

# AGARD

ADVISORY GROUP FOR AEROSPACE RESEARCH & DEVELOPMENT  
7 RUE ANGELLE 92200 NEUILLY SUR SEINE FRANCE

AGARD CONFERENCE PROCEEDINGS 543

## Multiple Mechanism Propagation Paths (MMPPs): Their Characterisation and Influence on System Design

(Les Trajets de Propagation des Ondes  
à Mécanismes Multiples (MMPP):  
Caractères et Incidences sur  
la Conception des Systèmes)

DTIC  
ELECTE  
MAR 02 1995  
S G D

*Papers presented at the Electromagnetic Wave Propagation Panel Symposium, held in  
Rotterdam, The Netherlands, 4th-7th October 1993.*



NORTH ATLANTIC TREATY ORGANIZATION

DISTRIBUTION STATEMENT A

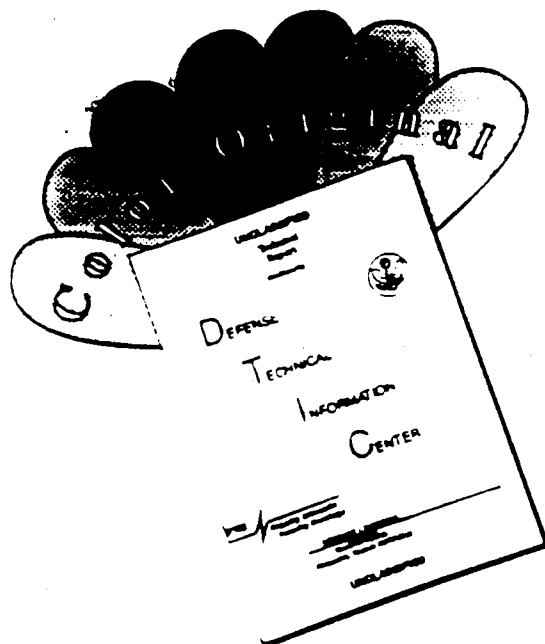
Approved for public release;  
Distribution Unlimited

19950227 028

Published July 1994

*Distribution and Availability on Back Cover*

# DISCLAIMER NOTICE



THIS DOCUMENT IS BEST QUALITY AVAILABLE. THE COPY FURNISHED TO DTIC CONTAINED A SIGNIFICANT NUMBER OF COLOR PAGES WHICH DO NOT REPRODUCE LEGIBLY ON BLACK AND WHITE MICROFICHE.

# AGARD

ADVISORY GROUP FOR AEROSPACE RESEARCH & DEVELOPMENT

7 RUE ANCELLE 92200 NEUILLY SUR SEINE FRANCE

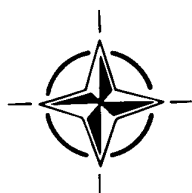
## AGARD CONFERENCE PROCEEDINGS 543

### Multiple Mechanism Propagation Paths (MMPPs): Their Characterisation and Influence on System Design

(Les Trajets de Propagation des Ondes  
à Mécanismes Multiples (MMPP):  
Caractères et Incidences sur  
la Conception des Systèmes)

Accession For	
NTIS	CRA&I <input checked="" type="checkbox"/>
DTIC	TAB <input type="checkbox"/>
Unannounced <input type="checkbox"/>	
Justification _____	
By _____	
Distribution / _____	
Availability Codes	
Dist	Avail and / or Special
A-1	

Papers presented at the Electromagnetic Wave Propagation Panel Symposium,  
held in Rotterdam, The Netherlands, 4th-7th October 1993.



North Atlantic Treaty Organization  
*Organisation du Traité de l'Atlantique Nord*

# The Mission of AGARD

According to its Charter, the mission of AGARD is to bring together the leading personalities of the NATO nations in the fields of science and technology relating to aerospace for the following purposes:

- Recommending effective ways for the member nations to use their research and development capabilities for the common benefit of the NATO community;
- Providing scientific and technical advice and assistance to the Military Committee in the field of aerospace research and development (with particular regard to its military application);
- Continuously stimulating advances in the aerospace sciences relevant to strengthening the common defence posture;
- Improving the co-operation among member nations in aerospace research and development;
- Exchange of scientific and technical information;
- Providing assistance to member nations for the purpose of increasing their scientific and technical potential;
- Rendering scientific and technical assistance, as requested, to other NATO bodies and to member nations in connection with research and development problems in the aerospace field.

The highest authority within AGARD is the National Delegates Board consisting of officially appointed senior representatives from each member nation. The mission of AGARD is carried out through the Panels which are composed of experts appointed by the National Delegates, the Consultant and Exchange Programme and the Aerospace Applications Studies Programme. The results of AGARD work are reported to the member nations and the NATO Authorities through the AGARD series of publications of which this is one.

Participation in AGARD activities is by invitation only and is normally limited to citizens of the NATO nations.

The content of this publication has been reproduced directly from material supplied by AGARD or the authors.

Published July 1994

Copyright © AGARD 1994  
All Rights Reserved

ISBN 92-835-0750-9



*Printed by Specialised Printing Services Limited  
40 Chigwell Lane, Loughton, Essex IG10 3TZ*



## Theme

In many practical systems involving EM wave propagation, energy is transferred from transmitter to receiver via multiple propagation paths or mechanisms. This may enhance system performance by providing redundancy and improving the potential for diversity combining, or by improving the system LPI/AJ and survivability characteristics. Conversely, if a multiple mechanism propagation path (MMPP) is not recognised as such, a system design may be somewhat mismatched to the actual characteristics of the propagation path, and its full performance potential not realised.

There are numerous operational situations in which EM energy, whilst nominally being propagated via a specific primary mechanism, may also be transferred by alternative independent, or partially independent, mechanisms. These alternative mechanisms may have very different characteristics in terms of diurnal and seasonal variability, and may also exhibit very different delay, Doppler spread, time dispersion, range, etc. properties from those of the primary mechanism. Both primary and alternative mechanisms should be taken into account in the design and operation of systems, otherwise the full performance potential may not be realised. A recognition of the true nature of a propagation path may stimulate new system design insights.

Past attempts to reach performance limits from a single propagation medium have not been successful or cost-effective. Systems based upon a combination of media can be a cost-effective method of providing the required communication connectivity even in highly stressed environments.

## Thème

Dans bon nombre de systèmes pratiques faisant appel à la propagation des ondes électromagnétiques, l'énergie est envoyée du transmetteur au récepteur par la voie de trajets ou de mécanismes de propagation multiples. Ceci peut améliorer les performances du système soit en assurant une certaine redondance et en permettant une meilleure diversité combinée, soit en améliorant le système LPI/AJ et les caractéristiques de survivabilité. Inversement, si un trajet de propagation à mécanismes multiples (MMPP) n'est pas reconnu comme tel, la conception d'un système donne risque d'être mal adaptée par rapport aux caractéristiques réelles du trajet de propagation, et il se pourra que ses performances potentielles ne soient pas exploitées au maximum.

Il existe de nombreuses situations opérationnelles où l'énergie électromagnétique, quoique, en principe, propagée par un mécanisme primaire spécifique, peut également être transférée par d'autres mécanismes, partiellement ou totalement indépendants. Ces mécanismes alternatifs peuvent avoir des caractéristiques très différentes sur le plan de la variabilité diurne et saisonnière, et peuvent également présenter des caractéristiques de retard, d'étalement Doppler, de dispersion temporelle, de portée etc. très différentes de celles des mécanismes primaires. Les mécanismes primaires, comme les mécanismes alternatifs, doivent être pris en compte lors de la conception et la mise en œuvre des systèmes, sinon le vrai potentiel des performances risque de ne pas être réalisé. L'appréciation de la vraie nature des trajets de propagation pourraient donner de nouveaux aperçus en ce qui concerne la conception des systèmes.

Les tentatives qui ont été faites dans le passé pour obtenir la limite des performances d'un seul milieu de propagation se sont avérées soit non-rentables soit inefficaces.

# Electromagnetic Wave Propagation Panel

**Chairman:** Dr J.H. Richter  
Naval Command, Control and Ocean  
Surveillance Center  
RDT&E Division, Code 54  
San Diego, CA 92152-5230  
United States

**Deputy Chairman:** Dr D.H. Höhn, apl. Prof.  
FGAN  
Forschungsinstitut für Optik  
Schloss Kressbach  
D-7400 Tübingen  
Germany

## TECHNICAL PROGRAMME COMMITTEE

### Co-Chairmen

Dr P.S. Cannon  
Radio Propagation Group  
Space & Communications Department  
D-Block  
Defence Research Agency  
Malvern, Worcs. WR14 3PS  
United Kingdom

Prof. M. Darnell  
Department of Electronic Engineering  
University of Hull  
Hull  
HU6 7RX  
United Kingdom

### Members

Dr E.P. Baars  
FGAN-FHP  
Neuenahrerstrasse 20  
D-5307 Wachtberg-Werthoven  
Germany

Dr P.A. Kossey  
Ionospheric Physics Division (GPI)  
Geophysics Directorate/Philips Lab.  
Hanscom AFB, MA 01731-5000  
United States

Mr L. Martin  
CNET/PAB/SHM  
38-40, rue du Général Leclerc  
92131 Issy les Moulineaux  
France

Dr G. Nourry  
Communications Research Center  
Radio Propagation Laboratory  
3701 Carling Avenue  
PO Box 11490, Station H  
Ottawa, Ontario, K2H 8S2  
Canada

Dr H. De Pedro  
Radio Branch  
Communications Division  
SHAPE Technical Center  
PO Box 174  
2501 CD The Hague  
The Netherlands

Dr J.H. Richter  
NCCOSC  
RDT&E Division, Code 54  
San Diego, CA 92152-5230  
United States

Prof. A. Van Der Vorst  
Hyperfrequencies UCL  
Bâtiment Maxwell  
B-1348 Louvain-la-Neuve  
Belgium

## PANEL EXECUTIVE

Lt-Col. R. Cariglia

**Mail from Europe:**  
AGARD-OTAN  
Attn: EPP Executive  
7, rue Ancelle  
F-92200 Neuilly-sur-Seine  
France

**Mail from USA and Canada:**  
AGARD-NATO  
Attn: EPP Executive  
PSC 116  
APO AE 09777

Tel: 33(1)47 38 57 68  
Telex: 610176 (France)  
Telefax: 33 (1) 47 38 57 99

# Contents

	Page
<b>Theme/Thème</b>	iii
<b>Electromagnetic Wave Propagation Panel</b>	iv
	Reference
<b>INTRODUCTION</b>	
Session Chairman: Prof. M. Darnell	
<b>Highly Survivable Communications: Complementary Media Packet Switched Networks</b> by D. Yavuz, F. Eken and N. Karavassilis	1
<b>ASPECTS OF SYSTEM DESIGN TO EXPLOIT MMPPs</b>	
Session Chairman: Dr D. Yavuz	
<b>QOS Driven Routing in Packet Switched Networks of Multiple Transmission Media</b> by C. Tamvaclis	2
<b>A MMPP Communications System for the Frequency Range 2-200MHz</b> by M. Darnell, P. Walker, N.G. Riley and G. Vongas	3
<b>Modelling and Simulation of HF/VHF MMPPs</b> by N.G. Riley, M. Darnell and G. Vongas	4
<b>Adaptive Error-Control Schemes for 2-200 MHz Multiple-Mechanism Propagation Paths</b> by B. Honary, M. Darnell and G. Vongas	5
<b>ASPECTS OF SYSTEM DESIGN TO EXPLOIT MMPPs (cont.)</b>	
Session Chairman: Dr P.A. Kossey	
<b>Passive Monitoring for Automated MMPP Communication Systems</b> by N.G. Riley	6
<b>The Relative Importance of Meteor Burst and other Long Distance Polar Cap Propagation Modes in the Low VHF Band</b> by P. S. Cannon, J. A. Weitzen, J. Ostergaard and J. E. Rasmussen	7
<b>Etude des Variations Rapides et Lentes de la Puissance Reçue lors de Liaisons VHF par Diffusion Troposphérique</b> par O. Ravard, F. Chevrier, L. Bertel et J. C. Le Jannic	8
<b>Les Problèmes de Codage dans les Canaux à Trajets Multiples</b> par C. Goutelard	9

**LOS SYSTEMS: PROPAGATION ANALYSIS  
AND MODELLING OF MMPP EFFECTS**

Session Chairman: Dr K.H. Craig

<b>Terrain and Refractivity Effects on Non-Optical Paths</b> by A.E. Barrios	<b>10</b>
<b>Méthodes d'Evaluation de l'Effet des Conduits à la Surface de la Mer</b> par M. Fournier	<b>11</b>
<b>Paper 12 withdrawn</b>	
<b>Propagation des Ondes Haute Fréquence en Milieu Urbain et en Tunnel Routier</b> par M. Liénard, P. Mariage, S. Baranowski et P. Degauque	<b>13</b>

**LOS SYSTEMS: PROPAGATION ANALYSIS AND MODELLING OF  
MMPP EFFECTS (cont'd)**

Session Chairman: Dr E.P. Baars

<b>A Wideband Propagation Simulator for High Speed Mobile Radio Communications</b> by P. Bussan, J.C. Le Jannic, G. El Zein and J. Citerne	<b>14</b>
<b>Combined Effects of Atmosphere and Terrain on UHF/Microwave Paths</b> by M.F. Levy	<b>15</b>
<b>Modelling Tropospheric Ducting Effects on Satellite-to-Ground Paths</b> by H.V. Hitney	<b>16</b>

**LOS SYSTEMS: PROPAGATION ANALYSIS AND MODELLING OF  
MMPP EFFECTS (cont'd)**

Session Chairman: Prof. A. Van der Vorst

<b>The Lorentz Reciprocity Theorem as a Consistency Test for Propagation Models</b> by R. A. Paulus	<b>17</b>
<b>Modelling of Microwave Propagation and Clutter in a Maritime Environment</b> by M. H. Vogel	<b>18</b>
<b>Simulation of the Impact of Atmospheric Turbulences on Millimeter-Wave Communications Systems</b> by H. Vasseur and D. Vanhoenacker	<b>19</b>

**LOS SYSTEMS: MEASUREMENT OF MMPP EFFECTS**

Session Chairman: Dr J.H. Richter

<b>Propagation Measurements on a Troposcatter Link in the Canadian High Arctic</b> by C. Bilodeau and K.S. McCormick	<b>20</b>
<b>Large Bistatic Angle Clutter Depolarization Study</b> by D.J. McLaughlin, E. Boltnew, J. Barclay, R.S. Raghavan and M.J. Sowa	<b>21</b>
<b>Time Behavior and Frequency Response of the Microwave Propagation Channel during Multipath Propagation</b> by D. Rana, M. Sylvain and A.R. Webster	<b>22</b>

**LOS SYSTEMS: MEASUREMENTS OF MMPP EFFECTS (cont'd)**

Session Chairman: Mr J. Rogge

<b>Development of a Fast Sampling System for Estimation of Impulse Responses of Mobile Radio Channels</b> by P. Melançon	23
<b>Line-of-Sight Multipath Propagation Measurements at 15 GHz over 500 MHz Bandwidth</b> by M. Touati, G. El Zein and J. Citerne	24
<b>Experimental Study of the Helicopter-Mobile Radioelectrical Channel and Possible Extension to the Satellite-Mobile Channel</b> by V. Blanchetière-Ciarletti, M. Sylvain and P. Lemenn	25
<b>Comparative Study of C- and KU-Band Propagation Mechanisms beyond the Horizon</b> by U.H.W. Lammers, R. A. Marr, R.K. Crane and M. Wennemyr	26

**LOS SYSTEMS: MITIGATION OF MMPP EFFECTS**

Session Chairman: Dr U. Lammers

<b>Angle Diversity on Digital Microwave Links: Antenna Design and Experimental Results</b> by D. Beaufort and L. P. Ligthart	27
<b>Mitigation of Effects of Multiple Path Nulls at Super-High Frequencies through Diversity and Networking</b> by N. Dave	28
<b>Multipath Impact on Ground-Based Global Positioning System Range Measurements: Aspects of Measurement, Modeling, and Mitigation</b> by G. J. Bishop and E. A. Holland	29
<b>Impact of Propagation Mechanisms on Global Navigation Satellite System Performance</b> by S. Riley, P. Daley and P. Raby	30

**PROPAGATION ASPECTS OF HF MMPPs**

Session Chairman: Prof. M. Darnell

<b>Mitigation of the Effects of F Layer Irregularities by using Multiple Paths</b> by J. Aarons	31
<b>Electromagnetic Wave Reflection from Irregular Plasma Layers</b> by K. Papadopoulos, R. Short and R. Shanny	32
<b>The Effects of Multihop HF Propagation on the Performance of OTH Backscatter Radars</b> by J. Buchau, G.S. Sales, S. Dandekar, B. Weijers and D. Reynolds	33
<b>Comportement Temporel et Spatial des Trajets Multiples dans les Propagations Ionosphériques en Incidence Oblique: Mesure Fractale des Perturbations</b> par C. Goutelard, J. Caratori et L. Barthes	34

**Paper 35 cancelled**

**SYSTEM ASPECTS OF HF MMPPs**

Chairman: Prof. C. Toker

- DAMSON - A System to Measure Multipath Dispersion, Doppler Spread and Doppler Shift on Multi-Mechanism Communications Channels** 36  
by N. C. Davies and P. S. Cannon

- Identification des Modes et Trajets de Propagation sur des Liaisons HF à l'Aide d'un Gonipolarimètre** 37  
par A. Edjeou, L. Bertel et V. Massot

**SYSTEM ASPECTS OF HF MMPPs (cont'd)**

Chairman: Dr P.S. Cannon

**Paper 38 cancelled**

- Geographical Diversity Combining to Exploit Multi-Mechanism Propagation** 39  
by M. Darnell and T.J. Speight

**Paper 40 withdrawn**

- Superresolution Direction Finding Algorithms for the Characterisation of Multi-Moded H.F. Signals** 41  
by M. A. Zatman and H.J. Strangeways

- Mesures d'Angles d'Élévation en HF par une Méthode Haute Résolution utilisant la Diversité de Polarisation** 42  
par C. Demeure, A. Ferréol et J-L. Rogier

- Measurements of Radar Backscatter from the Ocean Surface at 94 GHz as a Function of Wind Speed, Direction and the Modulation by the Ocean Waves during the SAXON-FPN Experiment** 43  
by H.-H. Fuchs

- Calibration du Sondeur à Rétrodiffusion de l'Ile Losquet en Présence de Multi-Trajets** 44  
par F. Gauthier, J.Y. Le Saout et R. Fleury

- List of Participants** LP

# HIGHLY SURVIVABLE COMMUNICATIONS: COMPLEMENTARY MEDIA PACKET SWITCHED NETWORKS

Dr. D. Yavuz  
Dr. F. Eken  
Dr. N. Karavassilis  
Communications Division  
SHAPE Technical Centre  
P.O. Box 174  
2501 CD The Hague  
The Netherlands

## ABSTRACT

The requirement for highly survivable communications (HSC) for essential command functions in military operations does not need any justification. The ability to communicate under extreme jamming levels and adverse propagation conditions, including high altitude nuclear events, is a very important requirement. There are also many natural disaster related requirements that also need such highly survivable communications.

The prevalent and in a sense classical, approach to provide highly assured connectivity can be summarized as follows: *Take a particular propagation medium and try to obtain the ultimate performance from it.* There are many examples of this philosophy some successful most not. Our, approach on the other hand, is to use **complementary multi-media** or **mixed-media** where communication links utilizing essentially commercial-off-the-shelf (COTS) equipment are integrated using packet radio (PR) techniques. There is also, in our view, an even more fundamental, recently discovered consideration why the expectation of continuous incremental refinement of a system using a given single media may not be achievable. This is derived from the theory of "**deterministic uncertainty**" or more popularly known as "**theory of CHAOS**", systems whose state space behaviour has fractal characteristics. We will elaborate on this novel argument.

**Complementary multi-media** approach has been the focus for all HSC communications activities at STC since 1982. The original STC studies and prototypes were in response to requirements of broadcasting (i.e. one-way transmission) information. A high frequency (HF)/meteor burst (MB) system was developed/prototyped/tested demonstrating the cost effectiveness of the approach. These results are reviewed.

More recently, in 1992 STC has completed the development/test of an Open Systems Interconnection (OSI) HF packet radio protocol as no such open or non-proprietary protocol exists. This protocol has been fully tested, documented and made available to all NATO nations/industries. These extensive results show that significant improvements in throughput of up to many times are obtained. A similar development for an OSI MB protocol has also been completed and combined with the HF protocol to obtain an OSI HF/MB link layer protocol with unique properties for HSC networks. Description of these protocols and the relevant results are presented.

The conclusion is that, HSC networks using standard COTS transceivers/modems with OSI PR protocols can provide highly survivable connectivity, by providing the most important ingredient of survivability, **media diversity**.

## 1. The Butterfly Effect

Early in the sixties, Edward Lorenz, a research meteorologist at MIT working on weather modelling with his graduate students, discovered what we now refer as

"**CHAOS**", unexpected or unpredictable behaviour of the solutions of sets of non-linear dynamical equations, more appropriately called "**deterministic randomness**". Later on, he also coined the term "**butterfly effect**", which can be expanded as for example "the flapping of the wings of a butterfly in Rio to-day, may result in a storm in the Central Asian steppes in two weeks time". What he had discovered was subsequently destined to be, in the opinion of at least the first author of this paper, probably the **most important development in the area of dynamical systems theory** this century.

Lorenz and his students at MIT were modelling meteorological phenomena using relatively simple sets of non-linear differential equations. The number of simultaneous equations they used ranged from 3 to 12, all deterministic, some non-linear, differential equations. Even with just three equations of the form

$$dx/dt = -\alpha x + \alpha y \quad dy/dt = \beta x - y - xz \quad dz/dt = -\gamma z + xy$$

relating  $x(t)$ ,  $y(t)$ ,  $z(t)$  with  $\alpha$ ,  $\beta$ ,  $\gamma$  constants, they were obtaining unexplainable result; predictions corresponding to a few days ahead were totally different with what should have been the "same" initial conditions. The initial conditions were rational numbers with 3,4 numbers after the decimal and were clearly of considerably higher resolution than for example local temperature measurements for meteorological reports. They had actually encountered the "**chaos**" effect or "**butterfly effect**"; the non-linear nature of the equations was such that extremely small changes in the initial conditions were resulting in totally different outputs. Subsequently, chaotic or fractal trajectories in state-space came to be associated with such effects in the solutions of coupled non-linear dynamical equations.

It is of historical significance that, more than ten years later, the National Meteorological Research Center in Maryland under directorship of Prof. von Neumann embarked on "Global Atmospheric Research Program" claiming to reach the goal of predicting weather/precipitation over all areas of north American continent, for periods up to one year ahead. This activity, employing many Ph.D.s and graduate mathematicians/engineers, at its peak, was using more than 100 000 simultaneous equations, mostly non-linear, to model the weather [Gleick 88]. Late in the eighties the implications of Lorenz's work almost two decades ago, was slowly appreciated and the goals scaled down. Now, we know that, weather predictions more than about a week ahead is essentially impossible under normal dynamical conditions that characterise atmospheric events. We can easily predict that next summer will be warmer than next winter at a particular location. This prediction is based on the linear model that states that the level of sun energy impinging in summer is order of magnitudes higher than in winter. However, the model for predicting a given weather parameter on specific day more than a few days ahead is generally highly non-linear and a meaningful prediction is not possible. The level of accuracy and density of input initial conditions required for such long term predictions is such that literally many billions of sensors of very high levels of accuracy and dynamic range

would be required; i.e., the inputs must be as close to real numbers as possible, not rational numbers with few significant digits. The term "butterfly effect" concisely but elegantly describes this "fact of life".

It is not difficult, at least conceptually, to extrapolate from the above to our field, propagation related predictions. We also deal with highly non-linear coupled dynamical relationships and the chaotic behaviour implicit in many such systems will limit the accuracies of possible predictions. Due to the relative novelty of the area, little specific work has been done in the area of actually identifying/analyzing chaotic behaviour in, say, prediction/modelling of signal propagation/reflection through/from the ionosphere. However, it does not take much imagination to anticipate that the associated non-linear processes must possess some chaotic characteristics and fractal state trajectories hitherto undiscovered, because we have not been looking for them. This, in turn implies that, when working with non-linear phenomena, refining the solutions without considering the chaotic events can lead to irrelevant or even misleading conclusions. The important summary message from the above can be summarized as, "if you are using non-linear models for any kind of prediction watch out - check your state-space for fractal behaviour!"

We will now proceed onto practical application aspects of basing HSC on MM systems.

## 2. Cost - Performance Trade-off Aspects

In the preceding section we have outlined a fundamental theoretical limitation that must be considered if attempts are made to refine a single media (propagation through which entails non-linear interactions) system towards its ultimate performance, to enable highly survivable communications.

There is also a more easily appreciated, pragmatic reason for basing HSC on complementary multi/mixed media (MM) systems that are essentially COTS. The cost vs performance curve of most products follows a saturation type curve, excluding the infrequent technological breakthrough type developments. Typically, for example, the "90% performance level" is obtained at reasonable cost but the additional "10% enhancement" can involve much additional expenditure [Figure 1] and in some cases even technical risks. In the context of HSC, it is far more cost-effective to combine two (or more) complementary COTS systems each providing say "90% performance" from their media, than to attempt to push the performance of one of the media towards its ultimate limits. The Regency Net program for highly survivable HF data communications under stressed conditions, is a good example of the attempt to obtain the ultimate performance from the HF media. The universal modem program exemplifies a satecom programme for HSC, again under similarly stressed conditions. The system examples in the following will describe STC activities, including on-air trial results, that demonstrate cost-effectiveness of HSC links/networks based multi/mixed media concepts.

## 3. Broadcast Mixed Radio Media System Example

In 1983 STC was tasked to develop a system for an "essential command function" which required a broadcast radio link of low capacity but extremely high reliability in terms of providing connectivity at all times to a few hundred locations spread out over ACE (Allied Command Europe). The messages would originate from a few locations in and around SHAPE HQ. In the following years a system concept based on complementary multi/mixed media, HF and Meteor Burst (MB) was developed, analyzed, a prototype built and extensively tested over various on-air links. The conclusions of this activity was that, HF and MB complement each other well and that highly reliable low capacity data links can be set up using the two media [TM-803]. Meteor Burst systems have unique properties of interest in military applications; they are inherently protected from jamming unless the

jammer is within radio line-of-sight of the receiver or is located close to the transmitter [Yavuz 91]. Long distance beyond LOS radio communications, SATCOM and HF both do not provide such inherent ECM protection but have other advantages/disadvantages. Though still considered esoteric, MB hardware can be described as essentially VHF radio transceivers with appropriate modulators and a PC. Like any media MB also has disadvantages; maximum link distances of about 2000 Km, daily/monthly/seasonal variations [Figure 2], random intermittent availability, low throughput. However the combination of HF/MB results in an extremely robust, cost effective systems. STC has operated various broadcast MB links for about five years documenting much useful information on this media [TN-470]. In fact, other media, SATCOM, terrestrial (Eg PTT) links can also be integrated into MM links/networks as required to provide even higher levels of survivability by increasing the media diversity options [TM-893, TN-366, TN-494]. The broadcast trials and related MM analysis, simulation and tests have provided the impetus for further work in the area of non-broadcast packet radio (PR) systems which will now be described.

## 4. Open/Non-proprietary Packet Radio Protocols

The MM work at STC originated with broadcast requirements, but it was clear right from the outset that open packet protocols were the key for the integration of different media for more general MM HSC requirements. Unfortunately HF data communications at higher than conventional teletype rates, is dominated by proprietary store and forward type protocols. Except through the use of AX.25 terminal node controllers (TNC) built for the Ham Radio community, there is essentially no possibility for setting up HF data/message links using equipment from different sources at the two ends. This is clearly an unacceptable state of affairs and STC initiated an open HF PR protocol development activity in 1989. In 1992 the full description of an OSI data link protocol for HF packet radio was published after extensive analysis, laboratory simulator tests and on-the-air evaluations [TN-492, TN-506, TN-507, TM-930]. In parallel a similar activity for an open MB protocol and an integrating activity to combine the two protocols to obtain a MM (HF/MB) protocol was pursued and completed. We are now in a position to establish HF, MB, and HF/MB data links using open protocols that are OSI both in letter and spirit. The HF protocol software has already been provided to many companies and to various NATO national organizations and can be requested from STC.

Security aspects of PR links and particularly networks is an active area of development. The data portions of the packets or frames can be protected to any level of security desired through various encryption algorithms. The protection of the control portions of the packets/frames (preambles, synchronisation flags, address fields, control fields, etc.) is complicated by the conflicting requirements of inherent flexibility expected of PR networks and the complexities of key management. The most significant threat against PR networks is the denial of service (DOS) attacks which could for example retransmit packets to saturate the links/networks so that they can not be used. Although DOS attack does not provide any information to the attacker if the data is properly protected, it can reduce significantly the throughput and give the attacker the satisfaction of having disrupted communications. DOS attack can be prevented by time + key protection of the control portions of the packets/frames using, for example the DES algorithm chips (or software with fast processors) as for example explained in TN-803. Another form of vulnerability that is sometimes considered is traffic flow security which entails the attacker attempting to gain useful information from the changes in the rate of flow of packets/frames. This can be readily circumvented by arrangements for dummy traffic when such threats are considered likely. Detailed exposition and analysis of the security of PR networks is beyond our scope and the above discussion is intended to give only a very brief overview.



#### 4.1 STC OSI Data Link Protocol for HF Packet Radio (HF - SDLP)

Due to changing requirements and the availability of high-speed modems utilizing adaptivity and excision, HF communications is destined to play an increasingly significant role in future military communication systems. Both reliability of data communications and available throughput over HF has improved significantly over the last decade with the advent of high-speed single tone modems employing sophisticated signal processing schemes for adaptive equalization and interference excision. Little has been available in terms of an OSI Data Link protocol to utilize the high-speed single-tone modems for packet communications over HF and to support internetworking with the Connectionless Network Protocol (CLNP).

STC data link-layer protocol (SDLP) provides robust and efficient packet communications over HF channels using standard multi-rate single-tone HF modems. The protocol conforms with the OSI description of a connection-oriented link layer service and incorporates features specifically designed for the HF environment [TM-930].

This protocol will be used for the transatlantic HF sub-network (STC-Canada) of the Communications Systems Network Interoperability (CSNI) multinational project (and possibly other HF subnetworks). The CSNI project will also demonstrate packet radio (PR) interoperability with satellite links and other tactical and commercial networks.

The HF OSI Data Link protocol developed at STC provides both connection-oriented (CO) and connectionless (CL) Data Link Services. The protocol supports multiple Data Link users (up to 20 in the present implementation) simultaneously over a single radio channel.

Both half-duplex and full-duplex HF modem operation can be supported by SDLP. The protocol is intended for point-to-point use and does not incorporate any frequency management or Automatic Link Establishment (ALE) functions. The protocol design offers the flexibility to implement these functions according to the specific requirements of the user.

An important form of adaptivity incorporated into the protocol (in addition to a selective automatic repeat request (ARQ) mechanism) is adaptive control of the modem speed. Extensive testing [TN-506] has shown that the throughput achievable using this simple adaptive mechanism and a judiciously chosen but fixed link-layer frame length is very nearly as great as that which can be achieved when both the modem speed and frame size are made adaptive. A second major feature of the protocol is the incorporation of a mechanism that reduces the frequency of collisions when used with half-duplex radio equipment. Additional features of the protocol include packet segmentation, use of low-overhead frame structures and a prioritized channel access scheme for networking applications.

Some of the important features of the HF SDLP are summarized below:

- Adaptive modem speed control.
- Selective automatic repeat request (ARQ).
- Collision avoidance and collision recovery mechanisms to reduce the probability and effects of collisions occurring over half-duplex links.
- Segmentation of long data packets.
- A single byte "connection reference number" rather than the full link address is carried by the link-layer frames to minimize the overhead.

- Prioritized channel access for connection-oriented Data Link Service.
- Robust connection management and data acknowledgement procedures.

The STC HF Data Link protocol has been implemented in software [TN-507] and tested extensively in the laboratory environment using ionospheric channel simulators. Simulator testing was used to establish the performance of the protocol using standardized channel conditions and enabled performance comparison with the performance of the AX.25. The protocol is particularly suitable for use with the new generation of adaptively equalised, single tone HF modems (NATO STANAG 4285, US MIL-STD-110A) and the simulation/trial results presented below are with such modems.

Half-duplex performance of the STC Data Link Protocol was measured using a modem interleaving of 0.6 sec. over a channel with 2 path, 2 ms delay spread and 2 Hz fading rate. Rockwell Collins MDM 2001 HF modems were used for the tests. The half-duplex performance of the protocol is shown in Figure 3. In Figure 3, in addition to the performance of the STC protocol, performance of the AX.25 protocol is also plotted. The AX.25 half-duplex performance was measured using the same (MDM 2001) modems over the same channel conditions. Since AX.25 has no speed adaptation feature the performance was measured at two different modem speeds, 1200 and 2400 bps. The performance of the STC protocol is superior to the AX.25 across the full SNR range. Note that even at a high SNR there is significant difference in performance between the two protocols. This is due to the fact that AX.25 can transmit a maximum of 8 data frames at a time, whereas the STC protocol can transmit 30 frames consecutively.

Full-duplex performance of the STC protocol was measured using two-way data transfer. The full-duplex mode of operation of the MDM 2001 modem was used with 0.6 sec. interleaving. The results are shown in Figure 4 for the same channel conditions indicated previously. The two curves plotted in Figure 4 indicate the throughput measured in each direction simultaneously.

The STC HF Data Link Protocol was tested on-the-air using a link between STC and the remote site in Staelduinen. The Staelduinen site is located at a distance of 25 km from STC. The tests on this link were done in daytime hours at a frequency of 6.98 Mhz. Past experience and observations made during the trials indicated that, at the frequency used during these tests, propagation was solely via sky-wave. No attempt was made to change the frequency in order to optimize the performance. During the test period, this frequency supported sky-wave communications on the test link starting around 9:00 am. The sky-wave link terminated shortly after the sun set, around 5:30 pm.

The on-the-air tests were carried out in the half-duplex mode. The averaging period for the throughput measurements was 30 min. The tests were conducted over a time period covering December 1992 and February 1993. Throughput measurements were made in half hour slots beginning at 9:30 am and ending at 5:00 pm.

The one-way throughput measurements recorded in the half hour slots during the test period were averaged for each time slot and shown in Figure 5. The number of measurements made on each half hour slot during the test period are also displayed in Figure 5. As indicated in Figure 5, the throughput averaged over the test period was relatively low at 9:30 am, due to weak propagation, but then increased to 1400 bps at 10:00 am. Between 10:00 am and 4:00 pm the average throughput fluctuated between 1200 bps and 1600 bps. After 4:00 pm, the average throughput gradually decreased due to the combination of interference and worsening propagation conditions.

The significance of the results shown in Figure 5 is that even without frequency management a high average throughput (above 1200 bps) could be sustained over a continuous 6 hour daytime period. There were observed instances of interference and weakening of propagation during the test period. The remedy for such impairments is of course frequency management, which is considered as a necessary component of a complete system design.

Some on-the-air test data was also obtained on a link between STC and Latina, Italy (approximately 1400 km). The HF OSI Data Link protocol was tested on this link on a daytime frequency of 14.69 Mhz. Throughput measured over 30 minute periods was recorded during different times of the day. The measurements covered a period of four days, 21,23,24 and 25 June 1993. The data obtained during these trials is shown in Figures 6 and 7. Similar to the Stael-duinen test results, the average throughput was high, with occasional periods of lower throughput due to interference or weak propagation. During the test period, a magnetic storm occurred at the time indicated in Figure 7.

Overall these results and others not discussed here have shown that sustainable average data rates in excess of 1 Kbps over difficult short links (high angle sky wave) and more typical long distance links, is readily obtained with simple frequency management. With more sophisticated frequency management, for example using automatic link establishment/maintenance (ALE/M) techniques, the protocol can be expected to provide throughput approaching 2 Kbps (excluding ALE/M overheads).

#### 4.2 STC OSI Data Link Protocol for Meteor Burst Communications (MB - SDLP)

This full-duplex protocol is a culmination of much analysis and experience over real links accumulated at STC over the past years. It is the result of a pragmatic systems level approach rather than an attempt to push the boundaries of capability of MBC systems to further heights through sophisticated signal processing approaches. The absolute requirement was that the protocol must be open in the OSI sense be easily integrated into the OSI network layer through CLNP as in the HF-SDLP case.

The link layer issue that is probably the most important in defining a MB protocol is the manner in which channel probing should be implemented. This process determines the availability of suitable trails between the transmitter and receiver so that data transmission can immediately start [Yavuz 91]. The two basic approaches are:

- (a) utilizing special short probing frames or packets,
- (b) using data frames themselves to probe the channel.

After extensive study of the related trade-offs, STC experimental results and the information available from other sources, it was concluded that there is a very small advantage in using special probing frames. However, this small advantage can be negated by the additional complexity and processing time requirements [TN-380]. The STC protocol, therefore, implements implicit probing with the data frames in the transmit queue. This permits efficient operation with standard PC processing through a robust, generic single frame type in both directions. The frame structure has sufficient flexibility to handle all necessary functions. More detailed information can be found in STC TN-547.

The other features that make this protocol efficient for use on MB links are:

- (1) Selective ARQ (automatic repeat request) is used as opposed to go-back-N. This ensures that all frames with good CRC check are utilized.

- (2) Acknowledgement (ACK) information about all received frames are piggy-backed on the data frames.
- (3) Quick reset procedure is provided to flush both transmit and receive queues.
- (4) Fast modem synchronization: user selectable number of preamble characters is transmitted before each frame.

A number of timers are also implemented to cater for the occurrence of small probability but possible events. Two most important are:

- (a) **NO\_ACK** timer: If the time since the last received ACK exceeds this timer duration (user selectable with default=15m) the transmit buffer is flushed and transmission stops. Next data frame transmitted has reset bit set.
- (b) **NO\_DATA\_RX** timer: The receiver keeps sending ACK frames for the duration of this timer setting (user selectable with default=15m) after it has received the last valid data frame. This ensures that the transmitter will receive the last ACK. For non-bursty channels this timer can be set to a few seconds.

Like the HF protocol described above, this MBC protocol can also run stand-alone, accepting data from a keyboard/PC or can be interfaced to a higher layer protocol to which it offers CL (connectionless) data link layer services. PDUs (Protocol Data Units) given to the MBC link layer by the network layer are buffered, segmented if necessary and transmitted. At the receive end converse is performed and the PDUs are reassembled and given to the Network layer in the same order they entered on the transmit side.

The protocol has been and is being used with 5 Kbps DBPSK modems built at STC for the broadcast MB trials but can be used with any modem with a standard synchronous RS 232 interface and Tx, Rx clocks.

Results of tests and on-air trials performed with this protocol indicate that throughput obtained under comparable conditions are at least comparable to published results with other (proprietary) protocols. Because STC work is focused on the use of MB as component of a multi/mixed media HSC system we will present the results as a component of our MM activities in the following section. These indicate that, both as a stand-alone MB data-link protocol and as a component of a mixed media service the results are excellent. The implementation is possible with standard hardware, the protocol is open and can be provided to any NATO entity to enable interoperable MB communications.

#### 4.3 STC Mixed Media Protocol - HF/MB (SMMP)

This protocol or mixed-media controller efficiently combines a MBC link and an HF link into a new "virtual link" which offers all the advantages of multi/mixed media operation. HF and MB are especially suited for integration as a MM unit because of excellent complementary nature of the two media and the similarity of the RF technology required for implementation.

Specifically:

- The MM link is more robust. If any of the sub-link media fail due to propagation, persistent interference and/or malfunction the other will automatically offer connectivity.

- Anti-jamming properties are greatly improved. A great deal more effort has to be expended to disrupt links over dissimilar media as compared to a single medium. Specifically, in the case of MBC, the jammer has to be located either radio LOS to the receiver or very close to the transmitter [Yavuz 91].
- With both media operating the throughput is the combination of throughput of both media or sub-links.
- One link can be used as electronic order wire (EOW) if there is a problem with one of the media. In this special case of HF/MB, the latter can provide frequency change information as the HF link deteriorates and/or initiate an ALE operation.

All the above advantages are gained through the use of standard, low-cost COTS hardware. Equivalent levels of robust connectivity through the use of a single medium would require the development/procurement of expensive customized systems.

If two media like HF and MB are to be combined efficiently, real time information about their performance must be available. Any algorithm based on a-priori statistical information would not be adequate due to the continuous and dynamic changes in the propagation characteristics and interference environments of these two media. The STC MM protocol (SMMP) monitors the ARQ process of the two (or more if required) individual media in order to determine the rate at which they are successfully delivering frames or packets. The SMMP keeps active updated copies of the frame queues of the individual media at all times. A frame is given to a link for transmission if its queue size is less than a predefined max size and if the link has not ordered SMMP to stop the flow of frames. If at any time the queue size reaches its maximum size the link does not receive any frames until its queue is reduced.

SMMP does not introduce any ARQ process of its own, it simply relies on the ARQs on the individual links. The protocol needs only 2 bytes of overhead per frame as shown in Figure 8. The frame sequence number is restricted to the range 0-255 and thus the maximum transmit window size is 128. The aperture of the Tx window (difference between the numbers of the first and last frames) can not be greater than 127.

An important feature of the protocol is the fact that the frames delivered to the individual links are "not forgotten". If a frame has been "stuck" in a link then SMMP automatically enters its "robust" mode. In this mode, all frames stuck in the slower medium are also given for transmission to the faster medium so that all possible resources are applied to push through the stuck frames. A frame is considered stuck if one of the following low-probability but possible events occur:

- A frame has been in the queue of a link for a duration greater than a prespecified value (default = 3m, but user selectable).
- Frames are available for transmission, at least one medium is free to accept frames but the aperture of the Tx window has reached its maximum value 127 because the first frame of the Tx window is stuck in the queue of the other medium.

After stuck frames are given to both media, eventually they are ACKed. As soon as this happens both media queues are flushed to avoid retransmissions of already ACKed frames and the SMMP returns to its normal mode, giving frames to the individual links according to the rate at

which they can successfully deliver them.

The transfer between the normal and the robust modes occurs automatically and in a way which is transparent to the higher layers. As seen by the network layer, the SMMP provides a CL link layer service. SMMP is totally responsible for the combination of the heterogeneous links as efficiently as possible and guarantee reliable delivery of the frames.

SMMP can also run stand-alone with messages generated locally by an operator or can be interfaced to a network layer, as with the other STC packet radio protocols. The interface between the network layer and all these protocols is the same. Figure 9 shows the position of the SMMP in the OSI stack. Figure 10 gives a schematic diagram of the STC MM test-bed. It should be mentioned that, although we are utilising separate standard PCs for the three link layer protocols, these could, in principle, all be combined in a single processor with an appropriate multitasking operating system. Messages to be transmitted by the MM system can be originated by users on a standard LAN interfaced to SMMP through a CLNP router as shown in Figure 10. The incremental costs associated with integrating given HF and MB systems is extremely low, the three processors, two for the link layer protocols and one for the MM controller and the software. STC developed software is available to all NATO national/commercial organisations at no cost for implementation in open systems to attain the goals of increased levels of interoperability at all levels.

Before the above solution was adopted, alternative ways of combining heterogeneous media at higher OSI levels were considered but were found to be unacceptable. For example, the use of CLNP in conjunction with an intelligent router (IR) could be considered. This IR would "direct the traffic" to the various links connected to it based on some derived "cost" information. The standard interface between Link layer and Network layer does not permit ACK information to be passed up to the Network layer. Therefore a transport protocol like TP4 would need to be used to ensure reliable delivery of data, initiate retransmissions, etc. Since the updating of the cost information could not be in real time, the router could, for example, redirect a stuck frame/packet to the same link in which it was originally stuck. Just as importantly, the overhead of the TP4 protocol is very large and if retransmissions at TP4 level occur frequently, the efficiency of the links/networks degrade rapidly. Combination of heterogeneous links at Network and Transport Layer is only acceptable for "well behaved" media (e.g. ISDN, fibre-optic, SATCOM, ... type links) whose performance can be predicted using near-real-time or non-real-time information. In such cases retransmissions only occur rarely and when they do, the router will have enough information not to direct the retransmitted frames to the link which was originally responsible for this retransmissions.

With highly dynamic, "non well behaved" links like HF or MB, the advantages of combination are achieved only if done at the link layer. The Mixed-Media controller cannot pretend that it is connected to some "generic" links and apply the same general rules to all of them. To be effective, the MM controller must take into account the peculiarities of the individual links. The only way this can be done is by making use of the low-level (link-level) ARQ information in real-time as is the case in our implementation and as is borne out by the trial results reported below.

Figures 11 and 12 present actual on-air test results over a 1400 Km link between STC and Latina (Italy). Figure 11 gives the average throughput in bps in 30 minute blocks of measurements, individually, over the two media, HF and MB utilising the protocols described in sections 4.1 and 4.2 above. No attempt was made to improve the night time HF performance through better frequency management, intentionally, so that the complementary nature of the two media could be clearly exemplified. As seen in Figure 12, combination of the two media through SMMP as described above,

ensures continuous connectivity with throughput ranging between highs of few Kbps (corresponding to sporadic-E on MB and/or good HF conditions) to lows around 50 bps when only low trail density MB is the only available option. Figure 11 exemplifies a non-typical period during which the MM link is forced to rely on only one media for an extensive period. Normally both links contribute to the throughput in a more dynamic way. With the enhancement of the HF link frequency management the contribution of the HF sub-link during the night-time hours (Figure 11) would be greatly improved. More detailed information on these tests is available in **TN-548**.

It should be noted that, SMMP also provides a simple but effective way to implement ALE/M. Since the MB component is essentially available at all times with sufficient capacity to exchange HF frequency management information, it is possible to implement an HF/MB system that would require absolutely no operator intervention. Such a system would be restricted to a maximum of about 2000 Kms because of the limitations of MBC (unless MB relaying is implemented). For example a simple implementation would be to use the MB component to initiate the search of a new frequency through the ALE module (US MIL-STD-188-110A is the only open COTS system available at this time) when certain throughput decrease conditions are met on the HF sub-link. We are in the process of implementing these and related concepts in the STC MM Test-Bed.

## 5. Conclusions

The momentous political developments of the past years has undoubtedly reduced threat levels but the requirement for highly survivable communications (HSC) under a wide range of possible scenarios can not be questioned. The ability to communicate under extreme jamming levels and adverse propagation conditions, including disruptions due to man made nuclear events, is still a very important requirement. There are also many natural disaster related requirements that also need such highly survivable communications.

This paper shows that the most cost effective way to provide highly survivable data/message communications is to utilise packet protocols over a combination of radio and terrestrial media, utilising standard, off-the-shelf hardware.

The approach that has generally been followed for highly survivable communications in the past, is to develop custom systems using a single propagation media and attempt to obtain the ultimate performance from that particular system at that point in the technological time-scale. Relatively new developments in the area of non-linear systems described loosely as "chaos theory" indicate that there are fundamental limits in predicting many natural phenomena, for example weather prediction. Extrapolation of such results to the propagation estimation area would indicate that similar limits exist. As a result, combination of proven, COTS systems to provide MM connectivity is the most effective approach to highly survivable communications.

At STC Complementary multi-media approach has been the focus for all HSC communications activities since 1982. Results of STC trials are presented, both for early broadcast links and more recent packet radio links. In the past few years STC has completed the development/test of an Open Systems Interconnection (OSI) HF, MB and MM (HF+MB) packet radio protocols. These protocols have been documented and made available to all NATO nations/industries. These protocols have been described and relevant results presented.

The overall conclusions is that, HSC networks using standard COTS transceivers/modems with OSI PR protocols can provide highly survivable connectivity, by providing the most important ingredients for survivability, media diversity, and internetworking.

## References

1. James Gleick, "CHAOS - Making a New Science", Heineman, London 1988.
2. STC TM-803 "System Level Description of ISB" Elvy, Nes, Rawles, Widdicks, (NC) 1986.
3. D. Yavuz, "Meteor Burst Communications", IEEE Communications Magazine, 1990.
4. STC TN-470 "STC-Latina MB Broadcast Link 1986-1991" Karavassilis, Sekreve, (NU) 1992.
5. STC TM-893 "Emergency Communications in Stressed environments" de Pedro, (NC) 1990
6. STC TN-366 "Multimedia Overlay for Special Purpose Communications in NATO" de Pedro, (NC) 1991
7. STC TN-494 "CLAMMS (Communications level Analysis of Mixed Media Systems) - STC mixed media simulation/analysis model" de Pedro, (NU) 1993
8. STC TN-492 "Connection-oriented OSI data link protocol for HF Packet Radio", Eken, Clark, (NU) 1992
9. STC TN-506 "Laboratory and Field Tests of the IIF OSI Data Link Protocol", Eken, Voordouw, (NU) 1992
10. STC TN-507 "IIF OSI Data Link Protocol Implementation Using TMS-320C30 DSP", Eken, Voordouw, (NU) 1992
11. STC TM-930 "IIF OSI Data Link Protocol", Eken, Clark, Voordouw, (NU) 1993 (Overall summary of TN 492, 506, 507)
12. TN-547 "STC OSI MBC Data Link Protocol" (MB-SDLP), Karavassilis (NU) 1993
13. TN-548, "STC OSI Mixed-media Protocol" (SMMP), Karavassilis (NU) 1993
14. NATO STANAG 4285
15. MIL STD-188-110A
16. MIL STD-188 141A US Mil. Std. for Automatic Link Establishment (ALE) Interoperability and Performance Standards for Medium and High Frequency Radio Equipment, Sept/1988, US Army ISEC

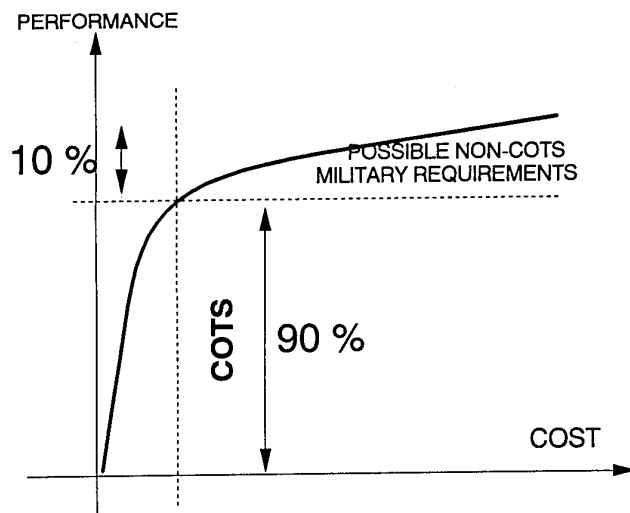


Figure 1. Cost-vs-Performance

### SEASONAL VARIATION OF AVERAGE, MORNING AND AFTERNOON VALUES OF METEOR INTERARRIVAL TIMES

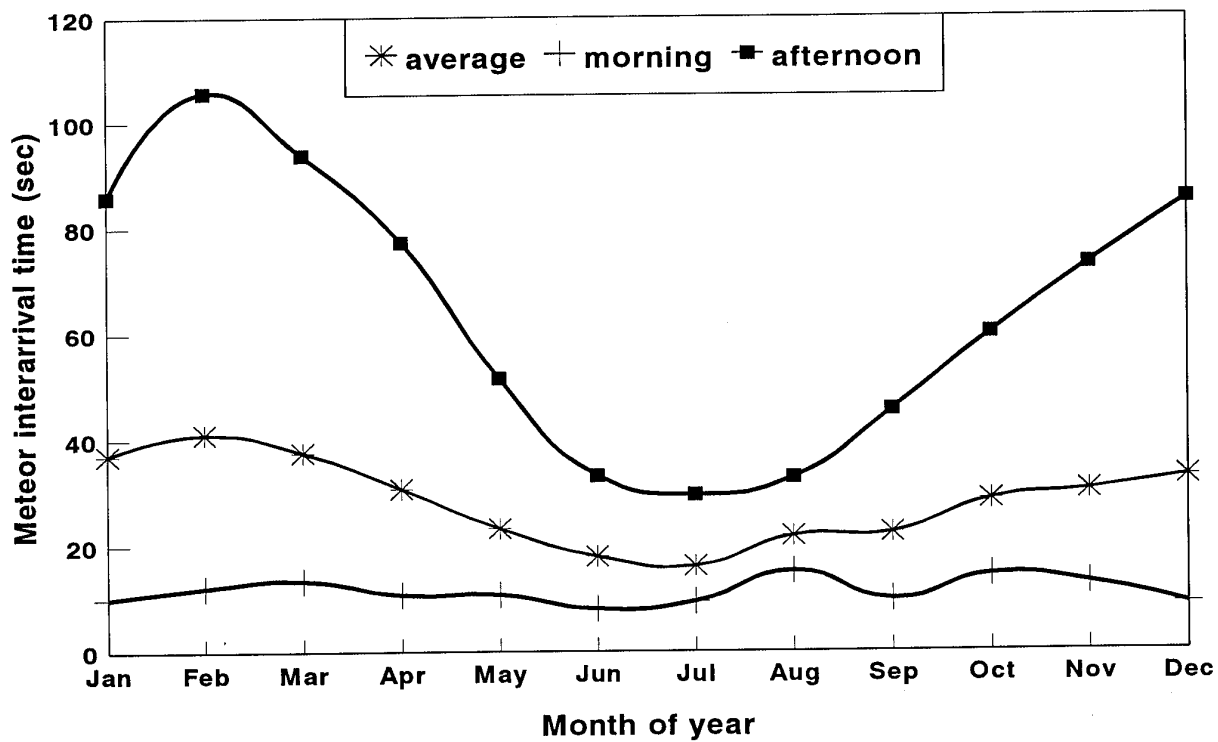


Figure 2. Seasonal variations of meteor interarrival times.

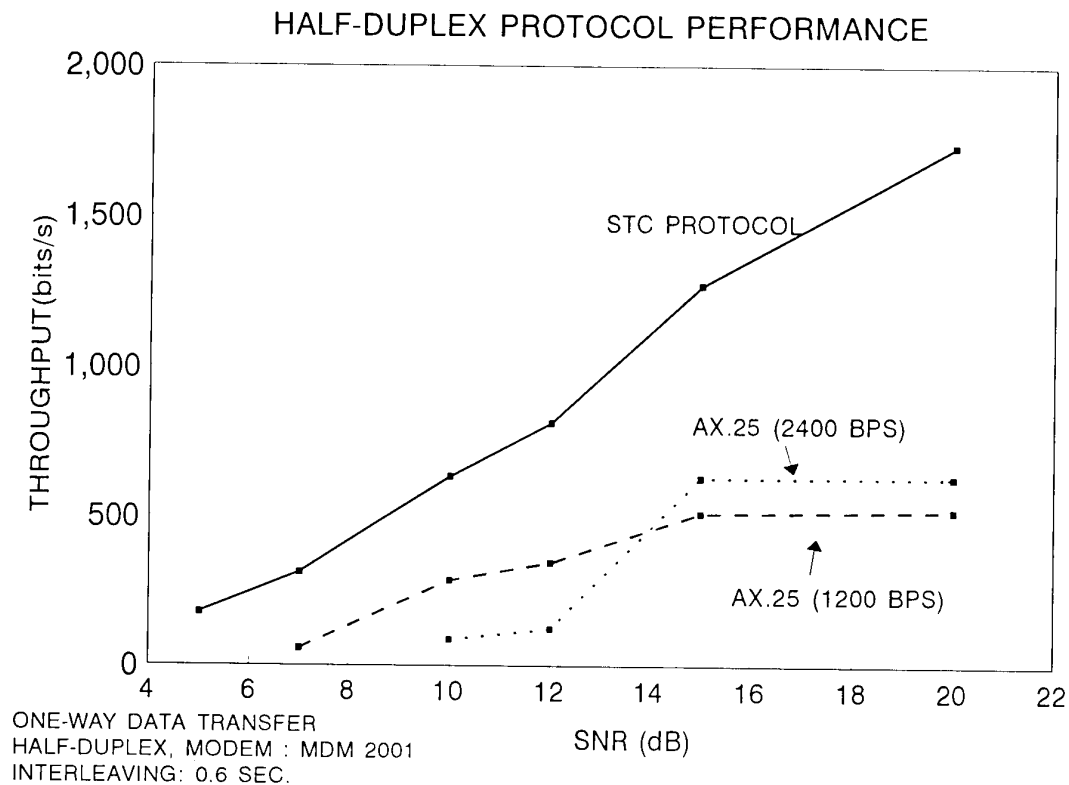


Figure 3. Simulator test results for half-duplex HF protocol.

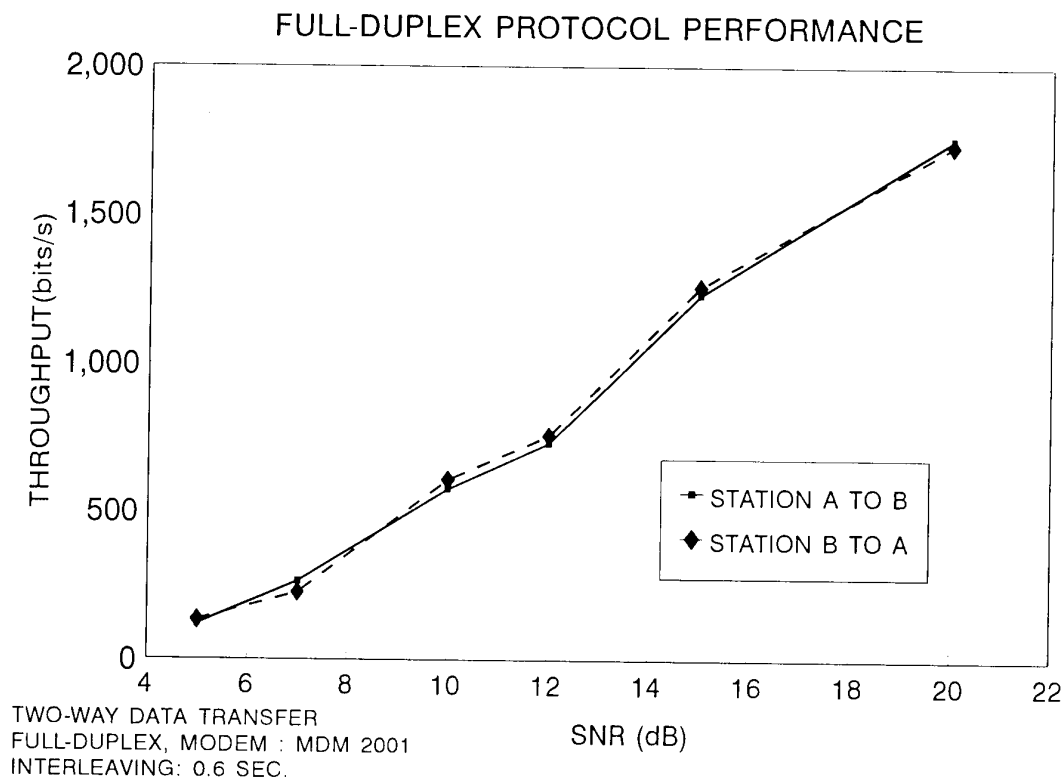


Figure 4. Simulator test results for half-duplex HF protocol.

# ON-THE-AIR AVERAGE THROUGHPUT STC-STAALDUIN, DEC 1992 - FEB 1993

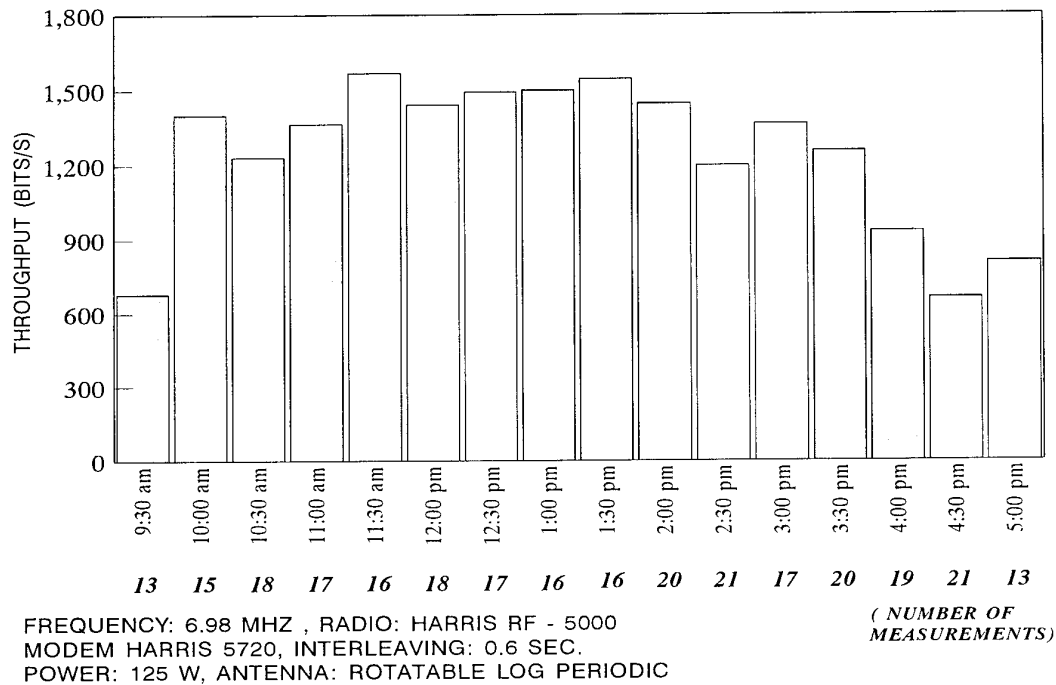


Figure 5. On-the-air HF test results, STC-Staelduinen.

# ON-THE-AIR THROUGHPUT STC-LATINA, 21, 23 JUNE 1993

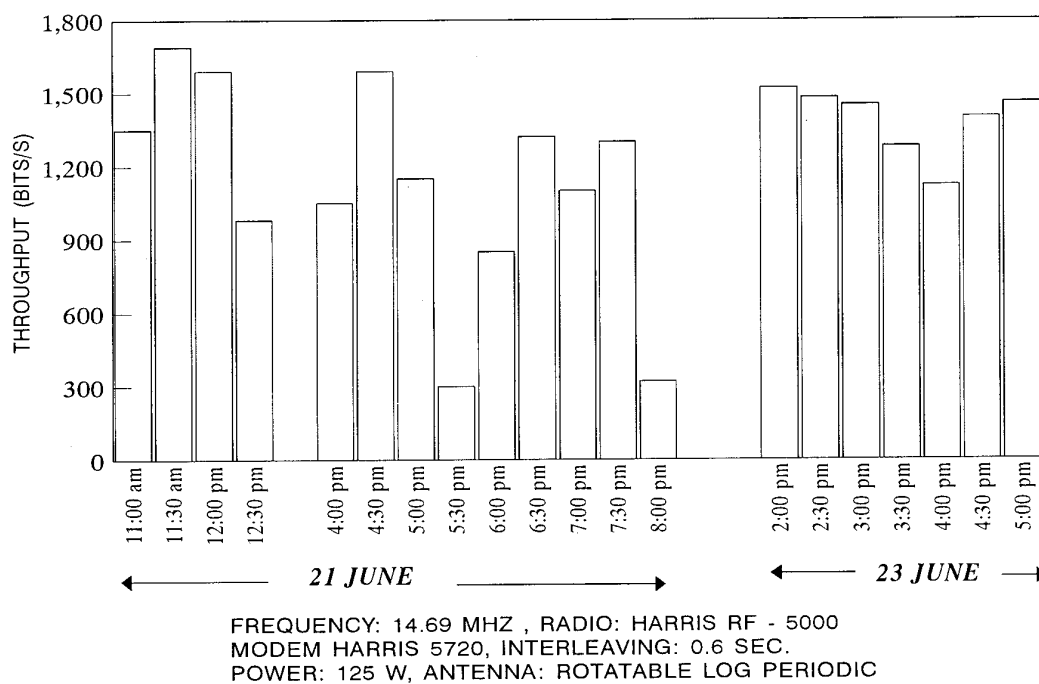
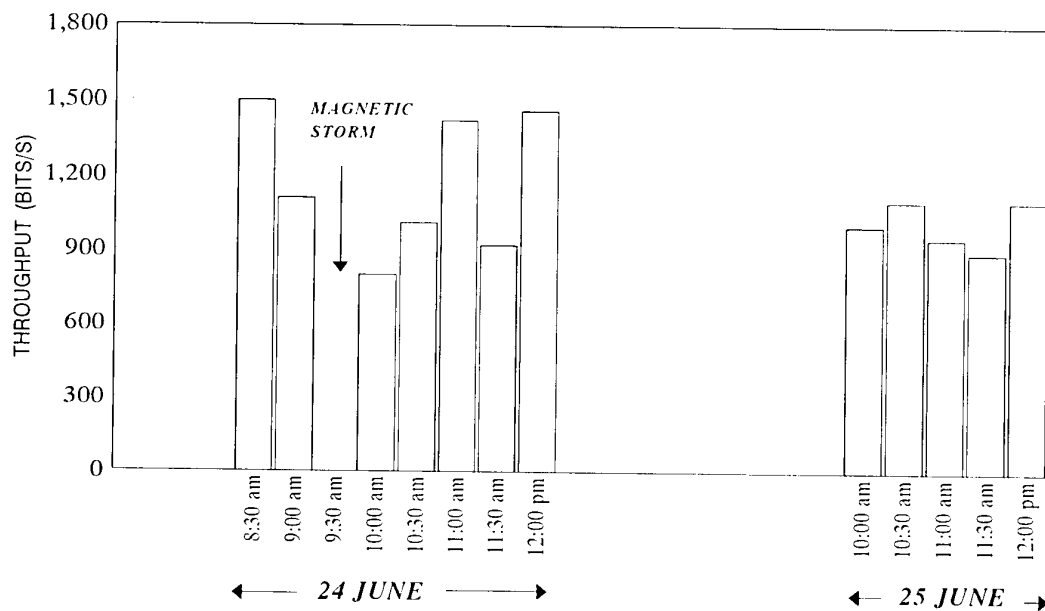


Figure 6. On-the-air HF test results, STC-Latina.

# ON-THE-AIR THROUGHPUT STC-LATINA, 24, 25 JUNE 1993



FREQUENCY: 14.69 MHZ , RADIO: HARRIS RF - 5000  
 MODEM HARRIS 5720, INTERLEAVING: 0.6 SEC.  
 POWER: 125 W, ANTENNA: ROTATABLE LOG PERIODIC

Figure 7. On-the-air HF test results, STC-Latina.

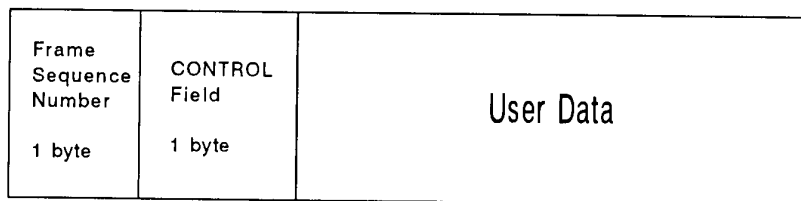


Figure 8. SMMP frame structure.



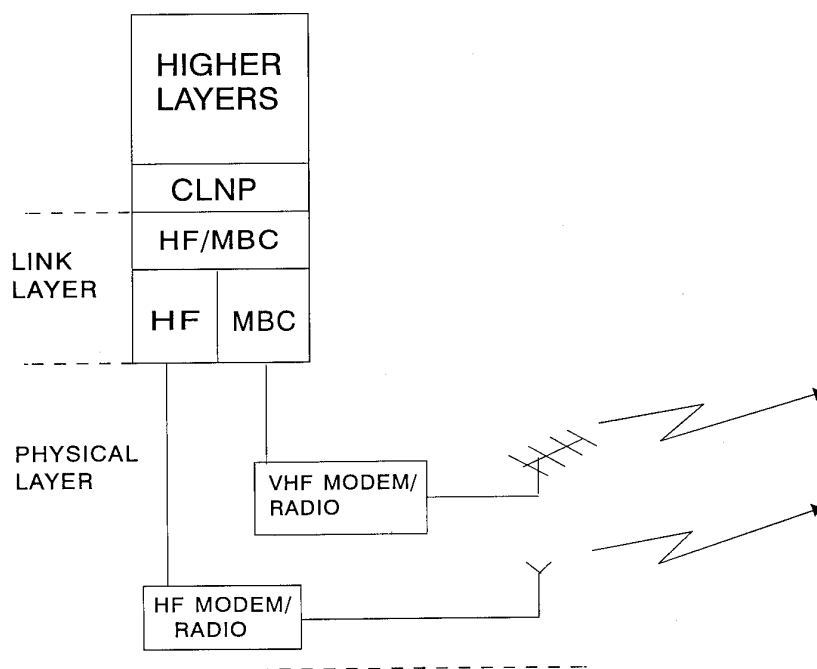


Figure 9. Relative position of SMMP sublayer in the OSI stack.

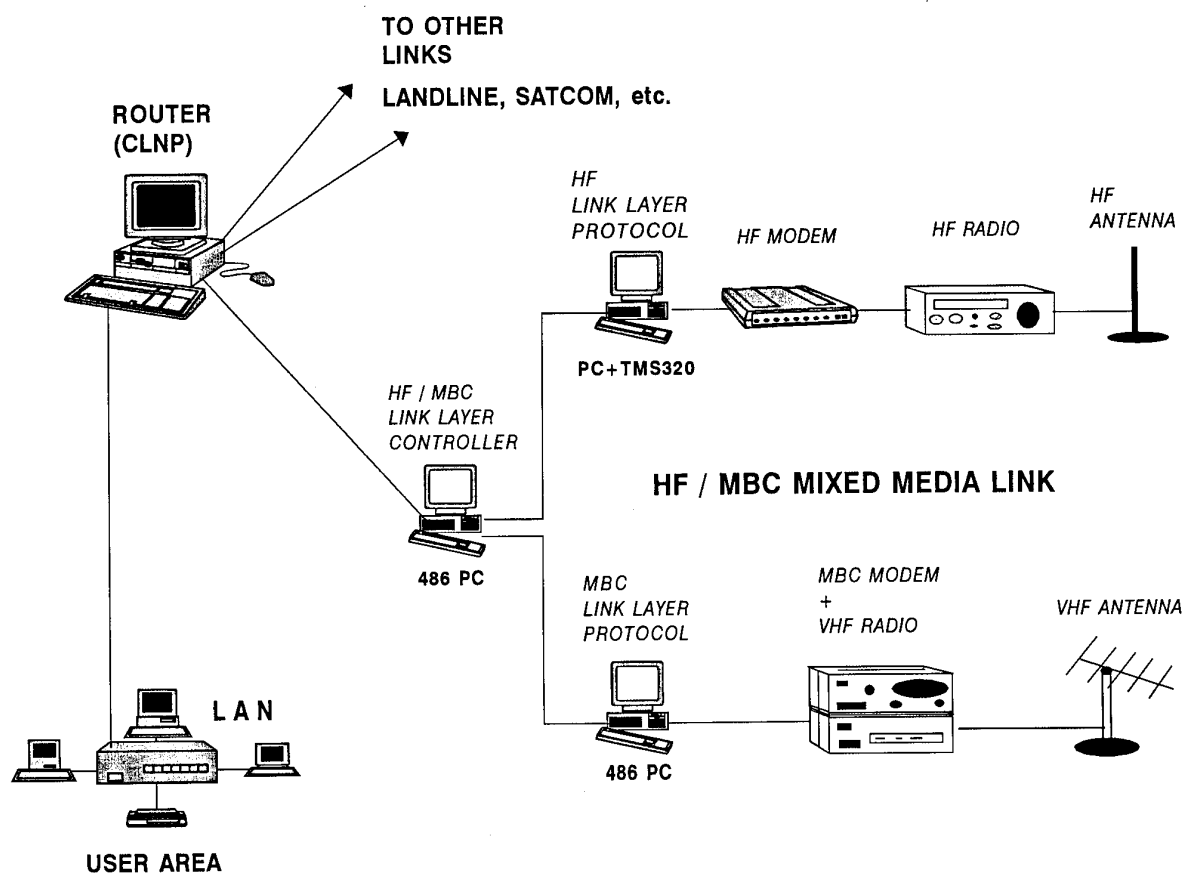


Figure 10. STC Multi/mixed Media Test Bed.

STAELDUIN-LATINA Mixed-Media Trials  
24/6/93 - 25/6/93

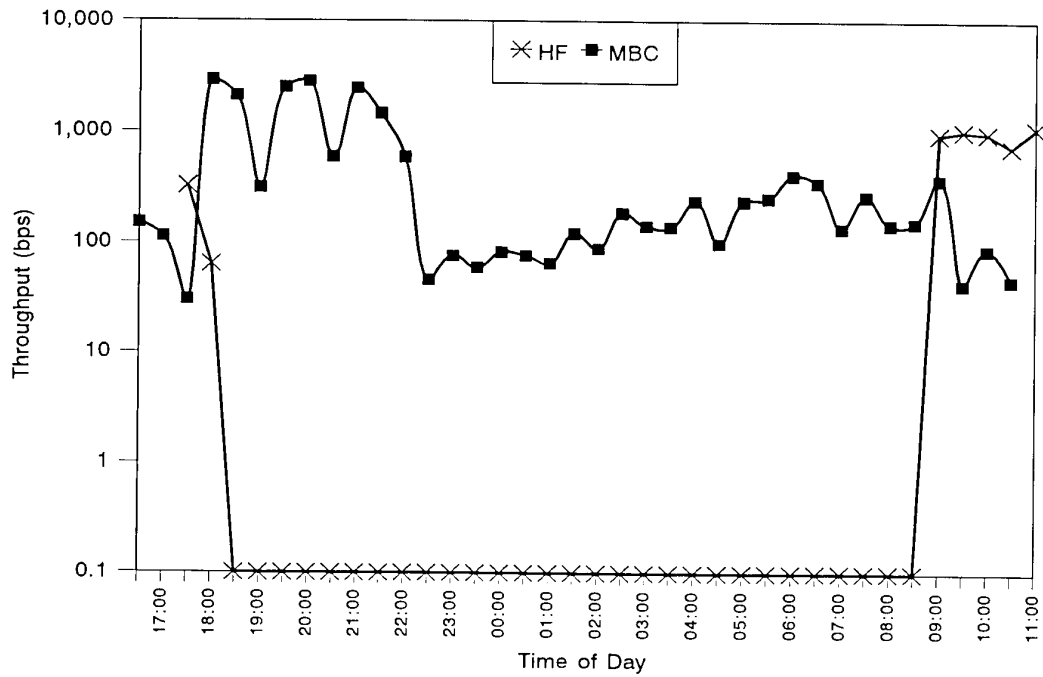


Figure 11. Staelduinen-Latina MM trial results.

STAELDUIN-LATINA Mixed-Media Trials  
24/6/93 - 25/6/93

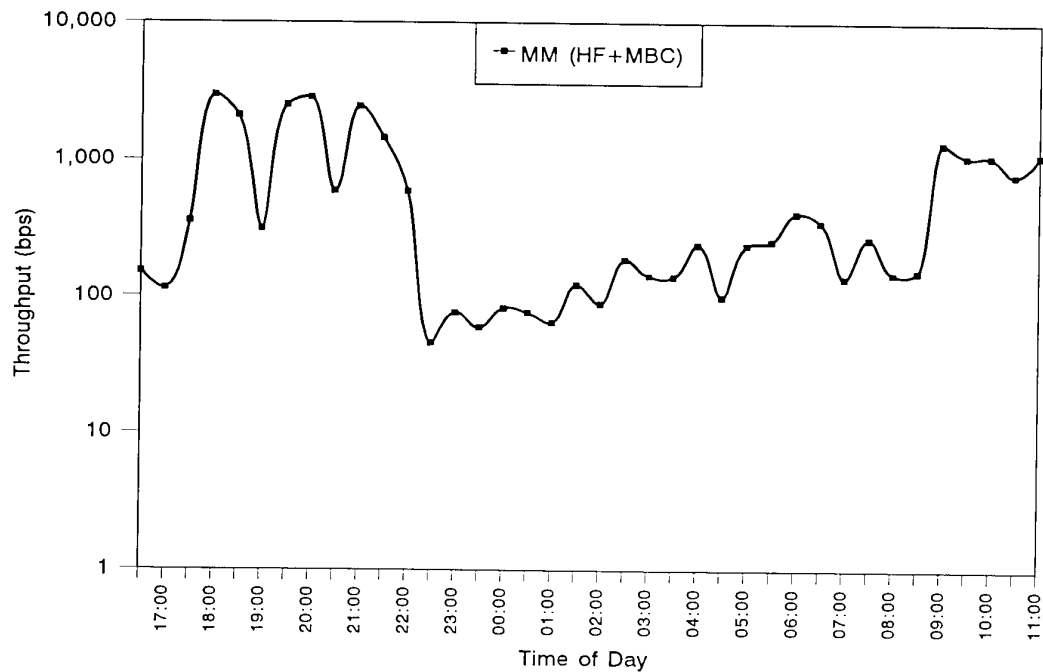


Figure 12. Staelduinen-Latina MM trial results.

## DISCUSSION

**Discussor's name :** P. Cannon

**Comment/Question :**

**Comment on Dr. Richter's Question:** For communications to mobiles, a typical satellite data rate is only 2.4 kbit/s and so such data rates mesh in well with HF and MB systems.

**Question 1:** In your HF OSI system the maximum data rate is 2400 bits/second. What overhead does your protocol impose and what is the consequential maximum information rate?

**Question 2:** There are plans to specify a robust waveform which will replace the MIL STD in certain circumstances. Will a significant change in the modem waveform require a radical rethink of your OSI protocol or is the latter readily adaptable.

**Author/Presenter's reply :**

Indeed, as Dr Cannon correctly states the capacities offered by truly mobile satcom terminals particularly under stressed (jamming, nuclear effects) conditions is of the order of a few kbps or even less.

**Question 1 :** The STC HF Data Link protocol (HF-SDLP) will provide slightly less than 2 kbps net with a US MIL-STD or NATO STA 4285 (at 2400 bps) modem over an ideal link. As I have shown, we have typically measured average net throughputs of 1 to 1.5 kbps over "good" HF links. We can say that the overhead of the protocol is about 20%; full details can be found in Ref 11 - STC TM-930.

**Question 2 :** We are closely following the so-called "HF-ECCM Waveform" activities within the NATO-TSGCE Sub-Group 11 and have made various contributions. The uncertainties and delays associated with these activities have convinced us that we should concentrate on the available COTS 4285 and MIL-STD modems which we feel have excellent performances and are now available at continuously decreasing costs from various manufacturers.

I do not think that our protocol would be directly applicable to what I know of the waveform being discussed. If and when such a waveform is available in COTS systems/modems with unambiguously demonstrated superior performance, I have no doubt that we can apply our knowledge from HF-SDLP development to the efficient use of such a protocol.

**Discussor's name :** J. H. Richter

**Comment/Question :**

1. Why are your multi-media confined to the HF-band and only slightly higher frequencies used for meteor-burst communications? What about VHF, UHF, microwave (including troposcatter and satellite) communications?

2. If higher data-rate channels are available, would they be used with the low data rates shown in your analyses?

**Author/Presenter's reply :**

1. and 2. I did not intentionally want to give the impression that HF and VHF/MB are the only possible media. Our work at STC is focussed on these plus satcom (SHF or UHF), but most of our on-air experience has been with HF and VHF/MB. It is of course, very difficult to combine media which have largely differing capacities. Our work is focussed on communication requirements that need modest/low capacity and an absolute guarantee of connectivity being available in highly stressed environments.

## QOS DRIVEN ROUTING IN PACKET SWITCHED NETWORKS OF MULTIPLE TRANSMISSION MEDIA

C. Tamvaclis  
Shape Technical Centre  
P.O. Box 174, The Hague  
The Netherlands 2501 CD

### SUMMARY

This paper discusses the application of Quality of Service (QoS) driven routing on packet-switched, heterogeneous networks. It is assumed that the network makes use of multiple transmission media of different types including narrowband radio based media such as those used in military tactical and emergency networks, e.g. ECCM SATCOM, HF radio etc.. A critical problem in the operation of such networks is the volatile performance of the transmission media, compounded by the fact that each transmission medium may respond differently to stress conditions. QoS driven routing provides an effective way to handle transmission media performance fluctuations and optimising the use of all the available communication resources. QoS driven routing means that packet routes are selected according to a global optimisation criterion that takes into account not only network connectivity, but also the application QoS requirements, and the currently available QoS from the network links. A routing architecture is described for implementing QoS driven routing on a connectionless internetwork of multiple transmission media. This architecture is based on the use of civilian networking standards and it is implementable using commercial off-the-shelf equipment.

### 1. INTRODUCTION

The interconnection of military strategic, tactical, and emergency networks has been given increasing attention in recent years as the military requirements shift towards the creation of multinational forces, increased mobility, and better inter-service coherence [Ref. 1]. Historically, most military networks have been built as transmission medium specific, custom-made systems, dedicated to particular services, commonly voice or messaging. The survivability and reliability of these networks have long been questioned [Ref. 2]. Their dependence on specific transmission media and their limited connectivity mean that adverse effects on the transmission medium, or any equipment failure may cause long disruptions in the service provided to the network users.

An internetwork is inherently more survivable than its constituent subnetworks, due to the increased link redundancy. Internetworking can compensate for poor transmission medium performance by routing traffic to other media. This capability is even more desirable in the military environment because transmission media respond differently to stress conditions. In order to exploit intelligently the capability to switch traffic from one medium to the other, there has to be a method of evaluating link performance dynamically. For optimum allocation of communication resources, the selection of transmission medium should also take into account the quality of service (QoS) requirements of the network users, as QoS requirements can vary considerably among different applications. For example it may be acceptable to switch

store-and-forward message traffic to a 300 baud link but that switching would be unacceptable for real-time voice.

This paper describes an internetworking scheme employing QoS driven routing that is well suited to the creation of heterogeneous networks with transmission media of volatile performance characteristics. The building blocks are independent subnetworks that can be transmission medium specific and which may have significantly differing capabilities. The objective is to provide a network data transfer service with the following characteristics :

- Multiple data applications with different quality of service requirements can be served concurrently,
- The quality of network service is optimised dynamically against variations in the traffic load, the subnetwork performance, and the network topology, seeking to tolerate disruptions with graceful degradation as opposed to sudden failure.

It is assumed that the constituent subnetworks offer a point-to-point data packet transfer service. Data packet switched modes of operation are becoming more widespread on military networks because of the expanding need for data services in support of the C<sup>2</sup> function, and the demand for local area network (LAN) to LAN interconnection [Ref. 1,2,5].

The proposed internetworking scheme is based on the use of existing civilian standards, and particularly the Open System Interconnection (OSI) Standards produced by the International Standards Organisation (ISO). Conformance to OSI standards is now official NATO policy [Ref. 3]. OSI provides the interoperability advantage of international open system standards and the cost advantage of using commercial off the self equipment [Ref. 4]. The proposed internetworking scheme does not require the subnetworks to be OSI conformant. Instead, it seeks to impose an OSI compliant internetworking structure on top of the subnetworks.

### 2. CONNECTIONLESS INTERNETWORKING

Fig. 1 depicts a heterogeneous network consisting of multiple subnetworks connected through standalone intermediate systems (IS). The purpose of the IS (also called routers or packet switches) is to perform the subnetwork switching function, i.e. to select the path through which the data will travel to reach their destination end-system (ES). This is known as the (inter)network routing function. In this scheme each subnetwork may have its own internal routing mechanism and it may be connection-oriented (for example X.25 or ISDN) or connectionless. The IS appear to each subnetwork as end systems. All traffic (data packets) coming from the network end-users is directed to the IS. The latter determine the optimum route, i.e. the subnetworks to be traversed, and forward the data along the selected route from one IS to the next until the packet reaches an IS which can communicate directly with the

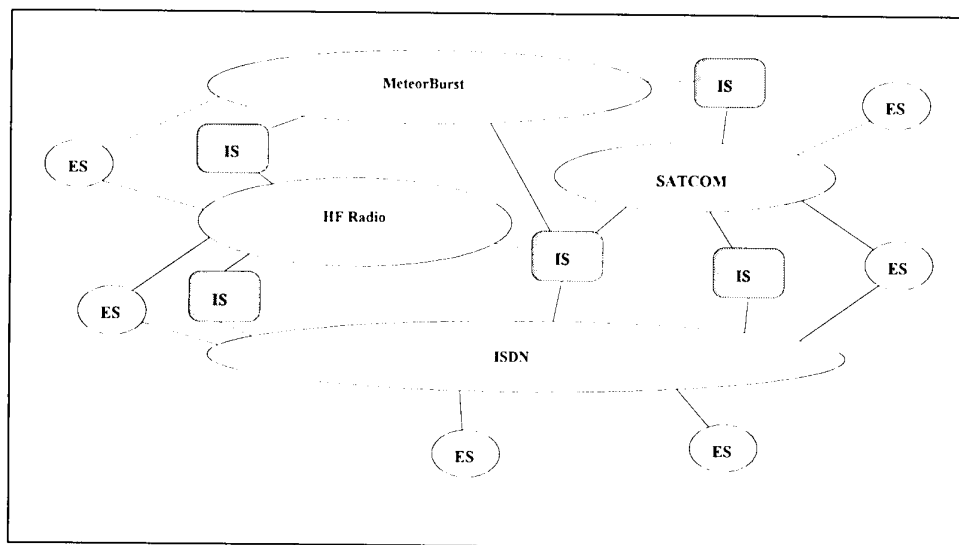


Fig. 1 A multi-transmission media internetwork

destination ES. The network operates in a connectionless mode meaning that each packet is routed independently, and that a new routing decision is made on each IS traversed by a packet.

The reason for adopting a connectionless routing function is that there are OSI routing information exchange standards available for this mode that are now widely supported in commercial routers [Ref. 5]. This is not the case for connection-oriented routing.

Fig. 2 depicts the OSI conformant protocol profile that applies to connectionless (inter)networks. An OSI conformant network must be able to support a wide range of applications. Each application may employ a separate application protocol profile (OSI layers 5-7). The transport service can be connection-oriented or connectionless to suit the requirements of different applications. The transport protocol ensures end-to-end communications reliability and implements flow control.

There are two applicable transport protocols, namely the Transport Protocol Class 4 (TP4) providing a connection oriented service, and the Connectionless Transport Protocol (CLTP) providing a connectionless transport service. Either transport protocol can run over the (subnetwork independent) Connectionless Network Layer Protocol (CLNP). The latter deals with the forwarding of data packets over the subnetworks from the source end-system to the destination. The network routing function operates in parallel with CLNP. There are two network layer routing protocols used, between end systems and intermediate systems (IS-9542), and between intermediate systems (IS-10589 and also IS-10747).

The subnetworks must provide a connectionless point-to-point packet transfer service. On subnetworks that do not provide such a service, it is derived through subnetwork specific access functions (SnAcc in Fig. 2). The SnAccs handle all subnetwork specific access protocols (for example HDLC/X.25). SnAcc functions are implemented externally to the subnetworks (router interfaces). The subnetworks themselves need not be OSI compliant. The data transfer service provided by the SnAcc functions does not have to be reliable, and it does not have to protect against packet duplication or loss of sequencing. The transport or higher protocols take care of

any data errors. Nevertheless a reliable subnet service is desirable because end-to-end retransmissions can be inefficient, especially in multihop networks [Ref. 8 and 9].

### 3. THE ROUTING FUNCTION

The selection of subnetworks for forwarding data is part of the network routing function. The objective of the routing function is to distribute efficiently the traffic load over the available connectivity and at the same time to ensure that the network users receive a reasonable quality of service.

The OSI (intradomain) routing mechanism for connectionless internetworks is defined in the standard IS-10589. This standard (also known as the IS-IS intradomain protocol) specifies a link state routing scheme [Ref. 6], where each IS maintains a routing information base (RIB) containing the addresses of all IS and also their adjacencies (links). The RIB maintains for each link a set of attributes including "cost" values in terms of a set of four metrics (discussed in Sec. 4.1). The least cost path (calculated as the sum of the costs of the links traversed) is considered as the best route for the particular metric. The RIB is kept up to date through the exchange (between the IS) of link state protocol data units (LSPs). This exchange is regulated through the routing information exchange protocol specified in IS-10589. Every change in the status and/or attributes of a link or IS causes an LSP to be generated and circulated through the network. Whenever an IS receives a new LSP (recognised by its sequence number and age) it recalculates its forwarding information base (FIB) which is the set of least cost paths between all ES to ES destination pairs. A separate FIB has to be kept for each routing metric supported by the IS.

The IS-10589 allows the hierarchical partition of the network into areas and domains as shown in Fig. 3. Partitioning is used to constrain the circulation of LSPs and limit the size of the RIBs and FIBs. The IS-10589 standard defines two levels of IS. Level 1 IS operate within an area. Level 2 IS provide the routing between the areas within a domain. Level 1 and 2 IS select routes on the basis of the link state mechanism described above. Communication with other routing domains occurs through specifically assigned Border IS (BIS). The BIS select routes according to rules defined by the routing

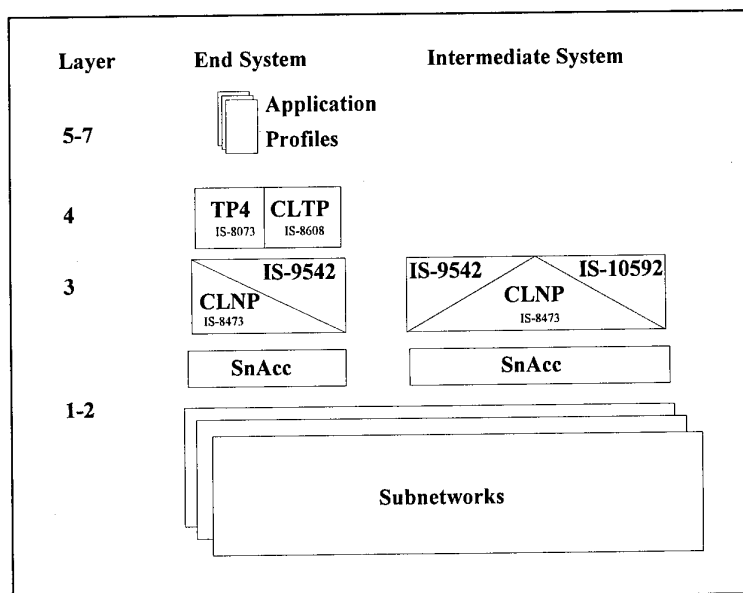


Fig. 2 OSI Protocol Profile for a connectionless internet

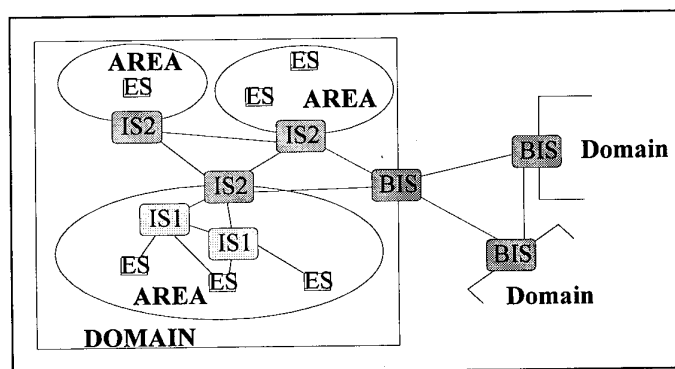


Fig. 3 Hierarchical Routing

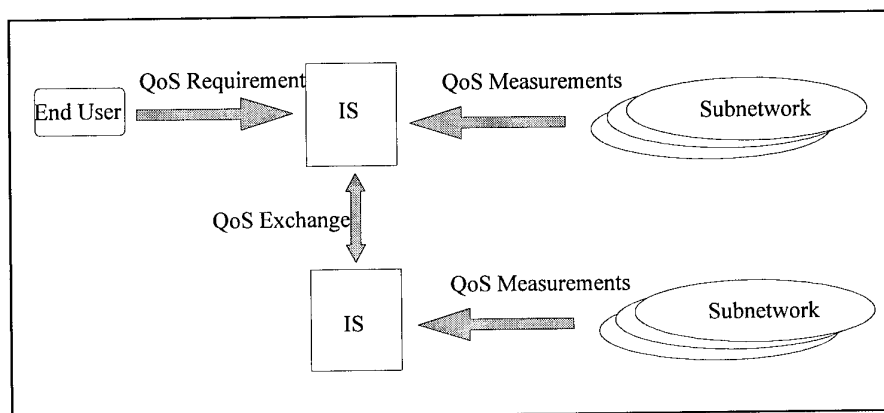


Fig. 4 Quality of Service driven routing

domain authorities (policy based routing [Ref. 6]). The standard IS-10589 defines the protocols exchanged between level 1 and between level 2 IS. There is a separate interdomain routing protocol

The IS-10589 internetworking scheme provides a routing mechanism which dynamically adapts to any changes in the connectivity of the network. Nodes (ES and IS) and subnetworks/links can be deployed or removed at any time and the

relevant information is automatically circulated through the appropriate IS and ES. A rapidly converging routing algorithm (link state) is used, which has been proved self-stabilising [Ref. 6]. The IS-10589 includes procedures for overcoming area partitioning in case of subnetwork failure or fragmentation. As for the bandwidth overheads, simulations on narrowband internetworks have shown that the TP4/CLNP protocol overhead is modest [Ref. 7-9]. The main source of data overheads is the CLNP header which can be 60 bytes

**Table 1**  
**CLNP Globally Unique QoS Field**

Bit	Usage
5	Routing decisions should favour sequencing over low transit delay
4	Congestion experienced
3	Routing decisions should favour low transit delay over low cost
2	Routing decisions should favour low residual error probability over low transit delay
1	Routing decisions should favour low residual error probability over low cost

long (per packet). It is possible however to reduce this overhead to 10 bytes through a header compression protocol [Ref. 11]. The routing information overheads are discussed further in Sec. 4.2.

QoS driven routing can be introduced into a IS-10589 conformant network by exploiting some of the standard's optional features. QoS driven routing requires that the route selection function takes into account the QoS offered by the subnetworks and the QoS requirement of the applications (see Fig. 4). With IS-10589 this can be achieved by calculating the link costs from the observed performance of the subnets and by using the QoS requirement of the applications to select the routing metric. For this scheme to work, the following requirements have to be met :

- the application QoS requirements must be signaled to the network service provider;
- the network data packets must carry an application QoS requirement label;
- the QoS being delivered by the subnetworks must be monitored ;
- the subnetwork QoS must be signaled the routing function.

The issues involved in QoS signalling within the protocol profile of Fig. 2 are considered in the following section.

#### 4. QOS SIGNALLING

Quality of Service is the measure by which the service-user and the service-provider judge the effectiveness of the service. The introduction of a consistent QoS framework in ISO OSI standards is a major unresolved issue [Ref. 10]. For the purposes of this discussion, it is sufficient to consider only those QoS parameters that relate to the characteristics of the network service. In this respect the commonly used QoS parameters are : minimum acceptable and target throughput, the maximum acceptable end-to-end delay, the maximum acceptable probability of message loss, the maximum acceptable probability of incorrect delivery, and the residual error probability. There may be separate QoS requirements per instance of communication (e.g. dynamic QoS allocation). Users may be assigned different priorities. Different priority rankings may imply distinct QoS entitlements.

Fig. 5 depicts the flow of QoS information over the protocol stack of Fig. 2 (obviously more than one IS may be involved

in any end-to-end communication). Two types of QoS flow can be distinguished:

##### a. Between remote systems

QoS information is exchanged among peer entities through communication protocols. These exchanges are subject to the constraints of the OSI protocols used.

##### b. Within each system

QoS information is exchanged between user and provider through service and management interfaces. These exchanges are beyond the scope of OSI standards.

In Fig. 5, type (a) flows may occur between peer application entities (using any of the layer 5-7 protocols), between peer transport entities, and between peer network entities (subject to CLNP and the routing protocols). There may also be QoS exchanges within the subnetworks. QoS exchanges need not be supported at all levels. For QoS driven routing, only network layer QoS exchanges are necessary, possibly complemented by either transport layer or management QoS exchanges (see Sec. 5). Additionally, QoS information must be supplied within each system to the network service provider (flow type b) per service request, because the network service is connectionless. There are two ways in which this can be achieved :

- through the layer service interfaces (application to transport to network), or
- through the management interface of the network or transport layer (there has to be a procedure by which the QoS requirement per service data unit is derived)

The limitations of QoS support in OSI protocol and service definitions are illustrated in Table 1 which lists the QoS provisions in the service and protocol specifications of each OSI layer in Fig. 2. It can be seen that there is no consistency in the QoS parameter definitions from layer to layer and even between the service definitions and the protocol definitions for the same layer. For example, the cost parameter appears on the network layer. No corresponding cost provision has been made in layers 4 and up.

#### 4.1 QoS exchanges in the network layer

The CLNP standard (IS-8473) allows for an (optional) QoS field in the protocol header. The standard defines a format for this field, called "globally unique", consisting of a single byte (see Table 1). It is also possible to use a source-address specific or a destination-address specific QoS field formats of variable length. Address-specific formats (may be up to 255 bytes long) are supposed to be defined by the routing/addressing domain authorities.

The CLNP standard does not specify any particular use for the QoS field (see Table 1), but the OSI intradomain routing protocol [(IS-10589) does have a use for it. There are up to four different routing metrics (link capacity, delay, cost, and error probability). The QoS field can be used to select the metric to be applied when calculating the "shortest" route. When a CLNP packet carries the "globally unique QoS" field, then only bits 1 to 3 of the QoS field are to be taken into account and the routing metric is selected as shown in Table 4. According to IS-10589, when an intradomain IS receives a data packet carrying no QoS field or having a QoS field of



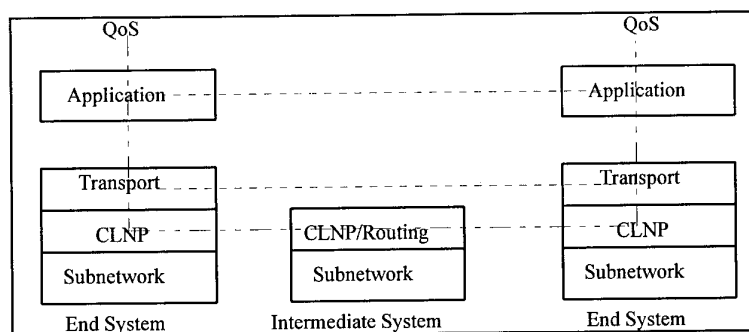


Fig. 5 QoS Information Flow

unknown format, it should apply the default metric (link capacity) for further routing of that packet.

**Table 3**  
**Router Metric Selection by QoS**  
(globally unique format)

Bit 1	Bit 2	Bit 3	Metric
0	0	0	cost
1	0	0	capacity
0	1	1	capacity
0	1	0	cost
0	0	1	delay
1	1	0	error
1	0	1	delay
1	1	1	error

#### 4.2 QoS driven transmission medium selection

IS-10589 requires the maintenance by the routing function of a dynamically changing link state RIB containing the current metrics for all known (e.g. advertised) subnets. Each IS advertises the costs per supported metric of all the subnets to which it is attached. These values may range from 1 to 63 (default is 20). The IS-10589 does not define any particular method for determining costs considering it an implementation issue. In practice, commercial OSI routers use preset subnet costs, usually configurable through their management interface.

As explained in Sec. 3, QoS driven routing can be introduced in a IS-10589 conformant network by dynamically adjusting the link costs on the basis of performance measurements collected from the subnets. Fig. 6 illustrates how QoS driven routing can be added to a commercial OSI router. A cost generation entity receives performance measurements and status reports extracted from the subnetwork access interface and/or the modem (if available). This entity calculates periodically or on an event-driven basis the costs to be assigned to the subnetwork per routing metric. The calculated cost is fed into the router RIB, and the IS to IS routing function circulates through an LSP the new value (if there is a change) to the other IS of the same level. Similar cost generation entities have to be attached to each router on the network. The cost generation algorithms (see Sec. 4.3) may differ per subnet but they must be consistently applied throughout the routing domain.

According to IS-10589 every change in a network link (cost or status) causes an LSP to be generated and propagated to all the IS of the same level and within the same area for level 1, or within the same domain for level 2. In QoS driven routing the link costs are recalculated periodically, consequently

there will be a regular routing traffic load imposed on the network. Furthermore, the routing function will need some finite amount of time to adapt to each change, i.e. to reach the state where all RIBs are synchronised. The periodic cost changes mean that the network will be going through periodic transient periods of suboptimal routing (the routing protocol provides safeguards against lockups such as eternal looping).

#### (a) The routing information traffic load

This issue is critical on low bandwidth subnetworks, such as HF radio and ECCM SATCOM. The routing information traffic consists primarily of LSPs. Each LSP needs to traverse each network link once<sup>1</sup> due to the flooding scheme used to propagate them through the area or domain. The size of an LSP is 27 bytes plus a variable part consisting of connectivity information (e.g. a list of applicable area addresses, adjacent neighbor addresses, and associated link costs) and authentication information. A typical LSP should therefore be up to 128 bytes long including the subnetwork data overheads. Consequently the average amount of routing information on each link will be of the order of Rate-of-QoS-Reports (RQR) kbits/sec, where

$$RQR = \frac{(\text{the number of IS})}{(\text{QoS measurement period, sec})}$$

For example an area of 10 IS with a QoS measurement period of 100 sec would have an average routing traffic load of the order of 100 bits per second, which is well within the capability of 2.4 Kbits/sec links. However, an area of 100 IS would need a QoS measurement period of 1000 sec to stay within the same limit.

#### (b) The routing function adaptation speed

The routing function completes its adaptation to a network link status/cost change when all the IS of the same level and within the same area/domain have received a copy of the corresponding LSP, and they have calculated the new FIB. The QoS measurement period must be long enough to allow the routing function to stabilise before a new change is circulated. In other words the transient period must be less than the QoS measurement period.

The period during which the routing function is in a transient state consists of:

- the update propagation time through the area or domain, and
- the recalculation time for the FIB (the list of least cost routes for each destination).

The update propagation time depends on the diameter of the area/domain and consists of propagation delay, transmission delay, and queueing delay. For 2.4 KBit/sec links the transmission delay would be 0.5 sec per hop. The propagation delay on SATCOM links would also be of the order of 0.5 sec per hop. The queueing delay is more difficult to quantify but it is likely to exceed by far the propagation and transmission

<sup>1</sup>Broadcast subnets are treated as a pseudonode and the LSP is multicasted. Thus on a broadcast subnet of N IS, two LSPs will be circulated instead of N-1 per cost change.

delay especially on narrowband military networks. The queuing delay depends on the type of interleaving and medium access used over the subnet as well as the overall traffic load. For example the universal NATO modem might add a delay of 5-6 sec because of the interleaving scheme used. Similar delays can be added by some slot based TDMA schemes used over SATCOM and HF [Ref. 9]. Hop delays on military narrowband networks may therefore reach 10 sec or more excluding queuing due to user traffic. In these cases LSP traffic should be allocated the highest priority to give it precedence over user data to keep the queuing time to a minimum.

The FIB calculation time is the time needed to recalculate the least cost paths for all potential destinations. This time becomes more significant in comparison with the update propagation time as the area or domain becomes larger. The FIB calculation time is proportional to the number (RQR) of updates/sec. In a 100 router domain with a 100 sec QoS update period, each router has to execute 1 FIB update per second. It has been found that a 386 CPU at 33 MHz can update the FIB (per metric) for a network of 100 IS (30 end systems per IS) in approximately 500 msec.

#### 4.3 Subnet Cost Generation

The IS-10589 standard allows for four possible routing metrics, of which only one (the default) is mandatory. The four metrics are defined in the ISO standard as follows :

a. Bandwidth (default) : Measure of the subnetwork capacity. It is preferable to define this metric as a measure of the remaining free capacity of the subnet. Queue length can be used as traffic load indicator. The counts of packets delivered, dropped, and retransmitted, indicate the percentage of error-free traffic.

b. Delay : Measure of subnetwork service transit delay from Service Access Point (SAP) to SAP. The delay should include any queuing delay on the subnetwork access interfaces.

c. Error : Measure of the subnetwork service residual error probability. The residual error probability is defined as the ratio of total incorrect, lost, and duplicate sds to total sds accepted for transmission (IS-8348).

d. Expense : Measure of the monetary cost of utilising the subnetwork. If monetary cost is not a consideration (as it happens in many military networks), the expense metric could be used to distinguish between types of subnetworks with regard to their suitability for a particular application. This would be an application imposing a composite requirement on throughput and delay and error performance (for example real-time voice).

Costs have to be normalised to the range 1-63, hence the cost calculation need not be very precise. The above metric definitions suggest that there is no need for complicated performance measurements on the subnets. The following subnet information should be sufficient :

- Transit delay
- Queuing delay
- Count of data packets/bytes accepted for transmission
- Count of data packets/bytes successfully delivered
- Count of data packets/bytes dropped
- Number of retransmissions

The above information can be calculated at the subnetwork interface if it cannot be extracted from the modem. Given the bursty nature of packet communications, the measurements should be in terms of sliding averages. The minimum sampling period has to be limited by the maximum rate at which it makes sense to circulate LSPs through the network so that there is sufficient capacity left for user traffic and there is sufficient time for the routing function to synchronise its FIBs.

## 5. ADDITIONAL OPTIONS

### 5.1 Interdomain Routing Protocol

The routing scheme described in the previous section is based on the OSI intradomain routing protocol (IS-10598). QoS driven routing can be extended to the case of internetworks spanning multiple routing domains. There is an OSI interdomain routing protocol (IDRP, IS-10747), which has been designed to support policy based routing. The IDRP has been specifically designed to operate over large networks [Ref. 6]. For this reason it is connection oriented avoiding the routing information flooding scheme used by IS-10589. The IDRP applies a distance-vector routing algorithm, which means that route optimisation is local and not global as in IS-10589.

QoS driven routing is feasible with IDRP, as this protocol provides for the exchange of link QoS attributes. The QoS parameters supported are: transit delay, error probability, cost, link capacity, security, and priority (source and destination specific QoS formats are also supported). The IDRP allows for link selection on the basis of link attributes. Multi-transmission media selection with IDRP would require that the subnetworks are treated as separate routing domains. The following table lists the advantages and disadvantages of IDRP relative to the IS-IS protocol for multimedia selection.

Advantages	Disadvantages
Lesser communications overhead on the network	Route selection is optimised locally and not globally
Firewall protection	Slower convergence on link cost or network topology changes
No need for global routing policy coordination	Does not handle routing within a domain (but can coexist with IS-10589)
Safeguards against policy inconsistencies within a domain	Less stable as a standard and not available commercially (yet)
Operates on top of CLNP and NLSP, hence it can make use of network security services	
Selective forwarding of reachability information	

Given the static nature of IDRP, the most effective configuration in a multidomain network, from the point of view of QoS driven routing, may be to create a routing domain federation consisting of a transit domain interconnecting the

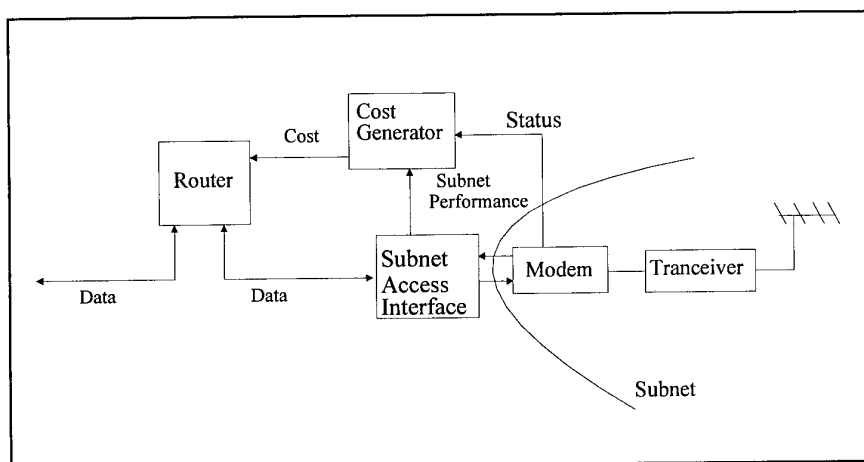


Fig. 6 Implementation of QoS driven subnet selection

participant domains. The transit domain should include only subnets connecting more than one participant. Within each domain including the transit one, the IS-IS protocol must be used for optimum QoS driven routing performance. For traffic between participant domains and the transit domain the IDRP must be used. Then, CLNP npdus would be directed to IDRP routers (BIS) who would make the appropriate routing policy decisions (e.g. filtration) and then pass the npdus to the transit network for transfer to the destination domain BIS according to the IS-10589 QoS routing scheme.

### 5.2 Domain specific QoS format

Both CLNP and the OSI routing protocol standards allow for source and destination specific QoS fields in the pdu headers. This feature can be exploited to extend the rather limited globally unique QoS format (see Table 2). It is also possible to assign different meanings to the four routing metrics allowed in the IS-IS protocol. Decision tables or algorithms will have to be specified to enable the routers to select the appropriate metric from the npdu QoS label. Interoperability with non conformant routers would be maintained, except for the fact that such routers will always revert to the default routing metric (link capacity).

### 5.3 Security Service Configuration

The protection parameter (see Table 1) can be used to enable the use of NLSP or any particular NLSP service (confidentiality, integrity etc.). With IDRP, the protection parameter may also be used as a criterion for selecting subnetworks or for communicating reachability information to other domains. However, COTS implementations of higher layers (4-7) do not necessarily pass through the protection parameter.

### 5.4 QoS adjustable Transport Connection operation

Under the TP4 protocol, the operation of transport connections is based on periodic acknowledgements, retransmissions, and on flow-control through a sliding window mechanism. Retransmission periods, acknowledgment frequencies and window sizes (effectively maximum queue sizes) could be adjusted dynamically taking into account both the QoS requirements of the Transport Connection users and incoming

QoS observations from the network service. However, this is not commonly supported in COTS implementations of TP4.

## 6. CONCLUSIONS

A QoS driven routing scheme has been described which is based on the IS-IS intradomain OSI routing standard (IS-10589). This scheme requires a connectionless internetwork. It exploits the dynamic link cost exchange features of the IS-10589 to enable transmission media selection on the basis of performance measurements from the network links. At the same time, user QoS requirements are taken into account by selecting the routing metric on the basis of these requirements.

The proposed scheme can be used with standard commercial off-the-shelf routers. Two functions have to be added, namely a subnet monitoring function and a metric generation function. The former may reside on the router subnet interfaces, while the latter has to operate over the management interface of the router.

The proposed scheme offers the advantages of dynamic adaptation to changing transmission media conditions, as well as changes in the network topology (addition and removal of nodes and subnetworks). There is considerable scope for adding to the sophistication of the transmission media selection function through the definition of new cost generation algorithms and link performance measurements.

The ongoing Communication System Network Initiative Project [Ref. 12], which is a international cooperative project of six NATO countries, has adopted a routing scheme along the lines described in this paper. It is hoped that CSNI will provide a definitive demonstration of the feasibility and effectiveness of the proposed QoS driven routing approach

## 7. REFERENCES

1. Webb T.C. and Widdicks J.A., "NATO Communications Post-CFE - An STC Perspective", PP-292, STC, The Hague Netherlands, Nov. 1990
2. Jones C. A. et al., "Multimedia Communication : The promise and the reality", Symposium on Packet Radio, STC, The Hague, Netherlands, 18-20 April 1989.

3. NATO AC/259-D/1218 (rev.), "NATO Technical Interoperability Standards Transition Strategy", Oct. 1989
4. Robinson J.L., "Data Radio Design for OSI Interconnection", TN-151, STC, July 1987
5. Robinson J.L. and Tamvaclis C., "Connectionless OSI for communications networks in ACE", TN-248, Nov. 1989
6. Perlman R., "Interconnections : Bridges and Routers", Addison Wesley, 1992
7. Robinson J.L. and Tamvaclis C., "Protocol Profiles for Packet Radio", PP-277, STC, The Hague, Netherlands, May 1990
8. Tamvaclis C. and DePedro H., "Open Systems Architecture for Multimedia Interoperability", IEEE Military Communications Conference, McClean Virginia, USA, 4-7 Nov. 1991
9. Hind R., "Evaluation of the OSI Transport Protocol Class 4 for use with SATCOM links", TN-512, STC, The Hague, 1993
10. Sluman C., "Quality of Service - The Holy Grail or a Waste of Time", Symposium on Military Communication Networks Interoperability and Standards, STC, The Hague, Netherlands, 8-11 June 1993
11. Koelman W.A., "CLNP Header Compression, A subnetwork-Independent Approach", TN-491, STC, The Hague, Netherlands, Dec. 1992
12. Bot A., "Communication Systems Network Interoperability : A cooperative R&D project", Symposium on Military Communication Networks Interoperability and Standards, STC, The Hague, Netherlands, 8-11 June 1993

**Table 2**  
**OSI Layer QoS Parameters**

Layer	Parameters	Negotiation	Notes
Messaging (X.400)	expiry time, reply time, importance, sensitivity, latest delivery, message security, precedence	No	All parameters are optional. The last three are MMHS enhancements.
Connection -Oriented Transport Service	Protection, Priority, Connection Establishment QoS: (Delay, Failure Probability) Data Transfer QoS: (Throughput, Transit Delay, Residual Error Rate, Connection Resilience Transfer Failure Probability) Connection Release QoS: (Delay, Failure Probability)	Yes	Negotiation takes place only during connection establishment. The responding entity or user may reduce but not increase the requested QoS. Notification of QoS changes is not required.
Connectionless Transport Service	Protection, Priority, Transit Delay, Residual Error Rate	No	Notification of QoS change is not required.
Connection -Oriented Transport Protocol	Protection, Priority, Transit Delay, Residual Error Rate, Throughput	Yes	All parameters are optional. Performance parameters are applicable to the data transfer phase only. There is no QoS maintenance function.
Connectionless Transport Protocol	None	No	TS QoS may be used to activate the checksumming option.
Connection-Oriented Network Service	Protection, Priority, Cost, Transit Delay, Residual Error rate	No	Notification of QoS changes is not required.
Connectionless Network Protocol	Protection, Priority, Lifetime, QoS (see Sec. 4)	No	All parameters are optional. They may be taken into account in route selection. User data may be delivered at a different QoS.
Connectionless DataLink Service	Protection, Priority, Transit Delay, Residual Error Rate	No	Notification of QoS changes is optional.
Connection- Oriented DataLink Service	Protection, Priority, Throughput, Transit Delay, Residual Error Rate Connection Resilience	No	On connection establishment, the user indicates the required QoS and the provider replies with the available QoS. Notification of QoS changes is optional. The provider may use QoS for link protocol selection.

## **DISCUSSION**

**Discussor's name :** K. S. Kho

**Comment/Question :**

You said that the QoS driven metrics could utilize COTS routers. Would it not be difficult to modify/add commercial software?

**Author/Presenter's reply :**

No, since these would not be modifications but additions, communicating with the router via interfaces.

# A MMPP Communications System for the Frequency Range 2-200MHz

M. Darnell<sup>1</sup>, P. Walker<sup>1</sup>, N. Riley<sup>1</sup>, G. Vongas<sup>2</sup>

<sup>1</sup>Hull-Lancaster Communications Research Group  
Department of Electronic Engineering  
University of Hull  
Hull HU6 7RX  
UK

<sup>2</sup>DRA Portsdown  
Cosham  
Hampshire  
PO6 4AA  
UK

## 1. SUMMARY

This paper describes the work being carried out to realise a robust digital radio communications system, operational over the frequency range 2-200MHz, which will utilise the existence of multiple mechanism propagation paths (MMPPs) in order to maximise link-availability. The system incorporates a substantial element of PC-based Digital Signal Processing (DSP).

This work is essentially a unification of several areas of on-going research within the Hull-Lancaster Communications Research Group (HLCRG) on the application of PC and DSP technology in radio system design.

## 2. INTRODUCTION

The traditional approach to radio communications systems design is to attain an optimum level of performance for a single radio propagation mechanism occurring over a limited frequency range, e.g. ionospheric refraction at HF, line-of-sight space wave at VHF, etc. Under operational conditions for such systems, any co-existing mechanisms which may occur from time to time are ultimately regarded as undesirable potential noise sources and detrimental to system performance. With the increasing availability of relatively cheap and powerful digital signal processing (DSP) hardware, along with frequency-agile, software-controllable radio equipment, the past few years have seen a move towards systems which have the facility to adapt their channel coding functions according to varying channel capacity. This is particularly prevalent at HF (2-30MHz), where channel conditions can fluctuate severely. The consequence of this development is that interest has been expressed in the exploitation, on an opportunistic basis, of multiple propagation mechanisms occurring over a broader frequency range than conventional systems, within a structured, adaptive framework containing a significant element of DSP processing for the channel coding functions.

A PC-based communications system is being developed which will operate over a nominal frequency range of 2-200MHz, and which will exploit the existence of alternative propagation paths for a given transmitter-receiver configuration, as shown in simple diagrammatical form in figure 1.

## 3. MECHANISM DIVERSITY AND THE DIGITAL APPROACH TO SYSTEM DESIGN

The main propagation mechanisms that can occur over the frequency range 2-200 MHz are listed in table 1, together with their relevant characteristics. Of particular interest is the troposcatter mode which has traditionally been associated with UHF and microwave systems. Recent work, however, has shown this to be exploitable in the low-VHF band [1][2]. A co-ordinated approach to the utilisation of the listed mechanisms within a DSP-based environment has yet to be accomplished, even though the technology to do so has been available for a number of years. The reasons for this are easily identifiable:

- (i) the time taken for new designs to become operational is relatively long - a minimum of several years;
- (ii) designers still have a tendency to think in conventional analogue terms;
- (iii) the nature and potential of the propagation medium, especially below 100MHz, is not yet fully appreciated.

With a digitally oriented approach to design, the generation of signals and processing algorithms can fully exploit the unique capabilities of DSP devices, rather than simply replicating functions traditionally implemented in analogue form. One implication of this philosophy is that, although the system functionality is limited by the capabilities of the DSP hardware, the software can be altered to such a degree that a terminal can function as a channel monitoring and evaluation system in one mode [3], and as an adaptive MFSK modem in another [4].

## 4. CHANNEL EVALUATION FOR MMPP SYSTEMS

The most fundamental characteristic of any practical radio system, especially when mobile terminals are involved, is a time-varying information transmission capacity, typically due to the combined effects of signal fading, Gaussian noise and non-Gaussian noise sources, e.g. co-channel interference. Over such channels, it is conventional to employ fixed channel encoding/decoding (CE/CD) procedures; this implies that the CE/CD may be insufficiently robust at times of low capacity, whereas, when the capacity is high, the channel may well be under-utilised. Variations in channel capacity may be

short-term, e.g. due to vehicle movement, or longer-term, due say to diurnal changes in the state of the propagation medium. Clearly, improved channel utilisation can only be achieved if the channel state is monitored continuously, and then information derived from that state used to initiate adaptation of the CE/CD parameters; real-time channel evaluation (RTCE) provides a means by which this can be done.

RTCE has been an important element of radio communication system design for approximately the past two decades; this is especially true of HF (2-30 MHz) long-range, ionospheric skywave communications [5][6][7]. Over this period, architectural evolution of radio system design has progressively widened the possibilities for extracting RTCE data, particularly from the normal operating signals of the system. Here, the application of RTCE techniques within MMPP system architectures is introduced.

#### Multi-functional Coding

A concept known as multi-functional coding (MFC) [8] has been developed within HLCRG over the past few years. MFC seeks to unify the elements of CE/CD, i.e. modulation/demodulation, error-control encoding/decoding, synchronisation, multi-user encoding/decoding, etc., within a structured analytical framework and a common processing environment. Since all the elements of CE/CD tend to be interactive, the practical problem, given a communications requirement, is how best to apply various adaptive CE/CD algorithms and the available processing power in order to optimise the overall system performance. The weighting applied to, and the parameters of, the different CE/CD functions will vary according to the channel state; thus, RTCE is an essential source of control data for an MFC-based communication system. At the transmitter, any adaptation of the CE will be comparatively slow unless a high capacity feedback link from transmitter to receiver is available, which often cannot be realised in practice. At the receiver, however, detailed RTCE data is immediately available for short-term adaptation of the CD procedures. Consequently, the nature of the RTCE at transmitter and receiver may well be significantly different. Figure 2 is a schematic diagram of an MFC-based communication system incorporating RTCE.

The following sections of this paper will consider the various types of RTCE potentially useful in a MMPP environment. Emphasis is given to RTCE procedures which can be implemented within flexible digital terminal architectures comprising conventional microprocessors and DSP devices. Finally, the manner in which particular forms of RTCE can be applied in a specific radio communication system architecture will be discussed.

#### 4.1 Basic Classes of RTCE

In general, RTCE procedures can be classified as either "active" or "passive". Active RTCE requires special probing signals to be radiated by the transmitter, with corresponding analysis algorithms at the receiver. Passive RTCE, on the other hand, makes use of naturally occurring signals - either the communications traffic associated with the system itself, or unrelated "transmissions of opportunity". The types of RTCE considered here will normally make use of embedded processing at the receiver, i.e. within the processing

architecture which is already provided to fulfil the communications functions.

Note that it is also possible for any active RTCE functions at the transmitter to be performed in an embedded manner using the processing architecture already available for communications signal generation. A further sub-class of passive RTCE makes use of off-line propagation and noise/interference models; again, these can take the form of software routines running within the existing system architecture.

A distinction can also be made between RTCE techniques primarily intended to monitor the state of the channel currently passing communications traffic, and those intended to rank a set of alternative channels in terms of their ability to carry a specified form of traffic; these will be referred to as current channel (CC) and alternative channel (AC) techniques respectively.

Figure 3 shows the above classifications diagrammatically.

To date, little attention has been given to the design of communication systems such that the extraction of RTCE data is facilitated. It is important to stress that in digital architectures, the availability of potential sources of RTCE is greatly enhanced, as will be indicated later. In general, an adaptive communication system should have both CC and AC RTCE types; these will normally make use of distinct algorithms.

#### 4.2 Active RTCE Techniques: AC Mode

The best known form of active RTCE in the HF band is ionospheric sounding in which energy is radiated over part, or the whole, of the frequency band. The majority of special-purpose sounders radiate a linear frequency modulated (LFM) signal, or "chirp", across the band of interest; after transmission over the propagation path, this signal is mixed with a synchronised LFM frequency sweep at the receiver, with the mixer output then being subjected to spectrum analysis. The output of this spectrum analyser can be shown to be proportional to the unit impulse response function of the channel [9][10]. A 2-dimensional projection of the raster of impulse responses is termed an "ionogram" and allows the channel multi-path structure to be displayed as a function of frequency.

Many other active RTCE procedures have been developed for operation in a limited set of assigned channels, rather than across the whole HF spectrum. Examples of these include the Channel Evaluation and Calling (CHEC) system [11] and Automatic Link Quality Analysis (ALQA) [12]. Essentially, these employ a special purpose probing transmission for channel evaluation, coupled with a link establishment protocol. These can also be classified as AC RTCE techniques.

It is now possible to implement embedded ionospheric sounding systems of various types using flexible processing power at transmitter and receiver [13][4]. Hence, when the system is not passing communications traffic, it can be configured as a sounder simply by means of software changes. The nature of the sounding process can be made extremely adaptable, for example, the sounder can be used to

scan the complete band or, alternatively, it can scan selected sub-bands of particular interest to the user. Also, it is possible to vary the nature of the sounding, depending upon, for instance, electromagnetic compatibility (EMC) constraints or maximum available transmitter power. A HF DSP-based sounder developed within HLCRG [4] will be adapted to run using the VHF receivers utilised in the MMPP system under development. This will be facilitated by the employment of a broadband flexible modulator, also developed within HLCRG, which is not restricted to 3kHz RF channels (see section 6.1).

#### 4.3 Passive Embedded RTCE Techniques: CC Mode

A number of passive RTCE techniques, compatible with embedded processing [8], will now be briefly described. In all cases, the output of the passive RTCE process can be related directly, or indirectly, to the received signal-to-noise ratio (SNR). This is logical since the performance of any particular CE scheme will be influenced primarily by SNR. The schemes below can be classified as CC techniques.

##### Soft-decision Data

Soft-decision data, in the form of the demodulator output waveform amplitude, phase margin, etc., can be used as a measure of confidence for detection decisions. Trends in soft-decision levels can give an indication of channel state [8].

##### Error Control Decoder Metrics

In a convolutional decoder, the metrics associated with the most likely path through the decoding trellis and the next most likely path can be continuously compared. The greater the difference between the two, the higher the channel SNR [14].

##### Synchroniser Output

The output of a synchronisation preamble detector will, under noise-free conditions, have a certain peak-to-sidelobe ratio (PSR) which will depend upon the type of preamble sequence used. As channel conditions degrade, so also will the synchroniser PSR [15]; this degradation can again be calibrated in terms of a reduction in received SNR.

##### Data Statistics

If the data to be transmitted has predictable statistics, these can be compared with the statistics of the received data - a process known as "statistical real-time channel evaluation" (SRTCE). The nature of any differences can be related to channel state [16]. This is a non-parametric form of RTCE, in that the technique is independent of the specific forms of CE/CD being employed at any time.

##### Zero-crossing Characteristics

Prior to demodulation, the zero-crossings of the received signal can be analysed within a defined bandwidth. The characteristics of the zero-crossing data can again be related to channel state [17]. Zero-crossing analysis can also be viewed as a non-parametric form of RTCE since it may be applied before the CD process.

#### 4.4 Passive Embedded RTCE Techniques: AC Mode

Following are passive embedded RTCE techniques which can be used in the AC mode.

#### Template Correlation

Template correlation [18] is a technique designed to allow optimum placement of a narrowband wanted signal within an assigned channel bandwidth when narrowband noise/interference is present. A template of the channel noise/interference spectral profile is first obtained using an FFT algorithm; this is then subjected to frequency domain cross correlation against another template corresponding to the ideal wanted signal spectral profile. The minimum value of the cross correlation function indicates the optimum position for the wanted signal within the channel bandwidth, i.e. where the wanted signal and unwanted background have least similarity. It is also possible to employ template correlation for optimum signal format selection by cross-correlating the background noise/interference profile against a range of possible wanted signal templates; again, the minimum correlation value indicates the preferred signal format.

#### Passive Monitoring of Transmissions of Opportunity

A number of classes of signals normally present in the HF band can be passively monitored in order to extract information about the current state of the propagation path [19]. Signals of this type, which can be identified unambiguously, include:

- (a) broadcast service transmissions;
- (b) standard time/frequency transmissions;
- (c) oblique ionospheric sounder transmissions;
- (d) radio beacons;
- (e) background noise/interference.

The information derived from the monitoring process can be compared with that predicted from off-line propagation analysis programs to establish the general state of the ionospheric medium. Also, conditions for a given wanted path can be inferred from interpolation/extrapolation of data from reasonably similar paths.

#### Embedded Propagation Analysis

In recent years, a number of HF propagation analysis models, compatible with PC computational power, have become available [20]. These can be embedded within the processing elements of the communication system terminal architecture and run for the different frequency channels assigned to the system, prior to starting communication. The data obtained can be used to initialise other RTCE procedures, e.g. to restrict the frequency range over which sounding is carried out, thus improving the overall efficiency of the channel characterisation process.

### 5. RTCE AND ALE WITHIN AN MMPP COMMUNICATION SYSTEM ARCHITECTURE

#### 5.1 Definition of Automatic Link Establishment(ALE)

As radio systems have become increasingly automated, the concept of automatic link establishment (ALE) has evolved to describe the "start-up" phase of communications; however, there is also a tendency for ALE to be confused to some extent with RTCE. ALE has a wider scope than RTCE, but will normally incorporate some of the types of RTCE outlined in this paper.



A proposed definition of ALE is as follows:

*"ALE is a term used to describe the protocol involved in the start-up phase of an automatic radio system by which the functions of RTCE, channel encoding and decoding, encryption and decryption, and system control are co-ordinated in order to meet specified user requirements."*

In addition, the ALE procedures should ensure a smooth and automatic transition from start-up to the "running" (or transmission) phase, whilst maintaining the required grade of service. It should be noted that, with the advent of flexible digital architectures, there is no reason why a given radio system should be limited to a single ALE mode; rather, the ALE protocol can be made adaptive in response to channel state, user requirements and interoperability constraints. Figure 4 is a schematic illustration of how the available processing power is distributed during the ALE process.

In the context of MMPP systems, future developments in the generation and use of RTCE data which appear to offer promise include:

- (a) the inclusion of a predictive (or trend) element in the output of an RTCE process;
- (b) increased emphasis upon the use of non-parametric forms of RTCE;
- (c) the coalescing of propagation analysis models and RTCE data within embedded on-line frequency management systems;
- (d) the design of radio communication systems to facilitate the extraction of RTCE data;
- (e) greater integration of CE/CD and RTCE.

The next phase of the RTCE investigation for the MMPP system will be to identify specific techniques which can be incorporated within the DSP-based architecture, and which can provide the required data for broadband frequency management. Different mechanisms require different techniques; for example, meteor burst propagation can only be quantified on the basis of statistical models, whereas ionospheric skywave, troposcatter, sporadic-E etc. are all amenable to some form of real-time probing.

## 6. HARDWARE CONSIDERATIONS

### 6.1 Broadband Modulation

In order to fully exploit the range of propagation mechanisms occurring over the frequency range 2-200MHz, a modulator capable of a variety of operational modes is required: the communications system being developed uses a module designed and built in-house which is capable, under RS-232 control, of SSB, ISB and DSB over the range 2-220MHz with an input bandwidth of up to 1MHz. An AT&T DSP-32C supplies the baseband signal to the modulator as two spectrally-similar waveforms, the DC offsets, amplitudes and relative phase of which determine the carrier and sideband levels. Sideband/carrier suppression of >50dB is typical. The fact that the offset, amplitude and phase adjustments are derived digitally ensures repeatability of signal levels and minimises component-related drift.

The modulator drives a broadband RF amplifier with a power level which is PC-controlled. This allows the radiated power at the antenna to be set in accordance with the propagation mechanism selected (e.g. 10s of watts for line-of-sight, few 100 watts for meteor-burst, etc.). A block diagram of the modulator is shown in figure 5. The baseband signal is first mixed up to 300MHz through an I/Q modulating process; the phase difference between the two versions of the baseband signal,  $\phi$ , will determine whether USB, LSB or DSB is produced. The 300MHz LO is then mixed with an oscillator varying from 302 to 500MHz to provide down conversion to the required final carrier (2-200MHz). The unwanted sum term of this mixing process is easily removed by a lowpass filter.

### 6.2 Antennas

Over the 2-200MHz range ( $\approx 6.5$  octaves) covered by the system, a large number of different antenna types are available for use depending on the application - land-mobile, aeromobile or fixed. Coverage of the whole of the frequency range of interest with a small number of antennas must involve a severe compromise of the gain achievable, especially if limited space is available or the antenna is required for a mobile application. An initial proposal for an antenna complement for the MMPP system is presented in the following section. This is divided into two situations: a base-station configuration when typical rooftop space is available, and a mobile configuration; both these situations need to be considered for the system under development since it is aimed primarily at aeromobile applications.

#### 6.2.1 Base-station Configuration

If transmitted power levels of up to a few 100s of watts are anticipated, then the most appropriate antennas would be a broadband fan-dipole for the lower end of the frequency range and a horizontal rotatable log-periodic for the higher range. The main problems to be expected with this configuration are that the low frequency antenna might not operate very efficiently at the extreme low frequency end of the range and that operational/siting considerations might preclude the use of a rotatable log-periodic. The former problem may be overcome with the use of a simple matched whip, whilst the latter would require the use of a fixed antenna. Use of a fixed antenna would mean that the directivity would be lost unless a switchable array were to be used, which would require more space for its deployment. A switchable array of four log-periodics pointing north, south, east and west would be feasible, although bulky. Alternatively, at the expense of 3 or 4 dB of gain, a simple broadband dipole could be used for the higher frequency range also.

Since both these antennas are capable of transmission and reception, there is no requirement to provide separate receive antennas. If additional receive antennas are required for monitoring purposes, however, a good choice would be an active monopole for the lower frequencies and/or an active dipole or horizontal log-periodic for the higher frequencies.

#### 6.2.2 Mobile Configuration

The choice of mobile antenna is severely limited if transmission and reception over a wide frequency range is required. At HF the choice is effectively limited to a whip antenna for transmission and reception, with the possibility

of active antennas for reception only. In some mobile applications, the use of a long wire may be considered if space permits. At higher frequencies, the choice is only slightly wider since space considerations would preclude the use of most of the antennas suggested for the base-station case in section 4.2.1 above. In the case of aeromobiles, antennas such as "towel rails" or slots could be used for transmission or reception but, as in other applications, these are often very inefficient and have poor bandwidth properties. A horizontal broadband dipole would be a reasonable choice for the higher frequencies in most mobile situations.

### 6.2.3 Proposed Antenna Complement for the MMPP System

In each of the two situations described above, base-station and mobile, a variety of antenna solutions could be proposed, depending on the exact circumstances in terms of available space, type of mobile etc. The following, however, would form the best compromise and cover the majority of situations:

#### Base-station:

(Low frequencies)	Horizontal fan dipole
(High frequencies)	Horizontal rotatable log-periodic

#### Alternate/additional:

(Low frequencies)	Whip for very low frequencies
(High frequencies)	Switchable array of horizontal log-periodics

#### Mobile:

(Low frequencies)	Whip
(High frequencies)	Horizontal broadband dipole

#### Alternate/additional:

(Low frequencies)	Long wire
(High frequencies)	Horizontal rotatable log-periodic
(Low/High)	Active monopole for monitoring
(High frequencies)	Various mobile-specific

## 7. SYSTEM CONTROL CONSIDERATIONS

The control protocols required for an MMPP communications system are considerably more complex than those for single-mechanism systems. The major additional factors which must be considered are as follows:

- (i) Channel evaluation for the range of mechanisms will be a composite of RTCE and the use of embedded statistical models;
- (ii) For RTCE purposes, it may be necessary to employ an auxiliary monitoring receiver, in addition to the receiver currently passing traffic;
- (iii) Propagation delays may differ substantially between mechanisms; for example, tropospheric propagation near the earth's surface will exhibit a propagation delay which is typically  $\approx 1$ ms less than that for a comparable path operating via F2-layer ionospheric refraction. Such a difference might correspond to several bit/symbol

intervals; clearly, switching rapidly between these two mechanisms would require re-synchronisation;

- (iv) It will be necessary to adapt the transmitted signal format/receiver processing procedures in response to the propagation mechanism in use at any time. For example, meteor-burst paths will exhibit low time dispersion, whilst HF skywave paths may suffer from severe multipath spreads of several milliseconds.

With the system architecture under development, making extensive use of DSP, the level of adaptation implied by (i) to (iv) above should be achievable.

## 8. CONCLUSIONS

This paper has outlined the main features of the design of an MMPP communications system to operate over the frequency range 2-200MHz. The system employs novel RF units and a highly flexible PC/DSP-based architecture.

To date, all hardware units of the system have been assembled and tested. System integration is currently in progress and on-air trials are planned for 1994.

## 9. ACKNOWLEDGEMENT

The authors wish to express their gratitude to the UK Defence Research Agency (DRA) for their support of the work described in this paper.

## 10. REFERENCES

- [1] Darnell, M., Riley, N. & Melton, D. "Tropospheric Scatter Propagation in the Low-VHF Band", 7<sup>th</sup> International Conference on 'Antennas and Propagation', IEE Pub.No.333, April 1991.
- [2] Forsse'n, K.G. "Troposcatter Data Transmission Tests at 30MHz", Proc. Nordic Shortwave Conf. "HF-89", Faro, Sweden, August 1989.
- [3] Gallagher, M. & Darnell, M. "An economic ionospheric sounding system using standard HF radio system elements", IEE 5th Int. Conf. on "HF radio systems and techniques", CP-339, Edinburgh, 1991.
- [4] Clark, P. & Darnell, M. "An Adaptive DSP-Based MFSK Modem", 1<sup>st</sup> International Conference on 'DSP for Communication Systems', Sept 1992, University of Warwick.
- [5] Darnell, M. "Channel evaluation techniques for dispersive communications paths" in "Communications systems and random process theory", Ed J.K. Skwirzynski, Sijthoff & Noordhoff, The Netherlands, 1978.
- [6] CCIR: "Real-time channel evaluation of ionospheric radio circuits", Report 889, Doc. of XVth Plenary Assy., ITU Geneva, 1982.
- [7] Darnell, M. "Embedded real-time channel evaluation techniques", AGARD Lecture Series No. 145 on "Propagation impact on modern HF communication system design", 1986.

- [8] Darnell, M. & Honary, B. "Multi-functional coding schemes applicable to secure communication", IEE 2nd Int. Conf. on "Secure communication systems", London, 1986.
- [9] Coll, D.C. & Storey, J.R. "Ionospheric sounding using coded pulse signals", Rad. Sci. J of Research, Vol. 69D(10), 1964.
- [10] Barry, G.H. & Fenwick, R.B. "Techniques for real-time HF channel measurement and optimum data transmission", AGARD CP-173 "Radio systems and the ionosphere", Athens, 1975.
- [11] Stevens, E.E. "The CHEC sounding system", in "Ionospheric radio communications", Plenum Press, 1968.
- [12] Bliss, D.H. "Automated channel evaluation for adaptive HF communications", IEE 3rd Int. Conf. on "HF communication systems and techniques", CP-245, London, 1985.
- [13] Darnell, M., Hague, J. & Chan, A. "A global common-user HF propagation monitoring system", AGARD CP-442 "Propagation effects and circuit performance of modern military radio systems with particular emphasis on those employing band-spreading", Paris, 1988.
- [14] Darnell, M. "Adaptive channel coding", Proc. of 4th Meeting of SERC CDS Club, London, 1990.
- [15] Grayson, M. & Darnell, M. "Optimum synchronisation preamble design", Elec. Letts., Vol. 27, No. 1, 1991.
- [16] Zolghadr, F., Honary, B. & Darnell, M. "Statistical real-time channel evaluation (SRTCE) technique using variable length T-codes", Proc. IEE (I), Vol. 136, No. 4, 1989.
- [17] Grayson, M. & Darnell, M. "Adaptive synchronisation techniques for time-varying dispersive radio channels", IEE 5th Int. Conf. on "HF radio systems and techniques", CP-339, Edinburgh, 1991.
- [18] Jowett, A.P. & Darnell, M. "Automatic channel selection using template correlation", Elec. Letts., Vol. 23, No. 22, 1987.
- [19] Masrani, K. & Riley, N.G. "Use of passive monitoring techniques in HF radio systems", IEE 5th Int. Conf. on "HF radio systems and techniques", CP-339, Edinburgh, 1991.
- [20] Davies, K. "Ionospheric radio", Peter Perigrinus Ltd., 1990.

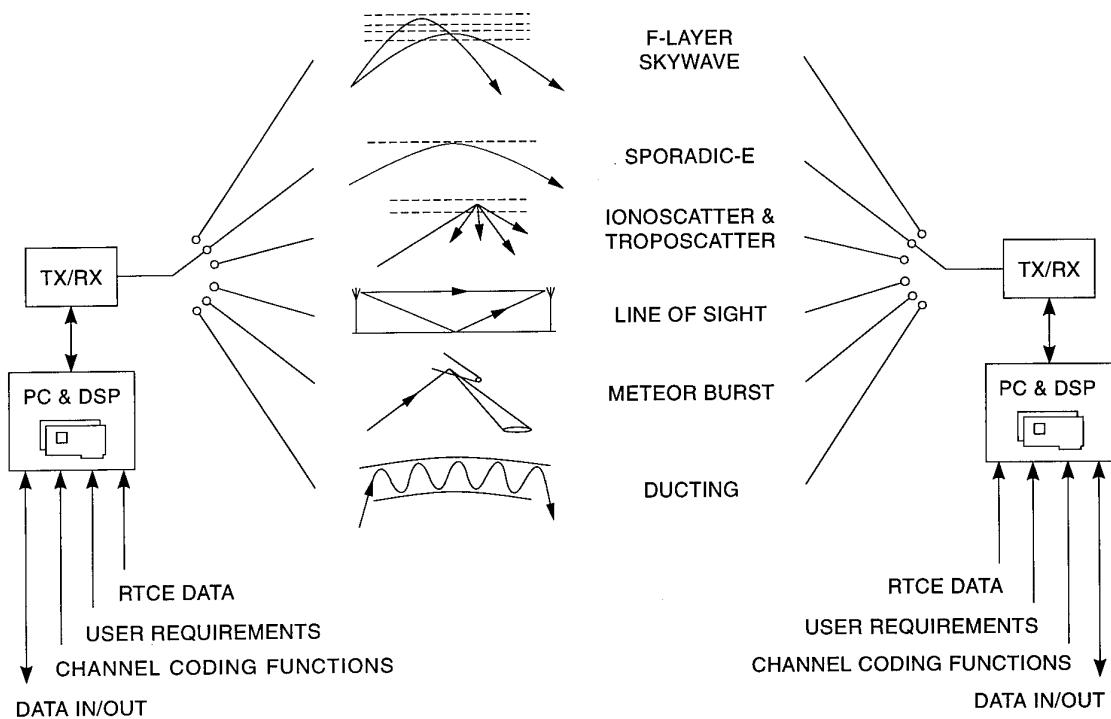


Figure 1 : Multiple-Mechanism System Concept

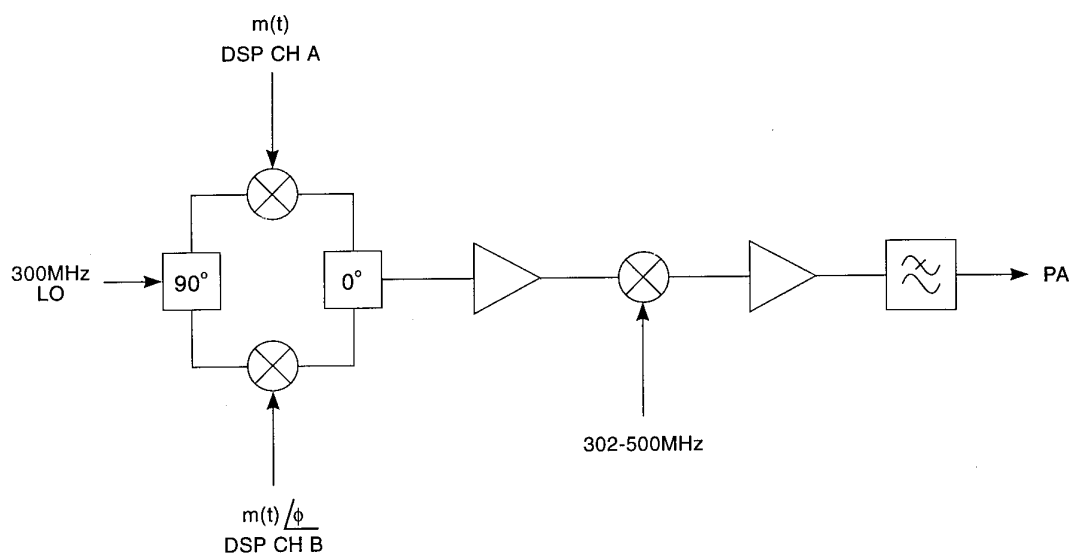


Figure 5 : 2-200MHz Modulator

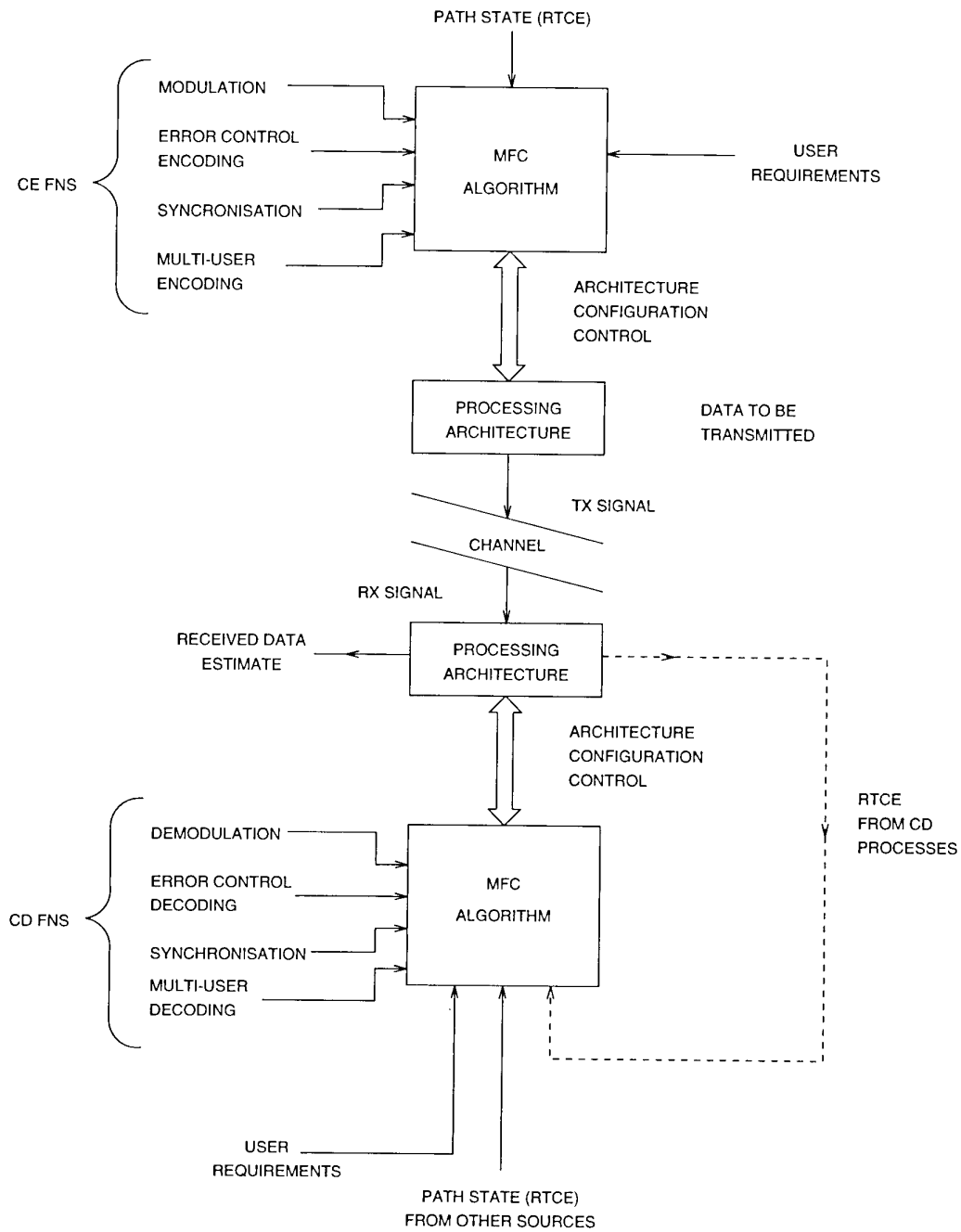


Figure 2: An MFC-based communication system

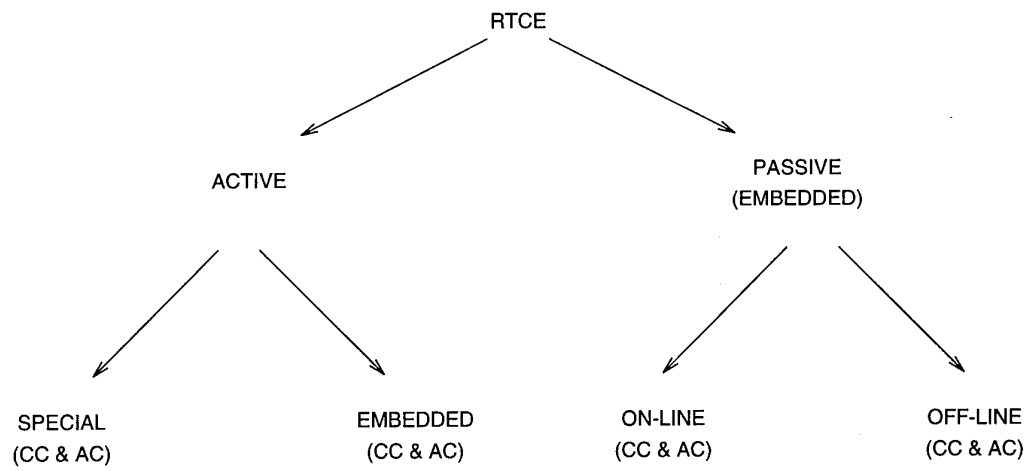


Figure 3 : RTCE classification

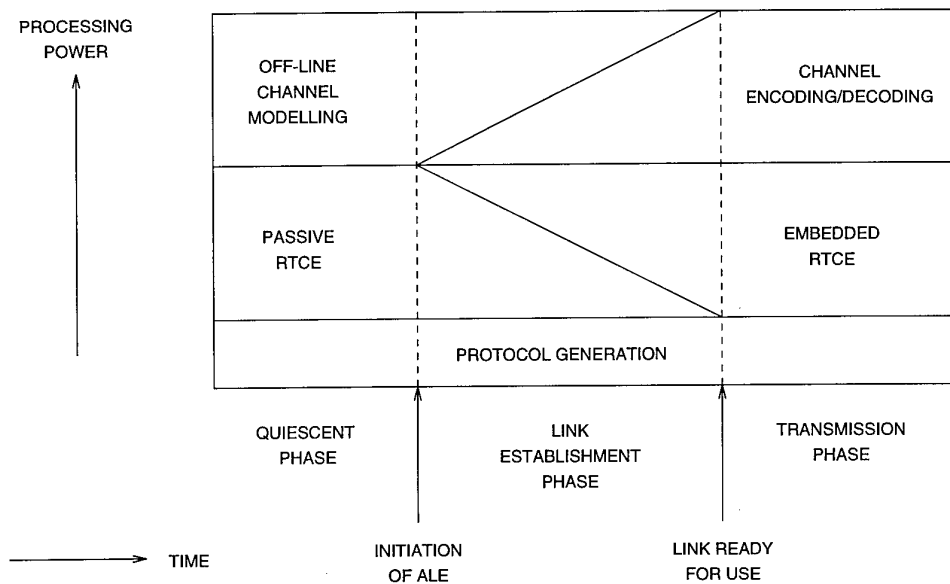


Figure 4 : Schematic illustration of the ALE process

Mechanism	Range	Amplitude, Phase & Frequency variability	Modulation formats supported	Availability	LPI/AJ Properties
Surface wave	to around 500km	A : low P : some F : low	Multi-tone PSK	high	good
Normal Skywave	to worldwide	A : high P : high F : low	MFSK	highly variable (depends on system and path parameters)	poor
Sporadic-E	to around 2000km	A : high P : high F : low	MFSK	variable (depends on location, season, etc.)	fair
Metcor-Burst	from around 250km to 2000km	A : high P : variable F : variable (fading in tail)	PSK MFSK	high, but intermittent (1% duty cycle)	very good
Ionosscatter	from around 250km to 2000km	A : high P : high F : low	MFSK	high if Effective Radiated Power high	poor
Troposcatter	to around 400km	A : high P : high F : low	MFSK	high if Effective Radiated Power high	fair
Line-of-Sight	to a few 10s of km	A : low P : low F : low	AM, FM MFSK Multi-tone PSK Multi-amplitude PSK	very high	good
Ducting	to a few 100s of km	A : variable P : variable F : low	MFSK	unpredictable, depends on location and met. conditions	good

Table 1 : Characteristics of Exploitable Mechanisms

## DISCUSSION

**Discussor's name :** E. P. Baars

**Comment/Question :**

Your paper briefly describes a number of RTCE techniques. Could you evaluate the relative effectiveness of the different approaches? Can you please comment on the zero crossing technique and its relation to SNR.

**Author/Presenter's reply:**

The most effective techniques are those which provide both modal structure and SNR information, i.e. the sounding and/or monitoring of swept frequency signals (e.g. 'chirps'). Active sounding, whilst allowing the user to define the sweep format, is more computationally intensive; if scheduling demands preclude the use of active techniques, then passive monitoring of conveniently sited remote sounders would be considered. The choice of techniques therefore depends on location, processing power demands, spectral emission considerations, etc.

The zero-crossing technique can be calibrated directly in terms of bit-error rate or SNR by considering the variability of the zero-crossing points with respect to their expected values.

**Discussor's name :** K. S. Kho

**Comment/Question :**

How do you use the "ducting" information for your MMPP system?

**Author/Presenter's reply :**

The MMPP system described aims to provide system adaptivity appropriate to differing channel conditions as determined by evaluation (sensors incorporated into the system). If ducting is present, but indistinguishable from other modes, the adaptivity will still yield an appropriate protocol. If it is distinguishable, the ducting will be treated as a separate mechanism accordingly.



## MODELLING AND SIMULATION OF HF/VHF MMPPs

by

**N.G. Riley and M. Darnell**

Hull-Lancaster Communications Research Group, UK  
University of Hull  
Hull HU6 7RX  
UK

**G. Vongas**

Defence Research Agency  
Portsmouth West, Cosham  
Hants PO6 4AA  
UK

### 1. SUMMARY

Modelling codes exist for many of the propagation mechanisms which may prevail in the frequency range of approximately 2 to 200MHz and many of these models are embodied in CCIR recommendations. Within the past few years, a number of simulation codes have been developed for use within various projects carried out by the Hull-Lancaster Communications Research Group (HLCRG). The proposed paper will describe current work aimed at bringing together the various models and simulation codes in order to produce a realistic simulation of the multiple mechanism propagation path.

The multiple mechanisms under consideration conventionally include groundwave, ionospheric skywave, sporadic E, ducting and the various scatter modes. In addition, recent work carried out by the HLCRG has revealed that tropospheric reflection may be responsible for stable propagation which is usable in the frequency range 30 to 70MHz for short (up to 400km) over the

horizon paths. The development of a propagation model for this mechanism will be included in the presentation.

### 2. INTRODUCTION

Many radio systems are designed on the assumption that a single radio propagation mechanism persists and the parameters of the system are therefore optimised to make best use of that particular propagation mechanism. Examples are HF skywave systems and meteor-burst communication systems which have very different operational protocols optimised to these two quite different propagation mechanisms. In these circumstances, propagation modes other than the intended one often appear to the system as interference, resulting in reduced channel capacity in spite of an increase in received energy from the required transmission. Since the additional propagation mechanisms often occur sporadically, an adaptive system architecture is required to take advantage of them when they occur.

As an example, it is often found that the channel availability of meteor-burst is

far higher than would be expected, due to the coexistence of other propagation modes, including sporadic-E [1] and tropospheric modes [2]. The characteristics of the additional propagation modes are such that the protocols often used in meteor-burst systems do not make optimum use of this added channel capacity. Of perhaps greater significance is the fact that, in this particular case, the inherent security of the meteor-burst system due to the assumed unique path between transmitter and receiver, may be removed by the additional propagation mechanisms.

The frequency range 30 - 200 MHz possesses a number of advantages for use in over-the-horizon communications, including a diverse range of propagation mechanisms and the possibility of reasonably compact, medium gain antennas. Several systems which aim to utilise the frequency range 2 - 200 MHz and above, are in use or under development including that described in a companion paper [3]. In support of these developments, propagation modelling and simulation is needed which encompasses the range of propagation mechanisms available and allows realistic multiple-mechanism fading models to be derived for the bandwidths of interest.

The aim of this paper is to outline the modelling and simulation activities required and to describe in detail work carried out on characterisation of a tropospheric mode of propagation which is prevalent up to ranges of around 400 km.

### 3. MODELLING PROPAGATION MECHANISMS IN THE 2-200

#### MHz FREQUENCY RANGE

The propagation mechanisms which may be utilised by MMPP communication systems and their characteristic propagation ranges are summarised below:

<i>MECHANISM</i>	<i>RANGE(km)</i>
Surface Wave	to 500 (Sea)
Skywave	Worldwide
Sporadic-E	to 2000
Meteor-burst	250 - 2000
Ionospheric Scatter	250 - 2000
Tropospheric Scatter	to 400
Line-of-sight	few 10s
Ducting	few 100s
Tropo-reflection	to 400

Well-established modelling codes exist for most of these mechanisms, enabling the median signal strength associated with each possible mechanism to be calculated for a given propagation path. A brief description of available codes is included here, with emphasis on new results obtained for what has been termed tropo-reflection [2].

#### SURFACE WAVE

Propagation range depends on surface conductivity, frequency and to a lesser extent on surface roughness and the atmosphere above the surface. Three main models are available, the simplest being the introduction of a ground attenuation term into the free-space equation, valid over a limited range of path lengths and frequencies:

$$E = FMA(P_T)^{1/2} / d \text{ mV/m}$$

where

$FM(P_T)^{1/2}$     *Unattenuated field at 1km*  
*d:*                *Range in km*  
*A:*                *Attenuation factor,*  
                       *dependent upon the*  
                       *electrical constants of the*  
                       *surface.*

A more accurate method for homogeneous ground is given by Rotheram [4], which the CCIR recommend should be used with Millington's method for paths of mixed ground conductivity [5,6]. A final class of methods involves the use of diffraction over irregular terrain or specific well defined obstacles such as cliffs [7].

#### *SKYWAVE and SPORADIC-E*

Many modelling codes exist, providing long-term path parameters for a wide variety of operational requirements. A good review of available long-term prediction models is given by Rush [8]. In the work described here, a version of CCIR Sup252 is used [9]. It should be noted that such models do not address the short-term variability which is of vital importance in MMPP communication system design. This variability is discussed in section 4.

#### *METEOR-BURST*

Prediction models based on the radar equation can give an accurate estimate of the received power scattered from meteor trails [10] whilst a large body of data has been accumulated describing the rate of arrival, echo duration, line density and resulting channel capacity in a statistical manner. It has been noted that other propagation mechanisms such

as auroral scatter [10] and sporadic-E [1] can change the characteristics of the channel on longer paths whilst on shorter paths, tropospheric mechanisms can have a similar effect [11].

#### *IONOSPHERIC SCATTER*

Ionospheric scatter can occur at frequencies primarily in the HF and VHF bands. At HF its main effect is to create dispersion in the form of spread-f. In high latitudes, field-aligned irregularities can give rise to auroral scatter. As a communication medium, ionospheric scatter is most effective around 30 to 60 MHz. At these frequencies the median scatter loss may be modelled by a simple set of curves showing the variation of scatter loss with range for a number of different frequencies. The scatter loss exhibits a minimum at a range of about 1400 km, due to simple geometrical considerations, and increases at about 5dB per 10 MHz from 30 to 60 MHz. Again account needs to be taken of the short-term variability about this median loss.

#### *TROPOSPHERIC SCATTER*

Both theoretical and empirical models of tropospheric scatter propagation exist, the most widely used being one of the empirical models [12] which gives values for the annual median transmission loss as follows:

$$L(50) = 30 \log f - 20 \log d + F(d) - G_t - G_r + L_c - V(d_e)$$

where

*f:*                *Frequency, MHz*  
*G:*                *Antenna gains, dB*

- F*: Function of scattering angle, path length,  $d$  and surface refractivity  
*L<sub>c</sub>*: Aperture-to-medium coupling loss  
*V*: Function of path length and climate

#### *LINE-OF-SIGHT and DUCTING*

A simple estimate of median field strength due to line-of-sight propagation may be made by considering the combination of direct and ground-reflected rays:

$$E = 2 (E_1/d) \sin(2\pi h_t h_r / \lambda d)$$

where

- E<sub>1</sub>*: field at 1 km  
*d*: path length  
*h*: antenna heights  
 $\lambda$  wavelength

However, in most practical situations many more effects must be taken into account such as diffraction over obstacles and terrain, refraction in the atmosphere, curvature of the earth's surface, ducting and other effects, depending on frequency. In the current study the propagation paths considered have precluded a line-of-sight mode (see Figure 1, for example) and therefore a line-of-sight model has not been included.

#### *TROPO-REFLECTION*

Measurements have been carried out [2] of the signal received from a 47 MHz beacon at receiver sites at ranges of 100, 265 and 400 km from the transmitter. The measurements, examples of which are plotted over several days in Figure 2, show that for a significant proportion of

the time a usable signal is received with a path loss which is considerably greater than would be expected if the CCIR tropospheric scatter model (validated for frequencies above 2 GHz) were applied. Taken along with the high degree of correlation between the received signals and the short-term fading characteristics observed (described in section 4) it was concluded that the propagation mechanism observed is due to reflections from structured layers in the troposphere, in agreement with other observations [13,14]. The received signal is at a much higher level than meteor returns, when measured at the 265 km receiver. It was shown that the propagation mechanism was capable of reliable data transmission at baud rates in excess of 4 kbps.

Further measurements are being carried out to enable calibration of an empirical model of median path loss for this propagation mechanism.

For a given MMPP system configuration, the models described above allow calculation of the median received signal level associated with each propagation mechanism which is likely to contribute to the total received signal. At any specific instant, the received signal will depend upon the instantaneous combination of signals due to each mechanism, each of which can only be modelled in a statistical manner. It is therefore necessary to simulate the likely ensemble received field strength to derive a realistic MMPP fading waveform which can be used for system development.

#### **4. SIMULATION OF THE FADING CHARACTERISTICS OF MMPPs**

A DSP-based implementation of an MMPP simulator is currently under development, with the following specifications:

*Number of Paths*

Up to 5

*Operation*

Non real-time at present

*Parameters*

*Delay* 0 to >20 ms in 0.1 ms

*Doppler* 0 to 100 Hz in 1 Hz increment

*Fade rate* 0.1 to 25 Hz in a binary progression (May be omitted from any channel)

*Attenuation* 0 to >50 dB in 1 dB increment (Infinite atten. for deselected channels)

*Noise Source*

Gaussian white noise level variable from 0 to -40 dB (or Off)

The overall design of the simulator is shown in Figure 3. In order to provide a realistic simulation of MMPPs, appropriate fading models for each of the constituent propagation mechanisms must be provided. Over the short time scales of interest, many of the MMPP constituent mechanisms exhibit Rayleigh fading, including scatter mechanisms and HF skywave. Where two paths of approximately equal amplitude exist, simple Fresnel fading may occur, for example in the decay phase of a meteor trail.

Measurements on paths where tropo-

reflection is dominant [2] have indicated that three different types of fading may occur, as shown in Figure 4, which appear to correspond to single path, two-path similar amplitude and multiple path propagation. A particular type of fading may persist for tens of minutes at a time, lending evidence to the view that the propagation is due to relatively stable atmospheric layers.

## 5. CONCLUSIONS

The parameters of propagation models, including short-term variability, appropriate to the development of an MMPP simulator have been described with particular emphasis on results obtained from a study of tropospheric propagation in the low VHF band to ranges of about 400 km. These models and results are currently being incorporated into a simulator in support of system development described in a companion paper [3]. Future work will include consideration of wideband models for HF propagation mechanisms and further characterisation of the tropo-reflection mechanism.

## 6. ACKNOWLEDGEMENTS

The Authors gratefully acknowledge the support for this work given by the SERC and the Defence Research Agency, Farnborough.

## 7. REFERENCES

1. Weitzen, J.A., Cannon, P.S., Ostergaard, J.C. and Bailey, A.D., "Seasonal variations in meteoric and non-meteoric duty cycle in the polar cap and auroral regions", IEE Fifth International Conference on "HF Radio Systems and Techniques",

- p162-166, Heriot-Watt University, 1991.
2. Melton,D., Riley,N.G. and Darnell,M., "A model for trans-horizon propagation in the low-VHF band", Proc. IEE Eighth International Conference on Antennas and Propagation, IEE CP-370, Heriot-Watt University, UK, 1993.
  3. Darnell,M., Walker,P. and Vongas,G., "A MMPP communication system for the frequency range 2-200 MHz", AGARD Symposium on "Multiple Mechanism Propagation Paths (MMPPs) Their characterisation and influence on system design", Rotterdam, October 1993.
  4. Rotheram,S., "Ground-wave propagation", Proc.IEE, 128, Part F, p285-36, October 1981.
  5. Millington,G., "Ground-wave propagation over an inhomogeneous smooth earth", Proc.IEE, 96, Part III, p53-64, 1949.
  6. CCIR, "Ground-wave propagation curves for frequencies between 10 kHz and 30 MHz", CCIR Rec.368-5, Recommendations and Reports of the CCIR, Vol V, Geneva, 1986.
  7. CCIR, "Propagation by diffraction", CCIR Rep.715-2, Recommendations and Reports of the CCIR, Vol V, Geneva, 1986.
  8. Rush, C.M., "Ionospheric radio propagation and predictions - A mini-review", IEEE Trans. Antennas & Propagation, Vol.AP-34, No.9, p1163-1170, 1986.
  9. CCIR, "Second CCIR computer-based interim method for estimating sky-wave field strength and transmission loss at frequencies between 2 and 30 MHz, Supplement to CCIR Rep.252-2, Recommendations and Reports of the CCIR, Vol VI, Geneva, 1986.
  10. Weitzen,J.A. and Ralston, W.T., "Meteor scatter: An overview", IEEE Trans. Antennas & Propagation, Vol.AP-36, No.12, p1813-1819, 1988.
  11. Weitzen,J.A., "Communicating via meteor burst at short ranges", IEEE Trans. Communications, Vol.COM-35, No.11, p1217-1221, 1987.
  12. CCIR, "Propagation data and prediction methods required for trans-horizon radio-relay systems", CCIR Rep.238-5, Recommendations and Reports of the CCIR, Vol V, Geneva, 1986.
  13. Eklund,F. and Wickerts,S., "Wavelength dependence of microwave propagation for beyond the radio horizon", Radio Science, Vol.3, No.11, p1066-1073, 1968.
  14. Friis,H.T., Crawford,A.B. and Hogg, D.C., "A reflection theory for propagation beyond the horizon", Bell Sys. Tech. Journal, Vol.36, No.5, p627-644, 1957.

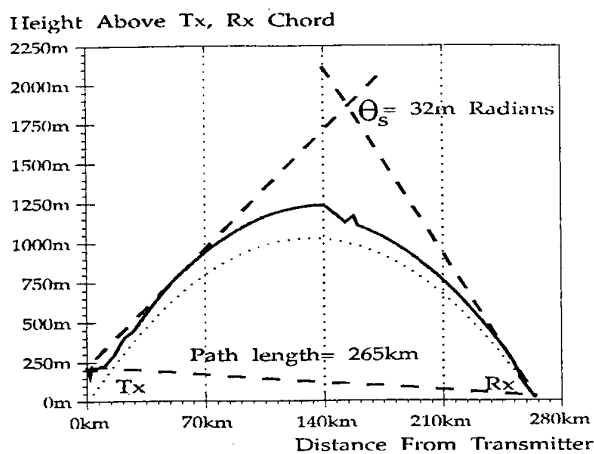
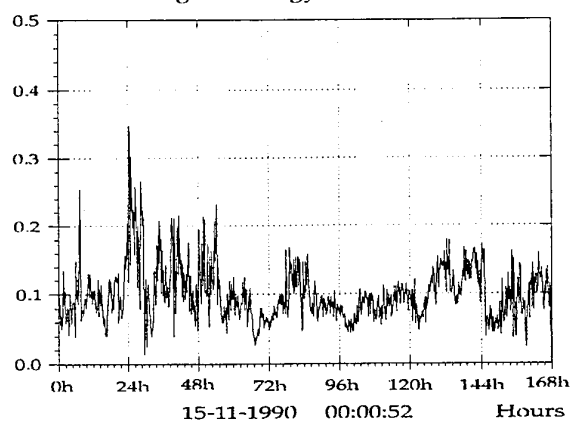


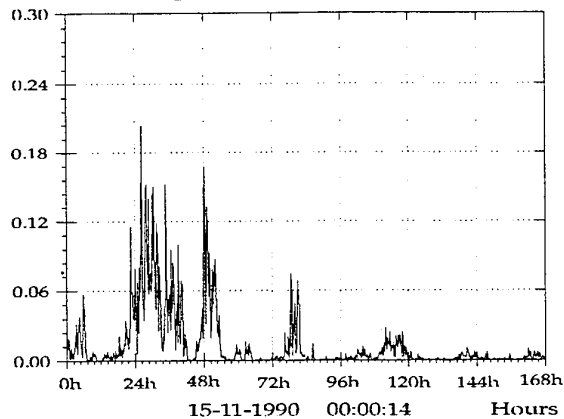
Figure 1: Typical tropo-reflection path profile

Normalised Signal Energy



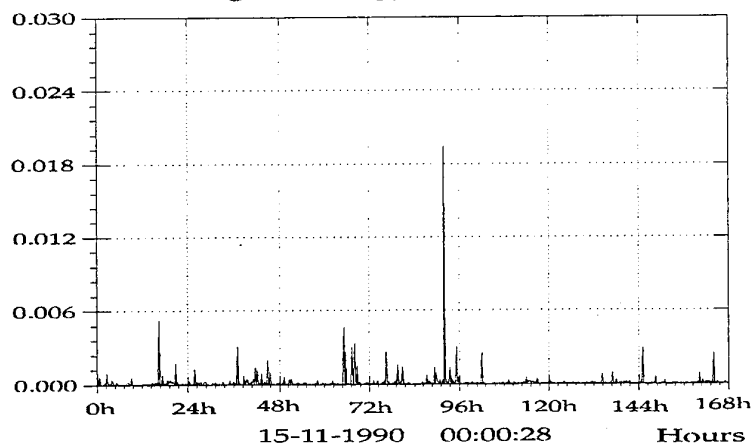
2a) Newbury - Warwick (100 km)

Normalised Signal Energy



2b) Newbury - Hull (265 km)

Normalised Signal Energy



2c) Newbury - Sunderland (400 km)

Figure 2: Long-term signal characteristics

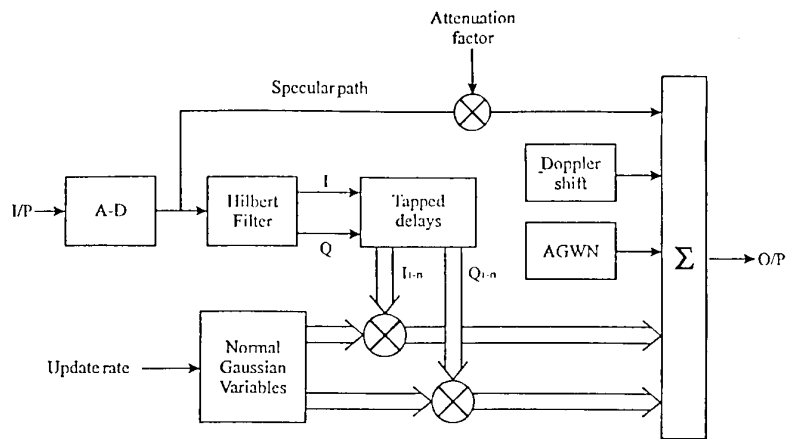


Figure 3: MMPP Simulator Design

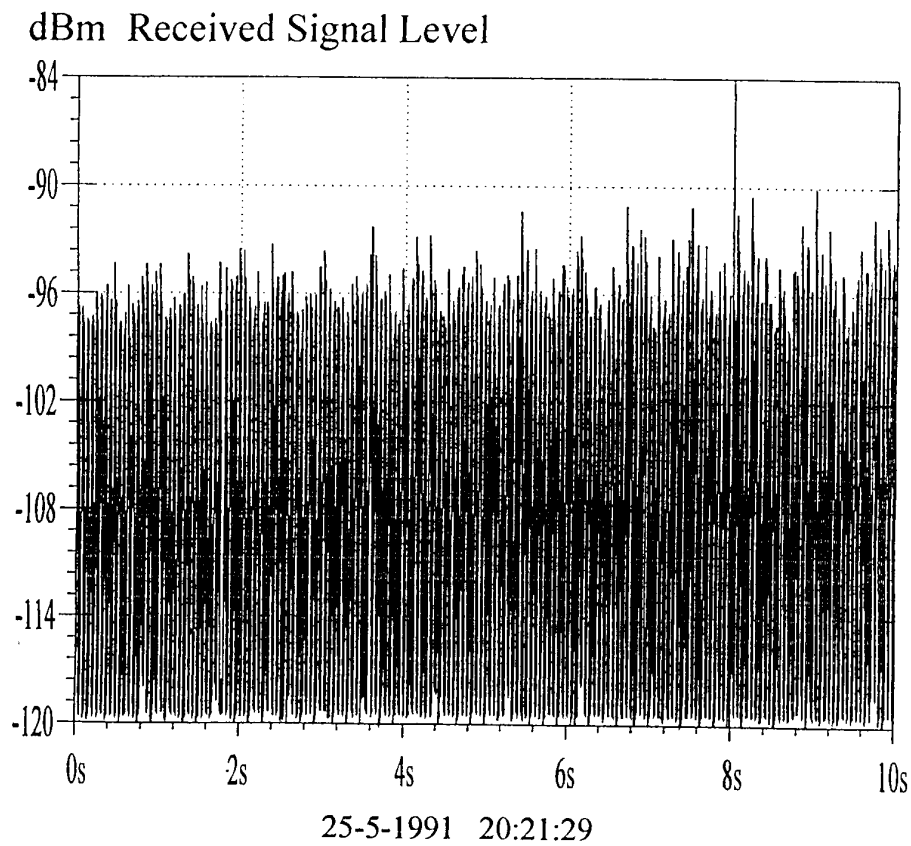
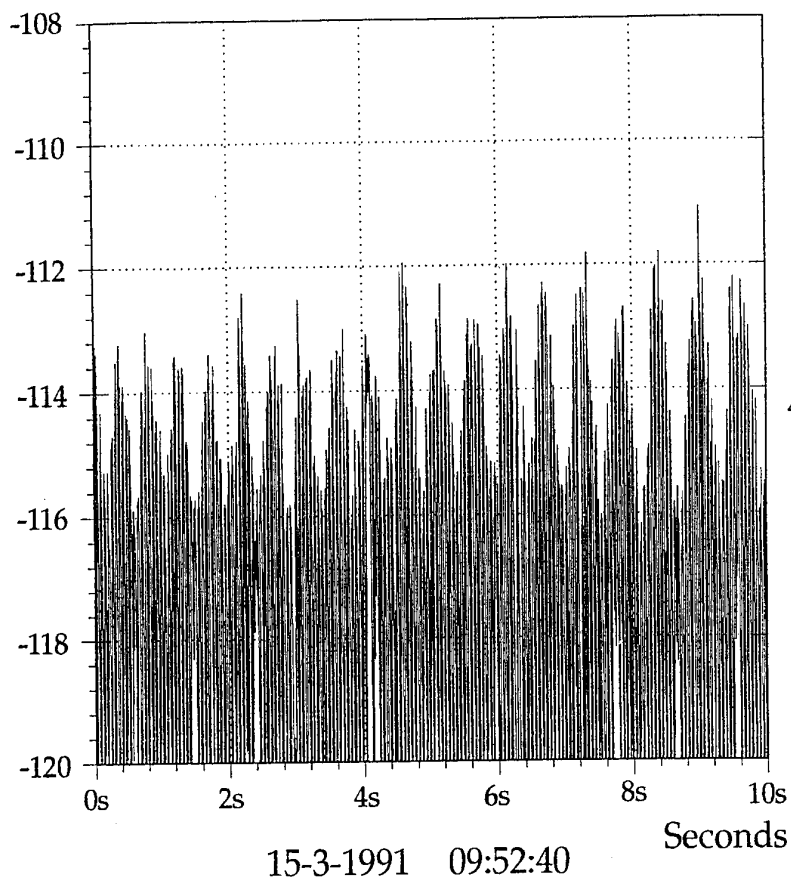


Figure 4: Short-term signal characteristics

4a) Little or no fading

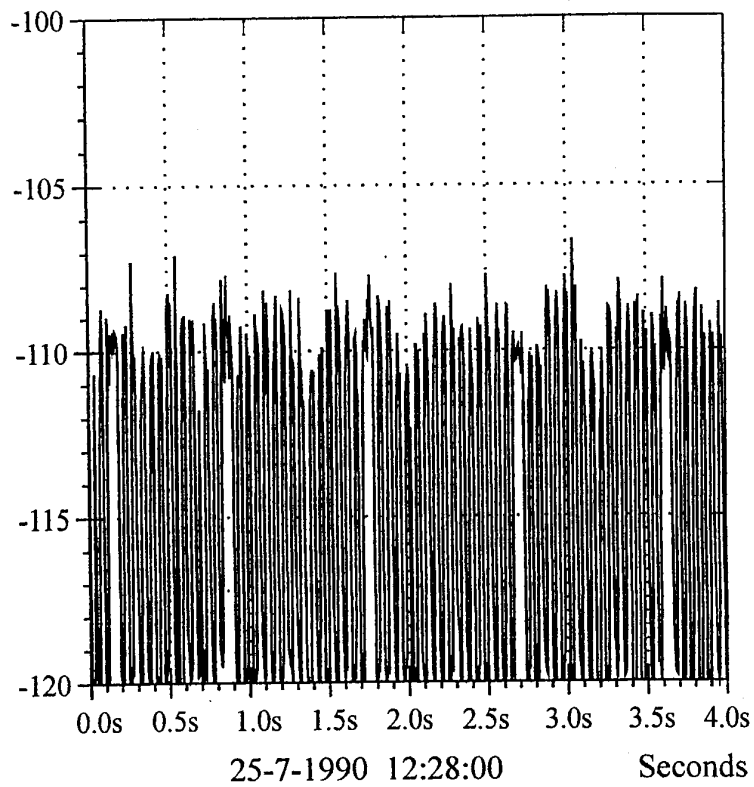


dBm Received Signal Level



4b) Periodic fading

dBm Received Signal Level



4c) Irregular fading

## DISCUSSION

**Discussor's name :** L. Bertel

**Comment/Question :**

1. En HF ou en propagation par réflexion sur les trainées météoriques les effets de polarisation associés à l'anisotropie des milieux nous semblent importants. Comment vos modèles et simulations prennent-ils en compte ces effets?
2. Dans votre modèle vous utilisez un doppler commun et constant pour toutes les voies. Croyez-vous que ce soit réaliste?

**Translation :**

1. *In HF propagation or when using propagation by reflection from meteor trails, it seems to me that the effects of polarisation associated with the ambient anisotropic are considerable. How do your models and simulations take these effects into account?*
2. *In your model you use a common and constant Doppler for all your channels. Do you think this is realistic?*

**Author/Presenter's reply :**

1. We have investigated polarisation effects and we have received signals on horizontal and vertical polarisation with at least 20 dB discrimination. However, we have no control over transmitter polarisation, which is horizontally polarised.
2. The design shown contained only a single channel module. The final design will contain around five "mechanism" channels, and I agree that the Doppler should be associated individually with each channel.

## ADAPTIVE ERROR-CONTROL SCHEMES FOR 2-200 MHz

## MULTIPLE-MECHANISM PROPAGATION PATHS.

B.Honary\*, M.Darnell\*\*, G.Vongas\*\*\*

## HULL-LANCASTER COMMUNICATION RESEARCH GROUP

- \*) Engineering Department, Lancaster University, Lancaster LA1 4YR, UK  
 \*\*) Department of Electronic Engineering, The University of Hull,  
 Hull HU6 7RX, UK  
 \*\*\*) DRA Farnborough, GU14 GTD, UK

## 1. Introduction

Modern radio communication systems are normally designed to exploit a given propagation mechanism in order to meet their operational requirements. This means that the parameters of such systems are, to a large extent, dictated by characteristics of a given propagation mechanism. Currently, most practical radio systems which make use of forward error correction (FEC), use one type of coding technique in order to provide a robust radio link against noise and interference in the channel. Consequently, these fixed coding methods tend to be ineffective for different channel characteristics. One of the most important parameters of a channel is its capacity. The greater the amount of redundant information added to the data, the greater the error protection offered to the data sequence, but obviously the efficiency of the channel falls by using a fixed coding for different channel conditions.

In Automatic repeat request (ARQ) systems, i.e. those that depend on feedback from the receiver as to the state of the received message, relatively low "overhead" check digits are required for reliable error detection. A properly designed system of this type can be very reliable [1], but under poor channel conditions the number of repetitions become excessive. Forward error correction techniques that can correct a mixture of burst and random errors are most suitable for predictable real channels.

Recently, an adaptive coding technique has been introduced [2,3]. The main purpose of an adaptive coding scheme is to permit only the necessary degree of error correction to be applied to the transmitted information according to the channel conditions.

The concatenated codes, first introduced by Forney [4], are formed by cascading two encoders, an inner and outer, where the first is usually a linear binary code, or a combination of two linear binary codes, and the outer is usually a multi-level Reed-Solomon (RS) code over  $GF(2^m)$ . An example of two-dimensional concatenated code is represented in Fig.1. It is known, that with choice of inner and outer codes, concatenated codes become very powerful codes for random and burst error correction.

The objective of the proposed paper is to investigate an adaptive concatenated codes, which can provide a more efficient error protection in the channels with different types of errors. The block diagram of the proposed technique is presented in

Fig.2. In this Figure: as an outer code two types of RS code ((15,9) and (15,7)), which allow correction of three and four q-ary ( $q=16$ ) errors are used. The interleaver/deinterleaver with degree  $j$ , is used to randomise burst errors. As an inner code we have chosen three binary codes, with different block length,  $n$ . Code No 1 is (5,4)(16,15) array code with  $n=80$ ,  $k=60$  and  $R=3/4$ . Code No 2 is (3,2)(3,2) array code with  $n=9$ ,  $k=4$  and  $R=4/9$ . Code No 3 is a cyclic (7,4,3) code with  $R=4/7$ . These codes provide us with different random error protection capability, which is related to guard space between burst of errors. To achieve an additional protection for bursty channels, we have implemented a majority logic encoder and decoder with degree of repetition  $i$ . That means, that each inner code is transmitted  $i$  times. Since length of the inner codes,  $n$ , is varying between  $n_3=7$  to  $n_1=80 \cdot i$ , the proposed technique provides an adaptive degree of protection for various types of channels.

At the receiver side, each incoming received segment of  $n$  digits is applied simultaneously to a majority logic gate. The majority logic gate compares the corresponding received digits, and chose the one which predominates. The output of the majority logic gate is fed into the inner decoder, which is matched with the inner encoder. To achieve additional energy gain, we have implemented a soft maximum likelihood decoding of array codes. Such a decoding technique was proposed recently [5] and allows performance improvement of array decoder.

## 2. Adaptive Encoders, Based on Concatenated Codes

## 2.1. Encoding of Reed-Solomon Codes.

As it was shown above, the proposed technique uses RS codes as an outer codes in the concatenated scheme. Reed-Solomon codes represent a very important and most widely used class of multi-level (non-binary) linear codes. They be viewed either as a sub-class of the BCH codes [5], or as a special class of Goppa codes [6].

An RS code over  $GF(q)$  ( $q$  always is greater than 2) is a BCH code of length

$$n = q - 1 \quad (1)$$

which allows correction of

$$t = \frac{n - k}{2} \quad (2)$$

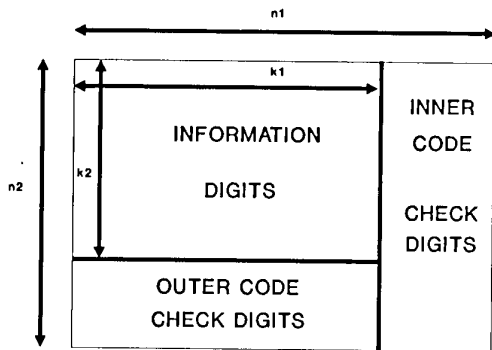


Fig.1. Block Diagram of a Concatenated Code Word

errors, where  $k$  is a number of information digits. Reed-Solomon codes are maximum distance separable (MDS) codes, since minimum Hamming distance  $d_{\min}$  is defined as

$$d_{\min} = n - k + 1 \quad (3)$$

and is equal to the maximum possible Hamming distance that an  $(n, k)$  code can have [6]. Therefore RS codes have highest possible minimum distance for their parameters and are very useful for correcting bursts of errors. For example, by choosing  $q=2^4$  and mapping into a binary representation, then the  $t$ -error-correcting RS code over  $GF(16)$  can be implemented as a linear code over  $GF(2)$ , which is capable of correcting any burst error pattern that does not effect more than  $t$  of the symbols in the original  $GF(16)$  version of the codeword.

The minimal polynomial of each element  $\alpha^i$  in case of RS codes is given as [7]

$$M^{(i)} = (x - \alpha^i) \quad (4)$$

and for a  $t$ -error-correcting RS code, the generator polynomial is defined as [7]:

$$g(x) = (x - \alpha)(x - \alpha^2) \dots (x - \alpha^{2t}) \quad (5)$$

For a chosen  $(15, 9)$  and  $(15, 7)$  RS codes over  $GF(16)$ , the generator polynomials are defined as follows:

$$\begin{aligned} g_{(15,9)}(x) &= (x - \alpha)(x - \alpha^2)(x - \alpha^3)(x - \alpha^4) \\ &\quad (x - \alpha^5)(x - \alpha^6), \quad t=3; \\ g_{(15,7)}(x) &= (x - \alpha)(x - \alpha^2)(x - \alpha^3)(x - \alpha^4) \\ &\quad (x - \alpha^5)(x - \alpha^6)(x - \alpha^7)(x - \alpha^8), \quad t=4. \end{aligned} \quad (6)$$

where the field elements of  $GF(16)$  must be expressed as polynomials.

## 2.2. Encoding of Array Codes.

Array codes were introduced by Elias [8] and have been widely used for both single and burst errors correction [9]. The essence of an array code is that the combination is based on a geometrical construction, the component codes are simple and decoding of array codes is relatively easy. The simplest array code is the row-and-column single parity check code, which is shown in Fig.3, and also is called a two-coordinate, bidirectional, bit and block

parity and has been widely used in data

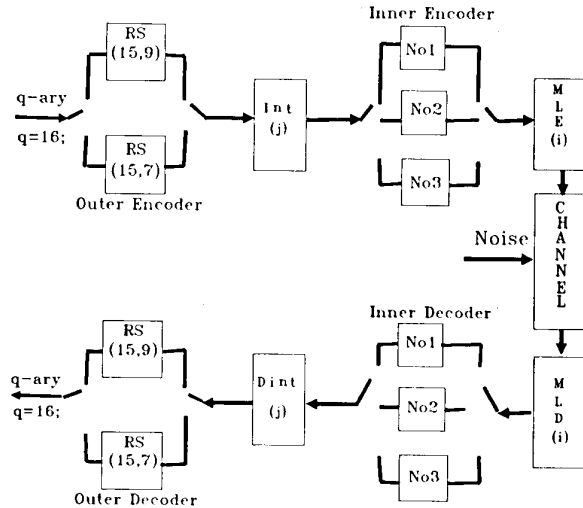
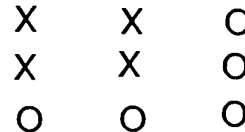


Fig.2. Block diagram of the concatenated technique.

transmission systems and computer memories [9]. Figure 3 illustrates an example for encoding of  $(3,2)(3,2)$  array code. The code may be square or rectangular and has parameters  $(n_1, n_2, k_1, k_2, d_{\min})$ , where  $(n_1, k_1)$  and  $(n_2, k_2)$  are row and column codes respectively, and minimum Hamming distance  $d_{\min}=4$ . These codes are easy and flexible to design and relatively simple to decode.

In this paper we show that array codes can be decoded with a low complexity, fast, trellis decoding algorithm, which provides maximum likelihood performance. We also introduce a simple procedure to construct the trellis diagram of any two-dimensional array code, and the algorithm is followed by a detailed example.



X - Information Digits

O - Parity Check Symbol

Fig.3. (9,4,4) Array Code

## 3. Decoding of Adaptive Concatenated Codes

### 3.1. Decoding of Concatenated Codes

As it follows from the block diagram of the proposed adaptive scheme, the decoding process consists of two steps. First decoding is done for each binary codeword as it arrives, and the corresponding check digits are removed (decoding of inner code). Then the  $n_2 \times k_1$  remaining symbols (Fig.1) are decoded according to the chosen RS code  $((15, 9)$  or  $(15, 7))$ . Therefore, every uncorrected error pattern at the output of the inner decoder will appear as a single error at the input of the outer decoder, since the outer decoder is a  $t$ -error ( $t=3$  or  $4$ ) correcting RS code. Thus all  $t$  error patterns of length not greater than  $n_2$  are correctable.

### 3.2. Decoding of Reed-Solomon Codes.

Since RS codes represent a class of BCH codes, the decoding procedure is similar to that for non-binary BCH codes: calculating the syndrome and computing the error locations and error values. The error location polynomial  $\gamma(x)$  and the error evaluator polynomial  $\omega(x)$  are defined as follows [8]:

$$\sigma(x) = \prod_{\beta \in B} (x - \beta) \quad (7)$$

$$\omega(x) = \sum_{\beta \in B} E_{\beta} \cdot \prod_{\substack{\gamma \in B \\ \gamma \neq \beta}} (x - \gamma)$$

and the Key equation for decoding of RS codes is given as follows [9]:

$$S(x) = \frac{\omega(x)}{\sigma(x)}, \quad \text{mod } G(x) = x^{2t} \quad (8)$$

Using the Key equation for decoding of RS codes, the decoding procedure can be outlined in five steps:

- (1) Calculate  $S_1, S_2, \dots, S_{2t}$ , from the received sequence;
  - (2) Find  $\sigma(x)$ , from the syndrome equations;
  - (3) Find the roots of  $\sigma(x)$  and hence the location of errors;
  - (4) Find  $\omega(x)$ , and also the values of the errors  $E_{\beta}$ ;
  - (5) Find the error pattern  $E = (E_0, \dots, E_{n-1})$ .
- The decoder of RS codes consists of the following four parts:
- (i) A buffer shift-register, with length between  $n$  and  $2n$ , depending on the speed of the decoder;
  - (ii) The syndrome calculator, which divides the incoming codeword by each irreducible factor of the generator polynomial.
  - (iii) A central Galois field processor, which calculates error location polynomials from syndromes.
  - (iv) An error location circuit, which finds the error pattern  $E = (E_0, E_1, \dots, E_{n-1})$  and corrects the errors when the erroneous digits leave the received word buffer.

### 3.3. Soft maximum likelihood decoding of array codes.

As it was shown in [10], array codes do not have the full power of block linear code of length  $n = n_1 n_2$ , and the conventional decoding algorithms [10] for array codes, do not make use of maximum power of the code and are not maximum likelihood decoding algorithms.

In this Section we show that array codes can be decoded with a low complexity, fast, trellis decoding algorithm, which provides maximum likelihood performance. These codes can be used effectively in combined coding and modulation (CCM) schemes for band-limited channels to give higher transmission rates than the same complexity conventional CCM schemes based on convolutional codes.

Trellis decoding was originally devised as a tool for decoding of convolutional codes [12], but it can also be used to decode block codes [13]. It has been shown by J. Wolf [13], that the trellis diagram of product code with symbols from  $GF(q)$  will have

$$N_s = \min[q^{k_1(n_2-k_2)}, q^{k_2(n_1-k_1)}] \quad (9)$$

states and can be constructed using the parity check matrix. However, if the size of array increases, the number of calculations, required to design a trellis diagram increases dramatically.

We show that the trellis diagram of any array code with symbols from  $GF(q)$ , where both row and column codes are single parity check codes, can be constructed easily. The number of states in this trellis diagram is given as:

$$N_s = q^{\min(n_1-1, n_2-1)} \quad (10)$$

The code can be square or rectangular in shape, and the trellis diagram can be obtained in the following manner [14].

1. Select the smaller of the two values  $n_1$  and  $n_2$  (say  $n_1$ ).
2. Choose the number of states  $N_s$ , and the trellis depth (number of columns),  $N_c$ , in the trellis diagram as:

$$N_s = q^{(n_1-1)}, \quad N_c = n_2 \quad (11)$$

3. Identify each state at depth  $p$ ,  $p = 0, 1, \dots, N_c-1$ , by a  $k_1$ -tuple  $q$ -ary vector,  $SP(A) = SP(a_1, a_2, \dots, a_{k_1})$ , where  $a_j = 0, 1, \dots, q-1$ , and  $j = 1, 2, \dots, k_1$ .

4. Identify the trellis branches which start and finish at depth  $p=0$  and  $p = N_c-1$ , as  $S_0(00\dots 0)$  and  $S_{n_2}(00\dots 0)$ , respectively.

5. The trellis branches at each depth  $p$ , which connect two states  $S_p(A)$  and  $S_{p+1}(B)$ , are labelled by a  $k_1$ -tuple  $q$ -ary vector  $C_p^A$ , which is determined in the following manner:

$$C_p^A = S_p(A) + S_{p+1}(B) \quad \text{mod } q \quad (12)$$

where  $A$  and  $B$  are all possible  $k_1$ -tuple  $q$ -ary vectors, and addition is on modulo  $q$ .

6. Each branch on the trellis diagram is labelled also with the second value  $D_p(A) = (a_1, a_2, \dots, a_{n_1})$ , which represents the output vector.

There are  $q^{(n_1-1)(n_2-1)}$  distinct paths through this trellis diagram, and each path corresponds to a unique codeword.

Example 1: Let the aim be to design the trellis diagram of the binary  $(9, 4, 4)$  array code, which consists of the  $(3, 2)$  row code and the  $(3, 2)$  column code.

1. Following the procedure, outlined above, we determine the number of states  $N_s = 4$ , and the trellis depth  $N_c = 4$ .

2. We identify each state at depth  $p$  ( $p=0, 1, \dots, 4$ ) by a 2-tuple binary vector  $S_p(a_1, a_2)$ , where  $a_i = 0, 1$ ,  $i=1, 2$ .

3. At depth  $p=0$  and  $p=4$  the trellis has only one state, namely  $S_0(00)$  and  $S_4(00)$  respectively.

4. The trellis branches at depth  $p=0$  are obtained as:

$$\begin{aligned} C_{00}^0(00) &= S_0(00) + S_1(00) = (00) \\ C_{00}^0(01) &= S_0(00) + S_1(01) = (01) \\ C_{00}^0(10) &= S_0(00) + S_1(10) = (10) \\ C_{00}^0(11) &= S_0(00) + S_1(11) = (11) \end{aligned} \quad (13)$$

and each state in second column,  $S_1(a_1, a_2)$ , is connected with the  $S_0(00)$  by one line, labelled according to (13). The set of transitions at next depth is obtained as follows:

$$\begin{aligned} C_{00}^1(00) &= S_1(00) + S_2(00) & C_{01}^1(00) &= S_1(01) + S_2(00) \\ C_{00}^1(01) &= S_1(00) + S_2(01) & C_{01}^1(01) &= S_1(01) + S_2(01) \\ C_{00}^1(10) &= S_1(00) + S_2(10) & C_{01}^1(10) &= S_1(01) + S_2(10) \\ C_{00}^1(11) &= S_1(00) + S_2(11) & C_{01}^1(11) &= S_1(01) + S_2(11) \end{aligned}$$

$$\begin{aligned} C_{10}^1(00) &= S_1(10) + S_2(00) & C_{11}^1(00) &= S_1(11) + S_2(00) \\ C_{10}^1(01) &= S_1(10) + S_2(01) & C_{11}^1(01) &= S_1(11) + S_2(01) \\ C_{10}^1(10) &= S_1(10) + S_2(10) & C_{11}^1(10) &= S_1(11) + S_2(10) \\ C_{10}^1(11) &= S_1(10) + S_2(11) & C_{11}^1(11) &= S_1(11) + S_2(11) \end{aligned}$$

(14)

and each state in the third column is connected to the previous set of states by 4 lines, which are defined according to (14). Following a similar procedure, the trellis branches at the last step will be obtained as follows:

$$\begin{aligned} C_{00}^2(00) &= S_2(00) + S_3(00) = (00) \\ C_{01}^2(01) &= S_2(01) + S_3(00) = (01) \\ C_{10}^2(10) &= S_2(10) + S_3(00) = (10) \\ C_{11}^2(11) &= S_2(11) + S_3(11) = (11) \end{aligned} \quad (15)$$

and state  $S_3(00)$  is connected to each state in the third column by one branch, which are labelled according to (15). The design of such a trellis diagram is very simple, and is shown in Fig.4.

The rate of array codes can be increased by adding columns (or rows) to the two-dimensional array. If the length of one

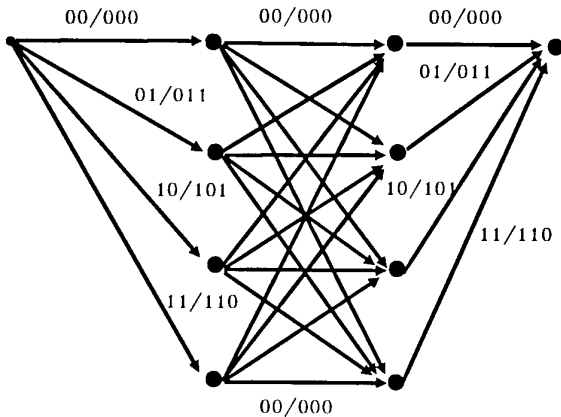
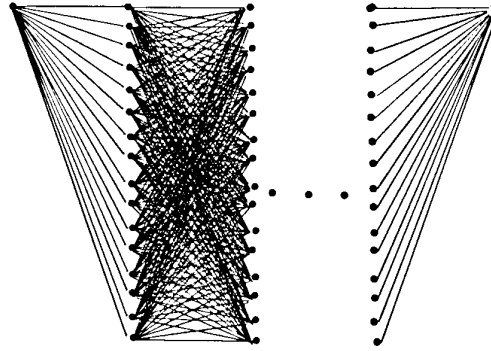


Fig.4. Trellis Diagram of (3,2)(3,2) Array Code

dimension is kept constant (assume the number of rows is fixed), the number of states of the trellis diagram will be fixed, and the code rate can be increased by appending more columns to the trellis. When the number of trellis states is fixed the increase in the depth of trellis adds a little complexity to the decoding procedure. Figure 5 illustrates the trellis diagram of such a (5,4)(16,15) array code.

Fig.5. Trellis Diagram of (5,4)(16,15) Array Code



Since the trellis diagram of an array code has been designed, one can proceed the soft maximum likelihood decoding of the code. The following example illustrates the procedure for the (3,2)(3,2) code.

Example 2. Let a transmitted codeword and corresponding received message for the (3,2)(3,2) code, denoted  $C$  and  $C^*$  respectively, be given in the array format as shown in Fig.6.

Because the minimum distance of this array code is four, with hard decision conventional decoding, the four errors indicated in  $C^*$  can not be corrected. The trellis decoding algorithm provides maximum likelihood performance and, with the utilisation of the unquantised data of the received message all four error can be corrected. The surviving path is obtained by calculating all the Euclidean distances to each state and choosing the one with the minimum value. The decoded codeword is shown in Fig.7.

$$\begin{array}{ccc} 0 & 1 & 1 \\ C = & 1 & 0 & 1 \end{array} \quad \begin{array}{ccc} \underline{0.2} & \underline{0.4} & 0.4 \\ C^* = & \underline{0.3} & 0.1 & 0.9 \\ & 1.0 & 0.9 & \underline{0.6} \end{array}$$

Fig.6. Transmitted and received codewords

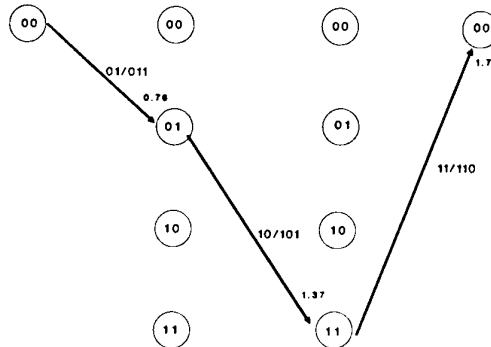


Fig.7. The surviving path after MLD

#### 4. RESULTS AND CONCLUSIONS

A computer simulation study for the above described techniques was carried out. The system was modelled and simulated using "C" language on an existing Sun-workstation. Figures 8-13 present computer simulation results for the proposed concatenated technique. As it follows from these results, repetition of inner code allows improvement of the performance under low  $E_b/N_0$ . However under higher  $E_b/N_0$  the bit error ratio is increased.

The system, which uses shorter inner code provides better performance under additive white Gaussian Noise (AWGN), however, the system with the longer inner code provides more reliable protection from the long burst of errors.

Fig.8. Adaptive Concatenated Code  
(15,9) RS + (9,4) Array Codes

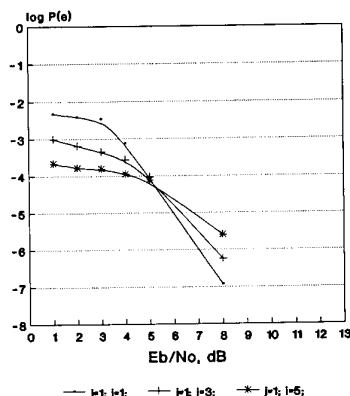


Fig.9. Adaptive Concatenated Code  
(15,9) RS + (7,4) Cyclic Codes

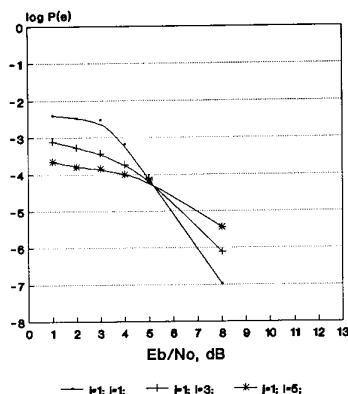
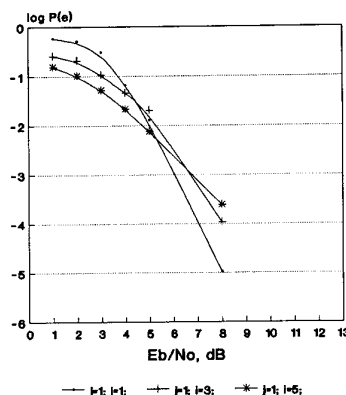


Fig.10. Adaptive Concatenated Code  
(15,9) RS + (5,4)(16,15) Array Codes



- system.-Proceedings of the "IEE Conference on HF Radio", Edinburgh, July, 1991.
3. Darnell M., Honary B., Vongas G. Adaptive communication system design for HF/VHF Multiple-mechanism propagation paths.- Proceedings of the MILCOM'92", October 1992.
  4. Forney G.D. "Concatenated Codes", MIT Press, Cambridge, Mass. USA, 1966.
  5. Reed I.S., Solomon G. Polynomial codes over certain finite fields.- SIAM-8, 1960, pp.300-304.
  6. MacWilliams F.J., Sloane N.J.A. The theory of error-correcting codes.- North Holland Publishing Company, 1977.
  7. Blahut R.E. Theory and Practice of Error Control Codes. Addison-Wesley Publishing Company, 1983.
  8. Sugiyama Y., Kasahara M., Hirasawa S., Namekawa T. A method for solving Key equations for decoding Goppa codes. - "Information and Control", v.27, 1975, pp.87-89.
  9. Berlekamp E.R. Goppa codes. - "IEEE Transactions on Information Theory", vol.IT-19, 1973, pp.590-592.
  10. Elias P. Error free coding. - "IEEE Transactions", vol.IT-4, 1954, p.p.29-37.
  11. Farrell P.G. Array codes. - "Algebraic Coding Theory and Applications". Ed. G.Longo, Springer-Verlag, 1979, p.p.231-242.
  12. Viterbi A.J. Convolutional codes and their performance in communication systems. - "IEEE Transactions on Communications", col.COM-19, N:5, October 1971, p.p.751-772.
  13. Wolf J.K. Efficient maximum likelihood decoding of linear block codes using a trellis.- "IEEE Transactions on Information Theory", vol.IT-28, No 2, 1982.
  14. Honary B., Markarian G., Darnell M. Trellis decoding technique for array codes.- Proceedings of the "Eurocode'92", Udine, Italy, October 1992.

#### REFERENCES

1. Lin S., Costello D.J., Miller M.J. Automatic Repeat Request error-control schemes.- "IEEE Communication Magazine", 1984, Vol.22, p.p.5-17.
2. Bate S., Honary B. Improved error protection techniques for HF communication

Fig.11. Adaptive Concatenated Code  
(15,7)RS & (5,4)(16,15) Array Codes

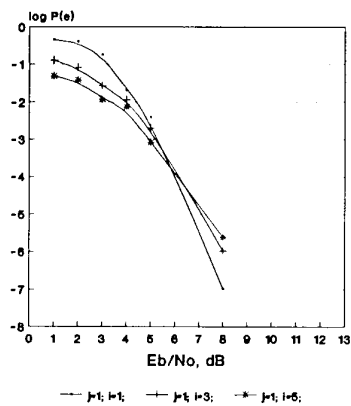


Fig 13. Adaptive Concatenated Code  
(15,7) RS + (7,4) Cyclic Codes

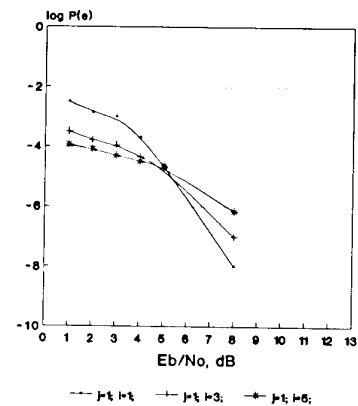
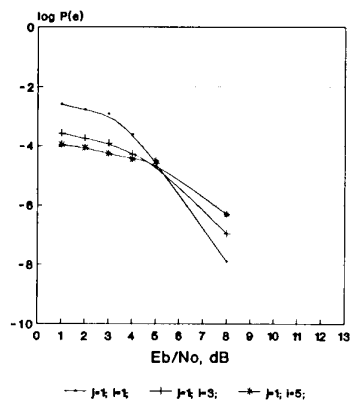


Fig 12. Adaptive Concatenated Code  
(15,7) RS + (9,4) Array Codes





## PASSIVE MONITORING FOR AUTOMATED MMPP COMMUNICATION SYSTEMS

N G Riley  
Hull-Lancaster Communications Research Group  
Department of Electronic Engineering  
University of Hull  
HULL, HU6 7RX  
United Kingdom

- Overall statistical occupancy measurements of the spectrum

### 1. SUMMARY

A recently completed study of passive sensing techniques for hf communication systems has shown that these sensing techniques can yield data which may be of use in the control of adaptive hf communication systems. The aim of this paper is to review work carried out to date on these techniques and to examine the feasibility of applying similar techniques to radio systems utilising higher carrier frequencies, up to around 200MHz, where many propagation modes other than ionospheric skywave may exist.

Whilst inputs for the control of adaptive radio systems may be derived from a number of sources, many techniques, such as pilot-tone soundings and the transmission of training sequences, involve radiation of signals which may be undesirable in a tactical situation. System control information may also be derived by monitoring other signals which are already present in related parts of the radio spectrum, allowing more covert operation and avoiding unnecessary pollution of the radio spectrum.

Derivation of such control information for use in hf systems has been studied in some detail, utilising the following types of radio signals existing in the hf band:

- Swept frequency sounder signals radiated by other uses of the hf spectrum
- Broadcast signals
- Standard Time signals
- Meteorological data signals (RTTY)

Some of these techniques would also be applicable to the multimechanism case, provided that the more complex propagation inversion, which is due to the greater range of propagation mechanisms available, can be taken into account. Additional, higher frequency, sources of RF energy which may provide data through passive monitoring, include aeronautical navigation beacons, amateur beacons and various types of radar signals. Use may also be made of low-orbiting satellite signals, although these present tracking problems in terms of doppler shift and give data mainly related to ionospheric scintillation and hence magnetic storm effects.

### 2. INTRODUCTION

A fundamental requirement for successful operation of an automated radio communication system in the HF/VHF bands is that the system has access to information describing both the current channel and alternative candidate channels. Conventionally, this information may be provided by several real-time channel evaluation (RTCE) methods [1] or by the use of off-line or embedded propagation prediction codes [2,3].

In the case where only a single channel is available or where interest is confined to the current operational channel, measures of the quality of the channel such as error rate, pseudo error rate or signal to noise ratio may be derived to drive automated procedures which select appropriate data rate, modulation format, error control protocol etc.

Where a small number of alternative radio channels exist and where propagation conditions are reasonably well behaved the above traffic-derived measures may be supplemented by results from propagation modelling codes coupled with some form of channel polling in order to optimise traffic throughput with reasonable efficiency whilst minimising the channel control processing overhead.

However, in the more typical case, where there may be many candidate channels spread over a large frequency range with diverse propagation conditions, channel polling becomes inefficient and propagation models less reliable, resulting in the increased use of active sounding to determine channel conditions. These conditions typically prevail in the HF band near to the maximum usable frequency (MUF) particularly in the high latitude region and in the low VHF band where propagation range is often an irregular function of carrier frequency, due to the availability of different propagation modes and mechanisms at various frequencies. In these conditions considerable system resource, in terms of time, digital signal processing (DSP), transmitted power and spectrum, is used in the channel management task. The increased use of sounder transmissions, as well as posing a tactical disadvantage, leads to pollution of the radio spectrum with resulting loss of overall channel capacity.

The aim of the work described in this paper is to attempt to reduce the system resource devoted to active channel sounding by monitoring radio signals of opportunity in the bands of interest and, by using background knowledge about the likely sources of transmission, to derive channel propagation data which can be used to either eliminate active sounding or to direct its use in a more productive manner.

To this end the following issues have to be addressed:

*What data can be derived from radio signals which are designed for other purposes?*

Some signals, such as swept-frequency sounder signals, are more useful than others. MUF data may be derived if several frequencies are available. Channel impulse response may be derived if the signal can be

processed to appear impulsive. Signals whose modulation type is known may yield error rate and hence signal-to-noise information.

*Can the signals be identified uniquely as to their transmission location?*

Swept-frequency sounder signals, time standard signals and some data signals can easily be identified. Broadcast signals require more care, since the same programme may be transmitted from a number of possible sites. Use of a knowledge-base and previous history can eliminate this problem to some extent.

*How can the data derived be applied to the control of the wanted system?*

Use may be made of embedded prediction models which may be updated on the basis of data derived from passive monitoring. Algorithms describing spatial correlation of effects such as MUF depressions under storm and non-storm conditions [4,5] must be used.

These issues will be addressed in detail in the body of the paper.

A central assumption is that a DSP-based system architecture is used, such as that described in [6]. A brief review of such a system architecture, adapted to include passive monitoring, is given in section 3 of this paper.

Studies have been carried out [7,8,9] to assess the usefulness of passive sensing techniques for provision of system control data for HF radio systems. Several types of radio signals existing in the hf band were studied to identify control information which could be extracted from each type of signal. These signals along with the techniques used and typical results are described in section 4.

With the introduction of multi-role radio systems covering the frequency range up to 200MHz and beyond [6] the channel evaluation and control function must also be extended to cover this extended frequency range. The application of passive monitoring techniques to these frequencies is investigated in section 5.

### 3. SYSTEM ARCHITECTURE FOR AUTOMATED MMPP

## COMMUNICATION SYSTEM UTILISING PASSIVE MONITORING

A simplified view of the architecture of an automated MMPP communication system utilising passive monitoring is shown in Figure 1. Each section is described briefly as follows:

### *Computer & Control*

This central part of the system consists of computer hardware which allows software implementation of many of the parts of the system described below, including modems, error control, signal acquisition and detection as well as system control. In the implementation under development by the Hull-Lancaster Communications Research Group (HLCRG) [6,10] the central computing and control function is performed by a 486-based personal computer supported by a DSP card using an AT&T DSP230C processor. The DSP card handles signal acquisition and processing including modem implementation whilst the PC runs propagation models, the knowledge base and performs system control. The system control function includes the allocation of computing and DSP resource to suit prevailing propagation conditions.

### *Monitoring Receiver and Traffic Transmitter/Receiver*

The monitoring receiver, controlled by the central computer, performs the passive monitoring task. Whilst it is not essential to include a dedicated monitoring receiver, the additional cost can probably be justified since the traffic transceiver will then always be free to pass traffic. Additionally, the monitoring receiver can then spend all of its spare time gathering statistical data which may contribute to the propagation data as described in section 4(v). In the HLCRG implementation the receivers are Watkins-Johnson type WJ-8607 with computer control, whilst the transmitter consists of a computer controlled custom-built ISB modulator and Kalmus RF amplifier.

### *Propagation Models*

Simple propagation models may be included for each expected propagation mechanism. These models allow interpolation to be carried out between data acquired from passive monitoring in order to match the

operational path conditions. The models include, for example, data on spatial correlation distance for MUF depressions, frequency/range/signal strength variation for tropospheric scatter and reflection as well as CCIR SUP252-based algorithms [11] for HF skywave propagation.

### *Frequency Allocations / Knowledge Base*

A table of frequency allocations is included in order that the monitoring receiver can perform statistical measurements as described in section 4(v). The knowledge base includes historical information on transmissions which can provide useful passive monitoring data including transmitter locations, transmission frequencies and schedules. The knowledge base will also contain updated decision weighting which is determined by the type of data provided by the monitored transmission, reliability data etc.

### *Own System Parameters*

Parameters of the system in use are included in order that passive monitoring data can be extrapolated to the operational system. Parameters include transmitter power / antenna gain, modulation type, geometry of the desired path etc.

### *Other Sensors*

In addition to passive monitoring of radio transmissions it may be possible to incorporate additional sensors of the type used in conventional short-term propagation forecasting, at a base, or transportable/deployable station. Work undertaken by the HLCRG has indicated that some of these sensors can be made in a cost-effective manner. Sensors may include:

**Magnetometer** - A low cost three-axis fluxgate magnetometer has been designed, which with suitable alignment can provide magnetic storm information, sudden storm commencements etc giving a predictive element to MUF calculations and warning of PCA events.

**Solar Radiometer** - Although more difficult to implement than the magnetometer, this device can in principle provide warnings of Shortwave Fadeouts and longer term forecasting of ionospheric storms.

*VLF Phase Recording* - Although requiring implementation of a separate receiver, this sensor can give indications of ionospheric height variation and resulting MUF effects by measuring the stability of the received phase of Omega navigation transmissions, which have the advantage of almost world-wide coverage.

#### 4. PASSIVE MONITORING SIGNALS AND TECHNIQUES - HF CASE

Signals from which systems control data may be derived by passive monitoring are described briefly along with comments on some of the processing techniques used:

##### *Swept frequency Sounder Signals*

Swept frequency sounding signals [12] are radiated by several administrations worldwide. A receiver has been developed by HLCRG based on a low cost computer controlled receiver with signal detection and analysis implemented on a DSP card. This offers a very cost effective way of obtaining data about the state of the ionosphere [13]. Work has subsequently been undertaken within the group to refine the technique and allow the simultaneous derivation of several ionograms. An example of an ionogram produced using this receiver is presented in Figure 2, for a path from Norway to Hull. An indication of the received signal strength is also shown at each frequency. Figure 3 shows a series of ionograms derived at 15-minute intervals from which short-term changes in propagation can be deduced. A simple algorithm was implemented to extract Maximum Observed Frequency (MOF) and Lowest Usable Frequency (LUF) from these ionograms. Left running as a background task, the monitor can produce plots such as that shown in Figure 4, which can be used to calibrate propagation models used to extrapolate to the operational path and frequency.

##### *Monitoring of Broadcast Signals*

Several types of information may be derived from the monitoring of broadcast signals. The most useful and simplest to derive concerns the time at which the broadcast frequency is observed to be just equal to the MUF for the path between the observer and the broadcast antenna. In particular, monitoring of a suite

of broadcast frequencies, for example 3, 6, 9 & 12 MHz from Berne, Switzerland, can as shown in Figure 5, yield data describing the variation of MUF versus time which can then be used to update embedded ionospheric models.

Signal strength information can also be derived which can be compared with previous data to determine channel quality. The use of measurements of frequency accuracy of the carrier was investigated and it was shown that such data may be of use in determining rate of change of effective reflection height, although this technique was not implemented fully.

The disadvantages of broadcast station monitoring are mainly associated with the difficulty of identifying the source of transmission with a good degree of certainty. However, experience has shown that certain broadcast stations are reliable for this purpose.

##### *Monitoring of Time Standard Signals*

Monitoring of time standard signals can provide similar data as that derived from broadcast signals. The time standard signals are, however, more reliable insofar as their source is often known more accurately and they are often available for greater periods of time. Again, suites of frequencies are often available eg 5, 10, 15, 20 and 25 MHz transmitted from Moscow as shown in Figure 6.

##### *Data links of various types*

In the UK the meteorological office have a number of radio teletype links supplying data from monitoring stations to the receiver station at Bracknell. Since the form of the transmitted data is known, to a certain extent, it is possible to demodulate the data using a DSP-implemented demodulator and extract error rate as an indication of channel quality. This technique has been successfully demonstrated and may be applied to a variety of reliable data links.

##### *Statistical Occupancy Measurements*

Wong et al [14] have shown that if the HF spectrum is sampled statistically across individual user bands (eg Broadcast, fixed services etc) the MUF characteristics can be determined if enough bands are available. It

has been shown that if enough sources are available it becomes possible to make a reasonable estimate of the average MUF for 4000km paths centred on the receiver site. The possibility of updating embedded predictions using MUF data derived in this way has been investigated. A computer-controlled HF monitor was constructed using an amateur-grade receiver. Typical "instantaneous" occupancy plots for the fixed services bands for night and day are shown in Figure 7.

#### *Use of passive monitoring data in system control*

Data derived from passive monitoring may be used to update an embedded prediction model, as illustrated in Figure 8, which may then be used to extrapolate parameters of the desired propagation path. Whilst extrapolation may be carried out in two dimensions using simple geometric considerations, due account must be taken of established data describing the changing spatial correlation length of ionospheric disturbances under various conditions [4,5]. Correlation may be carried out in real time, or on time series of historical data gathered by the system as illustrated in Figure 9. There is evidence that the degree of correlation of deviations of MUF from long-term predictions between various transmitters may yield data on storm conditions, but this has not been investigated within this study.

### **5. EXTENSION TO MMPP PROPAGATION IN THE 2-200 MHz FREQUENCY RANGE**

It is anticipated that many of the techniques described above would also be applicable to the multimechanism case, although the determination of the "inverse propagation" would in some cases be more complex due to the greater range of propagation mechanisms available.

Additional, higher frequency, sources of RF energy are available including aeronautical navigation beacons, amateur beacons and various types of radar signals. Use may also be made of low-orbiting satellite signals, although these present tracking problems in terms of doppler shift and give data mainly related to ionospheric scintillation and hence magnetic storm effects.

Data extracted from such monitoring must be related to prevailing propagation conditions in order that meaningful extrapolation to operational paths and frequencies may be performed.

A recent study carried out by the HLCRG [15,16] has shown that, in the low VHF band, signals propagate to ranges of up to 400km with lower loss than would be expected, suggesting a tropospheric reflection mechanism. Figure 10 shows the typical long-term variation of received signal whilst Figure 11 shows three distinct types of fading encountered regularly on such propagation paths at 47MHz. Such fading information may be used to determine optimum system parameters such as data rate and error control scheme. Further work is needed to characterise this propagation mechanism, particularly in terms of long-term spatial coherence length. The mechanism appears to be of significant importance to MMPP systems since it prevails in situations where the dominant mode is usually perceived to be meteor-burst. However, this mechanism lacks the uniqueness of path associated with meteor-burst and, unless recognised as such, could compromise any assumed anti-jam capability of systems operating over these path lengths.

### **6. CONCLUSIONS**

Studies carried out to date by HLCRG have shown that, in the HF case, passive monitoring may yield data of use in automated channel selection for adaptive radio systems. Further work is required to establish whether or not similar techniques can be used in the upper part of the MMPP propagation band, above about 50MHz. It is appreciated that many of the ideas described in this paper will not be applicable in a large scale conflict situation since many transmissions will be discontinued and many others will appear for which historical data is not available. However, it is felt that in normal circumstances the techniques of passive monitoring can be of use in aiding channel selection in automated radio communication systems.

### **7. ACKNOWLEDGEMENTS**

The Author gratefully acknowledges the support for this work given by GEC-Marconi

Communication Systems, Chelmsford and the Defence Research Agency, Farnborough.

## 8. REFERENCES

1. Darnell, M., "Real Time Channel Evaluation", AGARD LS-127 on "Modern HF Communications".
2. Darnell, M., "Embedded real-time channel evaluation techniques", AGARD LS-145 on "Propagation impact on modern HF communication system design", April 1986.
3. Uffelman, D.R. et al, "Real-time update of two HF channel evaluation models by oblique sounding", Report No 5246, Naval Research Lab., Washington D.C., 1984.
4. Milsom, J.D., "Frequency management of hf sky-wave circuits in Europe", Communications & Broadcasting, Vol.7, No.3, p23-30, 1982.
5. Davies, K. and Rush, C.M., "High-frequency ray paths in ionospheric layers with horizontal gradients", Radio Science, Vol.20, No.1, p95-110, 1985.
6. Darnell, M., Walker, P. and Vongas, G., "A MMPP communication system for the frequency range 2-200 MHz", AGARD Symposium on "Multiple Mechanism Propagation Paths (MMPPs) Their characterisation and influence on system design", Rotterdam, October 1993.
7. Masrani, K. and Riley, N.G., "Use of passive monitoring techniques in HF radio systems", IEE HF Systems and Techniques Conference, 1991.
8. Masrani, K. and Riley, N.G., "Passive sensing of radio signals in automated HF systems and the updating of off-line prediction models", IEE Antennas and Propagation Conference, 1991.
9. Masrani, K. and Riley, N.G., "Passive monitoring of HF radio signals in determining multipath", IEE Colloquium Digest 1990/2.
10. Gallagher, M. and Darnell, M., "Adaptive architectures for radio communication systems", 3rd Bangor Symposium on Communications, University College of North Wales, May 1991.
11. Dick, M.I. and Miller, B.H., "Microcomputer-based method for the estimation of HF radio-circuit performance", Proc. IEE Fifth International Conference on Antennas and Propagation, IEE CP-274, York, 1987.
12. Barry, G.H. and Fenwick, R.B., "Techniques for real-time hf channel measurement and optimum data transmission", AGARD CP-173, "Radio systems and the ionosphere", Athens, 1975.
13. Jowett, A.P., Darnell, M. and Riley, N.G., "Passive monitoring of chirpsounder transmitters as an aid to HF frequency management", IEE Colloquium Digest 1989/33.
14. Wong, N.F., Gott, G.F. and Barclay, L.W., "HF spectral occupancy and frequency planning", Proc IEE, Vol 132, Part F, No 7, 1985.
15. Melton, D., Riley, N.G. and Darnell, M., "A model for trans-horizon propagation in the low-VHF band", Proc. IEE Eighth International Conference on Antennas and Propagation, IEE CP-370, Heriot-Watt University, UK, 1993.
16. Riley, N.G., Darnell, M. and Vongas, G., "Modelling and simulation of HF/VHF MMPPs", AGARD Symposium on "Multiple Mechanism Propagation Paths (MMPPs) Their characterisation and influence on system design", Rotterdam, October 1993.

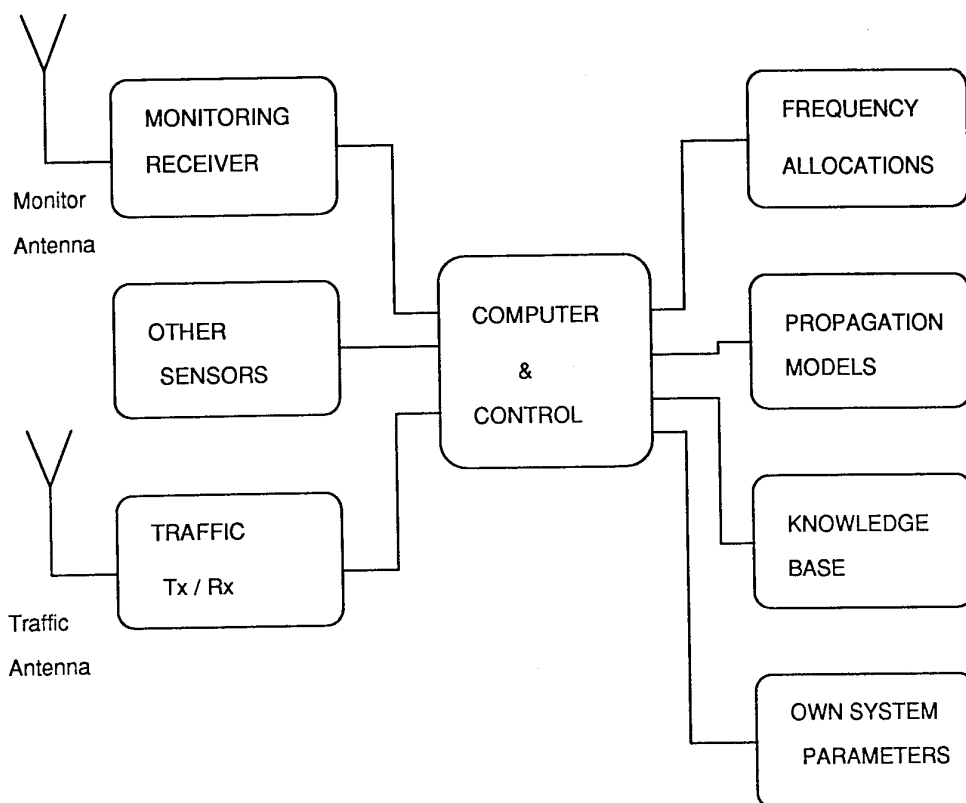


Figure 1: Architecture of an automated MMPP Communication system

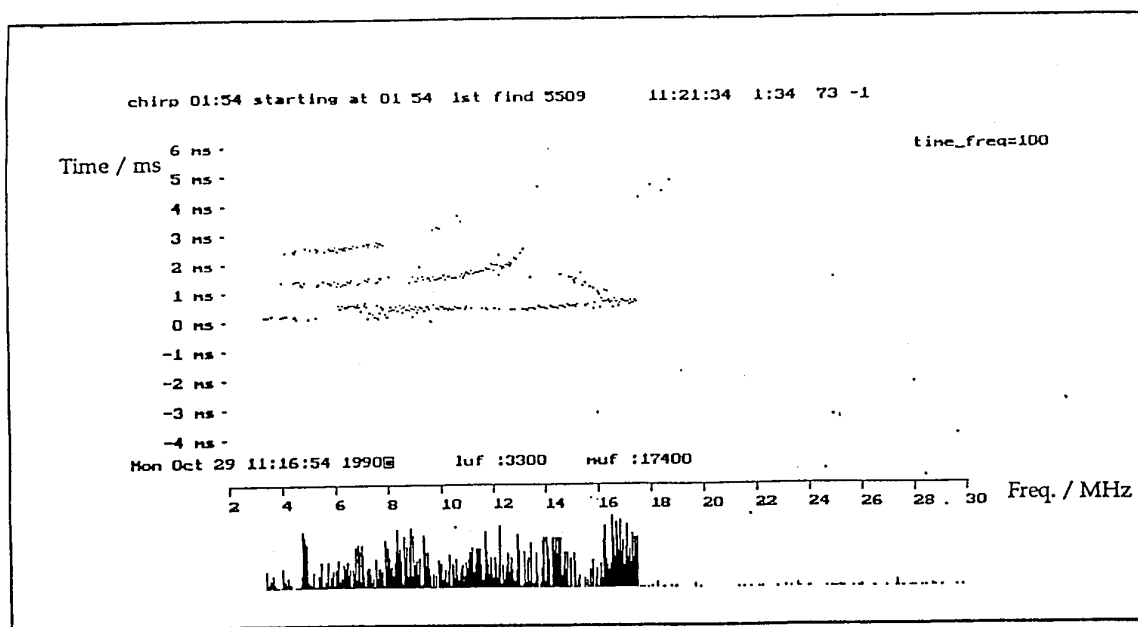


Figure 2: An example of an oblique ionogram received using PC/DSP/ICOM Rx  
Path: Norway to Hull, October 29th 1990, 11:16:45

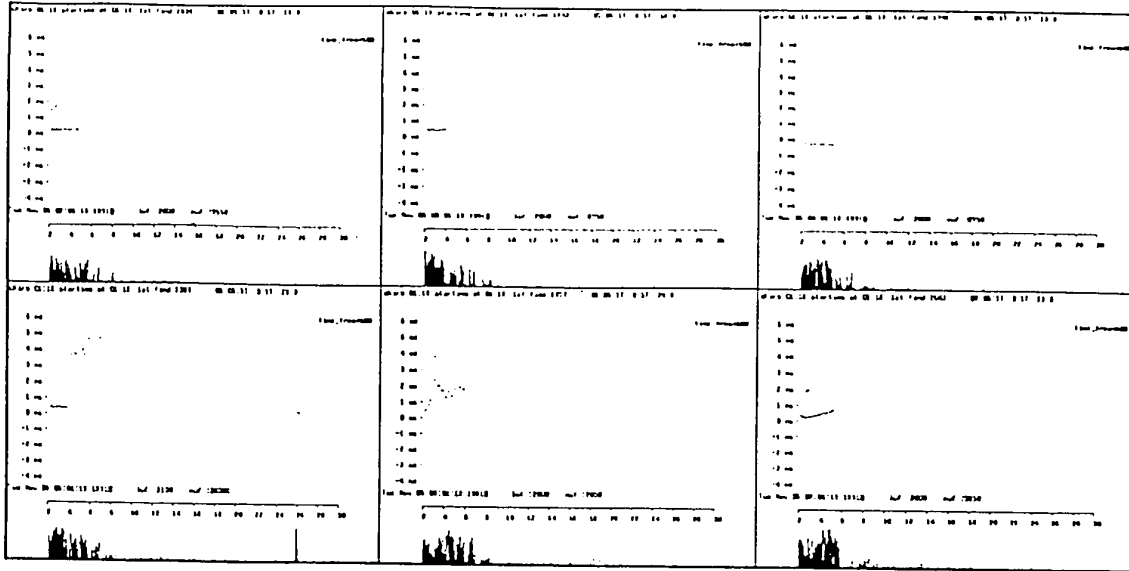


Figure 3: Typical set of oblique ionograms measured at 15-minute intervals

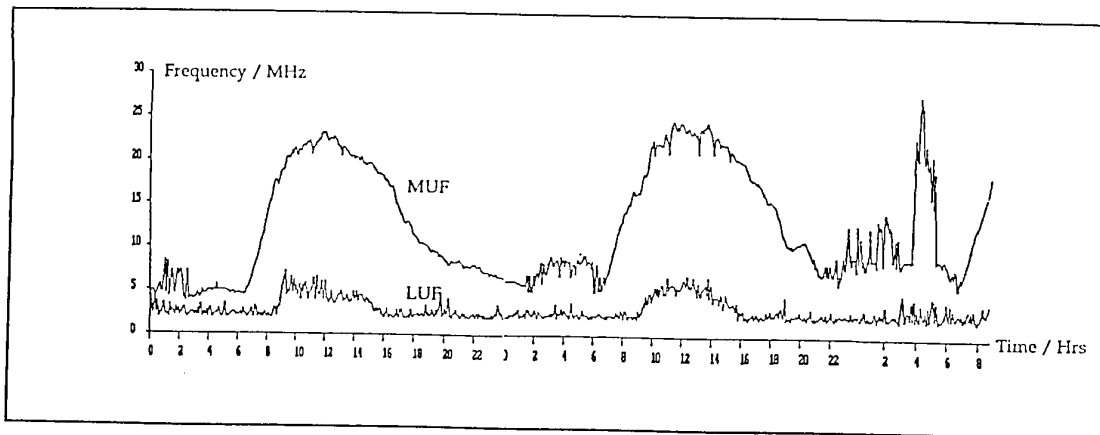


Figure 4: MUF plot derived from reception of swept-frequency sounder signal every 15 minutes over a two-day period.  
Path: Oslo to Hull.



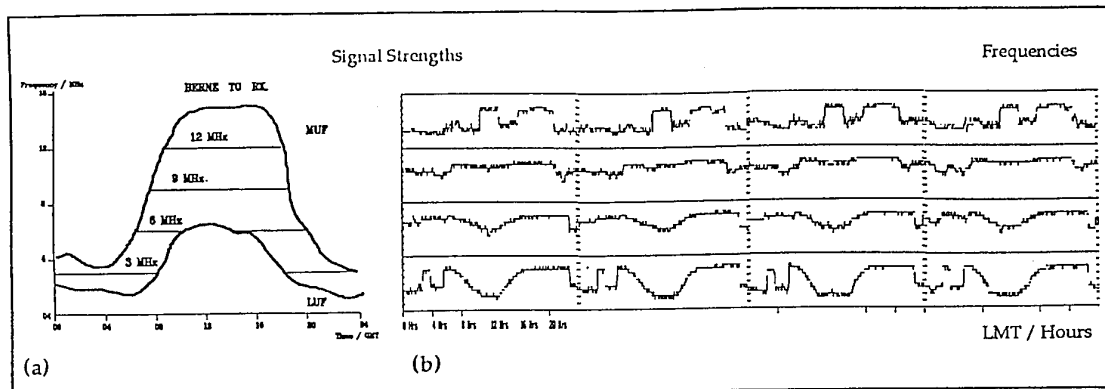


Figure 5(a): shows time during which broadcasts on a number of frequencies may be received, as governed by propagation conditions.

Figure 5(b): shows measured signal strength from Swiss Radio International throughout a four-day period.

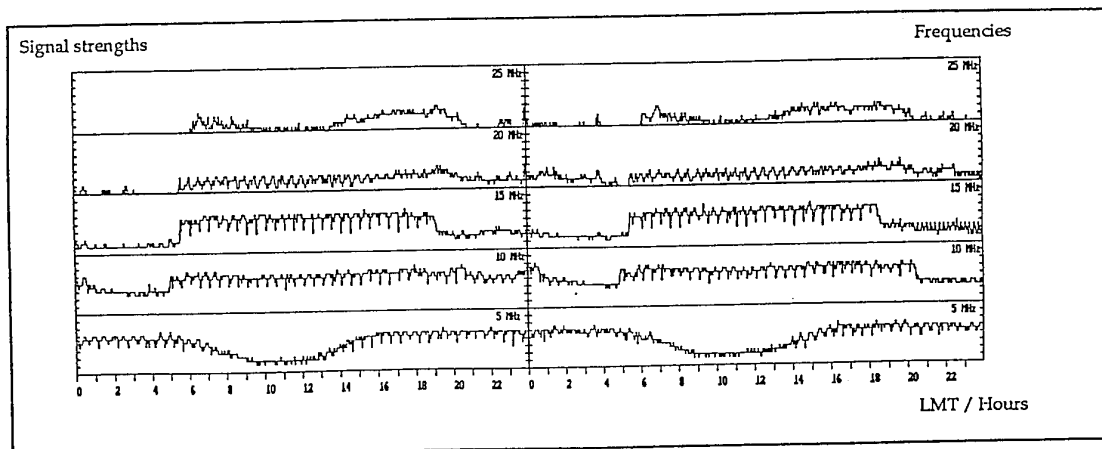


Figure 6: Measured signal strengths from the Standard Time Signal transmitted on various frequencies from Moscow. MUF effects may be noted.

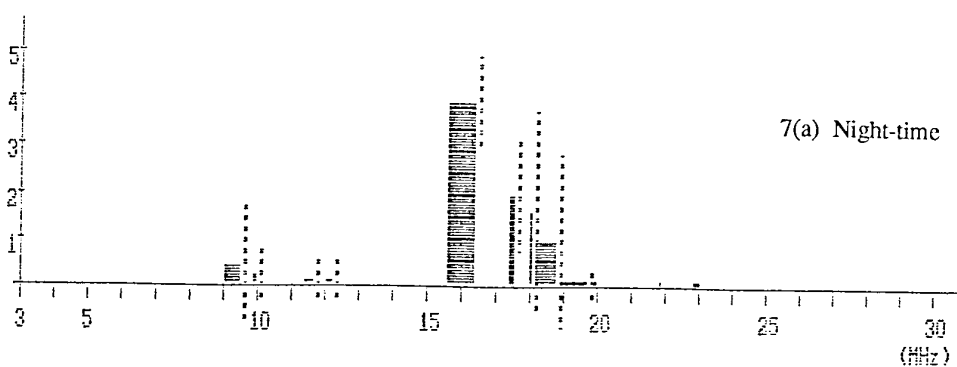
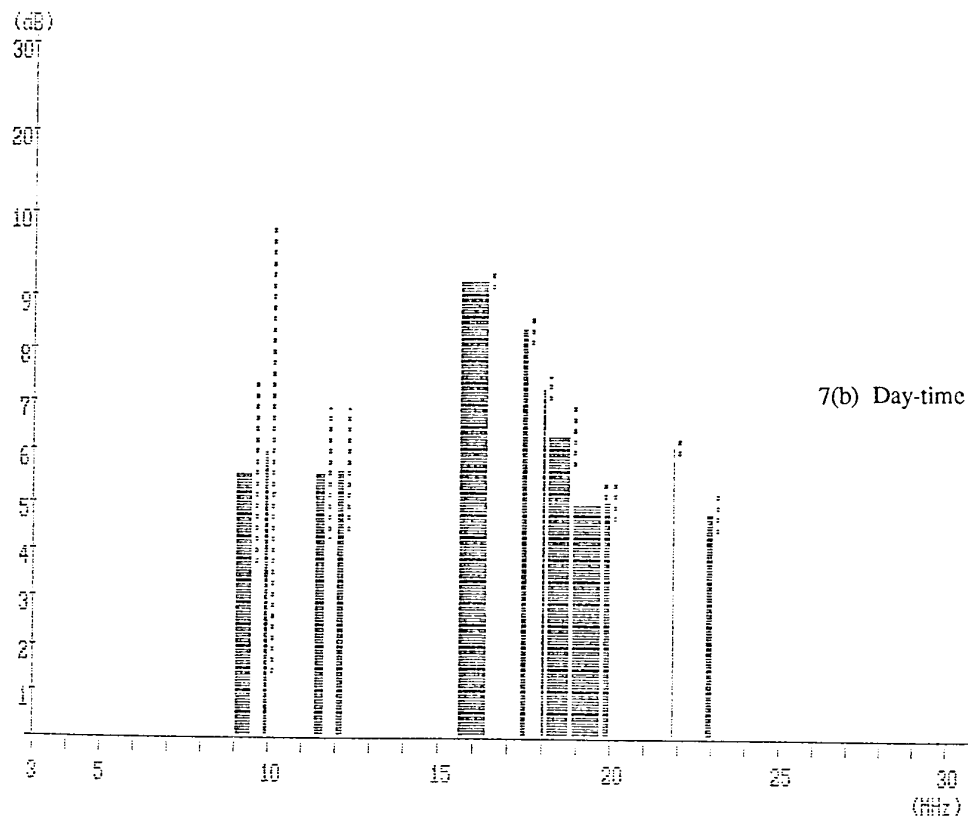


Figure 7: "Instantaneous" occupancy plots for the Fixed Service bands.

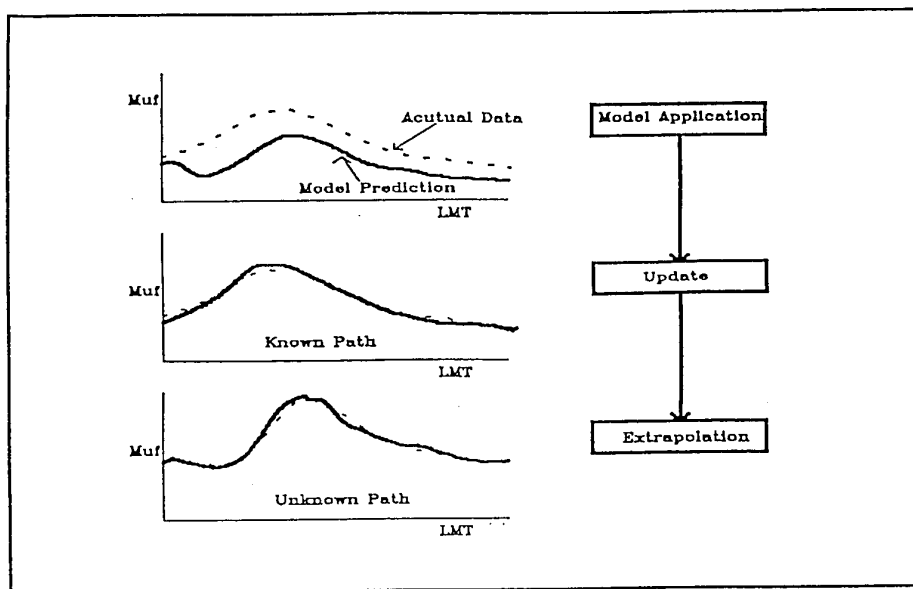
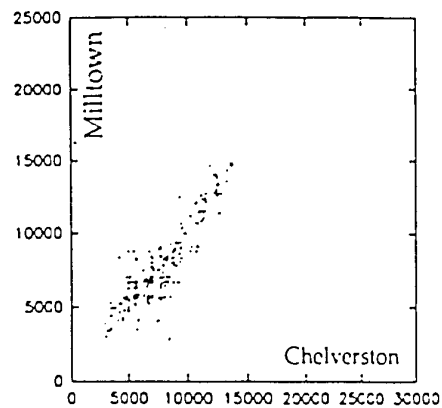
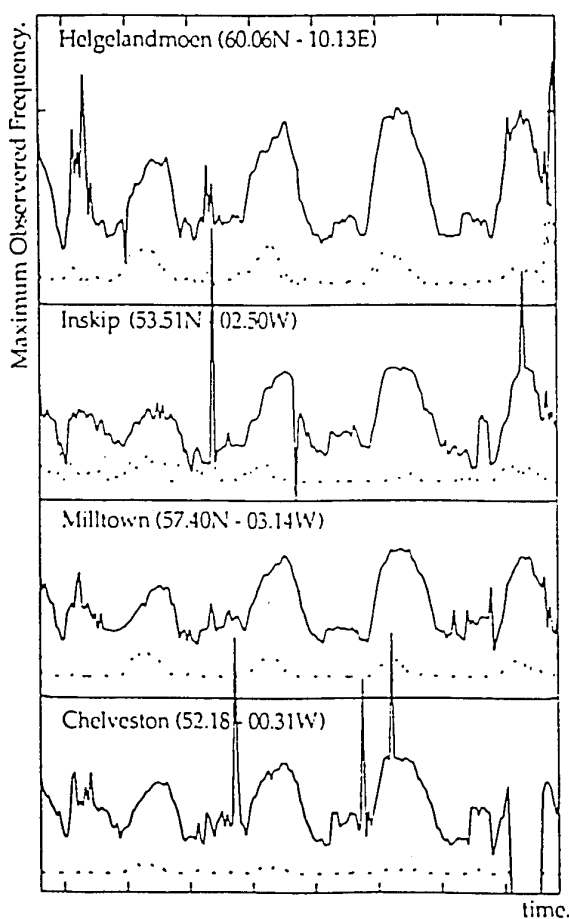


Figure 8: The principle of updating embedded prediction models



Scatter plot of Chelveston and Milltown MOFs.

	Chelveston	Norway	Inskip
Milltown	0.708	0.767	0.774
Inskip	0.698	0.677	-
Norway	0.612	-	-

Figure 9: Measured diurnal variations of MOF together with correlation coefficients

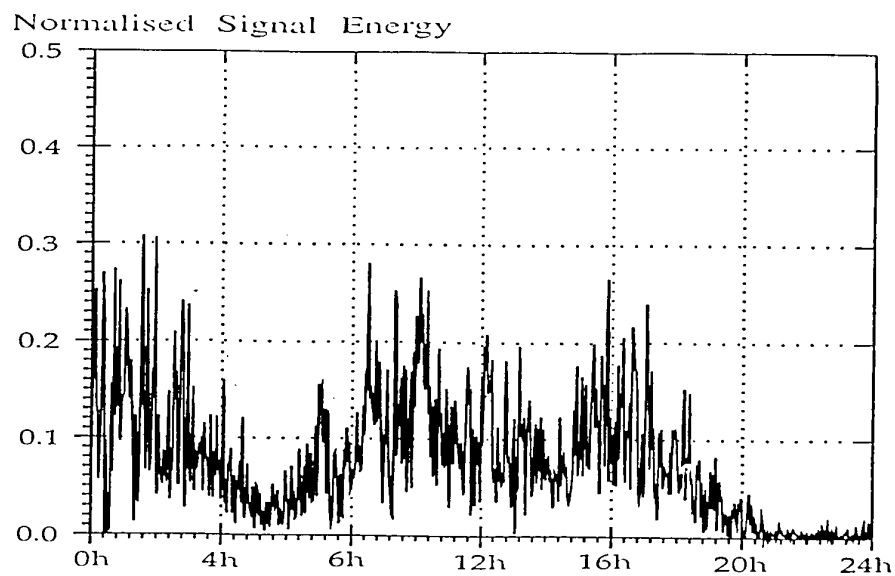
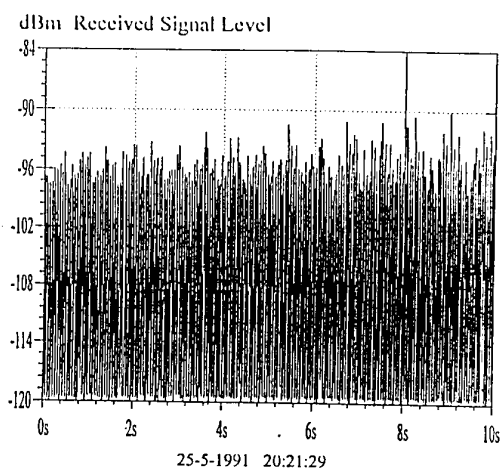
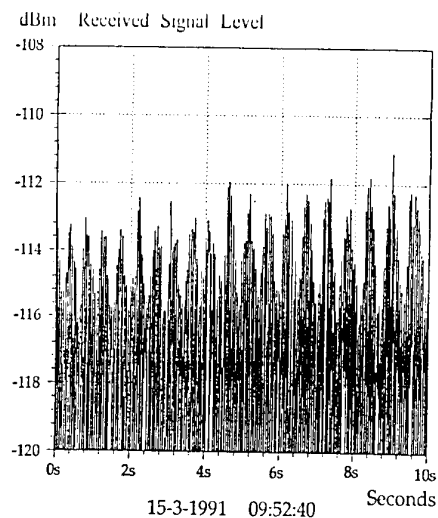


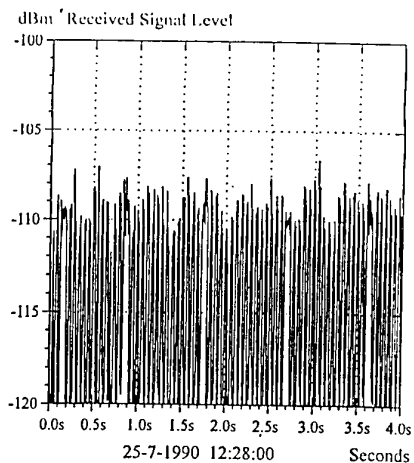
Figure 10: Long-term signal variation for Tropo-reflection mechanism



11(a) Little or no fading



11(b) Regular fading



11(c) Irregular fading

Figure 11: Short-term signal characteristics for Tropo-reflection mechanism

# THE RELATIVE IMPORTANCE OF METEOR BURST AND OTHER LONG DISTANCE POLAR CAP PROPAGATION MODES IN THE LOW VHF BAND

Paul S Cannon  
Radio Propagation Group  
Space and Communications Dept  
Defence Research Agency,  
Malvern, WR14 3PS, Worcs, UK

Jay A Weitzen,  
University of Massachusetts Lowell  
Center for Atmospheric Research  
Lowell,  
MA 01854, USA

Jens Ostergaard  
and  
John E Rasmussen  
Phillips Laboratory  
Geophysics Directorate  
Hanscom AFB  
MA 01731, USA

## SUMMARY

We have analysed the duty cycle from a very high frequency polar cap path in Greenland. We find that at 35 MHz and 45 MHz the path is often sustained by sporadic *E* layers rather than by meteor scatter. At the higher frequencies of 65 MHz and 85 MHz we find that the path is generally dominated by meteor scatter modes. The diurnal, seasonal and geomagnetic variations of sporadic *E* are examined and off line decision aid models are provided to evaluate the magnitude of multiple mechanism propagation on the path.

## 1. INTRODUCTION

Beyond Line of Sight (BLOS) meteor burst (MB) communications via meteor scatter propagation has been studied since the late 1950's and through this period there has been a steady improvement in system performance [e.g. Cannon and Reed, 1987]<sup>1</sup>. One important approach to system improvement has been the propagation experiment which aims to quantify throughput [e.g. Ostergaard *et al.* 1990]<sup>2</sup> and verify models [e.g. Cannon, 1986]<sup>3</sup>. More recently, however, Weitzen *et al.* [1993]<sup>4</sup> have drawn attention to the usefulness of one of these experiments to quantify high latitude, multi-mechanism propagation paths (MMPPs) for BLOS communications systems operating in the low very high frequency (VHF) band.

At high latitudes meteor scatter propagation is not the only BLOS propagation mode in the VHF band. Others may include 'wind shear' sporadic *E*, auroral *E* and *F* layer modes. On short links (under 200 km) tropospheric modes, as reported by Darnell *et al.* [1990]<sup>5</sup>, are also to be found; these introduce yet a further propagation mechanism.

The formation of wind shear sporadic *E* appears to be by plasma compression due to gradients in the vertical structure of neutral winds [Whitehead, 1970]<sup>6</sup>; this type of sporadic *E* dominates at mid-latitudes. A statistical study of wind shear sporadic *E* in Europe has been carried out by Edwards *et al.* [1984]<sup>7</sup> on frequencies between 59 and 77 MHz. This study showed an increase in May, a peak in June and cessation by

September with essentially no signals in winter. The signals are only present during daylight with a double peaked maximum before (~10 LT) and after local noon. The wind shear sporadic *E* summer maximum becomes more intense as we move to higher latitudes until it is altered by auroral zone influences [CCIR, 1990]<sup>8</sup>.

Auroral *E* is observed mainly at night and on ionograms it may exhibit retardation or no-retardation. The former is produced by a relatively thick layer whilst the latter is probably produced by a thin layer, by blobs or by partial reflection [Davies, 1990]<sup>9</sup>. It is to be noted that the zone of highest critical frequency does not coincide with the visible auroral zone [Davies, 1990]<sup>9</sup>. In the auroral zones, the dominant feature is the night-time-peak in the occurrence of sporadic *E* [CCIR, 1990]<sup>8</sup>. The summer peak of wind shear sporadic *E* disappears entirely in the centre of the visible auroral zone [Davies, 1990]<sup>9</sup> and is positively correlated with geomagnetic activity [Goodman, 1992]<sup>10</sup>.

In the polar cap, sporadic *E* is less well documented but extends in sun-aligned bands and appears to be negatively correlated with the substorm activity [Goodman, 1992]<sup>10</sup>.

MMPPs can be both an advantage and a disadvantage to the BLOS MB communicator operating in the low VHF band. If the communications system has been designed for operation as a MB only system then it may not be able to take advantage of the long opening times available via these other modes. Typically, the system may be constrained by limitations on the transmitter duty cycle. Conversely, if the terminal can tolerate long opening times the system availability can be increased substantially. The penalty, in so doing, is, however, a reduction in security and an inability to re-use frequencies in a network configuration. This follows because the ground illumination footprint for meteor modes is small whereas it is much larger for other ionospheric modes.

This paper investigates low VHF band MMPPs in the polar cap region. It will extend the work of *Weitzen et al.* [1993]<sup>4</sup> and in particular the paper will address the relative advantages of operating BLOS communications systems on a number of frequencies between 35 MHz and 65 MHz. Tropospheric propagation will not be addressed.

## 2. EXPERIMENT AND DATA ANALYSIS

For a number of years the United States Phillips Laboratory, Geophysics Directorate has operated meteor scatter data logging experiments on two paths in Greenland to support their research programme into meteor burst communications. One path nominally lies in the ionospheric polar cap and runs from Sondrestrom Air Base (66.98°N, 50.65°W) to Thule Air Base (76.55°N, 68.66°W) whilst the other path lies nominally in the auroral region with the transmitter again at Sondrestrom but with the receiver at Narssarsuaq (61.16°N, 45.45°W). The former path is 1210 km long and the latter is 690 km long. Figure 1 illustrates the path geometry and the nominal position of the auroral oval when  $Q = 2$ . This paper will only address the northerly polar cap path.

Sondrestrom to Thule transmissions take place on frequencies near 35, 45, 65, 85 MHz and are organised according to the schedule given in table 1. The measurement schedule is based on a two hour cycle with more time allocated to the higher frequencies where the average duty cycles are lower. Between each acquisition period, one minute is reserved for noise measurements at the subsequent frequency. The transmissions are 900 W continuous wave, constant amplitude signals, frequency modulated at 400 Hz. For both transmission and reception horizontally polarised antennas approximately 1.5  $\lambda$  above the ground are used. This height is suitable for mid-point illumination.

Data are collected on a PC based acquisition system and further processing and analysis are performed off-line [Ostergaard et al., 1985<sup>11</sup>; Weitzen, 1987<sup>12</sup>; Weitzen et al., 1993<sup>4</sup>]. An important part of this processing is the auto-classifier which for the purposes of the discussion herein is able to distinguish between meteor scatter and other non-meteor propagation paths. The autoclassifier is the means by which we can undertake the analysis of the large quantities of data which are required for this study.

TABLE 1. Schedule for Greenland Measurements

Time (UT)	Frequency (MHz), Thule to Sondrestrom
01.00 - 01.30	noise measurement
02.00 - 11.59	45
13.00 - 13.30	noise measurement
14.00 - 28.59	85
30.00 - 30.30	noise measurement
31.00 - 43.59	35
67.00 - 67.30	noise measurement
68.00 - 82.59	65

Times are given in minutes and seconds past the beginning of the even hour.

## 3. ANNUAL VARIATION IN NON-METEORIC AND METEORIC DUTY CYCLES

Figures 2a to 2d show the average annual variation in meteoric and non-meteor duty cycle for the polar cap Sondrestrom-Thule path at 35, 45, 65 and 85 MHz respectively. It seems most likely that the non-meteor duty cycle is dominated by sporadic *E*; the paths are all too long for tropospheric scattering and, particularly during the winter months, the *F*-region electron density is insufficient to sustain low VHF propagation.

### Non-Meteor Duty Cycle

The polar cap annual variation in non-meteor duty cycle is similar to that measured for sporadic *E* at temperate latitudes [e.g. Edwards et al., 1984]<sup>7</sup> which is generally considered to be due to a wind shear mechanism [e.g. Whitehead, 1970]<sup>6</sup>. The annual variation is most clear at 35 MHz and 45 MHz (Figures 2a and 2b) where the duty cycle is highest and the statistical errors smallest; in both cases the duty cycle peaks in June with raised values from May until September. This asymmetrical envelope with a fast rise and slow decay is similar to that measured by Edwards [1984]<sup>7</sup> in his temperate latitude studies in the low VHF band. At 65 MHz and 85 MHz (Figures 2c and 2d) the summer peak is still evident, although it occurs one month later.

During the non-summer months the non-meteor duty cycle drops to around 10 to 15% of the peak duty cycle. The 85 MHz variation exhibits a steep rise in November and December due to a sudden increase in 1989 which was not repeated in 1990. The reason for this sudden rise in duty cycle is not clear and maybe a statistical aberration.

Figures 2 helps us to understand the annual variation in non-meteor duty cycle but gives little intuition in respect to the daily variation. Figures 3 and 4 for 1989 and 1990 respectively combine both the daily and annual variations where each pixel is grey coded according to the duty cycle. Note that in each diagram the scaling is different. The time scale is given in universal time (UT) with local time (LT) and corrected geomagnetic local time (CGMLT) respectively 4 and 2 hours behind UT. Sporadic *E* driven by the wind shear method should be centred around mid-day LT but it is likely that polar cap sporadic *E* will be centred on geomagnetic mid-night

Figure 3 for 1989 and Figure 4 for 1990 graphically illustrate the summer day time peak at 35 and 45 MHz and the growth and decay of the daytime sporadic *E* either side of June. Only one summer day time peak is seen and this occurs around 18 UT (or ~14 LT); this is after the daytime morning peak often seen at mid-latitudes but before the time of the mid-latitude evening peak. Note, however, how that the sporadic *E* duty cycle remains high throughout the whole 24 hour period during mid-summer. At 35 MHz and 45 MHz it is clear that sporadic *E* occurs at night and also in the winter but is less frequent. There seems little suggestion, however, of any peaks in sporadic *E* during the winter but it is possible that the temporal measurement and plotting resolutions are too coarse. Binning by *k<sub>p</sub>* (see below) might be helpful in this respect. This latter sporadic *E* is unlikely to be generated by the wind shear mechanism.

Figures 3 and 4 also clearly illustrate the rapid fall in sporadic *E* duty cycle at the higher frequencies.

#### Meteoroid Duty Cycle

Figure 2a to 2d also describe the duty cycle at each frequency due to meteor propagation. The diurnal variation at 45 MHz has been discussed in some detail by Weitzen *et al.* [1993]<sup>4</sup> and will not be repeated here. Suffice to say that when non-meteoroid propagation duty cycle is high it obscures the meteor signals. From the viewpoint of the meteor scientist this is irritating but for the communications engineer it serves to highlight the dominance of sporadic *E* over meteor propagation. This obscuration is particularly evident in Figure 2a and 2b at 35 and 45 MHz where we would expect a strong summer time peak in meteor modes due to the northern latitude summertime showers. Some of these showers occur, however, during a period of high sporadic *E* activity which obscures the meteor signals. The annual variations at 65 MHz and 85 MHz do, however, show some evidence of the summertime peaks although even at these high frequencies the predominance of sporadic *E* during the summer months obscures the variation in meteor duty cycle. Both the 65 MHz and 85 MHz annual variations are very similar. Both show a dip in meteor propagation in the months of February and March and a subsequent rise to a peak in June. This is followed by a fall in July and a small rise again in August.

#### 4. RELATIVE THROUGHPUT

In Figure 5a to 5d we present the quotient of the two duty cycles on a month by month basis; values greater than unity indicate a dominance of non-meteoroid propagation modes. At 35 and 45 MHz non-meteoroid modes provide the principle communications mode throughout the year. This is an important result since it illustrates that so called MB systems operating at these frequencies are not in fact MB systems but more nearly sporadic *E* systems. At 65 MHz, however, the situation has largely reversed and meteor propagation dominates for 8 months of the year. The situation is more confused at 85 MHz where the data is less reliable but generally similar to 65 MHz. Without recourse to further modelling sophistication it is necessary to use frequencies as high as 65 or 85 MHz if MMPPs must be minimised.

The analysis leading to the above grouped together all of the meteor signals and all of the sporadic *E* for each month taking no account of their diurnal variations. Since meteor showers occur at different times of the day, because there is a diurnal variation in non-shower meteors and because sporadic *E* also exhibits a diurnal variation we expect that the quotient will vary as a function of time of day. In addition, we find that the law describing the incidence of sporadic *E* as a function of frequency is different depending on the type of sporadic *E*. Figure 6, therefore, shows the quotient for time bands 00-06 UT, 06-12 UT, 12-18 UT and 18-24 UT averaged over a month for each of the frequencies. Application of these, and similar, graphs will enable the system designer to better evaluate the impact of MMPPs on polar cap MB paths.

Moving up in frequency unfortunately minimises MMPPs at the expense of MB data throughput [Cannon and Reed, 1989]<sup>1</sup>. More sophisticated modelling may serve to minimise the MMPPs whilst allowing operation at the lower frequencies. In Figures 3 and 4 we have demonstrated that

there appear to be two different types of sporadic *E* in the polar cap; summer wind shear sporadic *E* and polar cap sporadic *E*. Figures 7 and 8 respectively describe the variation of sporadic *E* duty cycle as a function of the geomagnetic index *kp* for winter (February, March, October, November and December), data and summer data (May, June and July) at 35 MHz; similar results are apparent at 45 MHz. In winter the duty cycle decreases as *kp* increases where as no such relationship is apparent during the summer. Thus in the winter, when *kp* is low MMPPs will be common whereas when *kp* is high there will be few MMPPs. This knowledge can be used to further refine the model. Figures 9 and 10 give the quotient of non-meteoroid to meteoroid duty cycle for two conditions;  $kp < 2$  and  $kp \geq 2$ . When *kp* information is available these models give the most accurate estimate of MMPPs.

#### 5. CONCLUSIONS

Our measurements of duty cycle on a polar cap path have demonstrated that meteor burst systems operating in the polar cap will be subject to MMPPs. These may have deleterious or advantageous effects on system operation. The impact of MMPPs varies as a function of time of year, time of day, frequency and geomagnetic activity. By using the models presented in this paper the system designer can address the problems of MMPPs and if necessary take steps to avoid them. A future paper will address MMPPs in the auroral oval.

#### REFERENCES

- 1 Cannon, P. S. and A. P. C. Reed, The evolution of meteor burst communications systems, *J. Inst. Elec. Rad. Eng.*, 57, 101-112, 1987.
- 2 Ostergaard, J. C., J. A. Weitzen, P. M. Bench, P. A. Kossey, A. D. Bailey, S. W. Li, J. R. Katan, A. J. Coriaty and J. E. Rasmussen, Effects of absorption on high latitude meteor scatter communication, paper presented at IEEE MILCOM'90, Monterey, California, USA, 1990.
- 3 Cannon, P. S., Polarization rotation in meteor burst communication systems, *Radio Sci.*, 21, 501-509, 1986.
- 4 Weitzen, J. A., P. S. Cannon, J. C. Ostergaard and J. E. Rasmussen, High-latitude seasonal variation of meteoroid and non-meteoroid oblique propagation at a frequency of 45 MHz, *Rad. Sci.*, 28, 213-222, 1993.
- 5 Darnell, M., N. G. Riley, D. R. Melton, Beyond Line of Sight Radio Systems in the Low- VHF Band, 2nd Bangor Symposium on Communications, UK, 71-76, May 1990.
- 6 Whitehead, J. D., Production and prediction of sporadic-E, *Reviews Geophys. Space Phys.*, 8, 65-144, 1970.
- 7 Edwards, K. J., L. Kersley and L. F. Shrubsole, Interference from sporadic-E propagation at frequencies around 70 MHz, paper presented at IEE Third International Conference on Antennas and Propagation (ICAP'83), University of East Anglia, United Kingdom, Conf Publ No 219, 321-324, 1983.

8 CCIR, 2.-7., VHF ionospheric propagation in Annex to volume VI, XVIIth Plenary Assembly, Dusseldorf, CCIR, 1990.

9 Davies, K., Ionospheric Radio Propagation, NBS Monograph 80, Washington DC, USGPO, 1965.

10 Goodman, J. M., HF Communications Science and Technology, New York, Van Nostrand Reinhold, 1992.

11 Ostergaard, J. C., J. E. Rasmussen, M. J. Sowa, J. M. Quinn and P. A. Kossey, Characteristics of high latitude meteor scatter propagation parameters over the 45-104 MHz band, paper presented at Propagation effects on military systems in the high latitude region, Alaska, USA, CP 382, 1985.

12 Weitzen, J. A., A data base approach to analysis of meteor burst data, *Radio Sci.*, 22, 133-140, 1987.

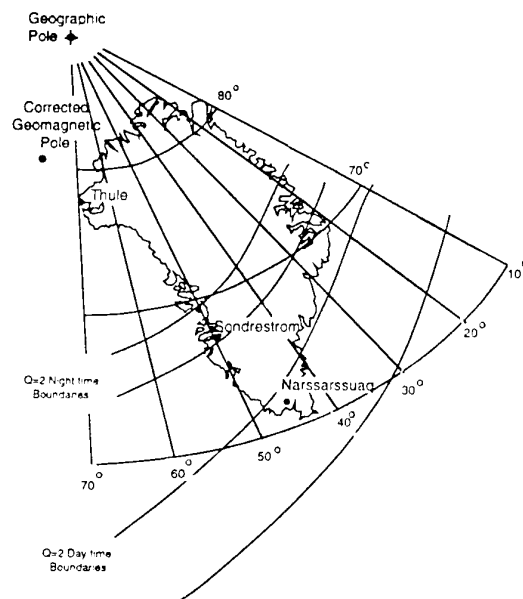


Fig 1. Measurement paths and the Q=3 boundaries of the auroral oval

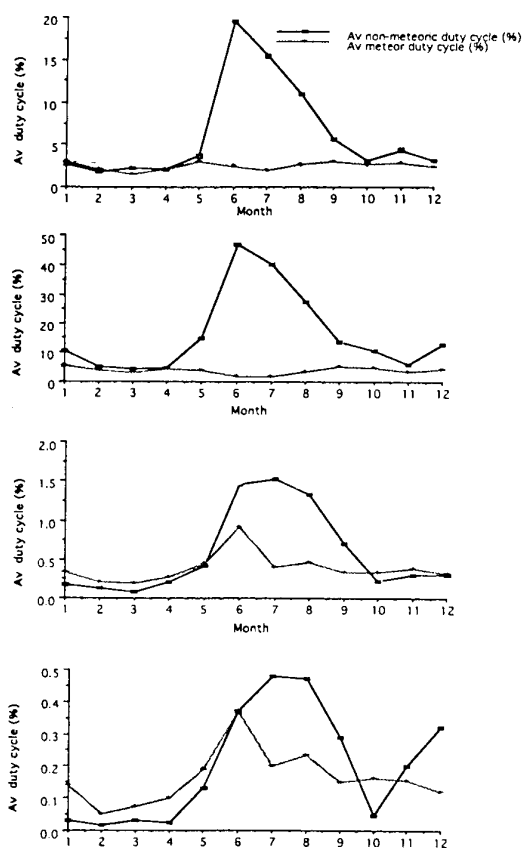


Fig. 2a to d, Non-meteor and meteor duty cycles for the path Sondrestrom to Thule at 35, 45, 65, 85 MHz respectively



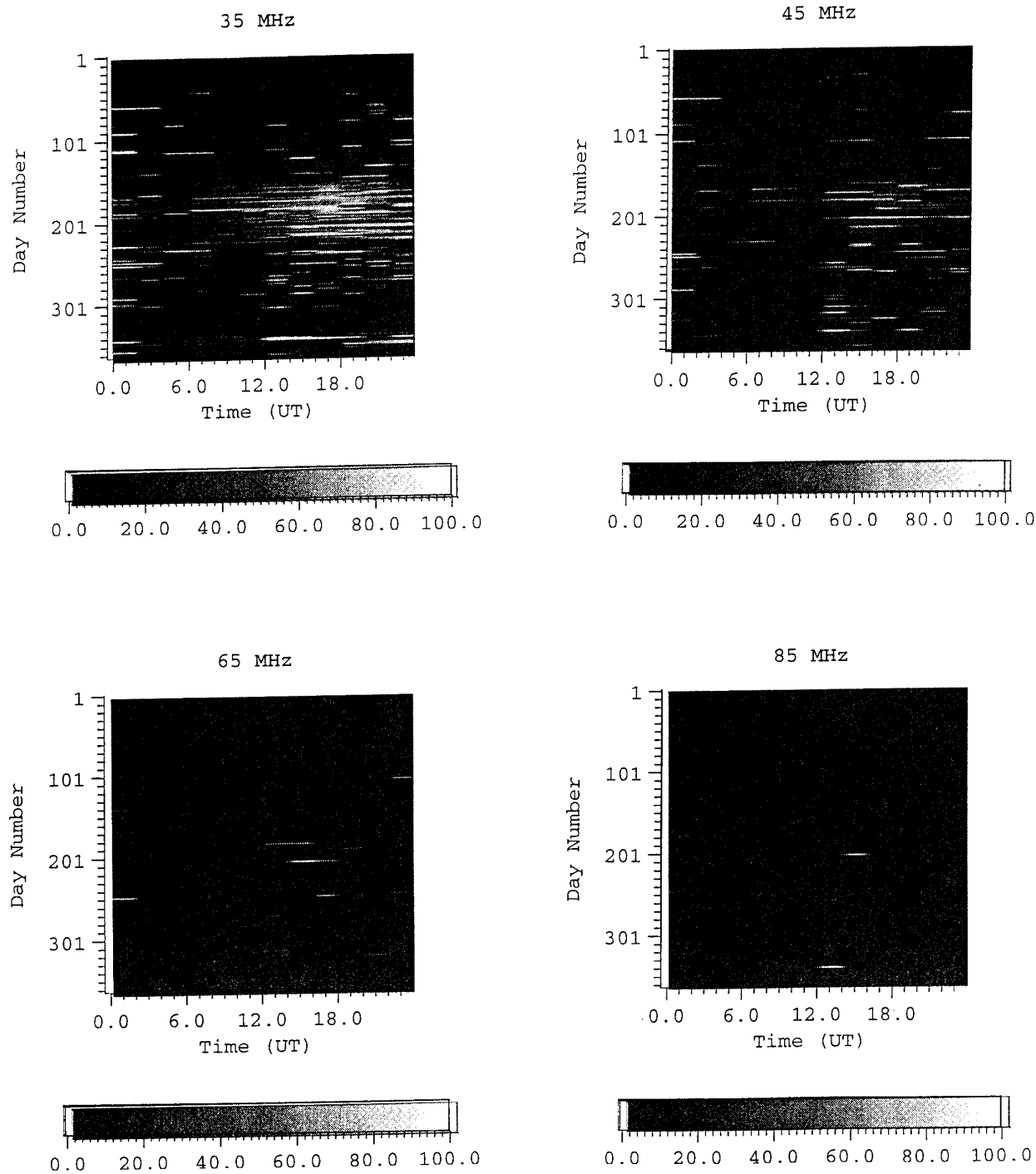


Fig. 3, Non-meteoritic duty cycle in 1989.

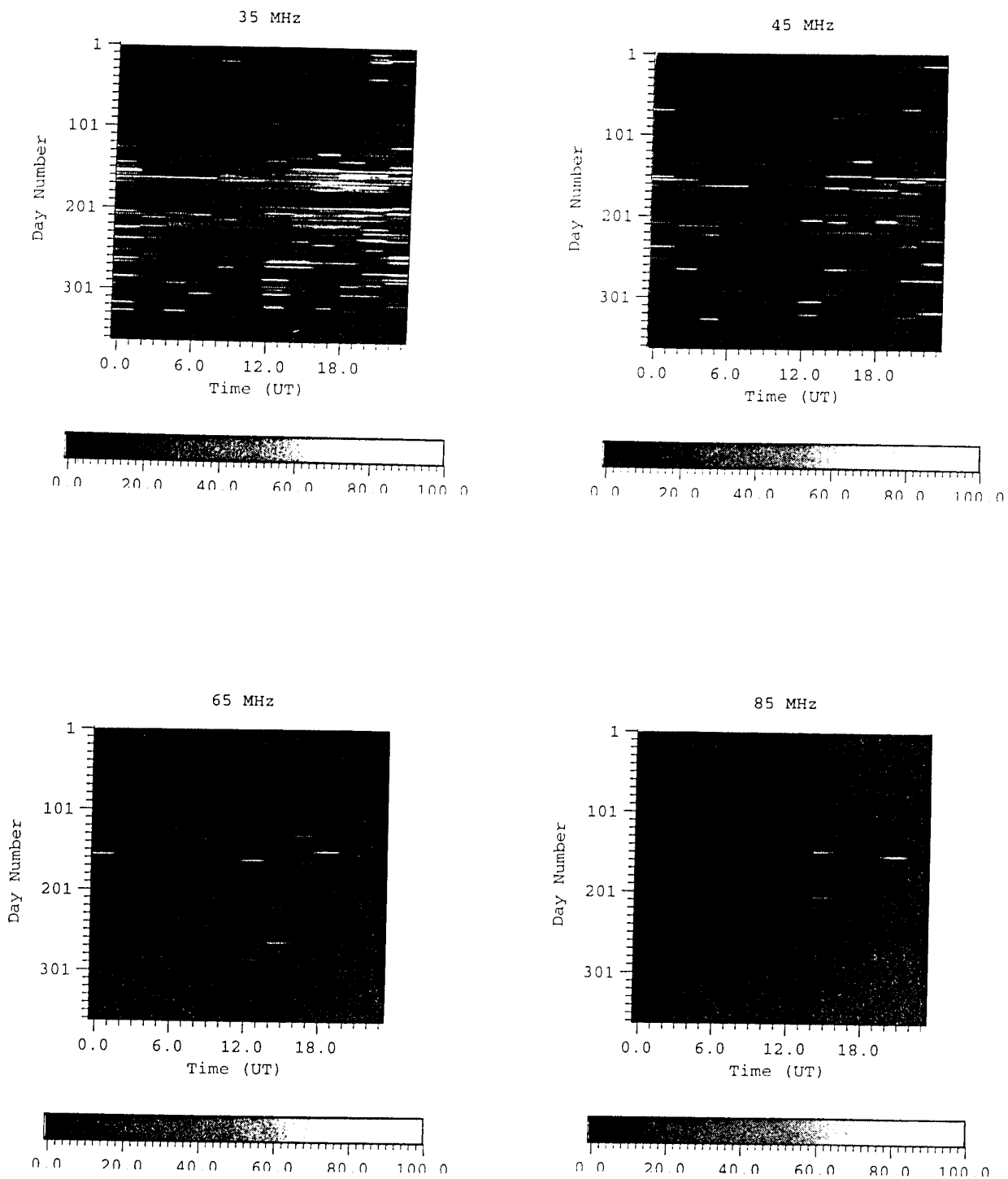


Fig. 4, Non-meteoritic duty cycle in 1990

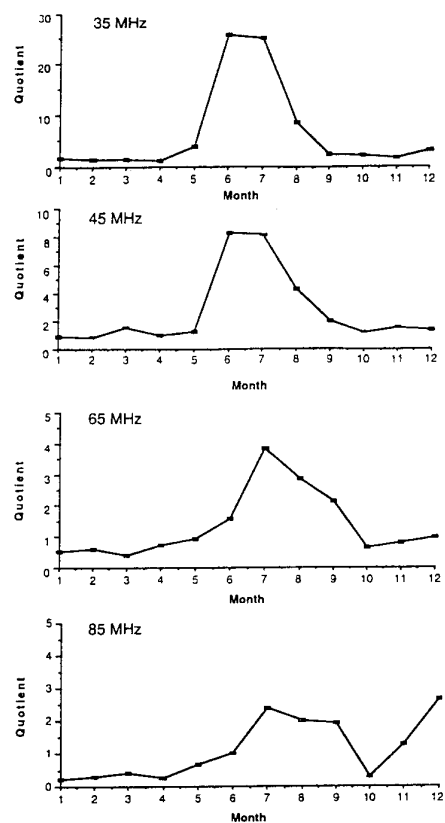


Figure 5a to d. Quotient of non-meteoritic duty cycle to meteoritic duty cycle

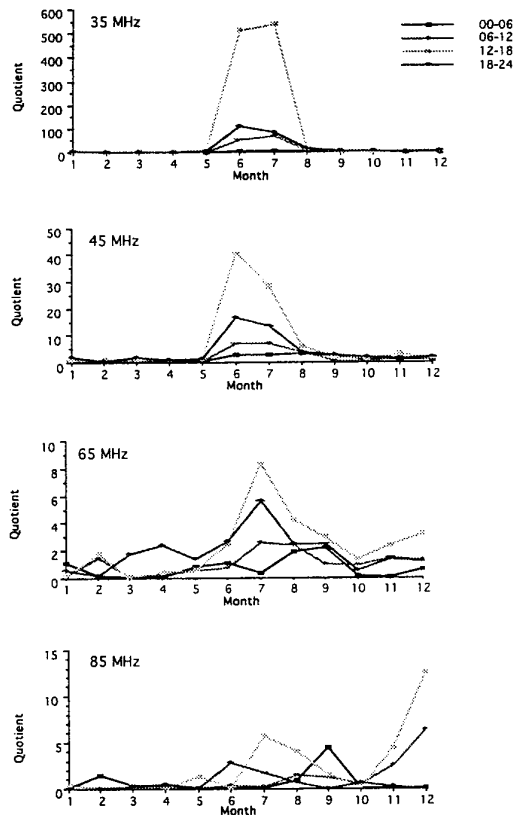
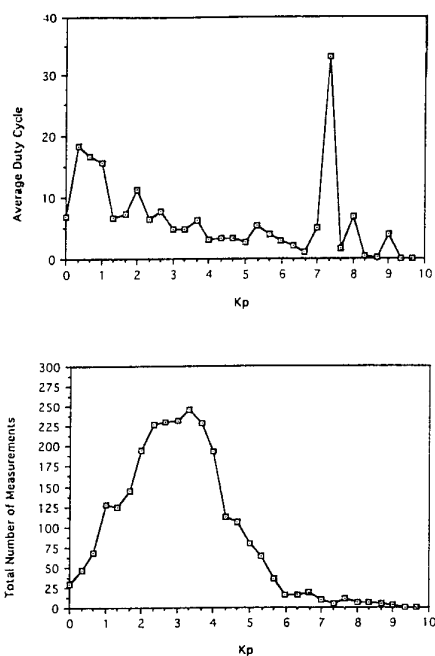
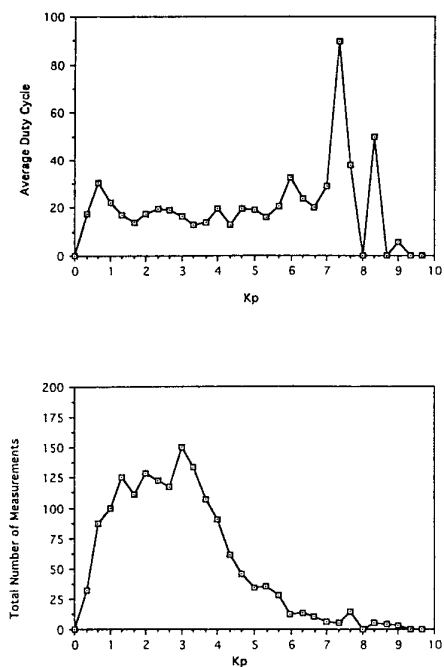


Fig 6. Quotient of non-meteoritic duty cycle to meteoritic duty cycle for various time windows.

Figure 7 Non-meteoritic duty cycle during the winter months as a function of the geomagnetic index  $K_p$ .Figure 8 Non-meteoritic duty cycle during the summer months as a function of the geomagnetic index  $K_p$ .

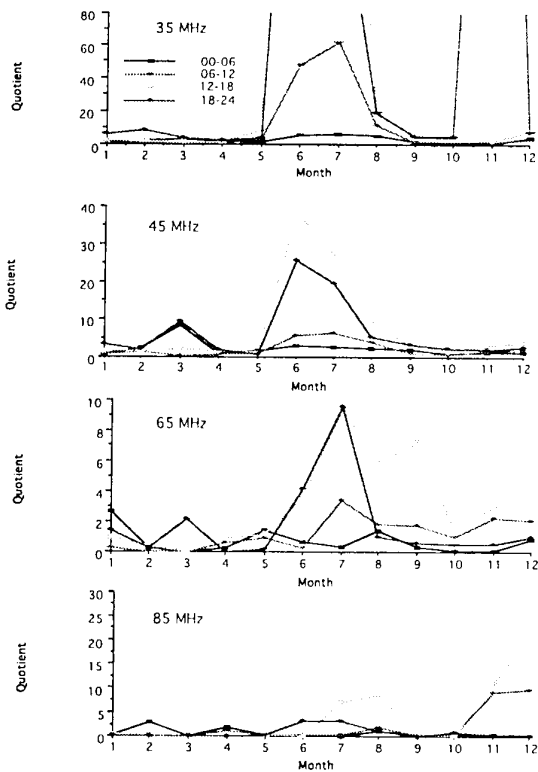


Figure 9, Quotient of non-meteor duty cycle to meteoric duty cycle for various time windows and when  $kp < 2$ .

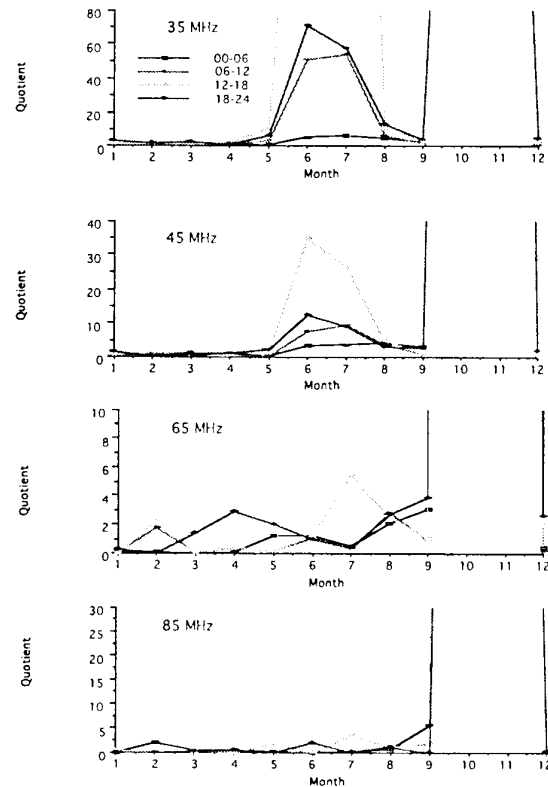


Figure 10, Quotient of non-meteor duty cycle to meteoric duty cycle for various time windows and when  $kp \geq 2$ .

## DISCUSSION

### 3. Discussor's name : U. Lammers

#### Comment/Question :

I noticed in your monthly ratio plots, particularly at the two higher frequencies, a discontinuity between the December and January data. Should not the curves be cyclical?

#### Author/Presenter's reply :

The discontinuity does not necessarily indicate a problem. Significant month to month variations can occur, for example due to meteor showers or due to variations in sporadic E. It is true, however, that the low duty cycle at the higher frequencies may affect the statistical stability of these results. We have tried to compensate for this lower duty cycle by making measurements for longer periods when operating on the higher frequencies. It is possible that we may not have fully compensated for the reduced duty cycle.

# Etude des variations rapides et lentes de la puissance reçue lors de liaisons VHF par diffusion troposphérique

O. RAVARD, F. CHEVRIER, L. BERTEL

Laboratoire de Radiocommunications - URA 834 - Université de RENNES 1  
Campus de Beaulieu - 35042 RENNES CEDEX - France

J.C. LE JANNIC

Centre ELectronique de l'ARmement  
CELAR - BP n°7 - 35998 RENNES Armées - France

## Abstract

*This paper deals with some experimental results. These correspond to radio link operating in the low VHF band (30 - 80 MHz) and in the range 300 - 500 km.*

*For those distances and frequencies, the received signal is affected by fast and low variations.*

*On the one hand, time-frequency analysis (waveleth transform) show that the mainly dominant propagation mode is due to partial reflection on random surfaces (sheets).*

*At a given time, only three or four reflections are significant and contribute to the received power.*

*On the other hand, statistics of low variations are examined and a log-normal distribution is observed. These low variations are correlated with meteorological data (radiosonde). Best correlations are obtained with atmospheric pressure, refractive index and hight of the tropopause.*

## 1. INTRODUCTION

Le mode de propagation, couramment nommé "diffusion troposphérique" apparaît pour des liaisons dont la distance est trop grande pour que le mode de propagation soit attribué au phénomène de diffraction (de 150 à 500 kilomètres). En fait, les mécanismes de propagation sont multiples et complexes. En effet, la troposphère constitue un milieu où le flux est globalement stable. Cependant, les flux locaux peuvent être de différentes natures. Ils seront laminaires ou turbulents suivant l'état local de l'atmosphère. Des inhomogénéités de l'indice de réfraction sont alors créées par ces différents flux (Misme [1] (partie 1, 2), VanZandt et al. [2], Röttger et al. [4]).

Ces inhomogénéités entraînent de multiples mécanismes de propagation : diffusion, réflexions partielles, spéculaires ou diffuses ; de plus, elles peuvent apparaître partout dans le volume commun aux antennes d'émission et de réception. Le signal reçu instantané est

alors la somme de plusieurs composantes, chacune correspondant à un trajet différent. La "diffusion troposphérique" VHF constitue donc un canal de transmission à trajets multiples où peuvent apparaître, a priori, plusieurs modes de propagation (Du Castel, Spizzichino [1] (partie 3)).

Durant la période Septembre 1992 à Septembre 1993, une expérimentation longue durée, visant à caractériser la propagation VHF par diffusion troposphérique, a été mise en place. Nous décrivons dans cet article l'ensemble des expérimentations. Nous exposons également les différentes analyses effectuées, dont l'objectif est de qualifier, en termes statistiques, le canal de propagation.

## 2. DESCRIPTION DES EXPERIMENTATIONS

Les expérimentations mises en place sur le territoire français comprennent quatre liaisons distinctes.

Le site d'émission se trouvant à Cholet, trois liaisons fixes correspondant aux sites de réception de Cazaux, Coulommiers et Haraumont ont pour longueurs au sol respectives 291, 332 et 506 kilomètres. La figure 1 représente la géométrie des trois liaisons fixes. Pour la quatrième liaison, la station de réception est déplacée tous les quinze jours environ.

Cette dernière station permet l'analyse de l'influence de différents paramètres, tels que : longueur de liaison, type et hauteur d'antenne, topographie des sites. L'aérien utilisé à l'émission est une antenne de type Disc-Cone placée à une hauteur de 18 mètres au dessus du sol. Les stations fixes utilisent des antennes de type Log-Périodique également placées à une hauteur de 18 m au dessus du sol. Pour la station déplaçable, les deux types d'antenne sont utilisés successivement (Disc-Cone et Log-Périodique) et leur hauteur au dessus du sol est comprise entre 11,5 et 30 mètres. Le tableau 1 regroupe les caractéristiques générales des liaisons et le tableau 2 représente les configurations choisies pour la station déplaçable.

Les mesures ont été effectuées pendant une année sans interruption, simultanément sur trois fréquences :  $F1 = 41,5$  MHz,  $F2 = 47,3$  MHz et  $F3 = 69.775$  MHz. Avec une période de 10 ms sur chaque fréquence, le niveau de puissance reçue est enregistré, la dynamique étant de 64 dB et la résolution de 1 dB. De plus, deux fois par seconde, le niveau de bruit est mesuré, l'émetteur ne fonctionnant pas à cette fréquence pendant la mesure. Dans ces mesures, aucune information de phase et de temps de groupe n'est disponible. Parallèlement aux mesures radioélectriques, la Météorologie Nationale nous a fourni, deux fois par jour pendant toute l'année de l'expérimentation, le profil vertical (obtenu par radiosondage) des paramètres météorologiques suivants : pression, température, température du point de rosée, direction et force du vent ainsi que la présence ou non de tropopauses. La résolution verticale des profils est de l'ordre de 500 m à 1000 m et correspond aux points caractéristiques de l'état de l'atmosphère (points où la pente du profil est modifiée de manière significative).

### 3. ANALYSE DES RESULTATS EXPERIMENTAUX

L'étude statistique du signal reçu peut être scindée en deux axes. D'une part, le signal observé est affecté de variations rapides autour de sa valeur moyenne ; d'autre part, cette moyenne subit des variations aléatoires au cours du temps. L'évaluation de cette moyenne se fait sur un intervalle de stationnarité (typiquement une minute) en tenant compte du bruit ambiant mesuré. En effet, la grandeur mesurée est

$\langle |S(t)|^2 \rangle$  telle que  $S(t) = X(t) + b(t)$  où  $b(t)$  est le bruit ambiant et  $X(t)$  le signal utile. L'estimation de la

puissance du signal utile  $\langle |X(t)|^2 \rangle$  est effectuée d'une manière très simple en soustrayant la puissance moyenne

du bruit  $\langle |b(t)|^2 \rangle$  à la puissance moyenne du signal reçu

$\langle |S(t)|^2 \rangle$ . Des erreurs d'estimation sont apportées lorsqu'un bruit stationnaire, toujours présent, se superpose un bruit de type impulsif. Afin d'évaluer la qualité de l'estimation, nous avons effectué les calculs pour une période où l'émetteur n'était pas en fonctionnement. Le signal utile est alors absent et le signal reçu s'exprime par  $S(t) = b(t)$ . Malgré cela, notre calcul donne une distribution de puissance du "signal utile" avec une médiane de -137 dBm (figure 2). Ceci correspond à ce que nous appelons le bruit d'estimation, situé à un niveau d'environ 18 dB en deça du niveau de bruit ambiant. Ainsi, lorsque le rapport signal à bruit moyen  $\langle |X(t)|^2 \rangle / \langle |b(t)|^2 \rangle$  est supérieur à -18 dB, ce qui est suffisant pour nos liaisons expérimentales,

la moyenne instantanée du signal utile  $\langle |X(t)|^2 \rangle$  peut être évaluée.

L'analyse des variations des moyennes estimées pour chaque minute de l'année constitue l'étude des variations lentes. Elle ignore les variations rapides du signal (variations sur la minute), qu'il s'agit tout d'abord de caractériser ces variations rapides.

### 4. ETUDE DES VARIATIONS RAPIDES

L'observation systématique d'enregistrements temporels a mis en évidence l'existence de signatures, souvent rencontrées, telles que celle reportée sur la figure 3. Cette signature caractérisée par de profonds et réguliers évanouissements, suggère que le signal reçu soit la superposition d'un petit nombre de composantes cohérentes.

Les réflexions des ondes sur des discontinuités d'indice, générées par des flux laminaires, peuvent être à l'origine du phénomène observé. Il est reconnu que ce type de propagation existe (Melton et al. [3], Röttger et al. [4]), mais il est intéressant d'étudier si celui-ci est caractéristique de la propagation VHF troposphérique transhorizon et s'il constitue un phénomène omniprésent ou éphémère. Les transformées temps-fréquence effectuées sur des périodes relativement longues peuvent en partie répondre à ces questions. L'utilisation de la transformée en ondelettes est particulièrement bien adaptée pour ce type de traitement, où le signal a des caractéristiques essentiellement non stationnaires. L'ondelette choisie et bien adaptée pour extraire des

composantes sinusoïdales d'un signal, est l'ondelette de Morlet.

Les figures 4 et 5 sont deux exemples de représentations temps-fréquence du module du signal reçu, effectuées par la transformée en ondelette de type Morlet. Notons que l'analyse est ici de type surabondante. La durée d'analyse pour chacune de ces représentations est de dix minutes (axe des ordonnées) et l'intervalle des fréquences est 0,5 - 15 Hz (axe des abscisses).

On peut remarquer qu'à chaque instant, une ou plusieurs composantes sinusoïdales peuvent être observées sur le module du signal reçu. La fréquence de chaque composante varie plus ou moins rapidement en fonction du temps, la modulation observée étant parfois linéaire. On peut également remarquer que la durée de chaque modulation peut s'étendre de quelques secondes à quelques minutes. Celle-ci peut être associée à la durée de vie du phénomène responsable de la propagation.

Les deux représentations temps-fréquence des figures 4 et 5 ne sont pas des cas particuliers et sont représentatives du comportement du canal dans la gamme VHF. Nous proposons donc, en accord avec les conclusions de certains auteurs (Voge [1] (partie 4, 5), Friis et al. [5]), qu'un mécanisme de propagation troposphérique transhorizon, au moins dans la gamme VHF, est de type multitrajet : chaque trajet correspond à une réflexion sur une couche, appelée feuillet, dont les dimensions horizontales sont suffisantes pour assurer la cohérence de l'onde réfléchi. Ces feuillets sont constitués par des discontinuités de l'indice de réfraction ou d'une de ses dérivées. Ils correspondraient à des flux laminaires et à un instant donné, seulement trois ou quatre de ces feuillets contribuent, de manière significative, au signal reçu (Spizzichino, Misme, Voge, Du Castel [1]).

## 5. ETUDE DES VARIATIONS LENTES

La puissance moyenne reçue instantanée est donc évaluée, sur une période supposée stationnaire de 1 minute, tout au long de l'année. L'étude des variations lentes consiste à caractériser, d'une manière déterministe ou statistique, l'ensemble des données ainsi calculées. Les caractéristiques météorologiques de la troposphère variant d'une saison à l'autre et également au cours de la journée, on peut s'attendre à observer deux types de variations lentes du signal reçu : variations diurnes et variations annuelles auxquelles on associe respectivement deux types d'analyses : l'analyse verticale et l'analyse horizontale.

### L'analyse horizontale

On cherche ici à caractériser la distribution statistique de la moyenne instantanée. Considérons une durée  $T$  d'observation du canal. Cette durée peut être divisée en  $N_c$  créneaux de  $N_m$  minutes chacun. On peut

alors évaluer la moyenne, la médiane et l'écart type associés à chaque créneau.

Sur chacun des créneaux, la densité de probabilité de la moyenne instantanée peut être considérée comme une loi log normale. La figure 6 est un exemple de distributions statistiques qui peuvent effectivement être considérées log normales. Ce point est en accord avec de nombreuses observations (Crawford et al. [6], Rice et al. [7]).

La figure 7 représente les variations de la médiane et de l'écart type pour une durée totale d'analyse de 6 mois et des créneaux d'une durée de 5 jours, associées aux trois stations fixes. Les mêmes types de résultats sont obtenus aux autres fréquences. La remarque essentielle suggérée par cette figure est l'absence de variation saisonnière déterministe significative, quelle que soit la fréquence. Naturellement, on ne peut pas affirmer qu'en moyenne, aucune variation saisonnière déterministe n'affecte la propagation VHF troposphérique transhorizon car il faudrait observer le canal pendant plusieurs années. Cependant, la période d'observation Septembre 92 - Septembre 93 a été stationnaire pour toutes les saisons.

La corrélation entre les puissances moyennes instantanées à différentes fréquences peut être visualisée sur la figure 8. Naturellement, plus les fréquences sont éloignées, plus la corrélation est faible. On apprécie l'avantage que pourrait apporter la diversité de fréquence sur ce type de liaison. On remarque également que lorsque les niveaux sont élevés, la corrélation est quasi totale, ce qui constitue un résultat intéressant. Des corrélations entre les différentes stations (figure 9) ont été effectuées : les niveaux moyens sur les stations de Coulommiers et Haraumont sont beaucoup plus corrélés car ces deux stations correspondent au même azimuth par rapport à la station d'émission.

Considérons les résultats relatifs à la médiane du signal utile en fonction de la durée de la mesure. La figure 10 représente l'écart type des médianes associées aux créneaux de durée déterminée en fonction de la durée de ce créneau. L'écart type diminue d'une manière significative pour des durées de créneaux supérieures à un jour et il devient faible ( $< 1$  dB) pour les créneaux supérieurs à environ un mois. Cette représentation très synthétique permet de montrer que le canal est affecté de variations temporelles aléatoires de période comprise entre quelques minutes et un mois. Ce résultat est de toute première importance puisqu'il montre qu'une évaluation significative de la qualité d'une liaison nécessite une période de mesure supérieure à deux mois.

### Analyse verticale

Cette analyse vise à caractériser les variations diurnes de la puissance reçue. Considérons une durée  $T$

d'observation du canal comprenant  $N_j$  jours de mesures. Partageons chaque jour en  $N_c$  créniaux comprenant chacun  $N_m$  minutes. Valeur moyenne, médiane et écart type sont évalués pour chaque ensemble de  $N_j$  créniaux correspondant au  $c^{\text{ème}}$  crénial de chaque jour.

La figure 11 représente l'analyse verticale pour la station de Cazaux pour une durée totale d'observation de six mois et des créniaux d'une minute. Les mêmes types d'observations sont faits pour les autres stations. Ce graphe montre qu'aucune variation diurne déterministe ne peut raisonnablement être associée, quelle que soit la fréquence. Ce résultat peut être généralisé quelle que soit la durée  $T$  d'observation (associée par exemple à chaque saison). Ceci est important car on peut imaginer que les variations diurnes associées à une saison peuvent compenser celles d'une autre. Ce n'est pas le cas ici.

### Corrélations avec les paramètres météorologiques

Les données météorologiques nous ont été fournies par la Météorologie Nationale. Celles-ci sont extraites des deux radiosondages journaliers, effectués à 00 h 00 et 12 h 00 TU. La période d'échantillonnage étant de 12 heures, la durée des créniaux d'analyses associés aux données de propagation est choisie au moins égale à cette période.

De nombreuses corrélations ont été effectuées entre données météorologiques et données de propagation. Les paramètres météorologiques choisis sont de plusieurs ordres :

- paramètres reflétant la situation météorologique globale : pression au sol, altitude ou température de la tropopause. Ces paramètres étant calculés soit d'une manière locale (une station) ou globale (moyennage sur toutes les stations),
- paramètres caractéristiques de la stabilité de l'atmosphère : gradient de température potentielle, nombre de Richardson,
- paramètres radioélectriques : coindice de réfraction, gradient moyen d'indice de réfraction.

De plus, ces corrélations ont été effectuées avec les mesures effectuées au sol ou en altitude, avec des durées de moyennage variables.

Nous ne présentons, dans cet article, qu'un échantillon réduit de résultats. Les meilleurs résultats ont été obtenus avec les paramètres suivants (diagrammes de dispersion figure 12) :

- la pression atmosphérique au sol,
- le co-indice de réfraction,
- l'altitude de la tropopause, fonction décroissante de sa température.

Les coefficients de corrélation obtenus sont en général compris entre 0.5 et 0.7, quelle que soit la fréquence ou la station choisie. La valeur maximum de 0.7 est obtenue lorsque la durée de moyennage est de

deux jours. De nombreux auteurs avaient déjà mis en évidence, à des fréquences plus élevées, les corrélations entre propagation et pression atmosphérique ou co-indice de réfraction au sol (Crawford et al [6], Tawfik [8]). Ici, la nouveauté apportée réside dans le fait que l'altitude ou température de la tropopause offrent de meilleures corrélations avec les données de propagation. De plus, des corrélations ont été effectuées avec des paramètres météorologiques estimés dans chaque tranche d'altitude (épaisseur typique : 1 km). La figure 13 représente l'évolution des différents coefficients de corrélation en fonction de l'altitude, pour la station de Haraumont et un moyennage - global pour les paramètres météorologiques - de un jour. On peut, à l'aide de ces graphes, situer la gamme d'altitude associée aux mécanismes de propagation entre un et dix kilomètres avec une prépondérance pour les faibles altitudes. Un des meilleurs coefficients de corrélation est obtenu avec la pression atmosphérique prise à une altitude d'environ trois kilomètres. On peut également observer que l'indice de réfraction offre une corrélation satisfaisante pour les tranches d'altitudes 4-5 km et 10-12 km, le coefficient de corrélation étant négatif pour la tranche 4-5 km et positif pour la tranche 10-12 km.

Naturellement, nous avons présenté ici les analyses effectuées en moyennant sur un ou deux jours et il est clair que les mêmes études devront être faites en utilisant d'autres échelles de temps (une semaine ou deux semaines par exemple Tawfik [8]).

Globalement, on peut conclure que les bilans de liaisons VHF troposphérique transhorizon sont meilleurs en situation anticyclonique qu'en situation dépressionnaire. Les situations météorologiques plutôt stables semblent donc être bénéfiques pour la propagation. Ceci est en accord avec les conclusions émises quant au mécanisme de propagation (§ 4), si l'on admet que l'apparition de feuillets troposphériques est en relation avec la stabilité à grande échelle de la troposphère. De plus, il semblerait que la qualité de la liaison soit également en relation avec le type de masse d'air en présence, et non seulement du climat, ce qui est, selon les connaissances des auteurs, un résultat nouveau.

## 6. CONCLUSION

Nous avons décrit dans cet article les résultats expérimentaux relatifs à une expérimentation longue durée (1 an) mise en place dans le but de qualifier les liaisons VHF troposphériques transhorizon. L'analyse des variations rapides du signal reçu nous permet de conclure que le signal reçu instantané est la somme d'un petit nombre de composantes cohérentes. Chacune de ces composantes serait l'effet d'une réflexion partielle sur un feuillet atmosphérique. La moyenne instantanée du signal reçu est affectée de variations dont aucune n'est apparue comme étant déterministe (pas de variations diurnes et pas de variations saisonnières). Cette moyenne



instantanée suit une loi log-normale dont les paramètres dépendent de la configuration de la liaison.

Les corrélations des données de propagation avec les paramètres météorologiques permettent de conclure que la qualité du mécanisme de propagation est en relation, non seulement avec la stabilité à grande échelle de l'atmosphère, mais également avec le type de masse d'air en présence.

Cette expérimentation longue durée a permis une bonne approche expérimentale des mécanismes de trajets multiples associés à la propagation VHF troposphérique transhorizon.

## Références

- [1] F. Du Castel, P. Misme, A. Spizzichino, J. Voge "Réflexions partielles dans l'atmosphère et propagation grande distance", Editions de la "Revue d'optique", 1960, Extraits des An. des Tel., Tome 13, n°7-8, 9-10, Tome 14, n° 1-2, Tome 15, n°1-2, 5-6.
- [2] T. E. VanZandt, K. S. Gage, J. M. Warnock "An Improved Model for the Calculation of Profiles of  $C_n^2$  and  $\epsilon$  in the Free Atmosphere from Background Profiles of Wind, Temperature and Humidity", 1981, 20th Conf. on Radar Meteorol., Nov., Boston, MA, Am. Meteorol. Soc., pp 129-135.
- [3] D. Melton, N. G. Riley and M. Darnel "A Model for Transhorizon Propagation in the Low-VHF Band", Avril 1993, IEE 8th Int. Conf. on Ant. and Prop., pp 749-754.
- [4] J. Röttger, C. H. Liu "Partial Reflection and Scattering of VHF Radar Signals from the Clear Atmosphere", Mai 1978, Geoph. Res. Letters, 5, n°5, pp 357-360.
- [5] H. T. Friis, A. B. Crawford, D. C. Hogg "A Reflection Theory for Propagation Beyond the Horizon", mai 1957, Bell. Syst. Tech. J., 38, n°3, pp 627-644.
- [6] A. B. Crawford, D. C. Hogg, W. H. Kummer "Studies in Tropospheric Propagation Beyond the Horizon", sept. 1959, Bell. Syst. Tech. J., 36, n°5, pp 1067-1178.
- [7] P. L. Rice, A. G. Longley, K. A. Norton, A. P. Barsis "Transmission Loss Predictions for Tropospheric Communication Circuits", 1967, NBS Tech. Note 101.
- [8] A. N. Tawfik, E. Vilar, L. Martin "Correlation of Transhorizon Signal Level Strength with Localised Surface Meteorological Parameters", Avril 1993, IEE 8th Int. Conf. on Ant. and Prop., pp 335-339.

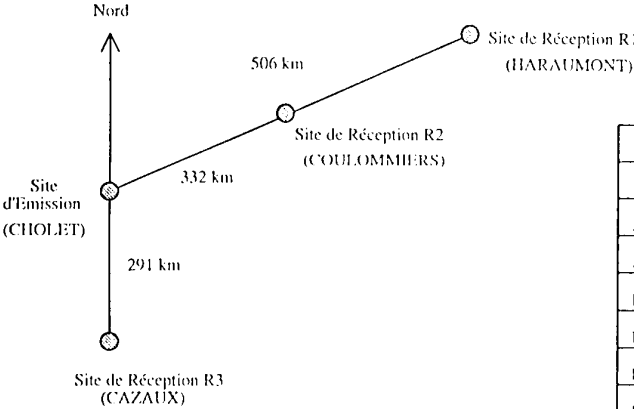


FIGURE 1 : Géométrie des liaisons.

Puissance émise	1 kw
Pertes coaxiaux	Environ 1 dB
Antenne émission	Disc-Cone (2 dBi)
Antenne réception (sites fixes)	Log-Périodique (6 dBi)
Polarisation	Verticale
Facteur de bruit réception	7 dB
Rythme binaire	24 kb/s
$E_b/N_0$ minimum nécessaire	6 dB
Bande de réception	25 kHz

TABLEAU 1 : Caractéristiques générales des liaisons.

SITES	DISTANCES / CHOLET	ANTENNE	HAUTEUR	DATE DES MESURES (JJ)
Coulomniers	332 km	LPV	11,5 m	3071400-3211000
Coulomniers	332 km	LPV	15 m	2911450-3071335
Coulomniers	332 km	LPV	18 m	3211025-3211210
Rocamadour	302 km	LPV	18 m	0351155-0531320
Lyon	443 km	LPV	18 m	0221415-0321030
Le Cranou	284 km	LPV	18 m	3511055-0050740
La Regine	472 km	LPV	18 m	0551340-0661205
Tasselot	413 km	LPV	18 m	0141625-0191540
Lannec	308 km	LPV	18 m	3251435-3351320
Le Portzie	318 km	LPV	18 m	3381405-3462305

TABLEAU 2 : Configurations de la station déplaçable.

Figure 2 : Distribution des moyennes instantanées  
Station CAZAUX (f2) - 28/03/93 18h19 / 29/03/93 07h10

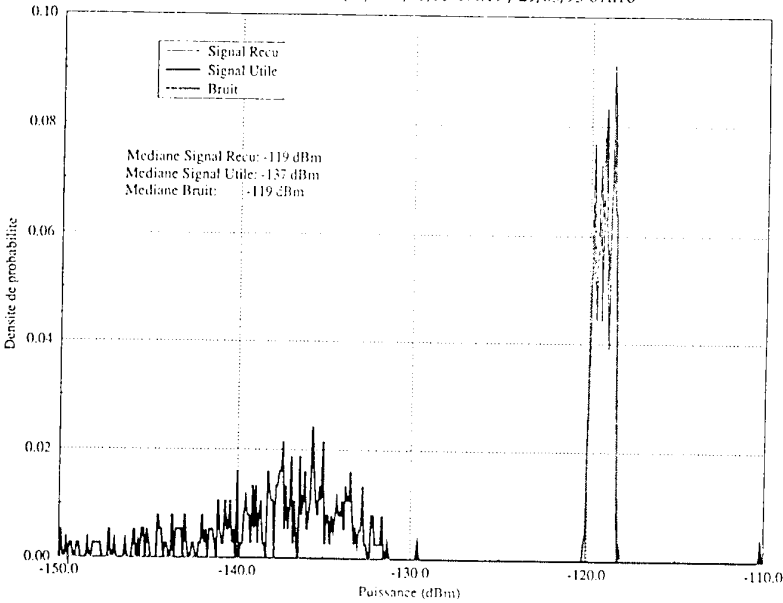


Figure 4 : Transformée en ondelettes  
Durée d'analyse : 10 minutes, fréquences : 0.5 - 5 Hz  
Date : 19/11/92 16h20

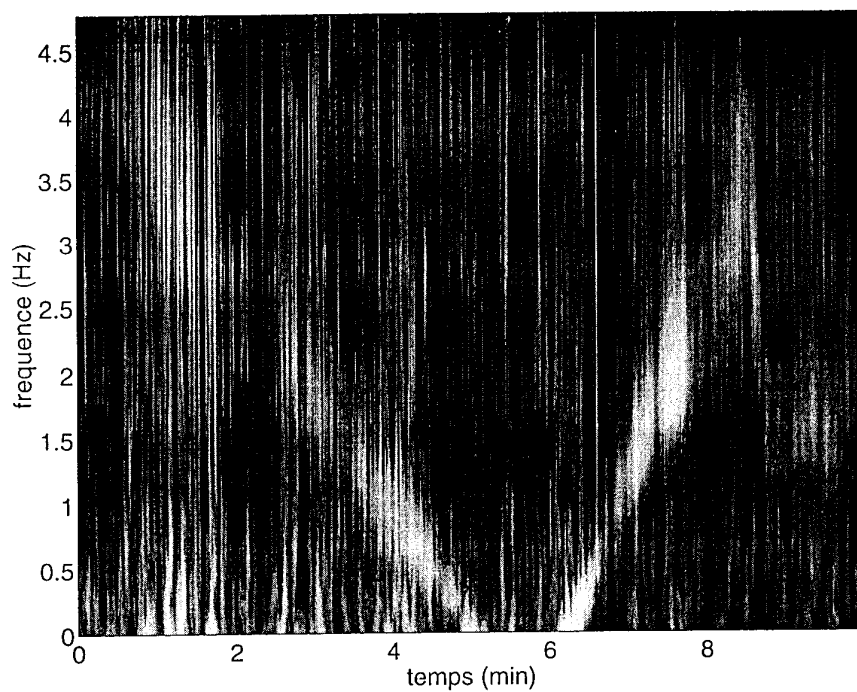


Figure 5 : Transformée en ondelettes  
Durée d'analyse : 10 minutes, fréquences : 0.5 - 5 Hz  
Date : 19/11/92 16h40

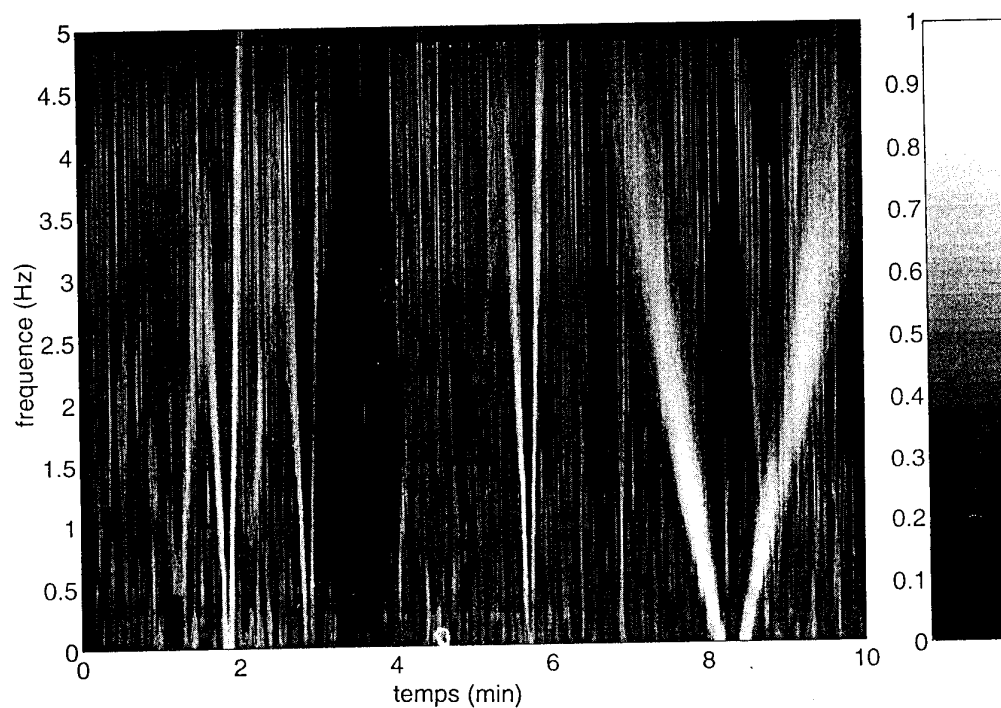


Figure 3 : Exemple de puissance reçue.  
Station CAZAUX - Date: 19/11/92 - Fréquence F3

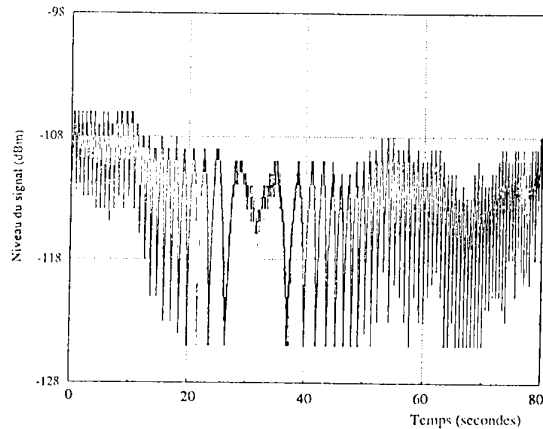


Figure 6 : Distribution des moyennes instantanées

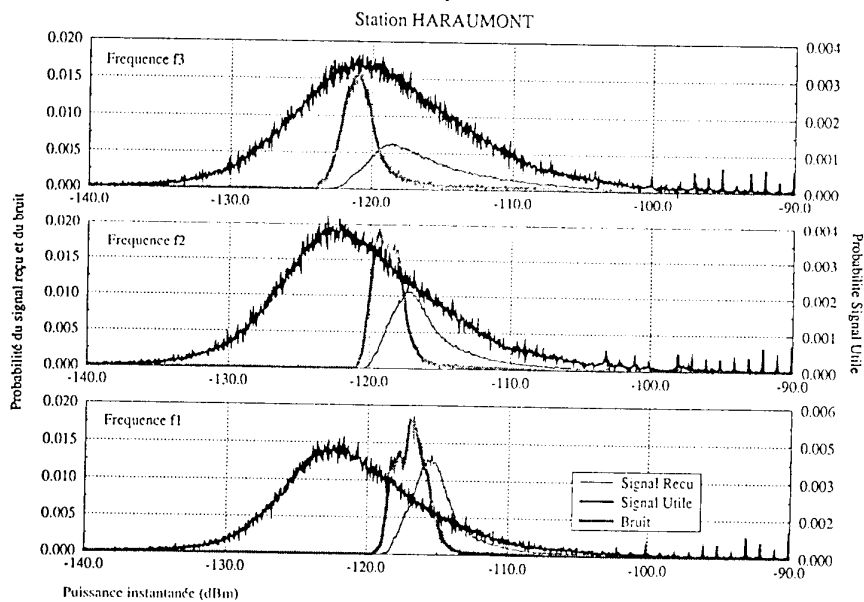


Figure 7 : Analyse Horizontale - Octobre 92 / Mars 93

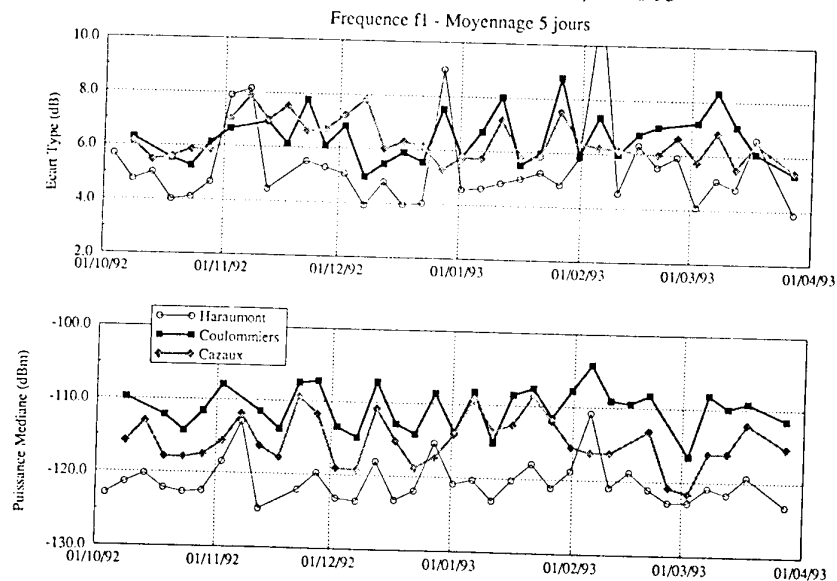


Figure 8 : Station HARAUMONT

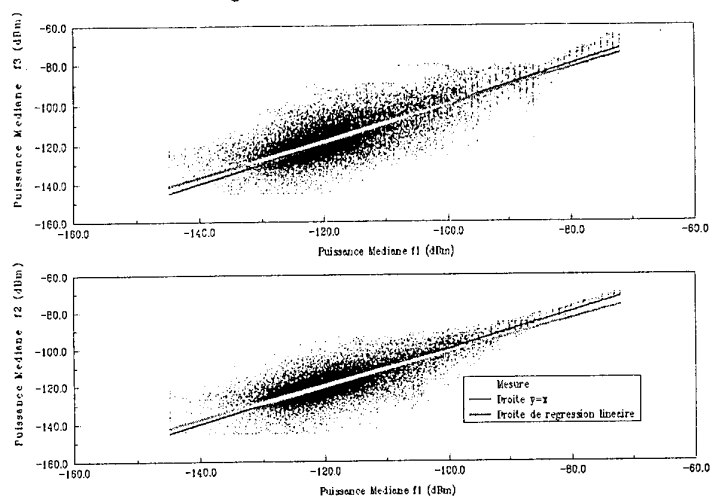


Figure 9 :

Comparaison entre station - Fréquence : 47.30 MHz  
Moyennage de 2 jours - Octobre 92 / Mars 93

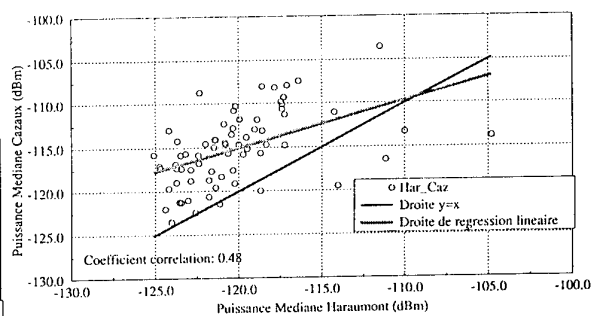
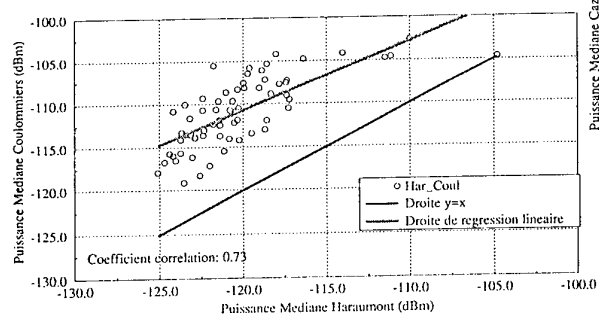


Figure 10 : Ecart type des médianes en fonction de la durée du créneau.

Station de CAZAUX - Octobre 92 / Mars 93

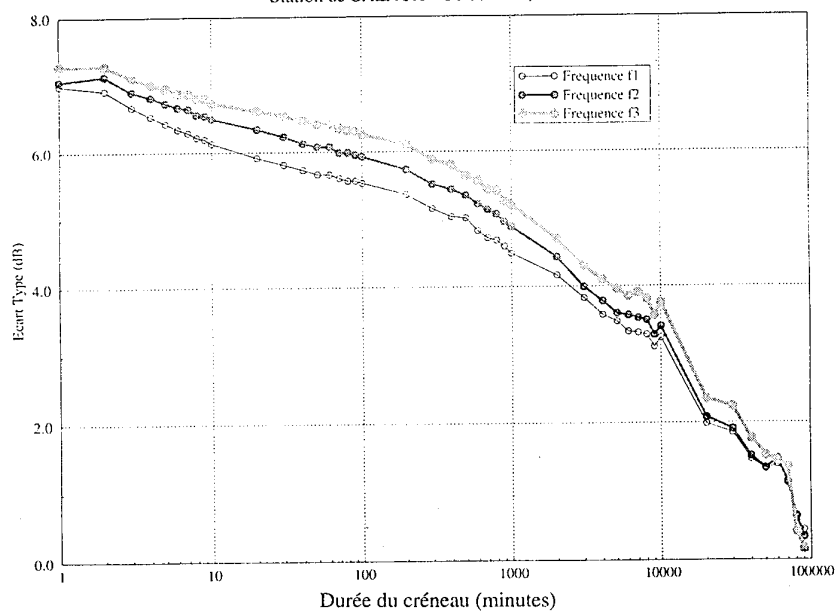


Figure 11 :

## Analyse Verticale Signal Utile

Station CAZAUX

Fréquence 41.50 MHz - Période : Octobre 92 / Mars 93

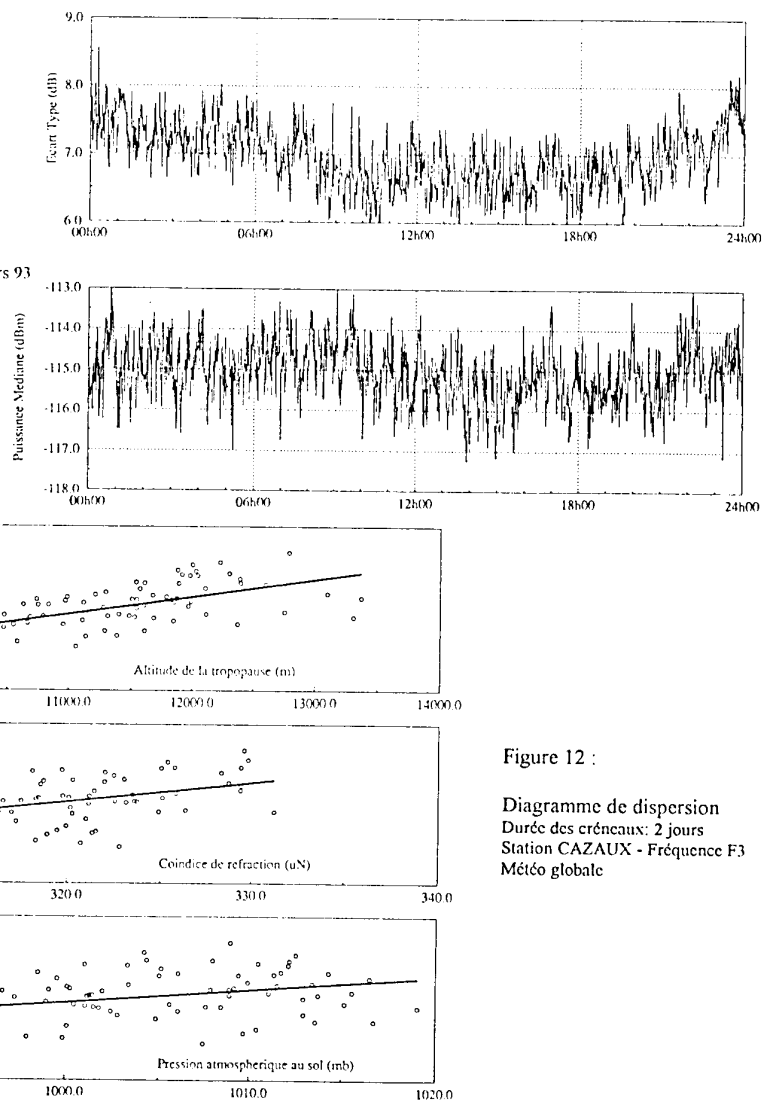
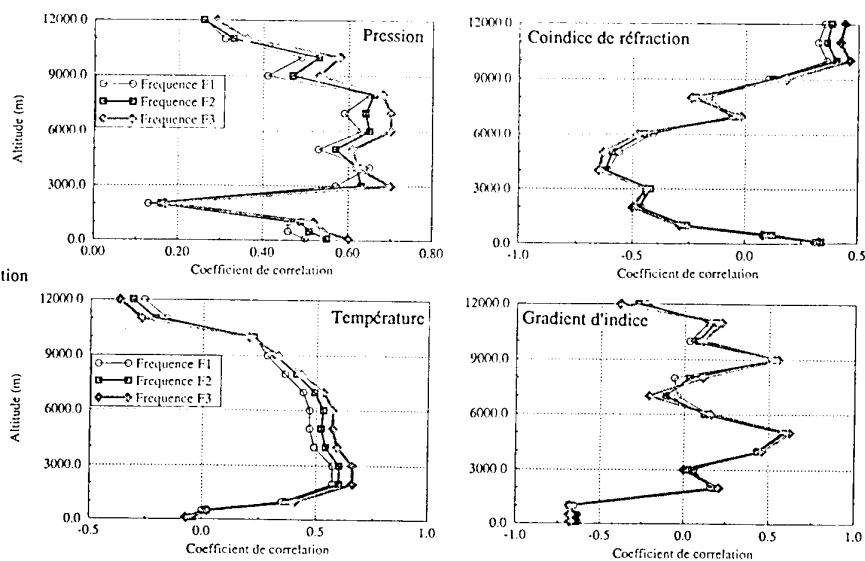


Figure 12 :

Diagramme de dispersion  
Durée des créniaux : 2 jours  
Station CAZAUX - Fréquence F3  
Météo globale

Figure 13 :

Evolution des coefficients de corrélation  
en fonction de l'altitude



## DISCUSSION

**Discussor's name :** W. Flood

**Comment/Question :**

1. What is the experimental data which leads you to conclude that for "tropospheric reflection" only 3-4 partial reflections occur?
2. You said that the model is in the process of being published. Can you give the reference for this publication?

**Author/Presenter's reply :**

1. Les transformées temps fréquences nous donnent de sérieuses indications à ce sujet, mais elles ne constituent pas une preuve absolue. En effet, pour cela, les traitements devraient être effectués d'une manière systématique, avec une détection du nombre de composantes présentes. Cependant, l'hypothèse, selon laquelle 3-4 composantes significatives sont présentes, est en accord avec les conclusions de certains auteurs [1]. Cette hypothèse est donc tout à fait discutable, mais le nombre de composantes n'intervient pas dans notre modélisation de canal.
2. Colloque SEE, "2ème Colloque Propagation du décamétrique à l'Angström", Mars 1993.

**Translation :**

1. *The time frequency transforms give us some fairly reliable indications on this point, but they do not constitute an absolute proof. In order to achieve that, processing would have to be carried out in a systematic manner, with detection of the number of components present. However, the assumption which states that 3 to 4 significant components are present is in agreement with the conclusions of certain authors (1). This assumption is therefore quite open for discussion, but the number of components is not involved in our channel modelling.*
2. *SEE Conference "Second Conference on Angström Decametric Propagation", March 1993.*

**Discussor's name :** C. Goutelard

**Comment/Question :**

L'effet saisonnier, dont vous présenterez des résultats entre novembre '92 et avril '93 est faible. L'aviez-vous constaté en dehors de cette période?

**Translation :**

*The seasonal effect, whose results you present for the period November 92 to April 93, is not very marked. Have you noticed it outside this period?*

**Author/Presenter's reply :**

Les données relatives à la période avril 93 à septembre 93 ne sont pas encore disponibles. Cependant, nous connaissons la tendance des résultats et il semblerait que l'effet saisonnier est également absent pour cette période et donc pour l'ensemble de l'année.

**Translation :**

*The data for the period April 93 to September 93 are not yet available. However, we know the trend of the results and it would seem that the seasonal effect is also absent during this period, and therefore during the whole of the year.*

**Discussor's name :** Prohoroff

**Comment/Question :**

Il serait intéressant de connaître les paramètres météorologiques qui interviennent ou interviendront dans la caractérisation de vos canaux de transmission. Ceux relatifs au soleil (ensoleillement, intensité et activité solaire) sont-ils pris en compte?

**Translation :**

*It would be interesting to know the meteorological parameters which are involved or which will be involved in the characterisation of your transmission channels. Do you take into account the sun-related ones? (Insolation, intensity and solar activity).*

**Author/Presenter's reply :**

Actuellement, dans notre modèle, aucun paramètre n'est pris en compte; il est adapté pour les liaisons associées à des climats de type tempéré car aucun autre climat n'a pu être testé. Cependant, nous espérons prendre en compte un ensemble de paramètres météorologiques dans les futures versions du modèle.

**Translation :**

*At present, no parameter is taken into account in our model; it is designed for links associated with temperate climates, as we have not been able to test any other type of climate. However, we hope to be able to take into account a whole set of meteorological parameters in future versions of the model.*



## LES PROBLEMES DE CODAGE DANS LES CANAUX A TRAJETS MULTIPLES

par

**C. Goutelard**

LETTI-Université Paris-Sud - 91405 Orsay Cédex  
France

### **I. - GENERALITES -**

Les canaux de transmission sont essentiellement multitrajets. Les trajets multiples sont introduits par des biréfringences du milieu comme dans l'ionosphère, par des inhomogénéités comme dans l'ionosphère et la troposphère, ou par des réflexions sur des obstacles comme dans les liaisons urbaines ou troposphériques.

Les trajets multiples créent des phénomènes d'interférence qui introduisent des modifications d'amplitude et de phase de la fonction de transfert du canal. La non stationarité des canaux complique leur utilisation, notamment dans les télécommunications numériques ou en télédétection.

La lutte contre les problèmes d'évanouissement fait appel à des techniques de modulation particulières ou à des dispositifs de codage. Le choix, à priori, d'une modulation pour réaliser un système de télécommunication entraîne souvent une complexité du codage nécessaire pour corriger les erreurs introduites par le canal.

Une méthode générale d'analyse des canaux et de choix de la modulation et du codage est proposée dans cette présentation. Il est montré que le choix optimum ne peut se faire sans une analyse de la répartition des erreurs qui dépend de la fonction de transfert du canal, mais également du bruit et des interférences.

A partir de la connaissance de la fonction de transfert, des interférences et du bruit, il est montré qu'une méthode générale peut être dégagée de façon à conduire à un modèle de répartition des erreurs à partir duquel les codes peuvent être choisis. Les codes à utiliser sont souvent d'une grande complexité. La technique de l'entrelacement peut être utilisée pour éviter des paquets d'erreurs, cependant la quasi périodicité des évanouissements qui apparaissent dans les canaux à trajets multiples rend l'entrelacement régulier souvent inefficace et il devient alors nécessaire d'envisager des entrelacements aléatoires ou pseudo-aléatoires. Les entrelacements aléatoires nécessitent un système de

désentrelacement séquentiel qui impose une synchronisation souvent préjudiciable à la bonne qualité de la transmission. Un entrelacement pseudo-aléatoire paraît plus favorable et une méthode d'entrelacement est présentée.

### **II. - CARACTERISATION DES CANAUX DE TRANSMISSION ALEATOIRES NON STATIONNAIRES - [1]**

On caractérise les canaux non stationnaires par leur réponse impulsionnelle  $h(t, \tau)$  qui représente l'amplitude du signal de sortie à l'instant  $t$ , à une impulsion de Dirac émise à l'instant  $t - \tau$ . Cette réponse impulsionnelle, que nous appellerons réponse bitemporelle, caractérise totalement le canal de transmission. Il est équivalent de représenter ce canal par la fonction de diffusion  $D(\gamma, \tau)$  qui est obtenue par la transformée de Fourier selon  $t$  de la réponse impulsionnelle ou par la fonction de transfert  $H(t, f)$  qui est obtenue par la transformée de Fourier selon  $\tau$  de la réponse impulsionnelle.

Soit

$e(t)$  le signal appliqué à l'entrée du canal et dont la transformée de Fourier est  $E(f)$ ,

$s(t)$  le signal à la sortie du canal et dont la transformée de Fourier est  $S(f)$ .

Trois relations équivalentes relient le signal  $s(t)$  à  $e(t)$ :

- Par la réponse bitemporelle :

$$s(t) = \int_{\tau} e(t-\tau) h(t, \tau) d\tau \quad (1)$$

- Par la fonction de transfert :

$$s(t) = \int_{\gamma} E(f) H(t, f) \exp(j2\pi f t) df \quad (2)$$

- Par la fonction de diffusion :

$$s(t) = \iint_{\gamma, \tau} e(t-\tau) D(\gamma, \tau) d\gamma d\tau \quad (3)$$

Dans les transmissions à travers des canaux multitrajets, on peut attribuer, à chaque trajet, une fonction de transfert propre  $H_i(t, f)$ . La fonction de transfert complète est donc donnée par la relation :

$$H(t, f) = \sum_{i=1}^I H_i(t, f) \quad (4)$$

où  $I$  représente le nombre total de trajets à travers le canal.

Le signal de sortie s'exprime alors par la relation :

$$s(t) = \sum_{i=1}^{I_1} \int_f E(f) H_i(t, f) \exp(j2\pi ft) df \quad (5)$$

où  $I_1$  est le nombre de trajets pris en compte dans le système de détection du récepteur.

La fonction de transfert globale de l'ensemble signal plus récepteur dépend du traitement de signal qui est associé.

- Dans les systèmes adaptatifs, le signal est traité par un filtre dont la fonction de transfert est théoriquement l'inverse de la fonction de transfert du canal.

- Des filtrages peuvent être effectués pour sélectionner une fonction de transfert du canal. Ainsi la séparation des modes de propagation par une discrimination temporelle réduit le nombre de trajets captés par le récepteur. Il en est de même si l'on effectue un filtrage spatial par un traitement d'antenne ou un filtrage sur la polarisation des ondes reçues.

La notion de fonction de transfert du canal doit être définie en prenant en compte les caractéristiques du récepteur. Par la suite nous définirons comme fonction de transfert du canal la fonction filtrée par le récepteur.

### III. - FONCTION DE TRANSFERT ET SIGNAL -

On appellera  $B$  la largeur spectrale du signal émis et  $D$  la quantité d'information transmise par seconde en Shannon.

Le produit (durée  $T_b$  bande  $B_b$ ) disponible pour la transmission d'un Shannon est donc donné par la relation :

$$T_b B_b = B/D \text{ Hertz-seconde} \quad (6)$$

Soit  $D_{s0}$  la densité spectrale de puissance du signal émis. L'énergie émise par Shannon est donc égale à :

$$E_b = D_{s0} \cdot B_b \cdot T_0 \quad (7)$$

qui est représentée par le volume élémentaire indiqué sur la figure 1.

La forme que l'on peut donner à la base ( $B_b T_b$ ) peut être variable. Dans les transmissions série  $T_b$  est petit, et dans les transmissions parallèles  $B_b$  est petit (figure 1).

La transmission consistant à utiliser un symbole par Shannon conduit à des erreurs généralement plus fortes que dans le cas contraire. Le spectre du signal reçu est le produit spectre du signal émis par la fonction de transfert du canal.

La figure 2a représente une fonction de transfert enregistrée sur une bande de 3kHz à travers le canal ionosphérique. La figure 2b représente une fonction de transfert relevée sur 500MHz à travers un canal hertzien. On peut constater de l'allure similaire des variations de la fonction de transfert. Nous nous intéresserons par la suite à la fonction de transfert de la figure 2a qui servira de base pour les raisonnements suivants.

Ces fonctions font apparaître les évanouissements, comme le montre la figure 3 qui représente une coupe de la figure 2a effectuée pour un niveau d'écrtage donné. On y voit apparaître les creux d'évanouissements dans lesquels la densité spectrale peut décroître de façon importante. Dès lors, si le volume élémentaire cité précédemment, ayant pour base  $B_b T_b$ , est situé dans l'un de ces creux d'évanouissements, la probabilité d'erreur croît de façon rapide. Ainsi, la transmission s'en trouve altérée. Si les creux d'évanouissements ont des durées longues, il s'ensuit l'apparition de paquets d'erreurs qu'il devient très difficile de corriger, même par des codes puissants, mais dont le décodage est évidemment complexe. On peut remarquer que la fluctuation de densité spectrale d'énergie à la réception est la cause la plus pénalisante quant à l'apparition des erreurs dans la transmission. Si la densité spectrale de puissance reçue était uniforme, on aurait une répartition aléatoire des erreurs sans apparition de paquets d'erreurs longs. Cette remarque conduit naturellement à deux constatations qui consistent à (figure 4) :

- Choisir, pour la base  $T_b B_b$ , une forme particulière permettant de couvrir une zone suffisamment large qui permettrait d'obtenir, pour chaque symbole, une densité d'énergie suffisamment voisine de la densité spectrale de puissance moyenne. Ce résultat ne peut

être obtenu de façon optimale, car les lois d'apparition des évanouissements sont extrêmement variables à l'intérieur d'un canal. Cette technique s'apparente à celle utilisée dans l'étalement de spectre où la base  $B_b$  se trouve élargie de façon considérable mais elle n'est cependant pas toujours utilisable.

- Grouper K Shannon pour former un signal. Dans ces conditions, la base disponible dans l'espace fréquence-temps s'exprime par :

$$T_s B_s = K \text{ B/D Hertz-seconde} \quad (8)$$

où  $T_s$  et  $B_s$  représentent le temps et la bande disponibles pour le signal transportant les K Shannon. La base étant plus étendue, la densité spectrale de puissance moyenne pour le signal s'approche davantage de la densité spectrale de puissance moyenne reçue et la probabilité d'erreurs s'en trouve diminuée.

Les techniques utilisant ce principe sont les modulations à  $2^n$  états et l'utilisation des codes. On peut également combiner le codage et l'étalement de spectre [2] ou enfin utiliser l'entrelacement. Le choix optimum de la base  $T_s B_s$  constitue le véritable problème à résoudre pour optimiser les transmissions. Il est possible de définir une méthode générale permettant d'aboutir au bon choix.

#### IV. - MODULATION ET CODAGE OPTIMUMS -

La qualité d'une transmission dépend de la fonction de transfert du canal, comme il l'a été montré précédemment, mais également de l'influence du bruit et des interférences.

Dans le développement qui suit, nous engloberons pour faciliter l'exposé sous le terme général de bruit, le bruit interne, le bruit externe (en particulier le bruit atmosphérique), mais également les brouilleurs et interférences. On appellera densité de puissance moyenne du bruit  $N_0$  donnée par l'expression :

$$N_0 = \frac{1}{B_s T_s} \int_{T_s} \int_{B_s} n(f, t) dt df \quad (9)$$

où  $n(f, t)$  est la densité spectrale du bruit à la fréquence  $f$  et à l'instant  $t$ .

On appellera énergie moyenne par Shannon la quantité  $E_b$  définie par la relation suivante :

$$E_b = \frac{1}{K} \int_{T_s} \int_{B_s} D_e(f) |H(f, t)|^2 dt df \quad (10)$$

où  $D_e(f)$  est la densité spectrale de puissance du signal émis qui n'est plus considérée comme une constante dans ce développement.

On définit les fonctions de distribution suivantes :

- La densité de probabilité pour que le rapport  $E_b / N_0$  soit compris entre  $x$  et  $x + dx$  :

$$p_0(x) dx = \text{Pr ob} \left\{ x < \frac{E_b}{N_0} < x + dx \right\} \quad (11)$$

Cette densité de probabilité se déduit des relations précédentes établies sur  $N_0$  et  $E_b$ . Il s'agit d'une caractéristique mesurable du canal.

- La probabilité pour que le rapport  $E_b / N_0$  reste inférieur à  $x$  pendant une durée comprise entre  $y$  et  $y + dy$  :

$$p_1(x, y) dy = \text{Pr ob} \left\{ y < \text{Durée} \left( \frac{E_b}{N_0} < x \right) < y + dy \right\}$$

Cette densité de probabilité est à deux dimensions : le seuil de la valeur  $E_b / N_0$  et la durée  $y$  durant laquelle cette condition est respectée. Cette loi se déduit des relations précédentes, c'est-à-dire des caractéristiques du canal.

- La probabilité d'erreur du modem pour un rapport énergie à densité spectrale de bruit donné :

$$P_e(x) = \text{Probabilité d'erreur du modem pour} \quad \frac{E_b}{N_0} = x \quad (13)$$

Ces 5 relations définissent totalement le modèle des erreurs.

La probabilité d'erreur moyenne  $P_e$  est donnée par la relation :

$$P_e = \int_0^\infty p_0(x) P_e(x) dx \quad (14)$$

La probabilité d'erreur moyenne est insuffisante pour définir un code de correction d'erreurs. Il est nécessaire de connaître la loi de répartition des erreurs que l'on traduit par une distribution de la longueur des paquets erronés et la probabilité d'apparition des erreurs isolées.

On peut caractériser ces deux distributions à partir de la relation suivante :

$$P_{e(x_0)} = \int_0^{x_0} p_0(x) P_e(x) dx \quad (15)$$

qui donne la probabilité d'erreur pour l'ensemble des cas pour lesquels le rapport  $E_b / N_0$  est inférieur à  $x_0$ .

On définit les paquets d'erreurs par leur densité d'erreurs  $d$ . Cette densité est fixée à priori, en fonction des caractéristiques des codes et la longueur  $L$  des paquets d'erreurs est définie comme la plus grande longueur que l'on peut trouver à l'intérieur du train numérique et dans laquelle la densité d'erreurs est égale ou supérieure à  $d$ . En d'autres termes, l'allongement de la longueur considérée, entraîne une densité d'erreur inférieure à  $d$ . Il est simple de voir que la densité d'erreur fixe la valeur de  $x_0$  de la relation précédente :

$$d = P_{e(x_0)} \quad (16)$$

La longueur des paquets d'erreurs ayant la densité  $d$  est définie par la distribution :

$$L(y) = P_1(x_0, y) \quad (17)$$

qui représente la probabilité de trouver des paquets d'erreurs de longueur  $y$  ayant une densité  $d$ .

On appelle erreurs isolées les erreurs que l'on ne peut grouper de façon consécutive dans un train numérique pour atteindre la densité des paquets d'erreurs  $d$ . Il est simple de voir que la probabilité d'apparition des erreurs est donnée par la relation :

$$P_{e_1} = \int_{x_0}^{\alpha} p_0(x) P_e(x) dx \quad (18)$$

Ces dernières relations définissent totalement le motif d'erreurs attachées à l'ensemble canal plus modem et sont suffisantes pour la recherche des codes les plus efficaces. Dans les propagations multitrajets les codes connus ne permettent pas toujours de corriger des erreurs de façon satisfaisante à cause des grandes longueurs de paquets qui apparaissent. Il est alors nécessaire d'utiliser, associé au codage la technique d'entrelacement.

## V. - ENTRELACEMENT PSEUDO-ALEATOIRE -

L'entrelacement a pour objectif de détruire les groupements des erreurs. Un entrelacement régulier aboutit à ce résultat à la condition que les périodes d'évanouissement ou les périodes d'apparition des

erreurs ne soient pas un multiple ou sous multiple du pas d'entrelacement.

Dans les canaux multitrajets les évanouissements apparaissent souvent de façon quasi périodique et résistent alors à des entrelacements réguliers. Les entrelacements, totalement aléatoires, nécessitent une synchronisation pour le désentrelacement, ce qui est une source de complications. L'entrelacement pseudo-aléatoire proposé évite les inconvénients cités ci-dessus.

On considère un vecteur code comprenant  $n$  symboles :

$$V_1 = \{s_1, s_2, \dots, s_k, s_{k+1}, \dots, s_n\} \quad (19)$$

où  $s_k$  figure le  $k$ ème symbole du vecteur code  $V_1$ .

L'étalement consiste à répartir ces  $n$  symboles sur  $m$  positions du train binaire comme le montre la figure 5 où  $N$  est le nombre de vecteurs de  $n$  symboles entrelacés avec un pas  $a$  dans le bloc de longueur :

$$L = m + (N-1)a$$

On peut définir un vecteur  $V$  binaire dont les symboles prennent la valeur 1 aux emplacements des symboles de  $V_1$  et la valeur 0 ailleurs. On repère  $V$  par la relation :

$$V = \{S_1, S_2, \dots, S_k, S_{k+1}, \dots, S_n\} \quad (20)$$

où  $S_k$  est la distance entre le symbole  $s_k$  et  $s_{k+1}$  du vecteur  $V_1$ .

Les lois d'entrelacement pseudo-aléatoires sont définies par la même loi d'entrelacement des distances  $S_k$  pour chaque vecteur code émis, et un pas d'entrelacement constant  $a$  entre deux vecteurs consécutifs (figure 5). On définit la loi pseudo-aléatoire par les relations suivantes :

$$\left. \begin{array}{l} S_k \neq S_h \\ S_k \geq S_m \end{array} \right\} \forall k, h \neq k \quad (21)$$

$$k, h \in \{1, 2, \dots, n-1\}$$

où  $S_m$  est une distance minimale imposée à priori.

Le problème se résume alors à rechercher, sous les contraintes définies par (21), un vecteur  $V$  à fonction d'autocorrélation aperiodique nulle en dehors du pic central pour tout  $\alpha$  tel que :

$$\alpha \in \{1, 2, \dots, N-1\} \quad (22)$$

Il faut enfin que, sur le bloc des  $m$  symboles transmissibles, le maximum d'entre eux soit utilisé pour la transmission des  $N$  vecteurs. Ceci conduit à définir le rendement  $\eta$  de l'entrelacement comme le rapport du nombre de symboles émis à la longueur  $L$  du bloc transmis :

$$\eta = \frac{n N}{m + (N-1)\alpha} \quad (23)$$

La solution de ce problème a été donnée dans [3] où il est montré que l'optimisation du rendement conduit au choix du nombre optimum de vecteurs défini par la relation :

$$N_{opt} = \frac{m-1}{n+1} \quad (24)$$

et que le rendement optimum s'écrit alors :

$$\eta_{opt} = \frac{N_{opt} n}{N_{opt} (n-1+\alpha) + (1-\alpha)} \quad (25)$$

qui est maximum pour  $\alpha = 2$ . Le rendement s'exprime alors par :

$$\eta = \frac{n}{n-1} \quad (26)$$

On peut constater que le rendement tend vers 1 lorsque le nombre de symboles par vecteur augmente. Ainsi, pour un code constitué par des vecteurs de 32 symboles :

- Le nombre optimum de vecteurs à entrelacer est de 37.

- La longueur du bloc est 1220.

- Le rendement de l'entrelacement est de 0,97.

Cette méthode d'entrelacement permet d'uniformiser la distribution des erreurs en évitant les longueurs de paquets d'erreurs trop importantes et de faciliter l'implantation de codes correcteurs à travers des canaux à trajets multiples.

## VI. - CONCLUSION -

Les transmissions à travers les canaux multitrajets sont caractérisées par l'apparition d'évanouissements profonds qui résultent d'un phénomène d'interférences. Ces évanouissements introduisent

des erreurs groupées que l'on peut combattre par des choix de signaux appropriés en groupant les symboles à transmettre de façon à obtenir des signaux élémentaires pour lesquels la densité spectrale de puissance reçue ne prend pas des valeurs trop faibles.

Cependant des erreurs groupées peuvent apparaître et une technique d'entrelacement devient nécessaire. L'entrelacement régulier, face à des canaux dans lesquels les évanouissements sont quasi périodiques, ne permet pas d'échapper, de façon systématique, au groupement des erreurs.

L'entrelacement par un processus pseudo-aléatoire apparaît alors efficace et les rendements de l'entrelacement peuvent être rendus très voisins de l'unité.

Cette solution apparaît économique quant à la complexité des codes utilisés lorsque l'entrelacement demeure cependant possible. La recherche optimale du signal et du codage doit cependant être effectuée simultanément car la résolution séparée de la recherche du signal et de la recherche du code reporte bien souvent l'allègement de la complexité de l'un sur l'accroissement de la complexité de l'autre.

## BIBLIOGRAPHIE

- [1] *Characterization of channels used for Wideband Transmissions.*  
C. GOUTELARD  
L.S. 172 AGARD : *Propagation Limitations for systems using band-spreading.*  
Paris-Rome-Boston - Juin 1990.
- [2] *Définition et construction de codes pseudo-orthogonaux.*  
C. GOUTELARD, F. CHAVAND  
*Annales des Télécommunications - Tome 33, n° 5-6 - Mai-Juin 1978.*
- [3] *Optimisation de l'entrelacement des codes dans les canaux à évanouissements sélectifs.*  
C. GOUTELARD  
*Colloque national "3 journées sur le codage" - Cachan - Juin 1983 - Vol. 1 n° 2 (1984)*

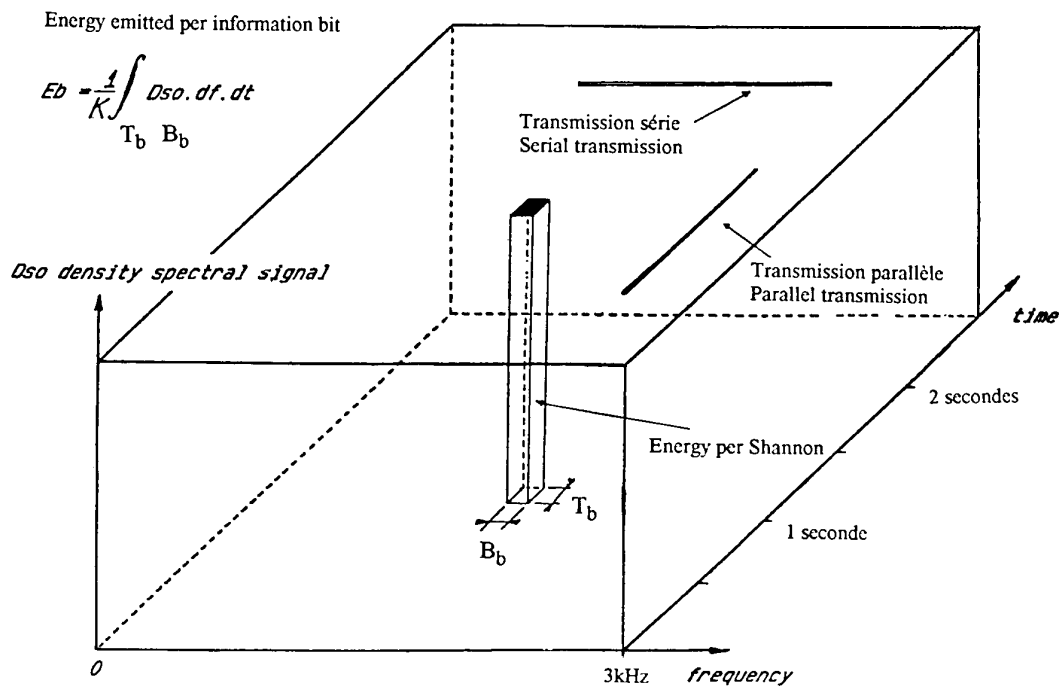
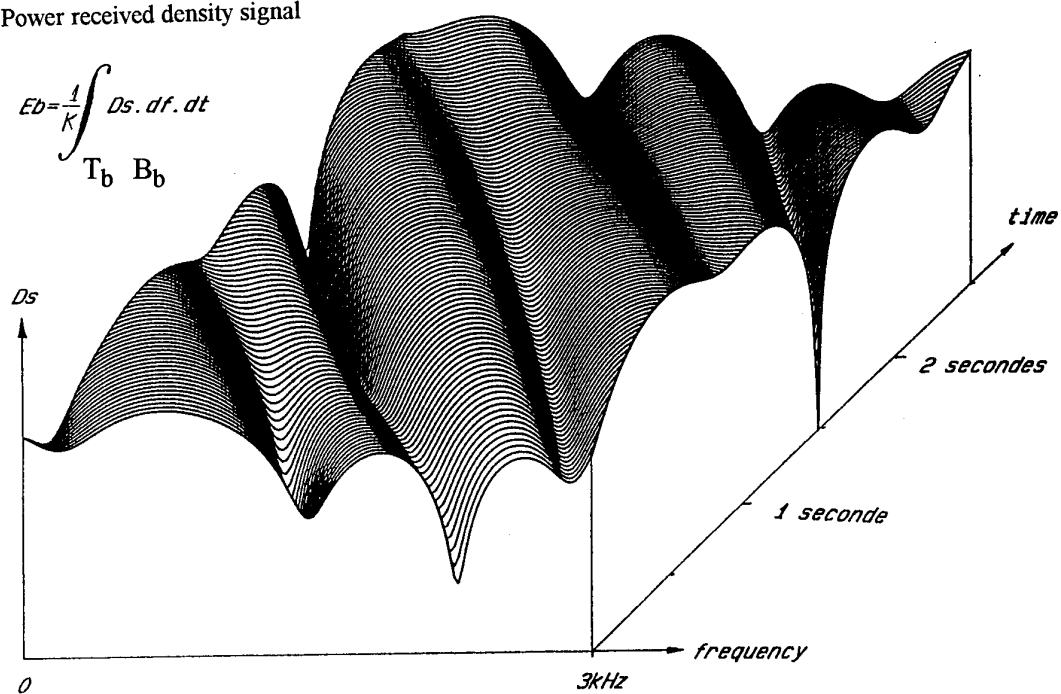


FIGURE 1  
Représentation de l'énergie émise par Shannon

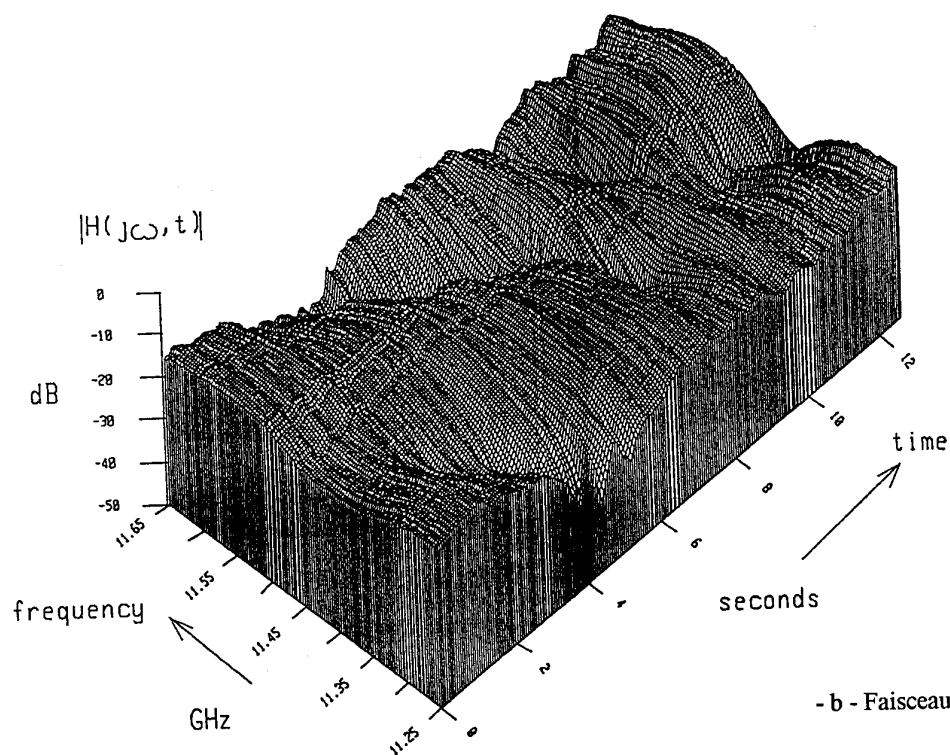
## RECEPTION

Ds Power received density signal

$$Eb = \frac{1}{K} \int_{T_b}^{T_b + B_b} Ds \cdot df \cdot dt$$



- a - Canal ionosphérique



- b - Faisceau Hertzien

FIGURE 2  
Fonctions de transfert mesurées.

- a -

Dans le canal ionosphérique. Document LETTI

- b -

Dans un faisceau Hertzien. D'après P. VILAR, L. MARTIN - IEEE - Ant. and Propag.

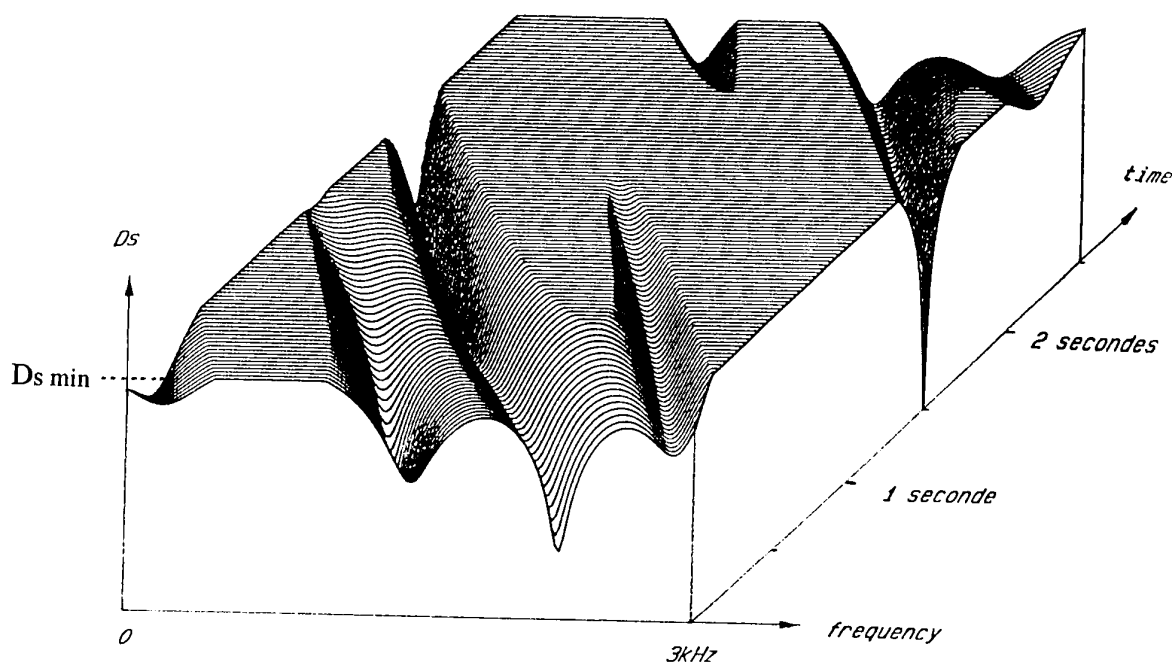


FIGURE 3  
Mise en évidence des évanouissements sélectifs profonds  
par une coupe de la fonction de transfert 2-a

### EMISSION

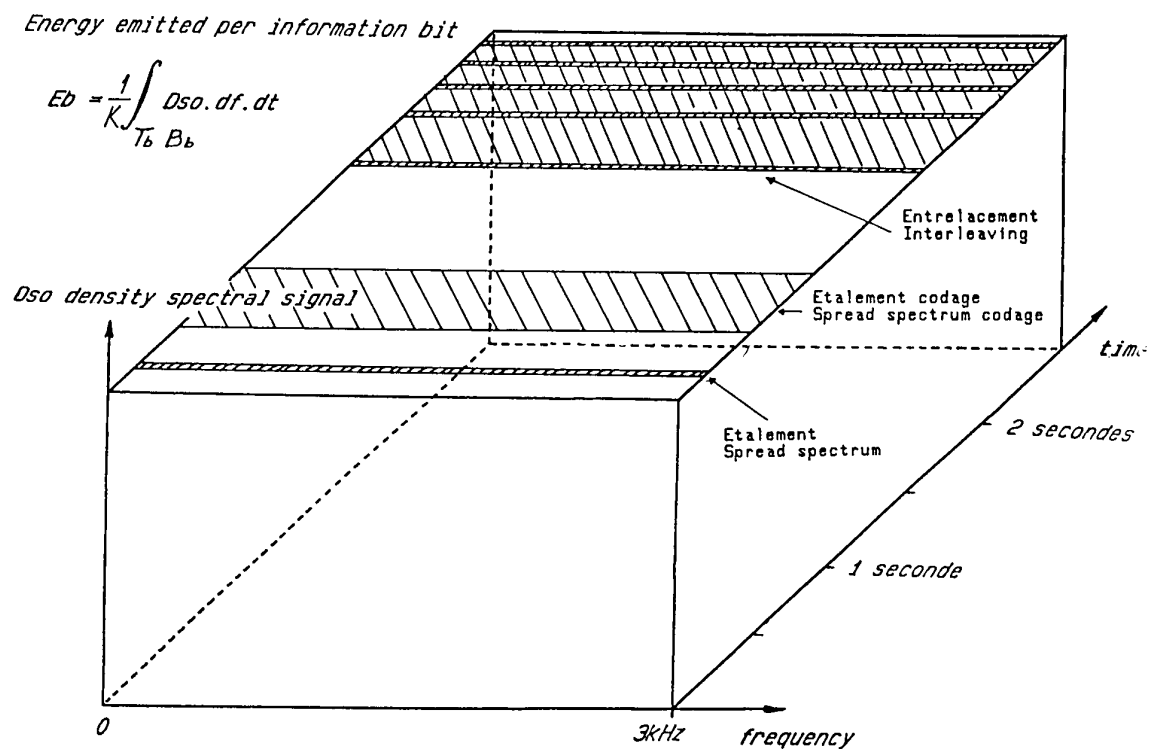


FIGURE 4  
Stratégie de répartition du volume d'énergie  
pour la transmission de K Shannon par un symbole



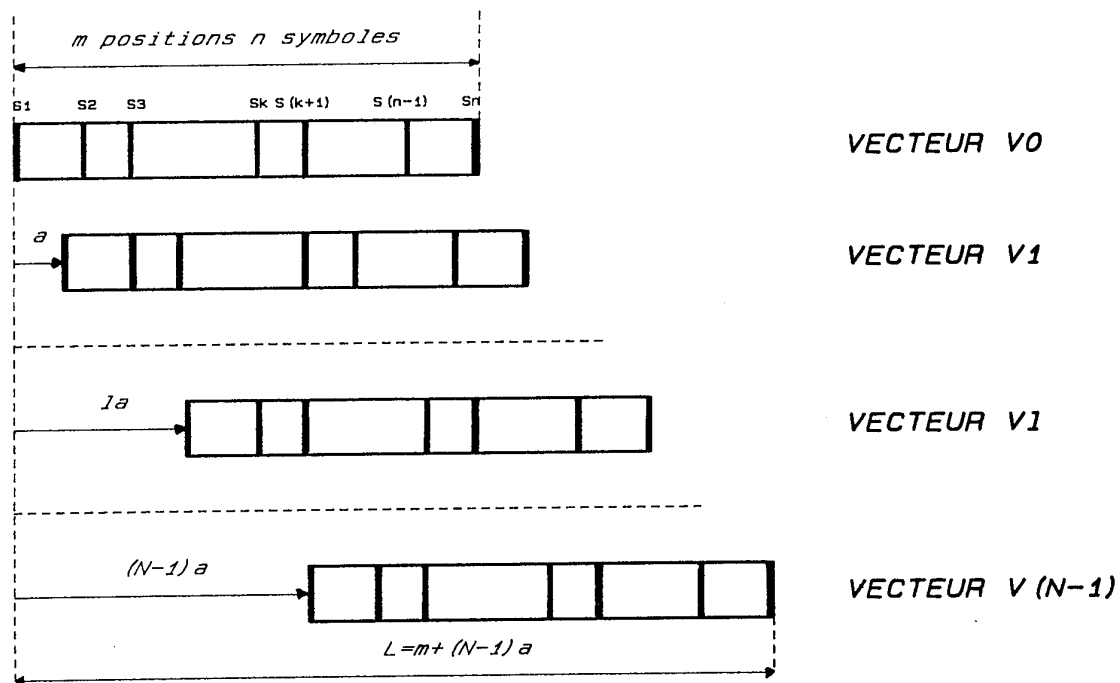


FIGURE 5  
Principe de l'entrelacement pseudo-aléatoire

## Terrain and Refractivity Effects on Non-Optical Paths

Amalia E. Barrios

Naval Command, Control and Ocean Surveillance Center  
Research, Development, Test and Evaluation Division

NCCOSC RDT&E DIV 543  
53170 Woodward Road  
San Diego, CA 92152-7385  
U.S.A.

### SUMMARY

The split-step parabolic equation (SSPE) method has been used extensively to model tropospheric propagation over the sea, but recent efforts have extended this method to propagation over arbitrary terrain. At the Naval Command, Control and Ocean Surveillance Center (NCCOSC), Research, Development, Test and Evaluation Division, a split-step Terrain Parabolic Equation Model (TPEM) has been developed that takes into account variable terrain and range-dependent refractivity profiles. While TPEM has been previously shown to compare favorably with measured data and other existing terrain models, two alternative methods to model radiowave propagation over terrain, implemented within TPEM, will be presented that gives a two to ten-fold decrease in execution time. These two methods are also shown to agree well with measured data.

### INTRODUCTION

Only recently has the ability been available to model terrain and range-dependent refractivity effects for microwave frequencies. Currently validated PE terrain models include FDPEM (Finite-Difference Parabolic Equation Model)[1], PARA[2], and TPEM[3]. While FDPEM is a finite-difference model, PARA and TPEM employ the split-step algorithm. The split-step algorithm is widely accepted as more numerically efficient than finite-difference methods, however, the split-step algorithm can still require a substantial amount of time for certain applications at high frequencies.

The original implementation of TPEM is based on a transformation introduced by Beilis and Tappert to model rough surface scattering for acoustic fields[4]. A straightforward solution of the flat earth parabolic wave equation, with the appropriate boundary condition for a perfectly reflecting terrain surface, would be very difficult, since the boundary condition would be range-dependent. The original coordinate system is transformed such that a simpler boundary condition can be applied to the resulting modified PE. The split-step algorithm is now used with a new modified refractivity defined by

$$m(z) = M(z) - z t''(x) * 10^6$$

where the normally defined modified refractivity, or M-unit, is

$$M(z) = \left[ n - 1 + \frac{z}{a} \right] * 10^6$$

$n$  is the refractive index,  $a$  is the earth's radius, and  $z$  and  $x$  are

the height and range variables, respectively[3]. A general height function describing the terrain is represented by  $t(x)$ , and  $t''(x)$  is the second derivative of the height function with respect to range. The M-unit, which normally accounts for the earth's curvature, is replaced with the  $m$ -unit which now also accounts for the radius of curvature of each segment of the terrain.

While this method has the advantage that it is mathematically rigorous and simple to implement, its main disadvantage is the necessity of handling large propagation angles inherent in the second derivative of the terrain. That is, if the terrain consists of steep slopes, wavefronts will reflect and propagate at large angles. Since the split-step algorithm utilizes the Fourier transform, and transform size is directly proportional to frequency and propagation angle, it is important to keep the size of the angles to a minimum. The height mesh size, determined by Nyquist's criteria, is defined as

$$\Delta z = \frac{\lambda}{2 \sin \theta}$$

where  $\lambda$  is the wavelength in meters, and  $\theta$  is the propagation angle with respect to the horizontal. Therefore, for a specified altitude and frequency, one desires  $\Delta z$  to be as large as possible so the transform size can be as small as possible. Keeping the transform size small results in a smaller and faster program. Even relatively small terrain slopes of  $5^\circ$  can be fairly restrictive within the split-step algorithm, as some reflected rays will be propagating at angles of  $10^\circ$  and greater. At 20 GHz the mesh size will then be approximately .043 meters. Using a 1024 point transform size one would only be able to determine loss contours up to an altitude of 44 meters - not very practical for a communications or target detection application. Two methods of including terrain effects within the split-step algorithm will now be presented in which the propagation angle, and hence  $\Delta z$ , become independent of the slope of the terrain.

### MODEL DESCRIPTION

#### A. BOUNDARY DECAY METHOD

The boundary decay (BD) method, simply stated, is the forced elimination of the field at heights below the surface of the terrain. The real and imaginary parts of the field are set to zero at array elements, or bins, corresponding to heights below the terrain surface, as shown in Figure 1. The elements of the field arrays are labeled  $f_i$ , where

$$f_i = x_i + jy_i \quad \text{for } i=0,1,2,\dots,n-1,$$

$n$  is the transform size, and  $x_i$  and  $y_i$  represent the real and imaginary parts of the field, respectively. The field is propagated from range step to range step, using the smooth earth SSPE algorithm (M-unit only), with array elements below the terrain surface constantly kept at zero value.

## B. BOUNDARY SHIFT METHOD

In the boundary shift (BS) method, field array elements are shifted up or down, depending on the slope of the terrain, by an amount equal to the number of bins corresponding to the height of the terrain surface. From one range step to the next, the field is shifted, then propagated via the smooth earth SSPE algorithm. As an example, in Figure 2 it is assumed that the height of the terrain at range  $r+dr$  corresponds to three bins ( $3\Delta z$ ). The field at range  $r+dr$  is obtained from the field at range  $r$  by shifting field elements down three bins (that is, the field value at bin #4 is moved to bin #1, the value at bin #5 is moved to bin #2, etc., with the three remaining bins in the upper part of the array now set to zero) and then propagated using the SSPE algorithm. On downward slopes the field arrays are shifted up with the lower elements of the array set to zero.

The BD and BS methods were arrived at not based on any sound mathematical or physical formulations, but on intuitive concepts and approximations to the more accurately obtained field via the coordinate transformation described above. Effectively, what the BD and BS methods fail to account for is the high-angle energy that is reflected off the ground surface. For ground-based transmitters and receivers, the upward reflected energy is not important for most applications and can be neglected. Also, since the terrain is now accounted for by systematically shifting or eliminating field arrays, large, even vertical, terrain slopes are no longer difficult to model. The mesh size,  $\Delta z$ , is now determined by the frequency and propagation angle (for desired coverage) without regard to terrain slope.

## RESULTS

Figures 3, 4, and 5 show coverage diagrams using TPEM and the BD and BS methods, respectively, for a single wedge centered at 50 km. The frequency is 1000 MHz with the transmitter height at 25 m. The propagation loss contours are defined by the gray scale at the bottom of the figures, and the environment is a homogeneous 300 m surface-based duct. The height/refractivity profile is shown in Table 1.

Height (m)	Refractivity (M-unit)
0.	339.
250.	368.5
300.	319.
1000.	401.6

Table 1. Height/refractivity profile for 300 m surface-based duct.

In Fig. 3 there is a pronounced reflection from the side of the wedge. Due to this reflection, energy is being propagated at very sharp angles. The coverage diagram for the same case using the BD method is shown in Fig. 4 and the diagram for the BS method is shown in Fig. 5. In both figures there is some energy reflection from the wedge that can be seen, but it

is not as pronounced as that shown in Fig. 3. This results from the fact that both the BD and BS methods ignore the larger angles, whereas it is necessary to account for these angles in TPEM. The main point to illustrate from these figures is the consistency of the BD and BS methods with TPEM in the calculation of propagation loss values for non-optical paths beyond the wedge, that is, at receiver heights below 400 m and ranges beyond 60 km. In Figs. 4 and 5 the main features of the diffracted fields are identical to that of Fig. 3 with some slight differences in detail.

Non-optical propagation measurements were taken at several bearings from Salisbury and Weymouth, U.K., for frequencies at 700 MHz and 12 GHz (Dr. K. Craig, personal communication). Terrain paths were chosen such that a variety of ground coverage would be included in the measurements. Four classifications of terrain coverage are given: terrain paths consisting primarily of forested areas are labeled "wooded", those paths consisting of smooth or un-vegetated land are labeled "uncluttered", paths consisting equally of wooded and uncluttered are "wooded/uncluttered", and paths of equally vegetated and uncluttered land are labeled "cluttered/uncluttered". Receiver ranges varied from 2 to 9 km for the 12 GHz measurements and from 3 to 20 km for the 700 MHz measurements. Receiver heights used were 10 m at both frequencies with two additional receiver heights at 5 and 15 m for the uncluttered paths at 12 GHz.

TPEM predictions for the different terrain paths vs. measurements at 700 MHz are shown in Fig. 6. A homogeneous standard atmosphere was used for the refractivity environment. Vertical and horizontal scales represent propagation factor (field strength relative to free space) in dB. An ideal fit of predictions to measured data would have all points lie on the diagonal line, but this rarely occurs. However, there is still good agreement between the predicted and measured fields for the uncluttered terrain paths, since the data points are spread fairly evenly above and below the diagonal. The correlation between predicted and measured fields was found to be .81. TPEM does not account for any vegetation effects, therefore, it is not surprising that it underestimates the losses for the wooded/uncluttered, cluttered/uncluttered, and wooded terrain paths. A comparison of predicted vs. measured fields using the BD and BS methods would give results similar to those in Fig. 6. If TPEM is believed to show good agreement with measurements (including the mismatch for vegetation-covered terrain paths, which is to be expected), then a more demonstrative example of the consistency of the BD and BS methods would be a comparison of the BD and BS predicted fields against those of TPEM. This is shown in Fig. 7. There is excellent agreement for both methods. Similar results are shown for 12 GHz in Figs. 8 and 9. A .76 correlation was found between predicted and measured fields at 12 GHz. However, TPEM again underestimates the losses measured for the partially wooded and cluttered terrain paths.

Many of the terrain profiles for the 12 GHz measurements consisted of relatively steep slopes, typically  $10^\circ$  to  $15^\circ$ , with a few having some as large as  $20^\circ$ . These were very taxing problems for TPEM and large transform sizes were required, resulting in long run times. These same terrain profiles posed no problem for the BD and BS implementations. No concrete run times are given, since time savings varied greatly depending on the terrain profile and range, but run times were reduced from two to ten times that required by TPEM. Also,

as shown by Figs. 7 and 9 no loss in accuracy of predicted fields resulted with the BD and BS methods.

## CONCLUSION

Two alternative techniques of modeling terrain effects within the split-step PE algorithm have been presented. These methods gave excellent agreement with the more mathematically correct method implemented in TPEM. Good agreement was shown between TPEM and measured diffracted fields over various terrain paths, and results from the BD and BS methods were shown to be comparable to TPEM.

## ACKNOWLEDGEMENT

Very great thanks to Dr. Kenneth Craig from Rutherford Appleton Laboratory for providing the diffraction field measurements. The measurements were made by National Transcommunications Ltd as part of the Radiocommunications Agency's contribution to the UK National Radio Propagation Programme. This work was sponsored by the Office of Naval Research, Technology Directorate.

## REFERENCES

1. Levy, M.F., "Parabolic Equation Modelling of Propagation Over Irregular Terrain", *Seventh Int'l Conf. on Ant. and Prop.* (ICAP 91), U.K., 15-18 April 1991.
2. McArthur, R.J., "Propagation Equation Modelling Over Irregular Terrain Using the Split-Step Parabolic Equation Method", IEE Conf. Pub. 365, *Radar 92*, pp. 54-57, 12-13 Oct. 1992.
3. Barrios, A.E., "Terrain Modelling Using the Split-Step Parabolic Equation Method", IEE Conf. Pub. 365, *Radar 92*, No. 365, pp. 66-69, 12-13 Oct. 1992.
4. Beilis, A. and Tappert, F.D., "Coupled mode analysis of multiple rough surface scattering", *J. Acoust. Soc. Am.*, Vol. 66, No. 3, pp. 811-826, Sept. 1979.

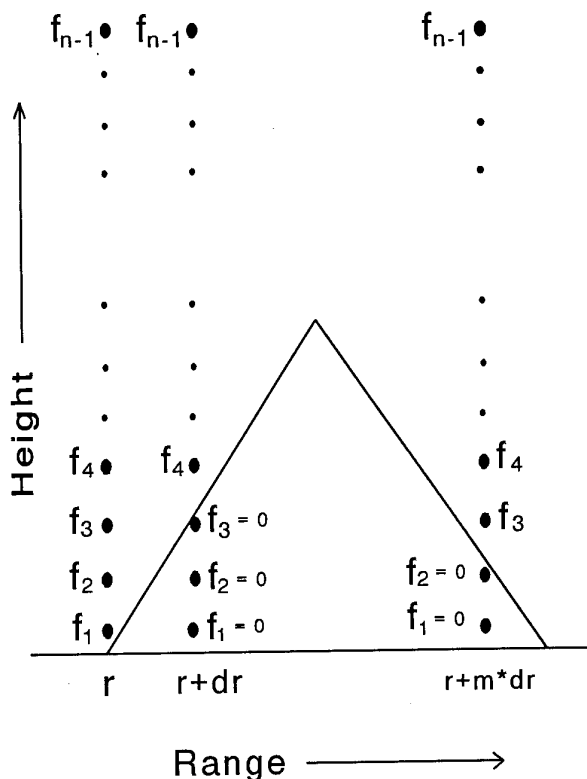


Figure 1. Boundary Decay (BD) method.

$$f_i = x_i + jy_i \quad \text{for } i=0,1,2,\dots,n-1$$

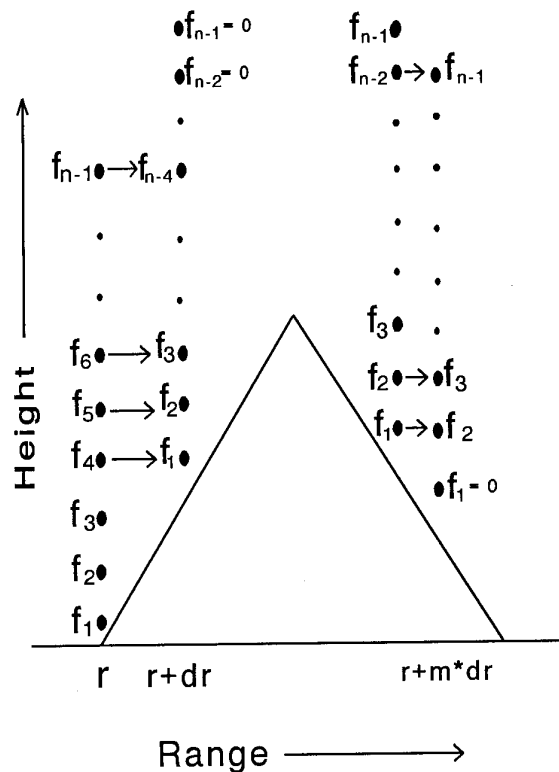


Figure 2. Boundary Shift (BS) method.

$$f_i = x_i + jy_i \quad \text{for } i=0,1,2,\dots,n-1$$

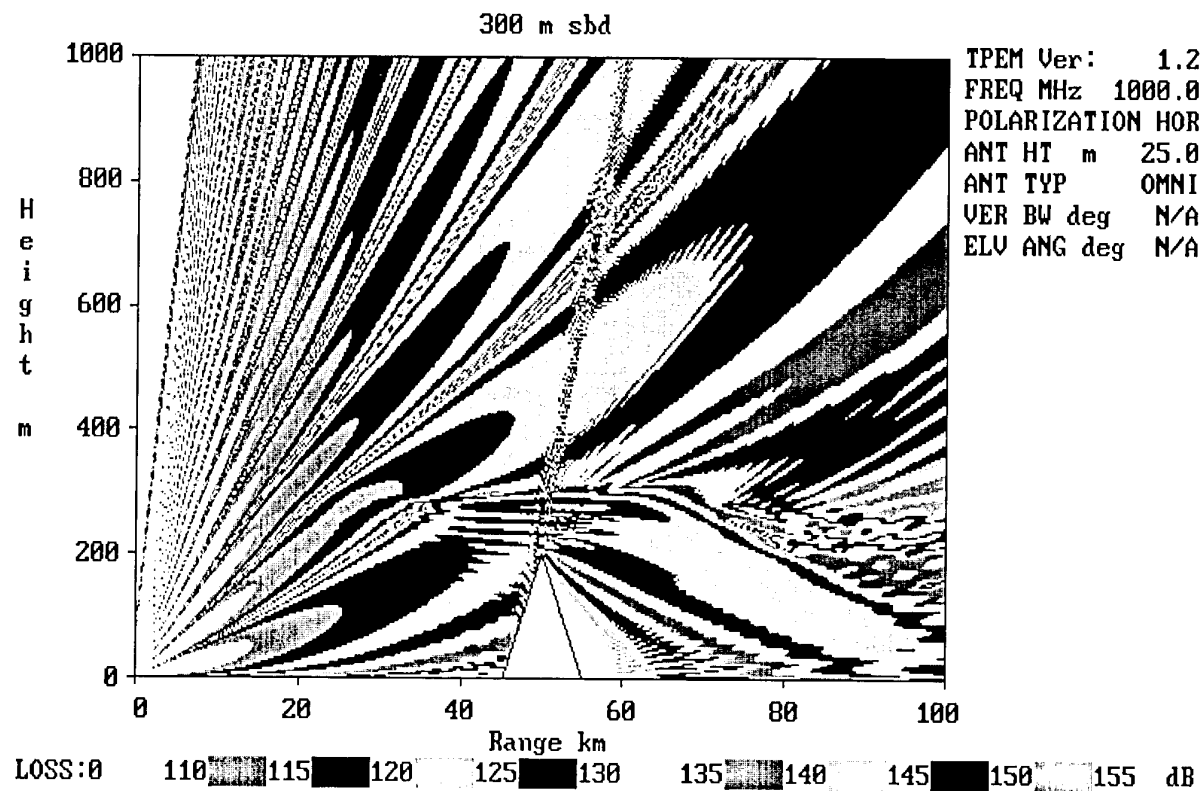


Figure 3. Terrain coverage diagram for 300 m surface-based duct from TPEM.

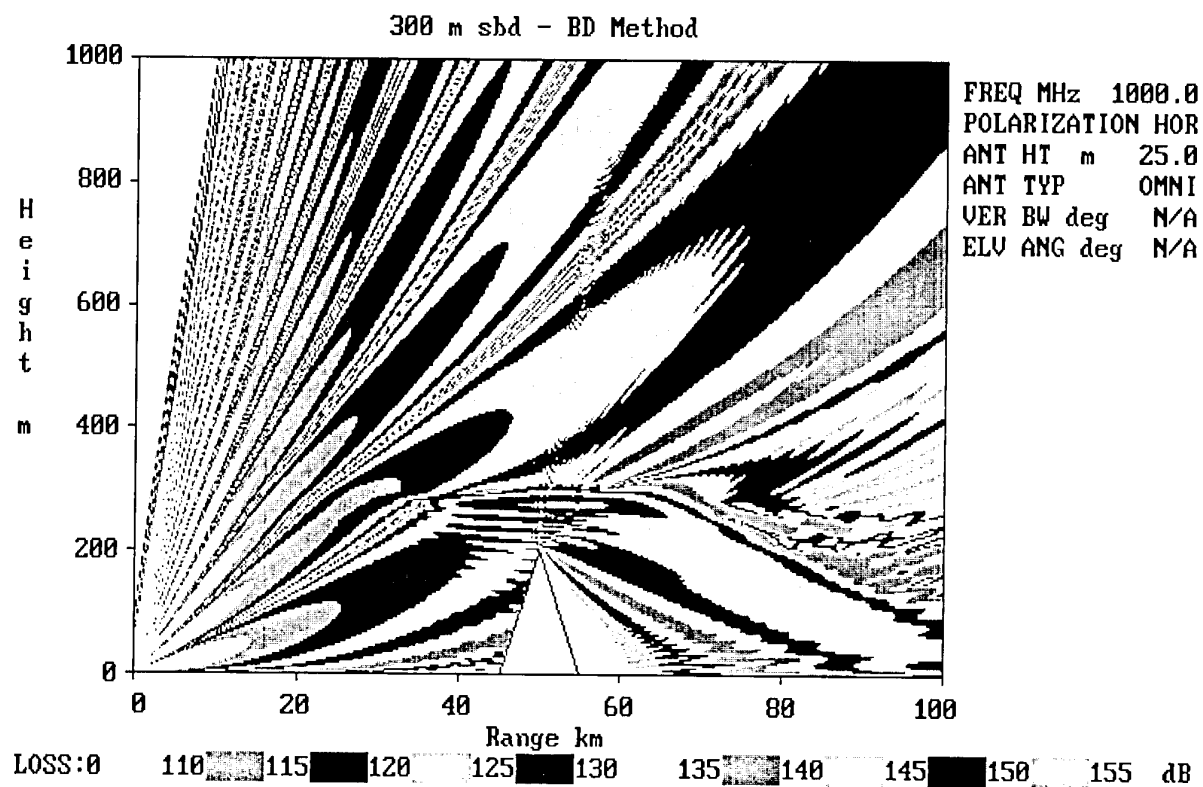


Figure 4. Terrain coverage diagram for 300 m surface-based duct using BD method.

### 300 m sbd - BS Method

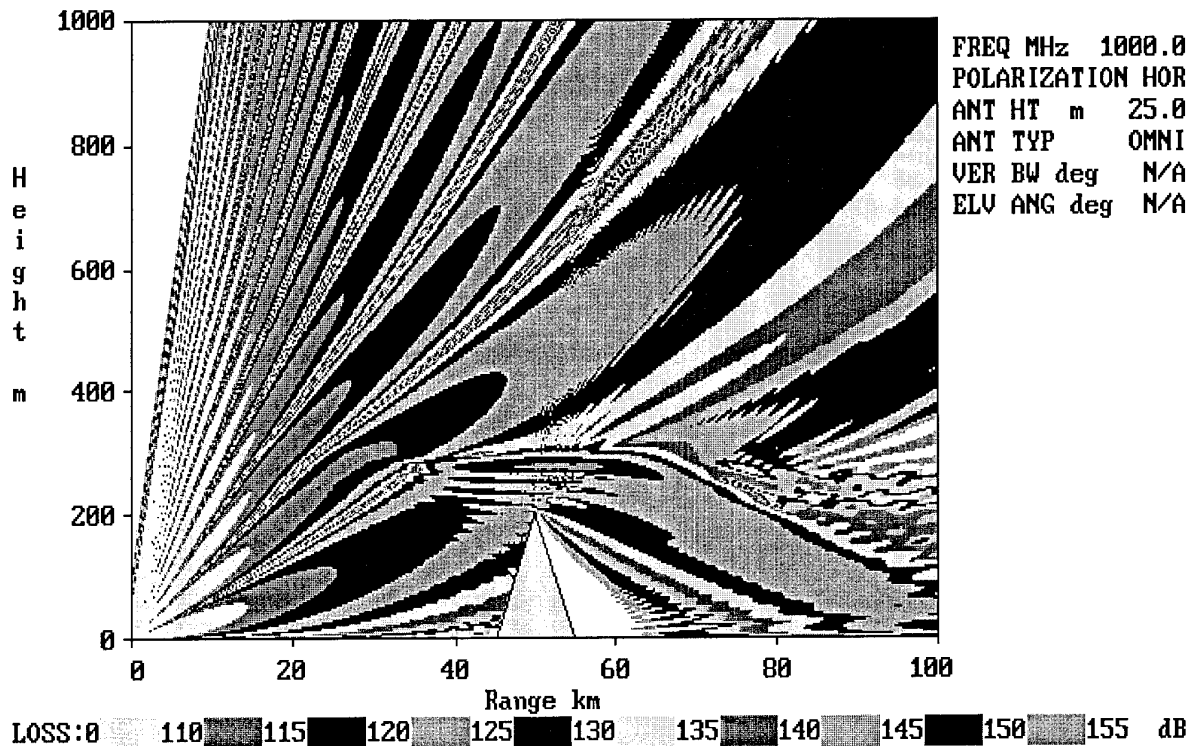


Figure 5. Terrain coverage diagram for 300 m surface-based duct using BS method.

TPEM (700 MHz)

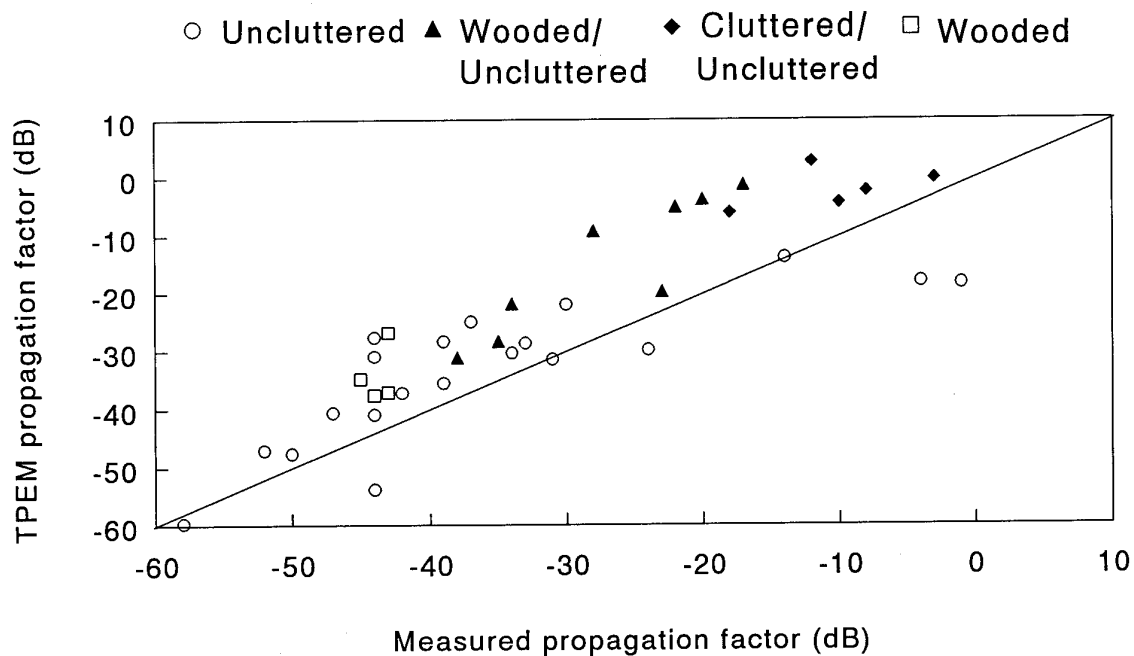


Figure 6. TPEM predicted vs. measured propagation factor at 700 MHz for various ground paths.

## BS & BD Model Comparisons-700 MHz

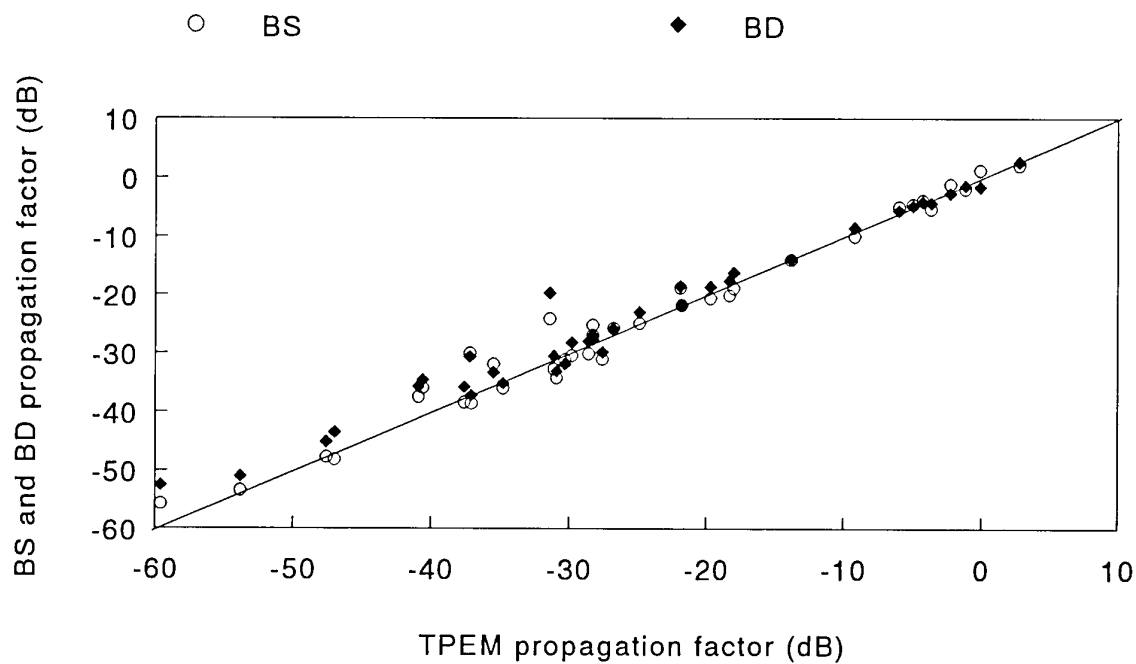


Figure 7. BS and BD vs. TPPEM predicted propagation factor for 700 MHz.

## TPPEM (12 GHz)

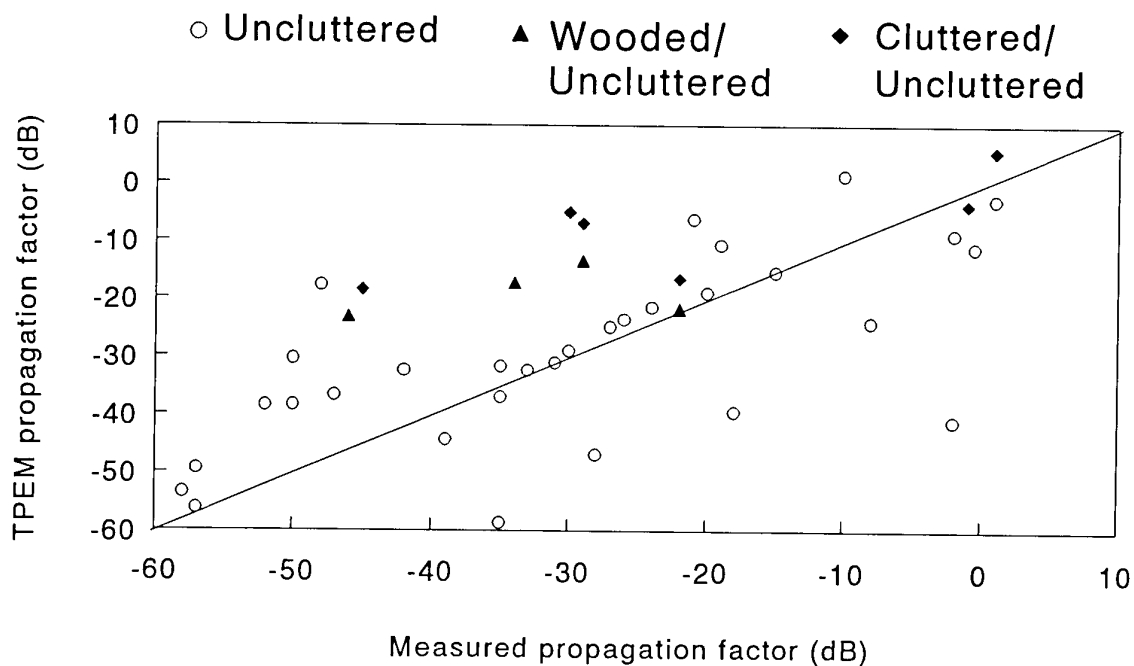


Figure 8. TPPEM predicted vs. measured propagation factor at 12 GHz for various ground paths.

# BS & BD Model Comparisons-12 GHz

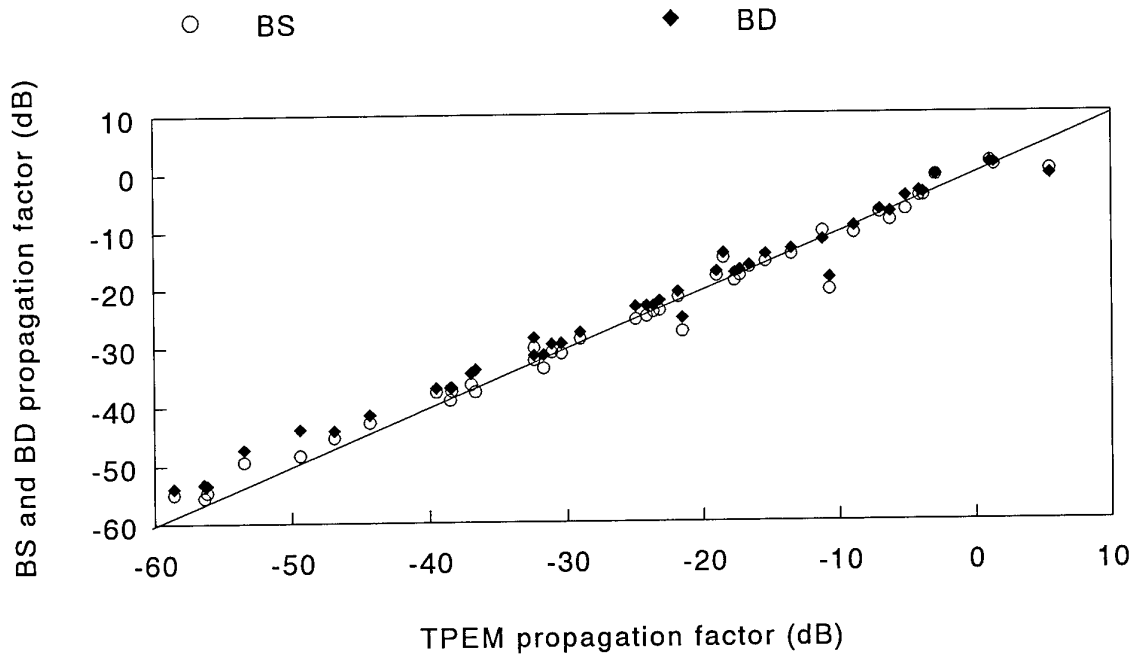


Figure 9. BS and BD vs. TPEM predicted propagation factor for 12 GHz.

## DISCUSSION

**Discussor's name :** G. S. Brown

### Comment/Question :

Why are some regions in both the 700MHz and 12GHz field strength shown as white? This occurs particularly in the near diffraction zone of a major terrain "bump".

### Author/Presenter's Reply :

The white zones are those regions of space where the signal level is below the color associated with the lowest plotted signal strength, e.g., for losses greater than 155 dB.



**Discussor's name : J. J. Costa**

**Comment/Question :**

1. The lobes seen on your "field strength" diagrams - are they not due to the antenna image (25m below the surface)?
2. What was the orientation of your transmitting antenna?

**Author/Presenter's Reply :**

1. Yes.
2. The antenna pattern modelled used a truncated omnidirectional pattern where a maximum angle is specified and solutions are determined only within this angle.

The elevation angle of the antenna is not applicable in this case.

**Discussor's name : K. H. Craig**

**Comment/Question :**

1. Since BS seems "more rigorous" than BD and is of similar complexity, I presume that you would recommend BS?
2. Would you like to comment on rough surface modelling in these methods?

**Author/Presenter's Reply :**

1. Yes, the BS method is a better approximation since it is consistent with the assumed symmetry about the terrain boundary. The BD method fails in cases in which propagation over urban (buildings) or cliff terrain is being modelled because it does not symmetrize correctly.
2. This is a very difficult problem, and it can be handled in several ways. One is to use the reflection coefficient reduction factor, as in the smooth earth case, but that involves certain problems. Another method is to introduce some small ground perturbations to simulate rough surface features.

**Discussor's name :** W. Flood

**Comment/Question :**

You indicated that the results are slope sensitive. How sensitive are the results to the size of the range step?

**Author/Presenter's Reply :**

The split-step algorithm is sensitive to the range step. The larger the range step the more error is introduced in the solution. An additional error for propagation over terrain is introduced dependent on the range step since the ground slopes are now approximated by a "staircase".

**3. Discussor's name :** K. S. Kho

**Comment/Question :**

Where have you published the TPEM algorithm?

**Author/Presenter's Reply :**

The description of the TPEM model has been published in the proceedings of the IEE Radar 92 Conference, and a paper giving a more detailed derivation and discussion of the model has been accepted for publication in IEEE Antennas and Propagation Transactions in the coming months.

## Méthodes d'évaluation de l'effet des conduits à la surface de la mer

Michel Fournier

Le Centre Thomson d'Applications Radars  
6 rue Nieuport  
78143 Vélizy-Villacoublay CEDEX  
France

### 1. RESUME

La propagation des ondes radioélectriques dans l'atmosphère est déterminée par l'indice de réfraction qui est sensible à la pression, à la température et à l'humidité de l'air. Au voisinage de la surface de la mer, il existe un fort gradient d'humidité lié à l'évaporation de l'eau ; ceci se traduit par une décroissance rapide de l'indice de l'air, l'indice de réfraction modifié passe alors par un minimum ce qui a pour conséquence du point de vue de l'électromagnétisme de créer un conduit de propagation au voisinage de la surface. Une source située à l'intérieur du conduit, c'est-à-dire à une altitude comprise entre celle du minimum de l'indice modifié et la surface de la mer voit la plus grande partie de son énergie rester captive à l'intérieur de ce conduit. Ceci a pour conséquence opérationnelle un accroissement considérable de la portée des matériels radioélectriques travaillant au voisinage de la surface de la mer. Par ailleurs, la propagation à l'intérieur du conduit est caractérisée par la présence de trajets multiples liés aux réflexions successives de l'onde électromagnétique sur la surface de la mer et sur le sommet du conduit. Il en résulte une série de renforcements et d'affaiblissements du champ se propageant dans le conduit.

Compte tenu de l'importance pratique de ces effets il convient de disposer de méthodes convenables d'évaluation. Dans cet exposé trois méthodes sont examinées :

- la méthode de l'équation parabolique,
- la méthode des modes,
- la méthode de l'optique géométrique.

La méthode de l'équation parabolique consiste à faire une approximation de l'équation d'onde en supposant que le champ se propage autour d'une direction privilégiée. Dans ces conditions on ramène l'équation de propagation à une équation aux dérivées partielles de type parabolique qui conduit à un algorithme aisé à mettre en oeuvre.

La méthode des modes permet de mener les calculs d'une manière entièrement analytique en supposant que le profil de l'indice suit une loi simple. Cette méthode constitue une référence analytique vis-à-vis des deux autres méthodes qui sont numériques.

La méthode de l'optique géométrique est une méthode asymptotique. Elle consiste à considérer la trajectoire des rayons issus de la source en résolvant l'équation de l'eikonale. L'intensité du champ électromagnétique peut être déterminée en adjoignant à l'équation des trajectoires, le calcul de la divergence du vecteur d'onde tangent au rayon passant par le point où le champ est évalué. On obtient ainsi un système d'équations différentielles ordinaires qui peut être résolu numériquement par la méthode de Runge-Kutta.

Chacune de ces méthodes est analysée et une comparaison entre elles est effectuée sur un certain nombre d'exemples concrets. Dans chaque cas on met en évidence les limites théoriques, les avantages et les limites d'emploi des trois méthodes exposées.

### 2. INTRODUCTION

La valeur de l'indice de l'air joue un rôle important en propagation troposphérique qui est très différente de ce qu'elle serait en espace libre. En radio-météorologie on caractérise l'indice non pas par sa valeur  $n$ , mais par le coindice défini par l'expression :  $N = (n - 1) 10^6$  ce qui permet d'utiliser des grandeurs numériques plus facilement manipulables : ainsi au voisinage de la mer  $N$  a une valeur d'environ 300. L'indice est fonction de la pression atmosphérique, de la température de l'air et de l'humidité. Aux fréquences radioélectriques  $N$  peut s'exprimer par la relation :

$$N = \frac{77.6}{T} \left( P + 4810 \frac{e}{T} \right)$$

$P$  est la pression atmosphérique en millibars,  $e$  est la pression partielle de vapeur d'eau en millibars et  $T$  est la température de l'air en degrés Kelvin.

Dans une atmosphère bien mélangée et stable, les lois de l'hydrostatique et de la thermodynamique font que la température, la pression et l'humidité décroissent en fonction de l'altitude. Cette variation peut être considérée comme exponentielle avec un gradient moyen au niveau de la surface de l'ordre de -40 unités  $N$  par kilomètre. Lorsque ces conditions sont réunies l'atmosphère est dite normale.

Les lois de l'optique géométrique montrent que dans une atmosphère à profil linéaire dont le gradient est négatif, les rayons issus d'une source électromagnétique sont incurvés avec un centre de courbure dirigé vers les indices croissants. Il en résulte que les rayons ont tendance à épouser la courbure de la terre ce qui conduit à une portée supérieure à ce qu'elle serait avec une atmosphère ayant un indice constant. Pour traduire ce phénomène d'une manière pratique, il est commode dans les calculs de propagation d'agrandir le rayon terrestre dans un rapport 4/3 et de supposer que tout se passe, en première approximation, comme si les rayons se propageaient en ligne droite. Il est de même commode d'utiliser la quantité :  $M = N + 10^6 h/a$  expression où  $h$  est l'altitude du point considéré et  $a$  le rayon de la terre. Cette quantité est appelée indice de réfraction modifié. Son utilisation permet de se ramener à la propagation au-dessus d'une terre plate surmontée d'une atmosphère d'indice de réfraction  $M$ .

Au voisinage de la mer les conditions d'équilibre atmosphérique ne sont pas toujours remplies à cause des échanges énergétiques qui se produisent entre l'océan et l'atmosphère résultant de la circulation des masses d'air. Ceci se traduit fréquemment par des conditions de propagation dites anormales qui résultent de fortes variations de l'indice en fonction de l'altitude. En général ces variations correspondent à un gradient négatif qui se manifeste par un phénomène de surpropagation : en effet lorsque le gradient est inférieur à  $-157 \text{ N/km}$  la courbure des rayons est inférieure au rayon de la terre et il en résulte des réflexions successives qui conduisent à une capture des rayons. Ces gradients négatifs sont en général dus à une inversion de température ou à une couche d'air sec surmontant une couche d'air humide. Dans ce cas on distingue : les conduits d'altitude dont l'épaisseur est de quelques centaines de mètres et qui sont situés à une altitude de l'ordre de mille mètres, le plancher de ces conduits n'atteignant pas la surface de la mer, et les conduits de surface dont le plancher est constitué par la surface même de la mer. Ces conduits ont au maximum quelques centaines de mètres d'épaisseur et produisent un accroissement considérable de la portée pour les bâtiments de surface dont la source se trouve automatiquement à l'intérieur. Cet accroissement résulte des réflexions successives et des trajets multiples entre le sommet des conduits et la surface de la mer.

Un autre type de conduit fréquemment rencontré est le conduit d'évaporation qui provient d'un très fort gradient négatif engendré par la variation de l'humidité à proximité de la surface due à l'intense évaporation causée par l'action du vent et de l'énergie solaire. Ces conduits dépassent rarement quelques dizaines de mètres, leur moyenne est d'environ 6 mètres pour les mers tempérées et de l'ordre de 10 à 15 mètres pour les mers tropicales. La variation de l'indice suit sensiblement une

loi log-linéaire. Du point de vue de la propagation le conduit d'évaporation joue un rôle très important : en effet, selon son épaisseur la source peut se trouver dans le conduit ou au-dessus de celui-ci. Dans le premier cas il y a capture avec un phénomène de surpropagation alors que dans l'autre cas il peut y avoir un trou de propagation dans lequel, par exemple, certaines cibles quoique proches peuvent ne pas être vues par les radars d'un bâtiment de surface.

Compte tenu de l'importance pratique de l'effet des conduits au voisinage de la surface de la mer, il convient de disposer de méthodes convenables d'évaluation de la portée des matériels utilisés. Dans le présent exposé trois méthodes de calcul de la propagation dans les conduits sont examinées :

- la méthode de l'équation parabolique,
- la méthode des modes,
- la méthode de l'optique géométrique.

### 3. METHODE DE L'EQUATION PARABOLIQUE

Pour mettre en oeuvre la méthode de calcul une fonction auxiliaire  $U(r, \theta)$  est introduite dans les équations de Maxwell exactes écrites dans un système de coordonnées sphériques  $(r, \theta, \varphi)$  dont l'origine est au centre de la terre :

$$\left| \frac{E}{H} \right| = \frac{U(r, \theta)}{r} (\sin \theta)^{-1/2} e^{-jk_r r}$$

$a$  = rayon de la terre

$k_0$  = nombre d'onde à la surface de la mer.

Les cas de la polarisation verticale et de la polarisation horizontale doivent être envisagés séparément.

Dans le cas de la polarisation verticale on ne restreint pas la généralité du problème en admettant que la source est constituée par un dipôle électrique vertical ce qui permet d'envisager un problème à symétrie cylindrique. Dans ce cas il est avantageux de s'intéresser au champ magnétique  $\vec{H}$ . Compte tenu de la symétrie de révolution  $\vec{H}$  n'a qu'une composante horizontale et le problème se ramène à un problème scalaire plan.

Dans le cas de la polarisation horizontale, il conviendrait en toute rigueur de considérer une source constituée par un dipôle électrique horizontal, mais dans ce cas la symétrie de révolution autour de l'axe passant par la source et le centre de la terre n'existe plus et il en résulte une certaine complication dans la formulation analytique du problème. Fock [1] a étudié ce cas en détail et a comparé les résultats obtenus au cas d'un dipôle magnétique vertical. Ces travaux montrent que, à des distances de la source supérieures à quelques longueurs d'onde, il y a identité entre le champ électrique engendré

par un dipôle électrique horizontal et le champ électrique engendré par un dipôle magnétique vertical. On ne restreint donc pas la généralité du problème en traitant le cas de la polarisation horizontale en considérant une source constituée par un dipôle magnétique vertical ce qui permet comme précédemment de traiter un problème scalaire plan en s'intéressant dans ce cas au champ électrique  $\bar{E}$ .

Dans les deux cas, en négligeant la dérivée seconde de  $U$  dans le sens de la propagation (dérivée par rapport à  $\theta$ ) l'équation de propagation s'écrit sous la forme simplifiée :

$$\frac{\partial^2 U}{\partial r^2} - 2j \frac{k_o}{a} \frac{\partial U}{\partial \theta} + k_o^2 \left( \frac{e - e_o}{e_o} + 2 \frac{r-a}{a} \right) U = 0$$

Le terme  $U(r, \theta)$  représente un terme d'atténuation dont les variations sont lentes comparativement à la longueur d'onde.

Les variations de l'indice atmosphérique sont introduites par le terme  $(\epsilon - \epsilon_o)/\epsilon_o$  où  $\epsilon$  est une fonction de l'altitude ( $r$ ) et de la distance ( $\theta$ ). Le terme  $2(r-a)/a$  revient à introduire une variation linéaire de l'indice de l'atmosphère qui tient compte d'une manière automatique de la rotondité de la terre tant que les altitudes considérées restent faibles par rapport à son rayon ce qui est toujours le cas pour le type de problème considéré ici (ceci est à rapprocher de la définition de l'indice modifié  $M$ ). L'équation aux dérivées partielles obtenue est du type parabolique dont l'avantage est le suivant : si  $U$  est connu sur une verticale correspondant à une certaine distance, alors les dérivées secondes par rapport à  $r$  sont également connues sur cette même verticale et l'équation permet de calculer les dérivées premières de  $U$  par rapport à  $\theta$ .  $U$  peut donc être calculé au pas suivant  $\theta + d\theta$  pour toutes les valeurs de  $r$ . Cette procédure peut être répétée aussi souvent que nécessaire conduisant ainsi à une solution pas à pas sur chaque verticale dans le sens de la propagation.

La solution obtenue par cette approximation n'est valable que si les relations ci-dessous sont vérifiées :

$$\frac{1}{e} \frac{\partial e}{\partial \theta} < 2m \quad \frac{1}{e} \frac{\partial e}{\partial r} < \frac{k_o}{m}$$

$$\theta > \frac{1}{2m^2} \quad k_o a \frac{\partial U}{\partial \theta} > \frac{\partial^2 U}{\partial \theta^2} \quad m = \left( \frac{k_o a}{2} \right)^{1/3}$$

Les deux premières relations indiquent respectivement une contrainte sur le gradient de l'indice en fonction de la distance et en fonction de l'altitude. La troisième relation traduit une contrainte sur la distance par rapport à la source. La quatrième relation est toujours vérifiée si les rayons ne sont pas trop obliques par rapport à la

direction de propagation. Dans les cas rencontrés en pratique, les gradients d'indice ne sont que de quelques unités  $N$  par mètre et les bornes données ci-dessus ne constituent pas une contrainte réelle. La contrainte sur la distance ne joue pas non plus aux fréquences considérées si bien que l'approximation parabolique se trouve parfaitement justifiée.

Pour résoudre complètement le problème différentiel il est nécessaire, outre l'équation aux dérivées partielles, de disposer d'une condition initiale et de deux conditions aux limites sur les frontières inférieure et supérieure du domaine de calcul.

Pour la frontière inférieure, la mer ayant une conductivité élevée, son influence peut être caractérisée par une impédance de surface ce qui constitue l'approximation de Léontovitch [2]. Elle consiste à écrire que le champ électrique tangentiel induit un courant proportionnel sur la surface :

$$\bar{E}_t = \sqrt{\frac{\mu_m}{\epsilon_m}} \bar{H}_t \times \bar{n}$$

expression où  $\bar{n}$  est la normale à la surface dirigée vers le centre de la terre,  $\mu_m$  et  $\epsilon_m$  sont les constantes électriques de l'eau de mer,  $\epsilon_m$  est ici la constante diélectrique complexe.

L'approximation de Léontovitch apporte une grande simplification au problème car seul est pris en compte le calcul du champ au-dessus de la surface de la mer. En toute rigueur, il faudrait aussi traiter le cas des ondes qui pénètrent le dioptré mer-atmosphère, mais aux fréquences considérées (fréquences radar) ces ondes sont très rapidement atténuées ce qui justifie l'approximation.

Une condition aux limites similaire sur la frontière supérieure du domaine de calcul est obtenue en exprimant le fait que l'onde doit s'éloigner de la source et tendre vers zéro lorsque le point d'observation est situé loin de celle-ci (condition de Sommerfeld).

Pour résoudre numériquement le problème il est nécessaire :

- de disposer d'une solution initiale,
- de mailler convenablement le domaine de calcul,
- de limiter le domaine vers le haut.

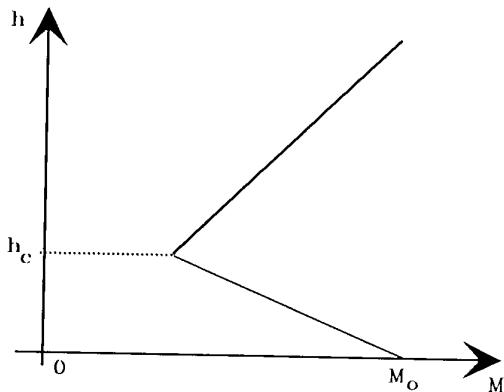
Un moyen efficace pour obtenir la solution initiale consiste à utiliser une méthode de rayons généralisée donnant le champ sur la première verticale de la grille de calcul. Le choix de la distance initiale joue un rôle important sur la précision de la solution obtenue. Une règle simple basée sur un raisonnement fondé sur l'optique géométrique donne  $s_o \approx 6\lambda/\alpha^2$ , dans cette formule  $\alpha$  est la demie ouverture du faisceau.

Pour mailler convenablement le domaine de calcul, il est nécessaire de tenir compte du caractère rapidement oscillant de la solution au fur et à mesure que l'on s'éloigne de l'axe du faisceau. La règle de maillage suivante :  $\Delta S = \lambda/5\alpha^2$  pour le pas en distance,  $\Delta h = \lambda/10\alpha$  pour le pas en altitude donne de bons résultats pour résoudre l'équation parabolique par un schéma aux différences finies du type Crank-Nicholson.

La nécessité de limiter le domaine de calcul vers le haut est un point délicat dans la mise en oeuvre de la méthode de calcul. Si aucune précaution n'est prise, il se produit une réflexion parasite qui engendre un terme perturbateur se propageant vers les altitudes décroissantes et qui vient rapidement altérer la solution lorsqu'on s'éloigne de la source. La méthode mise en oeuvre [3] pour empêcher ce phénomène consiste à agrandir le domaine de calcul vers le haut en y adjoignant une zone tampon avec des pertes de propagation dans laquelle la solution se trouve progressivement annulée jusqu'à la frontière supérieure (apodisation) et où le terme de réflexion parasite est très fortement atténué.

#### 4. METHODE DES MODES

Une solution analytique peut être obtenue dans le cas d'une atmosphère ayant un profil bilinéaire représenté par la figure ci-dessous :



Ce type de profil peut modéliser un conduit d'évaporation ou un conduit de surface.

L'écriture des équations de Maxwell assortie des conditions aux limites appropriées fournit une solution générale qui est donnée sous forme d'une intégrale de contour dans le plan complexe. A l'intérieur du conduit cette intégrale peut être évaluée par la méthode des résidus. L'atténuation par rapport à la propagation en espace libre est donnée par l'expression :

$$F = 2 \sqrt{\pi X} \sum_{m=1}^{\infty} e^{jA_m X} U_m(Z) U_m(Z_1)$$

X et Z expriment respectivement la distance et l'altitude en unités naturelles.  $Z_1$  correspond à l'altitude de la source. Les fonctions  $U_m(Z)$  et  $U_m(Z_1)$  sont les gains de hauteur du point courant et de la source. Ces fonctions sont solution de l'équation différentielle :

$$\frac{d^2 U_m}{dZ^2} + f(Z, A_m) U_m = 0$$

où  $f(Z, A_m)$  est une forme linéaire de Z et de  $A_m$  dont l'expression varie selon que l'on est à l'intérieur du conduit ou au-dessus.

Les termes  $A_m$  représentent les différents modes qui sont déterminés en écrivant que  $U_m$  vérifie la condition aux limites sur la surface. Compte tenu du caractère linéaire de la fonction  $f(Z, A_m)$  la solution donnant  $U_m(Z)$  est une combinaison linéaire de fonctions d'Airy.

La théorie des modes permet de montrer qu'il existe des modes captifs et des modes non captifs. Un mode captif se propage d'une manière privilégiée à l'intérieur du conduit et voit son amplitude diminuer rapidement au-dessus du conduit. Un mode non captif se propage d'une manière assez identique à l'intérieur et au-dessus du conduit. A l'extérieur du conduit il contribue d'une manière notable à la structure du champ électromagnétique dans la zone d'interférence.

La répartition de ces modes est fonction de la fréquence, de la géométrie du conduit ainsi que de la variation de l'indice à l'intérieur de celui-ci.

Les modes se propagent d'une manière différente à l'intérieur du conduit : leur atténuation en fonction de la distance varie avec l'ordre du mode considéré.

Il résulte de cette théorie qu'il existe pour un conduit une fréquence de coupure au-dessous de laquelle aucun mode n'est piégé.

L'influence du conduit se caractérise alors par une déformation de l'horizon radar et un déplacement de la zone d'interférence située au-dessus du conduit. Dans ce cas il y a un accroissement de la portée mais pas de phénomène de surpropagation.

La propagation à l'intérieur du conduit se traduit par un filtrage des modes ceux-ci tendant à être éliminés au fur et à mesure que l'on s'éloigne de la source. A la fin, la propagation ne se fait plus que sur un seul mode qui est le mode dominant.

Il convient de noter que dans un conduit les zones de renforcement et d'excitation du champ résultent de l'interférence entre les modes et non pas de l'interférence entre les rayons comme cela découle de la théorie de l'optique géométrique.

Les modes correspondent aux pôles de la fonction analytique qui est intégrée dans le plan complexe pour obtenir la solution du problème de propagation. Il s'agit de trouver les zéros d'une équation qui n'a pas de

solution algébrique. Seule une méthode numérique peut être mise en oeuvre et il se révèle que cette recherche dans le plan complexe est laborieuse. Une méthode utilisée est celle du suivi d'un paramètre (la hauteur du conduit) préconisée par Kerr [4] qui l'a appliquée avec succès au premier mode. Cette méthode peut être étendue aux modes supérieurs mais assez rapidement des difficultés numériques apparaissent et l'on doit, au fur et à mesure que l'on progresse dans l'ordre des modes, utiliser des développements asymptotiques adaptés à la région du plan complexe où l'on se trouve. Cette difficulté provient de la très grande dynamique des fonctions d'Airy, ainsi un zéro peut résulter de la différence de deux termes dépassant  $10^{12}$  en module ce qui correspond aux possibilités ultimes d'un calculateur numérique comme le VAX travaillant en double précision.

Les figures 1 à 6 correspondent à un conduit de 37 m de hauteur ayant un gradient de -500 N/km surmonté d'une atmosphère standard dont le gradient vaut -39 N/km. La source est à 10 m et la longueur d'onde est de 10 cm. Sur chacune de ces figures on compare à différentes distances la solution obtenue par la méthode des modes à celle fournie par la méthode de l'équation parabolique. Environ sept modes captifs sont pris en compte dont deux sont dominants. L'examen de ces différentes coupes en fonction de l'altitude montre une bonne concordance entre les deux méthodes. Pour la première coupe (cf. figure n°1) la discordance entre les deux solutions aux alentours de 80 m provient de la difficulté à calculer la série des modes dans la zone d'interférence au-dessus du conduit.

## 5. METHODE DE L'OPTIQUE GEOMETRIQUE

De par son essence même, la méthode de l'équation parabolique se trouve limitée dans un secteur angulaire voisin de la direction principale de propagation. Les limitations théoriques liées à l'approximation paraxiale sont exposées dans [5] en faisant appel à la théorie des opérateurs pseudo-différentiels. Dans une certaine mesure il est possible d'étendre la méthode à des secteurs angulaires plus larges mais cette extension nécessite des calculs supplémentaires qui, en augmentant le temps de calcul et la complexité de l'algorithme, font beaucoup perdre de son intérêt à la méthode.

D'un point de vue pratique une autre cause de limitation du secteur angulaire provient du fait que plus l'ouverture du faisceau est grande, plus il est nécessaire, pour une fréquence fixée, de réduire le pas d'échantillonnage vertical d'où là encore une augmentation du temps de calcul.

Dans le cas de l'étude de conduits, cette limitation angulaire joue peu, le domaine considéré s'étendant d'environ 100 kilomètres en distance à quelques centaines de mètres en hauteur. Dans ces conditions tout le domaine utile se trouve couvert avec une ouverture du faisceau de quelques degrés. Si l'on s'intéresse à un

domaine beaucoup plus étendu, par exemple 500 kilomètres en distance et 5000 mètres en hauteur, cette limitation angulaire va se faire ressentir et il est alors nécessaire de compléter le calcul du champ dans les secteurs angulaires où l'approximation parabolique n'est plus valable. La méthode de l'optique géométrique constitue dans ce cas une bonne approche alternative car elle permet de prendre en considération une atmosphère non homogène.

L'optique géométrique est une théorie asymptotique qui suppose que les fréquences considérées sont très élevées. En partant des équations de Maxwell, on admet que les champs électrique et magnétique, en adoptant la convention  $e^{i\omega t}$ , peuvent s'écrire :

$$\begin{cases} \vec{E} = \vec{e} e^{-j k_o S} \\ \vec{H} = \vec{h} e^{-j k_o S} \end{cases}$$

$k_o$  représente le nombre d'onde dans le vide :

$$k_o = \frac{\omega}{c} = \omega \sqrt{\epsilon_o \mu_o}$$

$c$  est la vitesse de la lumière,  $\epsilon_o$  et  $\mu_o$  sont respectivement la permittivité et la perméabilité du vide. La grandeur  $S$  caractérise la phase du champ électromagnétique : c'est la fonction eikonale utilisée en optique.

Les vecteurs  $\vec{e}$  et  $\vec{h}$  caractérisent l'amplitude et la polarisation du champ. Par définition les surfaces iso  $S$  ( $S = \text{cte}$ ) sont les surfaces d'onde.

Au sein d'un milieu sans perte comme l'atmosphère les équations de Maxwell, en supposant que  $k_o$  tend vers l'infini, se réduisent aux quatre relations ci-dessous :

$$\begin{cases} \vec{e} = -\frac{\eta_o}{\epsilon_r} \text{grad } S \times \vec{h} \\ \vec{h} = \frac{1}{\eta_o \mu_r} \text{grad } S \times \vec{e} \\ \vec{e} \cdot \text{grad } S = 0 \\ \vec{h} \cdot \text{grad } S = 0 \end{cases}$$

$\eta_o$  représente l'impédance du vide :

$$\eta_o = \sqrt{\frac{\mu_o}{\epsilon_o}} \sim 377 \Omega$$

$\epsilon_r$  et  $\mu_r$  sont la permittivité et la perméabilité relatives au point considéré  $\epsilon = \epsilon_o \epsilon_r$ ,  $\mu = \mu_o \mu_r$ .

Ces quatre équations montrent que localement le champ électromagnétique a une structure d'onde plane comme dans le cas de la propagation d'une onde électromagnétique dans un milieu homogène et isotrope :

- les vecteurs  $\vec{e}$  et  $\vec{h}$  sont orthogonaux au vecteur grad S et orthogonaux entre eux et le rapport des modules de  $\vec{e}$  et  $\vec{h}$  est égal à l'impédance d'onde locale :

$$\eta = \sqrt{\frac{\mu}{\epsilon}}$$

- du point de vue énergétique, en chaque point de l'espace la densité d'énergie électrique est égale à la densité d'énergie magnétique ;
- le vecteur de Poynting défini par :

$$\vec{I} = \frac{1}{2} R_e (\vec{e} \times \vec{h}')$$

est dirigé dans le sens du gradient de S. Il représente le flux de puissance rayonnée par unité de surface et il est, en un point donné, orthogonal à la surface d'onde.

En éliminant  $\vec{e}$  ou  $\vec{h}$  entre les quatre équations données ci-dessus, on aboutit à l'équation de l'eikonale :

$$|\text{grad } S|^2 = n^2$$

où n est l'indice de réfraction :

$$n = \sqrt{\epsilon_r \mu_r}.$$

Il s'agit d'une équation aux dérivées partielles du premier ordre de type non linéaire qui est résolue d'une manière classique par la méthode des lignes caractéristiques. Les trajectoires des lignes caractéristiques peuvent être calculées à l'aide d'un système d'équations différentielles ordinaires. Elles s'identifient aux rayons introduits d'une manière intuitive en optique géométrique élémentaire, localement, elles sont orthogonales aux surfaces d'onde  $S = \text{cte}$ .

Le principe de la conservation de l'énergie dans un milieu sans pertes s'exprime d'une manière absolument générale par la relation :

$$\text{div } (\vec{I}) = 0$$

ce qui signifie que le flux d'énergie est conservatif, en particulier l'énergie électromagnétique propagée dans un tube de rayons reste conservée. Le problème du calcul de la variation de l'amplitude du champ électromagnétique le long d'un rayon se réduit au calcul de la variation de

la section locale du tube élémentaire. La méthode d'Ugincius [6] est basée sur cette remarque et permet de calculer analytiquement l'intensité du champ.

Son principe consiste à définir deux vecteurs auxiliaires  $\vec{A}$  et  $\vec{B}$  induits par des déplacements infinitésimaux du site et du gisement d'un rayon dont la trajectoire est définie dans un repère sphérique  $(r, \omega, \phi)$  centré sur la source :

$$\vec{A} = \left( \frac{\partial \vec{r}}{\partial \omega} \right)_s \quad \vec{B} = \left( \frac{\partial \vec{r}}{\partial \phi} \right)_s$$

Ces expressions sont calculées en laissant S constant,  $\vec{A}$  et  $\vec{B}$  sont les dérivées partielles relativement à  $\omega$  et à  $\phi$  du vecteur position du point courant sur la surface d'onde considérée. Le flux d'énergie à l'intérieur d'un tube de rayons étant conservatif, l'intensité du champ électromagnétique égale au module du vecteur de Poynting est donnée d'une manière rigoureuse par :

$$I = \frac{f(\omega, \phi) \sin \omega}{(\vec{A} \times \vec{B}) \cdot \vec{t}}$$

$f(\omega, \phi)$  est la puissance rayonnée par la source dans la direction du rayon considéré (en watts par stéradian). L'évolution des vecteurs  $\vec{A}$  et  $\vec{B}$  le long d'un rayon est régie par un système d'équations différentielles ordinaires qui peut être intégré en même temps que celui qui décrit la trajectoire des rayons. En adjoignant les conditions initiales appropriées, on dispose, par cette méthode, de tous les éléments permettant de calculer la trajectoire des rayons et en chaque point d'une trajectoire de déterminer le terme de phase S et l'intensité du champ électromagnétique.

Pour obtenir une reconstitution cohérente du champ en chaque point de l'espace où peuvent passer plusieurs rayons il est nécessaire que S soit connu avec le maximum de précision : S doit être évalué sur toute la trajectoire d'un rayon avec une erreur très inférieure à la longueur d'onde de la source d'émission. Le système différentiel régissant les grandeurs caractéristiques suppose implicitement que l'indice est une fonction dérivable de la variable d'espace au moins à l'ordre deux. Dans la pratique les coupes de l'indice atmosphérique en fonction de l'altitude sont obtenues par des moyens expérimentaux qui conduisent souvent à une représentation par segments de droite. A la frontière entre deux segments il y a discontinuité du gradient de l'indice et la dérivée seconde n'a pas de sens. Il est donc nécessaire pour conserver toute la précision de la méthode de calcul de réactualiser le système différentiel au passage d'une couche à l'autre. D'autre part certains rayons sont réfléchis sur la surface de la terre (mer) et il convient là aussi de réactualiser le système différentiel lorsqu'un rayon passe par un point spéculaire.



Ce problème peut être traité d'une manière analytique [7] en considérant les déplacements infinitésimaux de part et d'autre de l'interface responsable de la discontinuité et en identifiant les variations des grandeurs caractéristiques à partir de deux trajets différents aboutissant en un même point situé sur la frontière, le premier trajet étant effectué avant la discontinuité et l'autre après.

Si  $\bar{A}$  et  $\bar{B}$  deviennent nuls, individuellement ou les deux à la fois, l'intensité du rayon considéré devient infini : dans ce cas on est en présence d'une caustique. Si  $\bar{A}$  et  $\bar{B}$  s'annulent individuellement, il s'agit d'une caustique simple et la section droite du tube de rayons se trouve réduite à une ligne focale dirigée selon  $\bar{A}$  ou  $\bar{B}$ . Si  $\bar{A}$  et  $\bar{B}$  s'annulent en même temps la section du tube se trouve réduite à un point de focalisation. Il convient de noter que ces points singuliers du champ ne constituent pas une singularité pour le système différentiel intégré. Pour tenir compte de la présence de caustiques on incorpore dans le calcul un saut de phase  $-\pi/2$  lors du passage d'une caustique ( $\bar{A}$  ou  $\bar{B}$  nul) et un saut de phase de  $-\pi$  lorsque  $\bar{A}$  et  $\bar{B}$  s'annulent simultanément.

Les trajectoires des rayons et l'amplitude du champ peuvent être aisément déterminées en intégrant le système différentiel à l'aide d'une procédure de Runge-Kutta à l'ordre quatre.

Pour tracer une couverture radar il est nécessaire de connaître l'intensité du champ en chaque point d'une grille distance-hauteur. La première opération consiste à lancer un certain nombre de rayons judicieusement espacés en site de façon à couvrir sensiblement toute la zone étudiée. La phase  $S$  étant prise comme paramètre au cours de cette procédure, les coordonnées d'un point de la trajectoire des rayons ainsi que les grandeurs caractérisant le transport sont toutes des fonctions de  $S$ . Numériquement les points obtenus qui correspondent à des accroissements réguliers de  $S$  ne coïncident pas avec les points de la grille de calcul de la couverture radar. Il est donc nécessaire, à partir des points situés sur les rayons, de procéder à des interpolations numériques pour calculer l'intensité du champ sur les points de la grille distance-hauteur.

Deux types d'interpolations sont à effectuer. La première consiste en une interpolation le long d'un rayon sur deux points consécutifs de la procédure de Runge-Kutta encadrant une distance donnée sur la terre, ce qui correspond à une verticale de la grille de calcul. Cette interpolation est faite à l'aide d'une fonction spline d'ordre trois à partir de laquelle on réactualise toutes les grandeurs caractéristiques au point où le rayon considéré coupe la verticale. On obtient ainsi un point pivot qui ne coïncide pas nécessairement avec les points de maillage sur la verticale. La deuxième interpolation consiste en une interpolation sur une verticale de la grille de calcul : dans cette procédure l'intensité est calculée pour les

points, correspondant au maillage, situés entre deux points pivots obtenus de la manière décrite ci-dessus. La phase  $S$  qui est le paramètre le plus sensible et qui doit être connue avec le maximum de précision est calculée par interpolation sur les points de maillage à l'aide d'une fonction spline à l'ordre cinq lorsque les deux points pivots ne sont pas séparés par une discontinuité et par deux fonctions spline à l'ordre trois lorsqu'il existe une frontière de discontinuité entre les deux points pivots. Dans ce cas ces fonctions splines sont construites de part et d'autre de la discontinuité de façon à ce qu'elles se raccordent d'une manière continue ainsi que leurs dérivées premières sur la frontière de la discontinuité.

Tous les points de l'espace ne sont pas nécessairement atteints par un rayon et en un même point plusieurs rayons peuvent se croiser. Les interpolations doivent donc être effectuées en tenant compte de la configuration des rayons entre eux. Ceux-ci peuvent être classés en familles ou congruences et c'est à l'intérieur d'une même congruence que doit être effectuée l'interpolation entre rayons voisins. Ce classement des rayons en faisceaux de congruences doit être effectué au préalable et ceci constitue une des principales difficultés de la mise en oeuvre algorithmique de la méthode. Les interpolations sont donc effectuées sur une même verticale à partir de rayons correspondant à une même congruence et en chaque point de la grille de calcul les intensités relatives à chaque congruence sont sommées d'une manière cohérente.

Les figures 7 à 12 montrent les résultats d'essais effectués en vue de comparer d'une manière quantitative, dans le cas d'un conduit à profil bilinéaire, la solution fournie par l'équation parabolique à la solution obtenue à l'aide de l'optique géométrique. La longueur d'onde est de 10 cm. Le conduit considéré a une hauteur de 200 m et le gradient à l'intérieur du conduit est de  $-500$  N/km ; il est surmonté par une atmosphère standard ( $-39$  N/km). Le tracé de rayons de la figure 7 donne une idée de la complexité de la structure du champ et met bien en évidence la présence des caustiques simples (enveloppe des rayons) et des caustiques cuspidées (plusieurs rayons se focalisent en un même point).

La figure 8 correspond à une coupe en altitude de la carte du champ à une distance de 10 km de la source. On peut noter une très bonne concordance sur la position et l'amplitude des lobes d'interférence. Au-dessus de 100 m il existe une certaine divergence entre les deux solutions qui peut s'exprimer par le fait que les faisceaux ne sont pas apodisés de la même façon dans les deux méthodes. La divergence au-delà de 200 m provient du fait que le faisceau relatif à l'optique géométrique est sensiblement plus large que celui qui est utilisé dans la méthode de l'équation parabolique.

La figure 9 relative à une coupe à 25 km appelle les mêmes commentaires.

La figure 10 est plus complexe d'interprétation. Elle

correspond à une coupe à 50 km de la source. Sur les 80 premiers mètres il y a une zone d'interférences fortes et la concordance entre les deux solutions n'est pas très bonne, quoique les tendances générales soient respectées. Au-dessus de 80 m la concordance est bien meilleure. Entre 110 et 240 m la solution donnée par l'optique géométrique est beaucoup plus grossière que celle obtenue par la méthode de l'équation parabolique. Il convient de noter le trou situé entre 180 m et 220 m qui correspond à une zone non atteinte par les rayons. La concordance redevient très bonne au-dessus de 250 m, c'est-à-dire dans la zone d'interférence.

La figure 11 relative à une coupe à 75 km de la source suscite les mêmes commentaires. On remarque le trou de propagation entre 140 m et 310 m ainsi que la présence d'une caustique située à 140 m, c'est-à-dire sur le bord inférieur de ce trou.

La figure 12 correspond à une coupe à 100 km de la source. La concordance entre les deux solutions est assez confuse en-dessous de 100 m et bien meilleure au-dessus. Le trou de propagation se fait ressentir au-dessus de 200 m.

La comparaison effectuée met bien en évidence les limitations intrinsèques de la méthode de l'optique géométrique liées à son caractère asymptotique.

## 6. CONCLUSION

Trois méthodes de calcul de la propagation dans les conduits au voisinage de la surface de la mer ont été examinées :

- la méthode des modes,
- la méthode de l'équation parabolique,
- la méthode de l'optique géométrique.

La méthode des modes permet d'obtenir formellement une solution analytique dans le cas d'un conduit à profil bilinéaire. A l'intérieur du conduit de solution est fournie sous forme d'une série dont chaque terme correspond à un mode de propagation. Au-dessus du conduit, en particulier dans la zone d'interférence il est nécessaire de recourir à un développement asymptotique. La principale difficulté de mise en oeuvre de cette méthode réside dans la détermination des modes qui correspondent aux zéros d'une équation qui n'a pas de solution algébrique et qu'il faut évaluer par des procédés numériques. Cette recherche est délicate compte tenu de la très grande dynamique des fonctions d'Airy qui interviennent dans le calcul. Les temps de calcul qui en découlent font que cette méthode ne peut être envisagée comme un moyen opérationnel, en revanche elle constitue un précieux outil d'investigation pour fournir des solutions de référence qui permettent de tester les autres méthodes. Elle peut être étendue au prix de certaines difficultés numériques à des profils paraboliques ou à des conduits dont la hauteur varie en fonction de la distance. Dans ce cas la méthode n'a qu'un intérêt théorique car les temps de

calcul deviennent très longs.

La méthode de l'équation parabolique est conceptuellement simple. Elle est fondée sur la résolution d'une équation aux dérivées partielles du type parabolique qui constitue une approximation de l'équation de propagation. Elle conduit à un algorithme qu'il est aisé d'implémenter sur calculateur. La méthode de l'équation parabolique fournit un outil bien adapté au calcul de la propagation dans les conduits dans le cas où l'indice de l'air dépend à la fois de l'altitude et de la distance.

Elle est limitée à des ouvertures de faisceau de quelques degrés au maximum, ceci pour deux raisons : l'une théorique et l'autre pratique. La première raison découle des approximations qui sont faites lors du passage de l'équation aux dérivées partielles du type elliptique qui est rigoureuse à une équation du type parabolique qui est approchée. Les termes négligés dans cette approche ne sont petits devant les termes principaux que si l'on ne s'éloigne pas trop de l'axe de propagation (approximation paraxiale). La deuxième raison qui conduit aux fréquences considérées à une contrainte plus sévère que la précédente provient du fait que plus le faisceau est ouvert, plus l'échantillonnage numérique en hauteur doit être serré. Ceci conduit dans la plage des fréquences radar à des ouvertures de quelques degrés au maximum. Les temps de calcul sont fonction de la fréquence et croissent avec celle-ci. Ils sont de quelques minutes à 3 GHz pour un domaine de 1000 mètres en hauteur et de 100 kilomètres en distance.

La méthode de l'optique géométrique est une méthode asymptotique qui consiste à supposer que la fréquence est très élevée. On aboutit ainsi à une formulation simplifiée des équations de Maxwell dont découle la notion de rayons, les trajectoires de ces rayons sont obtenues en résolvant l'équation de l'eikonale.

L'intensité du champ électromagnétique peut être déterminée en adjoignant à l'équation des trajectoires des équations du transport qui permettent de déterminer la divergence du vecteur d'onde tangent au rayon passant par le point où le champ est évalué.

Cette méthode est conceptuellement simple cependant sa mise en oeuvre pratique conduit à un algorithme complexe, il est en effet nécessaire de déterminer très soigneusement les limites de chaque congruence de rayons à l'intérieur du domaine considéré pour obtenir une représentation correcte du champ. Ce qui a été gagné en simplicité conceptuelle se trouve donc perdu au niveau du calcul du champ par sommation cohérente de l'amplitude sur chacun des rayons dont il faut au préalable effectuer le tri, ce qui se révèle être laborieux au niveau algorithmique.

Le caractère asymptotique de la méthode de l'optique géométrique amène un certain nombre de limitations :

- le champ calculé est infini au passage d'une caustique ;

- elle ne peut s'appliquer à des conduits faibles (conduits de faible épaisseur ou à faible gradient) ;
- le champ n'est calculé que pour les points qui sont atteints par les rayons ; il n'est donc pas calculé dans la zone de diffraction, au-dessus d'un conduit et dans les trous de propagation des conduits ;
- il y a une transition brusque entre la zone éclairée et la zone de diffraction : dans cette zone correspondant à l'horizon radioélectrique la décroissance du champ se trouve mal évaluée ce qui peut être gênant d'un point de vue opérationnel.

En revanche, la méthode de l'optique géométrique présente les avantages suivants :

- le temps de résolution est court ;
- elle prend bien en compte les paramètres physiques décrivant le milieu (indice atmosphérique, rugosité de la surface) ;
- le diagramme de rayonnement de la source est aisément pris en compte ;
- il n'y a pas de limitation pour les grandes ouvertures du faisceau.

La méthode de l'équation parabolique et la méthode de l'optique géométrique constituent l'une et l'autre deux méthodes opérationnelles d'évaluation de la propagation dans les conduits au voisinage de la mer.

Il conviendrait, dans une étape ultérieure, de les marier au sein d'une théorie mixte qui allierait leurs avantages réciproques.

#### Remerciements

Cette étude a été réalisée sous contrat de la Direction des Recherches, Etudes et Techniques (Délégation Générale pour l'Armement).

#### Références

- [1] V.A. Fock  
Electromagnetic diffraction and propagation problems - 1965 - Pergamon Press - Oxford - London - Edinburg - New York - Paris - Frankfurt.
- [2] L. Landau, E. Lifchitz  
Electrodynamique des milieux continus.  
Editions MIR, Moscou 1969, P. 365-371.
- [3] M. Fournier  
Etude de la propagation dans une atmosphère inhomogène dans les directions horizontale et verticale par la méthode de l'équation parabolique.  
AGARD Conference Proceeding n°453 -  
Operational decision aids for exploiting or mitigating electromagnetic propagation effects. San Diego. California 15-19 May 1989. Pages 21.1, 21.13 -  
AGARD- 7 rue Ancelle Neuilly sur Seine France.
- [4] D.E. Kerr  
Propagation of short radio-waves -  
Dover publication Inc - New York 1965.  
Reprint 1987 : Peter Peregrinus Ltd on behalf the Institution of Electrical Engineers - London.
- [5] F.J. Ryan  
RPE : A parabolic equation radio assessment model.  
AGARD Conference Proceeding n°453 -  
Operational decision aids for exploiting or mitigating electromagnetic propagation effects. San-Diego California 15-19 May 1989. Pages 19-1, 19-10 -  
AGARD 7 rue Ancelle 92200 Neuilly sur Seine.
- [6] P. Ugincius  
Intensity equation in ray acoustics - Part I  
The journal of the Acoustical Society of America  
Volume 45 Number 1 1969. Pages 193-205.  
Intensity equations in ray acoustics - Part II (même référence) Pages 206-209.
- [7] J.C. Durand, P. Granier  
Radar coverage assessment in nonstandard and ducting conditions : a geometrical optics approach.  
IEE Proceeding - Vol. 137, Pt. F, n°2 - April 1990.  
Pages 95-101.

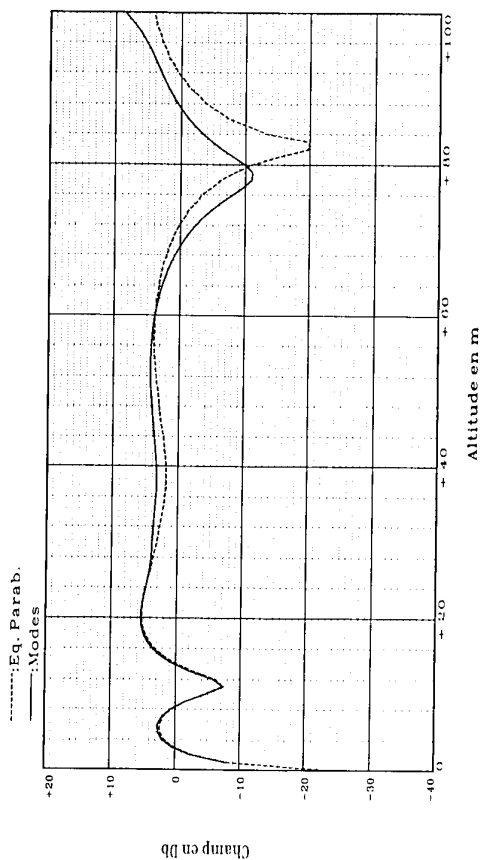


Figure n° 1 - Conduit bilinéaire. Coupe à 20 km.  
Comparaison entre la solution analytique et la solution numérique.

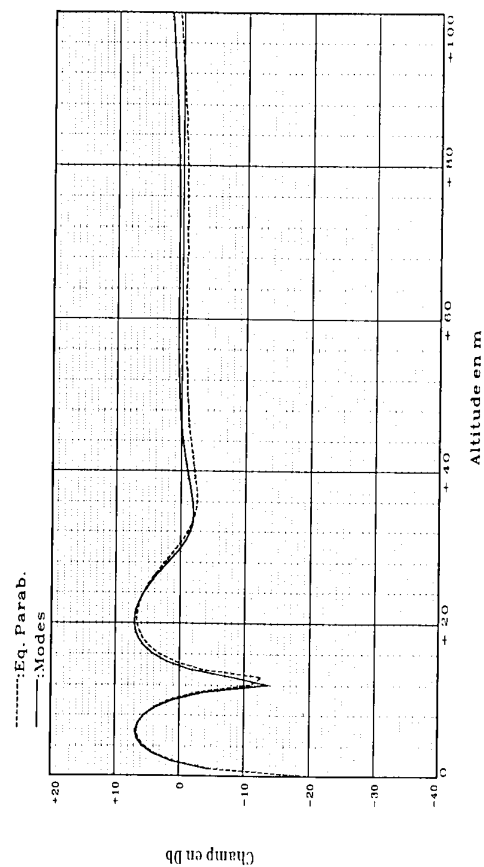


Figure n° 2 - Conduit bilinéaire. Coupe à 40 km.  
Comparaison entre la solution analytique et la solution numérique.

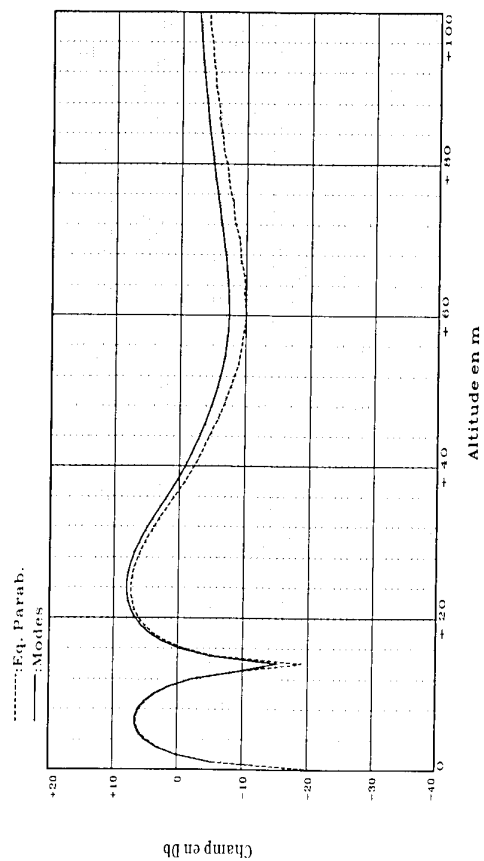


Figure n° 3 - Conduit bilinéaire. Coupe à 60 km.  
Comparaison entre la solution analytique et la solution numérique.

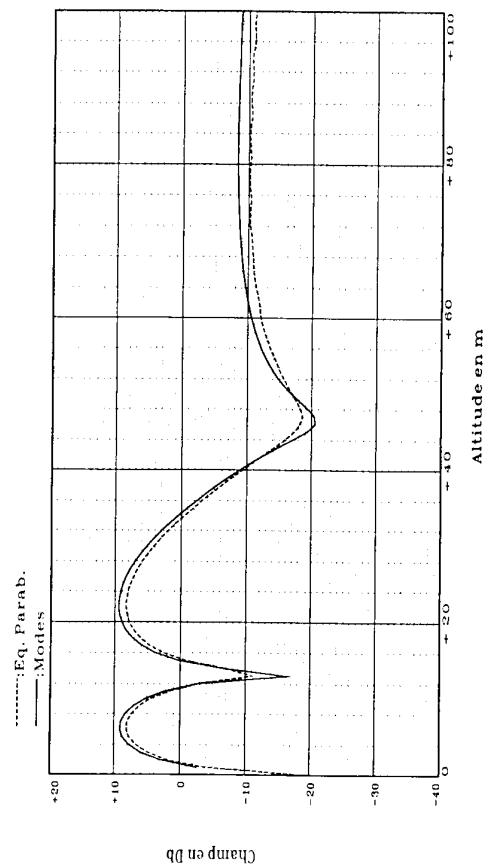


Figure n° 4 - Conduit bilinéaire. Coupe à 80 km.  
Comparaison entre la solution analytique et la solution numérique.

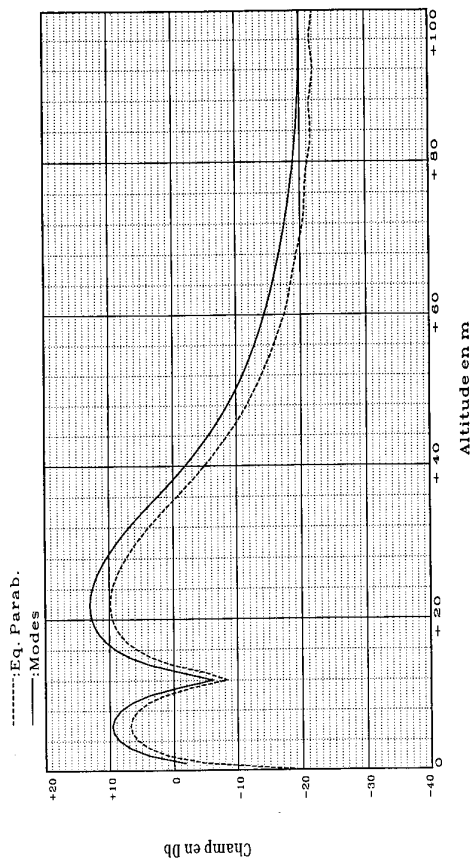


Figure n° 6 - Conduit bilinéaire. Coupe à 160 km.  
Comparaison entre la solution analytique et la solution numérique.

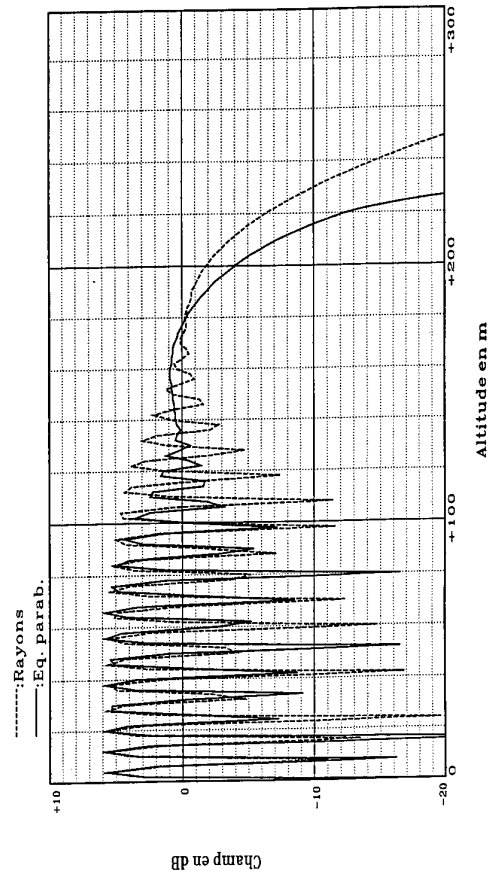


Figure n° 8 - Conduit bilinéaire. Coupe à 10 km.  
Comparaison entre l'optique géométrique et l'équation parabolique.

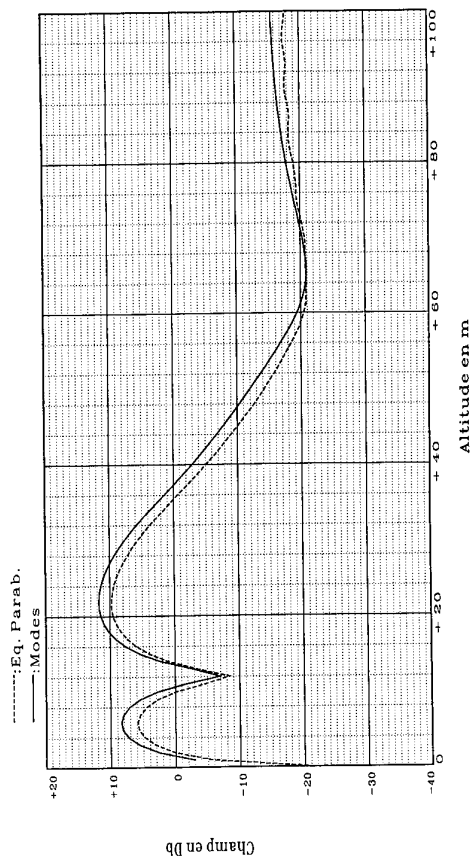


Figure n° 5 - Conduit bilinéaire. Coupe à 120 km.  
Comparaison entre la solution analytique et la solution numérique.

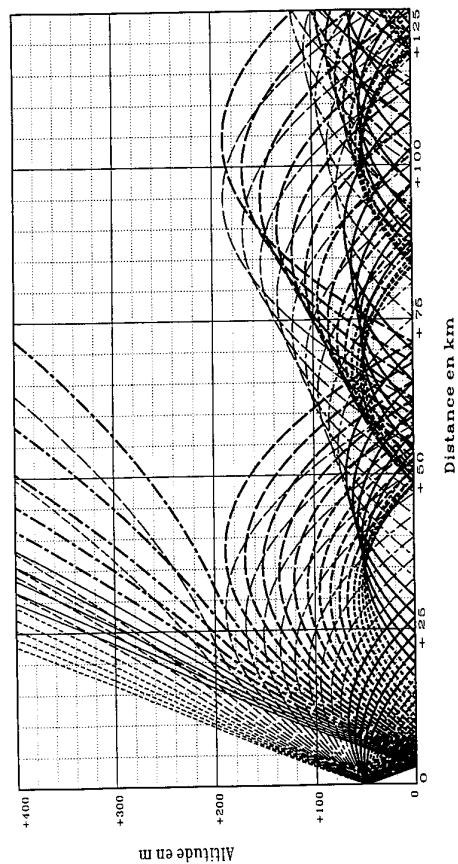


Figure n° 7 - Conduit bilinéaire. Trace de rayons.

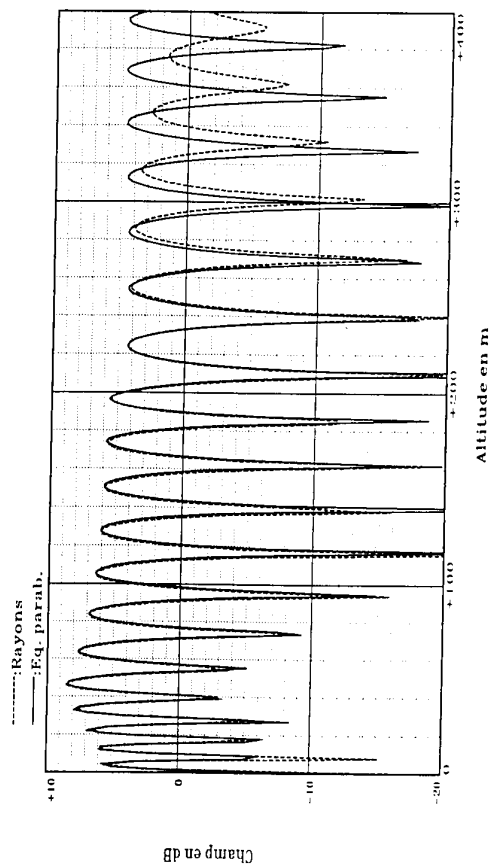


Figure n° 9 - Conduit bilinéaire. Coupe à 25 km.  
Comparaison entre l'optique géométrique et l'équation parabolique.

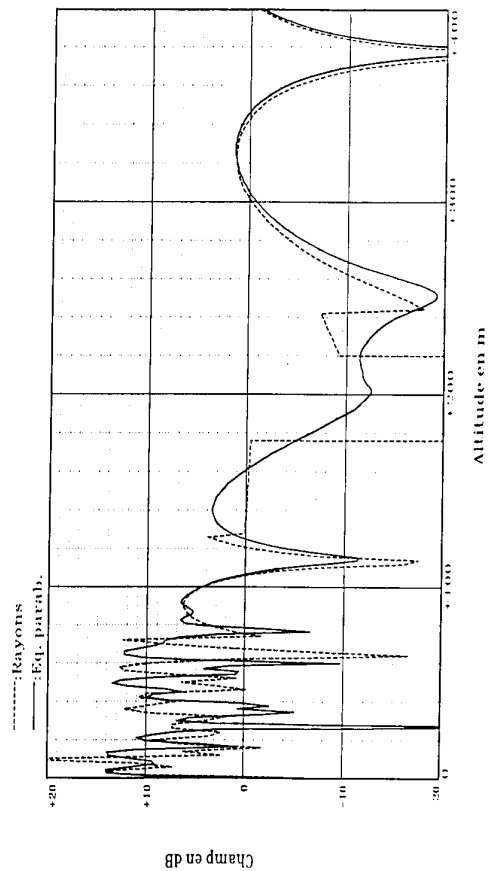


Figure n° 10 - Conduit bilinéaire. Coupe à 50 km.  
Comparaison entre l'optique géométrique et l'équation parabolique.

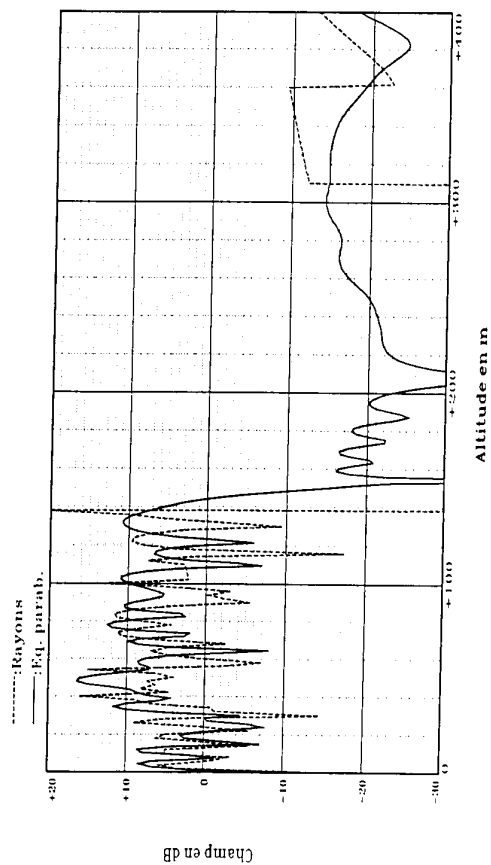


Figure n° 11 - Conduit bilinéaire. Coupe à 75 km.  
Comparaison entre l'optique géométrique et l'équation parabolique.

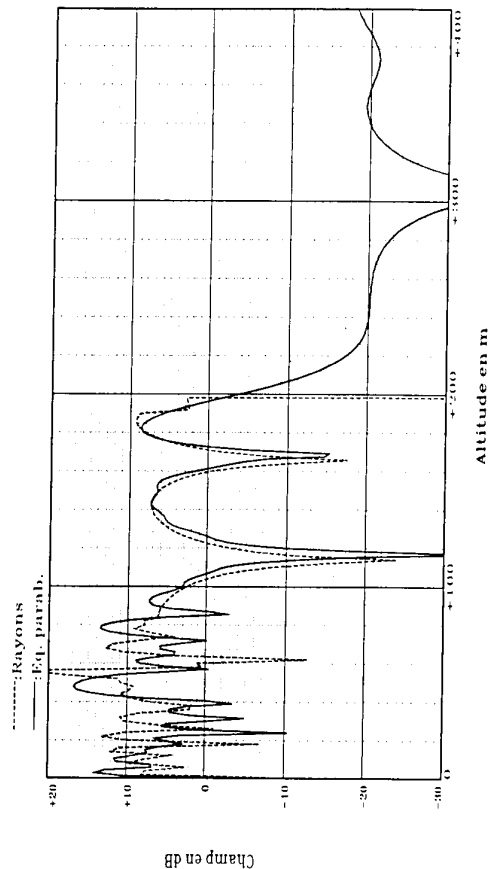


Figure n° 12 - Conduit bilinéaire. Coupe à 100 km.  
Comparaison entre l'optique géométrique et l'équation parabolique.

## DISCUSSION

**Discussor's name :** K. H. Craig

**Comment/Question :**

I (and others in the audience) have also compared mode theory and parabolic equation calculations, and have found excellent agreement if the input parameters are identical. Are your (relatively small) differences perhaps due to lack of mode convergence?

**Author/Presenter's Reply :**

Il conviendrait effectivement de disposer d'un programme plus performant pour calculer les fonctions d'Airy. On peut cependant noter que la convergence de la série est très suffisante à l'intérieur du conduit. La convergence devient beaucoup plus lente en dessus.

**Translation :**

*It would in fact be useful to have a more efficient program for calculating the Airy functions. However, it should be noted that the convergence of the series is still largely adequate inside the conduit. Convergence becomes much slower above it.*

**Discussor's name :** C. Goutelard

**Comment/Question :**

Dans la méthode de l'optique géométrique, les difficultés de calcul viennent du fait que la dérivée du profil vertical du coindice est discontinue. Si on introduit des gradients horizontaux, le problème devient encore plus difficile. En introduisant un profil dont la dérivée est continue ces inconvénients disparaissent et le profil devient plus réaliste à condition que les rayons de courbures soient choisis en fonction du pas d'incrément de la méthode de Runge-Kutta. Pensez-vous qu'une telle méthode soit applicable?

**Translation :**

*In the geometrical optics method, the difficulties of computation arise from the fact that the derivative of the vertical profile of the refractivity is discontinuous. If we introduce horizontal gradients the problem becomes even more difficult. By introducing a profile whose derivative is continuous we eliminate these problems and the profile becomes more realistic provided that the radii of the curves are chosen to fit the incrementation step of the Runge-Kutta method. Do you think such a method is applicable?*

**Author/Presenter's Reply :**

Il s'agit en effet d'une bonne idée qui peut conduire à un raccourcissement notable du temps de calcul. La seule difficulté provient de la question que l'on peut se poser sur le choix du raccord continu entre deux segments de profil. Sinon cela paraît tout à fait applicable.

**Translation :**

*It is in fact a good idea, and one which might reduce computation time considerably. The only difficulty lies in the choice of a continuous union between two segments of profile. Otherwise it seems perfectly applicable.*

**3. Discussor's name : H. V. Hitney****Comment/Question :**

1. In your presentation, you referred to the relative computer time required for each model. Can you give us an example of the actual time required by your PE model for the results you presented?
2. Do you plan to investigate a hybrid ray-optics and PE model?

**Author/Presenter's reply :**

1. 30 minutes sur calculatrice VAX ou 5 minutes sur une station de travail SUN.
2. On envisage effectivement de s'intéresser à un modèle hybride pour calculer en un temps raisonnable un domaine de 10 000 m en hauteur et 500 km en distance par exemple.

**Translation :**

1. 30 minutes calculation on a VAX or 5 minutes on a SUN work station.
2. We are in fact looking at a hybrid model for computing, in a reasonable time span; a domain of 10 000 m in height and 500 km in distance for example.



# PROPAGATION DES ONDES HAUTE FREQUENCE EN MILIEU URBAIN ET EN TUNNEL ROUTIER

M. Liénard, Ph. Mariage, S. Baranowski et P. Degauque

Université de Lille, Dept. Electronique

Bâtiment P3

59655 VILLENEUVE d'Ascq Cédex, France

## 1. SOMMAIRE

Les télécommunications entre une station de base fixe et un mobile se déplaçant à la surface du sol sont soumises à des réflexions multiples. Lorsque la fréquence de la porteuse est de l'ordre ou supérieure à 1 GHz, la plupart des obstacles situés entre l'émetteur et le récepteur ont des dimensions beaucoup plus grandes que la longueur d'onde et un modèle prédictif des conditions de propagation peut être basé sur la théorie des rayons et notamment sur la théorie uniforme de la diffraction (TUD). La première partie de cet article sera consacrée à un bref rappel du formalisme mathématique et à la façon d'introduire la permittivité complexe du sol dans les modèles théoriques. Dans le cas d'une propagation en milieu urbain, une comparaison entre les résultats obtenus à l'aide de la TUD et ceux basés sur des modèles approchés prenant en compte les diffractions multiples sera effectuée.

Une configuration géométrique importante pour laquelle les réflexions multiples jouent un rôle très important concerne les propagations en tunnel routier. L'étude sera menée en considérant successivement la propagation intrinsèque dans le tunnel, c'est-à-dire en supposant que celui-ci est infiniment long, puis la transition espace libre-tunnel. L'étude est effectuée dans le domaine fréquentiel puis temporel afin de mettre en évidence les fluctuations d'amplitude du signal et les retards dus aux trajets multiples. Les prévisions théoriques sont ensuite confrontées aux résultats expérimentaux.

## 2. RAPPEL DES DIVERSES APPROCHES THEORIQUES PERMETTANT DE TRAITER LES PROBLEMES DE DIFFRACTION

Dans le domaine des ondes hautes fréquences et hyperfréquences, les obstacles, tels qu'une colline lorsque la liaison s'effectue en rase campagne ou un bâtiment lorsque l'on se trouve en milieu urbain, créent des zones de masquage dans lesquelles le rapport signal sur bruit diminue dans des proportions importantes. Trois méthodes de prédiction numérique des pertes se dégagent lors d'une étude bibliographique. La première est la méthode d'Okumara-hata [2]. Elle utilise une série de formules mathématiques simples faisant intervenir des coefficients correcteurs dépendant des conditions générales dans lesquelles s'effectue la liaison. Cette méthode s'appuie essentiellement sur des résultats statistiques obtenus à partir d'une grande série de mesures effectuée au Japon dans des zones faiblement urbanisées.

La seconde méthode de prédiction est celle adoptée par le Comité Consultatif International des Radiocommunications (CCIR) [1] et qui rassemble plusieurs éléments de travaux effectués notamment par Hata, Epstein et Peterson, et Deygout [3]. Par la suite cette méthode sera désignée par la notation MCCIR.

Une autre solution consiste à utiliser la théorie uniforme de la diffraction (TUD). Dans le cadre de cette présentation, nous effectuerons une compa-

raison entre la formulation théorique de la MCCIR et celle de la TUD.

### 2.1 Méthode du CCIR

Dans cette méthode un obstacle quelconque est représenté par un demi-plan vertical parfaitement conducteur et les configurations géométriques dans lesquelles cette formulation sera applicable sont représentées sur la Figure 1. La solution s'appuie sur le calcul exact du champ lointain calculé à l'aide du principe d'Huygens. La solution scalaire du champ diffracté est donnée par la formule suivante :

$$E = E_0 \frac{\exp(-j/4)}{\sqrt{2}} \int_v^{\infty} \exp(j\pi t^2/2) dt \quad (1)$$

où la borne d'intégration  $v$  s'exprime en fonction des différents paramètres géométriques par la relation :

$$v = h \sqrt{\frac{2}{\lambda} \frac{(d_1 + d_2)}{d_1 d_2}} \quad (2)$$

$E_0$  étant le champ électrique qui existe en l'absence de l'obstacle. Si on suppose que les distances  $d_1$  et  $d_2$  vérifient l'inégalité  $d_1 \gg |h|$  et  $d_2 \gg |h|$  et en considérant que la longueur d'onde est très faible devant  $h$ , la borne d'intégration  $v$  est beaucoup plus grande que l'unité. En utilisant les développements limites des intégrales de Fresnel intervenant dans la formule (1), on montre que l'atténuation  $A$  due à l'obstacle et définie par :

$$A = 20 \log |E/E_0| \quad (3)$$

est donnée par l'expression suivante :

$$A = -6.4 - 20 \log (\sqrt{v^2 + 1} + v) \quad (4)$$

### 2.2 Méthode de la TUD

#### 2.2.1 Diffraction par un demi-plan métallique

Le point de départ de cette approche est la solution exacte de Sommerfeld qui prend en compte la nature vectorielle du champ électromagnétique et sa formulation a été développée dans de nombreux articles [4]. La TUD permet de tenir compte de la polarisation de l'onde incidente sur l'obstacle et le champ diffracté peut être calculé dans la région d'ombre profonde située juste derrière l'obstacle. Afin d'effectuer une comparaison entre les résultats issus de la TUD et de la MCCIR, envisageons la configuration géométrique représentée sur la Figure 2. La fréquence d'émission est de 900 MHz et, pour la TUD, on considère les deux cas où  $E$  est parallèle au bord du demi-plan et où  $H$  est parallèle à ce bord. La source est située à 5 km du demi-plan et définit l'altitude de référence 0 m. L'extrémité du demi-plan métallique est située à 100 m de hauteur par rapport à cette référence, l'altitude de réception étant successivement de 100 m et 150 m. Les courbes des Figures 3a et 3b donnent les pertes, exprimées en dB, en fonction de la distance OA entre le point d'obser-

vation et le demi-plan métallique. On remarque un accord très satisfaisant entre les deux approches excepté pour les faibles valeurs de OA dans le cas où  $h = 150$  m. Compte tenu des approximations utilisées dans le formalisme de MCCIR, l'équation (4) n'est valable que si  $v < -1$ , l'atténuation correspondante à cette valeur de  $v$  étant de 1.25 dB. On vérifie bien ce résultat sur la Figure 3b.

## 2.2.2 Diffraction par un dièdre métallique

Nous allons tout d'abord rappeler brièvement les expressions de la matrice de diffraction qui permet de calculer les composantes du champ diffracté par un dièdre métallique d'angle au sommet  $(2-n)\pi$ , et ceci à partir des composantes du champ incident. Le repère choisi est représenté sur les Figures 4a et 4b. Le plan incident à bord fixe est le plan contenant le rayon incident et le vecteur unitaire  $e$  tangent au bord au point d'incidence  $Q_0$ . Dans le cas d'un bord droit coïncidant avec l'axe des  $z$ , ce vecteur est le vecteur unitaire de cet axe. De même le plan diffracté à bord fixe contient le rayon diffracté et le vecteur  $e$ . La position de ces plans peut être repérée soit par les angles  $\psi$  et  $\psi'$  qu'ils font avec l'un des plans du dièdre qui contient le bord, soit par les vecteurs unitaires  $\psi$  et  $\psi'$  qui sont respectivement perpendiculaires au plan d'incidence et au plan diffracté. En effectuant la projection des champs sur les systèmes d'axes  $(S, \beta, \psi)$  et  $(S', \beta', \psi')$  de la Figure 4a, on montre /4/ que les composantes du champ diffracté se mettent sous la forme :

$$\begin{pmatrix} E^d_{\beta_0} \\ E^d_{\psi} \end{pmatrix} = (D) \begin{pmatrix} E^i_{\beta_0} \\ E^i_{\psi} \end{pmatrix} f(r) \quad (5)$$

L'indice  $i$  désignant le champ incident,  $f(r)$  est une fonction dépendant de la forme d'onde incidente sur le bord et  $D$  est la matrice de diffraction dont seuls les termes diagonaux  $D_E$  et  $D_H$  sont non nuls. Ils correspondent respectivement au cas où le champ électrique ou le champ magnétique incident sont parallèles au bord et se mettent sous la forme générale :

$$D_{E,H}(\psi, \psi') = D(\psi - \psi') \pm D(\psi + \psi') \quad (6)$$

Les expressions de  $D$  ont été déterminées notamment par Kouyoumian /4/ et permettent d'assurer la continuité du champ sur les frontières d'ombres géométriques.

## 2.2.3 Diffraction par un dièdre diélectrique

Il n'existe pas de solution exacte de ce problème mais plusieurs auteurs ont proposé des approches afin de prendre en compte la conductivité finie des matériaux. Comme nous l'avons signalé précédemment, les coefficients de diffraction permettent d'assurer la continuité du champ et les facteurs  $(-1)$  ou  $(+1)$  intervenant dans l'équation 6 peuvent être interprétés comme étant les coefficients de réflexion du champ électrique et du champ magnétique sur une surface métallique. Les expressions analytiques des coefficients de diffraction ont d'abord été étendues au cas d'une lame diélectrique mince /5/. La démarche qui a été suivie /5/, /6/ consiste à pondérer respectivement les deux termes  $D(\psi - \psi')$  et  $D(\psi + \psi')$  par les coefficients de réflexion  $R$  et de transmission  $T$  sur la lame afin de traduire la continuité du champ. Une approximation du coefficient de diffraction est donc donnée par la relation :

$$D_{E,H} = (1 - T_{E,H}) D(\psi - \psi') + R_{E,H} D(\psi + \psi') \quad (7)$$

Cette formule suppose cependant que les ondes de

surface soient négligeables et que la diffraction ne provienne que d'un seul point, ce qui implique que l'on néglige "l'effet de bord", c'est-à-dire la transmission par la face transverse de la lame.

Une généralisation de ces formules au cas de la diffraction par des dièdres diélectriques à pertes a été proposée par Luebbers /6/. Dans notre application les pertes dans le sol ou dans les murs des bâtiments sont suffisamment importantes pour négliger les rayons transmis à travers les parois. Cette hypothèse conduit donc à supposer que le coefficient de diffraction dans la zone d'ombre est équivalent à celui d'un matériau parfaitement conducteur. Par contre les coefficients de diffraction associés à la zone de réflexion s'exprimeront en fonction des coefficients de réflexion sur chacun des bords du dièdre diffractant. Dans de nombreuses applications, il faudra tenir compte des dimensions finies des arêtes qui provoquent elles-mêmes une discontinuité du champ diffracté. Ce phénomène se traduit par la diffraction du coin, intersection de deux bords droits, et qui produit un champ dans toutes les directions. Des formules empiriques ont été proposées par Sikta et al. /7/.

Afin de mettre en évidence l'influence de la conductivité et de la permittivité du milieu sur l'amplitude du champ diffracté, nous avons représenté sur la Figure 5 la variation des "pertes" exprimées en dB, dues à la présence de l'obstacle, les pertes étant définies comme étant le rapport entre le champ total et le champ direct en l'absence du dièdre diffractant représenté également sur la Figure 5. L'émetteur fonctionnant à 1 GHz est situé à 70 m de l'arête, le point de réception se déplaçant sur un cercle de rayon égal à 10 m et centré également sur l'arête. Les deux graphiques de la Figure 5 correspondent respectivement au cas où  $H$  et  $E$  sont parallèles au bord. On remarque que lorsque la conductivité du matériau varie de  $10^{-3}$  à  $10^{-1}$  S/m, l'atténuation du champ reste sensiblement la même. Une étude paramétrique a montré que dans la gamme des valeurs usuelles de  $\sigma$  et  $\epsilon_r$  des parois de bâtiment ou du sol, la valeur précise de ces paramètres n'est pas critique pour la détermination du champ diffracté. Dans l'hypothèse d'un dièdre parfaitement conducteur, l'écart devient beaucoup plus important, notamment pour une polarisation telle que  $E$  est parallèle au bord, les conditions aux limites imposant un champ nul sur la surface.

Dans la suite de l'exposé, cette approche basée sur la théorie uniforme de la diffraction en tenant compte de la conductivité finie des parois va permettre d'avoir des modèles prédictifs de la propagation des ondes dans un milieu complexe, et notamment en tunnel routier.

## 3. SIMULATION THEORIQUE DE LA PROPAGATION EN TUNNEL

### 3.1 Emission-réception à l'intérieur du tunnel

L'étude de la propagation d'ondes hautes fréquences en tunnel a déjà fait l'objet de nombreux travaux qui ont été publiés dans la littérature. Les dimensions transversales du tunnel étant bien plus grandes que la longueur d'onde, un tunnel de grande longueur se comportera comme un guide d'ondes surdimensionné dont les parois ont, pour la fréquence envisagée, une conductivité  $\sigma$  et une permittivité relative  $\epsilon_r$  équivalente. Le champ total peut être calculé à partir d'une théorie modale mais qui est lourde de mise en oeuvre. Une autre possibilité consiste à appliquer la théorie des rayons en considérant que la propagation des ondes à l'intérieur du tunnel est assurée par les réflexions multiples contre les parois, les coefficients de réflexion associés étant ceux d'une onde plane.

### 3.2 Emission à l'extérieur du tunnel

La théorie des rayons décrite précédemment ne s'adapte que très partiellement à la caractérisation d'un canal radio mobile étant donné que la zone critique se situe au voisinage de la transition tunnel-espace libre. En effet il est important d'évaluer la pénétration, à l'intérieur du tunnel, d'une onde extérieure (liaison de la station fixe vers le mobile) ou, inversement du rayonnement d'une antenne située à l'intérieur du tunnel vers l'espace libre.

L'approche théorique est basée sur une extension de la théorie des rayons qui prend en compte la diffraction par les coins et les bords dans le plan d'entrée du tunnel telle qu'elle a été décrite dans le paragraphe précédent.

Considérons dans un premier temps, une antenne S située hors du tunnel. Les rayons provenant de la source ou de son image par rapport au sol peuvent soit se propager directement dans le tunnel, soit se diffracter sur un des trois bords (AD, AB, BC), (Figure 6).

Dans le premier cas, les rayons incidents se propageront dans le tunnel avec de multiples réflexions. Pour une source décalée par rapport à l'axe longitudinal du tunnel, l'angle d'incidence sur les parois sera élevé, conduisant ainsi à un coefficient de réflexion faible et une atténuation linéique importante.

Dans le second cas, les rayons diffractés par une des arêtes du tunnel seront répartis sur un cône ayant le bord comme axe de révolution. Certains de ces rayons peuvent ainsi se propager à l'intérieur du tunnel sous incidence rasante donnant naissance à une onde se propageant avec une faible atténuation.

### 3.3 Traitement des données

L'étude des évanouissements du signal (couramment nommés dans la littérature *Fadings*) est très importante pour les systèmes de communication radio-mobile, la durée de ces évanouissements pouvant être suffisante pour dégrader la liaison. Ainsi nous ne focaliserons pas cette étude uniquement sur la détermination des paramètres caractérisant la propagation du champ électrique en tunnel tels que l'atténuation linéique, les pertes de couplage intérieur-extérieur, écart-type... mais aussi sur une statistique des évanouissements du signal apparaissant lorsque l'amplitude de celui-ci est inférieure à un niveau de référence donné.

De cette étude statistique nous déduirons les durées et les fréquences moyennes d'apparition des *fadings*. Pour une propagation en milieu urbain, les relevés d'amplitude de champ en fonction de la distance  $x$  émetteur-récepteur montrent qu'il existe des fluctuations rapides  $r(x)$  du signal, dites de Rayleigh et des évanouissements lents  $m(x)$ , (Figure 7).

Ces résultats ne sont pas directement transposables à notre étude puisque dans la plupart des expérimentations que nous avons faites, les tunnels étaient exempts de tout véhicule. La symétrie de translation liée à la géométrie propre du tunnel implique une distribution des évanouissements autre que celle de Rayleigh. Afin de faire abstraction de l'atténuation linéique provoquée par le tunnel, le signal sera "redressé", c'est-à-dire que l'on étudiera les fluctuations autour de sa valeur moyenne.

Le pas d'échantillonnage est fixé à 20 cm et définit ainsi une valeur minimale de durée d'évanouissement de 24 ms obtenue pour une vitesse du mobile égale à 60 km h<sup>-1</sup>. Soit  $X$  la largeur d'un évanouissement associé à une profondeur  $E_R$  donnée

(-10 dB par exemple) et  $Y$  la distance entre deux *fadings* successifs (Figure 8). Pour chaque fichier de valeurs de champ nous pouvons établir :

- . La fonction cumulative  $F$  des largeurs des évanouissements :  

$$F(X, \text{mètres}) = \text{probabilité}(X < X, \text{mètres}) \text{ pour } E < E_R$$
- . La fonction cumulative des distances séparant deux évanouissements successifs :  

$$F(Y, \text{mètres}) = \text{probabilité}(Y < Y, \text{mètres}) \text{ pour } E > E_R$$

Le temps moyen de durée des évanouissements ainsi que leur période d'apparition peuvent être déduits des expressions précédentes pour n'importe quelle vitesse du véhicule. Afin de fixer un ordre de grandeur de ces durées d'évanouissements une vitesse de 60 km h<sup>-1</sup> a été choisie.

## 4. FLUCTUATION DU CHAMP EN TUNNEL : COMPARAISON THEORIE - EXPERIENCE /8/

### 4.1 Emission et réception à l'intérieur du tunnel

#### 4.1.1 Etude dans le domaine fréquentiel

Les essais de propagation ont été effectués dans un tunnel de section rectangulaire, de 8 m de largeur et de 4.7 m de hauteur. L'antenne d'émission, de type Yagi, polarisée verticalement, est située à une hauteur de 4 mètres et à 1 mètre de la paroi du tunnel, l'antenne de réception étant un dipôle demi-onde. L'antenne réceptrice se déplace suivant l'axe longitudinal du tunnel sur une distance de 150 mètres. L'évolution de l'amplitude du champ en fonction de la distance émetteur-récepteur est représentée Figure 9a. On observe une atténuation de 15 dB sur les 150 premiers mètres. A 900 MHz et pour une telle distance les modes hybrides d'ordre supérieur ne sont pas encore totalement atténués. L'atténuation observée n'est pas représentative de l'affaiblissement linéique du champ qui serait obtenu sur une distance plus importante et pour laquelle le mode EH<sub>11</sub> deviendrait prépondérant. La simulation effectuée (Figure 9b) montre une bonne concordance entre les résultats expérimentaux et théoriques.

L'évolution du champ ne fait apparaître aucun évanouissement inférieur à -20 dB. Le seuil de référence choisi sera fixé à -10 dB pour l'étude statistique. Les différentes fonctions cumulatives sont présentées sur les Figures 10a et 10b. On peut noter que près de 75 % des *fadings* ont une largeur inférieure à 0,6 mètres et apparaissent à des distances inférieures à 35 mètres. Ces évanouissements sont donc peu fréquents et leur période d'apparition  $T_p$  est égale à 1,12 seconde, leur durée moyenne reste faible  $T_f = 30$  ms.

#### 4.1.2 Réponse impulsionnelle du canal

La caractérisation du canal a été effectuée à l'aide soit d'une méthode directe dans laquelle une impulsion ayant une largeur de 10 ns ou 20 ns à mi-hauteur module une porteuse à 900 MHz soit d'une méthode de corrélation basée sur l'émission d'une séquence pseudo aléatoire. Une étude statistique a porté sur 20 relevés de réponses impulsionnelles enregistrées pour diverses distances entre les antennes d'émission et de réception, placées toutes deux à l'intérieur du tunnel. La fonction cumulative des retards représentée Figure 11 indique que 75 % des retards sont inférieurs à 25 ns. De plus l'étude de la distribution d'amplitudes des échos montre également que 75 % d'entre eux ont subi une atténuation d'au moins 10 dB.

A partir d'autres essais effectués dans divers types de tunnel routier, on peut en déduire que le retard moyen pondéré est de l'ordre de 22 ns, la

dispersion des retards (ou moment d'ordre 2) étant de 6 ns.

#### 4.2 Emission à l'intérieur du tunnel et réception à l'extérieur

Pour un mobile situé à l'intérieur d'un tunnel et désirant communiquer avec une station de base, il est intéressant de connaître la façon dont le rayonnement extérieur va s'effectuer suivant la position de l'émetteur au sein du tunnel. Dans un premier temps nous avons tracé Figure 12 l'évolution du champ électrique en fonction de la distance émetteur-récepteur pour un tunnel infiniment long de section 5 m x 9 m. L'émetteur est situé à 3,5 m de la paroi et à une hauteur de 2,5 m.

Le champ rayonné à l'extérieur du tunnel est entièrement défini par la carte de champ dans le plan d'ouverture de celui-ci. Les simulations théoriques ont montré que cette carte de champ à une abscisse donnée était sensiblement la même dans un tunnel de longueur infinie ou non. En effet l'amplitude des champs dus à la diffraction sur les arêtes est faible vis-à-vis de celle associée aux champs réfléchis sur les parois.

Afin de mettre en évidence l'éventuelle influence de la position de l'antenne d'émission sur le rayonnement du tunnel, nous avons choisi deux positions particulières du mobile, suffisamment proches l'une de l'autre pour que la valeur moyenne du champ dans le plan d'ouverture soit la même mais décalée de telle façon que les cartes de champ soient très différentes. On peut ainsi choisir les abscisses associées aux points A et B de la Figure 12 (52 m et 57 m) pour lesquelles le champ en un point particulier (3,5 m du bord et 2,5 m de hauteur) passe respectivement par un maximum et un minimum. Une étude détaillée montre que la carte de distribution de l'amplitude et de la phase du champ dans le plan d'ouverture est très différente suivant que le mobile d'émission se situe au point A ou au point B.

Les diagrammes de rayonnement correspondant à ces deux configurations sont donnés sur la Figure 13. Les courbes sont pratiquement identiques pour des angles inférieurs à 10°, entraînant une atténuation de 25 dB par rapport au champ dans l'axe. Une étude paramétrique a montré que ce résultat est général et que le lobe principal est peu affecté par la position du mobile dans le tunnel.

#### 4.3 Excitation du tunnel

Afin d'étudier les pertes de couplage occasionnées lors de la transition espace libre-tunnel, l'émetteur a été disposé à 50 m à l'extérieur du plan d'entrée du tunnel et positionné successivement dans l'axe ou décalé de 25° et 45° par rapport à l'axe de ce tunnel. Les courbes, notées C<sub>1</sub>, C<sub>25</sub> et C<sub>45</sub> montrent une importante décroissance du signal lorsque l'émetteur n'est plus en visibilité directe. Un bon accord avec les prévisions théoriques a également été obtenu pour ces diverses configurations.

#### 5. CONCLUSION

Une étude du rayonnement des antennes placées en milieu confiné et notamment en tunnel routier a été effectuée. L'approche statistique basée sur les résultats expérimentaux a montré par exemple que dans 75 % des cas la largeur des évanouissements supérieurs à 10 dB n'excède pas 60 cm, la distance moyenne entre ces fadings étant de l'ordre de 35 m.

Pour des tunnels de courte longueur, une réémission n'est pas forcément nécessaire mais nous avons vu qu'un paramètre critique est la position angulaire  $\theta$  de la station de base extérieure par rapport à

l'axe du tunnel. En effet, les pertes de couplage, c'est-à-dire l'atténuation supplémentaire engendrée par le fait que cette antenne ne se situe pas dans l'axe, deviennent vite prohibitives (supérieure à 20 dB) dès que cet angle  $\theta$  dépasse 20 à 30°. Réciproquement lorsque le mobile émet depuis le tunnel, le diagramme de rayonnement vers l'espace libre est très étroit, le lobe principal étant dirigé dans l'axe. Nous avons montré également dans ce cas que, malgré une carte de champ dans le plan d'ouverture du tunnel dépendant très fortement de la position du mobile, le diagramme de rayonnement en espace libre reste sensiblement le même.

Une approche dans le domaine temporel a été menée pour les mêmes conditions d'excitation du tunnel. En se limitant aux échos n'ayant pas une amplitude inférieure de 20 dB à celle du plus fort signal, les retards maximums observés n'excèdent pas 30 ns. Ils sont donc tout à fait acceptables pour des systèmes tels que la radiotéléphonie cellulaire GSM, la largeur des bits élémentaires étant de 3,7  $\mu$ s, le retard maximum admissible étant de 15  $\mu$ s.

Il faut enfin noter que la comparaison entre les résultats théoriques et expérimentaux est tout à fait satisfaisante et par conséquent qu'un modèle basé sur la théorie des rayons permet une bonne prédiction de la couverture radioélectrique même dans une configuration compliquée comme celle d'un tunnel routier où de nombreuses réfractions et réflexions multiples se produisent sur des milieux dont les caractéristiques électriques (conductivité et permittivité) ne sont connues que très imparfaitement.

#### REMERCIEMENTS

Ce travail a été effectué dans le cadre d'un projet européen DRIVE en collaboration avec les partenaires suivants : INRETS/CRESTA (F), SIRT (I), ISSEP (B), ALCATEL Câbles (F), AEG Kabel (D).

#### REFERENCES

##### Comptes-rendus

1. CCIR, "Propagation dans les milieux non ionisés", vol. V, 1990.

##### Articles périodiques

2. Hata, M., "Empirical formula for propagation loss in land-mobile radioservices", IEEE Trans. on Veh. Tech., vol. 29, n° 3, 1980, pp 317-325.
3. Deygout, J., "Multiple knife-edge diffraction of microwaves", IEEE Trans. on A.P., vol. 14, n° 4, 1966.
4. Kouyoumian, R.G. and Pathak, P.H., "A uniform geometrical theory of diffraction for an edge in a perfectly conducting surface", Proc. IEEE, vol. 62, pp 1448-1461, 1970.
5. Burnside, W.D. and Burgener, K.W., "High frequency scattering by a thin lossless dielectric slab", IEEE Trans. on A.P., vol. 31, n° 1, pp 104-110, 1983.
6. Luebbers, R.J., "Finite conductivity uniform GTD versus knife edge diffraction in prediction of propagation path loss", IEEE Trans. on A.P., vol. 32, n° 1, pp 70-76, 1984.
7. Sikta, F.A., Burnside, W.D., Chu, T.T. and Peters, L., "First-order equivalent current and corner diffraction scattering from flat plate structures", IEEE Trans. on A.P., vol. 31, n° 4, pp 584-589, 1983.

8. Mariage, P., Liénard, M. and Degauque, P.,  
 "Theoretical and experimental approach of high  
 frequency waves in road tunnels", Submitted to  
 IEEE Trans. on Ant. and Prop., 1993.

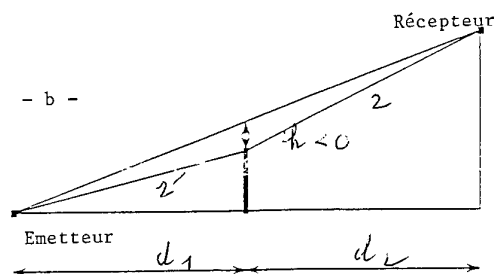
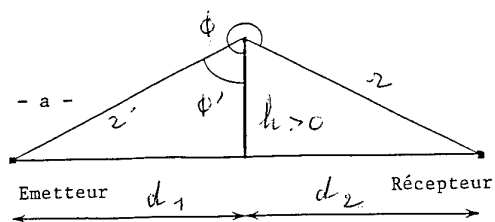


Figure 1 : Diffraction par une arête.  
 Configuration géométrique.

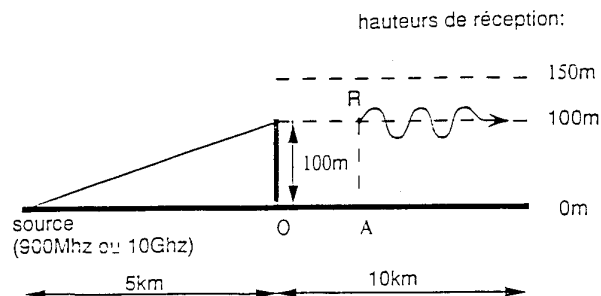


Figure 2 : Position de l'émetteur et du récepteur.

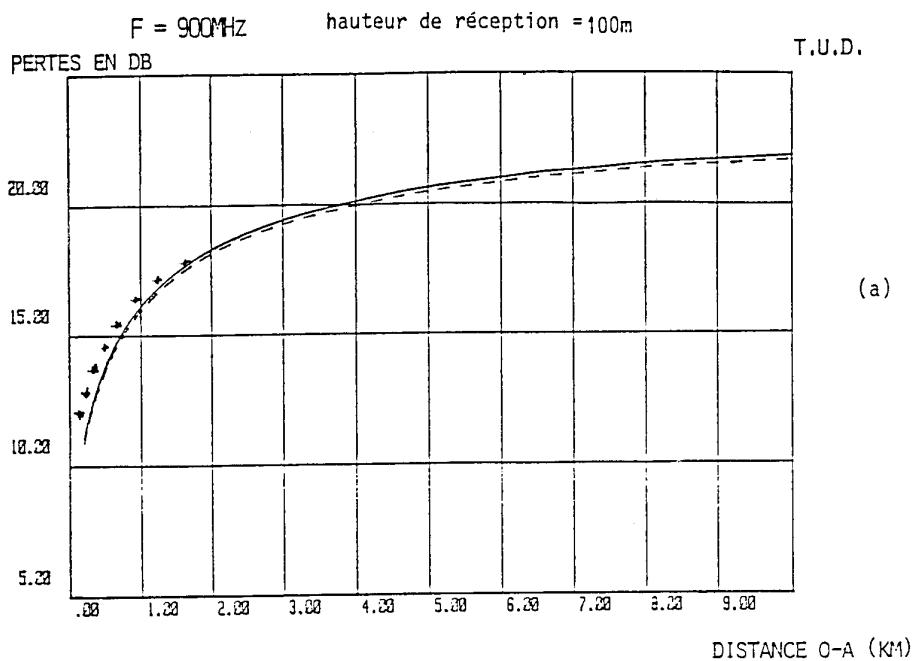


Figure 3a : Variation de l'amplitude des pertes dues à l'obstacle en fonction de la distance OA. — E parallèle au bord ; ---- H parallèle au bord ; + Résultats obtenus à partir de MCCIR. Hauteur du point de réception : 100 m.

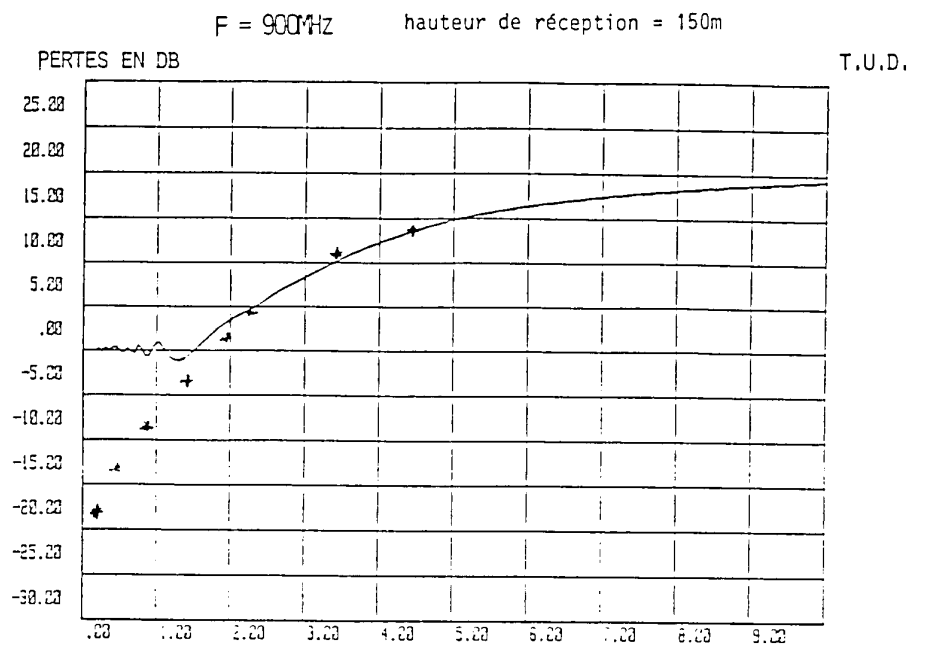


Figure 3b : Même configuration que celle de la Figure 3a mais pour une hauteur de réception de 150 m.

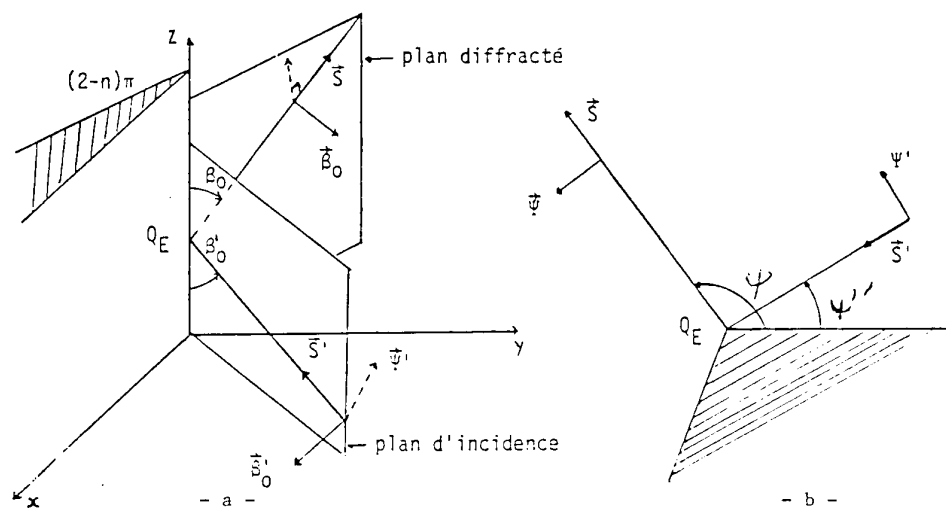
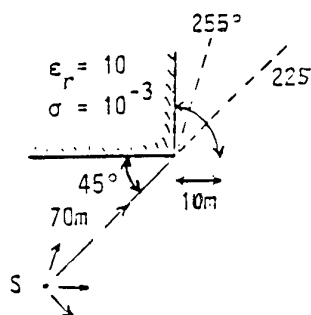
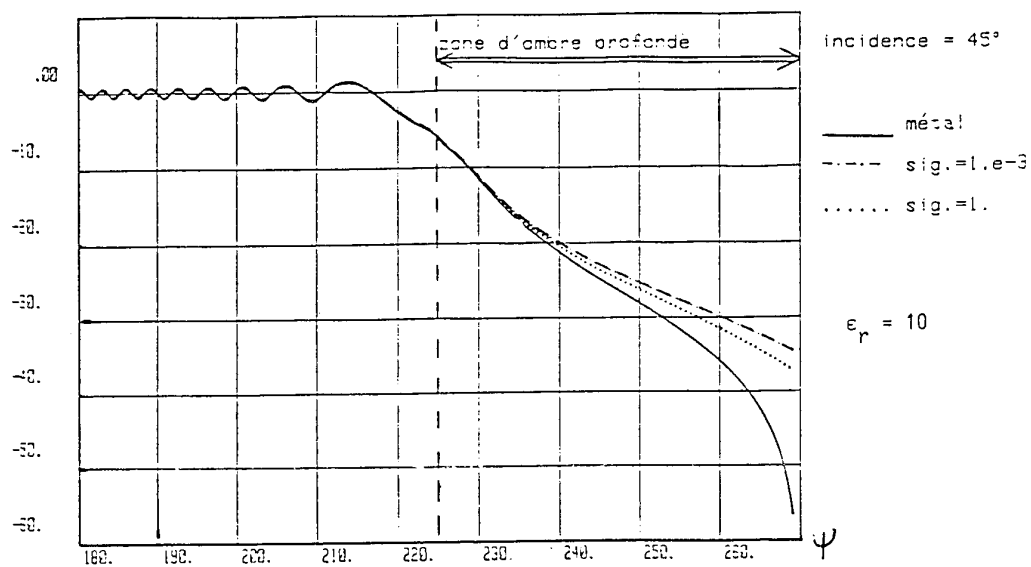


Figure 4 : Définition des divers paramètres géométriques.



dièdre à 90° E // bord F=1GHz E-R isotropes  
pertes en dB



dièdre à 90° H // bord F=1GHz E-R isotropes  
pertes en dB

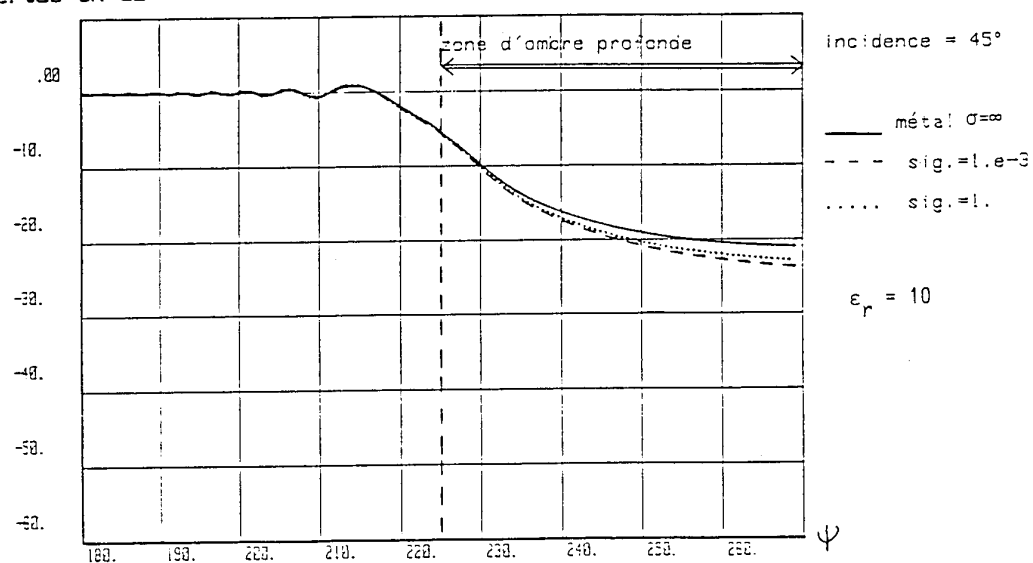


Figure 5 : Influence de la conductivité du dièdre sur l'amplitude du champ diffracté.

degrés

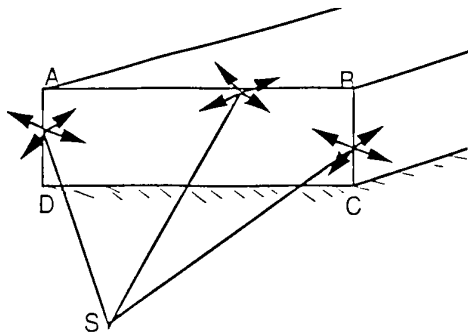


Figure 6 : Excitation du tunnel par une source extérieure.

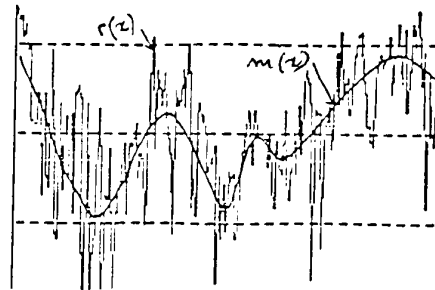


Figure 7 : Exemple d'enregistrement montrant les fluctuations lentes  $m(x)$  et rapides  $r(x)$  du signal.

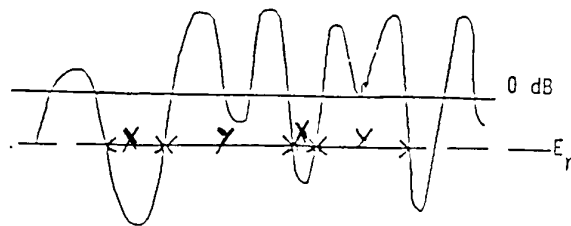


Figure 8 : Largeur des évanouissements X ayant au moins une profondeur  $E_r$  et distance Y entre deux évanouissements successifs.

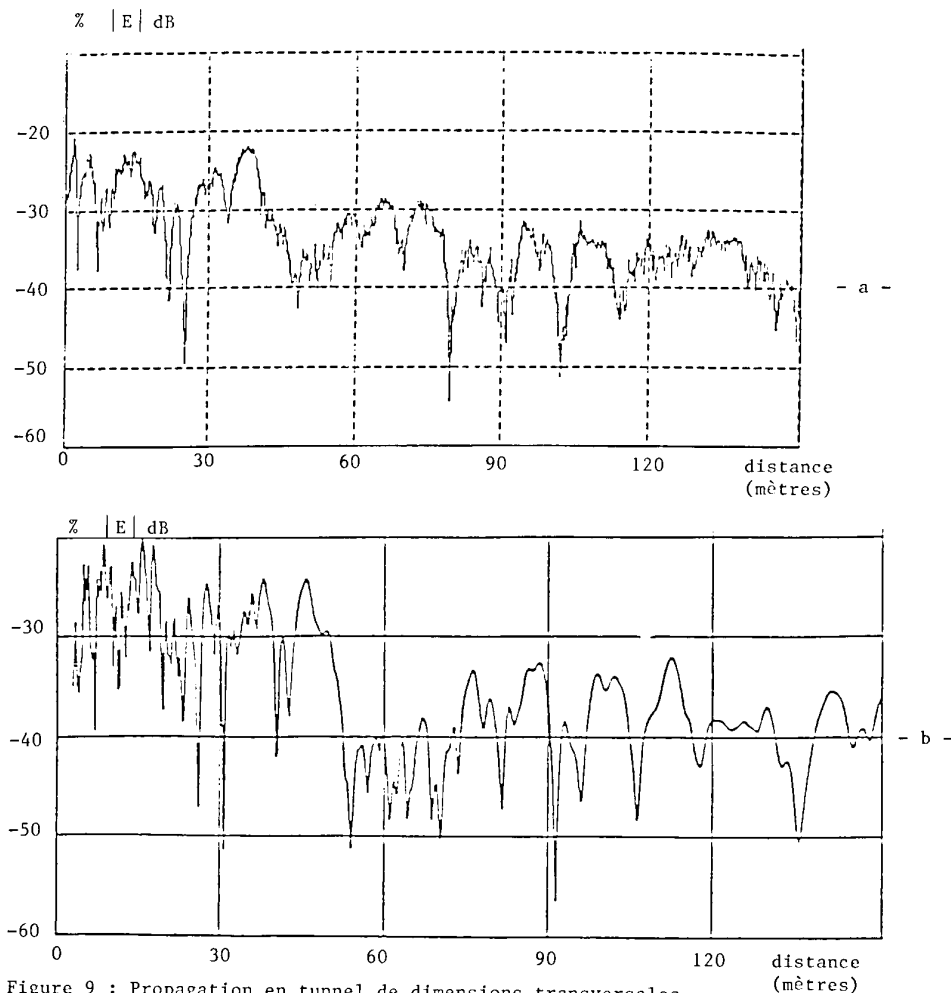


Figure 9 : Propagation en tunnel de dimensions transversales 4.7 m x 8 m. - a - courbe expérimentale ; - b - courbe théorique.



CUMULATIVE FUNCTION OF DISTANCE BETWEEN TWO FADINGS

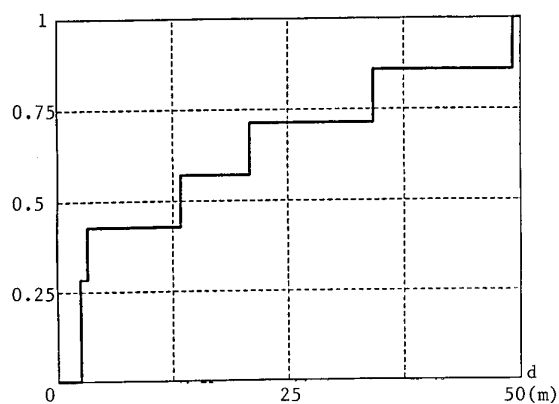


Figure 10a : Fonction cumulative des distances séparant deux évanouissements successifs.

CUMULATIVE FUNCTION OF FADINGS WIDTHS

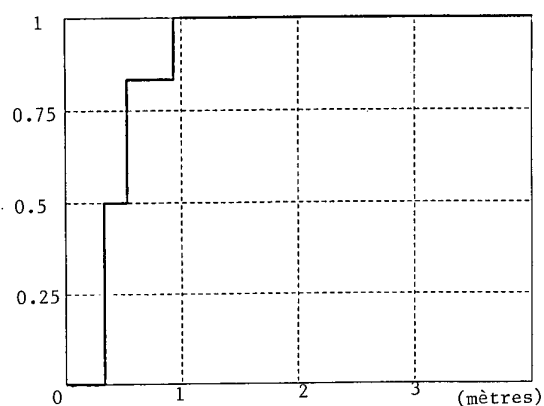


Figure 10b : Fonction cumulative des largeurs des évanouissements.

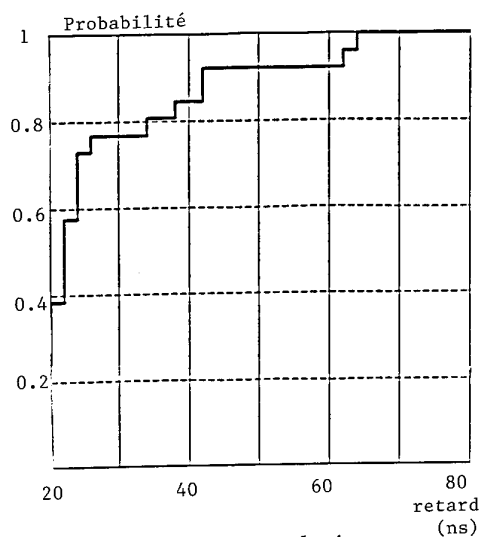


Figure 11 : Fonction cumulative des retards.

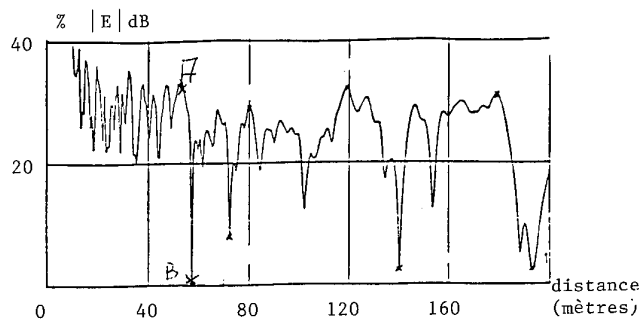


Figure 12 : Amplitude du champ en fonction de la distance émetteur-récepteur.

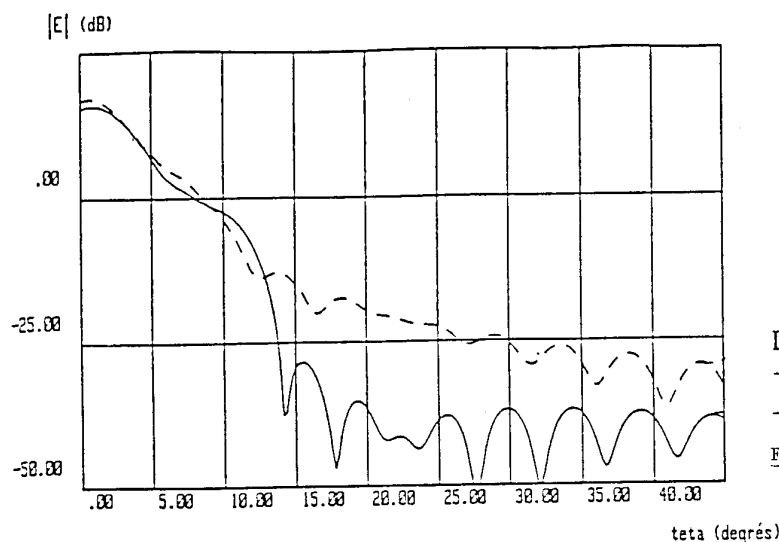


Diagramme de rayonnement

--- d=52 m  
— d=57 m

Figure 13

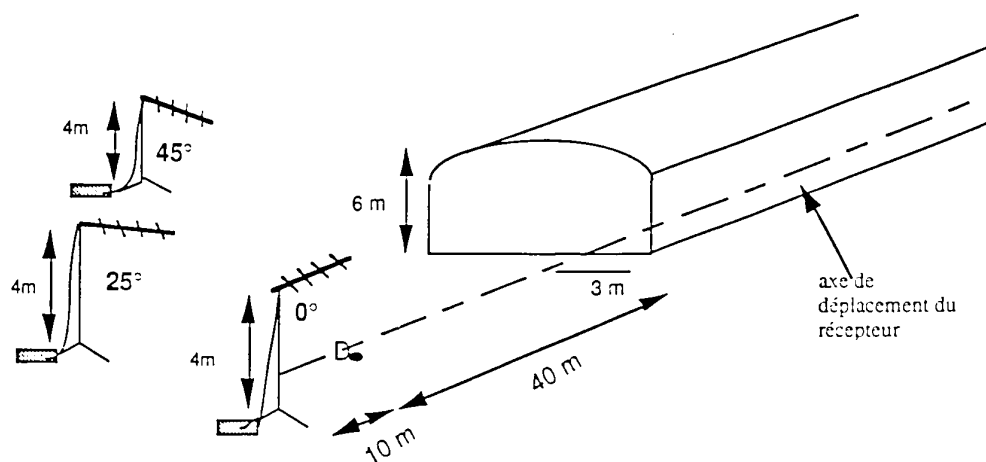


Figure 13a : Configuration géométrique montrant les positions successives de l'antenne d'émission.

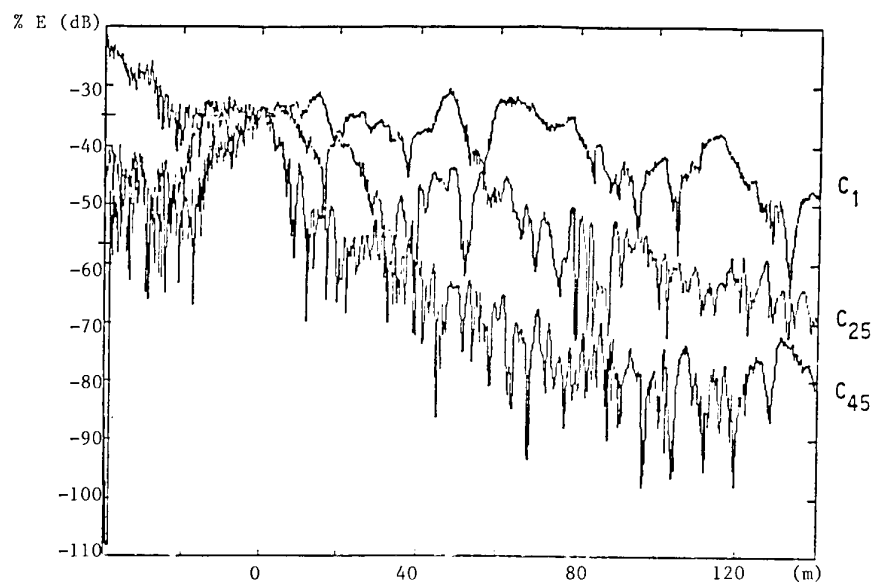


Figure 13 b : Amplitude du champ en fonction de la distance émetteur-récepteur. Le point 0 correspond à l'entrée du tunnel.

## DISCUSSION

**Discussor's name :** C. Goutelard

**Comment/Question :**

Vous avez présenté des résultats extrêmement intéressants, notamment pour les personnes qui auront à traiter le signal. Le tunnel est caractérisé et fait apparaître des effets caractéristiques de trajets multiples. Les tunnels sont en pratique, empruntés par de nombreux véhicules et le fading devrait tendre vers une loi de Rayleigh. Pouvez-vous donner votre opinion sur cette question?

**Translation :**

*You have presented some extremely interesting results, in particular for those who deal with signal processing. The tunnel is characterised and demonstrates the characteristic effects of multiple paths. In practice, the tunnels are used by a number of vehicles and fading should tend towards a Rayleigh law. What is your opinion on this question?*

**Author/Presenter's Reply :**

Il est exact que la distribution des évanouissements devrait tendre vers une loi de Rayleigh d'autant plus que cette loi statistique s'applique particulièrement au cas d'un mobile encaissé. On ne peut cependant pas l'assurer étant donné la configuration propre du tunnel qui est en symétrie de translation. Les résultats des mesures complémentaires, planifiées pour le mois de novembre, en tunnel routier, devraient lever cette incertitude.

**Translation :**

*You are quite right when you say that the distribution of fading should tend towards a Rayleigh law, especially as this statistical law applies particularly to an encased mobile. We cannot however concur, given the inherent configuration of a tunnel, which is transversely symmetrical. The results of the additional measurements, to be performed in a road tunnel in November, should remove this uncertainty.*

**3. Discussor's name :** S. Prohoroff

**Comment/Question :**

Est-ce que, dans le cas de l'émetteur extérieur au tunnel, la transmission ne passe pas de manière dominante par le rayon direct, ce qui ne nécessite pas nécessairement de régénération du signal?

**Translation :**

*If the emitter is outside the tunnel, isn't most of the transmission made by means of the forward ray, which does not necessarily necessitate signal regeneration?*

**Author/Presenter's Reply :**

Si on considère le cas particulier d'une station de base extérieure orientée suivant l'axe longitudinal du tunnel, la régénération du signal n'est pas nécessaire étant donné que le rayon direct est prépondérant. Cependant les autres configurations sont à prendre en considération car l'orientation d'un tunnel dépendant de l'infrastructure routière et non de la situation de la station de base. C'est pourquoi un modèle prédictif des variations du champs électrique est indispensable pour juger si une réamplification est nécessaire pour des émissions excentrées?

**Translation :**

*If we consider the specific case of a base station outside the tunnel, oriented along the longitudinal axis of the tunnel, signal regeneration is not necessary, given that the forward ray is predominant. However, the other configurations should be taken into consideration as the orientation of a tunnel depends on the road infrastructure and not on the position of the base station. This is why a predictive model of variations in the electrical field is vital in order to be able to judge whether reamplification is necessary for off-centred transmissions.*

# A WIDEBAND PROPAGATION SIMULATOR FOR HIGH SPEED MOBILE RADIO COMMUNICATIONS

P. BUSSON (1), J.C. LE JANNIC (2), G. EL ZEIN (3), J. CITERNE (3)

(1) SILICOM Région Ouest, 35700 RENNES (France)

(2) CELAR, 35170 BRUZ (France),

(3) LCST-INSA, URA 834, 35043 RENNES Cédex (France)

## Abstract

Multipath, jamming, listening and detection are the main limitations for mobile radio communications. Spread spectrum techniques, especially frequency hopping, can be used to avoid these problems. Therefore, a wideband simulation for multipath mobile channels appeared the most appropriate evaluation technique. It also gives useful indications for system characteristic improvements.

This paper presents the design and realization of a new UHF-VHF propagation simulator, which can be considered as an extended version of Bussgang's one[1]. This frequency hopping simulator (up to 100 000 hops per seconds) is wideband thus capable to deal with spread spectrum signals. As it generates up to 16 paths, it can be used in almost all mobile radio propagation situations. Moreover, it is also able to simulate high mobile relative speeds up to 2000km/h such as air-air communication systems.

This simulator can reproduce, in laboratory, 16 rays Rician or Rayleigh fading channels with a maximum time delay of about 15 ms. At the highest frequency of 1200 MHz, Doppler rates up to 2 kHz can be generated corresponding to vehicle speeds up to 2000 km/h. Let note that the Bussgang simulator was defined for narrowband and fixed radio communications. In both equipments, in-phase and quadrature signals are obtained using two numerical transversal filters.

The computerized evaluation procedure is the following: the input data are the procedure period, the step of calculation of tables corresponding to initial positions and the speed vectors of transmitter and receiver. Then, the type of link (ground-ground, ground-air, air-air, air-sea...) defines the number of paths, the Doppler rate and path losses characterizing the environment (plane, hilly earth, urban, suburban or rural areas). These data are kept constant during the overall procedure.

The computer creates four tables for numerical transversal filters:

- \* The table of coefficients which are calculated by noting that the envelope of the received signal follows Rayleigh or Rice distribution.
- \* The table of attenuations which are calculated for several VHF-UHF frequency bands taking into account the environment.
- \* The table of delays which vary between 125ns and 15 ms by step of 125ns.
- \* The table of noise (zero mean stationary Gaussian samples).

Simulation results were derived in various situations especially in terrestrial urban and suburban environments, where they could be compared with measurements. The main advantage of the simulator lies in its capacity to simulate the high speed and wideband mobile radio communication channels.

## 1. LA PROPAGATION RADIOMOBILE (VHF-UHF)

L'onde émise à partir d'un émetteur souvent fixe et captée par un récepteur mobile peut subir, surtout dans le cas de liaison en milieu urbain ou montagneux, des phénomènes de réflexions ou de diffusions dus aux obstacles rencontrés (arbres, immeubles, ...).

Dans ces conditions, la propagation se caractérise par une atténuation de la puissance moyenne reçue variant en  $D^{-\alpha}$  où  $D$  est la distance émetteur-récepteur et  $\alpha$  un coefficient compris entre deux et quatre, un effet Doppler dû à la vitesse du véhicule et provoquant un déplacement aléatoire de la fréquence porteuse, des évanouissements lents, non sélectifs en fréquence, traduisant l'effet de masque et suivant la loi log-normale[2].

De plus, dans un milieu urbain ou montagneux, on obtient des évanouissements rapides, dus à l'existence de trajets multiples. Ces évanouissements sont sélectifs en fréquence, arrivent environ toutes les  $\lambda/2$  et suivent une loi de Rayleigh en cas d'obstruction totale, sinon suivent une loi de Rice[3]. En général, ces trajets multiples se décomposent de la façon suivante :

- \* un trajet direct,
- \* une diffraction,
- \* une simple réflexion sur un obstacle proche du mobile,
- \* une réflexion multiple due aux bâtiments au voisinage du mobile,
- \* une réflexion multiple qui a subi auparavant une réflexion non locale causée par des masques de type collines, grandes constructions ...

Dans les liaisons radioélectriques actuelles, on cherche à augmenter le débit des systèmes numériques soit pour améliorer leur efficacité, soit pour accroître la confidentialité en particulier en utilisant les techniques d'étalement de spectre. Ainsi, on se trouve fréquemment dans des cas d'applications où les distorsions dans le canal jouent un rôle important dans la détermination de la qualité numérique.

L'étalement de spectre constitue un moyen efficace pour lutter contre l'effet des trajets multiples de la propagation. En effet, la technique de la séquence directe procure une discrimination temporelle aigüe des différents trajets. De même, la technique du saut de fréquence n'est autre qu'une forme de la diversité de réception en fréquence. Ce point est particulièrement intéressant pour améliorer la robustesse des communications avec les mobiles.

Ainsi, un simulateur large bande est la méthode la plus appropriée pour pouvoir tester les canaux de radiocommunications à évansion de fréquence.

## 2- MODELE DU CANAL

Une liaison radiomobile possède un canal non-stationnaire. Cependant, la caractérisation de celui-ci est extrêmement difficile. Par contre, celui-ci peut être caractérisé par un canal stationnaire sur des intervalles de temps réduits et par conséquent, dans des petites zones. Ces zones doivent posséder une valeur moyenne du signal reçu statistiquement constante et un environnement relativement inchangé. Ainsi, l'hypothèse de canal "WSSUS" est applicable [4,5]. Le canal est modélisé par une chaîne de diffuseurs non-corrélés en retard et en décalage Doppler.

Soit  $y(t)$  le signal émis donné par:

$$y(t) = R_e[y_e(t) \exp(j 2\pi f_c t)] \quad (1)$$

avec  $y_e$  l'enveloppe complexe du signal émis. Le signal reçu est représenté par l'équation (2) :

$$x(t) = k R_e \left[ \sum_i \rho_i y(t-\tau_i) \exp(j 2\pi(f_c - \mu_i)t - f_c(\tau_i + d\tau_i)) \right] \quad (2)$$

En général, les phases ( $2\pi f_c d\tau_i$ ) sont uniformément réparties sur l'intervalle  $[0, 2\pi]$  et indépendantes entre elles [2]. La description complète du canal est donnée par la connaissance de la densité de probabilité conjointe entre les amplitudes  $\rho_i$ , les retards  $\tau_i$ , et les décalages Doppler  $\mu_i$ . Cette formule est la formule de base utilisée pour la simulation du signal de sortie  $x(t)$ .

Une première description utilisant les paramètres à petite échelle a été proposée. Pour obtenir une parfaite description statistique du canal, une deuxième étape de caractérisation est proposée. Celle-ci étudie le comportement du canal à partir des moments obtenus pour des zones à petites échelles [4,6]. Ce type de canal a été appelé quasi-stationnaire au sens large ou "QWSS". Ensuite, nous pouvons déterminer les caractéristiques du canal à grande échelle en déterminant la valeur moyenne de plusieurs valeurs moyennes de retards et de la dispersion de ces retards obtenue sur un grand nombre de zones à petite échelle. Les variables  $\rho_i$ ,  $\tau_i$ , et  $\mu_i$  peuvent dans ce cas être considérées comme des variables aléatoires indépendantes. Les densités de probabilité des variables décrivent alors le canal.

## 3 - ETAT DE L'ART

Les premiers simulateurs étaient à bande étroite. Mais ceux-ci ne peuvent répondre aux problèmes d'étalement de spectre. Ainsi, des simulateurs à large bande ont été étudiés. Ces simulateurs ont été réalisés soit de façon logicielle, soit de façon matérielle, soit de façon mixte matérielle et logicielle.

L'utilisation d'un ordinateur permet une plus grande souplesse dans le choix des différents paramètres à simuler. En effet, les simulateurs [7] entièrement matériels possèdent tous des limitations dues aux différentes technologies employées soit en nombre de trajets, soit en valeur des retards, soit en décalage Doppler.

Les simulateurs entièrement logiciels ne peuvent répondre à nos besoins. En effet, il doivent pouvoir tester une paire d'émetteur-récepteur et donc acquérir des données provenant de l'émetteur. Ainsi, nous avons envisagé un simulateur de type mixte.

L'utilisation de filtres numériques identiques à ceux utilisés sur le simulateur du C.C.E.T.T. [8] permet une souplesse d'utilisation intéressante dans l'optique d'un simulateur à évansion de fréquence. En effet, les retards et le décalage Doppler sont programmables. Le nombre de trajets multiples réalisables sur celui-ci est largement supérieur au nombre théorique de trajets dans le cas d'une liaison dans un milieu fortement urbanisé [8]. Ce milieu possède le nombre de trajets le plus important.

Mais aucun de ces simulateurs ne peut répondre à la contrainte de l'évansion de fréquence. En effet, ils ne peuvent couvrir la gamme de fréquence UHF-VHF, souvent à cause des lignes à retard à ondes de surface. De plus, ils sont toujours destinés à des applications spécifiques pour des canaux urbains ou suburbains, mais non destinés à des applications allant des milieux de type urbain aux milieux de type maritime ou montagneux.

Le décalage Doppler de l'ensemble de ces simulateurs est limité en fréquence. Ainsi, on ne peut simuler que des vitesses de déplacement des mobiles allant jusqu'à 150 km/h [8]. Or, la simulation de la transmission de données entre deux avions doit être réalisée sur le simulateur envisagé ce qui oblige à accélérer le transfert des données aux niveaux des filtres numériques transversaux. Donc le simulateur devra posséder un bus à haut débit pour le transfert des données entre les mémoires de stockage et les filtres numériques transversaux.

## 4 - LE SIMULATEUR

Lors de la réception par un mobile dans une région fortement urbanisée, l'onde transmise parcourt des trajets de longueurs différentes comprenant des réflexions et des diffractions. C'est près du mobile que l'onde de chaque trajet est dispersée par des obstacles tels que les arbres, les immeubles, ... Il existe donc  $M$  ondes associées à  $M$  trajets différents et chaque onde est dispersée

en plusieurs sous-ondes  $N$ . Ainsi, le signal reçu peut s'exprimer d'après (2) par :

$$x(t) = k R_e \left[ \sum_{m=1}^M \sum_{n=1}^N \rho_{mn} y(t-\tau_{mn}) e^{j\alpha} \right] \quad (3)$$

$$\text{avec } \alpha = j 2\pi(f_c - \mu_{mn})t - f_c(\tau_{mn} + d\tau_{mn}) \quad (4)$$

où  $\rho_{mn}$ ,  $\tau_{mn}$  et  $\mu_{mn}$  sont respectivement l'affaiblissement, le retard et la pulsation Doppler de chaque sous-onde  $mn$ .

Cette expression peut-être simplifiée en considérant que les différences entre les retards  $\tau_{mn}$  sont très petits puisque les sous-ondes, issues de la même onde  $m$  prennent naissance sur des obstacles proches du récepteur. Ainsi, nous avons :

$$\tau_m = \frac{1}{N} \sum_{n=1}^N \tau_{mn} \quad (5)$$

Le signal reçu devient :

$$x(t) = k R_e \left[ \sum_{m=1}^M \rho_m y(t-\tau_m) e^{j\alpha} \right] \quad (6)$$

$$\text{avec } \alpha = j 2\pi(f_c - \mu_m)t - f_c(\tau_m + d\tau_m) \quad (7)$$

Cette équation montre que le simulateur doit réaliser les fonctions suivantes :

- \* effectuer les différents retards,
- \* faire varier les amplitudes et les phases de chaque signal retardé,
- \* sommer tous les signaux.

Le schéma de principe du simulateur est présenté à la figure 1. Le signal est décomposé par la partie radiofréquence en signal bande de base. La partie traitement de signal s'articule autour de deux filtres numériques transversaux, le premier pour la partie en phase et le deuxième pour la partie en quadrature. Le calcul des différents coefficients des filtres est réalisé en temps différé. Puis le signal est retransposé en signal radiofréquence et envoyé vers le récepteur. Ces deux parties vont être décrites ci-dessous.

## 4-1 Partie Radiofréquence

### 4-1-1 L'agilité en fréquence

L'agilité en fréquence, ou évasion de fréquence (EVF), consiste à émettre pendant un court instant à une fréquence donnée puis à changer de fréquence pour émettre à nouveau et ainsi de suite. A la réception, il convient de connaître la suite des fréquences utilisées à l'émission pour déplacer l'oscillateur local en conséquence, de façon à retrouver une fréquence intermédiaire de valeur fixe. Le même principe est utilisé pour le simulateur de propagation. La séquence de codage est envoyée sur un synthétiseur programmable, permettant ainsi d'obtenir une fréquence intermédiaire fixe. Ainsi, le simulateur permet de reproduire des liaisons avec des sauts classés ultra-rapides. En effet, on peut simuler jusqu'à 100 000 sauts par seconde à l'intérieur de

la sous bande sélectionnée. La commutation du synthétiseur s'effectue en 5  $\mu$ s. Le synthétiseur utilisé pour réaliser cette agilité de fréquence est à synthèse directe. Il possède une bande de fréquence allant de 1 MHz à 2400 MHz avec un pas de fréquence de 0.6 Hz. Son temps de commutation est de 50 ns. Les raies harmoniques sont situées à - 30 dBc sous la fréquence utile.

### 4-1-2 Transposition du signal radiofréquence

La sortie du synthétiseur programmable est divisée en deux parties, comme le montre la figure 3. Ainsi, le signal du synthétiseur sera utilisé pour la transformation radiofréquence-fréquence intermédiaire et pour la transformation fréquence intermédiaire-radiofréquence.

La fréquence intermédiaire est générée par un oscillateur à 21.4 MHz. Ce signal est ensuite divisé en deux : une partie en phase et une partie en quadrature. Ces deux voies sont divisées en deux pour générer deux signaux en phase et deux signaux en quadrature.

L'émetteur délivre un signal dont la fréquence varie de 30 MHz à 1215 MHz. Cette bande de fréquence est scindée en quatre sous-bandes : 30-88 MHz, 118-144 MHz, 225-400 MHz et 960-1215 MHz. La bande passante maximum du signal émis est de 10 MHz et sa puissance de 50 dBm. Pour réaliser le premier mélange, deux atténuateurs ont été placés en début de chaîne pour ramener le niveau d'entrée à un niveau fixe de 0 dBm. Le signal radiofréquence est converti en fréquence intermédiaire, puis transposé en bande de base. Le signal en fréquence intermédiaire a été scindé en deux pour pouvoir être mélangé avec un oscillateur possédant une composante en phase et une composante en quadrature.

La transformation analogique-numérique est réalisée par deux convertisseurs, un pour la composante en phase et l'autre pour la composante en quadrature. Cette transformation s'effectue par un convertisseur TRW 8 bits de type "flash". La conversion TTL-ECL permet de communiquer par l'intermédiaire d'un câble en s'affranchissant d'un certain nombre de parasites.

### 4-1-3 Transposition simulateur-récepteur

La transposition numérique-analogique permet de convertir le signal logique sur 8 bits en un signal en bande de base. Le circuit utilisé est un convertisseur 8 bits de TRW (THC 1018) dont la fréquence d'échantillonnage maximale est de 200 MHz. Le signal arrivant avec un niveau ECL est transformé en un signal de niveau TTL. Puis, il est démultiplexé pour obtenir deux trains numériques correspondant aux parties réelle et imaginaire de l'enveloppe complexe. Les deux trains numériques sont ensuite introduits sur les deux convertisseurs. Ainsi, nous obtenons le signal analogique en bande de base. Puis, le signal de la bande de base est transposé en fréquence intermédiaire. Les deux parties réelle et imaginaire du signal sont mélangées respectivement aux composantes en phase et en quadrature de l'oscillateur 21.4 MHz. La combinaison des deux signaux résultants permet d'obtenir le signal FI.

### 4-1-4 Le mélangeur réjecteur d'image

La transformation fréquence intermédiaire-radiofréquence est réalisée par un mélangeur réjecteur d'image. En effet, la

vitesse du saut de fréquence ne permet pas l'utilisation de filtre commutable à la sortie du simulateur. Ce mélangeur permet de rejeter la fréquence image et l'oscillateur local à -30 dB par rapport au signal utile.

#### 4-1-5 Le système radiofréquence

Le système radiofréquence est composé de cinq cartes au format VME. Celles-ci sont reliées entre elles grâce à un bus spécifique. Ainsi, ce bus comprend la carte d'atténuation du signal d'entrée, la carte de conversion numérique-analogique (CNA), la carte radiofréquence, la carte de conversion analogique-numérique (CAN) et enfin, la carte atténuateurs programmables.

#### 4-2 Partie Traitement de Signal

Les échanges de données entre le calculateur et les filtres numériques s'effectuent par l'intermédiaire d'un bus à haut débit de type VME, comme le montre la figure 3. Les données provenant de l'émetteur sont réparties sur 16 trajets différents. Sur chaque trajet, les données sont multipliées avec les coefficients calculés en temps différé. L'ensemble est ensuite retardé et additionné aux trajets précédents.

L'atténuation du canal se caractérise par une atténuation de la puissance moyenne reçue suivant la distance émetteur-récepteur, une atténuation suivant la fréquence, des évanouissements lents traduisant l'effet de masque et des évanouissements rapides dus à l'existence de trajets multiples. Ces atténuations et ces évanouissements vont être maintenant détaillés.

##### 4-2-1 Atténuation suivant la distance émetteur-récepteur

L'atténuation de la puissance moyenne reçue varie en  $D^{-\alpha}$  où  $D$  est la distance émetteur-récepteur et  $\alpha$  est un coefficient généralement compris entre deux (cas de la propagation en espace libre) et quatre (cas de la propagation dans une ville fortement urbanisée). Cette atténuation est définie suivant le type de milieu et le type d'urbanisation.

Des modèles prédéfinis sont introduits dans le simulateur pour un type de milieu donné dans le but d'une utilisation rapide du simulateur. Ceux-ci ont été définis après un certain nombre de campagnes de mesures [10].

##### 4-2-2 Atténuation lente

Cet affaiblissement est dû à la configuration du terrain et est connu sous le nom d'effet de masque. Celui-ci procure des évanouissements lents, non sélectifs en fréquence. Cet effet fait varier l'amplitude de l'enveloppe selon la loi de probabilité Log-normale [2].

La commande de l'atténuateur, envoyée par l'intermédiaire du bus VME sur l'atténuateur programmable, est réalisée sur sept bits, permettant ainsi une atténuation programmable de 127 dB par pas de 1 dB sur l'ensemble des trajets multiples. Pour éviter la superposition des raies de commutation au signal radiofréquence, la commande de l'atténuateur intervient pendant la phase de "non émission" du palier EVF.

Les atténuations suivant la distance et suivant l'effet de masque sont calculées en temps différé. Ces calculs sont réalisés suivant un échantillonnage spatial de façon à

obtenir un nombre de points suffisants pour simuler la décroissance lente du niveau du signal. Ainsi, cet échantillonnage permet aux atténuateurs de ne sauter que par pas de 1dB dans les milieux où l'atténuation varie rapidement, comme les milieux urbains ou montagneux.

##### 4-2-3 Atténuation rapide

Le mobile se déplace dans la géométrie des ondes stationnaires créées par interférence entre les ondes d'amplitudes et de phases variées, diffractées ou réfléchies à partir de l'onde émise par toute une série d'obstacles. La distance entre les nœuds de l'amplitude du champ reçu est d'environ  $\lambda/2$  pour une onde de longueur  $\lambda$ .

Le mobile parcourt cette distance à la vitesse  $v$ , l'espacement temporel entre deux évanouissements est donc de l'ordre de  $\lambda/2v$ . Ainsi, la fréquence d'apparition des évanouissements se situe au voisinage de  $2v/\lambda = 2fd$ , c'est-à-dire deux fois la fréquence Doppler correspondant à la vitesse de déplacement du véhicule.

Pour décrire cette modulation d'amplitude de l'onde reçue, modulation créée par la propagation à trajets multiples, il n'est pas possible d'analyser chaque situation instantanée car le nombre de données à prendre en compte est très grand, les valeurs étant difficilement mesurables. Le fading de Rayleigh est modélisé par une statistique des résultats mesurés.

Le nombre et la durée des évanouissements constituent un élément important de la qualité de transmission. Un évanouissement est observé quand le niveau du signal reçu  $r$  est inférieur à une valeur minimale  $R$ . Dans le cas d'un signal émis numérique, les évanouissements vont introduire des erreurs.

Si l'on désigne par  $t_i$  la durée du  $i^{\text{ème}}$  évanouissement, la fonction cumulative de probabilité de l'enveloppe permet d'écrire [2]:

$$t_i = T p(r \geq R) = T \left( 1 - \exp \left( - \frac{R^2}{E_0^2} \right) \right) \quad (8)$$

où  $T$  est la durée d'observation et  $E_0$  le champ reçu.

Ainsi, la durée moyenne des évanouissements pour le fading de Rayleigh est donnée par :

$$\bar{t} = \frac{\exp \left( \frac{R^2}{E_0^2} \right) - 1}{f_d \sqrt{2\pi} \frac{R}{E_0}} \quad (9)$$

Le canal présenté précédemment montre le cas le plus défavorable de la diffusion des signaux vers les mobiles. En réalité, le mobile peut souvent se situer dans un environnement où il existe une onde d'amplitude constante. A une fréquence donnée, la distribution de l'amplitude du canal suit la loi dite de Rice-Nakagami.

##### 4-2-4 Effet Doppler

Le signal reçu par un mobile en déplacement est soumis à une distorsion de fréquence appelée "effet Doppler". Soit  $f_c$  la fréquence d'émission, nous obtiendrons en réception



un déplacement de fréquence calculé à partir de l'équation (10) :

$$f_d = f_e \frac{v}{c} \cos \alpha_i \quad (10)$$

avec  $v$  la vitesse du mobile,  
 $c$  la vitesse de propagation de l'onde,  
 $\alpha_i$  l'angle formé par la direction du vecteur vitesse du mobile avec la direction du vecteur de propagation de l'onde transmise.

Pour un mobile terrestre soumis à l'action de nombreux diffracteurs et réflecteurs situés de façon quelconque par rapport à sa direction de déplacement, l'onde reçue est la superposition de  $M$  ondes incidentes. Ainsi en réception, on obtient une répartition d'énergie sur un intervalle de fréquence.

Pour un mobile en environnement urbain, l'énergie du signal reçu a une distribution uniforme en fonction de l'angle d'arrivée  $\alpha$  pris dans l'intervalle  $[-\pi, \pi]$ . Le spectre de puissance du signal reçu centré autour de la fréquence d'émission est donné par la relation (11)[2]:

$$P(f) = \begin{cases} E_r / \pi \sqrt{f_{\max}^2 - (f - f_0)^2} & \text{pour } -f_{\max} + f_0 < f < f_{\max} + f_0 \\ 0 & \text{ailleurs} \end{cases} \quad (11)$$

$$\text{avec } f_{\max} = f_0 v/c$$

Des études expérimentales, en UHF, ont montré que la forme du spectre Doppler dépend de la valeur des retards observés, ainsi que de l'urbanisation du milieu [11]. On pose  $G(A, f_1, f_2)$  la fonction Gaussienne définie par la relation (12):

$$S(f) = \frac{A}{\sqrt{1 - \left(\frac{f}{f_d}\right)^2}} \quad \text{pour } -f_d < f < f_d \quad (12)$$

Quatre modèles empiriques ont été proposés pour la forme du spectre Doppler.  
 Posons:

$$G(f) = G(A, f_1, f_2) = A \exp\left(-\frac{(f - f_1)^2}{2f_2^2}\right) \quad (13)$$

On obtient:

*\* le retard est inférieur à 500 nanosecondes*

Le spectre obtenu a la forme classique du spectre Doppler. Sa fonction est définie par l'équation (12).

*\* le retard est compris entre 500 nanosecondes et 2 microsecondes*

La fonction est une somme de deux fonctions Gaussiennes, définie par l'équation (14) :

$$S(f) = G(A, -0.8f_d, 0.05f_d) + G(A_1, 0.4f_d, 0.1f_d) \quad (14)$$

avec  $A_1$  inférieur à  $A$  de 10 dB.

*\* le retard est supérieur à 2 microsecondes*

La fonction est une somme de deux fonctions Gaussiennes, définie par l'équation (15) :

$$S(f) = G(B, 0.7f_d, 0.1f_d) + G(B_1, -0.4f_d, 0.15f_d) \quad (15)$$

avec  $B_1$  inférieur à  $B$  de 15 dB.

*\* cas d'un profil possédant un trajet direct et plusieurs trajets réfléchis*

Dans ce cas, on obtient une distribution de Rice définie par la relation (16) :

$$S(f) = \frac{0.41}{2\pi f_d \sqrt{1 - (f/f_d)^2}} + 0.91 \delta(f - 0.7f_d) \quad \text{pour } -f_d < f < f_d \quad (16)$$

Ces quatre modèles vont être utilisés dans le calcul des coefficients utilisés dans les filtres numériques.

### 4-3 Logiciel Temps Différé

Le logiciel temps différé permet de calculer les seize fichiers de coefficients représentant les trajets multiples nécessaires à la simulation. De plus pour chaque trajet, il doit associer au fichier une valeur de retard et une valeur d'atténuation.

#### 4-3-1 Calcul de la vitesse

La vitesse prise en considération sur le simulateur est la vitesse relative entre les deux mobiles ou entre le mobile et la station fixe. Cette vitesse permet de calculer la fréquence du générateur de renouvellement FR des coefficients. Une valeur de programmation VP va être déduite de cette dernière.

La loi de transformation  $FR = F(v)$  est liée à l'observation des évanouissements, à la statistique de leur répartition et à la nature des signaux traités. Ce calcul a été effectué à l'aide de l'équation (9). L'amplitude des évanouissements suit une distribution de Rayleigh. Le signal varie donc très vite durant un évanouissement profond. La durée moyenne  $t$  peut se mettre sous la forme de l'équation (17):

$$t = \frac{e\rho^2 - 1}{r \cdot f_{\max} \sqrt{2\pi}} \quad (17)$$

avec  $\rho$  l'atténuation qui est donnée par  $\rho = R^2/E_0^2$ . Elle est choisie arbitrairement à - 40 dB, correspondant à la valeur maximale des évanouissements perturbants le récepteur. La valeur FR est obtenue par  $TM = \tau$  et  $FR = 1/TM$ .

#### 4-3-2 Calcul de l'atténuation de chaque trajet

L'atténuation de chaque trajet, exprimée en dB par rapport au trajet principal, est appliquée comme facteur d'échelle à l'entrée du filtre numérique. La plus petite valeur pouvant être représentée est - 45dB, ce qui est supérieur à la valeur des évanouissements affectant le signal.

#### 4-3-3 Calcul des retards

Les différents retards sont calculés à partir du premier

trajet. Le retard introduit sur un trajet est transformé en période d'échantillonnage. Pour ce faire, la valeur du retard est divisée par 125 ns. Cette valeur correspond à un accès écriture-lecture d'une mémoire rapide.

Au total, quinze valeurs vont être calculées. Un seizième trajet doit être introduit. De par la structure du filtre FIR, ce retard entraîne un retard global sur l'ensemble des trajets. Ce retard va être fixé arbitrairement à  $T_{min}$  car il intervient sur l'ensemble des trajets.

#### 4-3-4 Calcul des coefficients pour un trajet

La transformée de Fourier d'un processus Gaussien étant elle-même Gaussienne, les coefficients générés par une loi normale peuvent directement aboutir à un spectre Gaussien. Ces coefficients sont ensuite filtrés par le canal, suivant les 4 types de filtre étudiés au §4-2-4. Le filtrage s'effectue ensuite par simple produit des coefficients complexes et des éléments du filtre.

Ensuite, une transformée de Fourier inverse permet la transposition du signal dans le domaine temporel. Afin d'obtenir une séquence de longueur correcte sans répétition des coefficients, la longueur du fichier a été fixée à 65536 échantillons. Cette valeur est dictée par le temps de calcul de la transformée de Fourier. Le calcul de cette transformée de Fourier est basé sur l'algorithme de Cooley-Tukey. L'échantillonnage se faisant à la fréquence  $2f_d$ , la durée totale de la séquence sera ainsi de  $(65536 / 2f_d)$ .

Après la transformation de Fourier inverse, les coefficients correspondent à une suite complexe temporelle échantillonnée à la fréquence  $2f_d$ . Une normalisation de ces nombres est ensuite réalisée, ceci afin d'obtenir une suite Gaussienne de variance unitaire.

Le tableau de données complexes Gaussiennes filtrées, normalisées et formatées à quatre octets par coefficient est ensuite enregistré dans un fichier de type "DATA.X", chaque fichier correspondant à un trajet.

#### 4-3-5 le logiciel

Le logiciel temps différé permet de définir le nombre de trajets utiles à la simulation d'un canal et de déterminer les trois paramètres de chacun de ces trajets. Les paramètres de ces trajets sont :

- \* la valeur du retard,
- \* la valeur de l'atténuation,
- \* le fichier de coefficients "DATA.X" correspondant à ce trajet.

Le programme débute par la définition du type de liaison à simuler. Sept types de liaison peuvent être définis : liaison sol-sol, liaison sol-air, liaison air-sol, liaison mer-mer, liaison air-mer, liaison mer-air et liaison air-air.

Après avoir défini le type de liaison, un choix de deux types de simulation est à effectuer. La simulation peut être faite soit suivant un type de terrain déterminé, soit suivant un trajet à simuler. Lorsque cette dernière est sélectionnée, l'utilisateur doit définir le nombre de trajets à simuler. Pour chaque trajet, il doit spécifier le retard qui doit être un multiple de 125 nanosecondes et l'atténuation du trajet par rapport au trajet le plus fort. Cette option est utilisée pour positionner le simulateur dans un cas

spécifique de simulation.

Si l'utilisateur opte pour la solution de la simulation suivant un type de terrain déterminé, il doit dans un premier temps sélectionner la bande de fréquence. Les quatre bandes de fréquence sont : 30-88 MHz, 118-144 MHz, 225-400 MHz et 960-1215 MHz. Au point de vue propagation, deux cas ont été envisagés : les fréquences inférieures à 200 MHz et les fréquences supérieures à 200 MHz. La différence entre ces deux sous-bandes réside dans le nombre de trajets à simuler.

Ensuite, le milieu de propagation est défini. Quatre types de milieu sont proposés : le milieu rural, le milieu suburbain, le milieu urbain et le milieu montagneux. Le nombre de trajets, déterminé suivant le milieu, la bande de fréquence et suivant le type de liaison, a été fixé à partir de données recueillies par différentes études. Ainsi, le programme va générer le nombre de trajets à simuler, les retards, les atténuations ainsi que les fichiers de données "DATA.X".

#### 4-4 Le système informatique

La partie numérique du simulateur de propagation s'articule autour d'un bus VME. Il est composé de douze cartes au format double europe 19":

- \* une carte système temps réel (Motorola MVME 147) possédant une sortie Ethernet pour connecter le simulateur à une station de travail ou à un réseau,
- \* une carte de conversion ECL/TTL et TTL/ECL qui permet de communiquer avec la partie radiofréquence du simulateur,
- \* une carte atténuateur reliée par l'intermédiaire d'un bus TTL aux atténuateurs programmables,
- \* huit cartes filtres numériques provenant du simulateur de propagation à large bande du CCETT et qui ont été modifiées pour répondre à notre application,
- \* une carte horloge et synchronisation.

#### 4-5 Le filtre numérique

Le signal radiofréquence numérisé, produisant un signal en phase sur 8 bits et un signal en quadrature sur 8 bits est distribué sur deux filtres numériques transversaux permettant de créer les différents trajets. Ces deux filtres numériques sont constitués de 8 cartes filtres numériques.

La carte filtre numérique est le centre du simulateur. Elle permet de combiner les données calculées et les données arrivant en temps réel de l'émetteur, comme le montre la figure 2.

Les 12 cartes sont reliées par le bus VME P1. Sur ce bus, l'ensemble des données calculées du filtre vont transiter. Le bus P2 est utilisé pour relier les cartes filtres entre elles, ainsi que la carte ECL/TTL et la carte horloge et synchronisation. Ce bus va supporter les données arrivant en temps réel des convertisseurs analogiques-numériques. De plus, il va récupérer les données après chaque filtre numérique et les envoyer vers les convertisseurs numériques-analogiques.

Les données arrivant des convertisseurs analogique-numérique se présentent sous forme de signaux ECL à l'entrée de la carte. Ceux-ci sont convertis en logique TTL.

Puis, ils sont démultiplexés pour donner sur deux fois 8 bits les parties réelle et imaginaire du signal appelées respectivement ER et EI. La fréquence d'échantillonnage  $F_{ech}$  est récupérée. ER, EI et  $F_{ech}$  sont envoyés à l'ensemble des huit cartes filtres numériques par l'intermédiaire du bus P2. La deuxième partie de cette carte effectue le multiplexage inverse. La carte récupère la sortie réelle et imaginaire des signaux après la dernière carte filtre numérique par l'intermédiaire du bus P2. Ces signaux sont multiplexés. Ensuite, les données TTL codées sur 8 bits sont converties en signaux ECL et envoyées au convertisseur numérique-analogique.

Chacune des huit cartes filtres numériques comporte deux trajets distincts. Ces trajets sont commandés par un microprocesseur de traitement du signal TMS 320C25. Ce processeur est utilisé pour synchroniser l'ensemble des données entre les FIFO (First In, First Out) et les multiplieurs. Cet échange va s'effectuer suivant la fréquence de renouvellement des échantillons. Ultérieurement, ce processeur sera utilisé pour effectuer le suréchantillonnage du signal calculé. Celui-ci sera utilisé pour calculer un certain nombre de coefficients supplémentaires dans le cas d'évanouissements profonds.

#### 4-5-1 Le multiplieur

Le multiplieur reçoit sur ses entrées le bus de données venant des FIFO et cadencé à la fréquence de renouvellement, ainsi que le bus de données venant de la conversion analogique-numérique et cadencé à la fréquence d'échantillonnage.

L'ensemble de ces données est multiplié à la fréquence d'échantillonnage. L'effet Doppler est simulé à ce niveau par la vitesse des données provenant des FIFO et arrivant sur le multiplieur. Le multiplieur utilisé est de type Plessey PDSP 16112. Il opère au même cycle d'horloge sur la partie réelle et sur la partie imaginaire des signaux d'entrée. A la sortie, nous allons obtenir un produit complexe.

#### 4-5-2 L'additionneur

Ce système permet d'additionner les données multipliées précédemment et correspondant à un trajet précis avec les données provenant des trajets précédents. Le premier trajet est additionné soit à la masse, soit à un bruit quelconque numérique. Cette addition s'effectue suivant la fréquence d'échantillonnage.

#### 4-5-3 La ligne à retard

La ligne à retard est constituée de RAM rapide de type Cypress comportant 8 kilo-octets. Ces mémoires possèdent un temps d'accès de 125 ns pour une écriture-lecture, ce qui constitue le retard minimum entre deux trajets. Le retard maximum est ainsi donné par  $8192 \times 125 \text{ ns} = 1 \text{ ms}$  par trajet donc au total 15 ms. Cette valeur maximale n'est jamais atteinte dans des liaisons VHF-UHF. Le dernier trajet possède un retard nul correspondant au premier trajet arrivant sur le récepteur.

Une suite de lecture et écriture mémoire de mots consécutifs a pour effet d'introduire un retard  $T_e$ . Ce retard est donné par le registre retard programmé précédemment.

## 5 - VALIDATION DU SIMULATEUR

Le but de cette partie est de démontrer la validité des phénomènes représentés par le simulateur. Différentes mesures vont permettre de valider les trajets multiples, et le décalage Doppler.

### 5-1 Mesures en porteuse pure

On applique à l'entrée du simulateur un signal en porteuse pure à 71 MHz avec un niveau de 0 dBm. Le signal sortant du synthétiseur est un signal à fréquence fixe de 48.6 MHz avec un niveau de +7 dBm. Ainsi, la fréquence en bande de base est de 1 MHz (la fréquence intermédiaire est à 21.4 MHz).

La sortie présente un signal à la même fréquence que le signal d'entrée dont l'amplitude varie aléatoirement entre 0 et -40 dBm.

Le signal en sortie du simulateur peut être observé sur un oscilloscope. Ce signal va dépendre de la vitesse relative des véhicules. La figure 4 présente les évanouissements de Rayleigh pour une vitesse des mobiles de 20 km/h à une fréquence de 910 MHz. On observe des évanouissements qui peuvent atteindre 40 dB.

### 5-2 Mesure des trajets multiples

Ces mesures vont permettre de visualiser les profils de trajets en fonction du temps, et ainsi vérifier les différents retards subis par l'onde.

#### 5-2-1 Mesure en impulsion

Le principe de cette mesure consiste à émettre de façon répétitive une impulsion de très courte durée, inversement proportionnelle à la bande d'analyse. La bande maximale du simulateur étant de 10 MHz, la largeur de l'impulsion sera donc de 100 ns et sera répétée toutes les 10  $\mu\text{s}$ . Ce temps est supérieur à la valeur maximale des retards observés dans une ville moyennement urbanisée.

Cette méthode est simple à réaliser, mais elle ne permet pas une analyse fine des retards à cause de l'incapacité de réaliser une impulsion très étroite précise. Il est donc impossible de visualiser des retards faibles. Sur la figure 5, on visualise l'impulsion émise et les différents retards introduits par le simulateur. Ainsi, on peut calculer par cette méthode, le retard introduit par le simulateur sur le signal. Ce temps de transfert est de 1,8  $\mu\text{s}$ .

#### 5-2-2 Mesure par un corrélateur à ondes de surface

Sur l'entrée du simulateur, nous appliquons un signal à 70 MHz avec étalement de spectre sur 10 MHz. La longueur du code est de 127 bits. Cette longueur est imposée par la technologie à ondes de surface. Le récepteur effectue la corrélation avec le signal issu du simulateur. Les pics de corrélation obtenus avec ce dispositif permettent de vérifier les différents retards. Un exemple de pics après détection est présenté à la figure 6.

### 5-3 Mesure du Doppler

La figure 7 présente un exemple de fonction de diffusion retard-Doppler pour une liaison de type urbain à 900 MHz.

Le retard maximal est de 5  $\mu$ s. Le nombre de retards est de 12. De même, la figure 8 présente un exemple de fonction de diffusion retard-Doppler pour une liaison de type rural à 900 MHz où le trajet direct est présent.

## 6 - CONCLUSION

La caractérisation du canal radiomobile est basée sur la représentation de celui-ci par un filtre linéaire variant aléatoirement dans le temps. La caractérisation par l'utilisation des fonctions de diffusion a permis d'obtenir l'expression du canal à simuler. Les variables aléatoires, déduites de cette expression représentant le retard, l'atténuation et le décalage Doppler, ont été décrites de façon statistique. L'étude des différents modèles empiriques, ainsi que les différents types de diffraction ont permis d'établir une prédiction de la puissance moyenne reçue.

Par comparaison avec les simulateurs de type "matériel", l'utilisation d'un simulateur de type mixte donne plus de facilité dans le choix des différents paramètres. Aucun des simulateurs existants dans la littérature ne peut répondre à la contrainte de l'évasion de fréquence. En effet, la façon de créer les différents retards par utilisation de ligne à retard à ondes de surface ne peut permettre de couvrir l'ensemble des fréquences de la gamme VHF-UHF. De plus, ils sont toujours destinés à des applications spécifiques pour des canaux urbains ou suburbains, mais non destinés à des applications allant des milieux de type urbain aux milieux de type maritime ou montagneux.

La partie radiofréquence permet la transposition du signal radiofréquence à saut de fréquence (la vitesse de saut maximale est de 100 000 sauts par seconde) en signal bande de base. Celle-ci possède une largeur de bande de 10 MHz.

La partie traitement de signal s'articule autour de deux filtres numériques transversaux. Ces filtres permettent de réaliser jusqu'à 16 trajets différents. Chaque trajet est séparé du précédent par un retard supérieur ou égal à 125 ns. Le retard maximal du dernier trajet est de 15 ms, ce qui est largement supérieur aux retards rencontrés dans les liaisons UHF- VHF.

La rapidité du renouvellement des coefficients des filtres numériques permet de simuler la vitesse relative entre les véhicules ou entre un véhicule et une station fixe. L'utilisation d'un bus à haut débit de type VME entre le calculateur et les filtres numériques permet de simuler une vitesse relative allant jusqu'à 2000 km/h.

## REMERCIEMENT

Ce travail a été supporté par "le Centre Electronique de l'Armement (CELAR)"

## BIBLIOGRAPHIE

- [1] J.J. BUSSGANG, E.H. GETCHELL, B. GOLDBERG et P.F. MAHONEY, "Stored channel simulation of tactical VHF radio links", IEEE Trans. on Com., Vol COM-24, N°2, Fev 76.
- [2] D. PARSONS, "The Mobile Radio Propagation Channel", Pentech Press, 1992.
- [3] W.C.LEE, "Mobile Communications Engineering", Mc Graw-Hill, 1982.
- [4] P. A. BELLO, "Characterisation of Randomly Time Variant Linear Channels", IEEE - Trans. Comm. Syst. vol.CS-11, Dec. 1963, pp. 360-393.
- [5] D.M. BALSTON, "Pan-European cellular radio : or 1991 and all that", Electronics & Communication Engineering Journal, IEE, January-February 1989.
- [6] A.S. BAJWA, "Wideband Characterisation of UHF Mobile Radio Propagation in Urban and Suburban Areas", British Thesis, August 1979.
- [7] A. DANIEL, G. EL ZEIN, M. SALEHUDIN, J. CITERNE, "Etude et réalisation d'un simulateur de canal radiomobile à large bande", Onde électrique, Vol. 68, N°2, Mars 88.
- [8] W. YI, J.C. LESAFFRE et Y. LEGOFF, "Un simulateur pour la diffusion en radio à modulation de fréquence vers les mobiles", Revue de Radiodiffusion-Télévision, N°98, 1987.
- [9] W.C.JAKES, "Microwave Mobile Communications", New-york : Wiley, 1974.
- [10] CCIR, 1986, "Recommendations and reports of the CCIR, Propagation in Non-Ionized Media", Vol V.
- [11] COST 207, "Digital Land Mobile Radio Communications", Final report, Commission of the European Communities, Mars 1984-Sept 1988.

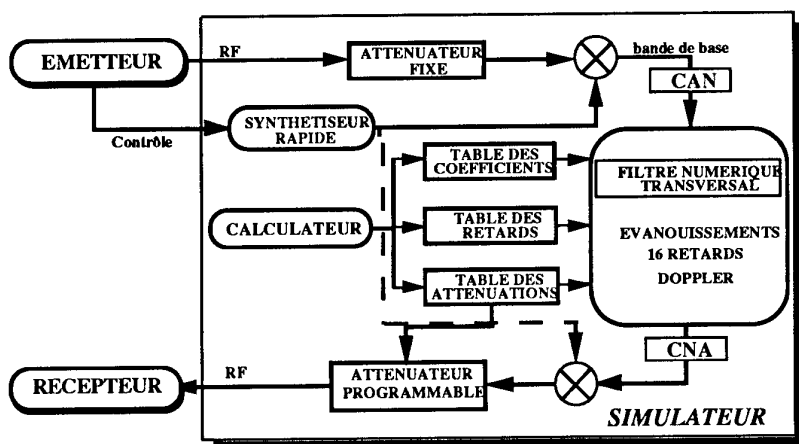


Figure 1 : Schéma de principe du simulateur

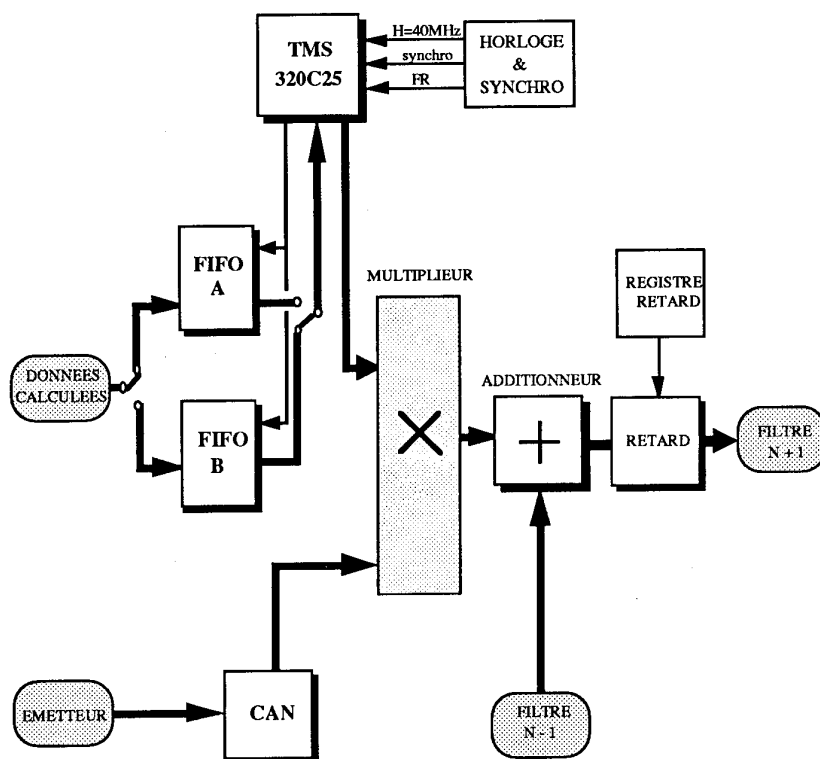


Figure 2 : Le filtre numérique

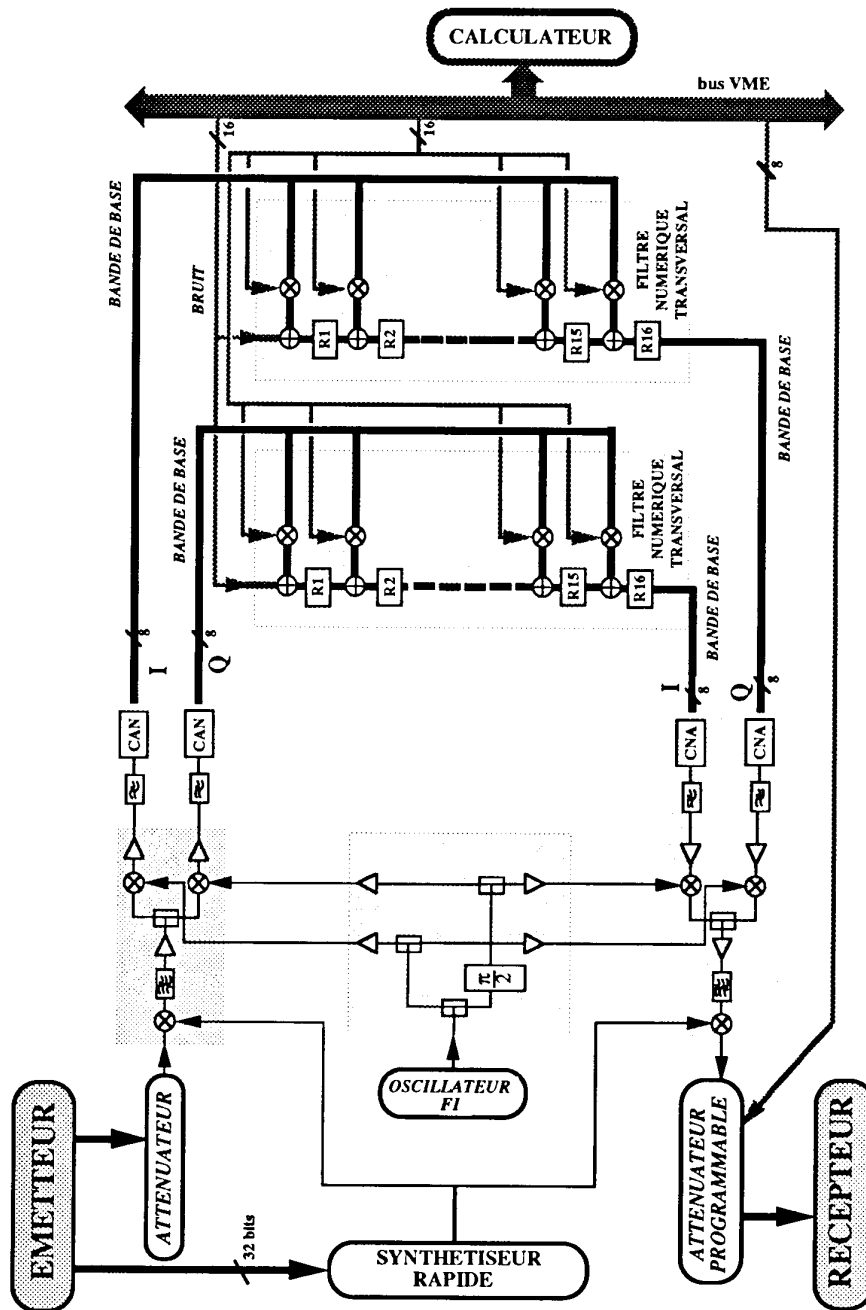
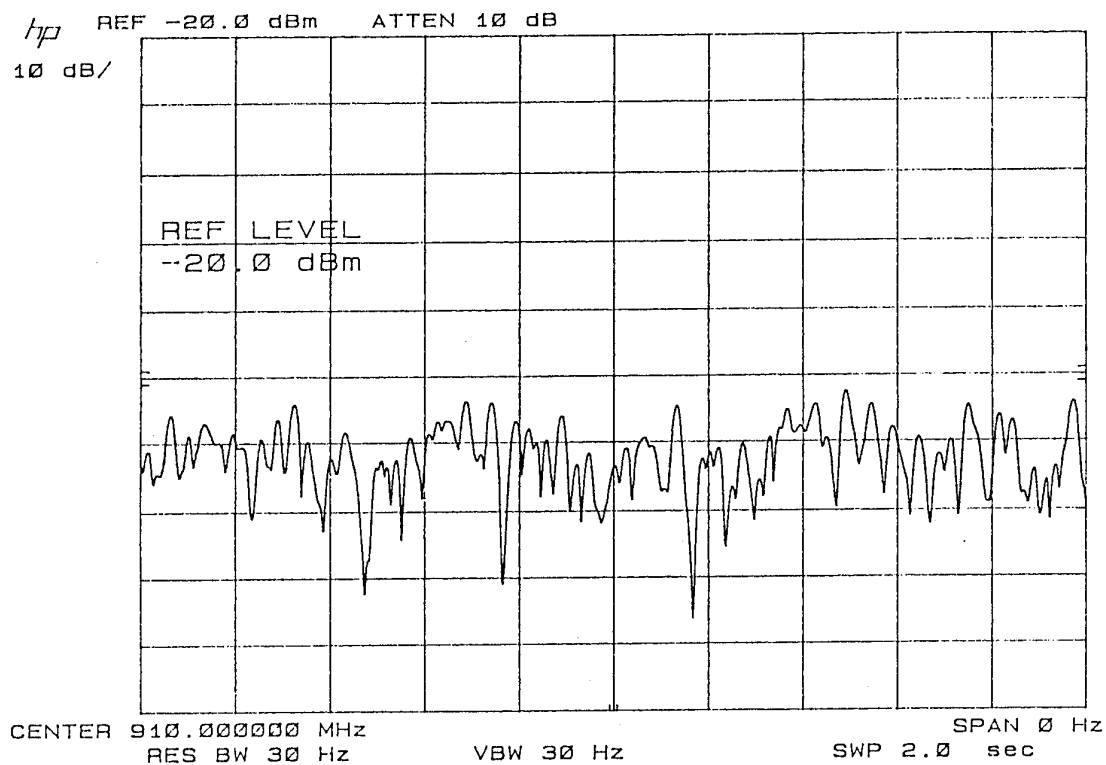
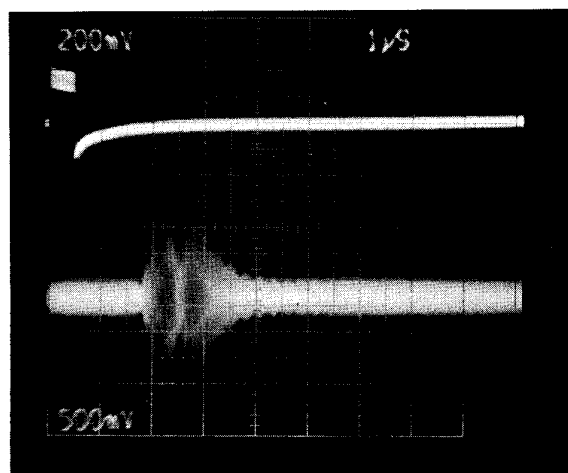


Figure 3: Schéma du simulateur



**Figure 4 :** Evanouissements simulés pour une vitesse de 20 km/h



**Figure 5 :** Mesure des retards en impulsion

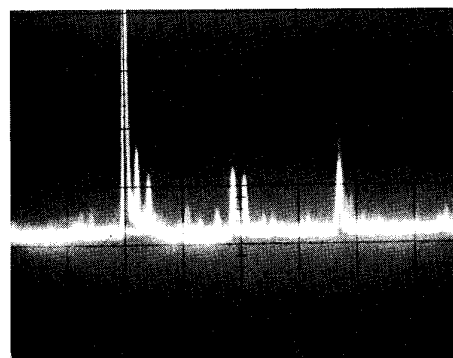


**Figure 6 :** Mesure des retards par un corrélateur

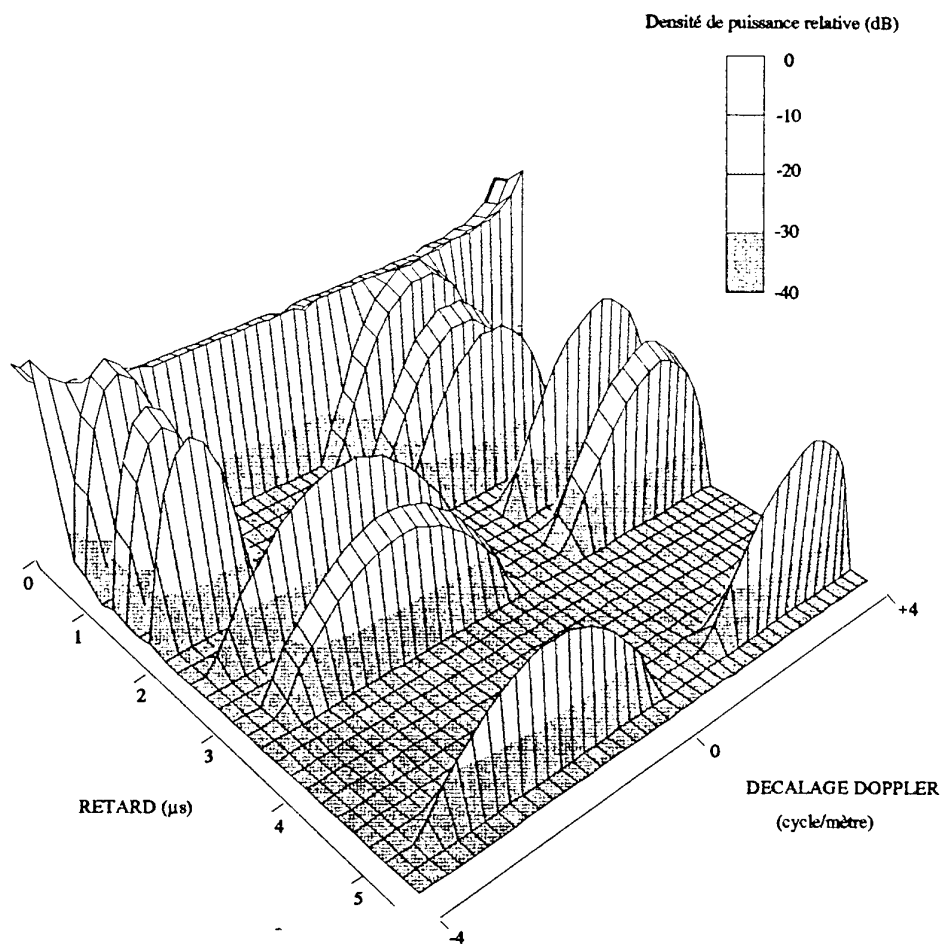


**Figure 7 :** Fonction de diffusion retard-Doppler pour une liaison de type urbaine à 900 MHz

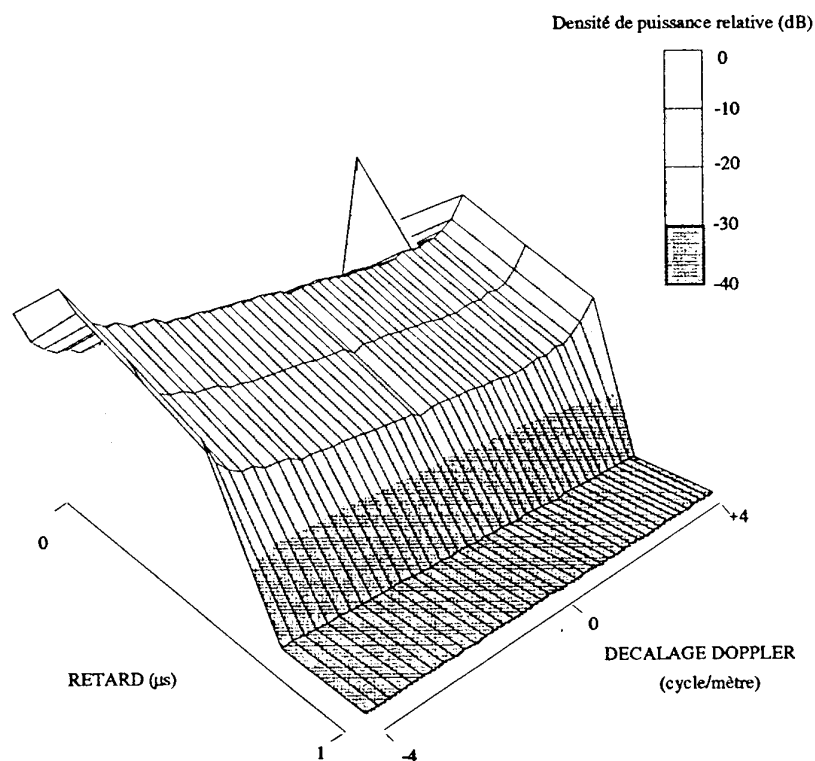


**Figure 8 :** Fonction de diffusion retard-Doppler pour une liaison de type rural à 900 MHz



## DISCUSSION

**Discussor's name :** C. Goutelard

**Comment/Question :**

Votre simulateur pourra-t-il être utilisé pour d'autres canaux que celui que vous avez mentionné et avez vous le projet d'introduire des modèles de bruit?

**Translation :**

*Could your simulator be used for channels other than the one you have mentioned, and do you intend to introduce noise models?*

**Author/Presenter's Reply :**

L'évolution vers la bande HF est en développement actuellement. En effet, les retards maximum possible correspondent aux retards de type HF. Le bruit est introduit au début des filtres numériques transversaux de façon numérique. Un modèle simple a été utilisé. D'autres modèles seront développés.

**Translation :**

*Development towards the HF band is in progress at the moment. In fact the maximum possible delays are HF type delays. Noise is introduced digitally on the input to the transverse digital filters. A simple model was used. Other models will be developed.*

## COMBINED EFFECTS OF ATMOSPHERE AND TERRAIN ON UHF/MICROWAVE PATHS

M.F. Levy  
Radio Communications Research Unit  
Rutherford Appleton Laboratory  
Chilton, Didcot OX11 0QX, UK

## SUMMARY

Radiowave propagation on mixed land/sea paths is affected by both atmospheric refraction and terrain effects. The parabolic equation method provides a numerical solution for calculation of field-strength in these circumstances. We give a few applications of the finite-difference PE method, which is particularly well-adapted to problems where ground effects are important. A case in point is that of detection of low targets above a rough sea surface. For air-defence applications, PE computing requirements are prohibitive. We describe a novel method, the horizontal PE method, which allows fast computation of signal strength in large domains, and apply it to calculations of radar coverage.

## 1. INTRODUCTION

Propagation on UHF/microwave overland paths is strongly affected by diffraction and reflection phenomena. Occasional multipath due to atmospheric refraction may also occur in the presence of ducting layers. On oversea paths, reflection from the rough sea surface interacts with the evaporation duct which is often present. The combined effects of these mechanisms are quite complex, and could not be modelled until recent developments of the parabolic equation method. The PE method has been used extensively in the last decade for modelling propagation over the sea [1, 2, 3, 4, 5], but implementations that can cope with irregular terrain have only appeared in the last three years [6, 7, 8, 9]. The finite-difference PE [6] has proved its usefulness for solving radiowave propagation problems in environments where an inhomogeneous atmosphere combines with a complex air/ground boundary. We briefly recall the basic ideas of PE modelling in section 2, and present a few applications of the finite-difference PE method to multiple mechanisms propagation paths in section 3.

For military applications, it is often desirable to calculate the electromagnetic field at long ranges and large heights. A typical domain for a 3 GHz radar might be 400 km in range by 10 km in height. PE calculations become prohibitively expensive for such large domains. Fortunately, we can take advantage of the fact that refractive index perturbations are normally confined to the lowest part of the tropo-

sphere. In section 4 of this paper, we present a novel method, the horizontal PE method, which gives a fast solution of the parabolic wave equation in the higher part of the domain, where the atmosphere is "standard". In section 5, we apply the method to calculations of radar coverage in large domains.

## 2. PE FRAMEWORK

This section gives a brief derivation of the 2-dimensional parabolic equation. We use cylindrical coordinates  $(r, \theta, z)$  and assume azimuthal symmetry. If we write a field component  $\psi$  as

$$\psi(r, z) = \frac{1}{\sqrt{kr}} \exp(ikr) u(r, z), \quad (1)$$

the scalar wave equation becomes in the far-field approximation

$$\frac{\partial^2 u}{\partial r^2} + 2ik \frac{\partial u}{\partial r} + \frac{\partial^2 u}{\partial z^2} + (n^2 - 1)k^2 u = 0 \quad (2)$$

Define the operator  $Q$  by

$$Q = \sqrt{\frac{1}{k^2} \frac{\partial^2}{\partial z^2} + n^2} \quad (3)$$

Equation 2 can be factored approximately as

$$\left( \frac{\partial}{\partial r} + ik(1 - Q) \right) \left( \frac{\partial}{\partial r} + ik(1 + Q) \right) u = 0 \quad (4)$$

The two terms represent the outgoing and incoming waves. It should be noted that this factorization neglects possible coupling between outgoing and incoming wave. The outgoing wave equation is then

$$\frac{\partial u}{\partial r} = -ik(1 - Q)u \quad (5)$$

Numerical solutions of Equation 5 rely on approximations of  $Q$  by rational functions. In this paper we use the narrow angle approximation,

$$Q = 1 + \frac{1}{2} \left( \frac{1}{k^2} \frac{\partial^2}{\partial z^2} + n^2 - 1 \right) \quad (6)$$

This yields the standard parabolic equation (SPE)

$$\frac{\partial^2 u}{\partial z^2} + 2ik \frac{\partial u}{\partial r} + k^2(n^2 - 1)u = 0 \quad (7)$$

Equation 7 can be solved by a marching process in range, knowing the field on the initial vertical and the boundary conditions at the top and bottom of the domain.

Fourier transform solutions are extremely efficient for propagation over a flat surface [1, 2, 4, 5]. More recently irregular terrain implementations have been developed [7, 8].

The finite-difference solution of Equation 7 has the advantage of providing a flexible treatment of boundary conditions allowing the representation of arbitrary-shaped terrain with range-varying surface impedance. An implicit Crank-Nicolson scheme gives a stable convergent solution [6].

We approximate the boundary condition at the air/ground interface with a surface impedance boundary condition,

$$\frac{\partial \psi}{\partial \vec{n}} = -ik\delta\psi \quad (8)$$

where  $\delta$  is the surface impedance. Since we try to express a non-local phenomenon with a local boundary condition, there are necessarily errors when the situation deviates from the case of plane-wave incidence on a smooth planar surface. However this is a decent approximation when the surface impedance varies slowly over the angular regime of interest. Also note that discontinuities in the surface impedance (mixed paths) are permitted, bearing in mind that that the PE solution is not correct at the discontinuity itself.

### 3. APPLICATIONS TO MMPPs

#### 3.1. Recovery effect on HF propagation

The recovery effect is an interesting feature of groundwave propagation which occurs when a vertically polarized wave reaches highly conducting ground after propagating over a high impedance portion of the path. The discontinuity at the boundary between the two segments of the path causes a sharp increase in signal strength.

This effect has been measured by Millington at a frequency of 3.3 MHz on a land/sea path. As integral equation solutions are also available for this case [10], it provides an interesting test of the finite-difference PE method. The source, vertically polarized, is located at ground level. The land-sea boundary is at a distance of 86 km from the transmitter. Figure 1 shows the results of the finite-difference PE simulation. They are seen to be in excellent agreement with those of [10], confirming the ability of the finite-difference PE to model groundwave propagation.

#### 3.2. Coastal effects

The planning of amphibious operations requires assessment of the combined effects of atmospheric refraction and diffraction over land. The finite-difference PE technique provides an ideal tool for this type of situation, since any terrain configuration and atmospheric variations may be used as input data. Figure 2 shows an example of propagation at 300 MHz in a strong surface duct over the sea, combined with diffraction over land. The modified refractivity profile over the first 110 km of the path is given in Table 1.

Table 1: M-profile for UHF example

Height (m)	M (M-units)
0	10
200	0
1200	118

An island is located on the path between 110 and 123 km. From 110 km, the surface duct weakens and the profile becomes standard (118 M-units/km) at 120 km from the source. It is interesting to observe how energy ducted to the island then gets diffracted over it and escapes as the duct weakens.

#### 3.3. Sea roughness

Effects of sea surface roughness on microwave propagation in the presence of ducting are notoriously difficult to model. The main reason for this is that although many sophisticated models exist for scattering by a rough surface, they usually assume that the propagation medium itself is homogeneous, although some advances have recently been made on scattering by a rough surface in a ducting medium [11]. Another common assumption is that no shadowing occurs, and this creates another difficulty at the very low grazing angles which are often of interest in naval applications.

In operational propagation packages, the usual fallback for rough surface modelling is based on a statistical approach: the reflection coefficient is calculated as a function of angle of incidence for particular types of rough surfaces, and this information is somehow incorporated in the algorithm which calculates the field. This method has several drawbacks: it is really a plane wave approach which assumes that the angle of incidence is a well-defined quantity. When anomalous propagation is present, it is not a straightforward problem to determine angles of incidence, and complicated spectral methods might be required. The fact that the reflection coefficient of a rough surface is very sensitive to the value of the angle of incidence allows little room for error.

Apart from this fundamental problem, shadowing is not tackled, and this type of method does not allow realistic descriptions of the sea surface.

The finite-difference PE allows direct numerical treatment of forward scattering by a rough surface which is represented explicitly as a sequence of facets. This works well for a perfectly conducting surface and horizontal polarization, when the boundary condition is that the field vanishes on the surface. More generally this method is applicable when the surface impedance of the material is slowly varying for the range of grazing angles which are needed in the problem (usually a few degrees). The surface does not have to be of a particular type, and refractive index variations are allowed as usual with PE methods.

This technique has previously been applied to sea clutter problems [12]. Here we are concerned with forward scattering. In the examples we present, the sea surface is obtained as a realization of a random process. We have used a directional version of the Pierson-Moskowitz sea spectrum [13], valid for fully developed wind seas. A 2-dimensional realization of the sea surface is obtained by filtering 2-dimensional white noise by the square root of the wavenumber spectrum, and taking an inverse FFT. One-dimensional profiles for PE simulations are extracted from the 2D results. Figure 3 shows a realization of the sea surface on a 2.5 km by 2.5 km square, obtained for a wind speed of 10 m/s and a wind direction of 45 degrees from the horizontal. Of course other models of the sea surface could be used, or even remote sensing measurements.

Figure 4 shows path loss contours for a 3 GHz source located at 15 m amsl, with a 20 m evaporation duct and a wind speed of 20 m/s. This is a very high sea (Douglas sea state 7) with an rms waveheight of 2 metres. It is worth noting that bunches of waves reaching 5 or 6 metres are then quite a common occurrence.

In Figure 5, we give path loss against range for a target at 5 m amsl and wind speeds of 0 and 20 m/s (sea states 1 and 7). The reduction of signal strength at sea state 7 is spectacular because the target can get obscured by high waves. Figure 6 shows short range effects for wind speeds of 0 and 10 m/s (sea states 1 and 4): at sea state 4 lobing is highly perturbed, with a slight reduction of signal at longer ranges.

#### 4. THE HORIZONTAL PE METHOD

As we mentioned in the introduction, in most tropospheric propagation problems, anomalous refractive index features only occur in the first few hundred metres (for evaporation or advection ducts, characteristic heights are of the order of 10 to 100 m).

Figure 7 illustrates the situation: below height  $z_0$ , the refractive index may exhibit 2-dimensional variations, and terrain features may be present. However above that height, the medium is in some sense standard. The "horizontal PE method", which was first presented in [14], is a novel method which permits the rigorous integration of Equation 7 if the field is known on the initial horizontal  $z = z_0$ .

The horizontal PE is applicable if the medium above  $z_0$  is independent of range and piecewise linear with height, with non-negative slopes. This covers the case of vacuum, and of a linear atmosphere in flattened Earth coordinates. An exponential atmosphere can be approximated by a suitable piecewise-linear profile. Ducting layers above  $z_0$  are of course excluded.

In what follows, we show that the solution of Equation 7 above  $z_0$  may be solved explicitly in terms of Laplace transforms. It should be noted that similar techniques have been used to derive transparent boundary conditions for a medium which is "standard" above a certain height [15].

We will assume that  $u(0, z) = 0$ ,  $z \geq z_0$ . This can be achieved rigorously by subtracting from  $u$  the solution to the standard problem in the whole domain. In practice it is usually more convenient to choose  $z_0$  sufficiently far from the source for the field above it to be negligible on the initial vertical.

In order to simplify notations, from now on we take  $z_0 = 0$ . We denote by  $\tilde{u}$  the Laplace transform of  $u$  with respect to range,

$$\tilde{u}(p, z) = \int_0^{+\infty} u(r, z) e^{-pr} dr, \quad \text{Re}(p) > 0 \quad (9)$$

With our assumptions, the Laplace transform of Equation 7 is

$$\frac{\partial^2 \tilde{u}}{\partial z^2} + (2ikp + k^2(n^2 - 1)) \tilde{u} = 0 \quad (10)$$

Here we treat the case of the linear atmosphere,

$$m^2(r, z) = 1 + az + b \quad \text{with } a > 0 \quad (11)$$

The solutions of Equation 10 can be expressed in terms of Airy functions. In order to conserve energy, we require a solution that is bounded in  $z$ . Using asymptotic expansions (see for example [16]), it turns out that the bounded solution of equation 10 can be written as

$$\tilde{u}(p, z) = C(p) \text{Ai}[\xi(p, z)] \quad (12)$$

where

$$\xi(p, z) = -(ak^2)^{1/3} z - \frac{k^2 b + 2ikp}{(ak^2)^{2/3}} e^{2i\pi/3} \quad (13)$$

It is convenient to invert this equation with the help of Fourier transforms by extending it to the imaginary axis [17]. Putting  $p = 2i\pi q$ , we obtain

$$u(r, z) = \mathcal{F}^{-1} \left\{ \frac{\text{Ai}[\xi(2i\pi q, z)]}{\text{Ai}[\xi(2i\pi q, 0)]} \mathcal{F}u(q, 0) \right\} \quad (14)$$

where the Fourier transform  $\mathcal{F}$  is defined by

$$\mathcal{F}u(q, z) = \int_{-\infty}^{+\infty} u(r, z) e^{-2i\pi q r} dr \quad (15)$$

Equation 14 is easy to implement with FFTs. The solution requires one initial FFT plus one inverse FFT per horizontal of interest.

Piecewise linear variations are a straightforward generalization of the linear case. The case of a constant atmosphere involves exponential functions instead of Airy functions and is easy to treat.

From the Nyquist criterion, we obtain an upper bound for the range resolution as a function of the wavelength and the maximum angle of propagation:

$$\Delta r \leq \frac{\lambda}{2\theta_{max}^2} \quad (16)$$

For propagation over flat terrain, it is often advantageous to use hybrid methods, restricting the use of the vertical PE to a narrow angular sector where refractive effects are important, resorting to faster algorithms (for example a simple ray-trace) at higher propagation angles where geometrical optics apply [18]. This in turn leads to far more efficient use of the horizontal PE, since the range step is inversely proportional to the square of  $\theta_{max}$ . For propagation over irregular terrain, this increase in efficiency is not available since PE techniques often have to be used over most of the angular domain of interest if correct modelling of ground reflections is required. Substantial speed-up is obtained nonetheless since integration heights for the vertical PE can be drastically reduced.

A further advantage of the method is that only horizontals of interest need to be tackled, thus enabling very fast calculations if only a few heights are required.

## 5. APPLICATION TO GROUND-BASED RADAR COVERAGE

In our first example, we compute the coverage diagram of a 3 GHz source located at a height of 75 m, for a domain of 400 km in range by 10 km in height. The required output resolution is 1 km in range and 20 m in height. We assume propagation over a smooth sea.

Table 2: M-profile for S-band example

Height (m)	M (M-units)
0	-9.8
100	2.0
200	0.0
1200	118

Table 3: M-profile for 1 GHz examples

Height (m)	M (M-units)
0	-33.4
300	2.0
350	0.0
1350	118

Suppose an elevated layer is present between 100 and 200 m (see Table 2). We can use the vertical PE method in the whole domain, or only up to 200 m, extending the solution to the whole domain with the horizontal PE. If we limit our angular sector to  $1.4^\circ$  from the horizontal, formula 16 gives  $\Delta r = 100$  m.

The computing requirements for the 2 methods are given below (the FFT sizes for the vertical PE are those used in the PCPEM package [19]).

- Vertical PE in the whole domain: 1600 FFTs of size 65336
- Vertical PE up to 200 m: 8000 FFTs of size 512
- Horizontal PE above 200 m: 490 FFTs of size 8192

Each of the two stages of the second method requires about 4% of the computing time of the first one. Memory requirements are 8 times smaller.

Figure 8 shows the reconstructed coverage diagram (vertical PE below 200 m, horizontal PE above). Figure 9 shows a comparison of path loss against height curves for the two methods, at 400 km from the source. The results are in such good agreement that the vertical PE curve had to be offset by 20 dB in order to be easily distinguished.

We now examine a case of propagation over irregular terrain. The source now transmits at 1 GHz, and is located 10 m above the ground. Here too, an elevated layer is present (see Table 3).

Figure 10 shows the reconstructed coverage diagram, using the finite-difference vertical PE up to 350 m, and the horizontal PE above. Figure 11 shows the reconstructed coverage diagram between 1000 m and

5000 m in altitude. In Figure 10, the vertical resolution is 2 m, while in Figure 11 it is 10 m. Since the field has been calculated on roughly the same number of horizontals in both cases, the computing time is similar.

Figure 12 shows a comparison of path loss curves at a height of 1000 m for vertical and horizontal PE. Once again the vertical PE results have been offset by 20 dB for clarity, since agreement is extremely good.

The horizontal resolution here was 10 m, giving propagation angles of up to 7°. With our current implementation of the finite-difference PE, integration up to 5000 m takes about 900 minutes on a transputer card. Integration up to 350 m takes about 60 minutes, while the horizontal PE for 465 horizontals (FFT size 16384) takes 25 minutes.

In conclusion, the horizontal PE method provides a rigorous and extremely efficient solution for extending coverage diagrams calculated in the non-standard part of the atmosphere to large domains.

## ACKNOWLEDGMENT

The research activity reported in this paper has been performed as part of the National Radio Propagation Programme at RAL and has been funded by the Radiocommunications Agency of DTI.

## References

- [1] G.D. Dockery, Modeling electromagnetic wave propagation in the troposphere using the parabolic equation, *IEEE Trans.*, **AP-36**, pp. 1464-1470, 1988.
- [2] K.H. Craig, Propagation modelling in the troposphere: parabolic equation method, *Elec. Lett.*, **24**, pp. 1136-1139, 1988.
- [3] M. Fournier, Analysis of propagation in an inhomogeneous atmosphere in the horizontal and the vertical direction using the parabolic equation method, *AGARD CP*, **453**, paper 21, 1989.
- [4] K.H. Craig and M.F. Levy, Parabolic equation modelling of the effects of multipath and ducting on radar systems, *IEE Proc.-F*, **138**, pp. 153-162, 1991.
- [5] J.R. Kuttler and G.D. Dockery, Theoretical description of the PE/Fourier split-step method of representing electromagnetic propagation in the troposphere, *Radio Sci.*, **26**, pp. 381-393, 1991.
- [6] M.F. Levy, Parabolic equation modelling of propagation over irregular terrain, *Elec. Lett.*, **26**, pp. 1153-1155, 1990.
- [7] R.J. MacArthur, Propagation modelling over irregular terrain using the split-step parabolic equation method, *Proceedings of Radar 92, IEE Conf. Pub.*, No 365, pp. 54-57, 1992.
- [8] A.E. Barrios, Terrain modelling using the split-step parabolic equation method, *Proceedings of Radar 92, IEE Conf. Pub.*, No 365, pp. 66-69, 1992.
- [9] S.H. Marcus, A hybrid (finite difference-surface Green's function) method for computing transmission losses in an inhomogeneous atmosphere over irregular terrain, *IEEE Trans.*, **AP 40**, pp. 1451-1458, 1992.
- [10] Z. Wu et al, Recovery effect in radiowave propagation, *Elec. Lett.*, **26**, pp. 162-163, 1990.
- [11] M.Spivack and B.J. Uscinski, Numerical solution of scattering from a hard surface in a medium with a linear profile, *J. Acoust. Soc. Am.*, **93**, pp. 249-254, 1993.
- [12] M.F. Levy, Parabolic equation modelling of backscatter from the rough sea surface, *AGARD CP*, **501**, paper 7, 1991.
- [13] C.L. Rino et al, Numerical simulation of backscatter from linear and nonlinear ocean surface realizations, *Radio Sci.*, **26**, pp. 51-71, 1991.
- [14] M.F. Levy, Parabolic equation solution of radiowave propagation problems on large domains, 2nd International Conference on mathematical and numerical aspects of wave propagation (SIAM), 1993.
- [15] R.A. Dalrymple and P.A. Martin, "Perfect boundary conditions for parabolic water-wave models", *Proc. R. Soc. London A*, **Vol. 437**, pp. 41-54, 1992.
- [16] F.W.J. Olver, *Introduction to Asymptotics and Special Functions*, Academic Press, 1974.
- [17] L. Schwartz, *Méthodes mathématiques pour les sciences physiques*, Hermann, 1979.
- [18] H.V. Hitney, "Hybrid ray optics and parabolic equation methods for radar propagation modeling", *Proceedings of Radar 92, IEE Conf. Pub.*, No 365, pp. 58-61, 1992.
- [19] K.H. Craig and M.F. Levy, A PC-based microwave propagation forecasting model, *IEE Conf. Pub.* **333**, 1.523-526, 1991.

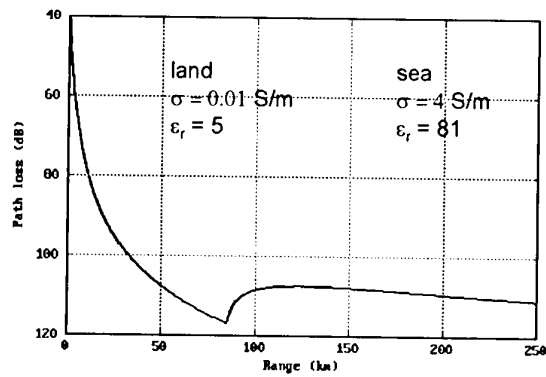


Figure 1. Recovery effect at 3.13 MHz.  
Land/sea boundary at 86 km

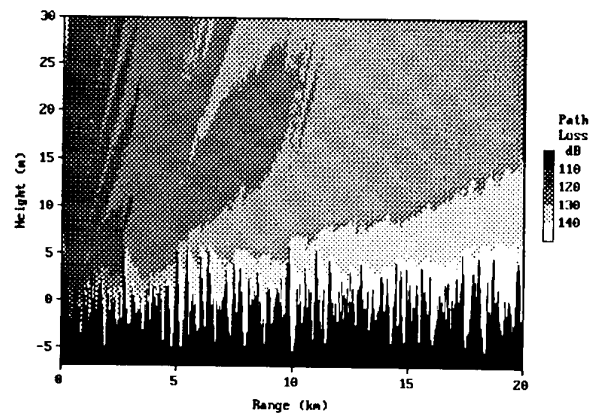


Figure 4. 3 GHz antenna over rough sea  
Wind speed = 20 m/s

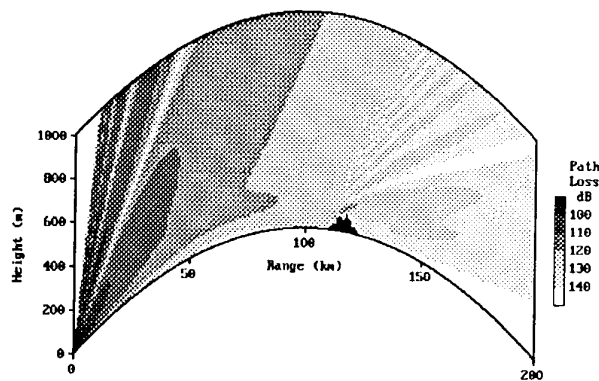


Figure 2. Coastal effects at 300 MHz

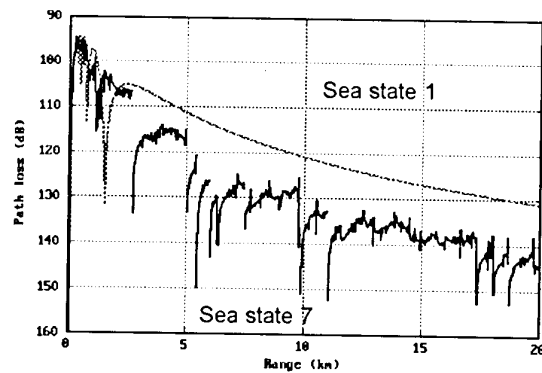


Figure 5. Roughness effects for target at height 5 m.

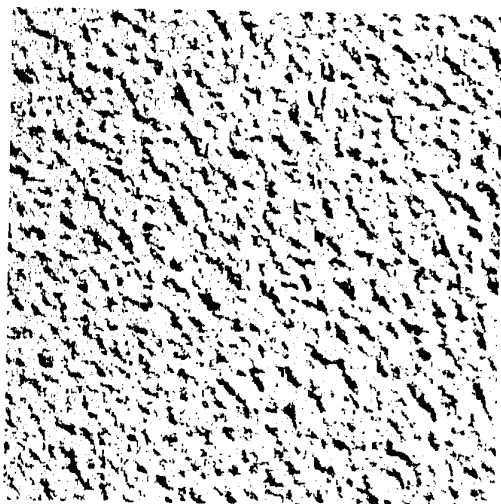


Figure 3. Realization of rough sea surface with  
directional Pierson-Moskowitz model.

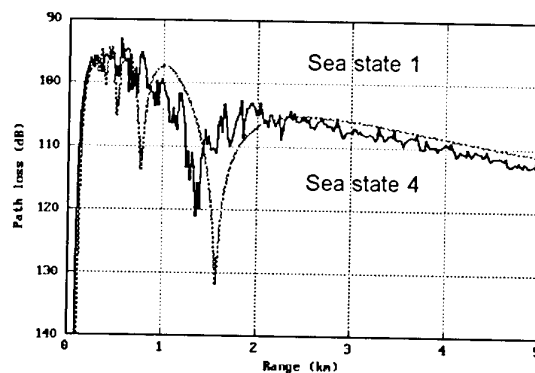


Figure 6. Roughness effects at short range for  
target at height 5 m.

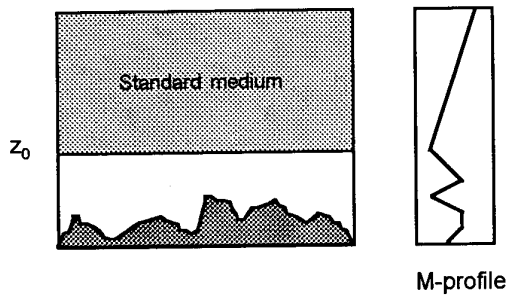


Figure 7. Framework for horizontal PE method

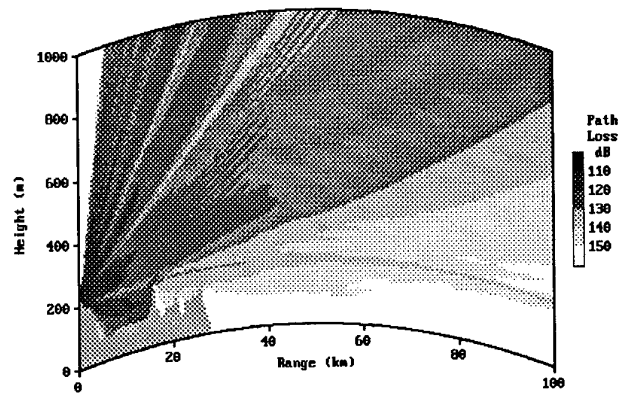
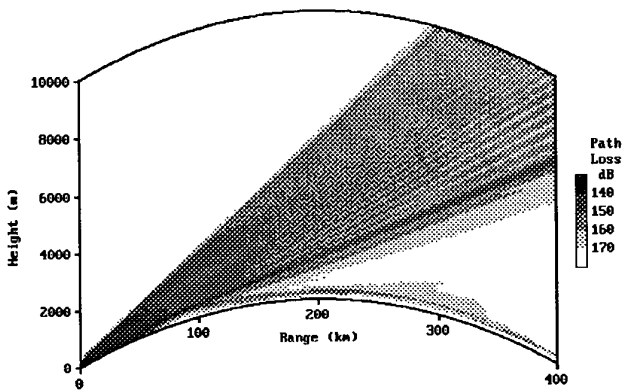
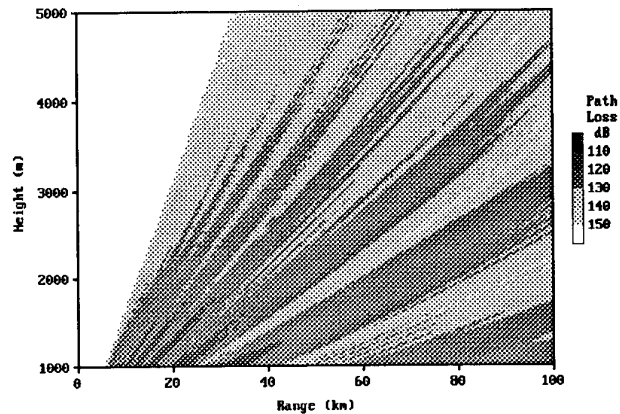
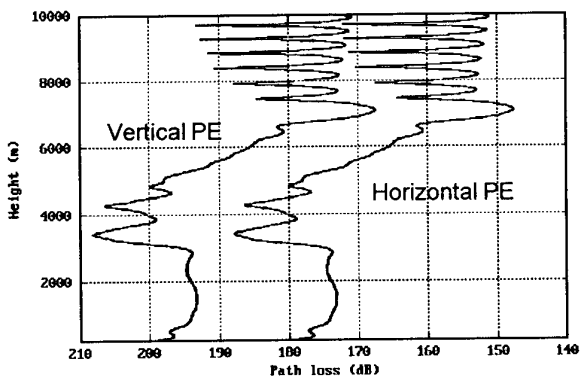
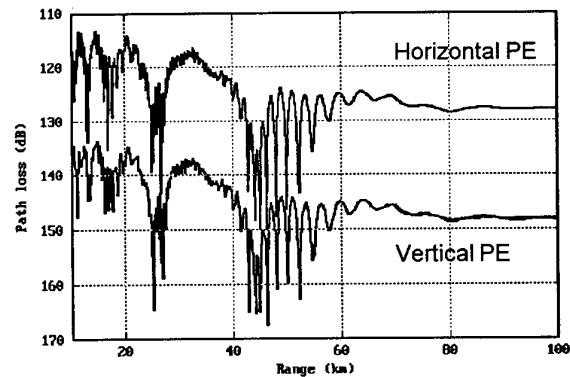
Figure 10. Coverage diagram of 1 GHz antenna  
Reconstruction with horizontal PE  
above 350 mFigure 8. Coverage diagram of 3 GHz antenna  
Reconstruction with horizontal PE  
above 200 m

Figure 11. High altitude reconstruction at 1 GHz

Figure 9. Comparison of vertical and horizontal PE at  
range 400 km (vertical PE curve offset by  
20 dB)Figure 12. Comparison of vertical and horizontal PE  
at height 1000 m (vertical PE curve offset  
by 20 dB)



## DISCUSSION

**Discussor's name :** E. P. Baars

**Comment/Question :**

Your paper describes modelling of the propagation path for radar detection and tracking. Results are presented for wide beam, mainly omnidirectional antennas. How can narrow beam radar antennas, side lobe effects and near-field/far-field problems be incorporated?

**Author/Presenter's Reply :**

The starter field on the initial vertical may be obtained in a number of ways. For microwave applications, the aperture field is readily calculated with a Fourier transform of the beam pattern in the far-field. At lower frequencies, it may be more appropriate to use near-field methods.

**Discussor's name :** M. Fournier

**Comment/Question :**

Sur les planches représentant la surface de la mer pouvez-vous indiquer dans quelle direction est le vent?

**Translation :**

*On the illustrations representing the sea surface, could you indicate the wind direction?*

**Author/Presenter's Reply :**

Le vent souffle dans une direction de 45 degrés par rapport à l'horizontale sur deux des planches présentées, et 30 degrés sur la troisième.

**Translation :**

*The wind is blowing from a direction 45 degrees to the horizontal on two of the illustrations shown and from 30 degrees on the third.*

**Discussor's name :** H. V. Hitney

**Comment/Question :**

I would like to comment that your horizontal PE method should be much better than the extended optics method used by RPO for the case of terrain, since the horizontal PE method should be able to account for multiple apparent sources, whereas the extended optics method can account for only one.

**Author/Presenter's Reply :**

Indeed HPE can cope with arbitrary terrain and refractivity features below the initial horizontal, provided horizontal resolution is fine enough to resolve the spectral structure of the signal.

## Modelling Tropospheric Ducting Effects on Satellite-to-Ground Paths

Herbert V. Hitney

Naval Command, Control and Ocean Surveillance Center

Research, Development, Test and Evaluation Division

NCCOSC RDTE DIV 543

53170 WOODWARD ROAD

SAN DIEGO CA 92152-7385

USA

### 1. SUMMARY

Satellite-to-ground propagation paths are frequently affected by tropospheric refraction and ducting at very low elevation angles. Common effects are substantial enhancements of signals at ranges that would normally be beyond the horizon, and severe distortions of the patterns created by the coherent interference of multiple propagation paths, in particular the direct and sea-reflected signals. Traditional methods to model tropospheric ducting effects, such as waveguide or parabolic equation methods, are difficult to apply to typical satellite heights. This paper will describe a parabolic-equation and ray-optics hybrid method to model these sometimes important effects, and compare modelled and measured results using a 1000-km high satellite transmitting at 1239 and 2891 MHz.

### 2. INTRODUCTION

Satellite-to-ground propagation paths require the consideration of a very high terminal, which is at least 200 km above the earth's surface. Traditional models that account for tropospheric ducting effects, namely waveguide and parabolic equation (PE) models, have great difficulties with such high terminal heights. Waveguide models are limited by the need to compute height-gain functions, which for practical purposes must not be too far removed from the ground or duct level. PE models are limited by practical fast Fourier transform sizes. For example, a 3 GHz application considering elevation angles up to 2 degrees and a terminal height of 1000 km would require a  $2^{20}$  transform size, which is beyond the practical limit for many computers, especially most personal computers. The model presented here is a hybrid method combining a PE model and an extended optics method that is based on the Radio Physical Optics (RPO) model [1]. The PE model uses transform sizes of  $2^{10}$  or less and is easily implemented on a personal computer. The extended-optics method is initialized by the PE model at its maximum height and uses ray optics methods to compute propagation effects at higher altitudes. Since only ray trace computations are required by this method, there is no practical limit to height provided a realistic refractivity profile is specified up to the satellite height.

RPO is a hybrid model that uses a split-step PE model for low elevation angles and low terminal heights. For elevation angles higher than those considered in the PE model, RPO uses a ray-optics model that traces both direct and surface-reflected ray paths to obtain a coherent sum of the two components. Full account is given for amplitude and phase variations induced by the vertical refractivity profile in this region. However, for terminal heights that are above the PE region and whose elevation angles are below the limit for the two-component ray-optics model, a special technique was developed. This method is called the extended-optics (XO) method, which traces a family of rays originating at the top of the PE region at

elevation angles determined by ray-optics methods. Along each ray, the propagation factor  $F$  (i.e. the ratio of the field strength to the free-space field strength) is kept constant at the value determined by the PE model at the top of the PE region. Reference [1] gives more details on this method, and gives a comparison of results using the RPO, waveguide, and pure PE models.

### 3. MODEL DESCRIPTION

The satellite-to-ground implementation of RPO works in the following manner. The PE model is executed in the normal way and propagation factor  $F$  is computed at ranges separated at a regular interval at the maximum PE height. At each range, an initial ray elevation angle is determined at the maximum PE height. A single ray is then traced up to the satellite from the maximum PE height using this initial elevation angle. Along this entire ray,  $F$  is assumed constant. The propagation loss from the source to the satellite is then computed from  $F$  using the slant range from the source to the satellite. Ground range of the satellite is also computed for use in displaying the results. By the principle of reciprocity, the propagation loss applies equally well to the case of a transmitter in the satellite and a receiver at the source location.

The PE model in RPO is a split-step model similar to that described by Craig and Levy [2] or Kuttler and Dockery [3]. However, it uses only real-valued sine transforms with a maximum of 1024 points. The sine transforms give exact results for horizontal polarization and approximate results for other polarizations. However, the extended optics method presented here should work equally well for other more exact PE (e.g., full complex or mixed sine/cosine transform) implementations. The 1024-point maximum transform size limits the RPO PE model terminal heights to about 2500 m at 1 GHz and 1500 m at 3 GHz for most environmental conditions. The PE model takes full account of range-dependent environments using the same parameter-interpolation method described by Barrios [4].

The initial elevation angle  $\beta$  of each ray at the top of the PE region is determined from ray-optics considerations in the following manner. If a reflected ray from the source exists at a given range  $x_0$  at the maximum PE height, then  $\beta$  is the elevation angle of this ray at that point. The greatest range at which reflected rays exist at the maximum PE height is called the optical limit. For ranges beyond the optical limit,  $\beta$  is given by

$$\beta = \sqrt{\beta_L^2 + 2 \times 10^{-6} (M - M_L)} \quad (1)$$

where  $\beta_L$  and  $M_L$  are  $\beta$  and modified refractivity at the optical limit, and  $M$  is the modified refractivity at the desired range. Note  $M = (n - 1 + z/a) \times 10^6$ , where  $n$  is the refractive index,

$z$  is height, and  $a$  is the earth's radius. For range-independent conditions,  $M_L$  and  $M$  are equal, so  $\beta$  is equal to  $\beta_L$  at all ranges beyond the optical limit.

In order to trace a ray up to the satellite height, the refractivity must be known at all altitudes between the maximum PE height and the satellite height. The ray trace methods and refractivity model used here closely follow those described by Anderson [5]. The refractivity model consists of a linear region, an exponential region, and a constant region. The linear region extends from the maximum PE height to 9 km. In this region, the refractivity  $N$ , defined as  $(n - 1) \times 10^6$ , decreases linearly from the value supplied by the user at the maximum PE height to a value of 105 at 9 km. The exponential region extends from 9 km to 50 km. In this region the refractivity is given by

$$N(z) = 105 e^{-0.1424(z-9)}, \quad (2)$$

where  $z$  is height in km [6]. The constant region extends from 50 km up to the satellite height. In this region, the refractivity is assumed to be 0 at all heights.

The ray trace method in the linear region assumes small elevation angles and computes ray position and elevation angle at 9 km using

$$\alpha_1 = \sqrt{\beta^2 + 2 \times 10^{-6} (1518 - M)} \quad (3)$$

$$x_1 = \frac{(\alpha_1 - \beta)}{10^{-6} dM/dz},$$

where  $\alpha_1$  is the elevation angle at 9 km,  $\beta$  and  $M$  are the elevation angle and modified refractivity at the maximum PE height,  $dM/dz$  is the modified refractivity gradient with height in the linear region, and  $x_1$  is the ground range. In this region, the ground and slant ranges are assumed equal.

The ray trace method in the exponential region numerically evaluates the integrals

$$x_2 = a \int_{\rho_9}^{\rho_{50}} \frac{d\rho}{\rho \sqrt{(\rho n/a)^2 - c^2}} \quad (4)$$

$$s_2 = \int_{\rho_9}^{\rho_{50}} \frac{\rho n d\rho}{\rho \sqrt{(\rho n/a)^2 - c^2}},$$

where  $x_2$  and  $s_2$  are the ground and slant ranges, respectively, in the exponential region,  $c$  is the ray characteristic given by  $1.001563 \cos(\alpha_1)$ ,  $\rho$  is the distance from the center of the earth to a point on the ray,  $\rho_9$  and  $\rho_{50}$  are the values of  $\rho$  at 9 and 50 km altitudes, and  $n$  is the refractive index corresponding to  $N$  given by (2). A 1 km step size for  $\rho$  is used to numerically evaluate the two integrals in (4).

The ray trace method in the constant region assumes the refractive index to be unity, and hence the rays are straight lines in this region. The ground and slant ranges,  $x_3$  and  $s_3$ , respectively, in this region are given by

$$x_3 = a \theta$$

$$s_3 = \rho_s \sin(\theta) / \cos(\alpha_2)$$

$$\theta = \frac{\pi}{2} - \alpha_2 - \sin^{-1} \left[ \frac{\rho_{50}}{\rho_s} \sin \left( \alpha_2 + \frac{\pi}{2} \right) \right] \quad (5)$$

$$\alpha_2 = \tan^{-1} \left[ \frac{\sqrt{(\rho_{50}/a)^2 - c^2}}{c} \right],$$

where  $\rho_s$  is the distance from the center of the earth to the satellite,  $\theta$  is the angle in radians at the center of the earth that subtends the ray segment in the constant region, and  $\alpha_2$  is the elevation angle of the ray at 50 km altitude. The total ground and slant ranges from the source to the satellite,  $x$  and  $s$  respectively, are then given by

$$x = x_0 + x_1 + x_2 + x_3$$

$$s = x_0 + x_1 + s_2 + s_3 \quad (6)$$

#### 4. RESULTS

The hybrid method described above was applied and compared to experimental measurements performed at Point Loma in the city of San Diego in 1978 using the P76-5 Wideband satellite in a 1000 km high orbit [5]. Relative signal strengths from transmitters on the satellite at 1239 and 2891 MHz were recorded versus time when the satellite was near the horizon for paths that were entirely over water. The horizontally polarized receiver antenna was located 34 m above mean sea level. The ground range of the satellite was computed from an orbital prediction program that had an absolute accuracy of  $\pm 4$  km. However, the ground station timing accuracy was  $\pm 1$  second, which resulted in a worst-case total error of  $\pm 14$  km.

Refractivity profiles were measured by radiosonde at the receiver location and indicated the presence of strong ducts near the surface. Two of the eleven measurement periods available were selected for presentation in this paper, namely 20 July 1978 1945Z and 28 July 1978 2000Z. The modified refractivity versus height profiles are given in Tables 1 and 2 for these observations. Figures 1 and 2 show plots of the lowest 1500 m of each profile. The 20 July case is characterized by a very strong surface-based duct extending to 360 m, while the 28 July case is characterized by an elevated duct extending from 250 to 790 m.

Figures 3 and 4 show comparisons of the hybrid model to the observations for the 1239 MHz signals on 20 and 28 July, respectively. The lower plot of each figure shows propagation loss on a gray-shade scale plotted versus height and range for the PE region only. The upper plot shows the propagation loss between the satellite and the ground station plotted versus satellite ground range in km. There is only an approximate relationship between the two range scales in each figure. For example, the maximum PE height is reached at about 30 km in the lower plot, which corresponds to an approximate ground range of 3100 km in the upper plot, and the maximum range of 375 km in the lower plot corresponds to approximately 3600 km in the upper plot. In the upper plots, the modelled loss between the satellite and the ground station is shown by the solid line, while the observed loss is shown by the dotted line. The observed data in all the figures were arbitrarily shifted vertically on the loss scale to best match the modelled results, since only relative amplitude of the signals was measured. Also, the observed data were arbitrarily shifted on the range scale up to 14 km to align the nulls at the closer ranges, based on the errors discussed above and the assumption that higher angles should be the least affected by refractive effects. Figure 5 shows results for the 2891 MHz case observed at the same time as Figure 3. The receiver antenna heights of 33.0 m for Figures 3 and 5, and 34.3 m for Figure 4, have been corrected for tide heights at the observation times. The maximum elevation angle considered in the PE model was 2 degrees for Figures 3 and 4 and 1.5 degrees for Figure 5.

## 5. DISCUSSION

Figures 3 and 4 indicate that the hybrid model is working reasonably well. For the surface-based duct case of Figure 3, it has certainly modelled the approximate loss levels observed at ground ranges exceeding 3500 km. These loss levels are the result of "leakage" of signals from the top of the well-formed duct evident in the lower plot of Figure 3. It is unfortunate that data were not recorded at ranges beyond those shown in Figure 3, for there was an ample signal-to-noise ratio available for more data, and the model would indicate similar loss values at substantially greater ranges. These results from Figure 3 are in contrast to the elevated duct case of Figure 4, where both the modelled and observed loss values increase rapidly near the 3500 km range. For the 2891 MHz case of Figure 5, the loss levels beyond 3500 km are also in rough agreement with the model, although the range intervals between nulls are much less than Figure 3 due to the higher frequency. The disagreement of the modelled and observed data at intermediate ranges is thought to be a result of range-dependent refractive effects that were not modelled, since there was no information on the atmospheric structure other than the radiosondes at the receiver site. Another source of modelled errors may be inaccurate knowledge of the refractivity profile very near the surface. Since the lowest height measured by the radiosondes was 43 m, the modified refractivity was extrapolated to the surface using the standard atmosphere gradient of 0.118 M/m in the modelling presented here.

Although better experimental validation should be performed on this model, it is thought that the hybrid technique is an accurate and efficient way to assess propagation effects on satellite-to-ground paths. The RPO execution times required for the results shown in Figures 3, 4, and 5 were approximately one minute each on an IBM/PC-compatible 486/50 MHz computer. The overall accuracy of the model is believed to be limited by the knowledge of the vertical and horizontal refractivity structure along the propagation path. It is apparent from Figures 3 through 5 that the satellite-to-ground loss patterns are sensitive to the refractive structure in the lowest few hundred meters of the atmosphere at ranges up to a few hundred kilometers, and that refractivity structure at longer ranges affects the patterns at likewise longer ranges. Also the model seems sensitive to the refractivity structure assumed very close to the surface and to the surface value of refractivity. A few cases were compared using different assumptions about surface refractivity and structure below 43 m, including the addition of a typical evaporation duct profile. Each case showed somewhat different results. It is thought that this transatmospheric model is more sensitive to the absolute value of surface refractivity than other models that consider only paths low in the atmosphere, where the surface refractivity is unimportant provided the gradients of refractivity are well known. In the transatmospheric case, the entire profile up to the vacuum of space must be considered, and the surface refractivity is thus related to the total refraction experienced along the path.

The limitations in the radio and environmental data measured in 1978 have led us to plan a new experiment using the Global Positioning System (GPS) satellites. The position of the GPS satellites is known very accurately, and receivers are readily available. The GPS frequencies of 1227.6 and 1575.42 MHz are close to those of Figures 3 and 4. We plan to make initial measurements similar to the 1978 measurements, but with emphasis on a better characterization of the refractivity structure to validate the model presented here. If the model is validated, it is our hope that we can use GPS signals measured near the horizon to infer the refractive structure of the

## 6. CONCLUSION

The hybrid model presented here appears to be an efficient and accurate method to model propagation on transatmospheric paths near the horizon. This model should be useful for many applications that consider propagation paths to very high altitudes near the horizon. One possible application is for modelling the detection and tracking capability of ground-based radars employed against theater ballistic missiles, such as the Scud missiles used in the recent Gulf war.

## ACKNOWLEDGEMENT

This work was supported by the Office of Naval Research, Technology Directorate.

## REFERENCES

- [1] Hitney, H.V., "Hybrid ray optics and parabolic equation methods for radar propagation modeling," IEE Conf. Pub. 365, *Radar 92*, pp. 58-61, 12-13 October 1992.
- [2] Craig, K.H. and M.F. Levy, "A PC-based microwave propagation forecasting model," IEE Conf. Pub. 333, *Proc. 7th Int. Conf. on Antennas and Propagation (ICAP 91)*, Part 1, pp. 523-526, 1991.
- [3] Kuttler, J.R. and Dockery, G.D., "Theoretical description of the parabolic approximation/Fourier split-step method of representing electromagnetic propagation in the troposphere," *Radio Sci.*, vol. 26, no. 2, pp. 381-393, March-April 1991.
- [4] Barrios, A.E., "Parabolic equation modeling in horizontally inhomogeneous environments," *IEEE Trans. Antennas and Propagat.*, vol. 40, no. 7, pp. 791-797, July 1992.
- [5] Anderson, K.D., "Inference of refractivity profiles by satellite-to-ground RF measurements," *Radio Sci.*, vol. 17, no. 3, pp. 653-663, May-June 1982.
- [6] Bean, B.R. and E.J. Dutton, *Radio Meteorology*, Dover Publications, Inc., 1968.

Height (m)	M units
43.0	364.8
204.1	380.0
349.5	396.4
359.2	323.8
386.8	326.4
617.3	355.5
1111.6	419.9
1540.1	481.8
1907.7	528.5
2749.4	642.9
3219.8	703.2
3545.5	748.0
4592.7	891.4
5430.8	1007.5

Height (m)	M units
43.0	359.0
133.0	373.8
465.3	410.8
487.8	396.5
593.2	391.3
787.0	388.7
1004.4	413.5
1543.1	486.3
1935.1	529.5
2517.5	644.1
2688.6	648.9
3217.4	723.2
3815.6	807.6
3925.5	829.1

Table 1. Modified refractivity profile for 20 July 1978 1945Z.

Table 2. Modified refractivity profile for 28 July 1978 2000Z.

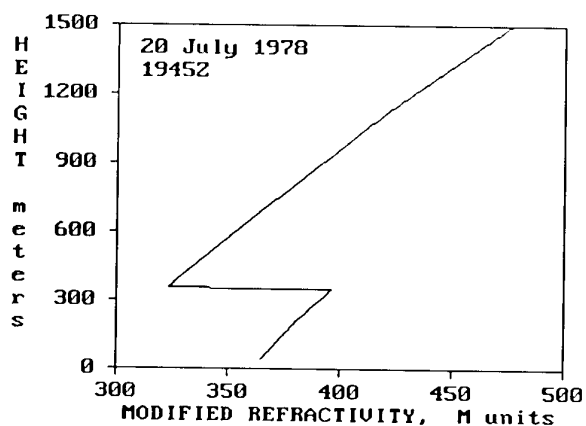


Figure 1. Modified refractivity profile for 20 July 1978 1945Z.

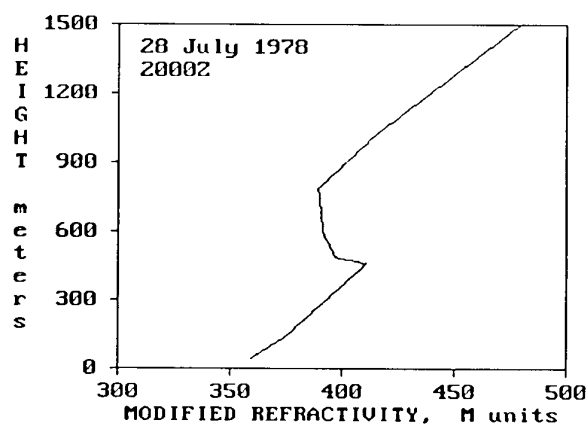


Figure 2. Modified refractivity profile for 28 July 1978 2000Z.

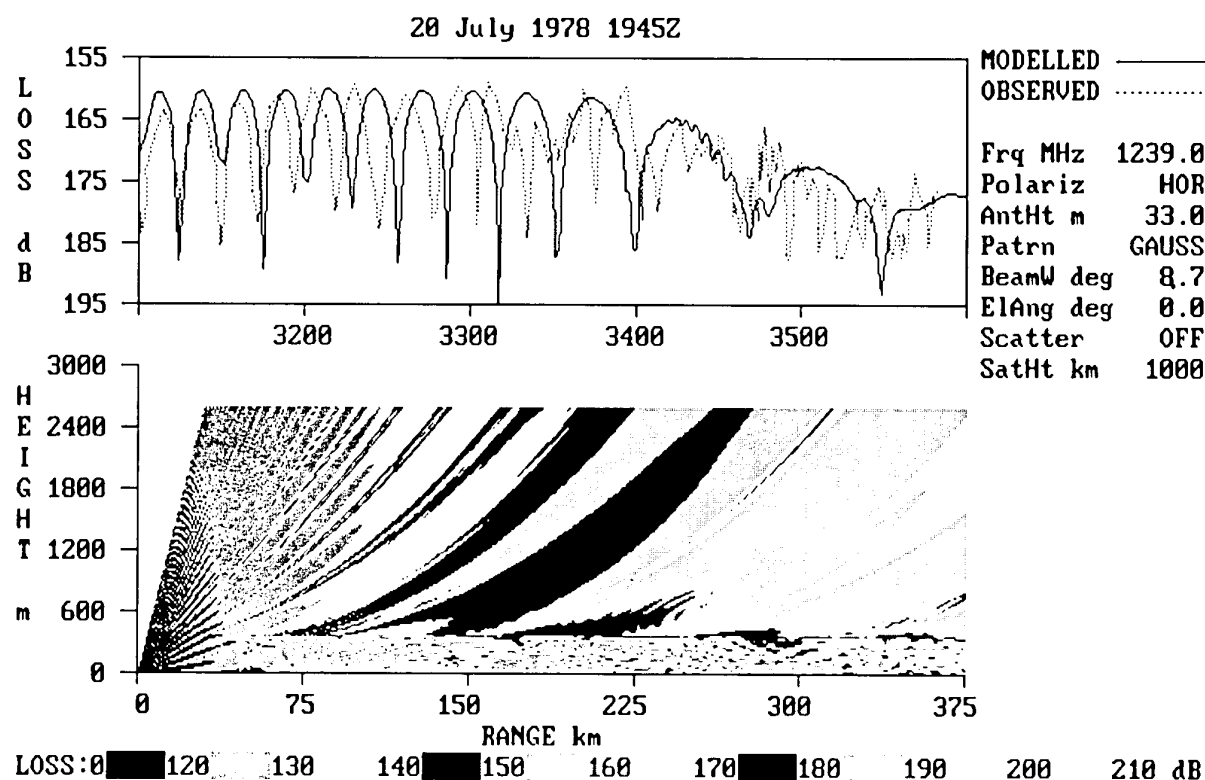


Figure 3. Hybrid model and observed data comparison for 20 July at 1239 MHz.

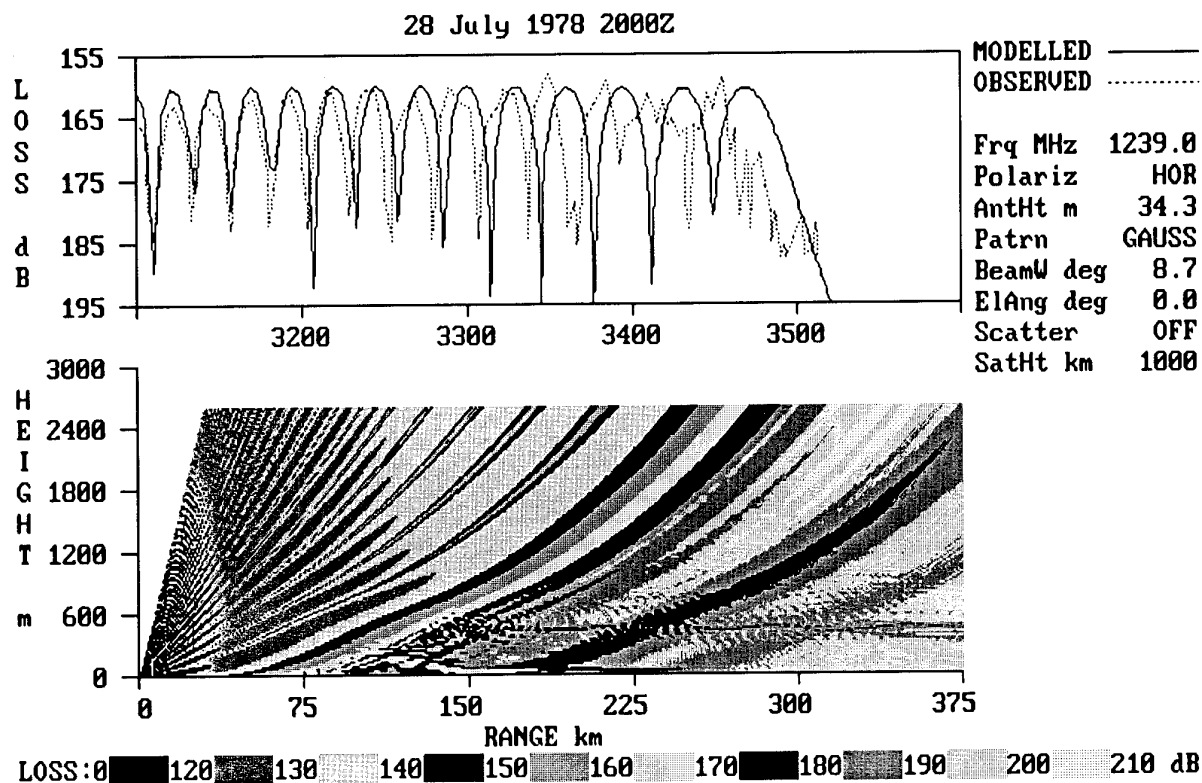


Figure 4. Hybrid model and observed data comparison for 28 July at 1239 MHz.

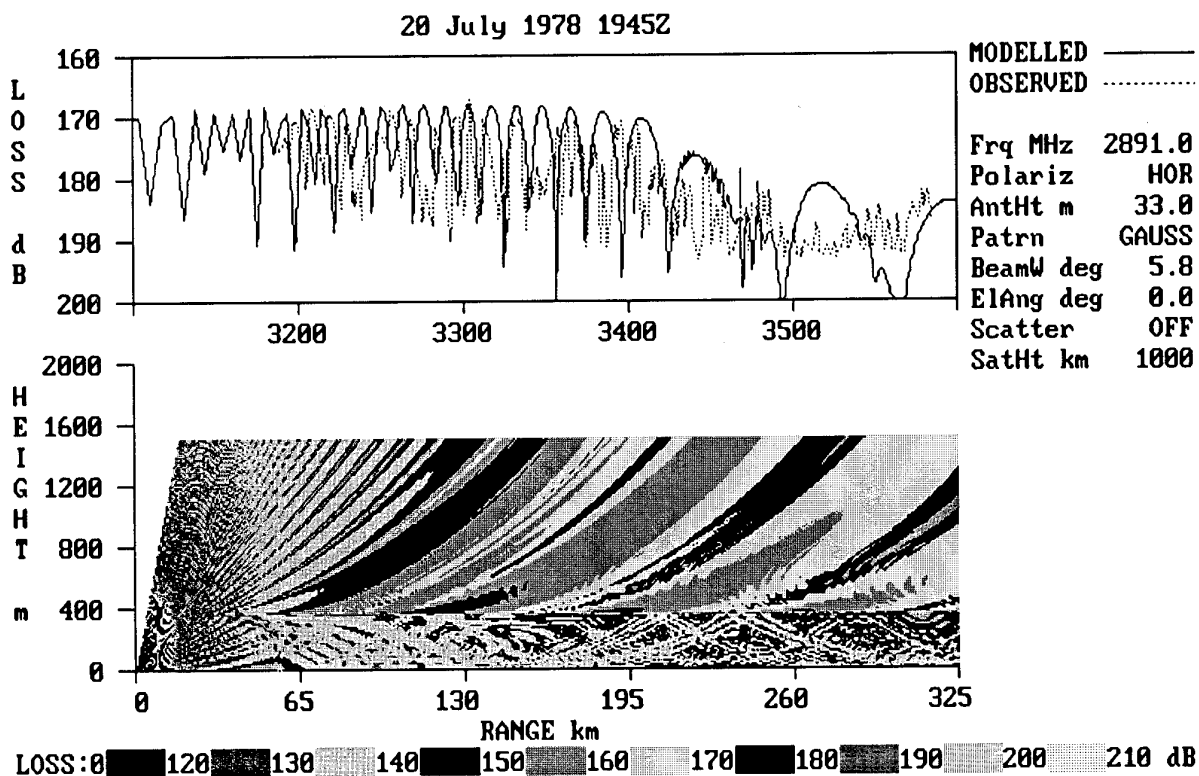


Figure 5. Hybrid model and observed data comparison for 20 July at 2891 MHz.

## The Lorentz Reciprocity Theorem as a Consistency Test for Propagation Models

Richard A. Paulus  
Naval Command, Control and Ocean Surveillance Center  
RDT&E Division 543  
53170 Woodward Road  
San Diego CA 92152-7385 USA

### SUMMARY

Modeling of electromagnetic propagation in the troposphere has been advanced in the last decade to the point where both the vertical and horizontal variation of refractivity can be accommodated readily. In particular, parabolic equation models inherently allow for lateral and vertical inhomogeneities. A hybrid ray-optics/parabolic equation model is utilized to predict propagation loss for a range-varying refractive structure to demonstrate the model obeys the Sommerfeld-Pfrang statement of the Lorentz Reciprocity Theorem.

### 1. INTRODUCTION

Many models have been developed for predicting radiowave propagation. Most of these models assume that the atmosphere is horizontally stratified and invariant in range. Hitney *et al.* (Ref 1) discuss waveguide techniques and an integrated model based upon a combination of parameterized waveguide predictions for diffraction and ray-optics techniques for optical region calculations. The integrated model, called the Integrated Refractive Effects Prediction System (IREPS), has been used in the U. S. Navy for well over a decade (Ref 2). Developments at Johns Hopkins University Applied Physics Laboratory (Ref 3) renewed interest in applying parabolic equation techniques to tropospheric propagation that were first used by Fock (Ref 4). Interest in the parabolic equation approach is due to several advantages,

including high-fidelity solutions in both the optical and diffraction region, computational efficiency due to Hardin and Tappert's split-step Fourier method (Ref 5), and the inherent capability to accommodate both the vertical and horizontal variation of the refractive structure. One approach to parabolic equation modeling of range-dependent conditions was proposed by Barrios (Ref 6). This method provides for smooth transitioning of various features between meteorological profiles using a linear interpolation in range for height/refractivity pairs which transition to like-numbered pairs in the next profile. This method has yielded excellent agreement between predicted fields and observed radio data.

In electromagnetic propagation work, reciprocity theorems have been applied in various forms (Ref 7) and reciprocity was used in IREPS to simplify optical region calculations. Of particular interest is the Sommerfeld-Pfrang statement of the Lorentz reciprocity theorem restated here from Ref 8:

*If  $A_1$  and  $A_2$  are two antennas situated at  $O_1$  and  $O_2$  respectively and having arbitrary orientations, and signals are first sent from  $A_1$  and received by  $A_2$ , and then sent with the same average power from  $A_2$  and received by  $A_1$ , then the intensity and phase of the electric field at the receiver  $A_1$  will be equal to that previously produced at  $A_2$ , regardless of the electrical properties and geometry of the intervening media (water, land, or combinations of these, stratified or otherwise*

*inhomogeneous atmosphere, of any degree of ionization, etc.) and the forms of the antennas.*

It is understood that the propagating medium must not change between the two transmission periods.

In the following sections, reciprocity is demonstrated in an inhomogeneous atmosphere utilizing a hybrid ray-optics/parabolic equation approach called the Radio Physical Optics (RPO) model (Ref 9), which uses the same profile interpolation scheme as Barrios.

## 2. SAMPLE REFRACTIVE DATA

The data used to develop the range dependent refractive structure were taken from Ref 10 which presented air temperature, sea temperature, and dew-point temperature in a south-to-north transect across an ocean front located southwest of Bermuda. Along with the mean wind speed, these data are utilized to infer the low-level refractive structure, commonly referred to as the evaporation duct. No propagation data were measured during this experiment so the meteorological data are

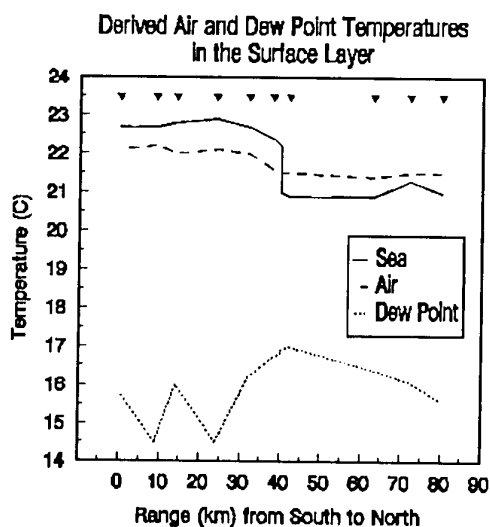


**Figure 1** Sea, air, and dew point temperatures derived from data taken during the Frontal Air-Sea Interaction Experiment (FASINEX) on February 17, 1986.

utilized here with the intent of simulating realistic range-varying conditions. The mean wind speed in the area was reported to be  $7.8 \text{ m s}^{-1}$ . The temperature data vs. range derived from Ref 10 are shown in Fig 1.

The ocean front is indicated by the sharp change in sea surface temperature at 40 km because a starting range of 0 was arbitrarily selected 40 km south of the front. The apex symbols represent the ranges where data were extracted to calculate the refractive profiles shown in Fig 2. The calculations follow the methods of Jeske (Ref 11). The profiles on the south side of the front are more concave and have a greater decrease in modified refractivity than those on the north side. These differences are related to the stability of the atmospheric surface layer (the lowest few tens of meters) over the ocean. Air on the south side of the front is cooler than the sea (thermally unstable) whereas the opposite is true on the north side of the front. The dots on the profiles in Fig 2 are located at the "evaporation duct height", the minimum on the profile and the dots on the range and M-units plane show the magnitude of the M-deficit. The concept of duct height is useful for two purposes. First, in open ocean conditions, the duct height can characterize the refractivity profile under the assumption of near-neutral stability (air temperature  $\approx$  sea temperature). IREPS parameterizes evaporation duct propagation in this manner since the normal condition over the ocean is near-neutral. Second, statistics of evaporation duct height have been compiled which can be applied to propagation problems (Refs 12, 13).

Finally, for simplicity in simulating the refractive structure, the surface layer refractivity profiles were allowed to asymptotically approach a constant gradient of  $0.125 \text{ M m}^{-1}$ . Typically, the surface layer profile must be merged with the boundary layer profile (Ref 14).

## 3. DEMONSTRATION OF RECIPROCITY



## FASINEX Evaporation Duct Profiles

◆ Front at 40 km

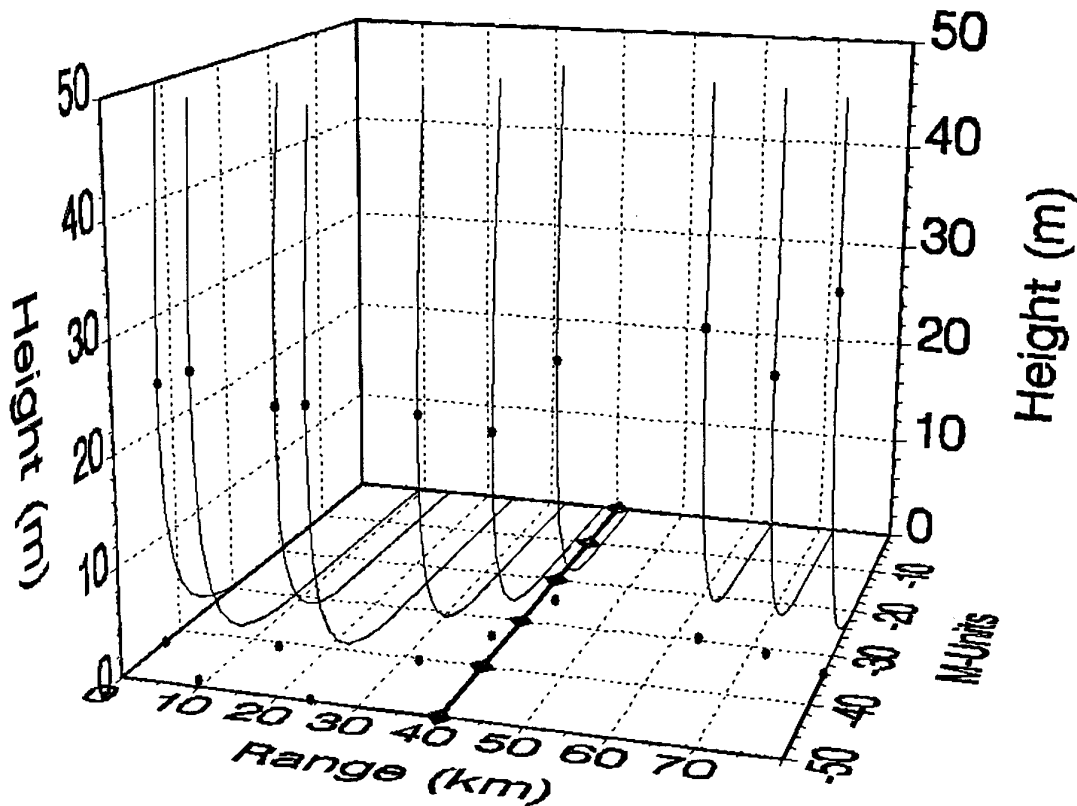


**Figure 2.** A plot of evaporation duct profiles derived from the FASINEX data. The profiles have been normalized to 0 M-units at the surface. The ocean front is located at a range of 40 km from the origin.

Lan and Tappert (Ref 15) showed that the acoustic parabolic equation method is reciprocal and demonstrated their numerical implementation showed this behavior. RPO, with its differing electromagnetic version of the parabolic equation and unique hybrid implementation, also exhibits Lorentz reciprocity. The RPO propagation model was run for transmitter heights at 10 m intervals from 10 to 80 m in altitude and for 3, 5, 10, and 20 GHz using the profiles in Fig 2 from left to right (representing a south-to-north direction). Likewise, RPO was run for the same transmitters using the profiles in Fig 2 from right to left. This approach yielded, for each frequency, 128 reciprocal paths, 80 km in length and perpendicular to the ocean front.

The geometries involved in these computer runs are such that the solutions obtained at the terminal ranges are essentially from the split-step parabolic equation model. Fig 3 is an example of the predicted propagation loss for a hypothetical 5 GHz transmitter at 20 m above the sea for a south-to-north path. Fig. 4 shows the predicted propagation loss for the same frequency and a 10 m transmitter for a north-to-south path. The coverage is distinctly different, due to both the inhomogeneous refractive structure and the difference in transmitter heights. The simulated environment is quite strongly ducting at this frequency as compared to the predicted coverage for a 10 m transmitter at 5 GHz under standard conditions (four-thirds earth radius factor) illustrated in

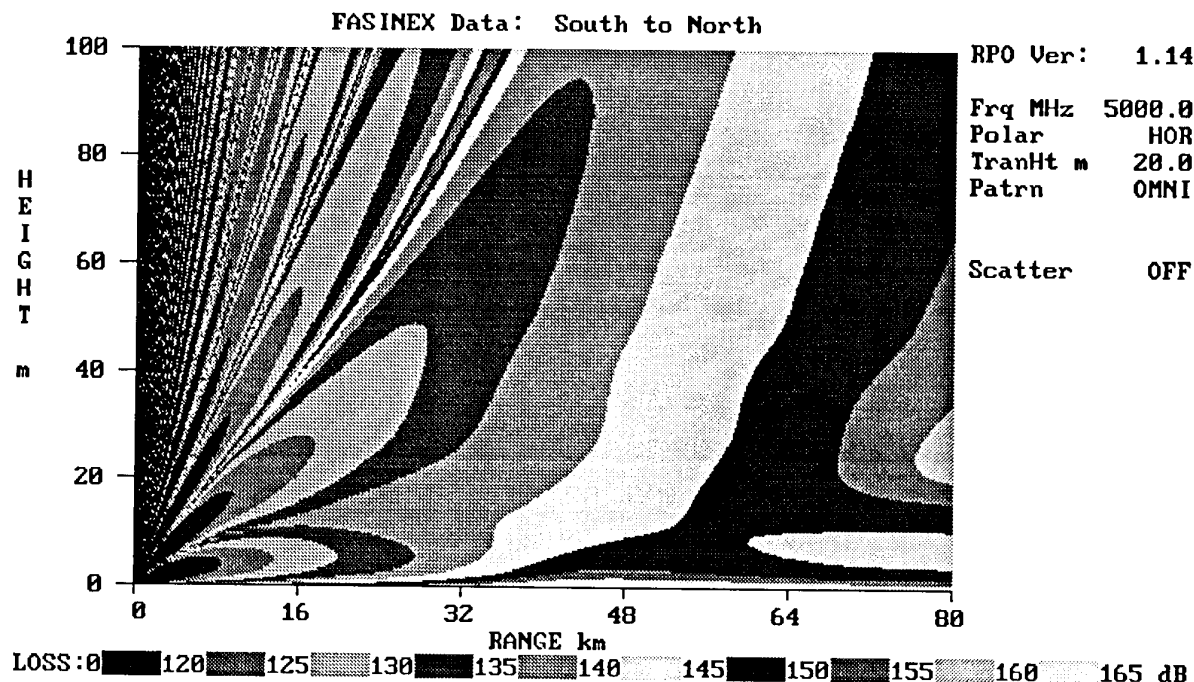


Figure 3. RPO predicted propagation loss on a south-to-north path across the ocean front for a 5 GHz transmitter located at an altitude of 20 m.

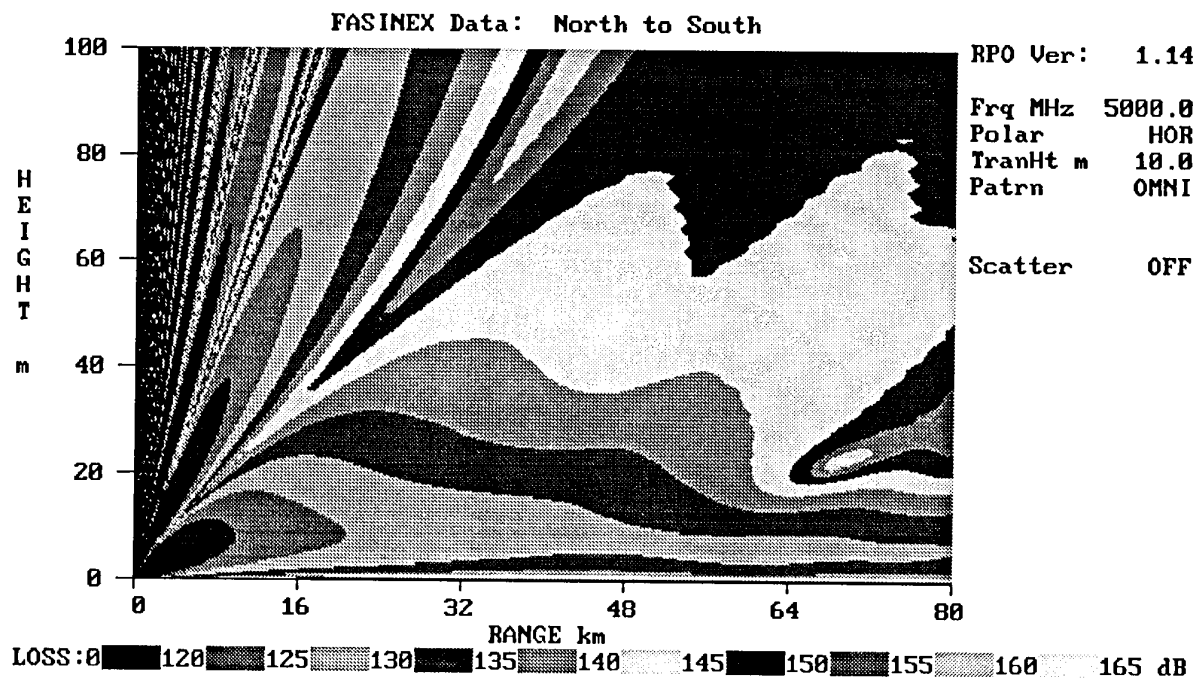
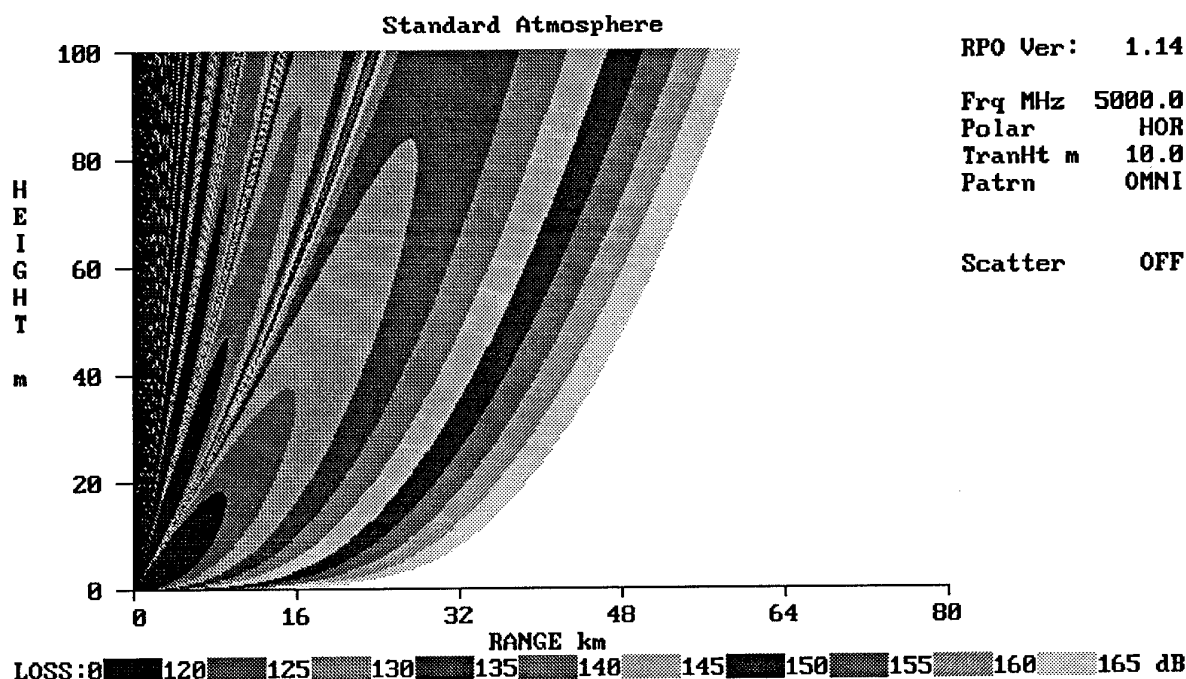


Figure 4. RPO predicted propagation loss on a north-to-south path across the ocean front for a 5 GHz transmitter located at an altitude of 10 m.



**Figure 5.** RPO predicted propagation loss for a 5 GHz transmitter located at an altitude of 10 m under standard atmosphere refractive conditions.

Fig 5. The Lorentz reciprocity theorem requires signals to be equal only at the terminals. To demonstrate this is the case for the RPO model predictions, Fig 6 shows propagation loss at 20 m altitude vs. range for a 10 m transmitter on the north side of the front and propagation loss at 10 m altitude vs. range for a 20 m transmitter on the south side of the front. From a range of approximately 10 km from the transmitters, the two propagation loss curves are several dB different, the north-to-south path being mostly above free space levels and the south-to-north path remaining below free space. However, at the full 80 km terminal range, the predicted propagation loss, in this case very near the free space value, is the same, in accordance with reciprocity. RPO produced reciprocity in all 256 comparisons.

Figs 4 and 6 may lead to the conclusion that higher signal levels result from being on the north side of the front. However, the dominant factor causing lower propagation loss is the transmitter height being at 10 m. Fig 7 compares propagation across the front for

terminals at the same height and the lower terminals have approximately a 24 dB advantage under this particular ducting condition. This phenomenon has been extensively examined for multiple frequencies and antenna heights in three ocean areas by Richter and Hitney (Ref 16).

#### 4. DISCUSSION

A simulated ducting environment, representative of range varying conditions in the open-ocean, was used to examine the capability of a high-fidelity propagation model to predict reciprocity in an inhomogeneous medium. The propagation model was shown to predict equivalent signal levels at the terminals for various frequencies and terminal heights. This capability is part of the verification and validation of the model.

**5. ACKNOWLEDGMENT.** This work was supported by the Office of Naval Technology, now the Office of Naval Research, Technology Directorate.

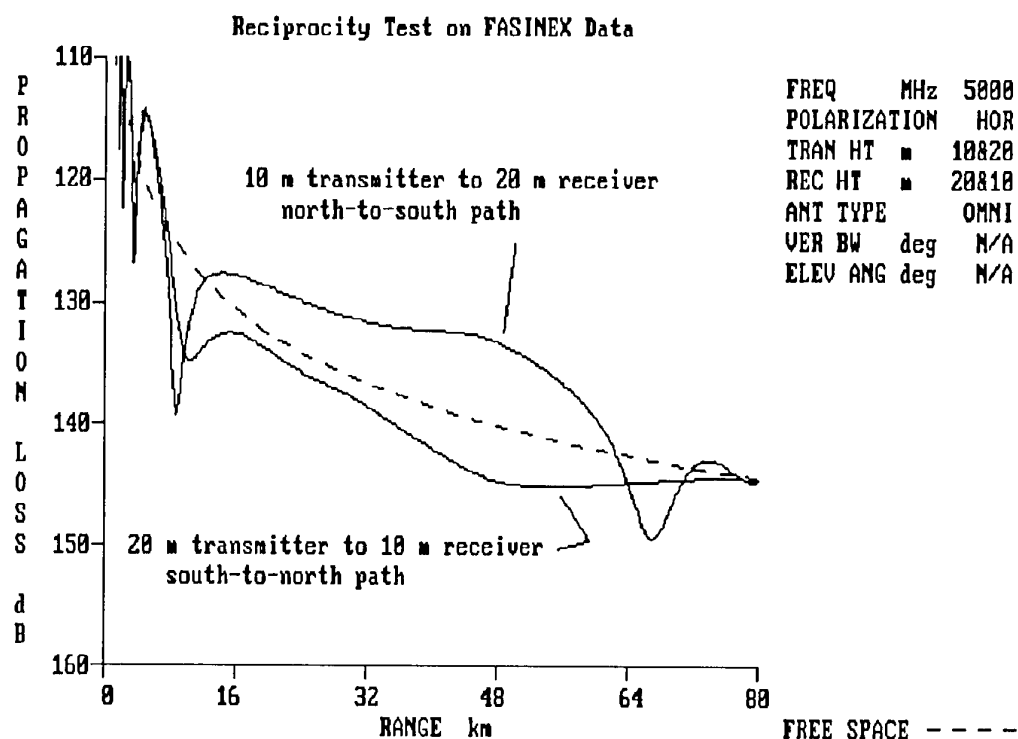


Figure 6. 5 GHz propagation loss vs. range at 10 and 20 m altitudes for a 20 m transmitter south of the ocean front and a 10 m transmitter north of the ocean front respectively.

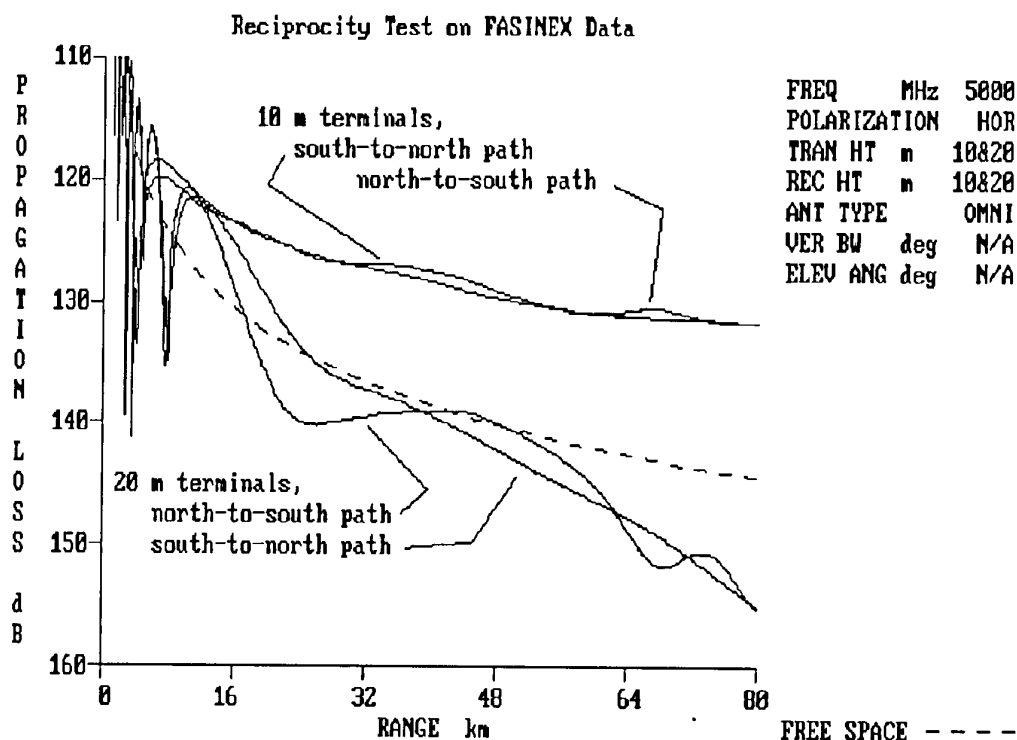


Figure 7. 5 GHz propagation loss vs. range between 10 m terminals on either side of the ocean front and 20 m terminals on either side of the ocean front.

## 6. REFERENCES

1. H. V. Hitney, J. H. Richter, R. A. Pappert, K. D. Anderson, and G. B. Baumgartner, Jr., "Tropospheric radio propagation assessment," *Proc. IEEE*, vol. 73, pp. 265-285, Feb. 1985.
2. L. Phegley and C. Crosiar, "The third phase of TESS," *Bull. Amer. Meteor. Soc.*, vol. 72, pp. 954-960, Jul. 1991.
3. H. W. Ko, J. W. Sari, and J. P. Skura, "Anomalous microwave propagation through atmospheric ducts," *Johns Hopkins APL Tech. Dig.*, vol. 4, no. 1, pp. 12-26, Jan.-Mar. 1983.
4. V. A. Fock, *Electromagnetic Diffraction and Propagation Problems*. New York: Pergamon, 1965, ch. 11-14.
5. R. H. Hardin and F. D. Tappert, "Application of the split-step Fourier method to the numerical solution of nonlinear and variable coefficient wave equations," *SIAM Rev.*, vol. 15, p. 423, 1973.
6. A. E. Barrios, "Parabolic equation modeling in horizontally inhomogeneous environments," *IEEE Trans. Antennas Propagat.*, vol. 40, pp. 791-797, Jul. 1992.
7. H. R. Reed and C. M. Russell, *Ultra High Frequency Propagation*. Cambridge, MA: Boston Tech. Publ., 1966.
8. S. Ballantine, "The Lorentz reciprocity theorem for electric waves," *Proc. IRE*, vol. 16, pp. 513-518, Apr. 1928.
9. H. V. Hitney, "Hybrid ray optics and parabolic equation methods for radar propagation modeling," *RADAR 92*, IEE Conference Publication No. 365, pp. 58-61, Brighton, England, U. K., 12-13 Oct. 1992.
10. S. J. S. Khalsa and G. K. Greenhut, "Atmospheric turbulence structure in the vicinity of an oceanic front," *J. Geophys. Res.*, vol. 94(C4), pp. 4913-4922, Apr. 15, 1989.
11. H. Jeske, "State and limits of prediction methods of radar wave propagation conditions over sea," *Modern Topics in Microwave Propagation and Air-Sea Interaction*, A. Zanca, ed., Reidel Pub., pp. 131-148, 1973.
12. H. V. Hitney and R. Vieth, "Statistical assessment of evaporation duct propagation," *IEEE Trans. Antennas Propagat.*, vol. 38, pp. 794-799, Jun. 1990.
13. H. V. Hitney and L. R. Hitney, "Frequency diversity effects of evaporation duct propagation," *IEEE Trans. Antennas Propagat.*, vol. 38, pp. 1694-1700, Oct. 1990.
14. K. D. Anderson, "Remote sensing of the evaporation duct using an x-band radar," *Remote Sensing of the Propagation Environment*, AGARD CP-502, pp. 3-1 to 3-9, Feb. 1992.
15. N. Lan and F. Tappert, "Modeling of reciprocity in the time domain using the parabolic equation method," *J. Acoust. Soc. Am.*, vol. 78, pp. 164-171, Jul. 1985.
16. J. H. Richter and H. V. Hitney, "Antenna heights for the optimum utilization of the oceanic evaporation duct," vols. 1 & 2, Naval Ocean Syst. Cen. (now Naval Command, Control and Ocean Surv. Cen., RDT&E Div.), San Diego, CA, Tech. Doc. 1209, Jan. 1988 (NTIS acc. nos. AD-A192 358/0/XAB and AD-A192 311/9/XAB).

## DISCUSSION

**Discussor's name :** M. F. Levy

**Comment/Question :**

The examples shown here test reciprocity in the parabolic equation region of RPO. Will this work be extended to more "hybrid" cases (for example a transmitter in the PE region and a receiver in the RO region)?

**Author/Presenter's reply :**

You are correct that only the PE portion of RPO was tested. The other regions of RPO could be tested using the same methods, but I believe we have not done this.

**Discussor's name :** A. van der Vorst

**Comment/Question :**

The Reciprocity Theorem has been theoretically proven long ago. It is valid for isotropic media. So, the present experiment proves that there is no anisotropic medium present in the configuration. Could you comment?

**Author/Presenter's Reply :**

It was certainly not the intent of this paper to re-prove the reciprocity theorem. It was used as a test to prove there were no errors made in the computer implementation of the PE model in RPO. We expected reciprocity to be preserved, and since it was preserved in all 128 cases studied, we conclude the range-dependent PE model is working properly. We have also used many other tests to validate the RPO models.

# MODELLING OF MICROWAVE PROPAGATION AND CLUTTER IN A MARITIME ENVIRONMENT

M.H. Vogel  
TNO Physics and Electronics Laboratory  
PO Box 96864  
2509 JG The Hague, the Netherlands

## SUMMARY

For a radar system in a maritime environment, the probability of detection of a target at a low altitude is strongly dependent on the conditions of the atmosphere and the sea surface. In order to determine the detection probability of a target at low altitude, these conditions should be taken into account. This paper presents numerical methods to calculate electromagnetic propagation in an evaporation duct and to calculate sea clutter returns.

## 1 INTRODUCTION

For a radar system in a maritime environment, the probability of detection of a target at a low altitude is strongly dependent on the conditions of the atmosphere and the sea surface. The presence of an atmospheric duct as well as roughness of the sea surface influence the propagation. Also, a rough sea leads to clutter returns. In order to determine the probability of detection of a target at low altitude, these effects should be taken into account.

In section 2, we present the split-step algorithm [1,2] for calculations on propagation. Well-known computer codes like PCPEM and PC-EMPE [3,4,5] use this algorithm. The effects of the atmosphere are included correctly, but the complicated influence of the sea is included in these codes only by means of a single roughness factor. Clutter is not considered at all. In section 3, we show how the sea swell can be incorporated in the split-step algorithm in order to make it more realistic.

In section 4, the Georgia Institute of Technology (GIT) method for the calculation of sea clutter is discussed [6]. In principle, this method can be combined with the method on propagation. We show how this can be done. The combination of results concerning propagation with data on the reflectivity of the sea surface from the GIT-model yields the clutter level that is observed by the radar.

Finally, in section 5 we recommend how to develop a computer code that includes propagation and clutter and that can be used in an operational environment. In an operational environment, a computer code like CARPET [7] should, in combination with the recommended code, give the probability of detection for a given target, taking into account the radar parameters, the propagation conditions and the sea clutter.

## 2 THE BASIC SPLIT-STEP ALGORITHM

### 2.1 Outline of the method

In this section, we present the parabolic equation with which microwave propagation in the troposphere can be modeled, and we show how the solution of this equation can be approximated with the split-step algorithm.

Starting with Maxwell's equations, one can derive an elliptic partial differential equation in spherical coordinates  $(r, \theta, \phi)$  that describes electromagnetic propagation over the (spherical) surface of the earth. Assuming azimuthal symmetry, the

coordinate  $\phi$  can be omitted. As we are interested in ranges up to about 50 km, which is small in comparison with the radius of the earth, we can apply the so-called earth-flattening transform [8]. This transform is given by

$$\begin{aligned} x &= a\theta \\ z &= a \ln(r/a) \approx r - a, \end{aligned} \quad (2.1)$$

in which  $a$  is the radius of the earth,  $x$  denotes the range towards the transmitting antenna and  $z$  the height above the earth surface. We also transform the field to a new variable  $u$  and make some approximations, which are justified when the computations are performed a large number of wavelengths from the antenna and for low elevation angles. Further, the horizontal refractivity gradient must be small.

In terms of the new coordinates  $(x, z)$ , the wave equation becomes

$$\frac{\partial^2 u}{\partial z^2} + 2ik \frac{\partial u}{\partial x} + k^2(m^2(x, z) - 1)u = 0, \quad (2.2)$$

which is the parabolic equation that governs low-altitude microwave propagation. In this equation,  $u$  is related to the electric field strength in case of vertical polarization and to the magnetic field strength in case of horizontal polarization. Further,  $k$  denotes the wavenumber and  $m$  denotes the modified refractive index, which is related to the refractive index  $n$  by  $m = n + z/a$ . The solution of this parabolic equation can be approximated more efficiently than that of the original elliptic equation.

When an elliptic equation has to be solved, boundary conditions on all boundaries are required. Furthermore, a very fine grid with a nodal spacing of a small fraction of a wavelength is required. Therefore numerical solution methods for such equations result in very large matrix equations. For our application, such matrix equations would be too large to be solved on present-day computers. A parabolic equation like Eq. (2.2), however, does not require a boundary condition on every boundary, nor does it require a very fine grid. To solve the equation numerically, a stepping procedure can be used, in which the solution at range  $x + \Delta x$  is calculated from the solution at range  $x$ . The step size can be many wavelengths. This stepping procedure is continued until a satisfactory distance from the transmitting antenna has been reached. One possibility for such a procedure is the Finite Difference Method, which is especially valuable for irregular terrain. Another possibility is the split-step algorithm, which is computationally more efficient for simple surfaces. In order to derive this algorithm, we write the parabolic equation as

$$\frac{\partial u(x, z)}{\partial x} = i[A(x, z) + B(z)] u(x, z), \quad (2.3)$$

where the operators  $A$  and  $B$  are defined as

$$A(x, z) = \frac{k}{2} [m^2(x, z) - 1], \quad (2.4)$$

and

$$B(x,z) = \frac{1}{2k} \frac{\partial^2}{\partial z^2} \quad (2.5)$$

The field at range  $x+\Delta x$  can approximately be expressed in terms of the field at range  $x$  by

$$u(x+\Delta x, z) = \exp[i\Delta x(A+B)] u(x, z). \quad (2.6)$$

The exponential is now split into three components. This split is one of many possibilities, none of which is exact. We obtain

$$u(x+\Delta x, z) = \exp(i\Delta x B/2) \exp(i\Delta x A) \exp(i\Delta x B/2) u(x, z). \quad (2.7)$$

Note that the operator  $B(z)$  is a differentiation with respect to  $z$ . In order to "multiply" the function  $u(x, z)$  with the operator  $\exp(iB(z)\Delta x/2)$ , we need the Fourier transformation. This transformation and its inverse are defined by

$$U(x, p) = F(u(x, z)) = \frac{1}{\sqrt{(2\pi)}} \int_{-\infty}^{\infty} u(x, z) \exp(-ipz) dz, \quad (2.8)$$

$$u(x, z) = F^{-1}(U(x, p)) = \frac{1}{\sqrt{(2\pi)}} \int_{-\infty}^{\infty} U(x, p) \exp(ipz) dp, \quad (2.9)$$

where  $p = k \sin \theta$  and  $\theta$  is the angle of propagation above the horizontal. Now, the application of the operator  $\exp(iB(z)\Delta x/2)$  to the function  $u(x, z)$  is implemented as follows:

$$u(x+\Delta x, z) = F^{-1} [ \exp(-i\Delta x p^2/4k) F(u(x, z)) ]. \quad (2.10)$$

So  $u(x+\Delta x, z)$  can be calculated from  $u(x, z)$  by applying two fourier transformations, two inverse fourier transformations and three multiplications in accordance with the equations just given. The scheme is presented in Fig. 1.

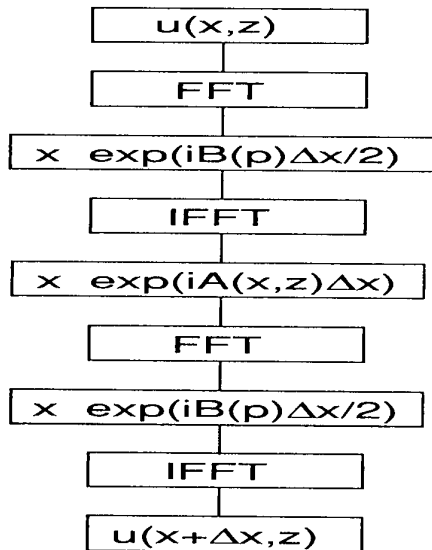


Fig. 1: The calculation of  $u(x+\Delta x, z)$  from  $u(x, z)$ .

The split-step algorithm to solve the parabolic equation is not exact. The error depends on the step size  $\Delta x$ , the frequency, and the refractive index gradients. By choosing smaller step sizes, the error can be made as small as desired, apart from round-off errors.

## 2.2 Implementation of the method

In order to implement the method just presented, we have to define a computational domain. The region we are interested in ranges in the  $x$ -direction from a distance of a few hundred meters from the transmitting antenna to a distance of about 50 km, and in the  $z$ -direction from sea-level ( $z=0$ ) to a height of about 40 m. The computational domain has to include this region of interest, and for efficiency reasons, it should not be much larger than this. We will now outline how this domain and its boundary conditions can be chosen.

In the first place, the sea is a good electrical conductor. In order to impose this as a boundary condition, the computational domain is extended to include negative  $z$ -values. Apart from the transmitting antenna at a specified height  $z>0$ , there exists an identical image antenna at the same "height" below zero. The initial field is the sum of the fields that are produced by both antennas. However, each "ray" from the image antenna is multiplied with the Fresnel reflection coefficient that belongs to the angle with which this "ray" crosses the line  $z=0$  (the sea surface). Also, the field from the image antenna is multiplied with a roughness factor  $p_r \leq 1$ . For a smooth sea,  $p_r$  approaches 1. The Fresnel coefficient and the roughness factor are given in [1]. This procedure ensures that at a distance of a few hundred meters from the transmitting antenna, where our computations start, the initial field for  $z>0$  includes multipath and roughness effects. The method chosen will give good results for a smooth sea surface. Only when the surface is very rough and the ducting is strong (so that a "ray" may strike the surface many times) the method becomes inaccurate for propagation distances of several tens of kilometers and more.

At the upper and lower boundaries of the computational domain, i.e. for the largest absolute values of  $z$ , we apply so-called absorbing boundary conditions. These boundary conditions have to ensure that the fields are not reflected at the boundary, and that a field that passes the upper boundary does not enter the computational domain at the lower boundary and vice versa. These requirements can be met by adding an imaginary component to the refractive index  $n$  in the upper and lower region of the domain, and/or by tapering the field. The computational domain is depicted in Fig. 2.

Having calculated the initial field, it is transformed to the variable  $u$  of the parabolic equation. After this, the split-step algorithm is invoked. For a frequency of 10 GHz and duct profiles that are not very strong, step sizes of a few hundred meters are possible. At each step, the sequence of FFTs, multiplications, and inverse FFTs is applied. If desired, at each step the field can be calculated from the actual function  $u(x, z)$ , and the path loss and propagation factor can be obtained as a function of distance. This can also be done after a specified number of steps.

The CPU time of the algorithm has been tested on a VAX 6310 computer. Each range step, with an FFT size of 1024, takes 0.33 second. The calculation of the path loss and propagation factor at each step costs only a very small fraction of this.

## 3 ADAPTATIONS TO THE ALGORITHM FOR AN IRREGULAR SURFACE

The split-step method presented in the previous section is suited for tropospheric propagation over a smooth surface.



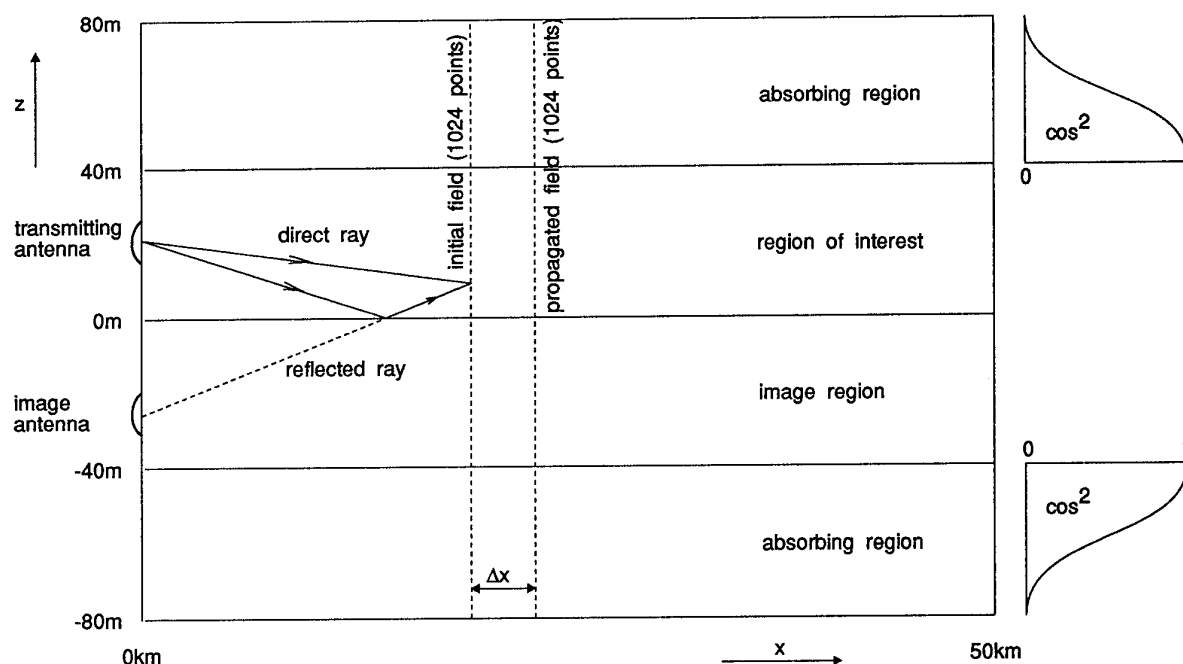


Fig. 2. The computational domain.

This surface should be a good electrical conductor. For an irregular surface, various authors have derived alternative parabolic equations or have adapted the split-step solution method. We will present the approach of Ryan [9], and show how an irregular surface (whose second derivative with respect to  $x$  exists) leads to a similar parabolic equation as the one we have discussed in the previous sections.

In section 2, we have applied an earth-flattening transform in order to obtain local coordinates  $x$  (range) and  $z$  (altitude). In this section, we apply an alternative earth-flattening transform. We again take for the range  $x$

$$x = a\theta, \quad (3.1)$$

but instead of an altitude  $z$  given by  $z \approx r - a$ , we now have a height  $h$  above the (irregular) surface, given by

$$h = a \ln(r/a) - \zeta(\theta) \approx r - a - \zeta(\theta), \quad (3.2)$$

where  $\zeta(\theta)$  is the terrain function that describes the elevation of the terrain or sea swell. We obtain

$$\left( \frac{\partial^2}{\partial h^2} + 2ik \frac{\partial}{\partial x} + k^2(m^2 - 1 - 2h\zeta''(x) + \zeta'^2(x)) \right) u(x, h) = 0. \quad (3.3)$$

In Eq. (3.3),  $\zeta'(x)$  denotes the first derivative of  $\zeta$  with respect to  $x$ , and  $\zeta''(x)$  the second derivative. Note that Eq. (3.3) for an irregular surface has the same structure as Eq. (2.2) for a smooth surface. Given an initial electromagnetic field, a refractivity profile and a terrain function, we can use the familiar split-step algorithm to solve the propagation problem. A limitation for the terrain function  $\zeta(x)$  is the requirement that its second-order derivative exist. There is no limitation that the surface should be a perfect conductor. Also for nonperfectly conducting surfaces suitable boundary conditions can be imposed numerically [10]. The method can therefore be applied not only to propagation over a sea surface with swells but also to propagation over a hilly terrain. This is

a significant advantage over the traditional split-step method, where the surface had to be smooth and perfectly conducting. A disadvantage of the method is its limited ability to calculate forward scattering by small waves on the sea surface. This would require extremely small step sizes. Therefore other methods have to be invoked to model this phenomenon.

#### 4 THE GIT CLUTTER MODEL

For the calculation of the reflectivity per unit area of the sea surface, several models exist [6,11,12,13]. As the reflection from the sea surface is a very complicated phenomenon, all these models are empirical. They give the reflectivity per unit area as a function of frequency, polarization, angle of incidence, sea state and wind direction. A comparison between these models reveals that the Georgia Institute of Technology (GIT) model yields much lower values for the reflectivity than the other ones, especially near grazing incidence. Reilly and Dockery [11,12,13] explain this discrepancy by suggesting that most experiments on sea clutter have been performed with an evaporation duct present whose characteristics are not known, while the GIT clutter model is based on experiments with a well-defined standard atmosphere (i.e. without ducting). Indeed, it is well known that in a maritime environment, evaporation ducts exist most of the time. These ducts in general change the angle under which the electromagnetic energy strikes the sea surface, and also lead to an increased propagation factor for low altitudes and long ranges, especially when the energy is "trapped" in the duct. These two effects give rise to a higher clutter level than the one that would be observed in a standard atmosphere. For this reason, Reilly and Dockery advise to use the GIT model first in calculations on clutter, and to make a correction for the actual propagation conditions in order to obtain the desired clutter level in situations when a duct is present. Taking this into account, the GIT clutter model generally provides an accuracy of about 5 dB [6].

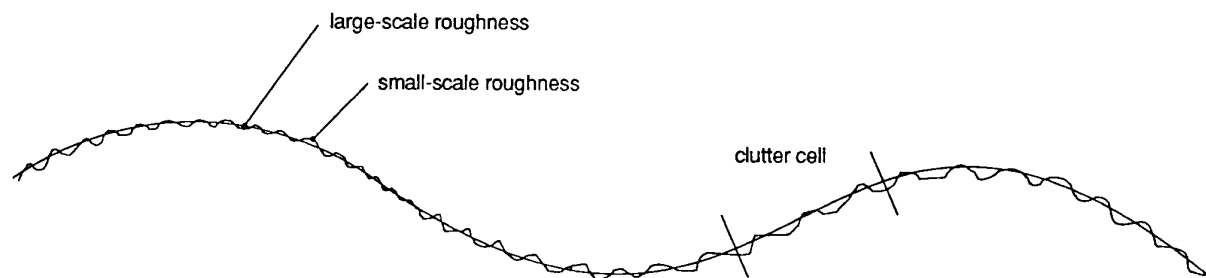


Fig. 3. Two-scale model of the sea surface.

We will outline how the GIT model can be used to calculate the clutter level in a situation with arbitrary atmospheric conditions.

In the first place, in any clutter model, including the GIT model, the angle under which the electromagnetic energy strikes the sea surface is very important. For near-grazing angles, i.e. angles of incidence  $\theta$  near zero, the reflectivity is proportional to the fourth power of this angle. Near and beyond the horizon, the angle cannot be determined geometrically, as the influence of the atmosphere on the direction of the electromagnetic waves is too large. A computer program for tropospheric microwave propagation should be used. When, for a certain range  $X$ , the vertical field distribution  $u(X,z)$  is known, the direction of propagation can be obtained by calculating  $U(X,p)$ , which is the Fourier transform of  $u(X,z)$ , as has been discussed in section 2 of this paper. As  $p$  equals  $k \sin \theta$  where  $k$  is the wave number, the location of the maximum of  $U(X,p)$  for negative values of  $p$  reveals the grazing angle at range  $X$ . When also the possible tilting of the sea surface due to a swell is taken into account, the angle under which the electromagnetic energy strikes the sea surface is known. In doing so, we implicitly assume that the sea surface can be decomposed into a large-scale swell that is not dependent of the actual wind speed and direction, and a wind-dependent sea structure. This is depicted in Fig. 3.

In the second place, knowing the reflectivity of the sea at a certain range, for the calculation of the clutter level the propagation factor should be taken into account. The reflectivity given by the GIT model corresponds to standard atmospheric conditions. We denote the propagation factor for this case by  $F_{st}$ . The received power (two way) will under standard atmospheric conditions be proportional to  $F_{st}^4$ . Under the actual atmospheric conditions, however, the received power will be proportional to  $F^4$ , where  $F$  is the propagation factor that is valid for the specific case under consideration.  $F$  follows from the computer program that calculates propagation. Now, in order to obtain the clutter level, the result of the GIT model should be divided by  $F_{st}^4$  and be multiplied by  $F^4$ .

## 5 CONCLUSIONS AND RECOMMENDATIONS

We have discussed numerical methods for calculations on microwave propagation and sea clutter.

For computations on propagation, the split-step method is very promising. As has been shown in section two, apart from an arbitrary atmospheric refractivity structure, also the large-scale roughness of the sea, the sea-swell, can be incorporated. The influence of the small-scale roughness, the capillary waves, on the propagation factor cannot be determined with this method. With this restriction, the split-step method yields the field strength at any distance from the antenna and at any altitude above the surface. This can be combined with the Radar Cross Section (RCS) of a (point) target in order to obtain the signal return from the target that is received by the antenna.

In order to establish a probability of detection, the clutter level also has to be calculated. To this aim, the Georgia Institute of Technology (GIT) clutter model is recommended. This model yields a reflectivity per unit area (clutter cell) of the sea surface, depending on the angle of incidence, the polarization, the radar frequency, the sea state and the wind direction. The angle of incidence is the sum of two components: the direction of propagation of the electromagnetic wave with respect to the horizontal and the tilting of the clutter cell by the sea swell. A combination of the reflectivity, calculated by the GIT-model, and the propagation factor, calculated by the split-step method, yields the clutter power at the receiving antenna.

Knowing the signal return from a (point) target and the clutter power at the receiving antenna, the signal-to-noise ratio is known for a specific scenario. The probability of detection of the target can then be determined. The computer codes recommended here can be linked to a radar performance assessment program like CARPET [7]. This approach would facilitate the optimum choice of radar parameters like frequency, polarization, pulse length, and pulse repetition frequency in an operational environment.

## REFERENCES

- [1] M.H. Vogel, "The split-step algorithm for microwave propagation modeling above a conducting surface", TNO Physics and Electronics Laboratory report nr. FEL-92-A430, February 1993.
- [2] K.H. Craig and M.F. Levy, "Parabolic equation modelling of the effects of multipath and ducting on radar systems", IEE Proceedings-F, vol. 138, no. 2, April 1991, pp. 153-162.

- [3] PCPEM User Guide, Signal Science Ltd., 20 Alexander Close, Abingdon, Oxon OX14 1XA, Great Britain, March 1990.
- [4] PC-EMPE User's Manual, Developed by Johns Hopkins University, Applied Physics Laboratory, Laurel, Maryland, U.S.A.; Distributed by Applied Technology Institute, 12960 Linden Church Road, Clarksville, MD 21029, U.S.A., 1989.
- [5] M.H. Vogel, "A comparison between several computer codes for calculations on microwave propagation", TNO Physics and Electronics Laboratory report nr. FEL-92-A435, March 1993.
- [6] M.M. Horst, F.B. Dyer, and M.T. Tuley, "Radar sea clutter model", Proc. Int. Conf. on Antennas and Propagation, Part 2, pp. 6-10, IEE Conf. Publ. 169, 1978.
- [7] A.G. Huizing and A. Theil, "CARPET: Radar performance analysis software and user's manual", Artech House, Boston, London, (ISBN 0-89006-636-1), 1993.
- [8] F.J. Ryan, "RPE: A parabolic equation radio assessment model", in: AGARD Conference Proceedings no. 453, "Operational Decision Aids for Exploiting or Mitigating Electromagnetic Propagation Effects", September 1989.
- [9] F.J. Ryan, "Analysis of electromagnetic propagation over variable terrain using the parabolic wave equation", Technical Report 1453, Naval Command, Control and Ocean Surveillance Center, San Diego, California, U.S.A., October 1991.
- [10] G.D. Dockery, "Modelling electromagnetic wave propagation in the troposphere using the parabolic equation" IEEE Trans. Antennas Propagat., vol. 36, no. 10, October 1988, pp. 1464-1470.
- [11] J.P. Reilly and G.D. Dockery, "Calculation of radar sea return with consideration of propagation conditions", Report number FS-89-042, Johns Hopkins University, Applied Physics Laboratory, Laurel, Maryland, U.S.A.
- [12] G.D. Dockery, "Method for modelling sea surface clutter in complicated propagation environments", IEE Proceedings, vol. 137, pt. F, no. 2, April 1990, pp. 73-79.
- [13] J.P. Reilly and G.D. Dockery, "Influence of evaporation ducts on radar sea return", IEE Proceedings, vol. 137, pt. F, no. 2, April 1990, pp. 80-88.

## DISCUSSION

**Discusser's name :** E. P. Baars

**Comment/Question :**

Forward and back-scattering are inter-related. In your simulation, both are modeled independently. To what extent does this affect the realism of the simulation?

**Author/Presenter's Reply :**

In calculations on forward propagation, only large-scale roughness is taken into account. Small-scale roughness certainly plays a role, but literature on this subject is scarce, and at present we have not decided how to incorporate it.

**Discussor's name :** G. S. Brown

**Comment/Question :**

Will the ducting of the rough surface scattered field be considered?

**Author/Presenter's Reply :**

Yes.

The ducting is taken into account twice: first to calculate the incident field on a clutter cell, and secondly to calculate the scattered field from this clutter cell as is observed by the radar system.

**Discussor's name :** K. H. Craig

**Comment/Question :**

A comment on your Figure 1 and text referring to it : if you are going to iterate the split-step algorithm in range, then of course the final IFFT at range  $N$  cancels with the first FFT at range  $N + 1$ . Thus only one FFT and one IFFT are required per step, plus an extra IFFT at any range at which the field is required to be output.

**Author/Presenter's Reply :**

This comment is correct. The final IFFT is only taken at those ranges where the field is required to be output.

**Discussor's name :** M. F. Levy

**Comment/Question :**

How do you compute the angle of incidence for the clutter calculation? This is not straightforward, as windowing techniques have to be used. Have you tested your techniques against Reilly and Dockery's?

**Author/Presenter's Reply :**

The angle of incidence follows from the FFT of the vertical field profile. It is true that this is not a straightforward calculation. This part of the model has not yet been tested.

## SIMULATION OF THE IMPACT OF ATMOSPHERIC TURBULENCES ON MILLIMETER-WAVE COMMUNICATIONS SYSTEMS

H. Vasseur, D. Vanhoenacker

Microwaves Laboratory U.C.L.  
Bâtiment Maxwell - 3, Place du Levant  
B-1348 Louvain-la-Neuve, Belgium

### 1. SUMMARY

By inducing scintillation of the transmitted signals, atmospheric turbulences affect both satellite and line-of-sight communication systems in the millimeter-waves range. After a characterization of the scintillation effect from theory and experiments, this paper presents two deterministic models developed at the Microwaves Laboratory U.C.L. for the simulation of scintillation. The first model accounts for the physical process of cloud induced turbulence that yields scintillation on satellite links and the second one deals with the turbulence in the lower atmospheric layer that affects terrestrial paths. These models allow to retrieve the turbulent configuration that produce scintillation, to simulate the scintillation effects on various links and finally to predict the impact of scintillation on the performances of communication systems.

### 2. INTRODUCTION

By inducing refractive index inhomogeneities, atmospheric turbulences yield multiple propagation paths both on satellite-earth and on terrestrial radio links. For radio-wave propagation in a clear-air turbulent atmosphere, one path remains preponderant and the scattered and diffracted field components are much smaller than the incident component. So, the time-varying small-scale variations of the atmospheric refraction generate rapid fluctuations of the amplitude, the phase and the angle-of-arrival of the received signals, called tropospheric scintillations, that become significant above 10 GHz.

On satellite-earth links, it has been observed that the strongest scintillations tend to occur during the passage of cumulus clouds through the propagation path. At 12 GHz, the cloud-induced turbulence yields, on a few meters receiving aperture, a peak-to-peak scintillation log-amplitude exceeding 3 dB on a 30° elevation path [1], while scintillation events of more than 15 dBtp have been measured on low-elevation links [2]. The scintillation intensity is proved to increase at higher frequencies, lower elevation and with smaller receiving antennas. The turbulence-induced scintillations influence on future low-margin VSAT communications systems at millimeter-waves cannot be neglected, especially at low elevation angles where long-term availability and performances are found to be predominantly governed by scintillation effects rather than rain [2].

On terrestrial links, scintillations are caused by turbulences in the atmospheric boundary layer. Up to now, only a few experiments have been undertaken to study in an extensive way the effects of atmospheric turbulences on line-of-sight radio links, but, according to some measurements, the turbulence theory and meteorological considerations, scintillation would certainly not be neglected on millimeter wave terrestrial communications systems. At 30 GHz, on a 4 km link, scintillation log-amplitude up to 5 dBtp could be measured. This scintillation amplitude grows with the frequency, the path length and with smaller receiving apertures.

The Microwaves Laboratory U.C.L. has developed deterministic models for the simulation of scintillation produced by clear-weather atmospheric turbulences. They are based on the physical mechanisms that create strong turbulences and yield significant scintillation of radio-waves. These models allow to retrieve the characteristics (size, temperature, humidity, ...) of a set of turbulent eddies from the measurement of the scintillation amplitude produced on a given link. They simulate the scintillation effect caused by such modelled eddies on millimeter-waves links characterized by the carrier frequency, the antenna aperture, the elevation angle or the length of the path. So, they offer the opportunity to assess the dependence of scintillation on various link parameters. Furthermore, they evaluate the influence of turbulences on the transfer function of the atmospheric channel during scintillation and finally, by using a communication systems simulating package (TOPSIM III), they predict the impact of scintillation on the performances (bit error rate, eyepattern) of communication systems.

### 3. THEORETICAL BACKGROUND

#### 3.1. Atmospheric turbulences

Turbulence is a feature of fluid flows that occurs at very high Reynolds number value. Turbulent flows are highly irregular and chaotic. Due to the random movement of fluid parcels, called turbulent eddies, turbulence carries out an intensive mixing of the fluid and then an homogenization of its physical features (temperature, humidity, ...). A turbulent flow can be regarded as a superposition of an average motion (laminar-like) and a fluctuating one. These fluctuations are caused by all sizes eddies; the largest ones receive their energy from interacting with the average motion and then break down in smaller and smaller eddies and transmit their energy in such a cascading process to the smallest eddies which are characterized by an intense viscous dissipation. The turbulent eddies sizes lie between the so-called outer scale  $L_o$ , of about 10 to 100 meters, corresponding to the instability of the medium, and the inner scale  $l_o$ , of about 1 mm, related to the fluid viscosity [2-5].

Atmospheric turbulences yield both time and space small-scale fluctuations of various features such as wind speed, temperature, humidity and refractive index. There are two main regions in the troposphere in which turbulence is likely to be strong [6] :

- in clouds, where turbulence results from the air entrainment process. It has been proved [1,7] that turbulence in cumulus clouds (especially fair weather cumulus) induces most of the scintillation effect observed on satellite link.

- in the lower part of the atmosphere, the surface boundary layer, where turbulent fluctuations produce the air mixing mechanism and are responsible for vertical transfer processes near the surface of the earth.

The well-known Kolmogorov theory of turbulence [2-5] assumes that, when the turbulent eddies sizes are far smaller

than the  $L_0$  outer scale and larger than the  $l_0$  inner scale of turbulence, respectively characterizing the introduction and dissipation of energy, in a so-called inertial subrange, the turbulent eddies can be considered as homogeneous and isotropic.

Although turbulence induces both space and time fluctuations of atmospheric features, the Taylor's frozen-in hypothesis [2-5], considered valid in most atmospheric turbulences, assumes that the eddies of a certain size  $l$  do not appreciably change their shape within the time required for the eddies to move the distance  $l$  and allows then to relate the space and time variations from the mean wind speed.

It must finally be pointed out that the major effect of the turbulence on the propagation of waves comes from the inhomogeneities of the refractive index  $n$  induced by the temperature and humidity turbulent fluctuations. The intensity of the turbulence can then be related to the structure function  $D_n$  and the structure parameter  $C_n^2$  of the index of refraction, which are directly proportional to the turbulent random variations of the refractive index.

### 3.2. Propagation of radio-waves in a turbulent atmosphere

Atmospheric turbulence affects the propagation of radio waves by creating random variations of the refractive index that yield amplitude, phase and angle-of-arrival fluctuations of the received signal, called scintillation. Scintillation may become significant above a frequency of a few gigahertz.

Amplitude scintillation is the most easily measured feature and is generally studied on beacons at fixed frequency. It can be characterized by:

- the log-amplitude  $\chi$  (in dB), that is the ratio of the instantaneous amplitude of the observed signal to the mean amplitude. This mean amplitude is generally calculated by a 60 seconds moving average filter [8], in order to separate rapid turbulence induced scintillation from "long term" time instability of the receiver or time variability of hydrometeors attenuation.

- the scintillation variance  $\sigma_\chi^2$  in  $\text{dB}^2$  or intensity  $\sigma_\chi$  in dBrms, that are respectively the variance and the root mean square value of the log-amplitude  $\chi$ . In order to be a good estimator of the instantaneous scintillation "level" and accounting for the time-variability of the scintillation intensity, the variance is generally calculated in a moving way on about one minute [9].

- the scintillation power spectral density  $W_\chi$  in  $\text{dB}^2/\text{Hz}$ , that is the spectrum of the scintillation log-amplitude. To insure a relevant signification to the scintillation spectrum, this spectrum has to be computed on a period within which the scintillation random process can be reasonably well considered as stationary. This approximation is valid only within a limited time of a few minutes [4-6] (generally about ten minutes [10]), during which the scintillation variance can be regarded as constant.

The problem of wave propagation through a turbulent medium has been quite well dealt in the literature. The theory was first attached to optical propagation [3] but afterwards extended to microwave transmission [4,11]. Thanks to this theory, statistical

characteristics of a scintillation event such as  $\sigma_\chi^2$  or  $W_\chi$  can be

related to the structure parameter  $C_n^2$ , which is a measure of the turbulence induced refractive index inhomogeneities. Theoretically, the scintillation spectrum  $W_\chi$  has the well-known pattern of a white noise low-pass filtered with a  $-8/3$  slope, for fully developed turbulence.

The major assumptions assumed to obtain the theoretical relations are:

- the Kolmogorov theory of turbulence is used to express the spectrum of the refractive index as a function of the structure parameter

- the incident wave is supposed to be a plane wave. Theoretical results are also available for the propagation of spherical waves [3, 5]. Their form do not vary significantly but the mean square log-amplitude fluctuations of a spherical wave are approximately 2.5 times smaller than the corresponding plane-wave fluctuations in the same conditions.

- a smooth perturbation method is used to determine the effect of refractive index inhomogeneities on wave propagation and that assumes weak scintillation:  $\sigma_\chi^2 \ll 1$ .

## 4. IMPACT OF ATMOSPHERIC TURBULENCES ON SATELLITE COMMUNICATIONS

### 4.1. Theoretical and experimental characterization of scintillation on satellite links

#### 4.1.1. Statistical distribution of the scintillation amplitude

Various studies have investigated the statistical distribution of the scintillation log-amplitude. It seems that a scintillation event is characterized by a stationary period of a few minutes (up to ten or fifteen minutes). Within this period, the scintillation log-amplitude distribution can be quite well fitted by a gaussian distribution which variance is the mean variance of the event during the period [12].

For a period longer than a few minutes, the distribution widens and the long-term probability density function of scintillation amplitude can be modelled by a gaussian distribution which variance follows a log-normal curve [13-15].

#### 4.1.2 Scintillation spectra

When the stationary period of a scintillation event has been determined, the scintillation spectrum can be calculated during this period. It is also possible to theoretically deduce the shape of the scintillation spectrum which is related to the measured scintillation variance of the stationary event. Measured and calculated spectra have been compared during scintillation events and are in very good agreement [16].

#### 4.1.3. Influence of the frequency

According to the theory, the scintillation variance  $\sigma_\chi^2$  increases

with the carrier frequency as  $f^{7/6}$ . By receiving two different beacons (12.5 - 20 GHz and 12.5 - 30 GHz) with the same antenna, the Belgian experiment with the Olympus satellite of E.S.A. allowed to experimentally investigate the frequency

dependence of the scintillation signals. It results that, on an event basis, there is a very good correlation between the signals received at different frequencies and that the measured frequency dependence is in general agreement with the theoretical law [9,17]. However, on a statistical basis (one year), first results from the Research Institute of the Deutsche Bundespost Telekom at Darmstadt seem to point out an higher measured increase of the scintillation variance with the frequency than theoretically predicted (as about  $f^{1.34}$ ) [12].

#### 4.1.4. Influence of the antenna aperture

The CCIR [18] proposes a theoretical relation to account for the influence of the receiving aperture on the scintillation. It predicts a decrease of the scintillation variance measured with a larger antenna, due to the spatial averaging on the receiving aperture. The theoretical expression of the antenna aperture smoothing effect on scintillation has been validated by experiments up to about 30 GHz [7, 19, 20]. Moreover, a larger antenna also induces a low-pass filtering effect on the scintillation spectrum with a steeper roll-off [21].

#### 4.1.5. Influence of the elevation angle

It is a fact that the scintillations are more intense on low elevation links. Scintillation amplitudes of 15 to 20 dBtp have been observed for elevation angles smaller than  $10^\circ$  at frequencies of about 10 GHz [2, 22-25].

According to the theory, the scintillation variance depends on the elevation angle as  $(\sin(\theta))^{-11/6}$ . This dependence is valid above about  $10^\circ$  elevation [22], but for lower elevation links some experiments have shown different elevation dependences of the observed scintillation variance :  $(\sin(\theta))^{-11/6}$  according to Hodge et al. [23],  $(\sin(\theta))^{-1}$  according to Vilar and Larsen [22] and  $(\sin(\theta))^{-2.6}$  according to Kurasawa et al. [24]. Furthermore, it seems that at low elevations the cloudy turbulences are not the principal cause of scintillations. No evidence of correlation has been found between the observation of scintillations on a low elevation link and the cloudy cover [25]. Another mechanism would be more likely to produce such intense scintillations : atmospheric multipaths [25].

#### 4.1.6. Diurnal and seasonal distribution of scintillation

Some experiments [26, 27] have shown that scintillation events have significant diurnal and seasonal dependences. Scintillations preferentially occur in summer and in the early afternoon. Correlations between scintillations and ground temperature or humidity has been obvious: higher are the temperature and humidity, more intense is the scintillation amplitude [15, 20, 25].

#### 4.1.7. Influence of rain

Scintillation has generally been investigated during clear-weather, but it also occurs in the presence of rain. In that case, scintillation (very short term variation) has to be separated from attenuation (rather long-term variation) by an adequate filtering. It has been proved that the scattering from raindrops could only be responsible for a small amount of the measured scintillation [28]. The scintillation can then be imputed to turbulence rather than to rain. Wind gusts however produce rapid attenuation variations that are superimposed on scintillation and prevent from distinguishing in the spectral domain scintillation and attenuation [12]. On a statistical basis, results from Darmstadt [12] show that the probability to have a given scintillation intensity is higher during rain than during clear-weather, this

can be attributed to the higher probability of the occurrence of cloud induced turbulence during rain.

### 4.2. Modelling of the cloud induced scintillation on satellite links

The Microwaves Laboratory U.C.L. is involved for more than ten years in the study of atmospheric turbulences and of their impact on satellite communications systems. The combination of measurements of turbulence induced scintillation, made first with the O.T.S. satellite at 12 GHz and now with the Olympus satellite at 12.5, 20 and 30 GHz, as well as theoretical developments produced a deterministic model for cloudy turbulences [1,16,29,30].

The model accounts for the physics of the air entrainment process that generates turbulent eddies in cumulus convective clouds from the mixing of two air masses of different temperatures and humidities and that induces refractive index inhomogeneities. The cloudy turbulent area responsible for scintillation is modelled by a layer of turbulent eddies of various sizes. Each turbulent eddy is represented by an homogeneous dielectric cell immersed in the surrounding medium. The geometry of the cell is cylindrical, although spheres seem more natural at first sight, for two different reasons : convection induces a geometry which is vertically elongated and more than one eddy may affect the earth-space link. The cylinders used in the model often represent more than one eddy and their height then represents the effective path in the turbulent layer (Figure 1). The cells are located at an altitude of about 2000 m, which typically corresponds to the upper boundary of a cumulus cloud and to the actual detected altitude of eddies [20]. The physical features of the surrounding medium are those of the medium outside the cloud, while the turbulent cells have the typical cloudy humidity and liquid water content; so, the model accounts for the small scale refractive fluctuations that produce scintillation. The sizes of the turbulent cylinders are about ten meters, in relation with the turbulent outer scale, and the cells are moved across the link with the mean wind speed. The influence of such dielectric cells on the electric fields emitted by a satellite and considered as plane waves has been determined by using the Kirchhoff-Huygens diffraction method, which is proved to be valid in that case [1]. The signal received by a parabolic antenna after diffraction by turbulent eddies has been calculated and, when realistic characteristics are chosen for the dielectric cells, it looks like actual scintillation [29, 30].

Furthermore, the atmospheric turbulent configuration that induces an observed scintillation event has been determined by inverting the model. Thanks to the turbulence theory and the physics of clouds, it is possible to retrieve from the observation of a scintillation event the physical and geometrical properties of a bidimensionnal network of turbulent cells that, by crossing the link under the wind effect, produce statistically the same scintillation characteristics on the simulated received signal as on the observed event. The physical features (temperature, pressure, humidity) of the surrounding medium at the turbulent layer height are determined from ground meteorological data assuming standard atmospheric profiles. The cells physical characteristics are considered to vary from surroundings only by humidity, because the turbulence induced humidity fluctuations is far the main cause of centimeter- and millimeter-waves scintillation. It is moreover assumed that the cloudy cylinders content suspended water droplets. The relative humidity of the cells has a cloud typical value around the saturation, while the liquid water content is about  $1 \text{ g/m}^3$ , the most plausible value for cumulus clouds.

Dielectric cylinders are characterized in such a way to verify all the theoretical relations between their physical and geometrical features, the measured scintillation characteristics and the link parameters (frequency, receiving aperture, elevation angle). Their influence on the satellite-earth path, when they cross the link with the assessed wind speed, is simulated and the cells are chosen in such a manner to induce the same simulated log-amplitude scintillation cumulative distribution as the observed event. That way, a sequence of turbulent cells is determined that produce on the satellite link a simulated scintillation statistically similar to the observed event. The modelled cells induce then the same peak-to-peak amplitude, the same mean scintillation variance and, because they satisfy the turbulence theory and they are moved with the actual wind speed, the scintillation spectrum calculated from the simulated event has the same pattern and the same corner frequency as the measured one.

So, physical modelling of cloud produced scintillation allows to extract the turbulent atmospheric configuration from scintillation measurement and to simulate the scintillation effect induced by this phenomenon on a satellite link.

The simultaneous measurements of the 12.5 and 30 GHz beacons of the Olympus satellite of the European Space Agency, at the Louvain-la-Neuve belgian station, with the same 1.8 m antenna, under a 30° elevation, offer a good opportunity to validate the model. From the scintillation event measured at 12.5 GHz, the eddies of the cloudy turbulent layer are retrieved. Their effect on the satellite link is then simulated at the 12.5 and 30 GHz frequencies. These simulated scintillation events are finally compared with the actual measured events at the same frequency.

This validation process has been performed on 25 events observed at Louvain-la-Neuve and the mean discrepancy between the measured and simulated scintillation effects on the basis of about 12 scintillation parameters (log-amplitude, variance, scintillation spectrum, corner frequency, ...) is less than 20% [16]. Moreover, the size of the modelled turbulent eddies and the refractive index structure parameter they induce are in good agreement with values found in the literature.

#### 4.3. Simulation of the influence of link parameters on scintillation

After having modelled the cloudy turbulent layer from scintillation data, it is possible to simulate its influence on various satellite links, characterized by their frequency, their elevation angle and their receiving aperture. It has been obtained [16, 31] that the simulated dependence of scintillation characteristics on link parameters are in very good agreement with theory and experiment. The results of the model corroborate the tendency of scintillation to increase with high frequency, small aperture and low elevation.

As examples, figure 2 shows the frequency dependence of the scintillation variance as simulated between 20 and 30 GHz from 20 modelled events. The regression line of the scatterplot (continuous line) is in good agreement with the theoretical dependence of scintillation on frequency (dashed line). Figure 3 plots the low-pass effect of a larger antenna on the scintillation spectrum as simulated at 20 GHz. The scintillation spectra simulated on a 1.8 m (continuous line) and 8 m (dashed line) are in very good agreement with the respective theoretical patterns determined from [21]. Figure 4 displays the influence of the elevation angle on the scintillation log-amplitude. The comparison of the scintillation simulated at 30° (continuous

line) and 15° (dashed line) elevation shows the increase of scintillation intensity at low elevation.

#### 4.4. Broadband characterization of the atmospheric channel during turbulences

Once modelled the cloudy turbulent eddies, not only the induced time-variant scintillation but also the frequency variation of the received signal for a fixed position of the cloud can be simulated. The simulation of the influence of turbulence in the frequency domain represents the transfer function of the atmospheric channel at a given time during the scintillation event. It has been shown [16, 32] that the coherence bandwidth of the simulated transfer function for a 30° elevation link with a 1.8 m receiving antenna is about a few tens of gigahertz, as experimentally observed [33]. But with a smaller antenna or at lower elevation, the turbulence induced transfer function seems to be more frequency selective and the coherence bandwidth can reduce to less than 1 GHz. So, atmospheric turbulences could limit the bandwidth of transmission at millimeter waves.

As an example, figure 5 shows the simulated transfer function amplitude of an atmospheric channel during turbulences for various elevation angles of the satellite link.

#### 4.5. Prediction of the impact of scintillation on the performances of communications systems

The atmospheric transfer function can then be used as a channel filter in a communication system simulation package, as TOPSIM, in order to quantify the impact of scintillation on the performances of realistic communication systems, in terms of bit error rate for example [16]. Figure 6 shows the simulation of the impact of a modelled scintillation event on the performance of a 30 GHz, coherent quadrature PSK communication system, transmitting 200 Mbit/s in a 100 MHz channel. The transmitter and receiver filters are raised cosines. The elevation angle is 30° and the antenna diameter is 1.8 m. The performance diagram displays the Bit Error Rate as a function of the mean  $E_b/N_0$  ratio. The continuous line represents the ideal BER curve, while the two dashed lines account for the extreme fluctuations of the performances during the extreme enhancement and fading of the scintillation event.

A further investigation [16] has proved that broadband communication systems could be dramatically damaged by scintillation at high frequencies, on low elevation links and with small receiving apertures.

### 5. IMPACT OF ATMOSPHERIC TURBULENCES ON LINE-OF-SIGHT COMMUNICATIONS

#### 5.1. Theoretical and experimental characterization of scintillation on terrestrial links

It has to be pointed out that it is difficult to clearly and completely characterize scintillation on line-of-sight paths because very few experiments have been undertaken to study this phenomenon and the environment of the experimental links is highly variable.

##### 5.1.1. Statistical distribution of the scintillation amplitude

Herben [34] has shown that on a period of about 15 minutes, the scintillation amplitude follows a gaussian distribution, this is in agreement with results obtained on earth-space path scintillation: within a stationary period, the scintillation log-amplitude distribution can be quite well fitted by a gaussian



distribution which variance is the mean variance during the period.

### 5.1.2. Scintillation spectrum

Most of the experimenters have proved that the measured scintillation spectrum has the theoretical pattern of a white noise low-pass filtered with a  $-8/3$  slope.

### 5.1.3. Influence of the frequency

According to the theory [3, 4], the scintillation variance is proportional to either the  $7/6$  power or the square of the frequency depending on the respective size of the outer scale of the turbulence  $L_0$  and  $\sqrt{\lambda L}$ , where  $\lambda$  is the wavelength and  $L$  the length of the link. The instantaneous measurements of the scintillation signal at two frequencies in London [35] give the opportunity to analyze the frequency dependence of scintillation. It appears that the scintillation variance seems to follow the theoretical laws: sometimes  $\sigma_\chi^2$  varies as  $f^{7/6}$

(if  $L_0 \gg \sqrt{\lambda L}$ ), sometimes as  $f^2$  (if  $L_0 \ll \sqrt{\lambda L}$ ) and when  $L_0 \approx \sqrt{\lambda L}$ , the frequency dependence lies between these two boundaries. There is however no indication on the occurrence of each case.

### 5.1.4. Influence of the length of the link

Theoretically [3, 4], the scintillation variance varies as  $L^{11/6}$ , if the outer scale of the turbulence  $L_0$  is far larger than  $\sqrt{\lambda L}$ , and as  $L$  in the opposite case.

### 5.1.5. Effect of the antenna aperture

The CCIR [18] predicts the smoothing effect of large receiving antennas on scintillation.

Only one experiment (Texas [36]) has run with two different antennas. The result is that the measured ratio of the scintillation variances of the large (4.9 m) to the small (0.1 m) aperture (between 0.6 and 0.9) is in general agreement with that predicted due to the effect of aperture smoothing (about 0.6). Moreover, the scintillation spectrum shows a steeper slope for the larger receiving antenna.

### 5.1.6. Refractive index structure parameter $C_n^2$

Various experiments (34, 37, 38) have deduced values for the refractive index structure parameter  $C_n^2$  from meteorological observations. Their results are that  $C_n^2$  could rise during the experiment up to  $1.5 \cdot 10^{-13}$  [34] or  $6 \cdot 10^{-12} \text{ m}^{-2/3}$  [37]. According to the theory, such values of the turbulence intensity could yield scintillation up to 4 to 5.5 dBptp on a 4 km link at 30 GHz.

### 5.1.7. Spherical or plane waves

Most of the experimenters assume the propagation of a plane wave. But, while the London experiment (36 and 55 GHz, 4.1 km) [39] has proved that the plane wave case gives closer fit to the measured scintillation spectrum than the spherical case, the Flatville experiment (173 GHz, 1.4 km) [37] found a good agreement between the theory for spherical waves and the measured scintillation variance.

### 5.1.8. Influence of hydrometeors

The Eindhoven [34] and Flatville experiments [37] have investigated the influence of rain on measured scintillation. Both experiments predict a broadening of the scintillation spectrum towards the high frequency component during rain, due to the incoherent scattering on the hydrometeors to be added to the turbulence induced scintillation. At Eindhoven, it was moreover observed an increase of the scintillation amplitude during slight rain, while, at Flatville, clear-weather during hot and humid summer days yields the severest scintillation events.

## 5.2. Modelling of the scintillation on line-of-sight paths due to turbulences in the lower atmosphere

The scintillation that affects line-of-sight links is due to turbulences in the surface boundary layer, the lower part of the atmosphere. According to the meteorological literature [40,41], in the lower atmosphere, intense turbulence with large eddies occurs during convective unstable conditions that can be especially met on sunny days, around noon. It is moreover generally assumed that the ground is fairly flat, so that an horizontal homogeneity of the mean features exists in this layer.

At the typical height of a radio link (about 50 m), it can be assumed [41,42] that the mechanical source of turbulence, related to the horizontal wind shear, may be neglected versus the buoyancy effects produced by the temperature and humidity upwards directed flux. The physical process that produces turbulent eddies can then be compared to a free convection mechanism and schematized as follows [42]. Turbulent eddies generated by the mean motion travel quasi-statically without any exchange of features with the surroundings. Because of the horizontal homogeneity, this turbulent transfer, established from regions with a higher mean concentration to such with a lower concentration, should be only observed in the vertical direction. The physical characteristics of the eddies (temperature, humidity, ...) in the place of their origination are equal to the averaged characteristics on this level. They are then conserved during the eddies ascent. Successively passing through the point of observation, the eddies cause fluctuations equal to the difference between the 'brought up' feature and the averaged one on the level of observation. After passing some finite length, called the vertical mixing length, which is proportional to the height above the ground (about  $0.4 z$ ) and is an approximation of the turbulent outer scale, the eddies dissolve into the flow and deliver the features which they carry. The vertical motion of these turbulent eddies should be at a speed of the order of a few to a few tens of centimeters per second. Finally, the turbulent eddies are horizontally transported across the link by the mean motion.

In order to model this physical process, we represent the turbulent eddies piled along the path by cylinders parallel to the horizontal link (cfr fig. 7). Considering an horizontal homogeneity, it is assumed that the mean temperature and humidity of the atmosphere vary with height according to standard profiles. The features of the air inside the cylinders correspond then to the temperature and humidity of the origination place where the eddies were formed before they ascend with the convective flux. So, the model accounts for the mixing process that produces refractive index inhomogeneities at the height of the link. Furthermore, the radius of each cylinder, which is related to the size of the spherical eddies piled along the path, can be theoretically assessed from the refractive index variations (depending on the origination height) and the length of the cylinder depends on the intensity

of the scintillation effect produced on the radio link. Finally, the cylinders move transversely across the link with the mean transverse wind speed.

In the same way as for the cloud produced scintillation, we have inverted this model in order to extract the characteristics of the turbulent configuration, represented by a bi-dimensional set of dielectric cylinders, that produces a given scintillation event on a certain line-of-sight link.

### 5.3. Simulations of the impact of atmospheric turbulences on terrestrial links

Once modelled the turbulent configuration, simulation of the scintillation amplitude can be performed on links characterized by the carrier frequency, the length and the antenna apertures.

As examples, figure 8 shows a scintillation event simulated at 30 GHz, on a 4 km link, with 1.8 m antenna apertures; it looks like actual scintillation amplitude. Figure 9 plots the scintillation spectrum of this simulated event; it is in good agreement with the theoretical pattern (dashed line). The dependence of the scintillation variance on the various link parameters can also be highlighted by this model: figure 10 represents a scatterplot of the scintillation variance simulated at 50 GHz versus variance at 30 GHz; the regression line follows a  $f^{1.4}$  frequency dependence, between the two theoretical asymptotic boundaries  $f^{7/6}$  and  $f^2$ .

Further investigations are needed to validate this model for scintillation on terrestrial links.

## 6. CONCLUSION

Both on satellite and horizontal links, atmospheric turbulences induced scintillation cannot be neglected above 10 GHz. In order to predict the impact of scintillation on millimeter-waves communication systems, two deterministic physical models have been developed. They allow to extract the characteristics of the turbulent eddies that yield scintillation, to simulate the scintillation effect on given links, to characterize the transfer function of the atmospheric channel during scintillation and finally to assess the influence of scintillation on the performances of communication systems.

A first model is dedicated to the cloud induced turbulence that affects space-earth paths. It has been validated thanks to measurements and gives results in good agreement with the theory. A second model, representing the turbulences in the lower atmosphere that damage line-of-sight links, is proposed. First results agree with theory, but further investigations and especially experiments are requested to improve and validate it.

## 7. ACKNOWLEDGEMENTS

The authors would like to thank Professor A. Vander Vorst for many fruitful discussions on this subject and the European Space Agency for having partially supported this research under ESA P.O.113272.

## 8. REFERENCES

- [1] Vanhoenacker, D., *Modèle radioélectrique pour la scintillation observée aux hyperfréquences sur les liaisons satellite-terre*, Ph.D. Thesis, U.C.L., April 1987.
- [2] Bryant, D.L., Low elevation angle 11 GHz beacon measurements at Goonhilly earth station, *BT Technology Journal*, vol. 10, n°4, pp. 68-75, October 1992.
- [3] Tatarskii, V.I., *The Effects of the Turbulent Atmosphere on Wave Propagation*, Israel program for Scientific Translations, Jerusalem, 1971.
- [4] Ishimaru, A., *Wave Propagation and Scattering in Random Media*, vol. 2, Academic Press, New York, 1978.
- [5] Nihoul, J.C., *Modèles mathématiques et Dynamique de l'environnement*, Ele, Liège, 1977.
- [6] Lumley, J.A., Panofsky, H.A., *The Structure of Atmospheric Turbulence*, John Wiley, New York, 1964.
- [7] Cox, D., Arnold, H., Hoffman, R., *Observations of Cloud-produced Scintillation on 19 and 28 GHz Earth-space Paths*, *Radio Science*, vol. 16, n°5, pp. 885-907, September 1981.
- [8] Rücker, F., *Description of the dynamic behavior of the Olympus beacon signals by the signal variance and fade slope*, *Proc. of the 15th OPEX meeting*, pp. 46-69, ESTEC, The Netherlands, April 1991.
- [9] Vanhoenacker, D., Matagne, J., Vasseur, H., Vander Vorst, A., *First Analysis of the Effect of Atmospheric Fluctuations on the 12.5, 20 and 30 GHz Olympus Beacons*, *First OPEX Workshop Proc.*, pp. 4.2.1.-4.2.7., ESTEC, The Netherlands, April 1991.
- [10] Vanhoenacker, D., Matagne, J., Vasseur, H., Vander Vorst, A., *Spectral Analysis of Scintillation Events from Belgian Olympus Experiment*, *Proc. 16th OPEX meeting*, pp. 32-40, Aveiro, Portugal, October 1991.
- [11] Clifford, S., Strohbehn, J., *The theory of microwave line-of-sight propagation through a turbulent atmosphere*, *IEEE Trans. Ant. Prop.*, vol. AP-18, n°2, pp. 264-274, 1970.
- [12] Vanhoenacker, D., *Impact of Atmospheric Turbulences on Earth-Space Propagation*, *The results of the Olympus Utilisation Program Conf.*, Sevilla, April 1993, to be published.
- [13] Mousley, T.J., Vilar, E., *Experimental and theoretical statistics of microwave amplitude scintillations on satellite down-links*, *IEEE Trans. Ant. and Prop.*, vol. AP-30, n°6, pp. 1099-1106, November 1982.
- [14] Ortgies, G., *Probability density function of amplitude scintillations*, *IEE Electr. Letters*, vol. 21, n°4, pp. 141-142, February 1985.
- [15] Banjo, O.P., Vilar, E., *Measurement and modelling of amplitude scintillations on low-elevation earth-space paths and impact on communication systems*, *IEEE Trans. Communications*, vol. COM-34, n°8, pp. 774-780, August 1986.
- [16] Vanhoenacker, D., Vasseur, H., Amaya, C., Vander Vorst, A., *Atmospheric Model for Cloud Produced Scintillation and Evaluation of its Impact on Communications Signals*, *ESA P.O. n°113272*, June 1992.
- [17] Vanhoenacker, D., Matagne, J., Vasseur, H., Vander Vorst, A., *Scintillation and depolarisation results from the Belgian Olympus experiment*, *Proc. 21st European Microwave Conf.*, pp. 961-967, Stuttgart, September 1991.
- [18] C.C.I.R., *Rapport 718-3, Propagation dans les milieux non ionisés*, vol. 5, 1990.
- [19] Herben, M., *The influence of tropospheric irregularities on the dynamic behaviour of microwave radio systems*, Ph. D. Thesis, T.U.Eindhoven, February 1984.
- [20] Rücker, F., Dintelmann, F., *Effect of antenna size on OTS signal scintillation and their seasonal dependence*, *Electr. Letters*, vol. 19, n°24, pp. 1032-1033 (part 2), November 1983.
- [21] Haddon, J., Vilar, E., *Scattering induced microwave scintillations from clear air and rain on earth space paths and the influence of antenna aperture*, *IEEE Trans. Ant. and Prop.*, vol. AP-34, n°5, pp. 646-657, May 1986.
- [22] Vilar, E., Larsen, J., *Elevation Dependence of Amplitude Scintillations on Low Elevation Earth Space Paths*, *Int. Conf. Ant. and Prop. (ICAP'89)*, I.E.E. Conf. Pub. 301, pp. 150-154, 1989.

- [23] Hodge, D.B., Theobald, D.M., Devasirvatham, D.M., Amplitude scintillation at 2 and 30 GHz on earth-space paths, URSI Comm. F Conf., La Baule, pp. 421-425, 1977.
- [24] Karasawa, Y., Matsudo, T., Characteristics of Fading on Low-Elevation Angle Earth-Space Paths with Concurrent Rain Attenuation and Scintillation, I.E.E.E. Trans. on Ant. and Prop., vol. 39, n°5, pp. 657-661, May 1991.
- [25] Larsen, J., Upton, S., Analysis of Propagation Data from Low Elevation Measurements in Denmark, Final Report ESA/ESTEC purchase order 101378, May 1991.
- [26] Vander Vorst, A., Vanhoenacker, D., Mercier, L., Fluctuations on the OTS-earth copolar link against diurnal and seasonal variation, Electr. Letters, vol. 18, n°21, pp. 915-916, 1982.
- [27] Ortgies, G., Rücker, F., Diurnal and seasonal variations of OTS amplitude scintillations, Electr. Letters, vol. 21, n°4, pp. 143-145, February 1985.
- [28] Ortgies, G., Amplitude scintillations occurring simultaneously with rain attenuation on satellite links in the 11 GHz band, 4th Intl. Conf. on Ant. and Prop., IEE Conf. Pub. 248, pp. 72-76, April 1985.
- [29] Vanhoenacker, D., Vasseur, H., Amaya-Byrne, C., Simulations of the effects of atmospheric scintillation on digital transmissions at centimeter and millimeter wavelengths, Int. J. of Infrared and Mm Waves, vol. 10, n°10, pp. 1215-1224, October 1991.
- [30] Vanhoenacker, D., Vasseur, H., Vander Vorst, A., Limitations de la largeur de bande dues aux phénomènes atmosphériques sur des liaisons spatiales de 10 à 300 GHz, L'Onde Electrique, vol. 72, n° 3, pp. 35-38, mai-juin 1992.
- [31] Vasseur, H., Vanhoenacker, D., Simulation of the Impact of Cloud Induced Scintillations on Satellite Links, 22nd Intl. Conf. on Ant. and Prop., I.E.E. Conf. Pub. 370, part 1, pp. 119-122, Edinburgh, March-April 1993.
- [32] Vanhoenacker, D., Vasseur, H., Vander Vorst, A., The Effects of Atmospheric Turbulences on Broadband Communication Channels above 10 GHz, I.E.E.E. Intl. Conference on Communications, vol. 2 of 4, pp. 1064-1068, Chicago, June 1992.
- [33] Cox, D., Arnold, H., Leck, R., Phase and amplitude dispersion for earth-satellite propagation in the 20-to-30 GHz frequency range, I.E.E.E. Trans. on Ant. and Prop., vol. 28, n°3, pp. 359-366, May 1980.
- [34] Herben, M., The influence of tropospheric irregularities on the dynamic behaviour of microwave radio systems, Ph. D. Thesis, Eindhoven University of Technology, February 1984.
- [35] Medeiros Filho, F., Jayasuriya, D., Cole, R., Spectral density of amplitude scintillations on a 55 GHz line-of-sight link, Electronics Letters, vol. 17, n° 1, pp. 25-26, January 1981.
- [36] Vogel, W., Davis, J., Mayer, C., Line-of-Sight Observations at 86 GHz with a Very Large and a Small Antenna, I.E.E.E., Trans. on Antennas and Propagation, vol. 32, n°2, pp. 113-118, February 1984.
- [37] R. McMillan, R. Bohlander, An Investigation of Millimeter Wave Propagation in the Atmosphere: Measurement Program, U.S. Army Research Office Contract Number DAAG29-81-K-0173, June 1987.
- [38] Helmis, C., Asimakopoulos, D., Caroubalos, C., Cole, R., Medeiros Filho, F., Jayasuriya, D., A quantitative comparison of the refractive index structure parameter determined from refractivity measurements and amplitude scintillation measurements at 36 GHz, I.E.E.E. Trans. on Geoscience and Remote Sensing, vol.21, n°2, pp. 221-224, April 1983.
- [39] Siqueira, G., Cole, R., Temporal-Frequency Spectra for Plane and Spherical Waves in a Millimetric Wave Absorption Band, I.E.E.E. Trans. on Antennas and Propagation, vol. 39, n°2, pp. 229-235, February 1991.
- [40] De Moor, G., Les théories de la turbulence dans la couche limite atmosphérique, Cours et Manuel, Ministère des transports, Direction de la Météorologie, France, octobre 1983.
- [41] Lumley, J.A., Panofsky, H.A., The Structure of Atmospheric Turbulence, John Wiley, New York, 1964.
- [42] S. Panchev, Dynamic Meteorology, Reidel Publishing Company, Dordrecht, 1985.

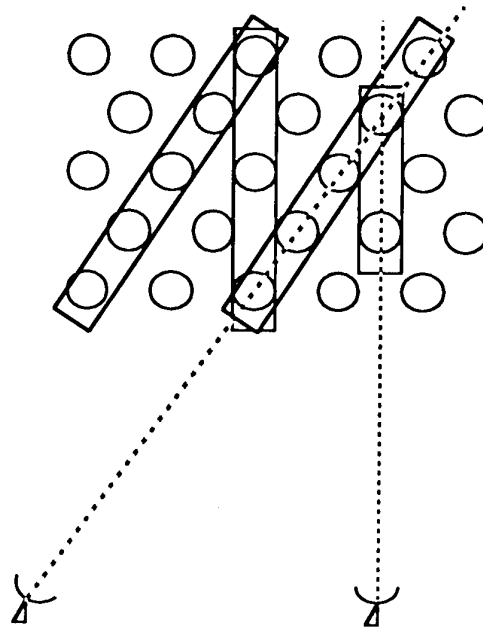


**FIGURE 1** Modelling of the cloud induced turbulence

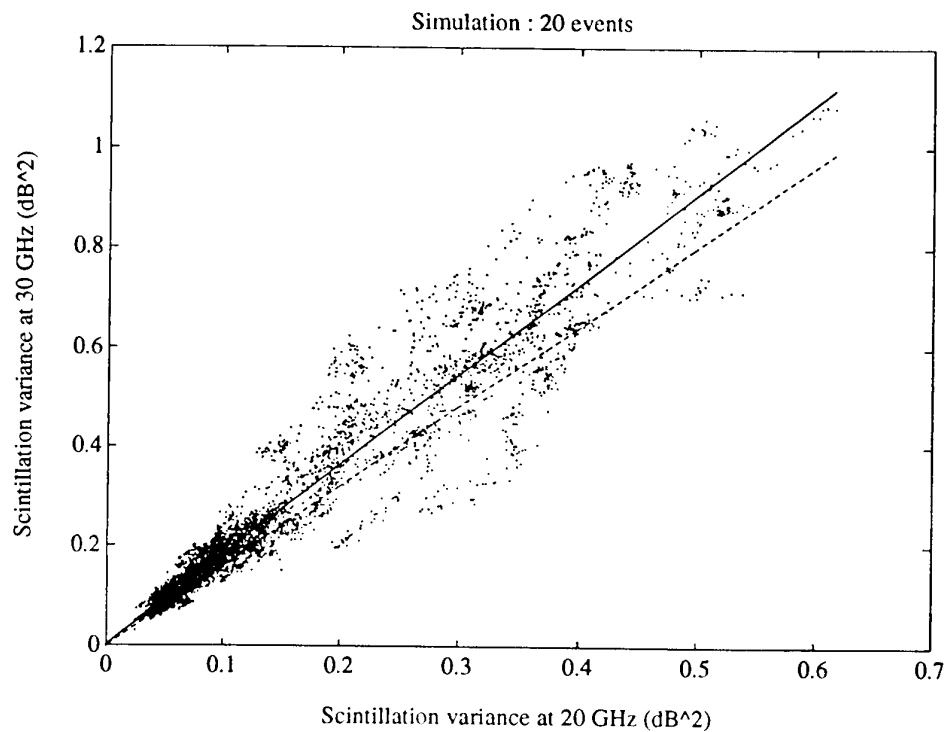


**FIGURE 2** Scatterplot of the scintillation variance at 30 GHz versus the variance at 20 GHz as simulated from 20 modelled events. The continuous line is the regression line and the dashed line corresponds to the theoretical dependence of scintillation variance on frequency. The antenna aperture is 1.8 m and the elevation angle  $30^\circ$ .

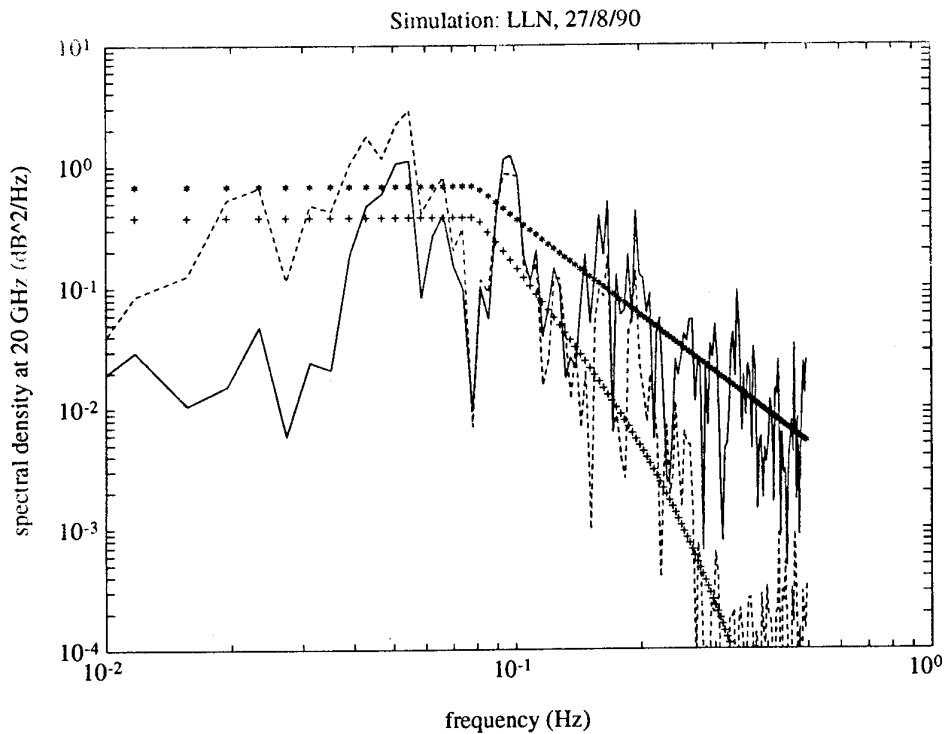


**FIGURE 3** Simulation of the scintillation spectra for a 1.8 m (—) and a 8 m (---) aperture, with their respective theoretical patterns (\*\*\*) and (+++). The frequency is 20 GHz and the elevation angle 30°.

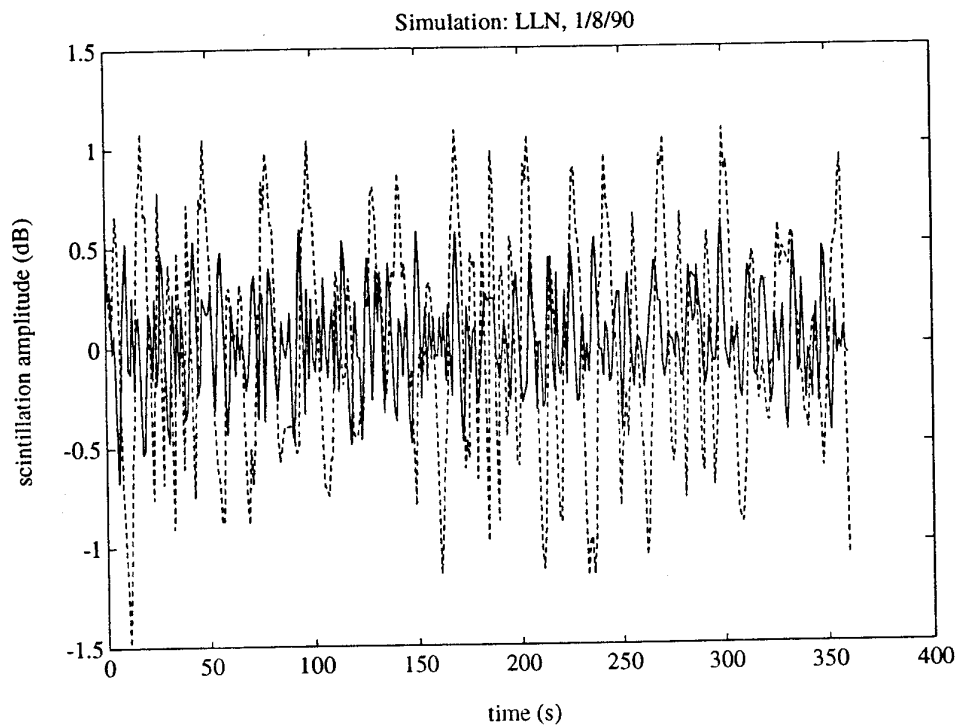


**FIGURE 4** Simulation of the scintillation amplitude for a 30° (—) and a 15° (---) elevation link. The frequency is 20 GHz and the antenna aperture 1.8 m.

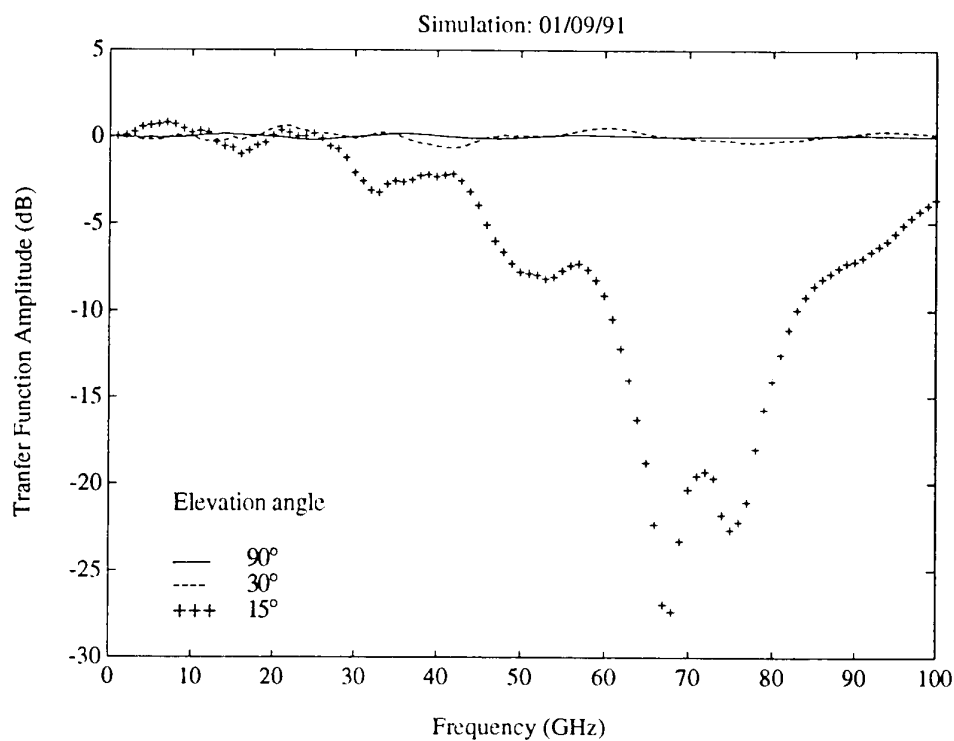


**FIGURE 5** Simulation of the transfer function amplitude during scintillation for various elevation angles. The antenna aperture is 1.8 m.

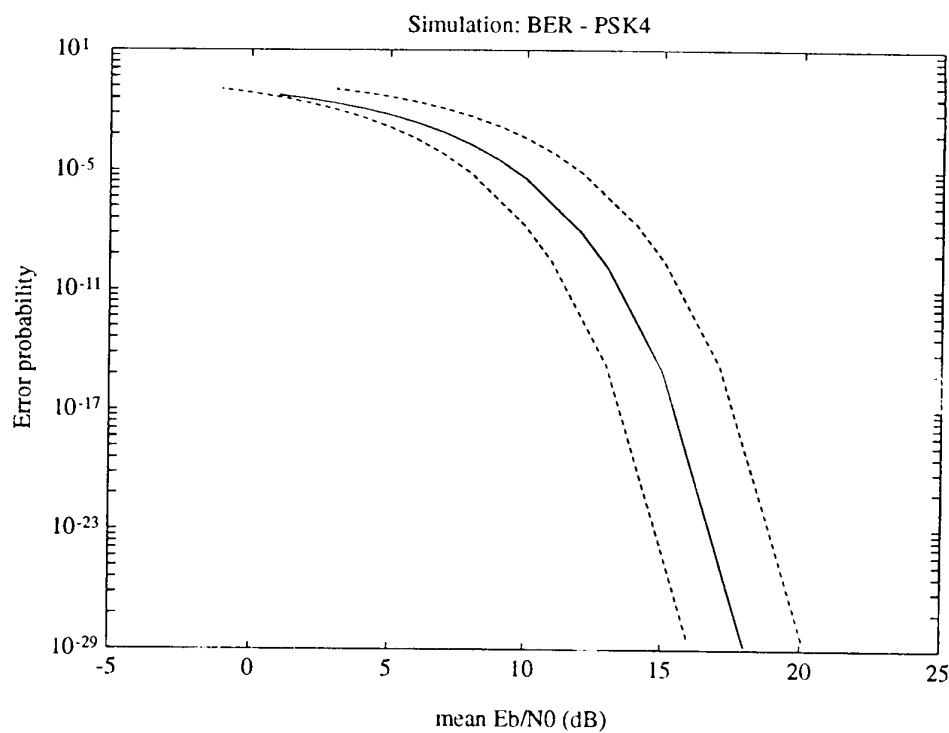


**FIGURE 6** Simulation of the bit error rate performances of a 200 Mbit/s QPSK communication link during a scintillation event. The carrier frequency is 30 GHz, the antenna aperture 1.8 m and the elevation angle 30°. The continuous line corresponds to the ideal performances and the dashed lines to the maximum enhancement and degradation of the performances during the considered scintillation event.

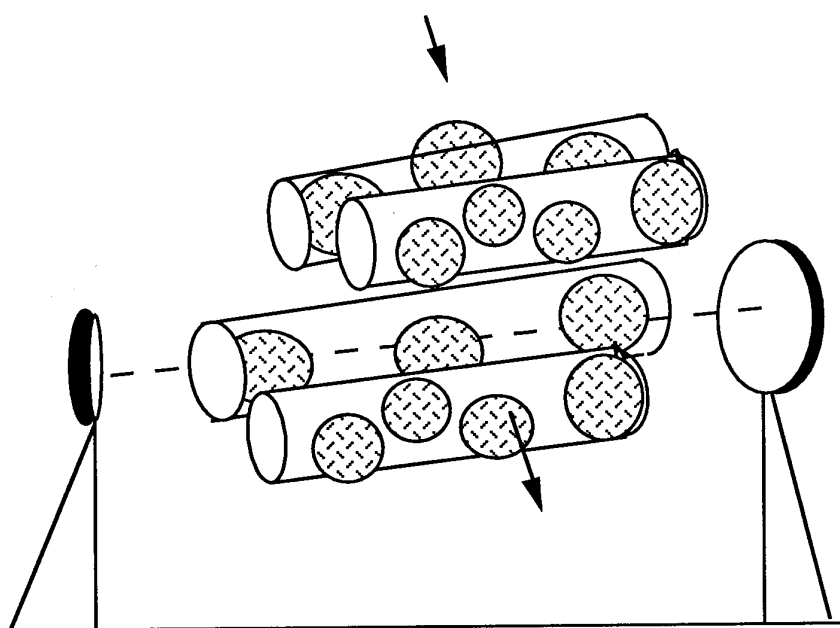


**FIGURE 7** Modelling of the atmospheric turbulences in the lower atmosphere

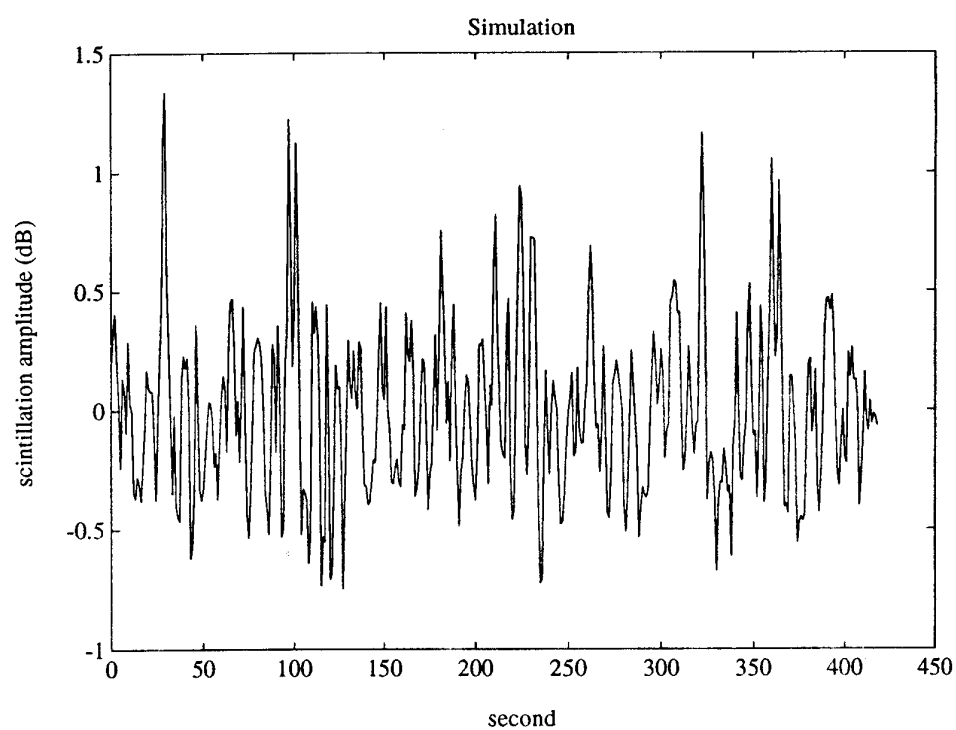


**FIGURE 8** Simulation of the scintillation amplitude on a 4km line-of-sight link, at 30 GHz. The antenna diameters are 1.8 m.

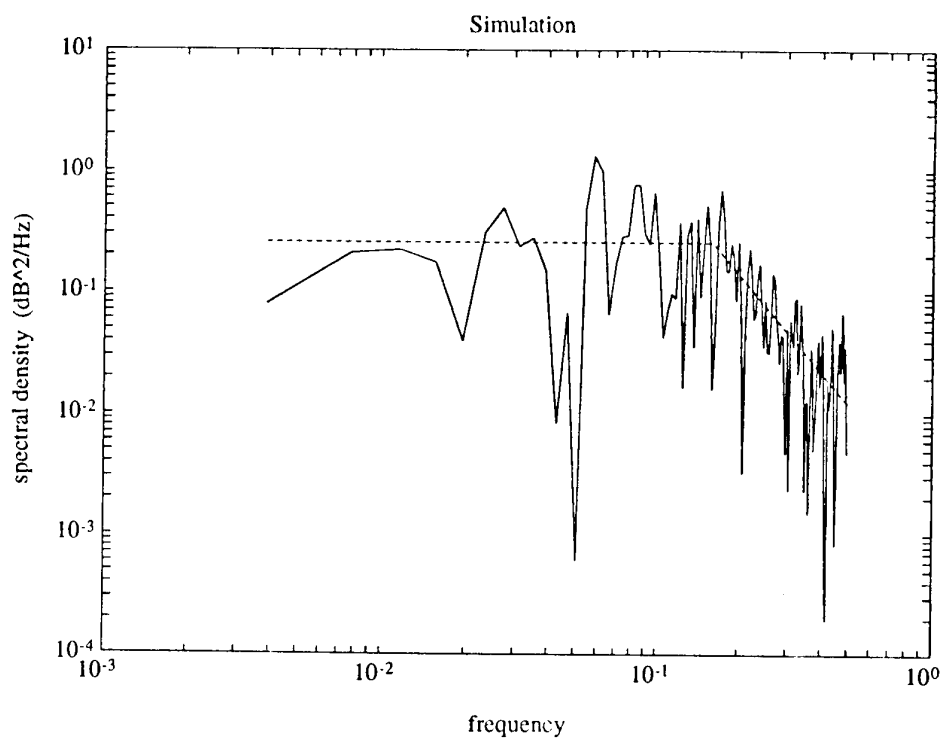


**FIGURE 9** Simulation of the scintillation spectrum on a 4 Km link, at 30 GHz, with 1.8 m antennas. The dashed line is the corresponding theoretical pattern.

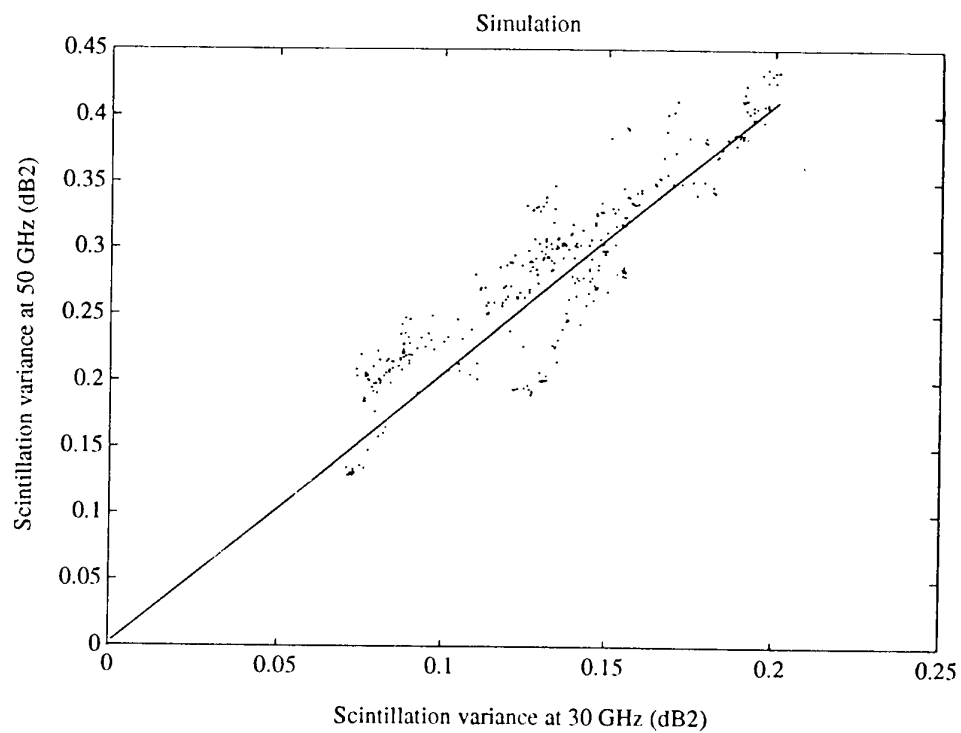


**FIGURE 10** Scatterplot of the simulated scintillation variances at 50 and 30 GHz, for a 4 Km link, with 1.8 m antennas. The continuous line is the regression line.



## DISCUSSION

**Discussor's name :** U. Lammers

**Comment/Question :**

In the slant-path model, you attributed scintillation to cloud turbulence. Is condensed water the important quantity here? How does cloud scintillation compare with that from clear air turbulent air columns all the way from the ground up?

**Author/Presenter's Reply :**

It has been shown experimentally that the cumulus clouds are responsible for scintillation measured at cm and mm wavelengths. The important parameter is the water vapor content in the clouds; this induces variations in the real part of the dielectric permittivity. The clear air turbulences are only important, in the frequency band of interest, at very low altitude (in the boundary layer). Above 100 m, they do not affect microwave propagation.

**Discussor's name :** E. P. Baars

**Comment/Question :**

Your paper mentions, that scintillation amplitude can be well fitted to a log-normal distribution. Does your model agree with this observation?

**Author/Presenter's reply :**

The earth-space model agrees with the log-normal distribution of the scintillation amplitude. Concerning the line-of-sight model, we do not have enough experimental data to check the log-normal distribution of the scintillation amplitude. Further experiments would be needed. Furthermore, the line-of-sight model has to be validated and probably improved. It is too early to show a conclusion.

## Propagation Measurements on a Troposcatter Link in the Canadian High Arctic

C. Bilodeau and K. S. McCormick

Industry and Science Canada  
Communications Research Centre  
P. O. Box 11490, Station H  
Ottawa, Canada  
K2H 8S2

### 1.0 SUMMARY

Experimental results of radio propagation measurements at 853 MHz are given for a 500 km troposcatter link in the Canadian High Arctic.

The experimental data were acquired using a narrow band measurement system that was developed to permit a transmitting power of only 100 Watts while using a 4.5 metre dish at each end of the link. The system includes a digital signal processor (DSP) receiver for signal strength computation and a high stability noise source reference for amplitude calibration. The main characteristics of this system are described in this paper.

Detailed fading distributions are presented for examples of slow and fast fading periods and compared with Rayleigh distributions. An estimate of the long term median path loss is made and compared with values predicted using accepted techniques. The results are believed to be the first ever presented for a microwave troposcatter link above the 80th parallel.

### 2.0 INTRODUCTION

The most northerly settlement in Canada is Alert, being located at more than eighty-two degrees north latitude, and well below the horizon for communications with a geostationary satellite such as ANIK. At the present time, communications to the south are provided by a line-of-sight radio relay system that runs almost five hundred kilometres from Alert to the weather station Eureka at eighty degrees north latitude. From Eureka, an ANIK satellite is visible at near zero degrees elevation angle. Two earth stations are operated at Eureka in a vertical site diversity system to provide satellite communications to the south.

Since for large portions of the year the individual relay sites between the two settlements are inaccessible, it was decided to investigate the possibility of providing a tropospheric scatter link as a backup communications facility which could be used in the event of a failure of the radio relay system. Although standard prediction techniques indicated that such a link would probably be feasible, we were not able to find reference to troposcatter systems operating at such latitudes. An experiment was therefore planned to verify the propagation predictions. A site survey was carried out in the late summer of 1988, and two sites were selected - a transmitting site about one kilometre from an HF installation at Alert, and a receiving site on top of a hill about five kilometres from weather station Eureka. The distance between the two sites is 476 kilometres.

### 3.0 DESCRIPTION OF THE EXPERIMENT

The terrain between Alert and Eureka is quite mountainous, with the terrain often rising precipitously from sea level. At Eureka in particular, it was difficult to find a site in reasonable proximity to existing power lines, but with a small horizon angle in the direction of Alert. A site with reasonable access was finally chosen about five kilometres distant from the Eureka weather station and two kilometres distant from a power line. The coordinates of this location are 80°02'00"N latitude, and 86°13'00"W longitude. Its elevation is 314 m above mean sea level, the horizon angle to Alert was measured to be 5.8 milliradians. At Alert, because of electrical power constraints, a site was chosen at 82°27'00"N, 62°38'00"W. (Note that the lines of longitude are closely spaced at these latitudes). This location is on a broad plateau 194 m above mean sea level. Its horizon angle in the direction of Eureka is approximately 18 milliradians.

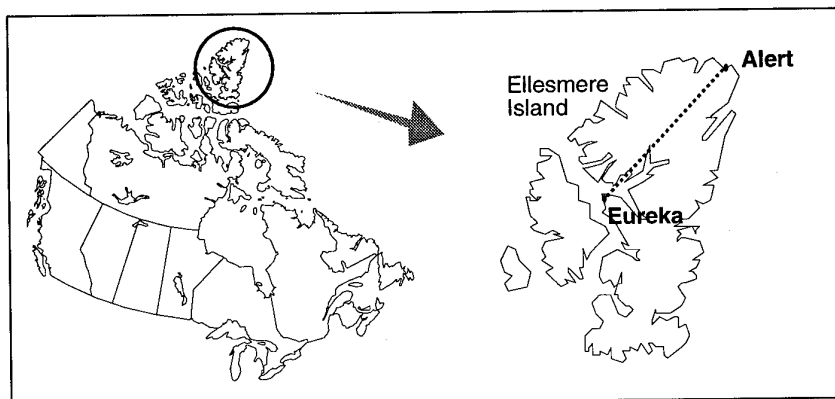


FIGURE 1.  
Canada, with expanded view  
of the experimental region in  
the High Arctic. Alert is the  
most northerly settlement in  
Canada.

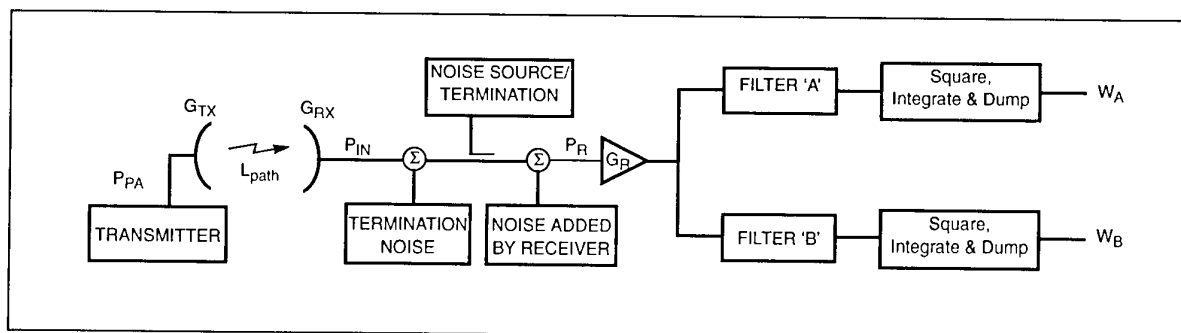


FIGURE 2. Simplified block diagram of troposcatter measurement system

Major constraints on the design of the experiment were the relatively long path length and consequent large path loss, and the difficulty of the site access at Eureka. No heavy equipment would be available for the erection of the receiving antenna - its size had to be such that it could be erected manually by a small number of people. The compromises that were reached in the experiment design are described in the next section.

#### 4.0 THE MEASUREMENT SYSTEM

Because of their size and complexity, troposcatter communication systems are typically expensive. The measurement system that was designed for this experiment minimizes expenditure, installation and maintenance costs. A 4.5 metre dish antenna, consisting of a two-piece grid reflector, was selected as a trade-off between the desired physical and electrical characteristics. An antenna of larger dimension and weight would have provided more gain but could not have been installed easily by a crew composed of only 3 or 4 people or without access to some heavy motorized equipment. A frequency of 853 MHz was chosen as a compromise between reasonable antenna gain and path loss.

A custom tower was designed so that the antenna is attached to a 114 mm diameter pipe. The dish is installed so that the direction of the grids is vertical, defining the plane of polarization. This precaution did not prevent snow from accumulating at times between the reflector elements.

Because of the relatively low transmit power, a foam-filled coaxial feed could be used, eliminating the need for pressurization equipment.

The transmitter is designed to provide a transmission of constant UHF power of 100 W (+50 dBm). A dual channel power meter with full remote-control capability is attached to a directional coupler for sampling the forward and reflected power on the transmitter's low VSWR transmission line. An automated power measurement sub-system was programmed to maintain the power level at the transmitter antenna feed input to within  $\pm 2.3$  W ( $\pm 0.1$  dB) of the nominal transmitted level. Losses from cables, couplers, sensor attenuators, etc., are all accounted for by the program. Power measurements, and corrections of the transmitted power level when required, are repeated four times per minute.

The antenna radiates a pure continuous wave (CW) produced by a low phase noise ( $< -82$  dBcHz<sup>-1</sup> at 100 Hz offset from carrier) signal generator having an excellent

long term frequency stability (aging rate better than 1 part in  $10^8$  per year).

Similarly, tight frequency tolerance is obtained at the receiver by phase-locking the receiver's local oscillators to a stable frequency standard. The use of a frequency standard at both the receive and transmit ends alleviates the need to perform frequent frequency-drift adjustments to accommodate a narrow receiver detection bandwidth of about 100 Hz.

The receiver must provide as much as 150 dB of signal amplification. Such a large overall amount of amplification is not easy to keep constant over wide temperature range or system life time. To minimize any amplification instability, the gain is distributed nearly evenly between the receiver's RF front end and two frequency down-conversion stages, one at 10 MHz, the other at 3 kHz. The first conversion provides good image rejection response whereas the second reduces the complexity of the analog-to-digital conversion circuitry. A special low noise amplifier (LNA) unit was designed and installed at the output of the receiving antenna feed. The components of the unit were mounted inside three miniature ovens to keep the operating temperature constant. In addition, a highly stable white noise source was coupled to the receiver signal main line to provide a reference power level for periodic (hourly) calibration of the LNA-receiver sub-system. The reference signal has less than 0.1 dB power variation over the temperature range of  $-50^{\circ}\text{C}$  to  $+50^{\circ}\text{C}$  and the unit introduces only 0.15 dB signal loss on the received signal path. The receiver has a noise figure of 0.90 dB.

The last stage of the receiver is implemented digitally after the signal has been digitized at a rate of about 10 000 samples per second. It is composed of two narrow band pre-detection filters, a square-law detector, and a post detection integrate-and-dump circuit as explained later. The nominal signal frequency at the output of the 2nd IF stage is 2800 Hz.

Equipment at both the transmit and receive sites operate unattended. Eureka, the nearest settlement to the receive site, is five kilometres away and a line-of-sight UHF telemetry link is used to relay the measurement data. Both sites are equipped with an uninterruptable power system able to sustain the equipment running for about 20 minutes during a main power line outage. The equipment is kept inside a  $1.5\text{ m} \times 3\text{ m} \times 3\text{ m}$  shelter where the temperature is regulated.

### 5.0 DATA PROCESSING AND ACCURACY

In this section, an expression will be derived to relate the path loss ( $L_{\text{path}}$ ) to the system parameters. A simplified model of the troposcatter measurement system is shown in Figure 2.

As mentioned in the previous section, the transmitting power is  $P_{\text{PA}} = 100$  W. Each antenna provides  $28.3 \pm 0.2$  dBi gain ( $G_{\text{TX}} = G_{\text{RX}}$ ) at 853 MHz, assuming a typical 50% antenna efficiency and a gain degradation factor of 0.9 dB.

Because of the high linearity of the system, the receiver can be modelled as a simple noiseless broadband RF amplifier preceded by a noise equivalent circuit to account for the thermodynamic degradation of the signal-to-noise ratio. The receiver has a gain  $G_r$  at the frequency of the carrier and the noise power added is determined from the receiver noise figure ( $\text{NF} = 0.90$  dB).

The noise reference behaves like a simple passive 50 ohm termination when turned off.

Two more elements of the model shown in Figure 2 are the finite impulse response (FIR) bandpass filters which limit the detection bandwidth of the measurements following the digitization of the 2nd IF signal. Both filters are implemented using real-time digital signal processing technology. Filter A is centred around the incoming signal frequency whereas filter B is adjacent to it but still well within the passband of the 2nd IF stage. This second filter is required to reject the incoming signal during the calibration intervals.

Finally, the last elements in the model are the power detectors following the two bandpass filters. Detection is accomplished by squaring and integrating the incoming samples over a fixed interval of time.

An expression for determining the path loss is easily derived by relating the transmitter output power  $P_{\text{PA}}$  to the receiver input power  $P_{\text{IN}}$ :

$$L_{\text{path}} = \frac{P_{\text{PA}} G_{\text{TX}} G_{\text{RX}}}{P_{\text{IN}}} \quad (1)$$

An expression is now needed to relate the receiver input power ( $P_{\text{IN}}$ ) to its output ( $W_A$ ). Two methods were used for determining the LNA-receiver sub-system power response. The first consisted of injecting a signal of known power and frequency, directly into the input of the unit. The detectors A and B output readings were then recorded. Figure 3 shows the calibration curve obtained in this manner for the A detector when varying the input signal level in 0.1 dB increments.

The power response is linear for a carrier to noise ratio (C/N) greater than about 10 dB. At lower C/N, the response degrades gracefully as the thermal noise of the receiver predominates. This non-linearity can easily be removed by subtracting from it the average noise power as measured by detector B. The receiver response then becomes a straight line, having a slope of 1 and an intercept with the ordinate axis at  $W_A = G_R$ , so:

$$W'_A = P_{\text{IN}} + G_R \quad (2)$$

where  $G_R$  is the receiver gain expressed in dB and  $W'_A$  is the detector reading corrected for low C/N ratios.

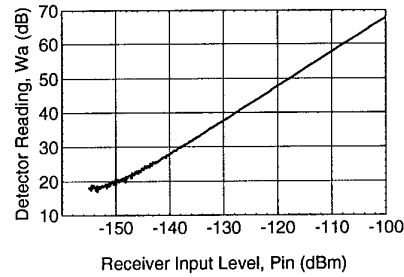


FIGURE 3. Power response for detector 'A'

The second method used for calibrating the LNA-receiver sub-system is a spot measurement of the readings obtained at the detectors output A and B when the noise source is turned 'ON'. Knowing the excess noise ratio (ENR) of the reference noise source and the equivalent noise bandwidth (ENB) of the detection filters, the reference noise power (RNP) can be found as follows:

$$\text{RNP} = 10 \log(kT \text{ENB}) + \text{ENR} \quad (3)$$

where:

$k$  is Boltzmann's constant ( $1.38 \times 10^{-20}$  mJK<sup>-1</sup>),  
 $T$  is the standard temperature (290K).

The ENR was measured to be 26.6 dB using a calibrated ENR meter. The ENB can be determined from the following equation:

$$\text{ENB} = \frac{\int_{-\infty}^{\infty} |H(\omega)|^2 d\omega}{|H(\omega_0)|^2} \quad (4)$$

where  $|H(\omega)|$  is the magnitude of the frequency response of the detection filter and  $\omega_0/2\pi$  is its centre frequency. For an FIR type of filter,  $H(\omega)$  is given by:

$$H(\omega) = \sum_{k=0}^{M-1} b_k e^{-j\omega k} \quad (5)$$

where the filter coefficients  $\{b_k\}$  are the values of the unit sample response of the filter and  $M$  is the filter length. Equations 4 and 5 were evaluated numerically over the frequency range of interest for filters A ( $M_A = 163$  coefficients) and B ( $M_B = 82$  coefficients) used in the experiment. Table 1 summarizes the results.

Table 1: Comparison of reference levels using the two calibration methods.

		Method 1	Method 2	$\Delta$
FILTER	ENB	$P_{\text{in}}$	RNP	$P_{\text{in}} - \text{RNP}$
	(Hz)	(dBm)	(dBm)	(dB)
A	140.6	-126.0	-125.9	-0.1
B	146.7	-125.7	-125.7	0.0

The third column of the table shows the signal level injected at the LNA unit input when applying the first method to achieve the same detector output readings as recorded for method 2. The results of both methods agree within 0.1 dB.

## 6.0 DATA ANALYSIS

Early in the design of the experiment, because of the remoteness of the location, it was recognized that the data collection for the experiment would have to be severely restricted. Personnel at the Eureka Weather Station agreed to look after the data recording computer, but the large number of signal measurements made (20 per second on each of the two signal channels) would have placed an impossible burden on them. Even with an effective data compaction scheme, the data storage requirements would have exceeded 300 kilobytes per hour.

Accordingly, it was decided to carry out as much preprocessing as possible at the recording site, and to retain only essential information on a routine basis. The data at the receiver were packetized, sent by telemetry to the weather station, and each hour the signal level density distribution for that hour, the median signal levels for each minute, each five minutes and the hour, the average power levels in both the signal and noise channels, a five-second sample of the actual data, and some housekeeping data were recorded. This scheme allowed the use of a single floppy disk each month, which was mailed to the laboratory in Ottawa.

For a few months, it was possible to transmit the original packetized data to Ottawa over a satellite link, in order to record samples of the details of the signal level characteristics.

In an experiment such as this, in which large volumes of data are recorded from a remote location, it is a significant problem to ensure that the data are valid: i.e. that there are no undetected periods in which either the transmitter/receiver/recording chain was faulty, or in which external factors affected the received signal. Since the original data were not generally available, a number of tests were applied to the data and these were plotted in a form that was easily scanned visually to detect anomalies. The following plots were generated for each day's data: the signal level density distribution and the cumulative signal level distribution for each hour, a time series of the median signal level distributions for each minute of the day, a time series of the hourly median signal level, noise level, and injected calibration power, the measured frequency offset between the transmitter and receiver and the twenty-four five-second samples of the receiver signal. As a final check, the difference between the ten percent and ninety percent levels of the cumulative signal distributed were calculated and plotted. (For a Rayleigh distribution, this value is expected to be 13.4 dB.) All these plots were put on a single letter-size page for each day, permitting a rapid visual scan of the data characteristics.

### 6.1 Signal Level Characteristics

The signal level characteristics are discussed under four headings:

- Fading rate
- Short term signal level fluctuations

### Long term signal level fluctuations Predictions

#### *Fading Rate*

The received signal level exhibited periods of both rapid and slow fading. Using data from the period for which all the packetized data were recorded, Figures 4 and 5 show typical examples of both these conditions. In each case, the horizontal line shows the median signal level calculated for a one-hour period. The signal levels typically rise above the median by more than 8 dB, and fall by more than 20 dB into the system noise.

One of the quantities of interest to the system designer is the "fade rate", defined as the number of two-way median crossings in a given time interval such as one minute or one hour. It was possible to calculate a number of these fade rates from the detailed signal level time series that were received in Ottawa, and the results are shown in Figure 6. In performing the calculation, a "hysteresis" zone was set up around the median to eliminate small fluctuations from affecting the results. In other words, a median crossing was not counted unless the signal continued its path sufficiently to exit the "hysteresis" zone. The fade rates were calculated for different values of the hysteresis zone, including one dB above the median to one dB below it, one dB above to three dB below, and one dB above to ten dB below. The results are shown in the Figure. Curves (a), (b), and (c) were calculated for all the available data for the month of April 1992, 398 hours. For the larger hysteresis zones, the number of fades included in the calculation decreases. There is perhaps a tendency for the higher fade rates to decrease more than the lower ones, but the change in slope of the curves is not large. The dashed line on the plot represents a linear fit to the (+1, -3) case.

#### *Short Term Signal Level Fluctuations*

Figure 7 shows a series of cumulative probability distributions calculated for data recorded during December 1992. Curves (a) and (b) show distributions calculated for one hour periods in slow and fast fading conditions, respectively. During slow fading, curve (a) appears to conform very well to a Rayleigh-type fading, as evidenced by the straight line characteristic extending from 0.01 percent to more than 99 percent of the hour, whereas curve (b) for the fast fading period departs from the straight line for percentages in excess of ninety percent. Similar behaviour is found for curves (c) and (d) which encompass data from complete days of slow and fast fading. Interestingly, when the distribution is calculated for the whole month, it is found to be essentially identical to curve (c). The 10-90 percent fading range in this case is found to be 12.2 dB, which is somewhat smaller than expected for Rayleigh fading (13.4 dB).

#### *Long Term Signal Level Fluctuations*

Of particular interest in this experiment was to gain a knowledge of the long-term signal level statistics. There was a concern that the cold, dry arctic atmosphere might exhibit unusual effects, particularly during the long winter night. Previous experience has shown that this atmosphere can be particularly stable from a propagation point of view, presumably because of the absence of diurnal solar heating and cooling. In this case it is the monthly signal level median values that are of interest. For each month, a distribution was formed of all the hourly median signal

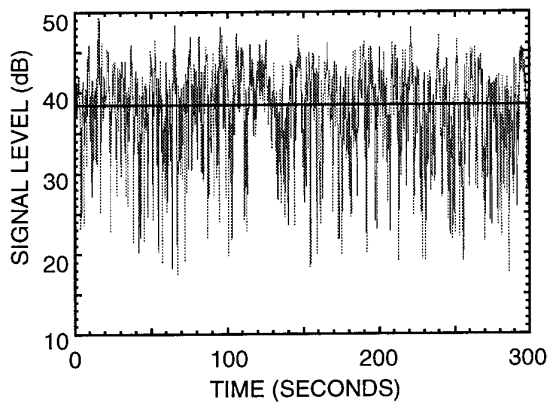


FIGURE 4. Example showing typical received signal level variations during a period of fast fading

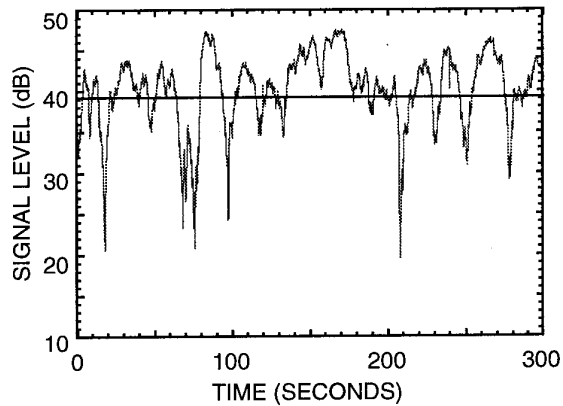


FIGURE 5. Example showing typical received signal level variations during a period of slow fading

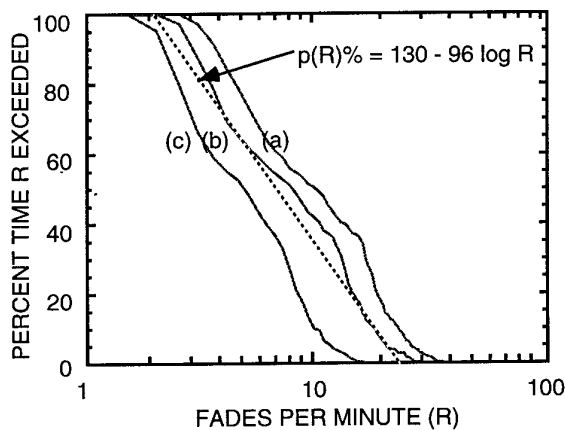


FIGURE 6. Fade rate distributions for the month of April 1992 with "hysteresis": (a)  $\pm 1$  dB, (b)  $+1/-3$  dB, (c)  $+1/-10$  dB (see text)

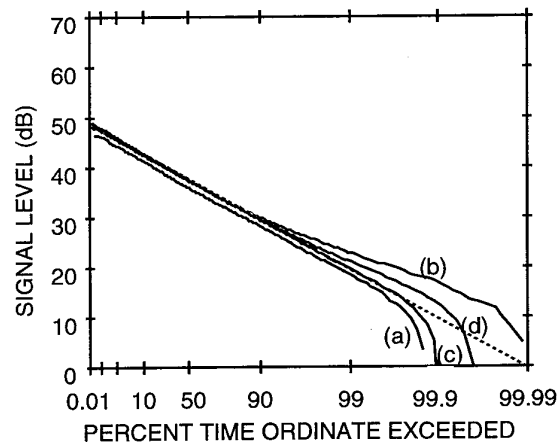


FIGURE 7. Cumulative distributions of data recorded during December 1992 for periods of one hour, (a) slow fading, (b) fast fading; and periods of several days (c) slow fading, (d) fast fading

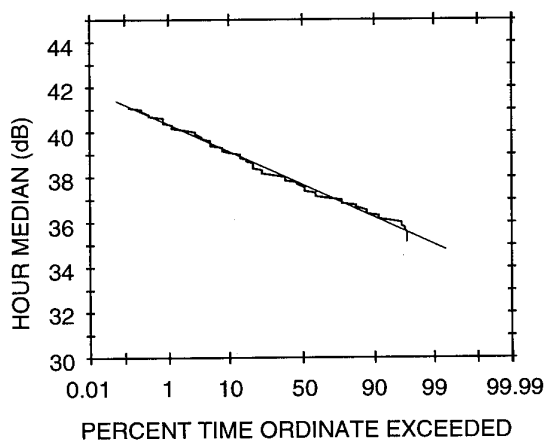


FIGURE 8. Cumulative distribution of hourly median signal levels for the month of December 1991

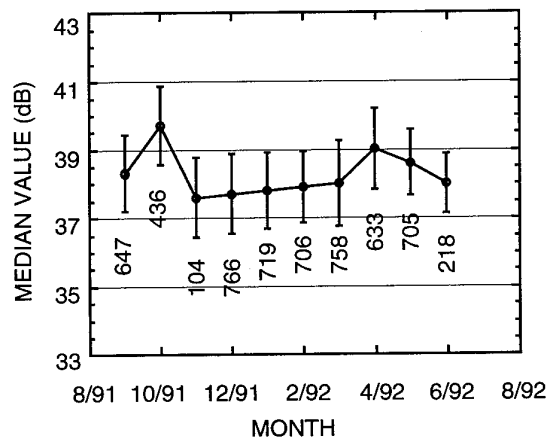


FIGURE 9. Monthly median values of the cumulative distributions of hourly median signal levels. The error bars indicate one standard deviation and each number, the available number of hour medians

levels for that month. An example for December 1991 is shown in Figure 8. Here the data are plotted on a Gaussian axis, and as expected the plot indicates that the medians follow a normal distribution. In this case, the monthly median value of the hourly medians is 37.7 dB, with a standard deviation of 1.1 dB. Figure 9 shows the monthly median values of the hourly medians for all the available data. In this plot, the numbers on the error bars indicate the number of hour medians that were used to form the corresponding distribution. The reason that in some cases they exceed the number of hours in the month is due to an artifact in the data recording setup. Sometimes the recording for a month extended a day or two into the following month. Figure 9 is remarkable in that it shows that the tropospheric scatter conditions on this path were extremely stable during the measurement period, particularly during the dark months November through March. During the total observation period, these median values were contained to within about  $\pm 1$  dB, with standard deviations of about 1 dB.

The next section will assume that a scale reading of 38 dB can be used to represent the long-term median for 50 percent of the time. Using the calibration curve of Figure 3, this value translates into a long-term received power of -129.5 dBm. Assuming a transmitter power of 100W, a total gain degradation factor of 1.8 dB for the two antennas, and equal receive and transmit antenna gains of 29.2 dB, we find a long-term path loss of 236.3 dB.

#### *Predictions*

Three different methods were used to predict the long-term median path loss  $L(50\%)$ . The first was through an in-house propagation prediction program, using a method based on NBS Tech. Note 101. The other two were CCIR methods as given by Roda (G. Roda, Troposcatter Radio Links, Artech House, pub., 1988, ISBN 0-89006-293-5). Where necessary a continental temperate climate was assumed since no information is available for a polar climate. These predictions yielded 231.2, 232.7, and 233.4 dB. In these calculations, the take-off angle for the transmitter is somewhat uncertain. It was assumed to be 18 milliradians, a value which was measured during the initial site survey, but which was unfortunately not verified during the actual antenna installation. (The sensitivity of the prediction to errors in take-off angle is about 0.3 dB per milliradian). The difference between the measured long-term median and the predicted values varies from 2.9 to 5.1 dB. Given the uncertainties in some of the experimental parameters as well as the prediction techniques, this agreement is considered acceptable.

#### **7.0 ACKNOWLEDGEMENT**

This work was supported by the Department of National Defence, Chief Research and Development. The Harris Corporation, RF systems Division, provided valuable advice. Special thanks are due to the personnel of the Atmospheric Environment Service, Weather Station Eureka, and to the OIC Fort Eureka.

## DISCUSSION

**Discussor's name :** K. S. Kho

**Comment/Question :**

Do you expect influence of bandwidth in the propagation (path) loss you have measured, since the actual signal will have a larger bandwidth compared to the bandwidth of the signal used for the measurements?

**Author/Presenter's reply :**

No. I think that the long-term median path loss will remain nearly the same. A larger bandwidth would affect things like the multipath spread values of course, but we wanted to keep the experiment simple and concentrate on the measurement of path loss only.

**Discussor's name :** U. Lammers

**Comment/Question :**

Does the path loss at these high latitudes change with the season; in other words, does humidity contribute to scattering?

**Author/Presenter's Reply :**

We did not get enough data to make a thorough season to season comparison. Winter is probably the worst season for propagation of tropospheric signals and what we observed in our analysis is that there was not much median signal level variation from month to month or season to season, at least for the data available.



## Large Bistatic Angle Clutter Depolarization Study

D.J. McLaughlin, E. Boltz, J. Barclay, R.S. Raghavan  
ECE Department  
Northeastern University  
Boston, MA 02115 USA

M.J. Sowa  
Rome Laboratory/ERCT  
Hanscom AFB, MA 01731-5000 USA

### SUMMARY

A bistatic radar test bed has recently been developed to measure the depolarization behavior of clutter at large bistatic angles in Eastern Massachusetts. Results presented in this paper describe the co- and cross-polarized S-Band NRCS for low resolution (300m by 300m) forested clutter cells viewed at low grazing angles. We also describe the variation in mean scattered power versus linear receiver antenna orientation angle for both vertical and horizontal transmitted polarizations. Measurements of a 20 km by 20 km region of rolling hills show that vertical copolarized NRCS exceeds horizontal copolarized NRCS by an average of 8 dB over a range of bistatic angles from 110 degrees to 160 degrees. The average polarization ratio is -12 dB for vertical transmitter polarization and -5 dB for horizontal transmitter polarization. For both transmitter polarizations and variable linear receiver antenna polarization, maximum scattered power was observed when transmitter and receiver antennas were copolarized while minimum received power was observed when the antennas were crosspolarized. Power fluctuation statistical distributions are approximately exponential for all linear receiver antenna polarization angles.

### 1. INTRODUCTION

Theoretical calculations for bistatic scattering from rough surfaces have shown that the ground clutter seen by a bistatic radar can be minimized by appropriate choice of transmitting and receiving antenna polarizations. Using both a physical optics (PO) model, and a combined PO and small-perturbation composite surface model, Papa et. al. (1986, 1991) predict significant variations in received power versus receiver antenna orientation (tilt) angle when rough surfaces are illuminated at large bistatic angles by vertically or horizontally polarized transmitter antennas. These theoretical calculations suggest that target detection performance using bistatic radars can be improved by choosing transmitting and receiving antenna polarizations in such a way that the clutter power level is minimized.

Few experimental measurements have been made for comparison with the theoretical predictions. Rao et. al.

(1991) studied the polarization behavior of deciduous trees at large bistatic angles using a high-resolution (200 MHz) bistatic radar system operating at S-Band. They measured the variation in received power versus linearly polarized receiver antenna orientation angle for both vertical and horizontal transmitted polarizations and compared their measured results with the composite surface calculations of Papa and Woodworth (1991). The scattering cell area for their experiment was 4 square meters. (The out-of-plane azimuth scattering angle was 75 degrees, and the incident and scattered grazing angles were 10 and 6 degrees, respectively in their experiment). Measured modulation depths (variation between maximum and minimum received power as the receiver antenna orientation is varied over a 360 degree range) were lower than those predicted by two-scale scattering models, but the general behavior of the variation was in good agreement with the model. Substantial variations in the statistical behavior of the clutter data were observed in this experiment as the receiver antenna was rotated. The coefficient of variation (normalized standard deviation of received power fluctuations) was observed to vary systematically with orientation angle, having a maximum value (0.65) at the orientation of minimum received power and having a minimum value (0.15) at the orientation of maximum received power. Since wider clutter distributions have a negative impact on detection performance, it is important to determine whether or not effects such as these exist in bistatic clutter returns from coarser resolution cells.

The bistatic radar test bed being developed by Northeastern University and USAF Rome Laboratory is described in the papers by Sowa et. al (1993) and Hartman (1993). We have recently used this system to measure the variation in mean bistatic clutter power versus linear receiver orientation angle for large (approximately 300 m by 300 m) forested clutter cells. We have also calibrated the system and measured the normalized radar cross section (NRCS) of tree clutter over a range of large bistatic angles for both copolarized and cross-polarized antenna configurations.

The test bed system and the results of these measurements are described in this paper. Section 2 describes the design, operation, and field deployment of the bistatic test bed. Section 3 describes fading

statistics, and presents measurement results showing mean power versus linearly polarized receiver antenna orientation angle for low-grazing angle forested clutter. NRCS measurements are presented in section 4 and conclusions are given in section 5.

## 2. BISTATIC TEST BED SYSTEM

A functional block diagram of the bistatic test bed system is shown in figure 1. The S-band transmitter is located at the USAF Phillips Laboratory/Rome Laboratory doppler weather radar site in Sudbury, MA. The 24 foot diameter prime focus parabolic antenna sits atop a hill, 370 feet above sea level and approximately 120 feet above the local terrain. It is currently configured for alternately transmitting vertically and horizontally polarized pulses 1  $\mu$ SEC wide at 2.71 GHz at a 200 kW peak power level and pulse repetition frequency (PRF) of 100 Hz. The bistatic receiver is located approximately 20 km east southeast of Sudbury at the Rome Laboratory Prospect Hill site in Waltham, MA. The receiver antenna is a linearly polarized standard gain horn antenna mounted on a waveguide rotary joint and installed on the laboratory rooftop, 500 feet above sea level and approximately 250 feet above the local terrain. An incoherent superheterodyne receiver located in the laboratory beneath the antenna filters, downconverts, and amplifies signals collected by the antenna prior to detection in a wide dynamic range (>80 dB) logarithmic detector. Integrated main-beam crosspolarization isolation levels for transmitter and receiver antennas are -25 dB and -18 dB, respectively. Specifications for the transmitter and receiver subsystems are summarized in figure 2.

Synchronous timing of the transmitter and receiver is accomplished using a line-of-site microwave link established between the two antenna sites. Two  $\mu$ SEC wide pulses are transmitted from Sudbury to Waltham using a pair of dedicated antennas and are detected at the receiver site for synchronizing the receiver data acquisition system. Bistatic returns are time-gated in order to separate clutter returns from different ranges.

The clutter region between Sudbury and Prospect Hill consists mostly of rolling hills covered with trees along with a few residential neighborhoods, and scattered industrial regions. Owing to the relatively large baseline distance between the transmitter and receiver sites and the low antenna elevations, the antennas view the clutter surfaces at grazing angles below approximately one degree. Figure 3 shows the measurement geometry in plan view, with the transmitter site shown at left and the receiver site shown at right. Closed contours are shown around prominent hills and elevated clutter regions that are within line-of-sight to both transmitter and receiver antennas. Also shown are one  $\mu$ SEC range delay contours, corresponding to the range-gates for this measurement geometry. Clutter resolution cell sizes, determined by the intersection of the transmitter

antenna beam with the range-gate geometry, are on the order of 300 m by 300 m. Since 1  $\mu$ SEC range gates are used to discriminate clutter returns from different ranges, interference from the direct path signal as well as forward scatter along the transmitter-receiver baseline precludes making measurements at bistatic angles greater than 160 degrees.

## 3. CLUTTER DEPOLARIZATION MEASUREMENTS

Below we describe a case study where we measured the variation of mean received power versus receiver antenna orientation (tilt) angle for both vertical and horizontal transmitted polarizations for a resolution cell at the top of tree-covered Goodman Hill in Sudbury, MA. This clutter region, indicated in figure 3, is 8 km and 12.5 km away from the transmitter and receiver sites, respectively. The out-of-plane azimuth scattering angle is 45 degrees corresponding to a bistatic angle of 135 degrees. The elevation of the clutter region is 100 feet above the local terrain.

Measurements were made at midday on April 21 and April 28, 1993. An anemometer located at the Sudbury site recorded 15-20 mph winds on April 21, blowing from south-southwest (205 degrees). On April 28, the wind speed was 10 mph from the northeast (44 degrees). The tree canopy was dry on both days.

### 3.1. Measurement Procedure

Depolarization measurements were obtained by rotating the receiver horn antenna in 30 degree increments over a 360 degree range, and measuring the mean scattered power level at each orientation angle. Figure 4 shows the instantaneous (pulse to pulse) fluctuations in received power observed over a typical 30 second record. Autocovariance analysis of records such as these indicates that the decorrelation time of the fading signal is approximately 0.5 seconds. Three minute records of received power were obtained at each receiver orientation angle and these records were then averaged to estimate the mean scattered power. Based on the observed decorrelation times for the data, we estimate that between 180 and 360 independent fading samples were included in each record. Assuming the probability distribution for scattered power is exponential, the rms uncertainty in the resulting estimates of mean power is below 0.3 dB (Ulaby, et al., 1986). Each 360 degree rotation of the receiver antenna required 90 minutes to complete.

### 3.2 Variation of Received Power Level versus Receiver Antenna Orientation Angle

Figure 5 shows the variation of received power level observed for both vertical (o) and horizontal (\*) transmitted polarizations for the April 21 data set. (Here a receiver antenna orientation of 0 degrees corresponds to a vertically polarized receiver). For vertical transmitted polarization, the maximum received power was observed at orientation angles of 0 degrees, 180 degrees, and 360 degrees (vertically polarized receiver antenna), and the minimum received

power was measured at 90 and 270 degrees (horizontally polarized receiver antenna). The ratio of maximum to minimum received power is approximately 7 dB. For horizontal transmitter polarization, the maximum received power was observed when the receiver antenna was horizontally polarized. Minimum received power was observed when the receiver antenna was vertically polarized. The ratio of maximum to minimum received power for the horizontally-polarized transmitter case is approximately 3 dB. The maximum received power for the vertical transmitted case exceeds the maximum received power for the horizontal transmitted case by 6 dB.

Measurement results from the April 28 data set are shown in figure 6. These measurements show the same general variation in received power versus receiver polarization angle as those of the previous week, the rms difference in the measurements from one week to the next being less than 1.5 dB. For horizontal transmitted polarization (o), the maximum mean received power level appears to be shifted away from the horizontal direction by 30 degrees, to orientation angles of 120 degrees and 300 degrees. Similar shifts were observed in the higher resolution measurements made by Rao et. al. (1991). We note that in the present measurements, however, the minimum mean power level is only 1 dB lower than that observed at 90 and 270 degrees, so caution must be used in interpreting this result. According to exponential fading statistics, a variation in mean power of 1 dB can be considered statistically significant, given the number of independent fading samples in these records. The vertically polarized transmitter results (\*) for the April 28 data set, however, show that the mean power observed with a vertically polarized antenna (0 and 360 degree orientation angles), can differ by greater than 1 dB when these measurements are obtained 1.5 hours apart. This indicates that either the scattering is nonstationary, with mean scattered power changing with time, or that the exponential statistic is inappropriate for estimating the residual fluctuations in the mean power estimates. In either case, this observation indicates that level differences below approximately 1 dB should be interpreted with caution.

### 3.3 Coefficient of Variation of Fluctuating Signals

Figures 7 and 8 show histograms of received power for both vertical transmit, vertical receive and vertical transmit, horizontal receive cases, for the April 21 data set. Also shown on the histograms are plots of the exponential probability density function. Normalized standard deviations for the vertical transmit, vertical receive and vertical transmit, horizontal receive cases are 1.0 and 0.8, respectively. The coefficient of variation (standard deviation normalized by the mean power level) versus receiver antenna orientation angle is shown in figure 9 for the data obtained on April 21. The coefficient of variation varies between 0.8 and

1.05, and shows no systematic variation versus receiver polarization angle. Similar results were observed in the April 28 data set.

### 4. BISTATIC NRCS MEASUREMENTS

The normalized radar cross section (NRCS) of approximately 30 different clutter regions was measured with the test bed using all four combinations of transmitter and receiver polarizations. Calibrated NRCS results were obtained by first boresighting transmitting and receiving antennas at each other and measuring the direct-path received power level:

$$P_{cal} = \frac{P_t G_t \lambda^2 G_r}{(4\pi)^2 R_{bl}^2}$$

where  $P_t$  is the transmitted power level,  $G_t$  is the transmitter antenna gain, and  $R_{bl}$  is the transmitter-to-receiver antenna baseline distance. The power level measured from an individual clutter cell is given by:

$$P_r = \frac{P_t G_t \lambda^2 \sigma^o A F_t^2 F_r^2}{(4\pi)^3 R_t^2 R_r^2}$$

where  $A$  is the area of the clutter cell,  $F_t$  and  $F_r$  are propagation factors, and  $R_t$  and  $R_r$  are the ranges between the transmitter and receiver antennas and the clutter patch, respectively. The propagation factors account for non-free space propagation effects between the antennas and the clutter cells. Computing the ratio of the equations given above and rearranging terms, the clutter cell NRCS is given by:

$$\sigma_F^o = \frac{\sigma^o}{F_t^2 F_r^2} = \frac{P_r R_{bl}^2}{P_{cal} (R_r R_t)^2 (4\pi)^2 A}$$

and is obtained from measurements of  $P_r$  and  $P_{cal}$  and knowledge of  $R_{bl}$ ,  $R_t$ , and  $R_r$ . Note that terms representing the propagation effects are included in the NRCS measurement result, since these effects are unavoidable at low grazing angles. In the discussion that follows, we restrict our consideration to those clutter cells for which a line-of-site propagation path exists between both the transmitter and receiver antenna terminals, as this eliminates the effects of shadowing from the measurement results. The scattering surface beneath the propagation paths contains primarily diffuse forward scattering elements, such as treetops, branches, and rough ground. While these scattering elements may have an impact on the measured NRCS values vis-a-vis the propagation factor, their impact is not likely to be as significant as would be the case when measurements are made in the presence of specular forward scattering elements such as the ocean surface.

#### 4.1 Copolarized NRCS Results

Figure 10 shows a vertically polarized NRCS image of the clutter region south of the Sudbury-Waltham baseline. Clutter cells having measured NRCS below -50 dB are likely to be shadowed from either the transmitter or the receiver, and the NRCS value shown for these cells is corrupted due to transmitter antenna sidelobes viewing adjacent, higher cells with higher NRCS values. Away from these regions, the NRCS values for clutter ranges from -19 dB to -50 dB. The range of bistatic angles for cells chosen in this study was 110 degrees to 160 degrees, corresponding to out-of-plane scattering angles from 70 degrees to 20 degrees, respectively. No systematic variation in NRCS versus out-of-plane scattering angle is apparent in these measurements. We attribute this to local terrain slope being the dominant factor controlling the NRCS variation at these low grazing angles. When horizontal polarization was used to illuminate the surface with both transmitter and receiver antennas, NRCS values were lower than the vertically polarized case. Throughout the image, the vertically polarized NRCS exceeds the horizontally polarized NRCS by 0 to 12 dB, averaging 8 dB.

#### 4.2. Crosspolarized NRCS Results

For vertical transmitted polarization and horizontal receiver polarization (VH), NRCS values were 5 to 20 dB below the co-polarized (VV) case. The average depolarization ratio (ratio of crosspolarized NRCS to copolarized NRCS) was -12 dB. For horizontal transmitted polarization and vertical receiver polarization (HV), NRCS values were 0 to 12 dB below the HH case. The average depolarization ratio for horizontal transmitted polarization was -5 dB.

#### 5. Conclusions

Maximum and minimum received power levels for this case study were measured when the linearly polarized receiver antenna was aligned parallel and perpendicular, respectively, to the transmitter antenna polarization. No systematic variation in the scattering statistics versus receiver polarization angle was observed in these measurements. The coefficient of variation, a measure of the dispersion of the received power probability distribution, varied between 0.8 and 1.05 over the range of receiver polarization angles reported in this study. This result contrasts the results of the wideband measurement results of Rao and Stevens (1991), who observed significantly narrower power fluctuation probability distributions in the locations of the null polarization angles and a substantial increase in the dispersion in the location of maximum power. The invariance in the statistical distributions measured in the present study is due to the large (approximately 300m by 300m) resolution cell sizes and the large number of scatterers in these cells.

The NRCS for vertical transmit and receive polarization exceeds the horizontal transmit/receive polarization

case by 8 dB on average. There is significantly more depolarization for horizontal transmitter polarization at large bistatic angles (-5 dB depolarization ratio) than for vertical transmitter polarization (-12 dB depolarization ratio).

A limitation in the present study was the coarseness in the angular rotation of the receiving antenna. Thirty degree increments in receiver antenna orientation angle were used between measurements, and consequently, fine details in the azimuth modulation patterns may not have been observed during these experiments. We plan to obtain additional measurements using finer step sizes (such as ten degrees) and observe scattering from a number of clutter regions within the measurement area described in figure 3. We have added a second receiver channel to the bistatic test bed receiver and have implemented a dual polarized receiver antenna. Our next measurements will focus on the short-time polarimetric behavior of the bistatic clutter as well as the long time averaged behavior at elliptical as well as linear receiver polarizations.

#### References

- [1] Hartman, A.J., "A Polarimetric Bistatic Radar Test Bed for Signal-to-Clutter Enhancement Studies," M.S. Thesis, Northeastern University, September, 1993. 135 pages.
- [2] Papa, R.J., J. F. Lennon, and R. L. Taylor, (1986), "The Variation of Bistatic Rough Surface Scattering Cross Section for a Physical Optics Model," IEEE Transactions on Antennas and Propagation, Volume AP-34, 1986.
- [3] Papa, R.J. and M.B. Woodworth, (1991) "Optimization of the Elliptically Polarized Diffuse Power Scattered from a Two-Scale Rough Surface," AGARD Conference Proceedings on Target and Clutter Scattering and their Effects on Military Radar Performance, AGARD-CP-501, Ottawa, Canada, May, 1991.
- [3] Ulaby, F.W, R.K. Moore, and A.K. Fung (1986), Microwave Remote Sensing, Active and Passive - Volume 2: Radar Scattering, Boston, MA, Artech House, 1986.
- [4] Rao, K.V.N., Stevens, W.G., and Medonca, J. (1991) Bistatic Scattering Statistics of Deciduous Trees", AGARD Conference Proceedings on Target and Clutter Scattering and Their Effects on Military Radar Performance, AGARD-CP-501, Ottawa, Canada, May, 1991.
- [5] Sowa, M.J., D.J. McLaughlin, and R.S. Raghavan, "A Bistatic Radar Test Bed for Signal-to-Clutter Enhancement Studies," Proc. 1993 Bistatic Radar Workshop, Griffis AFB, Rome, NY, May, 1993

## Discussion

### G.S. Brown (USA)

Do you have any plans for removing the "propagation factor" from the data so that a true bistatic NRCS can be produced?

### Author's Reply

At present, we are restricting our consideration to elevated clutter regions so that terrain blockage is not a dominant factor affecting the measurements. Diffuse multipath returns are likely to be present along with the bistatic clutter returns in the measurements, however, and our measurement system does not discriminate these signals. The propagation factor reported in our results is a "bookkeeping term" that accounts for these effects and cannot be removed. We are developing a portable 1 kW transmitter and plan to use that subsystem, along with the bistatic receiver, to make higher grazing angle measurements where propagation effects are less important and the propagation factor will not be needed.

### U. Lammers (USA)

Do you know what specifically in the terrain causes the bistatically scattered signal and the differences at vertical and horizontal polarization? Is it the internal structure of the vegetation?

### Author's Reply

Perhaps the dominant scattering mechanism is the

trees, whose trunks and limbs are predominantly vertical. This would explain the larger copolarized return for vertical transmitter polarization compared with the horizontal transmitted case. Other candidate scattering mechanisms are the leaves in the tree canopy and the soil on the surface. We plan to continue our measurements through the fall defoliation cycle to try to determine the significance of scattering from the canopy.

### W. Flood (USA)

Can you transmit V, H, RHCP, and either 45 or 135 degree linear polarizations? Then by measuring on reception the magnitudes of V and H, and their relative phase difference, you can compute the complete Mueller Matrix.

### Author's Reply

The high power transmitter can be configured to transmit either V, H, or RHCP, LHCP on alternate pulse repetition intervals and we do not have the flexibility to transmit other polarizations without a costly redesign of the transmitter front end. The transmitter and receiver are phase coherent, however, and we plan to rapidly switch between orthogonal linear polarizations to obtain the Mueller matrix. We will have the flexibility to transmit the waveforms you suggest using a new, portable 1 kW transmitter that we are developing, and we will investigate that idea.

## BISTATIC TEST RECEIVER IMPLEMENTATION

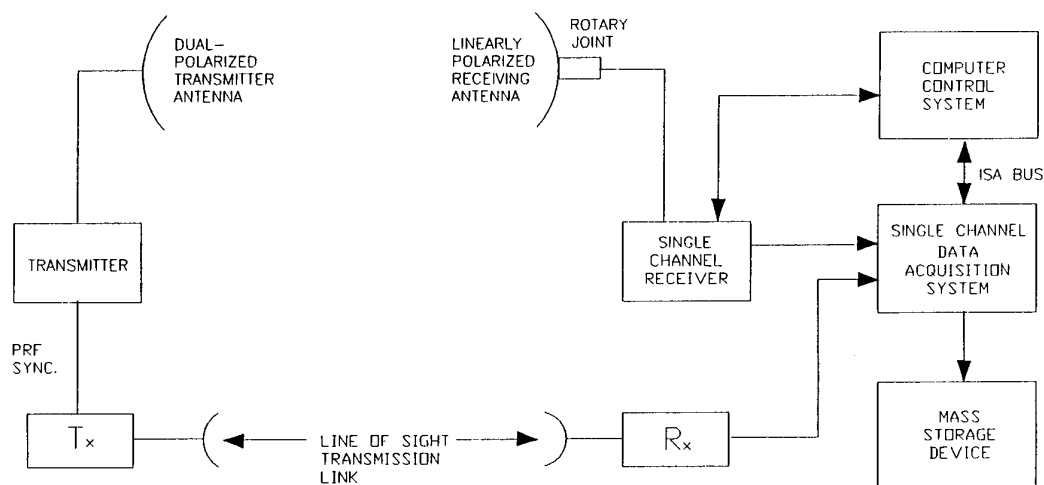


Figure 1 : Functional block diagram of the incoherent bistatic radar test bed

---

**Transmitter**

Center Frequency	2.71 GHz
Peak Output Power	83 dBm
Pulsewidth	200-1,000 nsec
Pulse Repetition Frequency	100-1,000 Hz
Bandwidth	100 MHz

**Transmitting Antenna**

Center Frequency	2.71 GHz
Gain	43.75 dB
3 dB Beamwidth	1 degree
Dimensions	24 ft diameter parabolic dish
First Sidelobe Level	-32 dB
Elevation	112 meters (ASL)
Polarization	Linear V/H

**Receiver**

Center Frequency	2.71 GHz
Bandwidth	3 MHz
Intermediate Frequency	30 MHz
Gain	-3 dB
Noise Figure	12.6 dB
Dynamic Range	80 dB
Detector	Logarithmic

**Receiving Antenna**

Frequency Range	S-Band (2-4 GHz)
Gain @ 2.71 GHz	15.15 dB
3 dB Beamwidth	27 degrees
First Sidelobe Level	-14 dB
On-Axis Cross-Polarization Isolation	18 dB
Elevation	150 meters (ASL)
Polarization	Linear (orientation variable with rotation)

---

Figure 2. Specifications for Transmitter and Receiver Subsystems

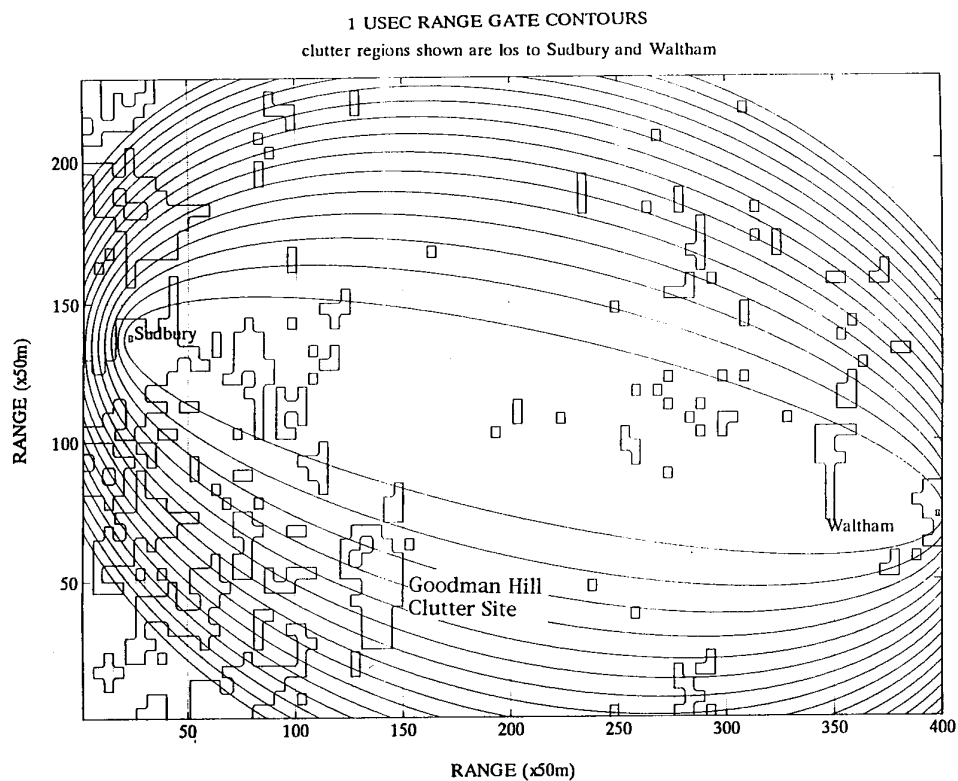


Figure 3. Plan View of Measurement Area showing 1 usec Constant Range Delay (Range Gate) Contours superimposed on LOS Clutter Regions.

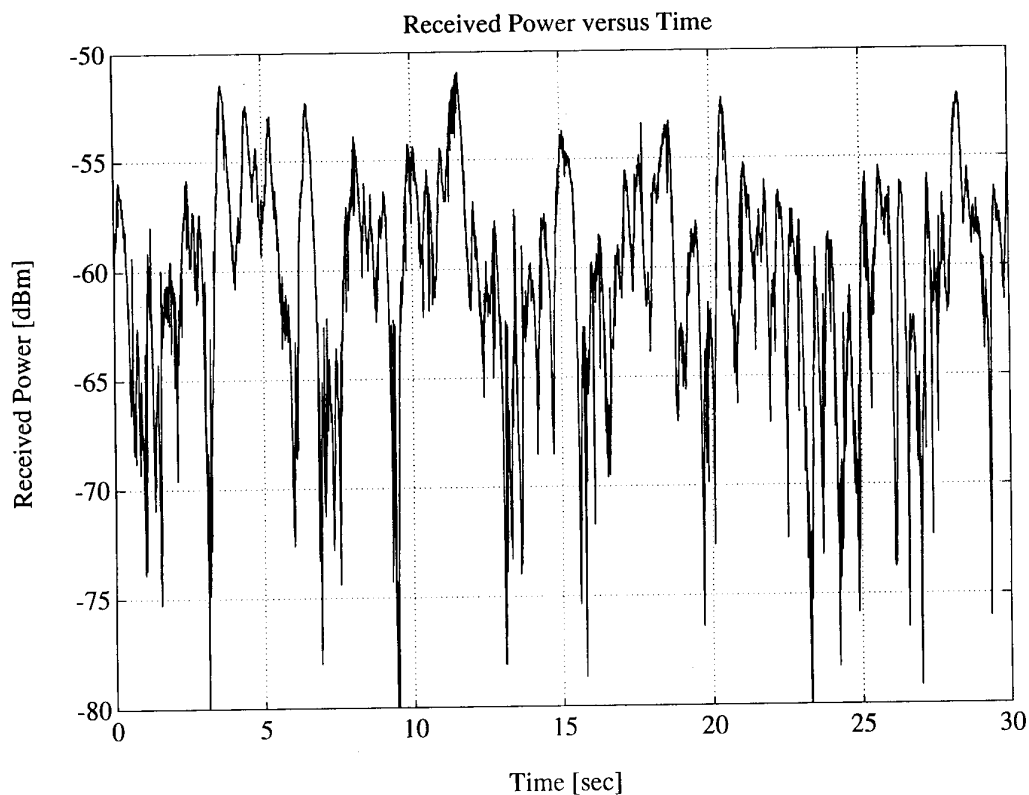


Figure 4. Typical 30 second segment showing Pulse-to-Pulse Variation in Bistatic Clutter Power Levels. Decorrelation Time is approximately 0.5 seconds.

Received Power versus Receiver Polarization Angle

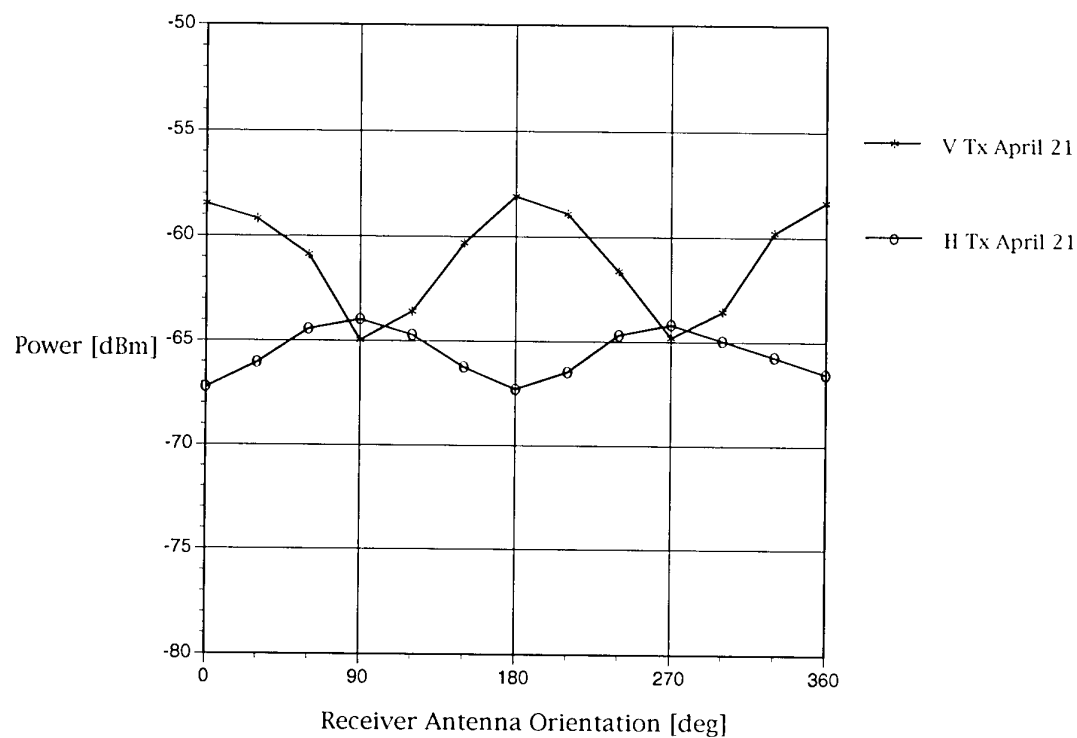


Figure 5. Variation of Received Power Level versus Receiver Antenna Orientation Angle.

Received Power versus Receiver Polarization Angle

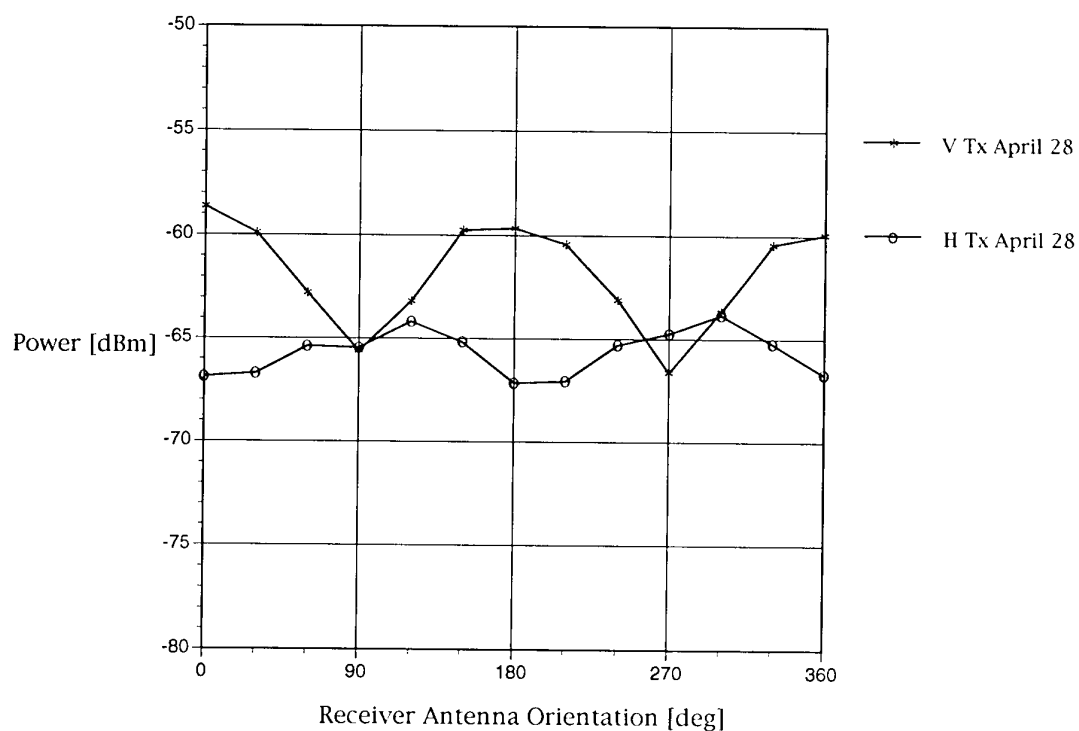


Figure 6. Variation of Received Power Level versus Receiver Antenna Orientation Angle.



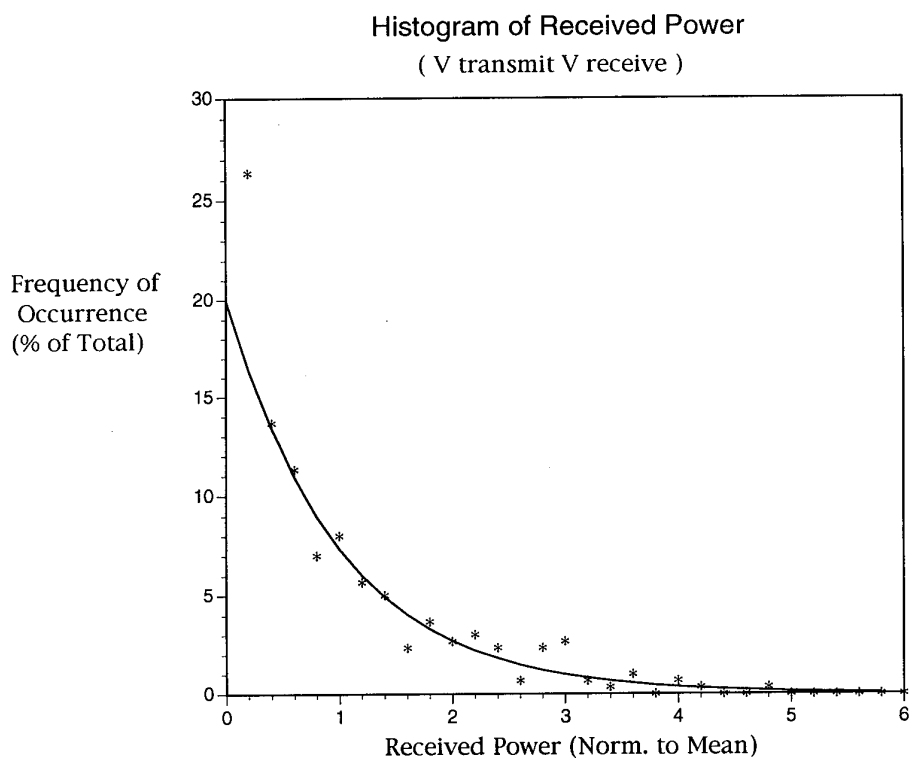


Figure 7. Histogram of Received Power for Vertical Transmit and Receive Polarizations. Solid line is Exponential Density Function.

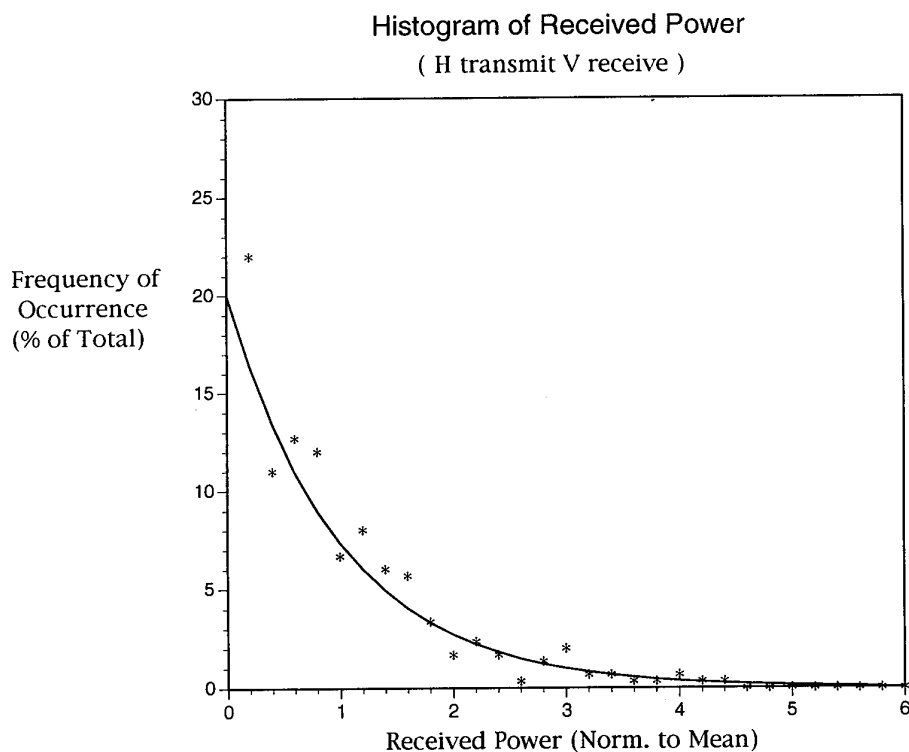


Figure 8. Histogram of Received Power for Horizontal Transmit, Vertical Receive Polarizations. Solid line is Exponential Density Function.

## Coefficient of Variation versus Receiver Polarization Angle

(April 21, 1993 )

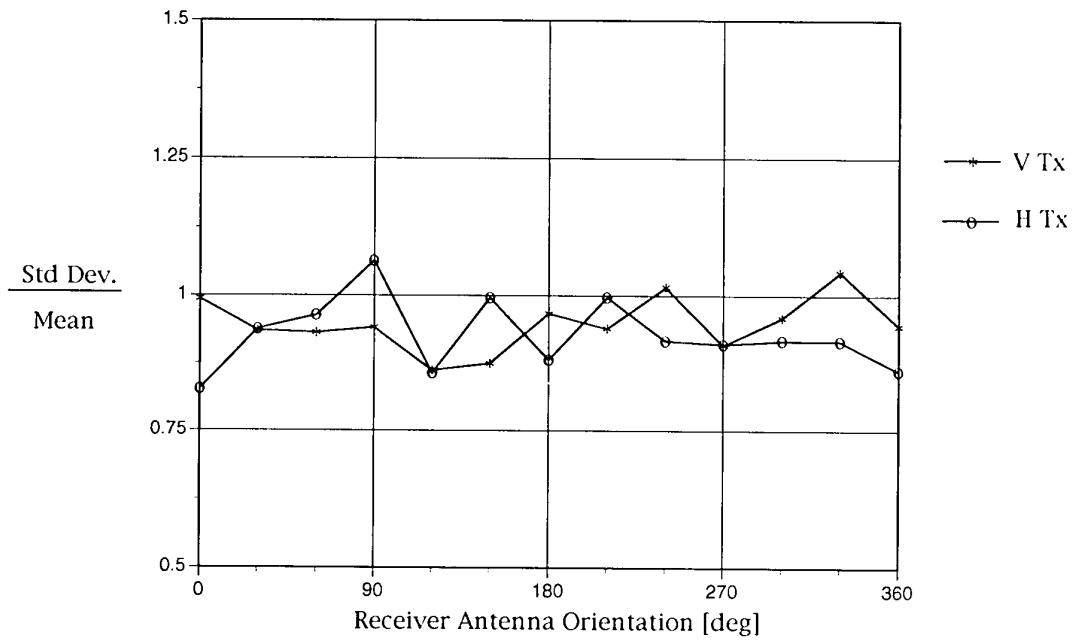


Figure 9. Coefficient of Variation (Normalized Standard Deviation) versus Receiver Polarization (orientation) angle for April 21 Data Set.

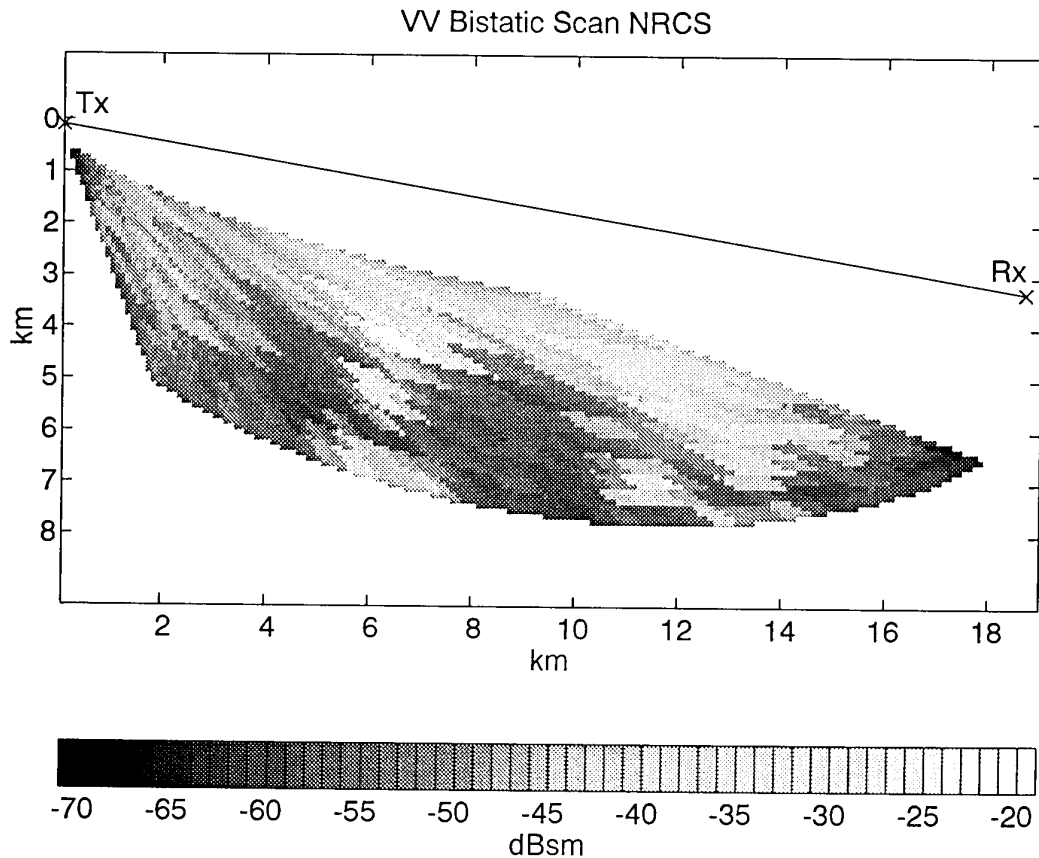


Figure 10. Bistatic Clutter Map Showing Calibrated NRCS for Vertical Transmitter and Receiver Antenna Polarization

# TIME BEHAVIOR AND FREQUENCY RESPONSE OF THE MICROWAVE PROPAGATION CHANNEL DURING MULTIPATH PROPAGATION

D. RANA<sup>†</sup>, M. SYLVAIN<sup>†</sup>, and A. R. WEBSTER<sup>\*</sup>

<sup>†</sup> C.R.P.E. (Unité mixte CNET/CNRS)

10-12 avenue de l'Europe

78140 Vélizy, FRANCE

<sup>\*</sup> Dept. of Electrical Engineering

University of Western Ontario

London, Ontario, Canada N6A 5B9

## SUMMARY

In this paper, ray-tracing simulation is used to model the dynamic behavior of the propagation channel in presence of a single super-refractive layer. Three typical mechanisms of layer formation and evolution are simulated according to experimental observations. 1) A ground-based layer formed by nocturnal cooling of the Earth's surface, its intensity increasing with time. 2) An elevating layer, that is a ground-based layer which weakens in rising, its intensity decreasing linearly with height. 3) An elevated layer formed when a warm dry air mass is produced in the upper atmosphere; this layer grows with time.

For each of these three types of layer, a ray-tracing program is used to compute the variations with time of the ray parameters and of the received signal level. As the statistics of the speed of layer formation and evolution are not precisely known, the time scale used in this study is somewhat arbitrary. However this technique allows one to identify three typical fading patterns and to help interpreting the physical mechanisms involved in the generation of multipath propagation. The frequency selective nature of the propagation channel bandwidth is then investigated over a 10.7-11.7 GHz in looking for the influence of each type of layer on the transfer function.

Some experimental evidence relating to, and confirming, the predicted behavior values is also considered.

## 1. INTRODUCTION

With the development of computers, ray-tracing simulations have allowed one to model correctly atmospheric multipath propagation on microwave line-of-sight links. However, the dynamic aspect of multipath propagation has rarely been considered in the various simulation studies which have been published (experimental studies have been presented by Sandberg [1980], Blanchetière-Ciarletti *et al.* [1989] or Li [1990], for instance).

In order to model the dynamic behavior of the microwave propagation channel, it is suitable to know

how super-refractive layers, which cause multipath, form and develop. In this study, we have used the experimental refractivity profiles presented by Ikegami *et al.* [1966]. These profiles have been obtained from relative humidity and temperature measurements made on a 312 m high tower located in Japan. As these authors did, we have distinguished three types of layer, according to their mechanism of formation and to their possible influence on the received signal.

These three typical layers, namely the ground-based, elevating, and elevated layers, are modeled in varying the parameters of a layer model. This model is the one given by Webster [1982]. A ray-tracing program is then used to compute the variations of the ray parameters and of the received signal level with time. However, one has to note that the time scale used in this study is somewhat arbitrary and that its relation with physical time depends on the speed of layer formation and evolution. In order to investigate the frequency selective nature of the propagation channel, the simulated frequency is varied to obtain the signature (time-frequency response) of each type of layer over a 10.7-11.7 GHz bandwidth.

The results presented in this paper should allow one to identify the various types of layer which may be observed on a microwave link. This knowledge should help building predictive methods more robust than those derived from a simple statistical analysis of experimental data.

## 2. RAY-TRACING CONSIDERATIONS

### 2.1 Atmospheric refractivity model

Tropospheric microwave propagation is mainly governed by the gradient of the refractive index  $n$ . Because the refractive index of the air is very close to 1, it is customary and convenient to use the refractivity  $N$  which is related to  $n$  by

$$N = (n - 1)10^6 \quad (1)$$

Although there is now some evidence that horizontal gradients may have a role to play on

microwave line-of-sight links (they modify the number of paths and the interference loci), the troposphere will here be considered as a horizontally stratified medium. In other words, the refractivity  $N$  will only depends on the altitude  $h$ .

In this paper, we will use the results of *Ikegami et al.* [1966]. These authors do not use the refractivity  $N$  but rather the modified refractivity  $M$  which is related to  $N$  by

$$M = N + \frac{h}{a} 10^6 \quad (2)$$

where  $a$  is the Earth's radius.

The simpler atmospheric model leading to multipath propagation consists in a standard atmosphere on which a single super-refractive layer (small height interval over which  $dM/dh$  is less than 0) is superimposed. This layer is assumed to be stable and uniform along the path. The formulation used to describe the atmospheric refractivity is the one given by *Webster* [1982]

$$N(h) = N_0 + kh + \frac{\Delta N}{\pi} \arctan \frac{[12.63(h-h_0)]}{\Delta h} \quad (3)$$

with  $\Delta N$  negative. In this model, the average refractivity profile is defined by a ground value of  $N$  ( $N_0 = 300$  NU) and a basic gradient ( $k = -0.04$  NU/m). The layer is characterized by its height  $h_0$  (in meters), its intensity  $\Delta N$  (in NU), and its thickness  $\Delta h$  (in meters) defined as the height range (centered on  $h_0$ ) over which occurs 90% of the change in  $N$ .

From relations (2) and (3), it is a straightforward matter to compute the duct intensity ( $\Delta M$ ) and the duct thickness ( $\Delta z$ )

$$\Delta z = \frac{2}{12.63} \sqrt{-\frac{12.63 \Delta N \Delta h}{0.117 \pi} - \Delta h^2} \quad (4)$$

$$\Delta M = 0.117 \Delta z + \frac{2 \Delta N}{\pi} \arctan \left[ \frac{12.63 \Delta z}{2 \Delta h} \right] \quad (5)$$

The duct exists only if  $\Delta N / \Delta h < -0.117 \pi / 12.63$ . The duct height is equal to the layer height  $h_0$ .

## 2.2 Ray parameters estimation

### Angle-of-arrival

The angle-of-arrival (AOA) is defined as the angle subtended at the receiver from the ray path to the local horizontal (positive if the ray is more elevated than the single atmospheric ray found for a standard atmosphere).

### Propagation delay

In order to define a propagation delay, it is necessary to first choose a propagation time of reference. This reference may be variable (propagation time of the stronger ray for a given atmospheric situation) or fixed (propagation time of

the direct ray for a standard atmosphere). In this study, we have chosen this second solution.

### Amplitude

Assuming no absorption loss and no horizontal refractivity gradient, the power density may be estimated in noting that the power launched within a small angular increment ( $d\theta$ ) arrives at the receiver spread out over a small height range ( $dh$ ). The amplitude associated with this ray is thus given by

$$A \propto \frac{d\theta}{dh} \Big|_{d\theta \rightarrow 0} \quad (6)$$

The above expression only considers the effects of refraction in the horizontal direction (ray focusing or defocusing). For a ground-reflected ray, it is also necessary to take into account the effects of Earth's curvature, surface roughness and reflectivity. Consequently, the amplitude of a ground-reflected ray has to be multiplied by a ground reflection coefficient  $R$ .  $R$  is given by

$$R = DR_0 R_s \rho_s \quad (7)$$

where  $D$  and  $R_0$  are respectively the divergence factor and the Fresnel reflection coefficient. Their definition is given in [*Livingstone*, 1970], for instance.  $R_s$  takes into account, if necessary, the fact that only a part of surface within the first Fresnel zone reflects specularly. Its expression is derived in *Rana et al.* [to be published] where the influence of the diffusely reflected power is also discussed.  $\rho_s$  is the specular roughness reduction factor, and it is given by the well-known relation [*Beckmann and Spizzichino*, 1963]

$$\rho_s = \exp \left[ -\frac{1}{2} \left( \frac{4\pi\sigma \sin \epsilon}{\lambda} \right)^2 \right] \quad (8)$$

where  $\lambda$  is the wavelength,  $\epsilon$  is the grazing angle of specular reflection, and  $\sigma$  is the standard deviation of surface heights. According to the values given by *Brutsaert* [1982], the parameter  $\sigma$  has been taken as 0.3 m for the fields and 4.87 m for the forests.

One may note that at grazing incidence,  $R_0$  is approximately equal to -1, and that for non directional antennas, it is not necessary to introduce antenna reduction factors in relation (7).

## 2.3 Example of ray-tracing

The ray-tracing technique is now applied to the experimental link Kemptville-Avonmore (Ontario, Canada). The terrain profile of this 50.6 km long link, as well as the four rays found for a standard atmosphere are shown in figure 1. The transmitting and receiving antennas are respectively at 150 m and 157 m above mean sea level. The operating frequency is 16.65 GHz (in the next two sections, our simulation results are compared with experimental observations made at this frequency). The ray parameters are given in table 1.

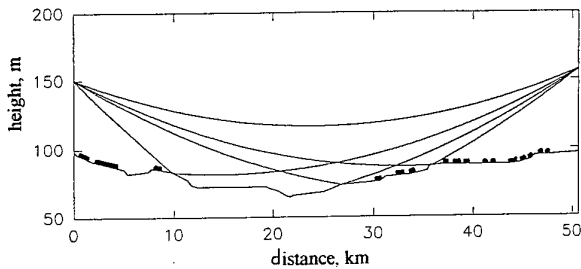


Figure 1. Path profile of the link-Kemptville-Avonmore. The rays plotted are those found by ray-tracing simulation for a standard atmosphere (flattened Earth representation used). The location of the forests is coloured in black.

Ray #	AOA, deg.	Amp, dB	Delay, ns	$d_r$ , km	$\epsilon$ , deg.
1	-0.2406	-28.5	0.433	10.00	0.1624
2	-0.2800	-21.4	0.246	26.80	0.0978
3	-0.3215	-34.6	0.220	36.00	0.1020
4	-0.1765	00.0	0.000	00.00	0.0000

Table 1. Received signal parameters obtained for a standard atmosphere. AOA and Amp are respectively the angle-of-launch and the amplitude. The delays are given relative to the propagation time of the direct ray (ray #4).  $d_r$  is the distance-of-reflection from the transmitter and  $\epsilon$  is the grazing angle.

### 3. TIME-VARIATIONS OF RAY PARAMETERS FOR THREE TYPICAL LAYERS

The atmospheric layer models used in this study undoubtedly consist in very rough approximations of what might be experimentally observed. These models do not allow one to consider small-scale variations of refractivity profiles. It is however likely that finer inhomogeneities cause very fast fluctuations of the received signal. In order to take them into account into a simulation study, it is possible to apply the ray-tracing technique to "fine" experimental atmospheric profiles as those presented by *Gossard et al.* [1984]. However, these profiles usually do not take into account horizontal inhomogeneities, and the limitations in resolution of the experimental equipment may lead to a biased estimation of these profiles. It is also permissible to model small-scale refractivity variations as a random process. This approach has been used by *Webster* [1991a] who considered the layer height as the random variable. In this paper, only large-scale variations of the refractive index have been investigated, as it is likely that small-scale variations do not modify significantly the overall trend of the ray parameters and received signal level.

The effects of three typical layers (ground-based, elevating, and elevated layers) have been simulated, according to the experimental observations of *Ikegami et al.* [1966], for the experimental link Kemptville-Avonmore mentioned in section 2. For each type of layer, the atmospheric refractivity model is presented,

and the variations with time of the ray parameters and of the received signal (computed as the vector sum of the rays) are given and discussed.

Concerning the presentation of the results, we have chosen to plot the M-profile rather than the N-profile. The direct ray parameters as found for a standard atmosphere are used as references, and the parameters of a given ray are not plotted if this ray amplitude is less than a given threshold (arbitrarily taken as -35 dB). The time scale used for the plots is arbitrary because the speed of layer formation and evolution is not precisely known. It may range from many minutes to several hours. For instance, the results presented in figure 26 of *Ikegami et al.* [1966] show a super-refractive layer elevating from the ground level to an altitude of 300 m in about two hours (from 22:30 to 00:30).

In order to illustrate the effects of the three types of layers considered in this paper, some experimental observations, obtained on the Kemptville-Avonmore link, are presented and interpreted according to the results of our simulations. Of course, refractivity measurements would be necessary to prove the rightness of our interpretation.

#### 3.1 Ground-based layer

A ground-based layer is formed by nocturnal cooling of the Earth's surface; it is thus usually observed after sunset and during the night. Its intensity  $|N|$  increases (in this example, from 0 to 50 NU with a step of 0.4 NU), while its height  $h_0$  and thickness  $\Delta h$  are kept constant (in this example, they are respectively equal to 135 m (above mean sea level) and 50 m).

Figure 2 shows the time variations of the M-profile, the received signal level and the ray parameters for this ground-based layer. As the layer gets stronger, the direct ray amplitude decreases and tends to a constant value of -10 dB. Its angle-of-arrival increases and its delay time (relative to the propagation time of the direct ray as found for a standard atmosphere) falls down to about -8 ns (the phase speed is increased by super-refractive conditions). However, one may note that the delay time difference between two rays is unlikely to exceed -3 ns. The received signal level is the sum of two components: a flat component due to a defocusing of the direct ray which leads to an average -10 dB level, and a time-varying component associated with the presence of ground-reflected rays.

The experimental data of figure 3 have been obtained using the experimental equipment described in section 4 (see also [*Webster and Merritt*, 1990]). There is some evidence that the results of figure 3 illustrate the effects of a ground-based layer on the received signal level. It seems likely that, in this example, the layer is sufficiently strong and close enough to the transmitter and/or the receiver to originate an average -20 dB level.

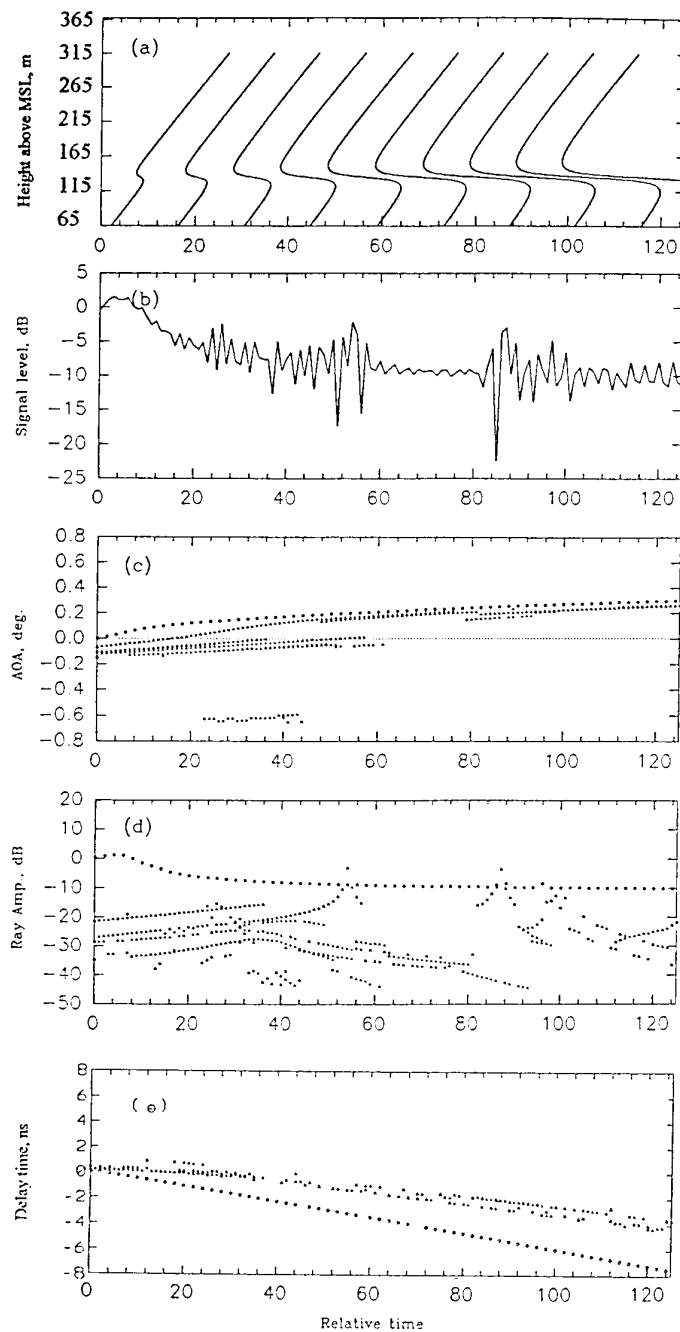


Figure 2. Variations of (a) the M-profile, (b) the received signal level, (c) the rays angle-of-arrival, (d) the rays amplitude, and (e) the rays delay time with time for a ground-based layer ( $h_0 = 135$  m). The angle-of-arrival, amplitude, and delay time of atmospheric rays (respectively ground-reflected) are represented by a  $\circ$  (respectively a  $\Delta$ ). A shift of 25 NU is applied to the profiles.

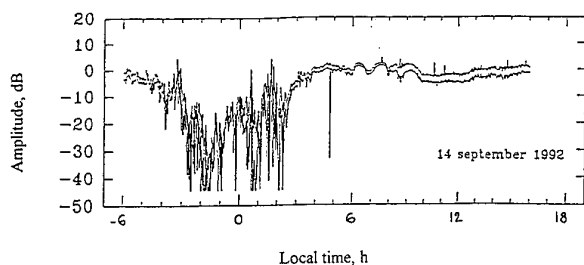


Figure 3. Amplitude of the received signal illustrating the effects of a ground-based layer. Shown is the reference channel of an antennas array (minimum and maximum over a one minute interval).

### 3.2 Elevating layer

An elevating layer is a ground-based layer which weakens in rising. This type of layer is usually observed just after sunrise [Sengupta, 1985]. The modelling of an elevating layer is such that the layer thickness  $\Delta h$  is kept constant and that the intensity of the layer is varied linearly with its height

$$\Delta N = \Delta N_i + (\Delta N_f - \Delta N_i) \frac{h_0}{h_{of}} \quad (9)$$

where  $\Delta N_i$  and  $\Delta N_f$  are respectively the initial and final value of  $\Delta N$ , and  $h_{of}$  is the layer height value for  $\Delta N = \Delta N_f$ . In the example of figure 4, we have taken,  $\Delta N_i = -10$  NU,  $\Delta N_f = -40$  NU, and  $\Delta h = 100$  m. The layer height  $h_0$  varies from 65 m (lower ground level on the Kemptville-Avonmore link) to 315 m (value of  $h_{of}$ ).

The effects of an elevating layer are shown in figure 4. As the layer height approaches the transmitter height (actually the lower terminal height), the direct ray amplitude becomes smaller and smaller, while its angle-of-arrival and propagation delay increase simultaneously. The associated received signal level decreases according to the defocusing of the direct ray (radio hole effect). Although it may be argued that the value of the ground reflection coefficient is a rough approximation based on simple assumptions, there is few doubt that the amplitude of such rays is sometimes higher than the amplitude of the defocused direct ray. As the ground reflection component is not stable (small variations of layer parameters affect significantly the number of ground-reflected rays and their parameters), the variations of the received signal are deep and fast. This result is usually summarized by "the lower the mean level, the greater the amplitude of the rapid fluctuations" [Olsen *et al*, 1986]. When the layer height is above the transmitter height, an atmospheric multipath propagation starts to occur. This mechanism lasts as long as the layer is strong enough and sufficiently close to the transmitter height.

There is a clear indication that the experimental data of figure 5 illustrate the effects of an elevating layer on the received signal. The continuous

defocusing of the direct ray with the layer elevation is followed by a short period of atmospheric multipath.

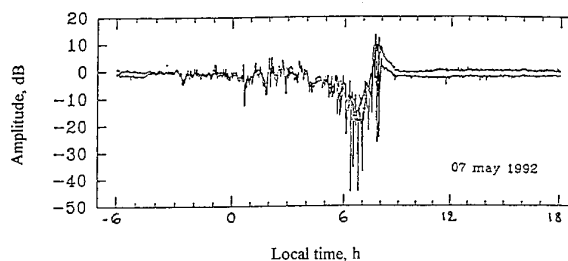


Figure 5. Amplitude of the received signal illustrating the effects of an elevating layer. Shown is the reference channel of an antennas array (minimum and maximum over a one minute interval).

### 3.3 Elevated layer

An elevated layer forms when a warm, dry air mass is produced in the upper atmosphere. It seems that this phenomenon mostly occurs during the night. This process is modeled by a layer which parameters  $h_0$  and  $\Delta h$  are kept constant (and respectively equal to 200 m and 100m). The layer intensity  $\Delta N$  is varied from 0 to -40 NU with a step of -0.25 NU.

Figure 6 shows the effects of an elevated layer. The direct ray and an additional atmospheric ray, the amplitude of which is slightly greater than the direct ray amplitude, combine to produce either constructive or destructive interference. The presence of a third ray which is mainly of atmospheric origin in this example but may be ground-reflected does not affect significantly the received signal level. The existence of an elevated layer is often associated with enhancements of the received signal.

It is likely that the experimental data of figure 7 give an illustration of the effects of an elevated layer on the received signal.

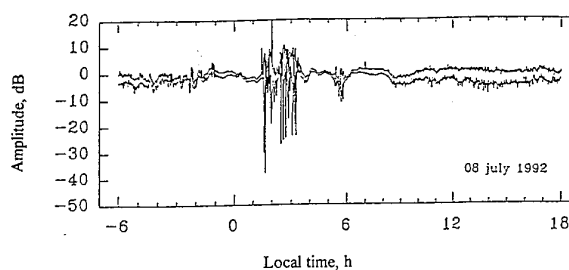


Figure 7. Amplitude of the received signal illustrating the effects of an elevated layer. Shown is the reference channel of an antennas array (minimum and maximum over a one minute interval).

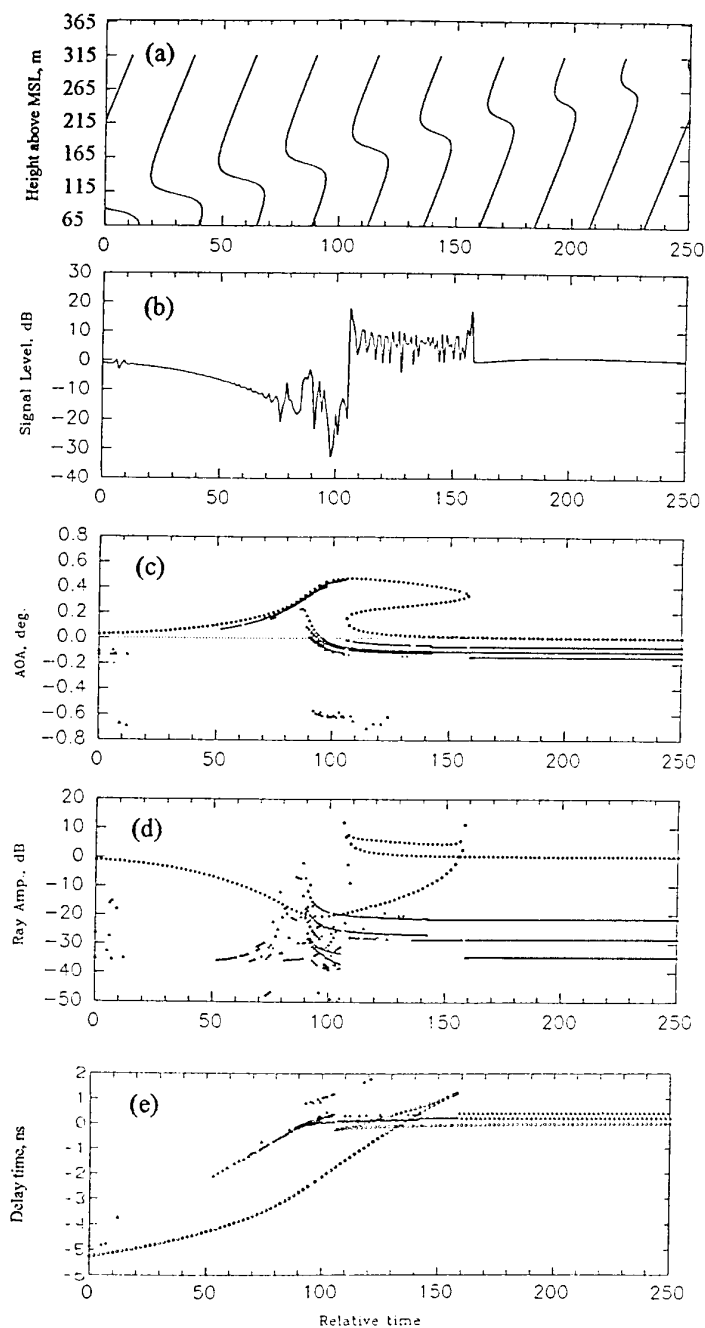


Figure 4. Variations of (a) the M-profile, (b) the received signal level, (c) the rays angle-of-arrival, (d) the rays amplitude, and (e) the rays delay time with time for an elevating layer. The angle-of-arrival, amplitude, and delay time of atmospheric rays (respectively ground-reflected) are represented by a  $\circ$  (respectively a  $\Delta$ ). A shift of 25 NU is applied to the profiles.



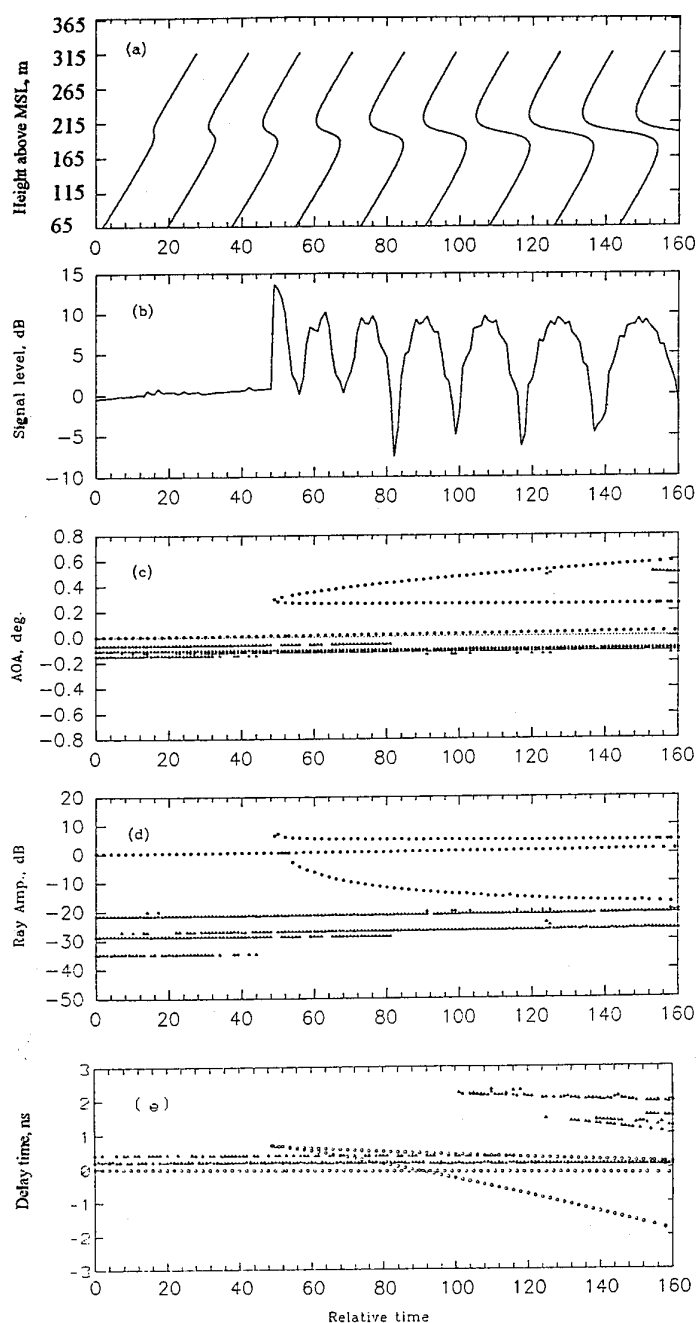


Figure 6. Variations of (a) the M-profile, (b) the received signal level, (c) the rays angle-of-arrival, (d) the rays amplitude, and (e) the rays delay time with time for a elevated layer. The angle-of-arrival, amplitude, and delay time of atmospheric rays (respectively ground-reflected) are represented by a o (respectively a  $\Delta$ ). A shift of 25 NU is applied to the profiles.

#### 4. COMPARISONS WITH COMBINED RAY ANGLE-OF-ARRIVAL AND AMPLITUDE MEASUREMENTS

The simulation results of section 3 are now intended to be compared with combined ray angle-of-arrival and amplitude measurements presented by Webster [1991b]. This should allow one to verify whether the variations of the ray AOA and amplitude as well as those of the received signal with time correspond to one of the mechanisms described in the previous section.

Experimental data from Webster [1991b] have been reproduced in figure 8. Let us first briefly describe the experimental equipment; a more complete description can be found in Webster and Merritt [1990]. The transmitter is a CW source operating at 16.65 GHz, while the receiver employs a wide aperture array of 16 pyramidal horns with a vertical separation of 0.75 m. The complex amplitude is sampled once per second across this aperture. A parabolic antenna located at the center of the array gives a phase reference and the reference channel amplitude. The basic processing of the raw data consists in a Fourier transform of the complex amplitude, which provides the angle-of-arrival spectrum. Side lobes levels are reduced by using a 40-dB Dolph-Chebyshev weighting function, and a 20 dB rejection threshold is applied to avoid a possible contamination by these side lobes.

Figure 8 shows the angle-of-arrival and the amplitude of each individual ray as well as the reference channel amplitude. As the characteristics of the array antennas and those of the reference antenna are not identical (for instance, the equivalent

beamwidth of the array is  $17^\circ$ , while this of the reference antenna is only  $2^\circ$ ), the reference amplitude can not directly be obtained as the vector sum of the individual rays. From the result of the analysis presented in section 3, the results of figure 8 can be qualitatively interpreted by the following sequence of events.

Refractivity measurements would again be necessary to verify the validity of our analysis. Although it is permissible to think that this analysis is qualitatively correct, it is not possible however to know whether the elevating layer combines with the ground-based layer to deeply reduce the level of the received signal and whether the ground-based layer becomes the elevated layer.

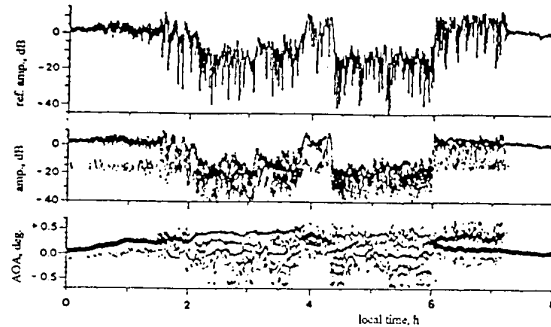


Figure 8. A summary of the activity during the early hours of September 10, 1988. Top: the amplitude of the reference channel. Center: the rays amplitude. Bottom: the rays angle-of-arrival with trace proportional to the amplitude (in decibel). Samples at 1-s interval. From Webster [1991b].

Time int., h	Experimental data Analysis	Type of layer
0:00 - 1:30	The direct ray AOA increases while its amplitude decreases.	Elevating
1:30 - 3:45	This mechanism continues and significant ground-reflected rays occurs. The received signal is the sum of a continuous component (flat fade associated with a defocused direct ray) and of a time-varying component (fast fades associated with ground reflections).	
3:45 - 4:10	A short period of atmospheric multipath associated with discontinuities of the AOA and the presence of high-amplitude elevated rays and of enhancements of the received signal follows.	Ground-based
4:10 - 6:00	Then a period of flat fading with an average -20 dB level occurs. Numerous ground-reflected rays may be seen.	Elevated
6:00 - 7:10	This flat fade period is followed by typical atmospheric multipath propagation; there are two high-amplitude rays of atmospheric origin, one them is the direct ray.	No layer
7:10 - 8:00	Normal propagation.	

Table 2. Interpretation of the experimental results of figure 8.

## 5. WIDE-BAND STUDY

### 5.1 Modelling consideration

It is easy to demonstrate from simple mathematical models of the propagation channel that the existence of several paths cause frequency selective fading. The frequency selectivity nature of the multipath propagation channel may also be easily observed for instance from Microwave Link Analyser (MLA) measurements, and such experimental observations abound in the literature ([Sandberg, 1980], [Martin, 1981], [Bundrock and Murphy, 1984], [Blanchetiere-Ciarletti et al., 1989],...). Nevertheless, we have found only very few theoretical or experimental studies trying to interpret the evolution of selectivity in terms of variation of the atmospheric profile.

In the frequency range of interest (centimeter wavelength), the ray parameters as given by the ray-tracing program do not depend on the value of the operating frequency (except the amplitude of ground-reflected rays). The signature (time-frequency response) of the propagation channel may thus be easily computed from a single set of parameters obtained for a given frequency.

On microwave line-of-sight links, propagation delays rarely exceed 10 ns. In varying the frequency of the resulting signal which is calculated as the vector sum of the rays, it is straightforward to show that the nodes and notches of the propagation channel transfer function are always separated by several hundreds of megahertz. It is thus a priori more interesting to study the transfer function over a wide bandwidth rather than over a medium bandwidth.

In this paper, we have chosen to investigate the signature of the three typical layers presented in the previous section over a 10.7-11.7 GHz bandwidth, which is the bandwidth allocated in France to high-bit rate LOS transmission.

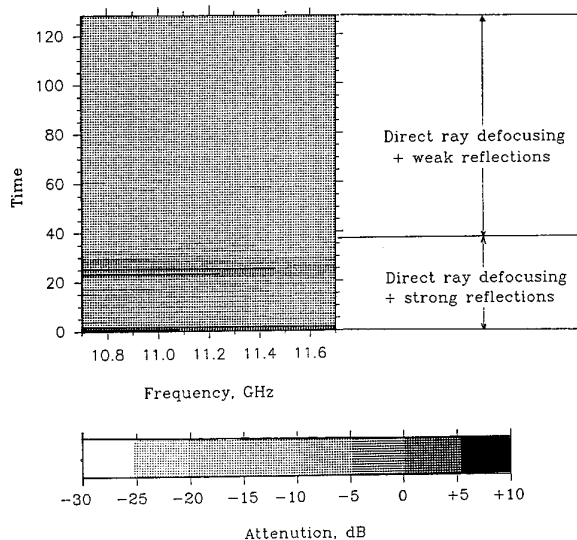


Figure 9. Signature of a ground-based layer. The characteristics of the layer are identical to those of figure 2. Sampling : 1 point every 10 MHz.

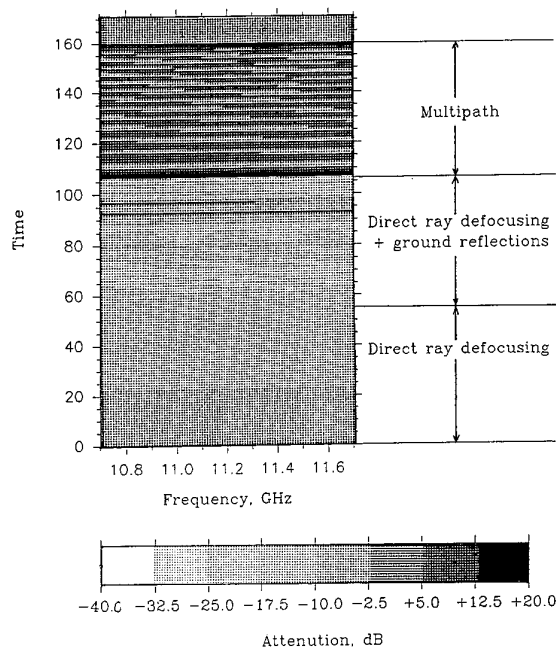


Figure 10. Signature of an elevating layer. The characteristics of the layer are identical to those of figure 4. Sampling : 1 point every 10 MHz.

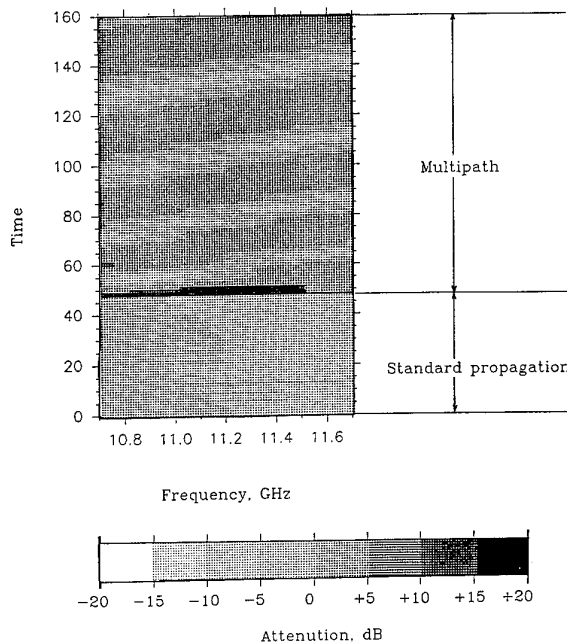


Figure 11. Signature of an elevated layer. The characteristics of the layer are identical to those of figure 6. Sampling : 1 point every 10 MHz.

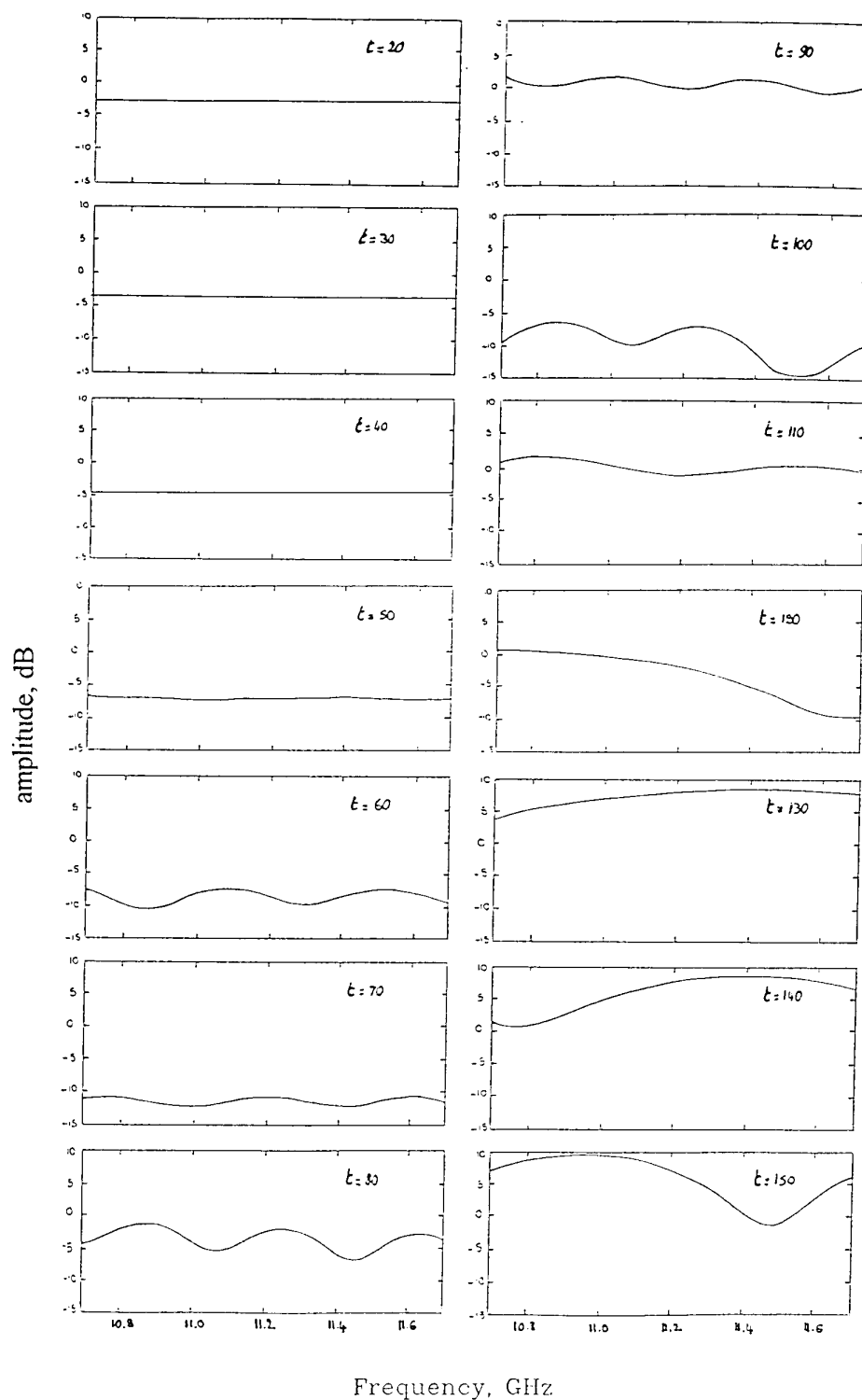


Figure 12. Sequence of transfer functions for the elevating layer which characteristics are given in figure 4.  $t$  indicate an arbitrary time, and the corresponding time-scale is identical to the one used in figures 4, 10, and 12.

## 5.2 Signature of the three typical layers

The results of figure 9, 10, and 11 show that the signatures obtained for the three typical layers presented in section 3 are significantly different from one another, and that each fading mechanism (atmospheric multipath, defocusing, and ground reflections) may be clearly identified. As long as the direct ray is not sufficiently attenuated to interfere with ground-reflected rays, a defocusing mechanism is associated with non selective fading. In presence of several paths (this includes the case of a defocused direct ray which amplitude is of the same order of magnitude than the amplitude of ground-reflected rays) the observed fading depend on the operating frequency.

As shown in figure 10, the three fading mechanisms previously considered (atmospheric multipath, defocusing, and ground reflections) are encountered for an elevating layer. In order to further investigate the effects of these mechanisms, we have thus found interesting to present the results of figure 10 in the form of a sequence of transfer functions (see figure 12).

As the propagation delays of the ground-reflected rays are longer than those of atmospheric rays, two or more notches may be found in the 1 GHz bandwidth during periods of strong defocussing (fig. 12, for  $60 \leq t \leq 100$ ), while atmospheric multipath propagation generally only leads to one notch of the transfer function (fig. 12, for  $t \geq 110$ ). These results apply to the 50.6 km-long Kemptville-Avonmore link, and the extension to other links would obviously require further investigation. However, it seems likely that ground-reflected rays have to be taken into account in a different way than atmospheric rays when modeling the transfer function, and that a two-frequencies diversity technique would be more appropriate to counteract the effects of atmospheric multipath fading than the effects of defocusing and ground reflections.

## 5.3 Comparison with experimental observations

One has to keep in mind that the time scale used in this study is arbitrary, and that it is not possible to derive directly quantitative information from the graphs presented in section 5.2. The experimental signature of figure 13 have been reproduced from [Blanchetiere-Ciarletti *et al.*, 1989]. Although these results have been obtained during a period where horizontal refractivity gradients were observed, there is a clear indication that the signature of figure 13 is similar to atmospheric multipath propagation (see figure 11 for comparison). An other experimental signature is presented in figure 13 of [Blanchetiere-Ciarletti *et al.*, 1989]. It does not seem to correspond to any of the signatures obtained in figures 9, 10, or 11. However, it has to be noted that it is associated with the presence of horizontal gradients, and that it has been recorded over a short period of time (60 seconds).

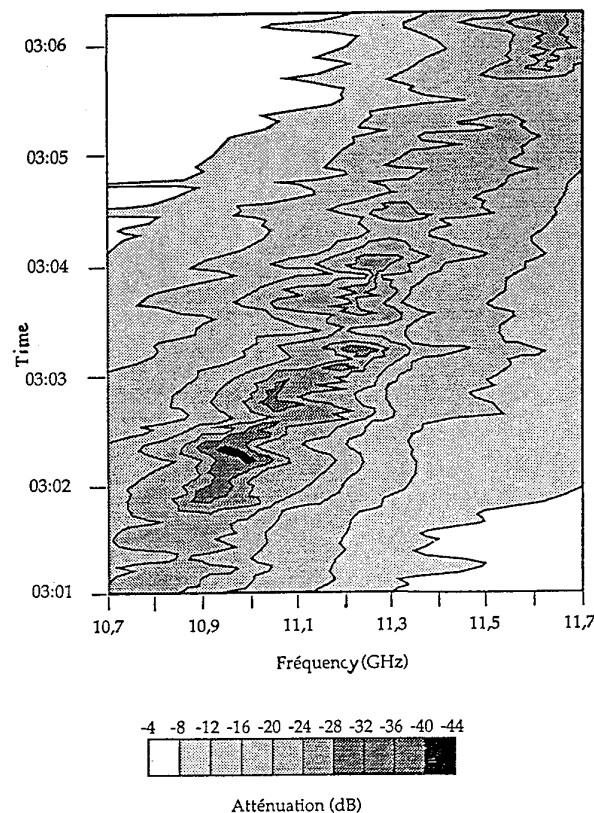


Figure 13. Experimental signature obtained on the Mont de Marsan-Maillas link (France) by Blanchetiere-Ciarletti *et al.* [1989].

## 6. CONCLUSION

The three typical layers (ground-based, elevating, and elevated) which have been studied in this paper are characterized by different behaviors of the propagation channel both in the time and in the frequency domains. This information is summarized by the channel signature which gives the amplitude of the received signal versus time and frequency. The analysis of these results should allow one to identify the atmospheric mechanisms leading to multipath propagation and hence to help estimate their probability of occurrence on a microwave line-of-sight link. In summary, the following appears to be relevant

- 1 - Long period of flat fading which may last several hours, are due to a defocusing of the direct ray associated with the presence of a ground-based layer. The level of the received signal can be 20 or 30 dB less than the free space level, depending on the characteristics of the layer. If the direct ray is sufficiently defocused, fast, deep, and frequency selective fading due to interferences with ground-reflected are superimposed to this flat fading.
- 2 - In presence of an elevating layer, the amplitude of the received signal decreases as the layer rises. It

reaches a minimum when the layer height is equal to the lower terminal height. Then a period of atmospheric multipath follows; this period lasts as long as the layer is strong enough and sufficiently close to the lower terminal height.

3 - Elevated layers cause atmospheric multipath fading. This type of fade is often associated with enhancements of the received signal.

4 - The frequency response obtained in period of direct ray defocusing plus ground-reflections is quite different from the one obtained in period of atmospheric multipath, mainly because of the difference between ground-reflected and atmospheric rays propagation delays. This result should be relevant to radio designers and engineers in modelling the transfer function of the propagation channel, and in estimating the effects of a frequency diversity technique. It seems likely that frequency diversity may be more efficient to counteract the effects of atmospheric multipath fading than space diversity while this second technique seems to be more appropriate to counter the effects of "defocusing plus ground reflections". Of course, this conclusion applied to the frequency bandwidth considered in this study (1 GHz).

The next step of this study should consist in measuring the speed of layer formation and evolution in order to estimate the period of observation of the fading mechanisms described in this paper. The same technique as the one presented in section 5 could also be applied to investigate the effects of atmospheric multipath and ground reflections over a narrower bandwidth (in the order of 20 or 30 MHz for instance).

**Aknowledgements.** The experimental work described here was supported in part by the Communications Research Centre in Ottawa and by the Natural Sciences and Engineering Research Council of Canada. The cooperation of Bell Canada is greatly appreciated.

#### REFERENCES

- Beckmann, P., and A. Spizzichino, *The scattering of electromagnetic waves from rough surfaces*, Pergamon Press, New York, 1963.
- Blanchetière-Ciarletti, V., J. Lavergnat, M. Sylvain, and A. Weill, Experimental observation of horizontal refractivity gradients during period of atmospheric multipath propagation, *Radio Sci.*, 24(6), 705-724, 1989.
- Brutsaert, W. H., *Evaporation into the atmosphere: theory, history, and applications*, D. Reidel Publishing Company, Dordrecht/Boston/London, p. 114, 1982.
- Bundrock, A. J., and J. V. Murphy, A broad band 11 GHz radio propagation experiment, *IEEE Trans. Antennas Propag.*, AP-32(5), 1984.
- Gossard, E. E., W. D. Neff, R. J. Zamora, and J. E. Gaynor, The fine structure of elevated layers: implications for over-the-horizon propagation and radar sounding systems, *Radio Sci.*, 19(6), 1523-1533, 1984.
- Ikegami, F., M. Haga, T. Fuguda, and H. Yoshida, Experimental studies on atmospheric ducts and microwave fadings, *Rev. Electr. Comm. Lab.*, 505-533, 1966.
- Martin, R., Relative amplitudes and delays during multipath fadings, *Proc. of IEE, international Conf. on Antennas and Propag.*, York, 1981.
- Li, Y., *Etude du comportement dynamique du canal hertzien pendant les périodes de trajets multiples*, Thèse de doctorat de l'université de Paris VII, Paris, France, 1990.
- Livingstone, D. C., *The physics of microwave propagation*, Englewood Cliffs, NJ: Prentice Hall, 1970.
- Olsen, R. L., L. Martin, and T. Tjelta, A review of the role of surface reflection in multipath propagation over terrestrial microwave links, *Proc. NATO AGARD, CP-407*, 2.1-2.23, 1986.
- Rana, D., A. R. Webster, and M. Sylvain, Origin of multipath fading on a terrestrial microwave link, *Annal. des Telecommun.*, accepted on June 9, 1993.
- Sandberg, J., Extraction of multipath parameters from measurements on a line-of-sight path, *IEEE Trans. Antennas Propag.*, AP-28(6), 743-750, 1980.
- Sengupta, N., Sunrise and sunset effects as observed on microwave propagation over a line-of-sight path, *IEEE Trans. Antennas Propag.*, AP-33(4), 441-445, 1985.
- Webster, A. R., ray path parameters in tropospheric multipath propagation, *IEEE Trans. Antennas Propag.*, AP-30(4), 796-800, 1982.
- Webster, A. R., and T. S. Merritt, Multipath angles-of-arrival on a terrestrial microwave link, *IEEE Trans. Commun.*, 38(1), 25-30, 1990.
- Webster, A. R., Rough elevated layers and tropospheric microwave propagation, *Antennas Propag. Society Symposium*, London, 1552-1553, 1991a.
- Webster, A. R., Multipath angle-of-arrival measurements on microwave line-of-sight links, *IEEE Trans. Antennas Propag.*, AP-39(6), 798-803, 1991b.

## Development of a Fast Sampling System for Estimation of Impulse Responses of Mobile Radio Channels

Pierre Melançon

Communications Research Centre

3701 Carling Ave, Ottawa, Ontario, Canada K2H 8S2

### 1. SUMMARY

This paper describes the features of measurement equipment developed to measure impulse response estimates of mobile radio channels in less than a ms per measurement. The development of such equipment was required to measure mobile radio channels in realistic operating scenarios, in a normal sized vehicle moving at typical speeds in different environments. Up to speeds of 70 km/hr, the measurement period is short enough to assume the equipment is measuring the same channel during the whole sampling interval. At the transmitter end of the measurement system, a wideband signal (10 MHz) is produced by modulating a carrier frequency with a 511 bit pseudo random sequence at 5 Mb/s and transmitted through the radio channel. The received signal is down-converted to 70 MHz and demodulated by a complex demodulator. The quadrature baseband signals at the demodulator outputs are then filtered and sampled at high speed by two fast digitizers. During this process, the data are stored in large memory banks to allow a fast sampling rate during a long period of time. Data are transferred to laser disks for further processing in the laboratory. Impulse responses of radio channels are estimated by performing a software correlation between a measurement system back to back reference and real time measurements. A minivan was modified to hold the receiver, digitizers, memory banks and the computer. A shaft encoder was attached to its rear left wheel to trigger measurements while moving. Features of the system are discussed along with the effects of data block length, signal to noise ratio, sampling rate, memory size and phase stability on the design of the measurement equipment. Finally, some measurement results are presented and discussed.

### 2. INTRODUCTION

Mobile radio channels are particularly interesting to study because of the many impairments that cause rapid, significant degradations in communication signal quality. A short list of phenomena includes deep multipath fading, shadowing, random fm, frequency selectivity, multipath propagation and Doppler spread. Good estimates of radio channel impulse response functions are necessary to characterize these phenomena. Based on such measurements, a radio engineer can predict signal degradation and loss of information.

Hardware correlators have previously been used [1,2,3] to estimate impulse responses in different environments, including: land mobile, cellular and indoor radio channels. Unfortunately, such measurement systems require long sampling times to estimate each impulse response. For example, a typical setup used for cellular radio channel measurements modulates a carrier at a chip rate of 10 Mb/s, uses a correlation rate of  $10^{-4}$  the chip rate (1 kHz) at the correlator and a pseudo random sequence of 511 bits. This results in a sampling time of 511 ms. Consequently, it is not possible to measure a channel changing at a rate of even a few hertz. Only truly static environments can be measured.

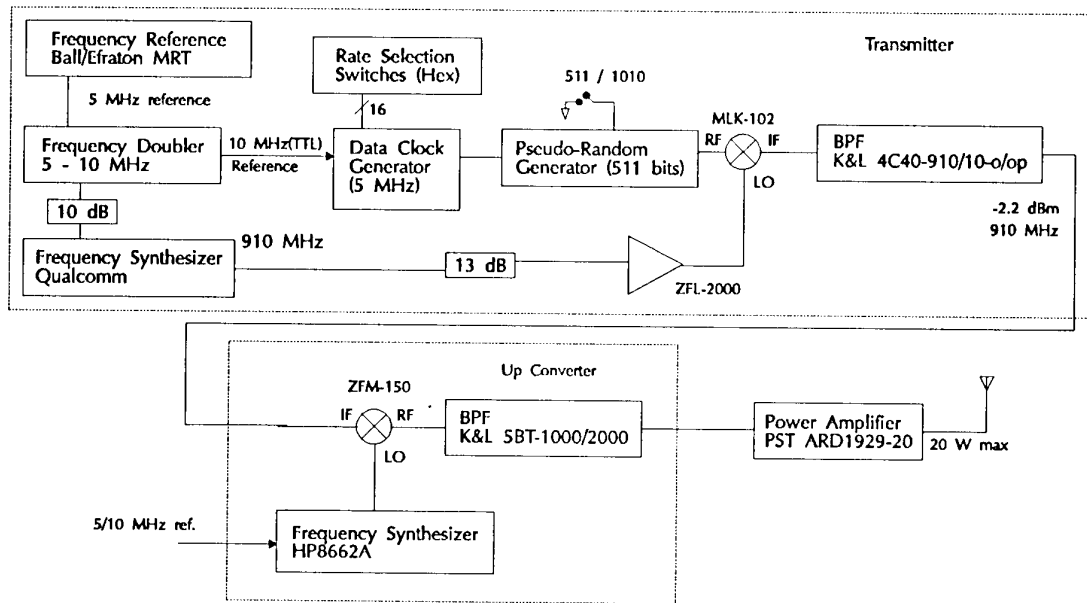
This paper reports a measurement system similar to the equipment presented by Levy [4]. The operation is similar to a hardware correlator except it directly samples the received

signal, stores the data on disk and processes it later by software. The system is very fast and sampling times of less than a half millisecond are possible for the implementation discussed here. The next section describes the impulse response measurement system. A discussion on the different tradeoffs in the design follows. Finally, some measurements are presented and discussed.

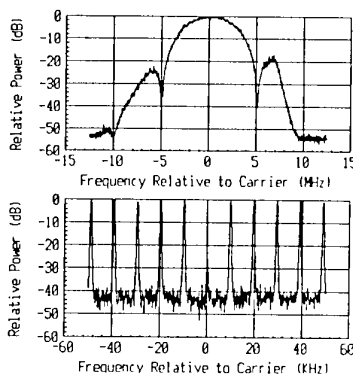
### 3. DESCRIPTION OF THE EQUIPMENT

Figure 1 shows the wideband transmitter configuration. It transmits a wideband radio signal which is produced by modulating a 910 MHz carrier with a pseudo random sequence. The Local Oscillator (L.O.) is modulated at 5 Mb/s by a 511 bits Pseudo Random Binary Sequence (PRBS). The resulting RF signal is then filtered by a 10 MHz bandpass filter (BPF) to keep only the first lobe of the signal. Then, it is up-converted to the frequency band of interest. A power amplifier provides a maximum output power of 20 W. Antennas used at the different frequencies are all omnidirectional monopoles with drooping radials. This type of antenna was selected because of its bandwidth, easy construction and radiation pattern which is practically independent of the location of the antenna on car roofs. Figure 2 shows the transmit output spectrum. The width of the first lobe is twice the chip rate (10 MHz) and the frequency separation between the frequency lines is 9.78 kHz. The spectrum has the  $\sin(x)/x$  shape with a slight distortion due to the filters. Because non-linearity in the transmitter or receiver can cause false echoes [4], great care was taken to use linear amplifiers to reduce distortions. The clock generator and local oscillators are locked in phase to a highly stable rubidium frequency standard to enable phase measurements.

The wideband receiver configuration is shown in Figure 3. In order to sample two channels quasi-simultaneously and make diversity measurements, two omnidirectional antennas are connected to a receiver with two separate front ends. Each front end amplifies and down-converts the RF signal to an IF frequency set at 70 MHz. An RF switch connects either one of the two input signals to a complex demodulator. At the demodulator output, the in-phase and quadrature baseband signals are filtered by two identical low-pass filters, each with a 3 dB cut-off frequency of 4 MHz to avoid aliasing. At 5 MHz, the rejection is 50 dB. These signals are sampled at 10 Msamples/s and the data is stored in memory banks of 32 MB (16 MB/channel). The data are transferred to laser disks with capacities of about 650 MB per disk. Laser disk storage was selected instead of a Digital Audio Tape (DAT) or 8 mm tape because of its random access feature. Data are processed simultaneously on several computers in the laboratory after field measurements. A single channel is measured by keeping the RF switch always connected to the same front end. Diversity measurements are taken by measuring the signal from one front end then switching to the other front end, then, after the measurement, the switch returns to its previous position and waits. Table I shows the measurement system specifications, each of which will be explained in the following section.



**Figure 1:** Wideband transmitter configuration



**Figure 2:** Output spectrum of transmit signal. The top plot shows the  $\sin(x)/x$  shape of the output signal. The bottom plot is an expanded view of the top plot centered at the carrier frequency.

Measurements are triggered by either time or distance. In both cases, when sampling is triggered, a block of data is acquired and stored in memory. Since the memory banks are limited in size, the trigger rate determines the duration of, or distance travelled during, an experiment. For a block size of 4096 samples per trigger, the maximum number of blocks that can be sampled in one run is  $4096 \times (32 \text{ MB} / (4096 \times 2 \text{ baseband signals}))$ . If measurements are triggered every metre, the maximum distance travelled is then 4.096 Km, or if they are triggered at 100 Hz a measurement lasts about 40 seconds.

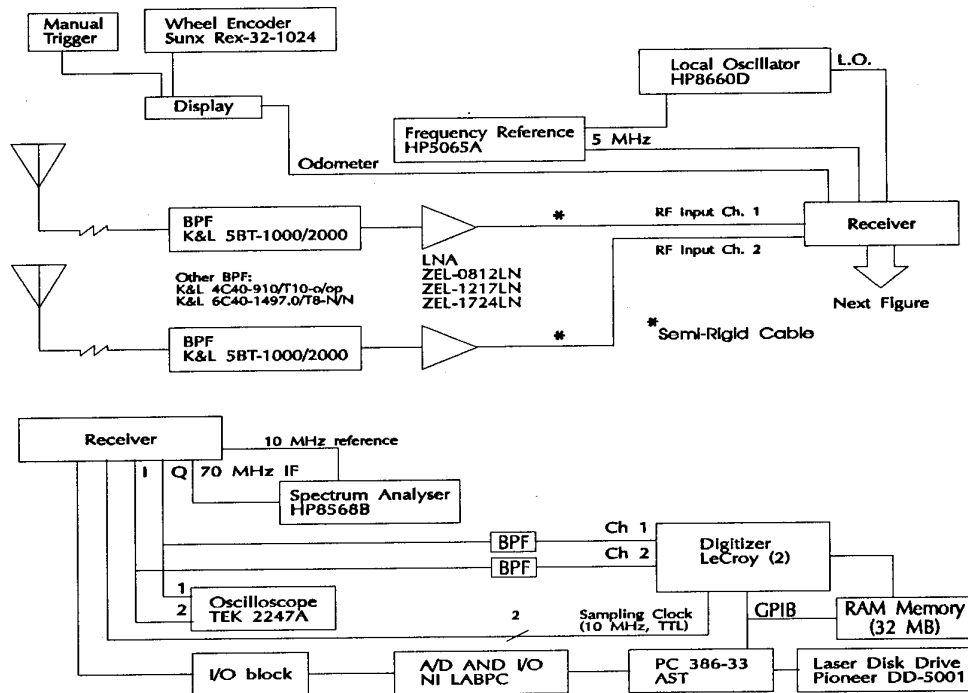
All equipment is mounted in standard 19 inch racks, 100 cm high. The transmitter fits in a special trailer equipped with a generator that can be set up at any transmitter site. The receiver racks are installed in a minivan. This is used instead of a normal

van or truck so as to simulate operation from a sedan as closely as possible. The AC power is provided by two different sources. A DC-AC inverter, equipped with batteries, converts the 12 - 14 V dc power from the car generator to 120 V AC. It powers the computer, disk drives and frequency standard. This inverter is used as an uninterruptible power supply and maintains power in case of power failure from the car. It also keeps the frequency standard warm and stable. A gasoline powered AC generator is mounted on the back bumper of the minivan to power the rest of the equipment. Distance travelled is recorded by monitoring a shaft encoder. The trigger distance can be set from 1 cm to several metres. Except for the frequency standard which is mounted on a foam cushion, there is no special suspension system to protect the equipment against vibrations and road bumps. The minivan suspension was tested and found to be sufficient. A special suspension was rejected because it uses several cm of much needed vertical space.

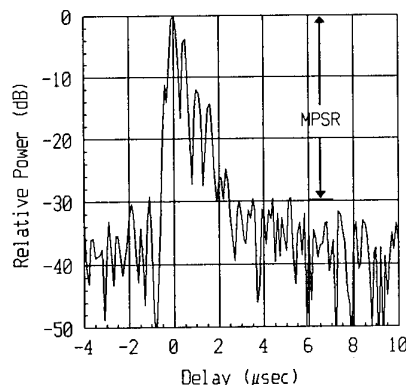
In a typical run, the transmitter is set-up on the side of the road. Then the receiver, mounted in the minivan, travels at normal traffic speeds and records the received signal. The system is designed to always start sampling at the same position in the PRBS. When the distance encoder triggers a measurement, it enables the sampling of 1 block of data. The digitizers start sampling when a new PRBS starts, no later than  $102.2 \mu\text{s}$  after the trigger. This feature permits ranging as explained in later paragraphs.

Figure 4 is an example of a measured impulse response estimate. Figure 5 is its Fourier transform. In figure 4, the Multipath Power Sensitivity Ratio (MPSR) indicates the power ratio of the strongest echo and the peak 'noise'. This 'noise' is composed of contributions from the correlation sidelobes as well as the receiver noise. In figure 5, the Fourier transform of a back to back reference measurement is superimposed on the plot. It clearly shows distortion due to multipath propagation. The reference curve is not a perfect  $\text{sinc}^2(x)$  because of the filters used in the measurement system.





**Figure 3:** Wideband receiver configuration



**Figure 4:** Example of a typical estimate of impulse response in a non line of sight path, downtown Ottawa. The MPSR is about 30 dB, delay spread is slightly more than 2  $\mu$ s and the first path is not the strongest path.

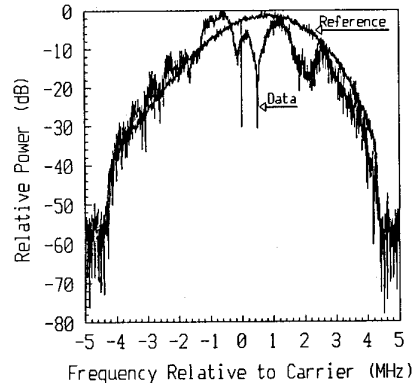


**Figure 5:** Spectrum of impulse response estimate shown in Fig. 4. The spectrum of the reference is superimposed to show the distortion measured.

#### 4. DATA PROCESSING

Impulse response estimates are obtained by computing the correlation between a block of sampled data and the reference signal. The reference is used in correlation computation instead of a copy of the baseband PRBS because it includes distortion due to the system hardware. Software correlation is done in accordance with the following algorithm:

1. Let  $x(t)$  and  $b(t)$  be finite-duration functions, where  $x(t)$  is the data sampled during an experiment, and  $b(t)$  is the back to back measurement. (Both blocks have the same length to simplify the data processing and this length is equal to  $2^N$ , where  $N$  is an integer value. Data blocks

contain more than one PRBS to reduce the noise level by averaging.)

2. Add zeros to double the length of each block. (These zeros are necessary to avoid overlap in the correlation process.)

3. Compute the Fast Fourier Transform (FFT) of each block,  $X(f)$  and  $B(f)$ .

4. Compute  $H(f) = X(f) B^*(f)$ , where  $B^*(f)$  is the complex conjugate of  $B(f)$ .

5. Obtain the correlation  $h(t)$  by computation of the inverse FFT of  $H(f)$ . (Since each data blocks is longer than one sequence, the resulting correlation has several sidelobes due to partial correlations.)

6. The highest peak is selected and the impulse response estimate is extracted by selecting 1022 points (the sampling period is 100 ns and the PRBS lasts 102.2  $\mu$ s) starting 100 before the main peak (Fig. 4) to include all precursors.

The execution time of this algorithm is long because of the large number of multiplications. Typically, on a 486/50 MHz PC, it needs about 3.5 s/impulse response, which means days of CPU time for a few hours of measurements.

### 5. SPECIFICATIONS OF THE MEASUREMENT SYSTEM

At 910 MHz, the maximum distance travelled during one sampling interval is less than a tenth of a wavelength at normal traffic speeds. It is assumed the radio channel does not change significantly over that distance. The minimum spatial sampling distance is set at a tenth of wavelength (3.3 cm). Previous measurements show that multipath spreads rarely exceed 30  $\mu$ s, except for a few measurements in mountainous terrain. The required unambiguous delay window must therefore be greater than 30  $\mu$ s. In order to enable the computation of good estimates of correlation bandwidth, which has been recorded to be as low as few tens of kHz [6,7] in urban areas, the spectral density of the probing signal is required to be less than 10 KHz. The minimum measured bandwidth is set at 6 MHz, equivalent to a TV channel. Diversity measurements (2 channels) are required to study space, pattern or polarization diversity as means to improve communications. A multipath signal power sensitivity ratio of at least 30 dB is necessary to achieve measurements at least as good as estimates from a hardware correlator. For measurements every half wavelength, with diversity, the recording distance required is greater than 200 m.

The pseudo random sequence length is 511 bits and its clock rate is 5 Mb/s. These two parameters set several specifications of the measurement system and they were carefully selected to fit our requirements. The 511 bits per sequence set the correlation sidelobes at -54 dB, well below the MPSR requirements. The 5 Mb/s was selected after several chip rates were tested to obtain the best time resolution for a bandwidth of 8 MHz. Fig. 7 shows the system output for chip rates of 1, 2, 5 and 10 Mb/s. Five Mb/s was selected because it results in a

narrow peak. Interestingly, high bit rates, such as 10 Mb/s, show a thinner peak but at the cost of a wider section at -30 dB. This is different from the correlation triangle because an important part of the first lobe is filtered out. The unambiguous delay is automatically set at 102.2  $\mu$ s (511 x 200 ns) and the spectral density is set at 9.785 kHz (1/102.2  $\mu$ s).

The maximum reliable trigger rate was found to be 500 Hz. This rate is set by the measurement period and triggering delay in the system. The minimum distance between two measurements is 1 cm. Two 8 bit high quality digitizers sample the in-phase and quadrature baseband signals at 10 Ms/s. They are rated at a maximum sampling rate of 100 Ms/s and yield 40 dB s/n at 5 Msamples/s for an input signal amplitude at 80% of maximum input. Each digitizer is connected to 16 MB of random access memory. Limited memory means that the number of samples per block of data is important. Data cannot be acquired continuously. At 10 Ms/s, digitizers will fill the memory in a little more than 1.6 s. Fig. 8 shows the effect of different block lengths on the impulse response estimate. Based on these plots, a block size of 4088 or more is considered sufficient to maintain a 30 dB MPSR. At 4096 samples/block and 16 MB of memory per digitizer, a maximum of 4096 blocks of data can be stored in memory. The block length also sets the duration of one measurement period and the maximum distance travelled during one experiment or run. For long runs and/or high speed measurements, 4096 samples/block was chosen to be the most suitable. This leads to a sampling period of 0.5 ms. Therefore, at 30 m/s, the distance travelled during one measurement interval is 1.5 cm, less than the tenth of a wavelength requirement at 910 MHz. For a trigger distance of 15 cm or around half a wavelength, the maximum distance travelled is 614 m for single channel measurements or 307 m for two channels diversity recordings.

The multipath power sensitivity ratio is required to be greater than 30 dB. Once the data block length sets the correlation gain, the only other way to improve the MPSR is to maintain a large signal to noise ratio at the input of the receiver. At first, it was thought an Automatic Gain Control (AGC) was necessary to maintain input signal levels to the digitizer above 80% of the maximum input. This was reasonable since the signal fades continuously. Unfortunately, this gain had to be tracked and recorded because different gains also mean different phase shifts. However, it was verified that if the receiver is set at a constant gain, the MPSR is not degraded very much. Measurements show that if an AGC is set to maintain the signal above 80% of the maximum level and under saturation, the MPSR is greater than 30 dB for input signal power levels above -100 dBm (Fig. 6). For power levels below -100 dBm, the receiver noise becomes important and the MPSR decreases linearly with the input signal power. On the other hand, if the receiver gain is set manually the MPSR is still more than 30 dB for strong signals and as the signal power decreases, only a 2 dB degradation is measured for input signal powers lower than -100 dBm. A similar test on a hardware correlator showed rapid degradation of the MPSR if the gain is not adjusted. Therefore, for a software correlator, the noise floor is set mostly by the correlation process, at least down to -100 dBm. This remarkable feature of a software correlator greatly simplifies measurements, which can be done over long distances even with fading and shadowing of the signal. The maximum propagation loss the equipment can tolerate with a MPSR greater than or equal to 30 dB is then, for a transmit power of 10 W (40 dBm), about 140 dB (40 dBm - (-100dBm)).

Two rubidium frequency standards are used to phase lock all the oscillators used in the measurement system. If only envelope

Sequence length	511 bits
Chip rate	5 Mb/s
Unambiguous delay	102.2 $\mu$ s
Spectral density	9.785 kHz
Frequency range	100 MHz to 2 GHz
Measured bandwidth	8 MHz
No. of rf channels	2
Minimum trigger distance	1 cm
Maximum trigger rate	500 Hz
Sampling rate	10 Ms/s
Digitizer	8 bits/100 MHz
Data block length	4096/8192
Block sampling time	$\approx 0.5$ ms/ $\approx 1.0$ ms
Maximum number of blocks	4096/2048
Memory size	16 MB/ channel
Multipath Power Sensitivity Ratio	>30 dB.
Stability	$1 \cdot 10^{-11}$ Hz/ 1 s

**Table I :** Specifications of the impulse response measurement equipment.

information is required, local oscillator frequency offsets of up to 1 kHz are acceptable.

## 6. TYPICAL MEASUREMENT RESULTS

This section presents examples of impulse response estimates measured with the system described above. Figure 9 compares the output of a hardware correlator measurement system to the output of the software correlator. The two impulse response estimates are for the same transmitter - receiver configuration and both systems show very similar results. The differences between the two plots are due to a better time resolutions of the hardware correlator. This measurement shows that both systems have the same output for static radio channels.

Fig. 10 shows impulse response estimates recorded quasi-simultaneously on two diversity channels, a specification unique to the measurement system. The main features of these measurements are very similar, but because of different vectorial additions of multipath within the equipment time resolution the exact position and amplitude of each path group is slightly different. Fig. 11 shows the instantaneous coefficient of cross-correlation between the structure of impulse response estimates measured from two antennas separated by 1.0 and 1.5 wavelength (15 cm and 22.5 cm) at 1.980 GHz. Measurements were made every cm and coefficients of cross-correlation were also computed every cm for a total distance of 64 cm. The two antennas were installed side by side across the roof of the vehicle. Measurements were done in line of sight (LOS) and non line of sight (NLOS) environments. For an antenna separation greater than or equal to 1.5 wavelength, it was found the two radio channels are uncorrelated, for both LOS and NLOS conditions. For a 1 wavelength separation the cross-correlation coefficient is very high ( $>0.9$ ) for LOS and varies from low to high (0.2 to 0.7) for when there is NLOS.

The final feature to be discussed here is ranging. It is possible to determine direction of arrivals and distance the echoes travelled by taking multiple measurements and using artificial aperture techniques. Fig. 12 shows some examples. The top plot is a reference measurement. It was measured at a known location, close to the transmitter with line of sight path. Because the phase stability is maintained with Rb frequency standards and sampling always starts at the same position in the PRBS, the software correlation does not drift and always maintains the same excess time delay for the same echo. The bottom plot shows an example of an impulse response estimate measured behind a hill, about 50 m from where the middle plot was sampled. Because the shortest path signal was greatly attenuated, the echoes from distant buildings have greater relative power. It follows that the received signal power decreased and the channel transfer function would be much more distorted by the presence of a longer multipath spread.

## 7. CONCLUSIONS

This paper discussed a fast data acquisition measurement system for the estimation of impulse responses of mobile radio channels. The most important feature of the equipment is its short measurement period of less than a millisecond. Estimates measured for time varying radio channels are believed to be more relevant than those measured with a hardware correlator because data are acquired on the move at speeds comparable to realistic operating speeds in mobile environments. In static environments, both systems give identical results.

The system is very versatile. It operates at any frequency between 100 MHz and 2 GHz with a bandwidth of 8 MHz. This bandwidth can be easily changed and adapted for other

applications. The system can also measure two channels quasi-simultaneously.

## 8. REFERENCES

1. Bultitude, R.J.C., Bedal, G.K., "Propagation Characteristics on Microcellular Urban Mobile Radio Channels at 910 MHz", IEEE J-SAC, Vol. 7, No. 1, Jan. 1989, pp. 20-30.
2. Cox, D.C., "Delay Doppler characteristics of multipath propagation at 910 MHz in a suburban mobile radio environment", IEEE trans. on Antennas and Propagation, vol. AP-20, September 1972, pp 625-635.
3. Cox, D.C., "910 MHz Urban Mobile Radio Propagation: Multipath Characteristics in New York City", IEEE Trans. on Communications, vol. COM-21, November 1973, pp. 1188-1194.
4. Levy, A.J., et al., "An improved channel sounding technique applied to wideband mobile 900 MHz propagation measurements", Vehicular Technology Conference VTC'90, 1990, pp. 513-519.
5. Van Rees, J., "Measurements of impulse response of a wideband radio channel at 910 MHz from a moving vehicle", Electronics Letters, 27th Feb. 1986, pp. 246-247.
6. Melançon, P. and LeBel, J., "A characterization of the frequency selective fading of the mobile radio channel", IEEE Trans. on Veh. Tech., vol. VT-35, no. 4, November 1986, pp 153-161.
7. Cox, D.C., "Correlation Bandwidth and Delay Spread Multipath Propagation Statistics for 910 MHz Urban Mobile Radio Channels", IEEE Trans. on Communications, vol. COM-23, November 1975, pp. 1271-1280.

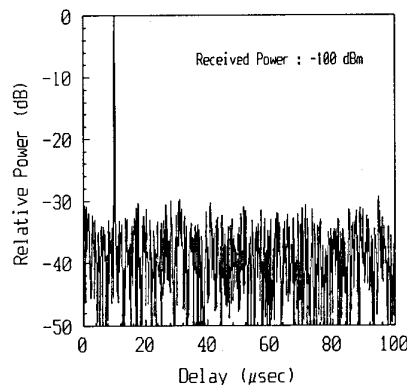


**Figure 6:** Impulse response estimate for a back to back measurement with an input signal of -100 dBm.

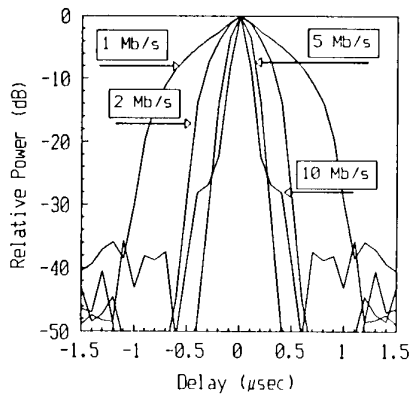


**Figure 7:** Effect of chip rate on time resolution.

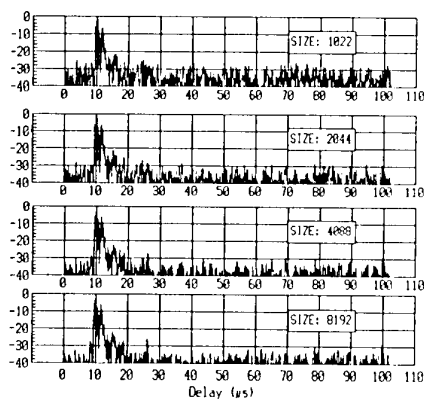


**Figure 8:** Effect of block size on the impulse response estimate. Block sizes of 4088 or larger are necessary to maintain a minimum MPSR of 30 dB.

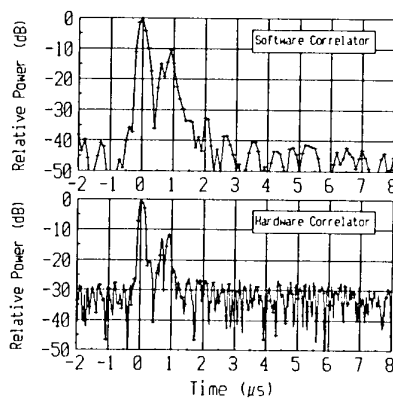


**Figure 9:** Comparison between impulse responses computed by a 10 MHz software correlator and a 20 MHz hardware correlator, for the same transmitter - receiver configuration.

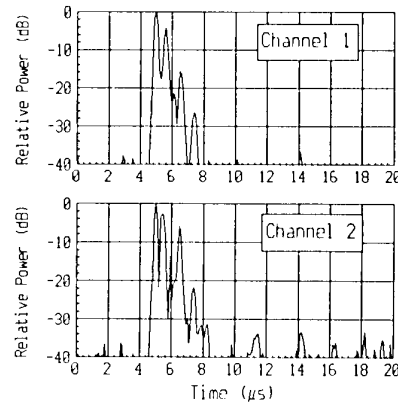


**Figure 10:** Comparison of two impulse responses measured simultaneously from two antennas separated by one wavelength.

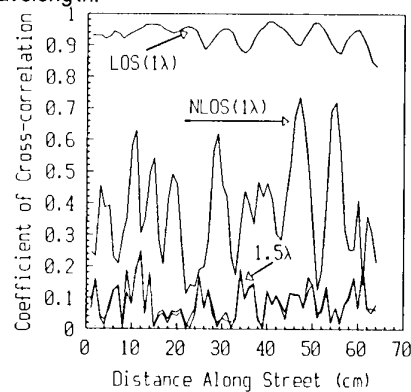


**Figure 11:** Cross-correlation between impulse responses measured from 2 antennas separated by 1.0 and 1.5 wavelengths in LOS and NLOS configurations.

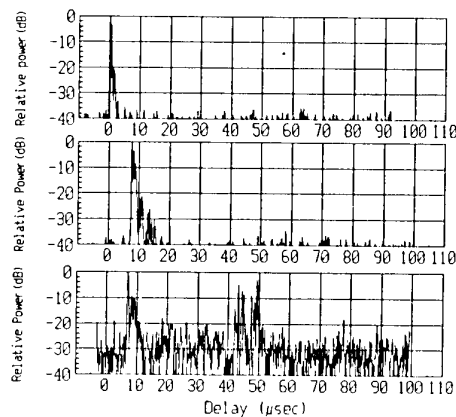


**Figure 12:** Ranging capability of the measurement system. The top plot is a reference at close range. The middle plot is at 2.25 km in LOS and the bottom plot is at 2.2 km in NLOS, where long excess delay echoes are from buildings located at 10 km from the transmitter.

## DISCUSSION

**Discussor's name :** G. S. Brown

**Comment/Question :**

Are you reasonably certain that the paths and scatterers which are causing your multiple returns are frequency independent over the bandwidth of your transmitted signal? If they are not, this could degrade the theoretical resolution of your system.

**Author/Presenter's Reply :**

Since the measurement system has only a 10 MHz bandwidth, I assume the returns are frequency independent.

# Line-of-sight Multipath Propagation Measurements at 15 GHz Over 500 MHz Bandwidth

M. Touati, G. EL Zein and J. Citerne

Laboratoire Composants & Systèmes pour Télécommunications  
URA CNRS 834, INSA 35043 Rennes Cédex  
FRANCE

## 1. ABSTRACT

An experimental wideband grazing radio link at 15 GHz has been set up on a 17.6 Km line-of-sight between Laillé and Rennes to measure the variations of the propagation medium characteristics (attenuation and group delay versus frequency) due to meteorological effects. For this, a meteorological system was set up at the receiver station in order to measure the variations of the meteorological parameters (temperatures, pressure, rain precipitation, speed and direction of the wind). Consequently, the atmospheric refractive index is obtained. A particular interest is given to the occurrence of multipath fading in clear air caused by low-level layering in the troposphere.

The collecting and recording of the propagation data (attenuation and group delay), from the MLA (Microwave Link Analyzer), and that which relates to the meteorological characteristics, from the meteorological station, are executed using a computer program in a sequential manner.

The channel impulse response, corresponding to each measured data, is calculated to deduce the number of rays detected and their different delays respectively. Besides this and using the meteorological parameters data acquired, the refractivity gradient is calculated in order to correlate the multipath fading occurrence to the meteorological parameters.

## 2. INTRODUCTION

Multipath propagation is a phenomenon in which the transmitted signal arrives to the receiver along more than one path. This phenomenon can happen under various atmospheric and geographic conditions [1] :

- Multipath propagation caused by atmospheric conditions may be due to stratified layers and inhomogeneities of the atmosphere, such as reflection from an inversion layer, partial reflection from an atmospheric sheet, refraction in an inhomogeneous layer and scattering by a turbulence. The variations of the atmospheric refractive index allows the signal power to travel from the transmitter to the receiver over two or more paths and thus with different delays.

- Multipath propagation caused by geographical conditions may be due to reflections from the ground, from buildings or objects and from mountains or hills.

Since the pioneering works of W. M. Sharpless, A. B. Crawford, W. C. Jakes and O. E. Delande [2-4], the adverse effects of multipath propagation on communication systems can be described in terms of selective fading and intersymbol interference, which degrade the performance of analog and digital radio communication systems in form of distortion and bit error respectively.

Occurrences of multipath fading limit the performance quality of high-speed digital radio systems operating on line-of-sight microwave radio paths. Consequently, the characterisation of the transmission medium or channel will allow us to evaluate this limitation and hence to make predictions on the transmission quality of the link.

The propagation medium is characterized by its multipath transfer function either in frequency domain by its attenuation and group delay responses or in time domain by its impulse response.

In order to study the phenomena cited above, an experimental 500 MHz bandwidth radio link from Laillé to Insa at 15 GHz, based on a Microwave Link Analyzer method, is realized.

## 3. THE EXPERIMENT SET-UP

The measuring equipment is installed on a 17.6 Km overland path. The transmitter station is mounted on a water tower at Laillé and the receiver station is mounted on a tower built at the LCST laboratory located in the campus of Insa (Institut National des Sciences Appliquées de Rennes).

The propagation path is over an area that is urban as well rural. The path profile of this link is given by Fig. 1. The characteristics of this link are :

- Height of the transmit antenna above the ground: 43 m.
- Altitude of the transmit station : 108 m.
- Height of the receive antenna above the ground : 26 m.
- Altitude of the receive station : 42 m.
- Hop distance : 17.6 Km.
- Transmit frequency : 15 GHz.

The schematic diagram of the measuring system is given by Fig. 2.

### 3.1. The transmitter

The transmitter station consists of an isolated shelter with a temperature regulator employed to limit the frequency shift. The signal delivered from the sweep generator is fed via a 1 W power amplifier into a 0.6 m diameter paraboloid antenna.

### 3.2. The receiver

The received signal through a 0.6 m diameter paraboloid antenna is applied to a low noise amplifier to guarantee the input specifications of the RF to IF converter. This device, based on the system developed by the CNET [5], performs the change of frequency as well as compression of the bandwidth of the incoming signal. The obtained signal is applied to the RME-5 of the MLA (device of Wandel&Goltermann) which gives the measurements of the attenuation and the group delay of the medium transmission.

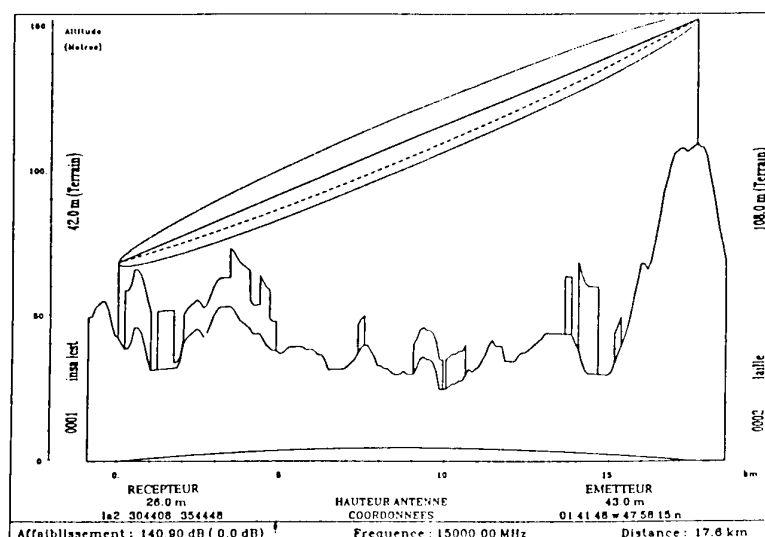


Fig. 1 : Path profile of Laillé-Insa link.

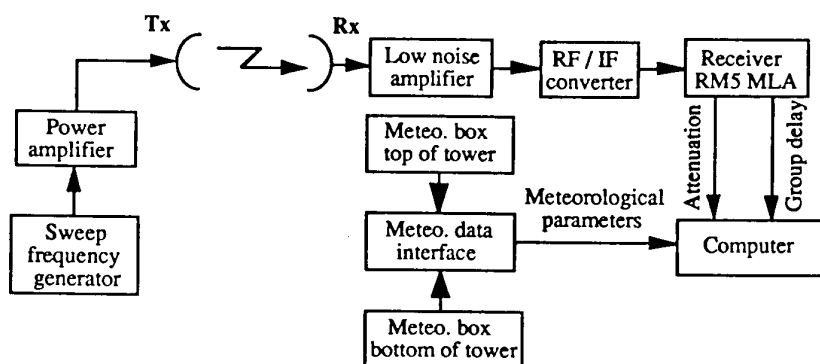


Fig. 2 : The schematic diagram of the measuring system.

Two meteorological boxes have been installed : the first at the top of the receiver tower gives the information of wet and dry temperatures, speed and direction of the wind. The second one at the bottom of the receiver tower gives the information of wet and dry temperatures, pressure and rain precipitation. Then a meteorological data interface performed by  $\mu$ MAC-1050 I/O (Analog devices) is used to control and monitor the meteorological instruments. The  $\mu$ MAC-1050 configuration and the I/O routines are executed from a host computer program.

The principle of the meteorological system performed in this study is similar to the one used in [6].

#### 4. THE DATA ACQUISITION SYSTEM

The connection of the receiver RME-5 and the  $\mu$ MAC-1050 to the computer are realized with the GPIB and serial interfaces respectively. The collecting and recording of the propagation data (attenuation and group delay versus frequency) and that which relates to the meteorological data (temperatures, pressure, rain, precipitation, speed and direction of the wind) are executed using a computer program in a sequential manner.

The acquisition program developed to acquire data is organized in three steps.

- During the first step an initialisation of the interfaces and the set up of the receiver RME-5 of the MLA is done by choosing the desired configuration.
- The second step consists to introduce the values of the total duration of the running system  $D_{acq}$ , the time duration  $I_{acq}$  between two successive acquisitions and the storage file index.
- The collecting and the recording of data is done in the third step.

If the attenuation level acquired is less than the threshold fixed to 4 dB under the free space conditions, the storage is done each time duration  $I_{acq}$  fixed during the second step. Otherwise, the storage is done faster with the minimum time duration given by our system (around three seconds) in order to capture the evolution of the occurrence of the fading.

Once the acquisition of the data is accomplished, their processing (calculation of the refractive indices of the up and the bottom of the tower, statistics on the fading and the

channel impulse response) is done on the HP 9000/835 computer.

## 5. RESULTS OF MEASUREMENTS

Propagation measurements have been made since the last week of September 1992 and the data is acquired daily, during twenty days, by fixing  $D_{acq}$  to 24 hours and  $I_{acq}$  to 10 minutes in the acquisition program.

The obtained results confirm the fact that severe multipath fading occurs in the early morning hours and late evening hours. An example of an occurrence fading events acquired, between 00:40:32 and 2:07:26 of 2 October 1992, is presented by the figures 3-a to 3-f.

Fig. 3-a shows the attenuation and group delay curves in 500 MHz frequency band acquired in the free space conditions. The curves are flat and the propagation characteristics are not deteriorated.

The figures 3-b to 3-f, acquired sequentially, show the occurrence of a multipath selective fading where the depth of the attenuation reaches - 15 dB from the free space considered by the Fig. 3-a. We also notice that the frequency selective power minima are accompanied by delay distortion maxima.

Some measurement results of the data acquired on 2 October 1992, such the one given by the figures 3-b to 3-f, suggest the existence at least of three components or rays. The two first components represent the direct ray and a reflected ray. The delay of the reflected ray in comparison with the direct ray can be evaluated from the Fig. 3-e. This figure shows a succession of power minima spaced out of 160 MHz, which correspond to a reflected component having a delay of 6.25 ns comparing to the direct ray. The third component could be a reflected ray, with small amplitude and big delay, which induce the small ripples given by the Fig. 3-f for example. These ripples are spaced out of 17 MHz corresponding to a delay of 58.8 ns, which is considerable and could be explained as lateral reflections.

The calculated channel impulse responses which correspond to the measurements data shown in Fig. 3-a to Fig. 3-f are presented by the Fig. 4-a to Fig. 4-f respectively. Fig. 4-a shows one main ray corresponding to the direct path while the figures 4-b to 4-f shows several components located at different delays. Fig. 4-f for example, shows the 6 ns component.

Using the meteorological parameters data acquired, both atmospheric refractive indices of the up and the bottom of the tower are calculated by using the relations given in [6]. Taking into account that the height between the two meteorological boxes is 15 m, the refractivity gradient is deduced. The behaviour of the refractivity gradient of the data file acquired on 2 October 1992 is given by the Fig. 5, where several abrupt changes are presented. From the propagation data acquired during this time, the observed severe multipath selective fading arrive mainly when a quick variation in the atmospheric refractivity gradient occurs. The variation of the refractivity gradient corresponding to the propagation data given by the figures 3-b to 3-f is located by the points A and B presented in the Fig. 5.

## 6. CONCLUSION :

In this paper an experimental propagation set up is presented which allows us to acquire propagation medium characteristics (attenuation and group delay curves in 500 MHz frequency band) and the meteorological parameters at the receiver station. Propagation measurements have been

conducted continually since September 1992 and during two months. The first results obtained show the occurrence of multipath fading happens when a quick change in the meteorological conditions is noted.

## ACKNOWLEDGEMENTS

The authors would like to thank Mr L. Martin of CNET for many useful advices and for providing facilities to undertake this work. Acknowledgement is also due to G. Grunfelder, Technician at LCST laboratory, for all his contributions in the realization of this experimental link.

## REFERENCES

- [1] C. P. Tou : "On combating multipath effects using spread-spectrum systems" AGARD Conf., proc. N° 332, pp 36-1;36-11, October 1983.
- [2] W. M. Sharpless : "Measurement of angle of arrival of microwaves" Proc. IRE, 34, N° 11, pp 837-845, 1946.
- [3] A. B. Crawford and W. C. Jakes : "Selective fading of microwaves" B. S. T. J., 31, N° 1, pp 68-90, 1952.
- [4] O. E. Delange : "Propagation studies at microwave frequencies by means of very short pulses" B. S. T. J., 31, N° 1, pp 91-103, 1952.
- [5] L. Martin and P. Leforestier : "Un analyseur de liaison pour le guide d'ondes circulaire" URSI, Com. A, C, E, pp 451-455, 1977.
- [6] L. Martin, R. L. Olsen and T. Tjelta : "Coïndice de réfraction, météorologie et affaiblissements sur les trajets en visibilité" AGARD Conf., proc. N° 407, pp 13-1;13-12, October 1986.



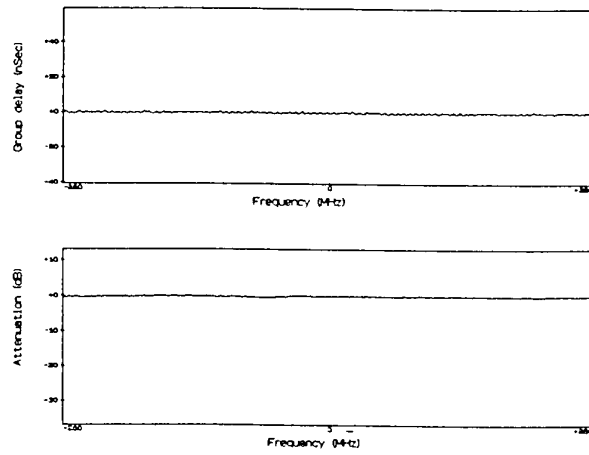


Fig. 3-a : Attenuation and group delay curves in 500 MHz frequency band.  
Acquisition N° 1, 00:40:33 / 2 October 1992.

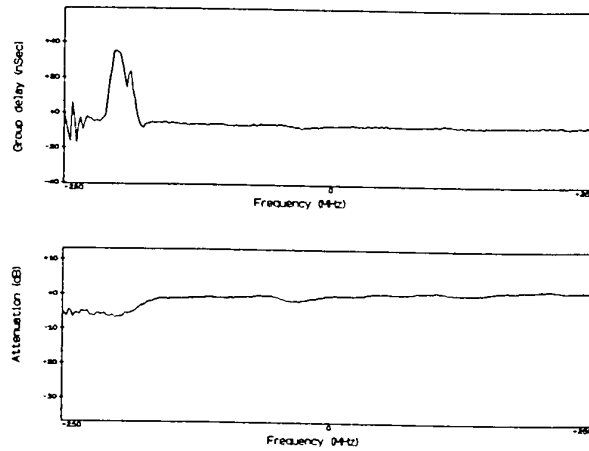


Fig. 3-b : Attenuation and group delay curves in 500 MHz frequency band.  
Acquisition N° 27, 01:41:13 / 2 October 1992.

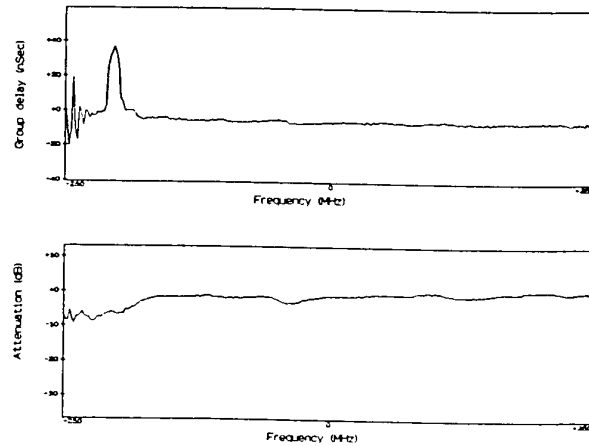


Fig. 3-c : Attenuation and group delay curves in 500 MHz frequency band.  
Acquisition N° 29, 01:41:22 / 2 October 1992.

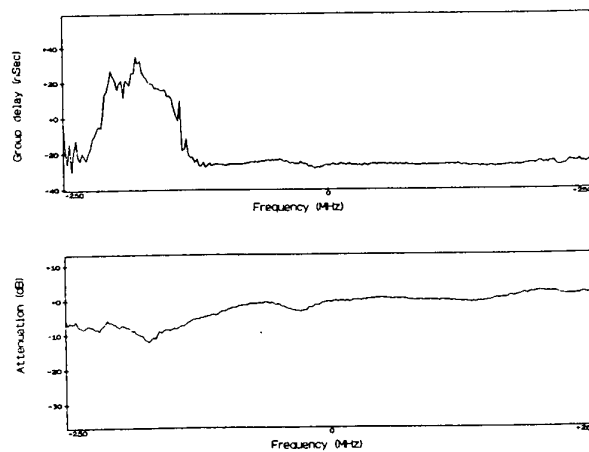


Fig. 3-d : Attenuation and group delay curves in 500 MHz frequency band.  
Acquisition N° 33, 01:49:02 / 2 October 1992.

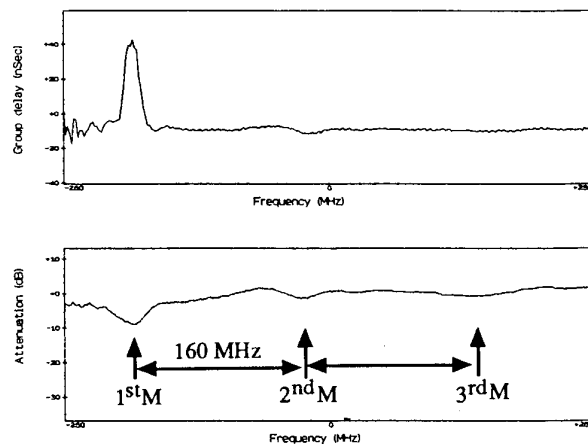


Fig. 3-e : Attenuation and group delay curves in 500 MHz frequency band.  
Acquisition N° 35, 01:50:48 / 2 October 1992.

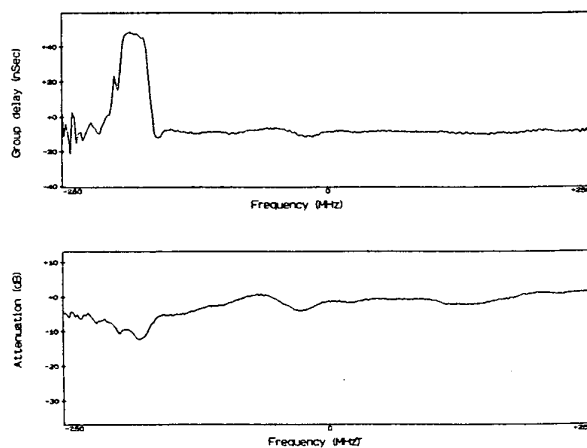


Fig. 3-f : Attenuation and group delay curves in 500 MHz frequency band.  
Acquisition N° 36, 01:50:53 / 2 October 1992.

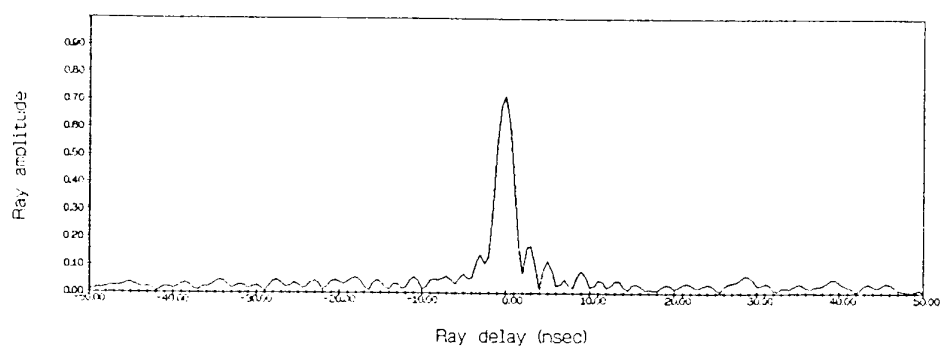


Fig. 4-a : The channel impulse response which corresponds to the measurements shown in Fig. 3-a.

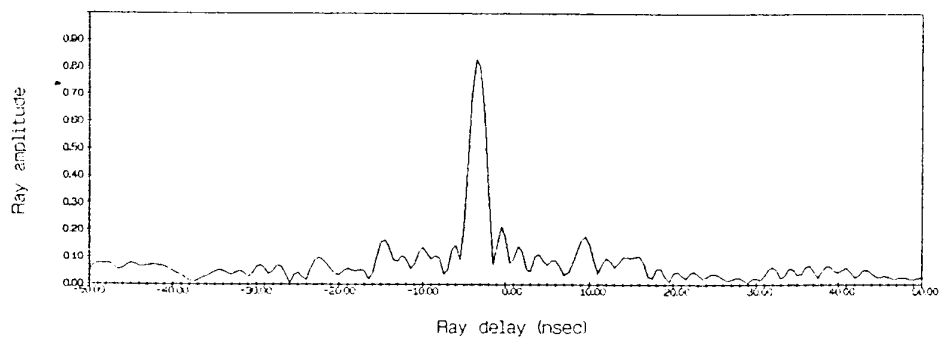


Fig. 4-b : The channel impulse response which corresponds to the measurements shown in Fig. 3-b.

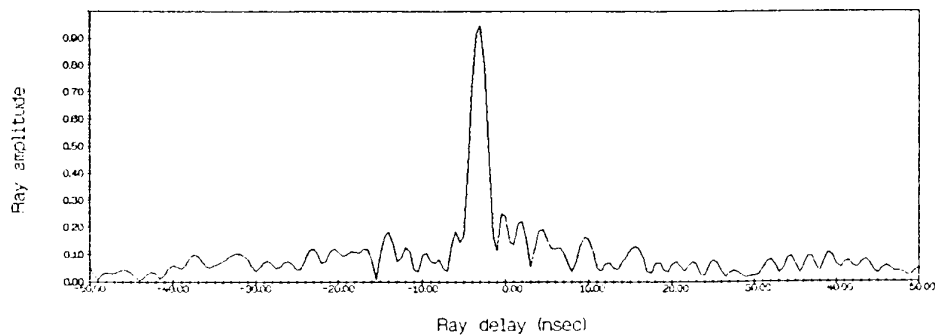


Fig. 4-c : The channel impulse response which corresponds to the measurements shown in Fig. 3-c.

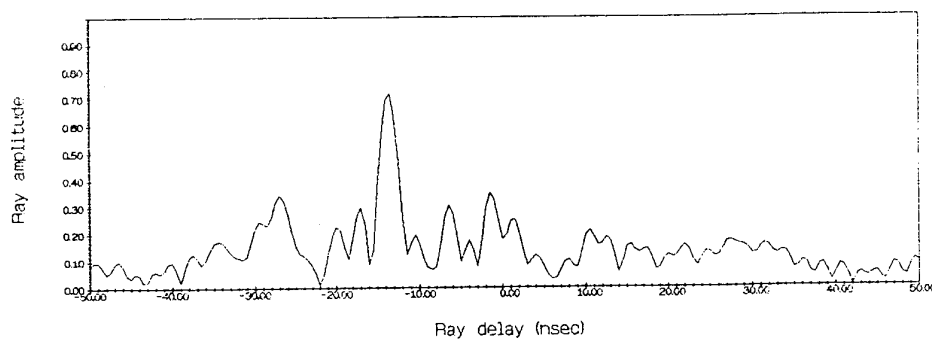


Fig. 4-d : The channel impulse response which corresponds to the measurements shown in Fig. 3-d.

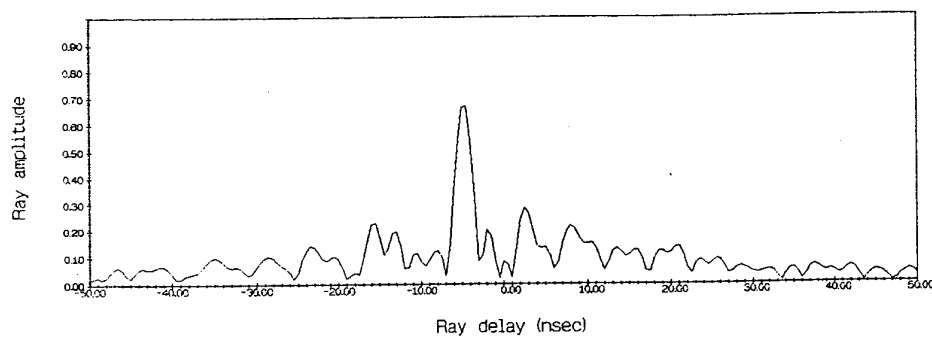


Fig. 4-e : The channel impulse response which corresponds to the measurements shown in Fig. 3-e.

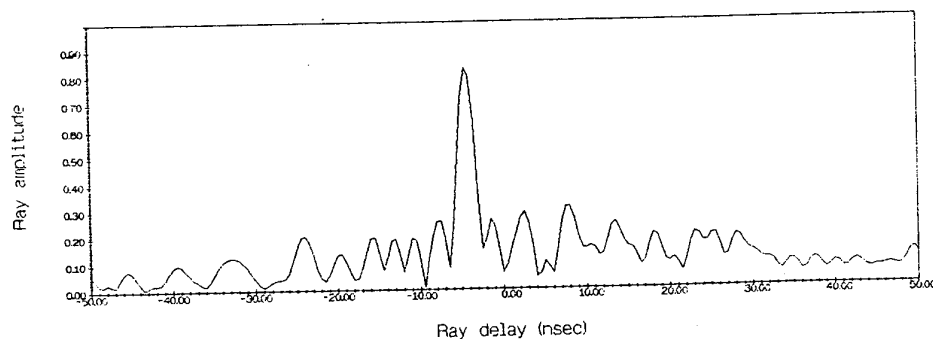


Fig. 4-f : The channel impulse response which corresponds to the measurements shown in Fig. 3-f.

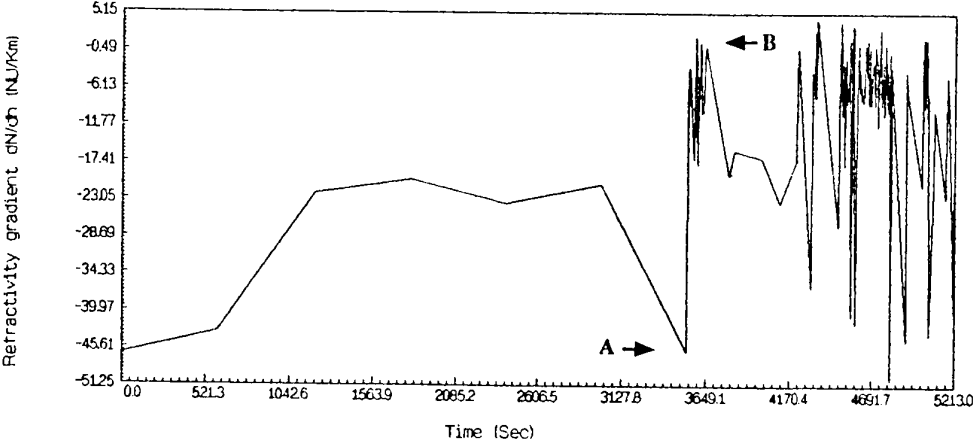


Fig. 5 : Refractivity gradient curve.

## DISCUSSION

**Discussor's name :** C. Goutelard

**Comment/Question :**

Les variations de la fonction de transfert, amplitude et temps de propagation dans la bande montrent que l'effet de distorsion est fortement marquée vers les fréquences inférieures et très peu ailleurs, alors que le retard que vous annoncez de 6ns, devrait marquer un effet voisin à d'autres endroits de la bande. Pouvez-vous commenter les résultats.

**Translation :**

*Variations in the transfer function, amplitude and propagation time in the band show that the distortion is highly marked towards the lower frequencies and scarcely noticeable elsewhere, whereas the delay you mention of 6 ns, should produce an effect in other places in the band. Can you comment on the results?*

**Author/Presenter's Reply :**

La sélectivité en fréquence du canal de transmission se traduit par l'apparition d'une atténuation quasi-périodique, due à une composante arrivant avec un retard de 6ns. Cependant, ces minimums d'amplitude n'ont pas la même valeur car les phénomènes de réflexion et de réfraction doivent varier en fonction de la fréquence.

**Translation :**

The frequency-selectivity of the transmission channel is shown by the appearance of a quasi-periodic attenuation, due to a component arriving with a delay of 6 ns. However, these amplitude minima do not have the same value, as reflection and refraction phenomena vary with frequency.

**Discussor's name :** Mr. K. S. Kho

**Comment/Question :**

Would a single meteorological station (top and bottom of the receiver tower) be sufficient for the measurements? Should it not be complemented by meteorological stations at for example the transmitter site or at the middle of the path?

**Author/Presenter's reply :**

Pour avoir une information plus complète sur la réfraction atmosphérique, il est vrai qu'il faut relever les données météorologiques sur plusieurs points de la liaison notamment au niveau de la base d'émission et à mi-distance émission-réception.

**Translation :**

*It is true that in order to obtain more complete information on atmospheric refraction we would need meteorological data from several points; and in particular, the transmission site and from the transmission-reception mid-point.*

**Discussor's name :** S. Prohoroff

**Comment/Question :**

Il serait intéressant de connaître la procédure de calibration qui permet d'accéder à une estimation de l'atténuation du canal, ainsi que la définition de la référence utilisée.

**Translation :**

*It would be interesting to know the calibration procedure which enables estimation of channel attenuation, as well as the definition of the reference used.*

**Author/Presenter's reply :**

La référence utilisée dans nos mesures est constituée par le signal reçu dans des conditions de propagation dite "normale". Cette méthode de calibration peut être améliorée en ayant des informations simultanées sur le signal émis et le signal reçu.

**Translation :**

*The reference used in our measurements comprises the signal received under "normal" propagation conditions. This method of calibration can be improved if we have simultaneous information on the signal sent and the signal received.*

# Experimental Study of the Helicopter-Mobile Radioelectrical Channel and Possible Extension to the Satellite-Mobile Channel

V. Blanchetiere-Ciarletti  
M. Sylvain  
P. Lemenn

C.R.P.E. (Unité mixte CNET/CNRS)  
10-12 avenue de l'Europe  
78140 Velizy  
France

## SUMMARY

The use of satellite seems to be an answer to the radioelectrical covering problem for the mobile communications, particularly in the low populated areas. Frequency bands at 1.5 and 2.5 GHz have been dedicated to these future services

Satellite-mobile links will be much more affected by propagation phenomena than the existing links between satellites and fixed stations. The reasons for that are twofold :

- The probable use of LEO (Low-Earth-Orbit) satellites instead of GEO ; such satellites will have to be received at relatively low elevation to limit their number.

- The use of mobile communication terminals with small and non directive antennas that must work in various environments instead of terrestrial stations located at carefully chosen places and equipped with large diameter paraboloids.

These propagation phenomena mainly consist in

- the fading of the signal level (shadowing of the link)
- a frequency selective fading due to multipath propagation.

The experience run by C.R.P.E. is aimed at a better understanding of the satellite-mobile propagation channel at fixed frequency as well as on a large band.

In this paper, we discuss preliminary results from a series of propagation measurements performed (by lack of any experimental satellite) on an experimental radio link at 1.45 GHz on a of 20 MHz bandwidth between an helicopter flying at a height of 2 km and a mobile receiver. The whole experiment has been run in a rural environment in Brittany (France).

In a first part, we illustrate the quality of the data collected during the experiment on a typical case study and give a possible physical interpretation of the observed phenomena.

Then we present statistical results concerning the various characteristics (attenuation and delay spreads) of the propagation channel.

Finally, we discuss the problem of using an helicopter (flying at a height of 2 km) as a substitute for a satellite at about 1000 km and try to estimate to what extent it is possible to use the data collected during this experiment to characterize the satellite-mobile channel. To do that, both the helicopter-mobile and the satellite-mobile propagation channels are simulated under the same environmental conditions.



## 1. DESCRIPTION OF THE EXPERIMENT

### 1.1 Experimental equipment

The experimental equipment consists in a versatile digital channel sounder which can be used in various environments (microcellular, macrocellular, helicopter-mobile, etc...) : it is only necessary to adapt in each case its frequency bandwidth, its type of antennas and the transmitted power level.

The transmitted signal is modulated by a pseudo random sequence with various possible choices for its length and bit rate; the impulse response of the channel is obtained from it by means of digitally implemented correlation [1]. The impulse response can be used to get fixed frequency attenuation, large band attenuation, selectivity parameters such as delay spread, correlation bandwidth...

The characteristics of the equipment during the helicopter-mobile experimental campaign are summarized in Table I.

frequency carrier	1.45 GHz
code length	511
bandwidth	25 MHz
transmitted power	20 W
polarisation	circular
antenna	spiral conical
antenna gain	3.9 dB

Table 1 : characteristics of the experimental equipment

With this configuration, it is possible to measure impulse responses of length about 20  $\mu$ s with a resolution of 0.1  $\mu$ s.

The transmitter was placed on board the CNET Ecureuil helicopter. The antenna was located under the helicopter, a mechanical device allowing its deployment below the helicopter runners during the flight.

The receiver was on board a mobile.

The radiation pattern of the transmitting and receiving antennas are presented fig.1. The difference between both is due to the metallic reflecting plane located above the car roof. The result of that is a flattening of the maximum and a change in the slope of the sidelobes.

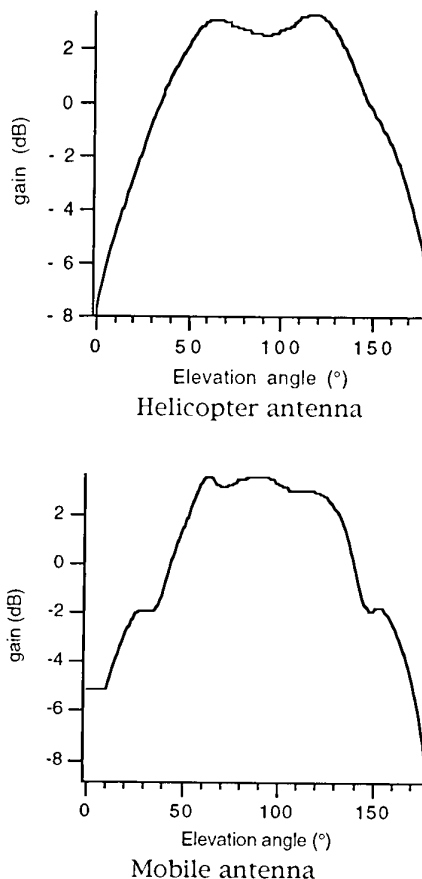


Figure 1 : Radiation patterns of the antennas.

The characteristics of the antennas have been chosen to give flexibility in the propagation equipment : they are large band antennas covering a complete hemisphere with small directivity. Of course, different types of antennas will be used for practical systems. It must be noted, however, that waves reflected from the ground in the immediate neighbourhood of the receiver, which need to be considered for future hand-terminals, are too much weakened by the antenna pattern to have noticeable effects.

### 1.2 mode of operations

Several experiments have already been performed with an helicopter simulating a satellite [2,3]. In most cases, however, the helicopter was following the receiving car, keeping as far as possible a constant relative position, both in distance and in azimuth. Such experiments are more appropriated to simulate transmission from a geostationary satellite than

with a LEO one ; in the latter case, even if its elevation probably remains the fundamental parameter, a coverage in azimuth is worthwhile. The mode of operation of the experiment has been defined in order to give a full coverage both in elevation (above  $10^\circ$ ) and in azimuth. The trajectory of the helicopter, designed as a "daisy" mode is represented in figure 2.

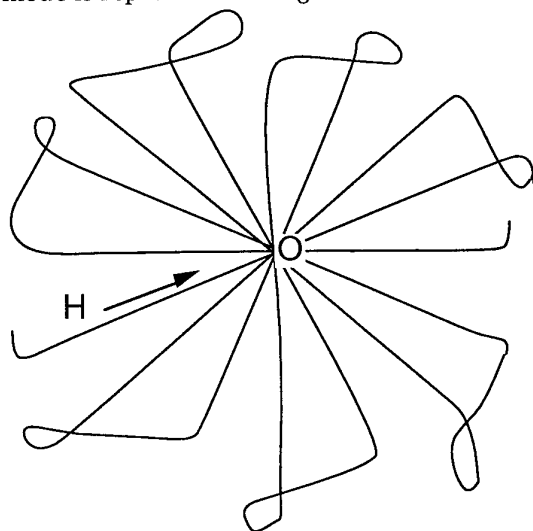


Figure 2 : "daisy" mode

The helicopter is flying according to the pattern drawn above while the car is fixed at point O or moving around this point.

It consists of radial crossings over a circular region, covering uniformly the azimuthal direction. The number of radial paths has been chosen so as to be covered by the helicopter (flying at 2000 m) at a speed of 200 km/h in a 3 single hours flight. The extremities of the crossings performed by the helicopter are predetermined and the course to follow is given to the pilot by a GPS system.

The receiver car can be either at a fixed position or following a circuitous route in the central part of the overflight area.

In such a mode of operation, it is necessary to know accurately the relative position of the helicopter versus the car in order to correct the received data from the effects of the variations in the distance between both and from those of the antenna patterns. The relative position is obtained by use of a GPS differential system [4]. The reference receiving station is located near the base airport. Comparing these signals with those received by the two GPS receivers on board

the helicopter and the car, allows to eliminate some of the atmospheric and ionospheric effects, as well as the voluntary degradation of the localization accuracy and to obtain a relative accuracy of the order of 10 m. The absolute positions are derived from the a priori known position of the reference receiver. The GPS system gives a new position approximately every second.

An inertial platform is onboard the helicopter, providing pitch and roll angles information. The skew angle is not known ; however this is of little consequence because the antenna radiation pattern is one of revolution.

Finally, the transmitted power is also recorded. The general synoptic of the experiment is given figure 3.

It is not possible, nor useful, to have continuous reception due to memory limitation. The principle is to collect a set of impulse responses about every second, which gives a resolution of  $1^\circ$  in elevation for an elevation of about  $40^\circ$ , this is sufficient for the statistical description of the channel.

Each individual set is composed of 20 impulse responses recorded every 2 ms. That is to say every 11 cm (for an helicoptere speed of 200 km/h). These data are too distant to make Doppler analysis, but can be used to analyse small scale fluctuations. They also could be averaged, if necessary, to improve the signal to noise ratio.

The time between two sets of acquisitions is used to transfer data to an optical disk.

The chronogram of data acquisition is presented in the following figure.

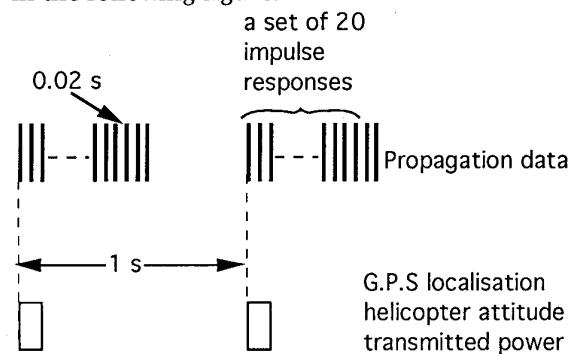


Figure 4 : chronogram of the data acquisition

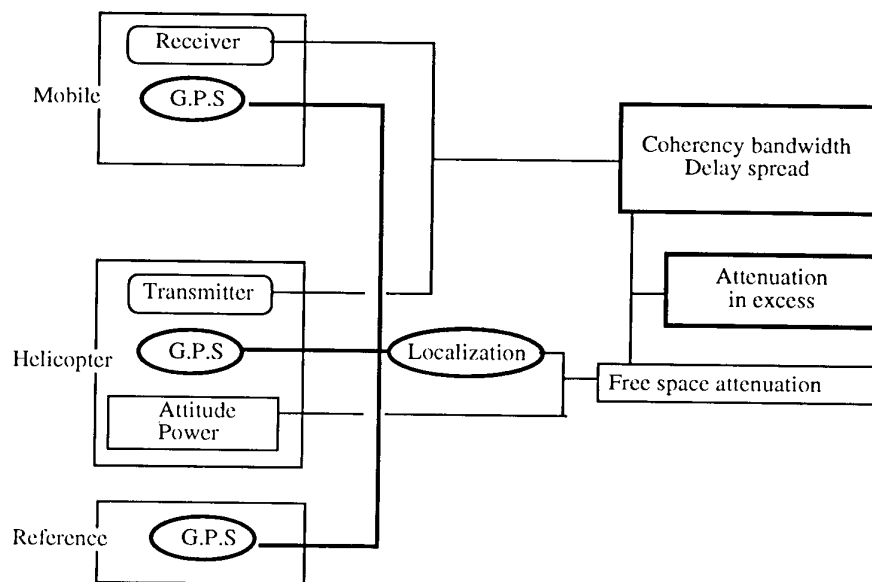


Figure 3 : data collected during the experiment.

- G.P.S. data giving the position of the transmitter(helicopter) and receiver (mobile car)
- Propagation data characterizing the channel
- Additionnal data (pitch and roll angle of the helicopter power of the transmitted signal)

### 1.3 Data used in this study

The data used here were collected in Brittany (France) in the neighbourhood of Lannion in February 1993. The whole experiment took place in a rural environment. The roads are rather frequently edged with trees and banks with only very few, generally low, buildings. The data presented in this paper have been drawn from one of the recorded "daisy".

### 2. Data overview

Figure 5 shows some of the results obtained during the first series of measurements made in Brittany near Lannion. Narrow and large band attenuations recorded during a passage of the

helicopter, as well as the free space attenuation calculated, are presented on the same graph. Thereafter, the free space attenuation is always taken as a reference and attenuations are presented in excess to this reference.

On the example of figure 5, we make clear the two kinds of impairments of the signal due to the environment :

- Important attenuation (at time 225 for example) up to 25 dB observed simultaneously in the narrow and large bands are probably due to probable shadowing
- Quick fading and enhancement of the narrow band level show the presence of multipath propagation.

As expected, these fluctuations become more important as the large band signal is weakened.

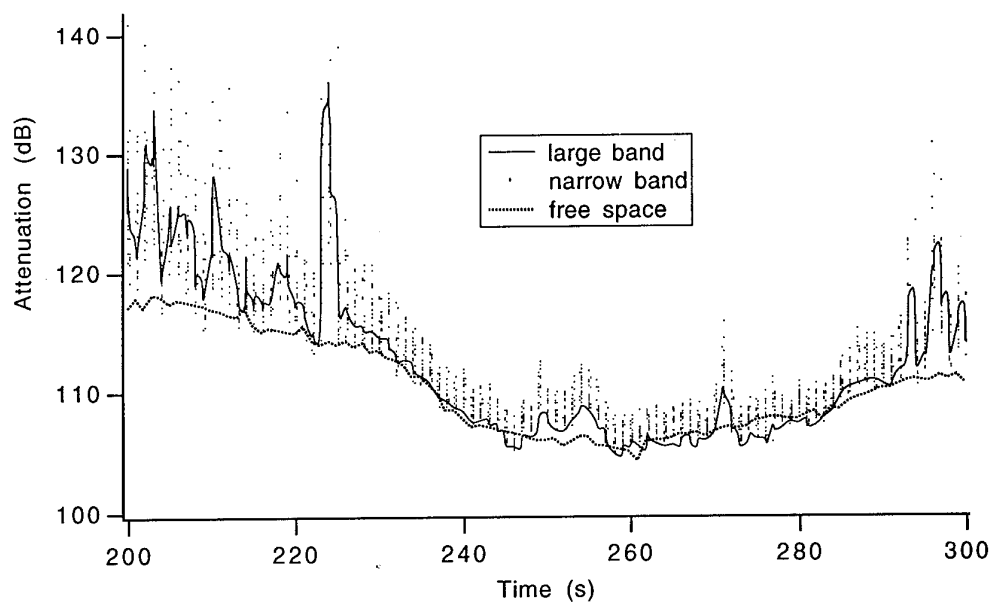


Figure 5 : large band (line) and narrow band (dots) attenuations recorded during a crossing of the helicopter.

The dashed line is the computed free space attenuation.

Figures 6a and 6b present some impulse responses collected during the same run.

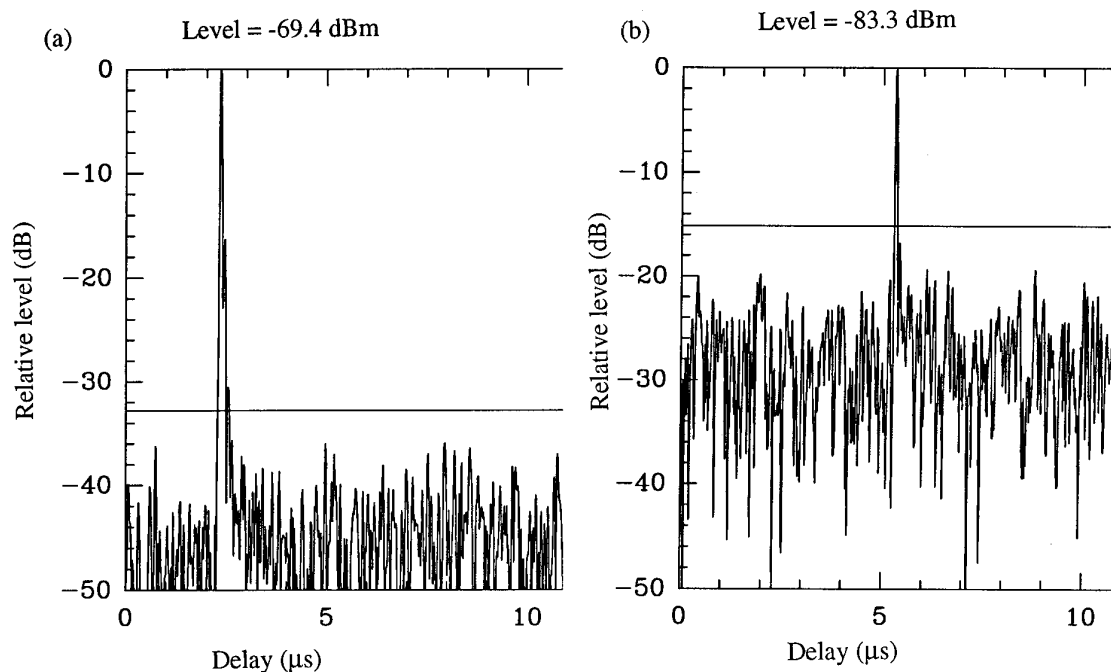


Figure 6: Impulse responses collected during the flight shown figure 5. The line represents the noise level.

(a) : response corresponding to time 250. Two paths with excess delays of approximately 0.1 and 0.2  $\mu$ s are observed in addition to the direct one.

(b) Response collected at time 225. Only one path can be retrieved. The signal to noise ratio is not good enough to see eventual others rays.

As previously stated, the environment of the mobile during this set of measurements was such as it leads to little impairment of the signal. As a matter of fact, the short duration of these responses is remarkable (less than  $0.4 \mu\text{s}$ ) and the number of retrieved rays is very low (2 to 4). The second ray is generally 10 to 20 dB under the level of the first one. This points out the fact that if the signal to noise ratio is too small (see figure 6-b) the computed selectivity parameters are not reliable. The data collected during this first series of measurements show that, unfortunately, the signal to noise ratio was not good enough at low elevation. This situation will be improved for the next campaign by averaging successive impulse responses recorded at a higher rate.

Anyway the delay spreads that could legitimately be calculated, lead to quite low values, between 20 and 40 ns. This result is in a rather good agreement with what is expected in the rural environment of the mobile.

### 3. STATISTICAL CHARACTERIZATION OF THE PROPAGATION CHANNEL

In the case of oblique links, multipaths are very seldom due to atmospheric refractivity (except may be at very low elevation (less than  $5^\circ$ )). Most often they are caused by nearby obstacles (buildings, trees, relief,...) generating reflected/refracted rays. For this reason, it seems reasonable to conclude that the behaviour of the propagation channel mainly depends on the link elevation. Hence, the statistics are presented according to different classes of elevation (from  $10^\circ$  to  $20^\circ$ , from  $20^\circ$  to  $30^\circ$ , etc...)

#### 3.1 Narrow and large band attenuations statistics

The results for narrow and large bands attenuations are presented figure 7-a et 7-b.

For the higher elevations (more than  $60^\circ$ ), the curves are in good agreement with what is observed in free space.

For the lowest elevations (less than  $40^\circ$ ) the behaviour of the channel is quantitatively different. The curves slope (fig.7-a et 7-b) is, roughly speaking, 10 dB per decade.

Signal enhancement is observed and strong attenuation up to 25 dB occurs (for 0.1 to 1% of the data).

Some differences can be noticed between the two sets of curves. The narrow band data shows smooth curves while the large band data is showing jumps corresponding to the shadowing situations. The narrow band data shows greater attenuations. Even when the direct ray is not shadowed (for elevation  $> 60^\circ$ ), the effect of the reflected/refracted rays can be responsible for an approximately 5 dB fluctuation.

Special attention must be paid to the  $40^\circ$ - $50^\circ$  elevation curve : the quick change in the slope suggests that a few measurements (4%) have been made in a shadowing situation while the others have been made for an unobstructed line of sight link. The corresponding non cumulative probability clearly shows two maxima.

#### 3.2 - Delay spreads statistics

As already mentioned in section 2.1, delay spread calculation requires a good dynamic of the channel response measurement. For this reason, statistics are not available for the lowest elevations (figure 8). The observed delays spreads values range between 20 ns to 70 ns, the latest value corresponding to an elevation angle smaller than  $20^\circ$ . The  $20^\circ$  to  $30^\circ$  elevation curve show the greatest delay spreads values but, for the reason given above, the statistics are biased. The percentage of short delay spreads ( $< 40$  ns) is clearly overestimated.

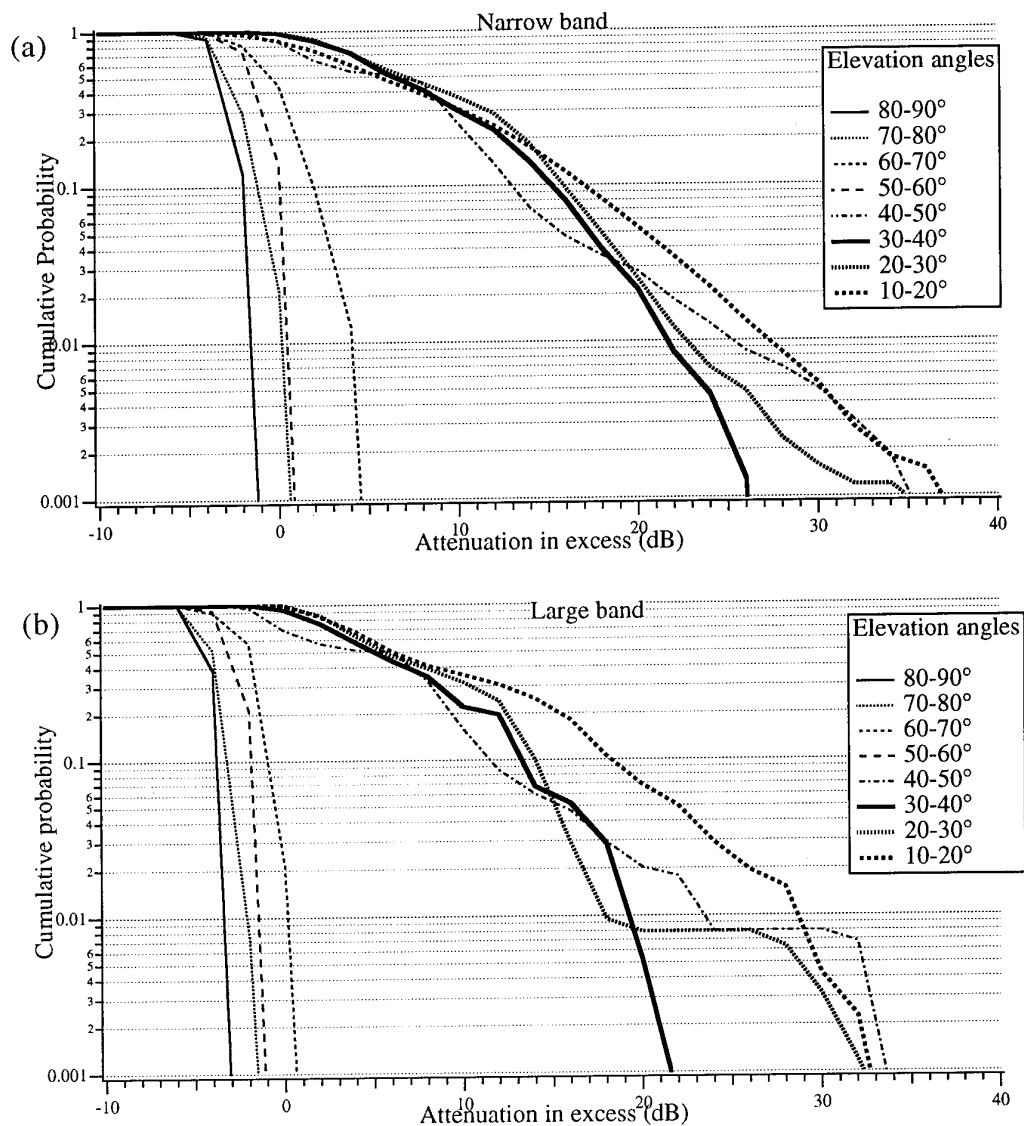


Figure 7 : Cumulative statistics for attenuation.

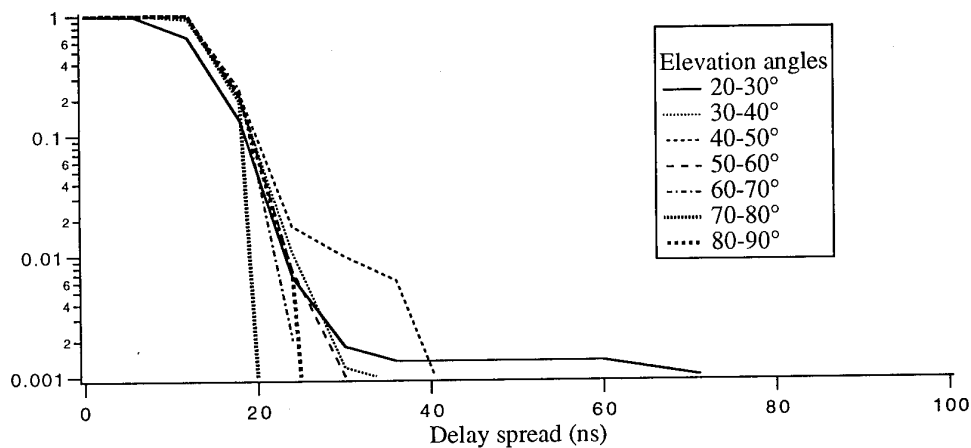


Figure 8 : Cumulative statistics for delay spreads

#### 4. POSSIBLE EXTENSION TO THE SATELLITE-MOBILE CHANNEL

We already pointed out the fact that data were collected using an helicopter (flying at 2000m) instead of a satellite (at 1000 km) and that the above results apply to the helicopter-mobile channel. A premature extension to the satellite-mobile channel could lead to erroneous conclusions. The object of this part is to compare the behaviour of the satellite and helicopter-mobile channel for a given simple environment (one obstacle) in order to evaluate if the data recorded from an helicopter experiment can help understanding the mobile-satellite channel.

##### 4.1 Simulation of the effect of an obstacle near the receiver

Our purpose is to get an order of magnitude of the effect of the transmitter height on the received signal. For this, we only take into account a simplistic situation with only one obstacle at a time in a two-dimensional geometry.[5]

Wave propagation between the transmitter and the receiver is handled by means of ray optic approximation, the different rays being characterized by their amplitude and delay. As far as oblique links are concerned, the effect of the atmospheric refractive index is of little importance and is therefore neglected in our simulation.

Three kinds of rays are thus considered (see fig.9) : direct, reflected and diffracted.

- The direct ray (1) is propagating along a straight line as in free space. This ray can be shadowed by obstacles near the receiver. The effect of the environment upon the direct ray only depends on the elevation (and azimuth) of the link and therefore would be identical for an helicopter and a satellite based transmitter.

- The diffracted ray (2) is given by the geometrical theory of diffraction. For any elevation, there is a diffracted ray. The trajectory of the diffracted ray is the same but the incident ray, and therefore the diffraction coefficient, depends on the transmitter height.

- The reflected ray (3) is observed if both the transmitter and the receiver are on the same side of the obstacle and if the obstacle is high enough ( this last condition depending on the transmitter height).

The coefficient of reflection applied to the ray intensity should depends on the angle of incidence as well as on the nature of the obstacle (electric properties and roughness of the surface). In our simulation, the coefficient of reflection is hold constant, equal to -3 dB for a building and to -10 dB for the relief.

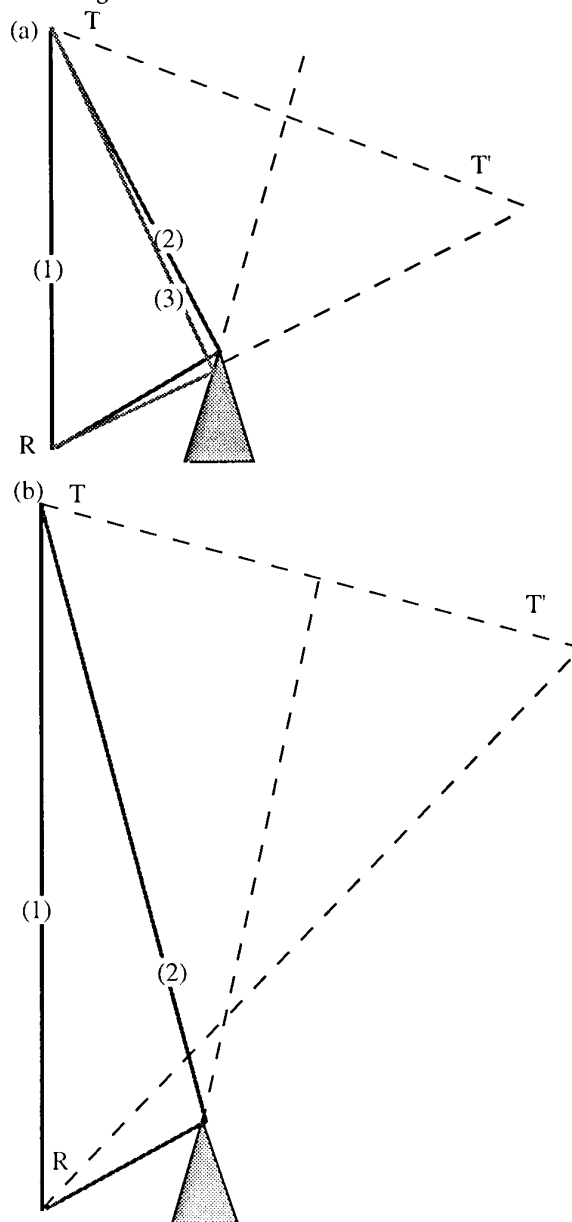


Figure 9 : Various rays arriving at receiver R with one obstacle (in grey) : direct (1), refracted (2) and reflected (3).

A low transmitter T (case a) gives 3 rays while a higher one case (b) only gives 2.

The two examples of figure 9 corroborate the importance of the transmitter height : for the two cases presented in figures 9-a and 9-b, the obstacle as well as the elevation angle are the same. Only the transmitter heights are different. The situation a leads to 3 rays while situation b (corresponding to a higher transmitter) only gives 2 rays, reflection being in that case impossible. This example makes it clear that the characteristics of the propagation channel really depend on the transmitter height.

The effect of the transmitter height has been studied for two kinds of typical obstacles.

- (A) buildings : vertical and rather low obstacle, giving a rather important reflection
- (B) relief : oblique, rather high obstacle (mountain) with weak reflections because of the roughness of the soil.

The characteristics of the two obstacles used in our simulations are described in the following table

	building (A)	mountain (B)
angle /ground	90°	45°
height	10-100 m	100 m-1 km
distance /mobile	100 m	100 m
coeff. reflection	-3 dB	-10 dB

Table II : characteristics of the obstacles taken as examples for the simulation

All these assumptions, concerning both the propagation model and the obstacle description, lead to a simple model that can still give a good order of magnitude of the differences expected between the helicopter-mobile and the satellite-mobile channels.

## 4.2 Results of simulations

### 4.2.1 Propagation delays

Of course, propagation time increases with the transmitter height. But only the relative delays of the multiple paths reaching the receiver are relevant for communication systems. The results concerning relative delays are presented figure 10.

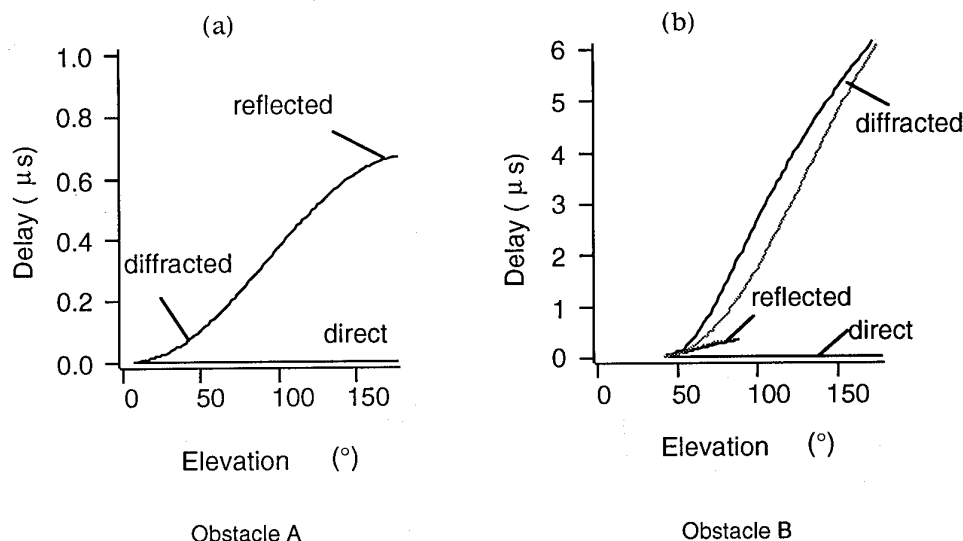


Figure 10 : Computed delays. The black curves are obtained with a transmitter height of 2 km while grey ones correspond to an height of 1000 km.

Figure (a) (resp. (b)) gives the results for obstacle A (resp. B).

On figure (a) grey curves are hidden by the black ones.



As expected, only the diffracted ray is observed at every elevation. The reflected ray appears for a very limited range of elevation ( at about  $180^\circ$  for a vertical obstacle, at about  $50^\circ$  for a  $45^\circ$  slope)

The computed delays are always longer for an helicopter than for a satellite. The differences between the two situations is much more important in case b (important relief) than a (building).

#### 4.2.2 Level of the rays

The levels of the existing rays are presented figure 11-a (resp. 11-b) for obstacle A (resp.B), with the two transmitter heights of 2 km and 1000 km.

The direct ray level changes with the elevation angle, this is due to the increase of the transmitter to receiver distance. This effect is more important for a low transmitter because of the larger relative variations of the path length. Like for the delays, the differences between satellite and helicopter are more important in case of obstacle B.

Using the computed delays and levels of the rays, one can get any selectivity parameter of the channel, as delay spreads, correlation bandwidth,...

Comparison of delay spreads observed for an helicopter and a satellite is shown. The delay spreads are computed for obstacles A and B. As expected, a change in the transmitter height does not bring any noticeable change for obstacle A. However, for obstacle B, the difference induce by the transmitter height can reach 70 ns.

#### 4.2.3 Temporal considerations

In preceeding sections, we have described, both from measurements and from simulations the behaviour of the propagation channel. Despite of its fundamental practical importance, this information is not sufficient for system planning purpose. One also need to know how the channel varies with time (a variation which is due mainly to the movements of the transmitter and receiver).

When considering such questions, care is needed to extend to the satellite case information obtained from an helicopter experiment. The difficulty comes from the fact that a uniform trajectory around the Earth corresponds to a uniform distribution of the polar angle distribution as measured from the Earth center, but a non uniform of the elevation angle as measured from the Earth surface. This second distribution differs all the more from an uniform one as the height decreases. As a consequence, the probability density of the elevation angle of

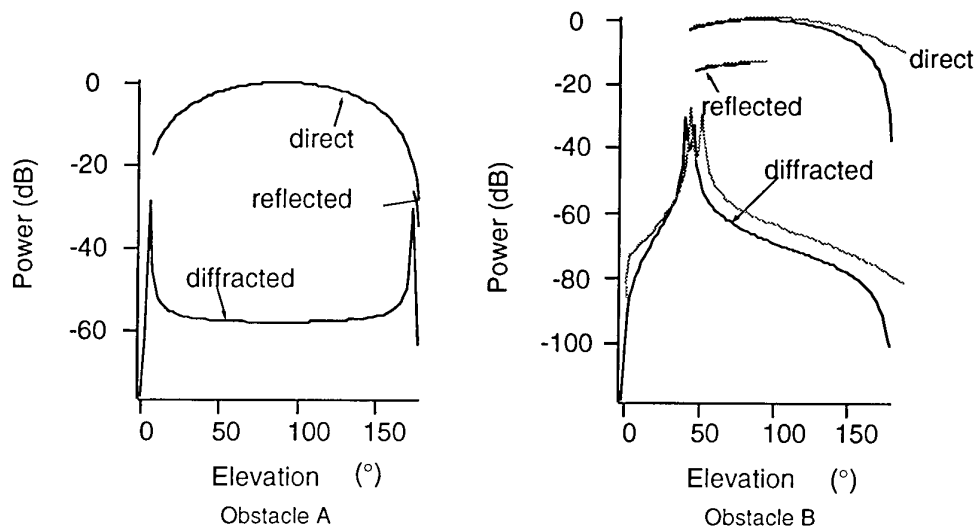


Figure 11: Computed level of the various rays.

The black curves are obtained with a transmitter height of 2 km while grey ones correspond to an height of 1000 km.

an helicopter seen from a point on the ground, differs from that of a satellite (fig.12).

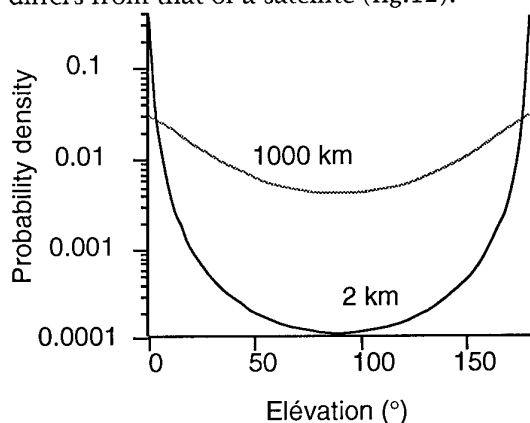


Figure 12 : probability density for a given elevation computed for two transmitter heights (2 km and 1000 km)

Some corrective computations are therefore needed to derive the percentage of time a parameter exceeds a given value, from its dependence on elevation, as presented previously.

#### 4.2.4 Conclusions

The results presented in this part, clearly show that as far as vertical and low obstacles are concerned data propagation obtained from helicopter measurements give a very good estimation of what could be observed with a satellite based transmitter. But as the obstacle becomes high (a mountain for example), differences are emphasized and conclusions about the satellite-mobile channel must be drawn very carefully.

### 5. CONCLUSION

We have presented in this paper some results of propagation measurements between an helicopter and a mobile receiver. The main goal of this campaign was to check the operational performances of the experimental device : the experimental site was therefore chosen so as to lead to only weak propagation impairments.

The presented results, however, illustrate the various propagation phenomena expected on such a channel, such as obstructions and multipath propagation.

It has been demonstrated that the data collected from the channel analyser give access to statistical results, concerning both level

attenuation and selectivity of interest for systems designers.

Of course, an helicopter is not a true substitute to a satellite. The simulations presented in the last section show, however, that the presented measurements can be boldly extrapolated to a satellite-mobile channel, except in mountainous regions. Taking into account the flexibility provided by an helicopter in varying the experimental configuration, it is probably one of the best choices in performing the necessary propagation measurements required for the planning of the future cordless universal communications systems.

CNET therefore plans to perform future campaigns, using the same experimental set-up, in various environmental conditions.

#### Acknowledgment

The authors wish to thank all the people who participated in the preparation and the realization of this experiment.

#### References

- [1] A.J. Levy, J.P. Rossi, J.P. Barbot et J. Martin (1990) An improved channel sounding technique applied to wideband mobile 900 MHz propagation measurements, Proc. of 40th IEEE Vehicular Technology Conference, pp 513-519.
- [2] J. Goldhirsh and W. Vogel (1990) An overview of results derived from mobile-satellite propagation experiments. Proc. of International Mobile-Satellite Conference, Ottawa, pp 219-224.
- [3] A.J. Bundrock and R.A. Harvey (1989) Propagation measurements for an Australian land mobile-satellite system, ATR, vol 23, n°1, pp 19-25.
- [4] J. Beser and B.W. Parkinson  
The application of NAVSTAR Differential GPS in the civilian community, (1984), in "Global Positioning System", vol. 2, pp 167-214, edited by the Institute of Navigation.
- [5] V. Blanchetière-Ciarletti and M. Sylvain (1993) Comparaison entre le canal de propagation satellite-mobile et le canal de propagation hélicoptère-mobile. Note Technique CNET NT/PAB/RPE/ETP/3167

## DISCUSSION

**Discussor's name :** C. Goutelard

**Comment/Question :**

Vous avez effectué une étude très intéressante sur l'effet de la basse troposphère et du sol sur des liaisons air-sol. Vous envisagez l'extension de ces mesures aux liaisons satellites-sol. Pour les fréquences utilisées par GPS, l'effet ionosphérique est très important. En bande X ou KU, il devient beaucoup plus faible. A quel domaine envisagez-vous de l'appliquer et comment prendrez-vous en compte l'effet ionosphérique?

**Translation :**

*You have carried out a very interesting study on the effect of the lower troposphere and of the ground on air-to-ground links. You envisage extending this measurements to satellite to ground links. On the frequencies used by GPS the ionospheric effect is considerable. It falls off in the X or KU bands. In what domain do you intend to apply it, and how will you take into account the ionospheric effect?*

**Author/Presenter's reply :**

Notre dispositif expérimental ne permet en effet de mettre en évidence que les phénomènes de propagation se produisant dans les basses couches de la troposphère mais l'objectif que nous nous sommes fixé est une meilleure connaissance de l'influence de l'environnement du véhicule mobile sur le canal de propagation.

L'effet de la traversée de l'ionosphère doit être étudié de façon indépendante.

Cependant, l'utilisation d'une polarisation circulaire permet de s'affranchir de l'effet Faraday. Quant aux scintillations, elles sont généralement assez faibles aux latitudes moyennes.

**Translation :**

*Our experimental device only actually shows propagation phenomena occurring in the lower layers of the atmosphere, but our aim is to improve our knowledge of the influence of the environment of the mobile vehicle on the propagation channel.*

*The effect of crossing the ionosphere should be examined separately. However, the use of circular polarisation enables us to overcome the Faraday effect. As for scintillation, it is generally quite weak in medium latitudes.*

# COMPARATIVE STUDY OF C- AND KU-BAND PROPAGATION MECHANISMS BEYOND THE HORIZON

Uve H. W. Lammers

Richard A. Marr

Rome Laboratory, 31 Grenier St., Hanscom AFB, Massachusetts 01731-3010

Robert K. Crane

Magnus Wennemyr

University of Oklahoma, 100 East Boyd, Norman, Oklahoma 73019-0470

USA

## 1. SUMMARY

At intervals over a period of several years, we conducted simultaneous troposcatter measurements at frequencies of 4.95 and 15.73GHz on a 161km path in the northeastern United States. This ensured a fair comparison within a largely unspecified but identical propagation medium. Besides signal level, both systems yielded Doppler information on the propagation mechanism. In addition, the Ku-band system provided delay resolution by pseudorandom phase modulation. On the basis of these data, three primary propagation mechanisms could be identified: clear air turbulent scatter, rain scatter, and ducting. Criteria are given for the identification of these mechanisms along with the resulting received signal level and delay spread distributions under each propagation condition.

## 2. BACKGROUND

At Ku-band, mobile military troposcatter links of about 100 miles pathlength benefit from the advantage of small, easily erectable antennas. They also provide relief for the crowded C-band which currently supports much of the tactical transhorizon communication. The high and potentially disabling attenuation in rain at frequencies above 10GHz is well known. However, forward scatter from rain is also substantially stronger than that from clear air dielectric inhomogeneities which normally supports troposcatter communication. Consequently, the feasibility of a short troposcatter link at high frequency depends on the spatial distribution of rain along the path and the tradeoff between enhanced scattering and enhanced attenuation. Tactical Ku-band troposcatter links can tolerate somewhat larger outages than commercial communication links.

Parl and Malaga [1] evaluate the frequency dependent behavior of a hypothetical 100km troposcatter path. Humid, turbulent air and light rain are assumed homogeneously distributed between the terminals. Figure 1 shows for antennas of fixed diameter the received signal level increasing with frequency and humidity, before beginning to drop off above 10GHz. Light rain with a drop size distribution according to Marshall and Palmer is added to the highest humidity curve (dashed line). Although only attenuation from uniform rain at a 5mm/h rate has been considered, the received signal level is still higher at 15GHz than the one based on a completely dry atmosphere. Scattering

from rain in the common volume would further increase the received signal level. Results from the NBS model are included for comparison. At higher rain rates, a uniform distribution along the path can no longer be assumed.

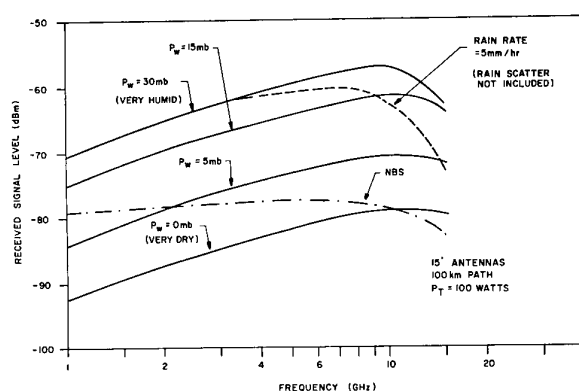


Fig. 1 Frequency dependent rain attenuation on a hypothetical troposcatter path

The objective of the measurement program was to evaluate the performance of a Ku-band troposcatter link under all weather conditions, including severe rain. The meteorological characterization of troposcatter paths has been notoriously difficult. A comparison of a Ku-band system against one at the currently used C-band under identical, if undefined meteorological conditions is, therefore, a useful method of evaluating the Ku-band system's performance. Identical meteorological conditions imply simultaneous measurements with identical common volumes. In turn, this requires scaled antenna sizes for both systems, i. e. the ratio of antenna diameters to be equal to the inverse of the frequency ratio. Our experiment was put together from previously existing hardware. This necessitated the compromise of somewhat unequal common volumes along identical paths, as will be seen. Apart from excessive path loss, the most detrimental weather related factor in modern digital scatter communication systems is excessive delay spread causing intersymbol interference. To measure this quantity, a RAKE system of 12.5Mb/s and later 400Mb/s pseudorandom biphasic switching rate was employed at Ku-band. This yielded a differential pathlength resolution capability of 80ft and 2.5ft, respectively. Depending on the bistatic geometry,

the 2.5ft pathlength resolution translates into a height resolution between 13m (near the top of the common volume) and 22.5m (near the bottom). Both systems were highly frequency stable to be able to attribute frequency changes of the received signal to atmospheric motion induced Doppler phenomena. The measured data made it possible not only to establish communication related parameters such as received signal level and multipath delay spread, but also to shed light on the prevalent propagation mechanism contributing to the received signals. The experiments were conducted under Air Force contract with Dartmouth College, the Air Force being responsible for transmitter design and operation and Dartmouth College carrying out the remainder of the tasks. The authors from Dartmouth College are now with the University of Oklahoma.

### 3. EXPERIMENTAL SCATTER PATH

The experimental systems were installed on a simulated tactical path with the transmitters on Prospect Hill in Waltham, Massachusetts and the receivers on Mount Tug in Lebanon, New Hampshire. Table 1 lists salient parameters of both systems.

Table 1. Troposcatter System Parameters

Frequency (GHz)	15.73	4.95
Distance (km)	160.9	
Transmitter Height (m)	159.4	
Receiver Height (m)	493.8	
Transmit Aperture (ft)	3	29
Transmit Beamwidth (deg)	1.52	0.48
Receive Aperture (ft)	3	10
Receive Beamwidth (deg)	1.52	1.46
Modulation (Mb/s)	12.5/400	None
Transmit Power (W)	225	30
Receiver Noise (dBm)	-144	-147

Identical common volumes at both frequencies would require the transmit antenna diameter at 15.73GHz to be 9ft. An attempt to operate the 29ft antenna with a dual frequency feed which underilluminated the aperture at Ku-band while fully illuminating it at C-band was not successful. Some measurements were made with the 29ft antenna transmitting a 0.15deg beamwidth at 15.73GHz. They will not be addressed here. In order to study a Ku-band link with a more practical transmit antenna size, a separate 3ft antenna was chosen for transmission. The 15.73GHz frequency used was determined by the available equipment, not current band assignments. The higher transmit power at the higher frequency offsets to some extent the fact that the power received from a path delay resolution cell within the common volume is lower than that available from the whole common volume.

The path profile in Figure 2 illustrates the common volumes possible with the available combinations of transmit and receive apertures.

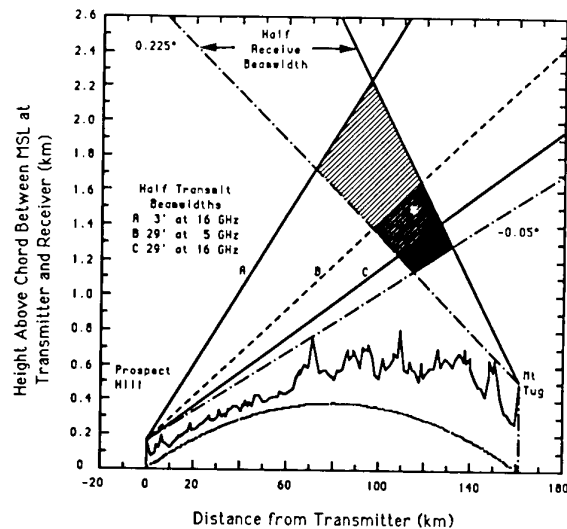


Fig. 2 Experimental path profile and common volumes at C- and Ku-band

Both transmit and receive beam axes were placed on their respective horizons for highest received signal levels under clear air conditions. The signals compared here originated within the black region with the 29ft transmit antenna at Ku-band, within the black and densely hatched regions using the same transmit antenna at C-band, and within the black, densely hatched, and lightly hatched regions with the 3ft transmit antenna at Ku-band. The path profile assumes a 4/3 effective earth radius. The minimum common volume height under standard refraction conditions is 1.1km above chord or 0.4km above local terrain. At Ku-band, using 3ft transmit and receive antennas, the common volume maximum height is 2.3km above chord or 1.6km above local terrain. The common volume in this case is 60km long. The path profile suggests that diffraction contributions to the received signals were insignificant.

### 4. PROPAGATION MODE DISCRIMINATION

A perspective view (Figure 3) of the transmit and receive beam half cones forming the common volume shows an elemental volume of scatterers  $S$  moving through the common volume with tangential (horizontal) velocity  $v_T$  and radial (vertical) velocity  $v_R$ . The total pathlength TSR is longer than the horizon path of minimum delay. Velocity component  $v_T$  typically is the crosspath wind component which, for beams accurately aligned in the great circle plane, does not result in a Doppler shift of the received signal, when averaged over all elemental volumes  $S$  within the common volume. This also requires that scatterers be distributed symmetrically on either side of the great circle plane. Velocity component  $v_R$  primarily represents the fall velocity of rain or other particulate scatterers. It leads to a Doppler shift of the received signal due to continuous shortening of the TSR path. Doppler shifts due to  $v_R$  do not average to zero over the common volume. The frequency drift between transmitter and

receiver was of the order of 0.1Hz maximum at Ku-band, making Doppler shifts of several hertz due to rain clearly distinguishable.

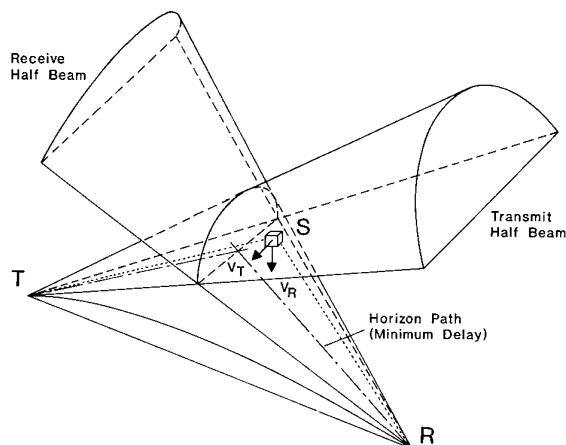


Fig. 3 Delay and Doppler shift on troposcatter path

The length of the TSR path or, more specifically, its differential delay relative to the minimum delay along the horizon path is a measure of the location of S. The differential delay is largely determined by the height of S within the common volume. To find the height from where a particular received signal component originates is straightforward when its difference in delay relative to a signal arriving with minimum delay on the horizon path is known. Lacking the latter signal, one has to rely on the independent timing between transmitter and receiver clocks. Synchronism between the two is difficult to maintain, even with Cesium beam frequency standards. If the frequencies of the two standards can be different by up to one part in  $10^{11}$ , it takes 250s in the worst case for transmitter and receiver phase codes of 400Mb/s to walk apart by 1 bit. This means that delay spread measurements which are taken over a short time duration are reliable. Height measurements within the common volume are trustworthy only when reference can be made to the horizon path.

Received signal levels on the Prospect Hill to Mount Tug path have been calculated as a function of relative delay for the path parameters given and under uniform turbulent clear air scatter conditions. Figure 4a shows the rapid onset and high level for the component arriving along the horizon path at maximum antenna gain. Received power decays exponentially with increasing delay, as components arrive from greater height in the common volume and with a scatter angle and antenna gain disadvantage. The distance in nanoseconds between the half power points of this curve is defined as the delay spread. Experimentally, finding the peak power (which was then halved before finding the crossing points) involved some averaging. The estimate for the delay spread is therefore a slightly conservative one. No estimate for the delay spread was

made, when the power was too close to the receiver noise floor.

Figure 4a simulates how narrow layers of higher scattering intensity would superimpose on the basic delay profile.

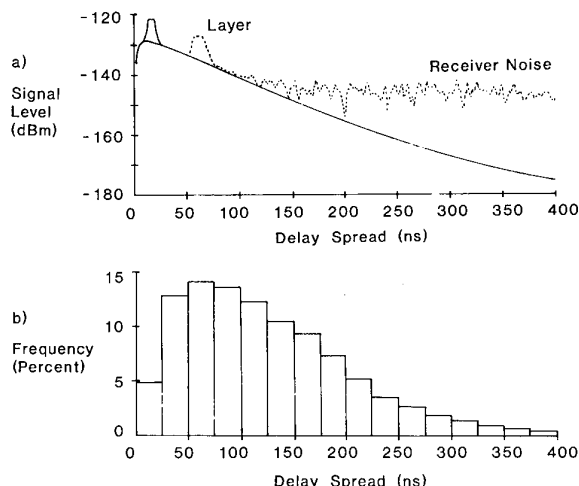


Fig. 4 Calculated and measured delay spread on Prospect Hill to Mount Tug path

It is currently thought that the troposphere contains a weak background turbulence. More highly turbulent layers, measuring from tens of meters to a few hundred meters thick and of up to several tens of kilometers in horizontal extent, lie within this background turbulence. Appearing randomly over time and space, these layers cause every part of the common volume to produce increased scattering at some time [2]. Figure 4b confirms the delay spread function of Figure 4a by measurement. Delay spread is plotted as a histogram of one week's observations, implying that scattering was uniform within the common volume when averaged over a large enough number of hours.

The characteristics of our data suggest that in addition to clear air scatter and rain scatter a third propagation mechanism contributed to a significant percentage of the signals received. This is ducting from elevated layers with sufficient vertical refractivity gradient. Such layers cannot be expected to extend over the whole length of the path, but over whatever distances they exist, they help to lower the scatter angle, increase the received signal level, and reduce delay spread. Reflection from a refractive layer requires a significant vertical refractivity change per unit wavelength. This is more likely to occur at C-band. In terms of wavelengths, ducting layers also appear to be smoother and therefore more effective at C-band. We believe that these three modes of propagation were most responsible for the transmission of signals from Prospect Hill to Mount Tug. As a result, we classified the data whose medians were determined on an hourly basis into three groups,

according to the dominant mode observed for each particular hour. The classification was done by computer and then checked manually to guard against statistical errors. The criteria used to decide the dominant mode of propagation were as follows:

- (1) Since only heavy rainfall produced significant Doppler shift at C-band, Ku-band was used to identify periods of rain. Any hour for which the median Doppler shift was above 2.75Hz and the maximum shift greater than 6Hz, was designated as an hour of rain.
- (2) Ducting was noticed mainly at C-band. This was identified by the presence of very strong signal levels, with the median values in excess of 17dB over the median Ku-band signal, and near-zero Doppler shift.
- (3) All hours not fitting the criteria above were classified as clear air turbulent scatter.

## 5. MEASUREMENT RESULTS

Measurements were carried out between May 89 and June 91, with a gap from July to December 90. Since insufficient data exist for a worst-month analysis, seasonal statistics have been compiled instead [3],[4]. In this context, winter is defined as December, January, February, spring as March, April, May, and so on. Table 2 lists the numbers of hours, at both frequencies, which were classified as clear air scatter, rain scatter, or ducting. Of a total of 5749 hours measured at Ku-band, 88.6 percent are in the first category, 9.7 percent in the second, and 1.8 percent in the third. The corresponding percentages out of a total of 1861 hours at C-band are 79.8, 14.7, and 5.5. Since fewer C-band than Ku-band data exist, and C-band provided the ducting criterion, some ducting may not have been classified as such at Ku-band. Note, however, that ducting conditions at C-band do not necessarily result in Ku-band ducting.

Table 2. Summary of Collected Data (In Hours)

	SPR 89	SUM 89	FALL 89	WIN 89	SPR 90	WIN 90	SPR 91	SUM 91	Total
<b>Ku-Band:</b>									
Clear Air	247	670	294	179	1472	796	1164	270	5092
Rain	40	148	36	-	137	4	134	56	555
Ducting	14	43	2	-	-	-	10	33	102
Total	301	861	332	179	1609	800	1308	359	5749
<b>C-Band:</b>									
Clear Air	247	670	55	-	-	-	244	270	1486
Rain	40	148	-	-	-	-	29	56	273
Ducting	14	43	2	-	-	-	10	33	102
Total	301	861	57	-	-	-	283	359	1861

It was found that the 80ns resolution afforded by the earlier 12.5Mb/s RAKE modulation was marginal in resolving delay spread within the common volume. This led to the installation of the 400Mb/s modulation. Delay spread measurements were made with low resolution through May 90 and with high resolution thereafter. We address here delay spread measurements

from the later period only. Signal level measurements pertain to the same period and to the earlier one as indicated. Data recording consisted of sampling the in-phase and quadrature outputs from the receiver's 120Hz wide low pass filter at a 250Hz rate. Sequentially, 60 in-phase and 60 quadrature samples each were taken for all 1023 taps of the pseudorandom code, meaning the transmitter and receiver code correlation was measured for all 1023 relative positions at the beginning of every hour. In the interest of higher speed, the range was then reduced to 241 taps, centered on the tap with maximum output as determined from the 1023 tap scan. A total of 16 scans of 241 taps each were performed during the remainder of the hour. From these sampling periods the hourly median signal level and delay spread were determined. The whole process repeated itself the next hour, i. e. the timing was reset once per hour with reference to the signal arriving along the horizon path.

It is interesting to compare C- and Ku-band data of summer 89, spring 91, and summer 91 in Table 2 when both systems operated simultaneously. In Figures 5, 6, and 7 the hourly median signal levels received at C-band are divided into five categories relative to their average median. The categories are, normal: within  $\pm 5$  dB of the median, amplified: more than 5dB but no more than 10dB above the median, strongly amplified: more than 10dB above the median, attenuated: more than 5dB but no more than 10dB below the median, and strongly attenuated: more than 10dB below the median. In each of these categories the hourly median signal levels received at Ku-band during the same hours were divided into identical categories relative to the Ku-band average median. The resulting five histograms show the distribution of Ku-band hourly medians parameterized in terms of the five C-band categories. Figure 5 displays the clear air data.

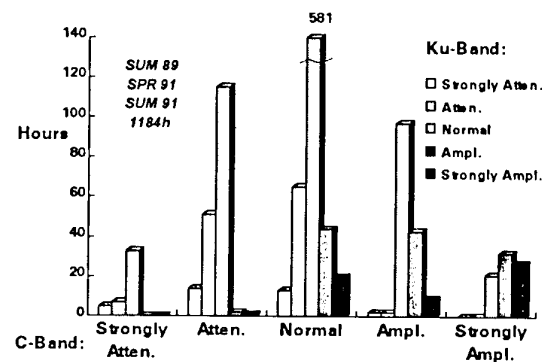


Fig. 5 Relative signal levels of Ku- vs. C-band, hourly medians, clear air

As an example, the center histogram shows (in hours out of a total of 1184 hours) the distribution of Ku-band signal levels when the C-band signal level was normal. The middle value is not drawn to scale. Values in the other categories of the center histogram are distributed fairly symmetrically. In the other histograms they are

appropriately skewed, as might be expected. This means, the more the C-band median moves to one extreme or the other, the less likely it is for the Ku-band median to move to the opposite extreme. It can be determined from Figure 5 that in the majority of cases (59.7%), levels are in the same category at both bands. In a substantial number of cases, however, medians at both bands were in adjacent categories (32.3%) and in non-adjacent categories (7.9%). The latter, in particular, is difficult to explain as a consequence of differences in the clear air scatter mechanism at the two wavelengths. The rigid incrementation into one-hour data segments and relative crudeness of classification criteria are under some suspicion in this context.

The rain data in Figure 6 are based on a much smaller total of 233 hours, leading to somewhat larger statistical uncertainty. Compared with the previous figure, all histograms have broadened, most visibly the one for normal conditions at C-band. As in the previous figure, the tendency for signal levels at both bands to move in the same direction is still noticeable. The cross-band comparison does not allow one to interpret rain either as an advantage or disadvantage at Ku-band. Subsequent figures will show the constructive trend of rain at Ku-band better. Ducting data in Figure 7 are based on a total of 86 hours which further increases statistical noise. Most hours again show normal levels at both wavelengths. Remnants of the skewedness of Figures 5 and 6 are visible. There is no obvious trend toward amplification or attenuation at Ku-band. In Figures 5 to 7 categories are referenced to the respective average medians for each band and propagation mode.

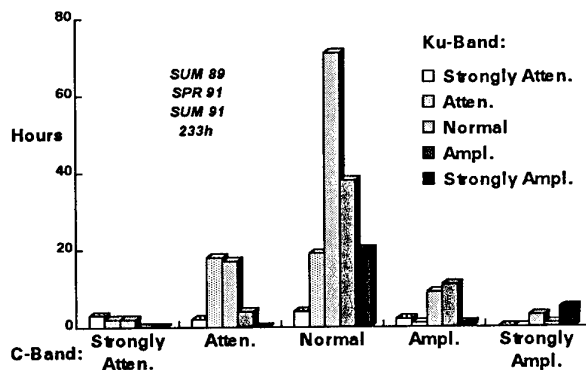


Fig. 6 Relative signal levels of Ku- vs. C-band, hourly medians, rain

To further investigate the effect of rain on troposcatter, the Ku-band rain data for winter 90, spring 91, and summer 91 were replotted in Figure 8. They are categorized as before but with respect to the average clear air median at Ku-band, derived from 2230 hours of data. In each of the seasons the histograms are skewed toward signal increases in rain relative to clear air. There were few rain hours in winter and rain rates were low enough for enhanced scatter to prevail over enhanced attenuation. The rain scatter advantage can be

seen during the other seasons as well. Notwithstanding this observation, there were cases where enhanced attenuation overtook enhanced scatter, either by high precipitation rate or by unfavorable distribution along the path.

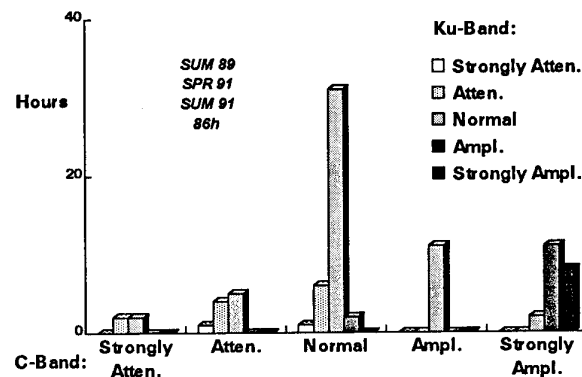


Fig. 7 Relative signal levels of Ku- vs. C-band, hourly medians, ducting

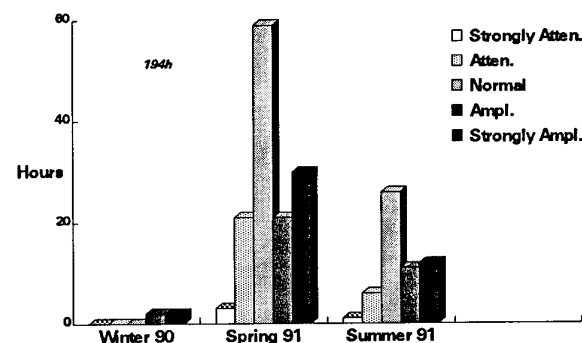


Fig. 8 Ku-band hourly median signal levels in rain vs. clear air average median

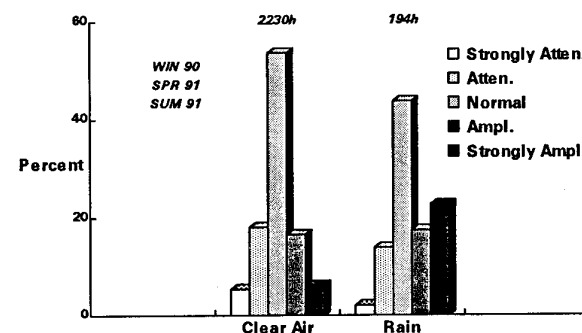


Fig. 9 Ku-band hourly median signal levels in clear air and rain vs. clear air average median

In a last comparison of this kind (Figure 9), we show histograms of both clear air and rain data, each added for the same seasons as in Figure 8.

All data are categorized with respect to the clear air average median. Because of the large difference in clear air and rain hours, 2230 and 194, respectively, populations in the categories are given on a percentage



basis. The lack of symmetry in the rain data is quite apparent in comparison with the clear air data. Again, in rain, signal levels are amplified more often than they are attenuated. Since both data sets are referenced to the clear air average median level, one notes that a larger number of hours are attenuated or strongly attenuated under clear air conditions than under rain conditions. This is true both on a percentage basis and in absolute numbers.

Signal level averages were also plotted on a diurnal basis. Ducting generally takes place during the night and early morning hours, when the wind speed is low enough to permit atmospheric layering. Later in the morning, when the sun warms the earth surface, turbulent activity in the air increases, leading to enhanced clear air scatter. While low rain rates cannot be associated with a specific time of day, thunderstorms and their high rain rates tend to occur later during the day. Since rain data are plotted separately, and since two summers are included in the data, one might assume heavy rain in the afternoon and evening hours to produce low signal levels. But then, a narrow cell of heavy rain well placed within the common volume could have just the opposite effect.

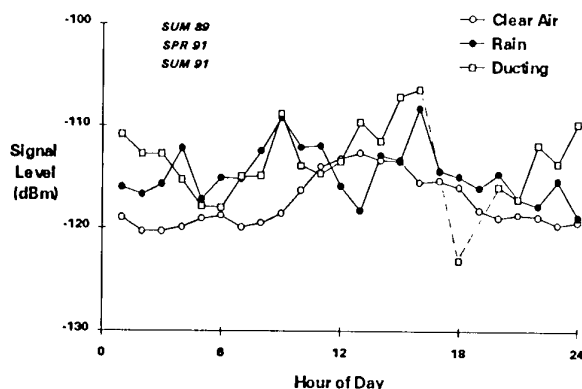


Fig. 10 Average diurnal variation in Ku-band signal level

Figure 10 shows the hourly medians of signal level, averaged over summer 89, spring 91, and summer 91 data and plotted versus the hours of the day. Scarcity of hourly data in the rain and ducting modes translates into averages of only a few measurements, a single measurement, or none at all at a particular hour. Periods where data are missing were connected by dashed lines. The limited number of points leads to little smoothing of the curves which makes it more difficult to discern trends. The clear air data in Figure 10 show the expected diurnal behavior. From around 0900h to 1200h the signal rises by about 7dB. It then drops back more gradually to its nighttime level. The seasonal increase from winter to summer, also quite noticeable in the data, is not revealed in this plot. The clear air signal level averaged over the whole day was -116.7dBm for our link. Rain signal levels vary more

substantially over the course of the day. There appears to be some upslope in the curve until midafternoon, and a downslope over the remainder of the day. Although this would confirm the behavior postulated earlier, the evidence is weak. There is no rationale to interpret the large peaks and valleys during the ascending portion other than the limited amount of data. At -113.6dBm, the average signal level over the day is 3.1dB higher than under clear air conditions. Ducting along the path is signified by excess signal levels and low Doppler spread at C-band. The ducting curve in Figure 10 has the highest average signal level (-112.7dBm) which exceeds the clear air level by 4dB and the rain level by 0.9dB. Curiously, although one may not be able to find a physical explanation for this, there exists a fairly high correlation between the fluctuations of the rain and ducting curves. The highest levels during ducting conditions occur around midday.

The final figure gives delay spread data on a diurnal basis for the spring and summer 91 seasons. Summer 89 was left out in Figure 11 because of the low delay resolution available during that period.

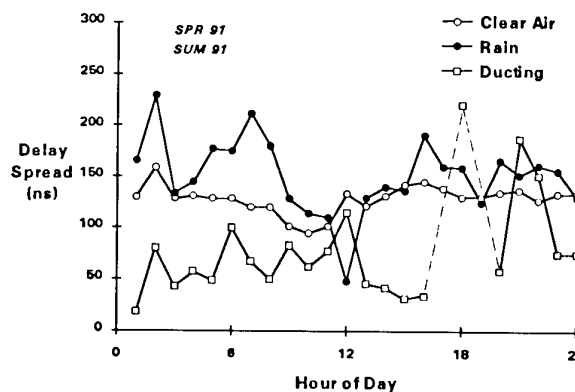


Fig. 11 Average diurnal variation in Ku-band delay spread

We found a delay spread of 128ns in clear air, averaged over the day and the seasons. Variation over the day is small. There is no significant effect of the midday signal increase on delay. Delays measured in rain were higher, as expected, because of the higher scattering efficiency of raindrops at larger scatter angles. The average of the rain curve is 151ns, not an inordinate increase over the clear air value. However, hourly median delay spreads in rain as high as 322ns were observed. There is no pronounced diurnal trend. Compared with signal levels in rain and ducting conditions, the corresponding delay spreads show a marked difference. In the ducting mode, delay spread is substantially less at least during the first half of the day, even in comparison with clear air. The average value was determined to be 81ns. This suggests that the ducting classification as implemented does have a bearing on Ku-band. Undue importance should not be assigned to the high excursions during the last quarter of

the day, since these are based on a low number of hours from one season.

## 6. CONCLUSIONS

The main purpose of the measurements reported here was to examine the frequently held notion that high attenuation and delay spread in rain would make troposcatter systems at frequencies beyond 10GHz impractical. Some evidence has been accumulated toward the contrary. On a relatively short path of 100mi length the excess attenuation caused by rain is more often than not outweighed by a more efficient process of scattering power out of the transmit beam into the receiver direction. To avoid having to specify the propagation environment in any meteorological detail, the experiment was conducted as a comparative study between similar C- and Ku-band paths. This allowed us to classify the data in terms of the prevailing propagation mechanism along the path. By its decision criteria and by the hourly median quantization of data this may not have done justice to all propagation phenomena along the path, in particular high intensity rains. Another drawback has been the limited amount of non-clear-air hours of data. Notwithstanding these limitations, the study shows that Ku-band troposcatter has potential as a mobile, tactical communication mode.

## ACKNOWLEDGEMENT

Funding for the contractual part of this work has been provided by the US Air Force Joint Tactical Communication (TRI-TAC) Program Office, Electronic Systems Division.

## REFERENCES

1. Parl, S. and Malaga, A., "Theoretical Analysis of Microwave Propagation", RADC-TR-84-74, April 1984.
2. Crane, R. K., "A Review of Radar Observations of Turbulence in the Lower Stratosphere", Radio Science, 15, 2, March-April 1980, pp 177-193.
3. Crane, R. K. and Prabhu, R., "Wideband Troposcatter", Final Report, GIT Subcontract E-21-T29, Dartmouth Coll., August 1991.
4. Crane, R. K. and Wennemyr, M., "Troposcatter at the Ku Band", Final Report, GIT Subcontract E-21-T44, Dartmouth Coll., November 1991.

# Angle Diversity on Digital Microwave Links:

## Antenna Design and Experimental Results

**D. Beaufort**

Royal PTT Nederland NV  
PTT Research  
P.O. Box 421  
NL-2260 AK Leidschendam  
The Netherlands

**Prof. L.P. Ligthart**

Delft University of Technology  
Dept. of Electrical Engineering  
Mekelweg 4  
NL-2628 CD Delft  
The Netherlands

### 1. SUMMARY

PTT Research and Delft University of Technology examined the merits of angle diversity for multipath fading reduction on digital microwave links. A dual-polarized hybrid reflector array, suitable for beam switching in the vertical plane, was designed and produced. The antenna specifications were based on extensive propagation studies.

The antenna was tested for two years on a 45 km hop in The Netherlands. It was found that *switching* between the antenna beams is superior to *adaptive (maximum power) combining*. Switching reduces the time that the Bit Error Ratio (BER) exceeds  $10^{-3}$  by a factor 27.

### 2. INTRODUCTION

On digital radio links, multipath fading may cause Intersymbol Interference (ISI). The ISI can be reduced significantly by adaptive equalizers, which are therefore widely used in high capacity digital microwave systems. However, with performance objectives and spectrum efficiency requirements becoming more stringent, additional countermeasures are often necessary. A common solution is space diversity: a second receiving antenna is installed at a certain distance from the main antenna. If the antenna separation is chosen properly, the signal degradation on the two antennas will normally be uncorrelated or even show negative correlation. Thus high performance improvement can be obtained, for example by adding the two signals in-phase to get maximum signal level at the receiver input (Maximum Power Combining or MPC).

An interesting alternative for space diversity is *angle diversity*. Angle diversity is based on the difference in Angles-of-Arrival of the received signal components: the fading is reduced by an appropriate change of the antenna pattern. A major advantage of angle diversity above space diversity is that it can be realized with only one reflector. This saves space and costs and makes angle diversity very useful in situations where the installation of a second reflector is impossible (for example on the roof of a building, on overcrowded radio towers or on masts that are too low for the required antenna separation).

In a joint project, Delft University of Technology and PTT Research examined multipath propagation characteristics related to angle diversity, which resulted in the design of a dual-polarized angle diversity antenna. A proto-type of this antenna,

that can be mounted in a standard parabolic dish, was tested for two-years on a radio link in The Netherlands.

This paper describes the angle diversity principles, the antenna design, the set-up of the field trial, and the measurement results.

### 3. ANGLE DIVERSITY

During multipath propagation, signal attenuation and spectrum distortion may occur, depending on the number of received signal components ("rays") and on the propagation delays and amplitudes thereof. The ray amplitudes are determined by the structure of the atmosphere and by the Angles-of-Arrival (AOA's) in combination with the receiving antenna pattern.

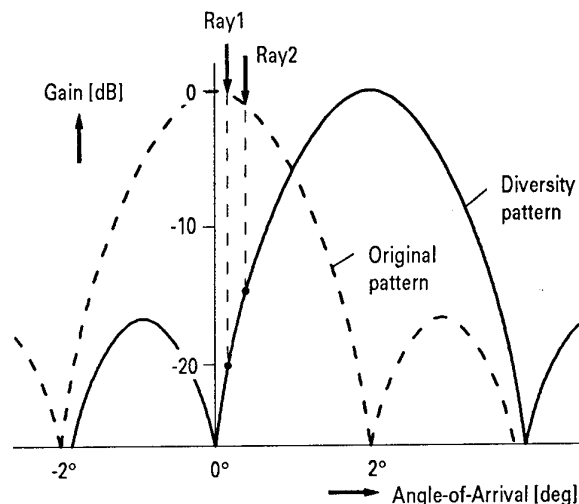


Figure 1: the principle of beam switching.

Measurements show that the AOA's of the dominating rays are mostly close to the nominal Line-of-Sight (LOS), e.g. within approximately  $\pm 0.5^\circ$  on a 30 km path [1]. Hence, the impact of the antenna pattern on the ray amplitudes is usually negligible: the rays are equally added. In the case of two-ray propagation this means that, if the rays arrive with equal amplitudes, a deep notch may occur in the signal spectrum. This situation changes if the antenna is shifted such that the multiple rays are received on the slope of the antenna beam,

as illustrated in figure 1. Now the antenna gain for one ray is lower than for the other. As a result notch depth decreases.

Angle diversity by beam switching is based on this principle. Under nominal propagation conditions the signal is received with an antenna aiming at the LOS. As soon as multipath fading leads to system degradation another antenna is selected, having some positive or negative elevation with respect to the LOS. Ideally, the different antenna patterns are integrated into a single feed system. The design of such a compact feed system with high XPD and low coupling between the ports is described in section 5.

From figure 1 it is evident that:

- the slope of the diversity pattern near the LOS determines to what extent the notch depth is reduced. The steeper the slope, the shallower the notch;
- all incident rays are attenuated by the diversity pattern and hence the average signal level, measured over a large bandwidth, will decrease. A steeper slope of the antenna pattern will increase the attenuation (flat fading).

In other words: the optimum diversity pattern follows from a compromise between the required reduction of selective fading and the permissible increase of flat fading.

#### 4. DESIGN CRITERIA

Studies of multipath propagation modelling to derive design criteria for angle diversity systems have been published earlier [2]. The propagation model starts with the calculation of the elevation AOA and the delay time of a "direct" ray. The direct ray is a ray that propagates from the transmit to the receive antenna given the link geometry and "standard" tropospheric conditions.

A "multipath" ray goes its path assuming a constant refractive index gradient that differs from the standard troposphere. The model calculates for this multipath ray an AOA-difference  $\alpha$  and a delay time difference  $\tau$ , both with respect to the direct ray. In this way a unique  $\alpha$ - $\tau$  combination is found for the specific constant refractive index gradient that is implicitly needed to obtain one specific multipath ray, affected by that gradient. Figure 2 shows the  $\alpha$ - $\tau$  relationship that results from a range of refractive index gradients.

The design of the antenna system is based on a two-ray propagation model where  $\alpha_1$ ,  $\tau_1$  and  $\alpha_2$ ,  $\tau_2$  are both points on the  $\alpha$ - $\tau$  curve, which is considered the worst case for selective fading. For digital radio links it is assumed that the BER performance objectives are satisfied as long as:

$$20 \cdot \log \left\| \frac{\tau_1 - \tau_2}{\tau_s} \right\| < FD - 6 \text{ [dB]}$$

where  $\tau_s$  is the symbol time, dependent on the bitrate and on the system modulation scheme, and FD is the two-ray fade depth in dB, expressed as:

$$FD = 20 \cdot \log \left\| 1 - \frac{a_1}{a_2} \right\|$$

where  $a_1$  and  $a_2$  are the ray-amplitudes after reception.

The needed change in pattern envelope follows from these requirements and from the assumed worst cases for the two rays. This approach is valid as long as the system flat fade margin is sufficiently large.

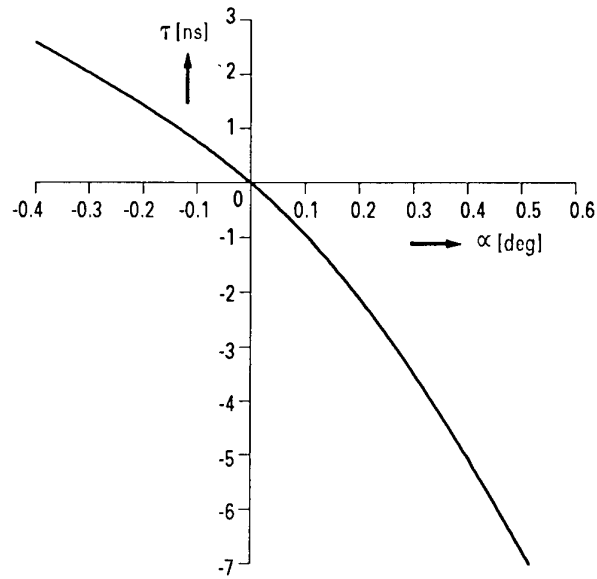


Figure 2: Angle-of-Arrival  $\alpha$  as a function of delay time difference  $\tau$  for linear refractive index profiles. Antenna height: 80 m; radio link distance: 40 km.

#### 5. ANTENNA DESIGN

The needed change in pattern envelope can be made by a focal-feed array system integrated in a 3 meter parabolic reflector with  $F/D = 0.3$  ( $D$  = diameter;  $F$  = focal distance = 0.90 m). Assuming beam steering by switching between single "activated" elements the requirements are:

- spacing around  $\lambda_0/2$  ( $\lambda_0$  is the free space wavelength)
- at least 3 elements for switching the elevation angle
- low side lobes in the reflector antenna patterns are only needed for the one coming from the centre element since this element is active most of the time (during non-multipath conditions)
- dual linear polarizations
- antenna pattern of centre element has to be rotationally symmetric.

Therefore a 5-element array with  $\lambda_0/2$  spacing was built. The 4 GHz band was selected for experiments (described in section 7). The array configuration is shown in figure 3.

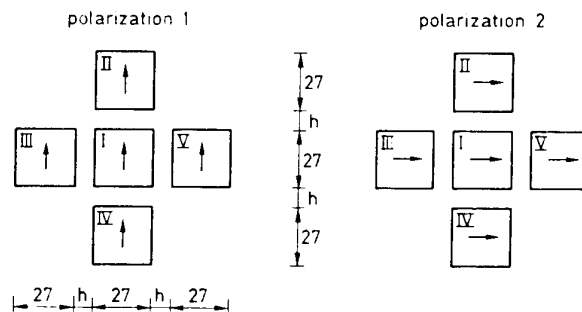


Figure 3: array of 5 dual polarized  $TE_{01}$  radiators with square cross sections (inner dimensions 27 x 27 mm).

Identical dual-polarized dielectric filled  $TE_{01}$  radiators with square cross sections of 27 x 27 mm were constructed. Unique in the radiator are the airgap wideband matching of the aperture (airgap length of 4.1 mm) and the use of two metal sheet

polarization dependent reflectors 1 and 2. A sketch of the element, with dimensions indicated, is drawn in figure 4 [3].

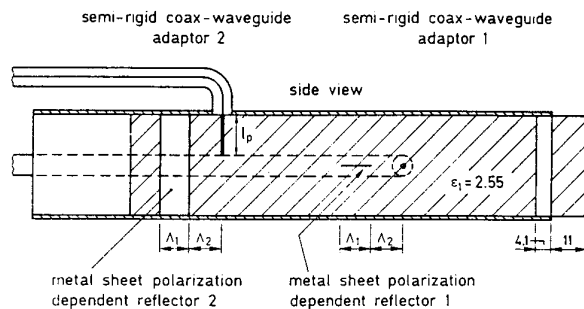


Figure 4: dual polarized  $TE_{01}$  radiator with square cross section.

Optimization of the element resulted into:

- VSWR < 1.3 from 3.85 to 4.50 GHz.
  - VSWR < 1.4 from 3.70 to 4.90 GHz.
  - Coupling between the two polarization ports < -40 dB.
- The mutual coupling between two elements at  $\lambda_0/2$  spacing is:
- E-plane coupling < -20 dB
  - H-plane coupling < -40 dB

Figure 5a shows co-polar patterns for horizontal and cross polar patterns for vertical polarization over an elevation angle from  $-6^\circ$  up to  $+6^\circ$  (azimuth angle  $0^\circ$ ). The co-polar patterns concern switched beam patterns of radiators I, II and IV as numbered in figure 3. The cross-polar patterns concern radiators I and IV only, because all cross-polar measurements are probably affected by ground reflections.

The calculated cross-polar patterns in figure 5b show good agreement with measurements. Differences can be explained because aperture blockage by the array and by the struts has been neglected.

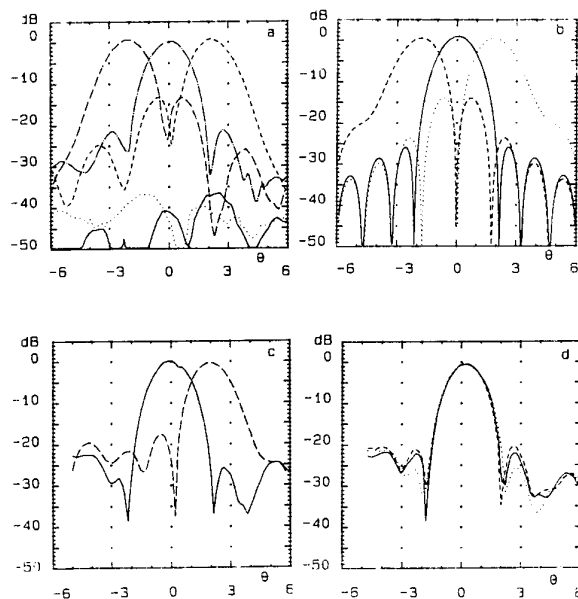


Figure 5: hybrid reflector array patterns. *a* co- and cross-polar, hor. polarization; *b* calculated co-polar; *c* co-polar, vert. polarization; *d* co-polar, hor. polarization, elevation  $-2^\circ$ ,  $0^\circ$ ,  $+2^\circ$ .

The rotational symmetry of the main lobe pattern is illustrated by the elevation co-polar patterns of radiators I and IV for vertical polarization (figure 5c), where the main lobes are similar to those in figure 5a. The azimuth co-polar patterns of radiators I, II and IV are shown in figure 5d for horizontal polarization and elevation angles  $0^\circ$ ,  $-2^\circ$  and  $+2^\circ$ , respectively. Differences with the elevation pattern for the centre element, as far as levels below  $-20$  dB are concerned, are probably caused by ground reflection effects.

## 6. SWITCHING OR COMBINING

In principle the antenna was designed for angle diversity by switching between the different elements ("beams"). Normally the centre beam, directed towards the LOS, is selected. When a certain threshold (for instance a BER-level) is exceeded, the receiving equipment switches to another beam.

As an alternative, the signals from the different beams could be added in-phase such that the signal level at the receiver input is always at maximum. This Maximum Power Combining (MPC) technique is very common for space diversity. MPC performs better than switching during periods of strong fading of all individual signals. Here switching would not help, whereas MPC might deliver a combined signal that is strong enough for error free demodulation.

It is, however, also possible that switching is superior to MPC. If only the strongest of the MPC-combiner inputs is severely distorted, the combiner output (which is dominated or even completely determined by the strongest input signal) will be distorted as well. In such a case a switch could perform better by selecting the weaker signal that is not distorted.

With space diversity, performance improvement by MPC will generally be higher than the improvement by switching, since the strongest signal is usually the less distorted. For angle diversity the situation is different. From figure 1 it was concluded that the penalty for the reduction of selective fading (distortion) is an increase of the flat fading (attenuation). Thus the strongest signal might very well be the most distorted, in which case MPC fails. Switching or combining by a different algorithm (for instance Minimum Dispersion Combining) would therefore be more appropriate for angle diversity. Experimental evidence for this conclusion, that is not often recognized, will be given in section 11.

## 7. THE EXPERIMENT

In July 1988, a field test started on the 44.6 km hop Lopik - Loon-op-Zand to evaluate the performance improvement by angle diversity [4]. The hop is almost completely flat and horizontal. The antenna heights are about 80 m at both ends; the terrain is open (mainly grassland), so there is no risk of obstruction. Table 1 summarizes the main link parameters.

From Lopik a 140 Mbit/s Pseudo Random Bit Sequence (PRBS) was transmitted at 3.81 GHz. The angle diversity antenna was mounted in Loon-op-Zand in a 3 m parabolic dish. The centre beam aimed at the Line-of-Sight and thus acted as the reference to an unprotected link.

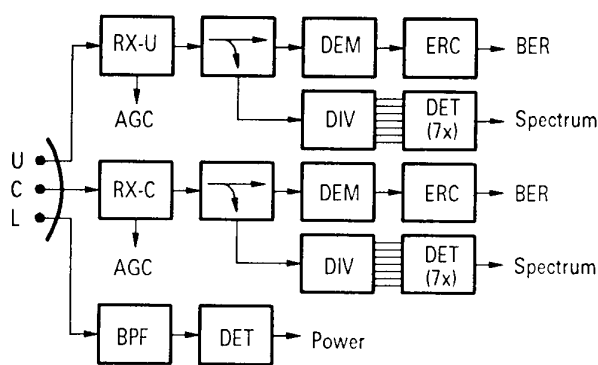
Two demodulating receivers (commercially available equipment) were connected to the centre beam and the upper beam, respectively. With error counters detailed information on the BER-performance of these two beams was obtained. Moreover the AGC-voltages of the receivers were sampled. From these the signal attenuation (flat fading) can be derived accurately. The IF amplitude spectra of the centre and upper beam signals

were also measured, using narrow band filters (at 7 frequencies from -15 to +15 MHz with respect to the centre frequency).

channel centre frequency	3.810 GHz
polarization	horizontal
modulation	16 QAM
system capacity	140 Mbit/s
channel bandwidth	40 MHz
nominal FFM (centre beam)	40 dB

Table 1: main link parameters.

Because a third demodulator was not available for the experiment, the BER-performance of the lower beam signal could not be determined. On the lower beam only the incident signal level within the radio channel bandwidth was measured.



U : Upper beam    RX : Receiver    BPF : Bandpass filter  
C : Centre beam    DEM : Demodulator    DET : Detector  
L : Lower beam    ERC : Error counter    DIV : Power divider

Figure 6: measurements at the receive site.

Figure 6 gives an overview of the measurement set-up at the receive site (Loon-op-Zand). The measured parameters were sampled once per second, except for the amplitude spectra which were sampled 5 times per second. The data were stored on the hard disk of a remote PC system during multipath events and otherwise only once per minute.

## 8. MEASURED FADING STATISTICS

Fading statistics can be derived from the AGC-recordings of the centre beam. The AGC-voltage was stored per second if the input signal level was at least 5 dB below the nominal level. Figure 7 shows the distributions based on 24 months (July 1988 – June 1990). The dashed lines each correspond to a 1 year period. The solid lines give the average worst month and the "overall" average year for the entire period.

According to CCIR Rec. 530-4, the deep fading region (i.e. below 0.1%) of the average worst month can be approximated by:  $p(A) = P_0 \cdot 10^{-A/10}$  %, where  $P_0$  is a constant that depends on the hop geometry and on a climatic factor  $K$ . The value for  $P_0$  that fits best to the measurements is about 60%. To obtain this value from equation (19) of Rec. 530-4,  $K$  must be set to  $1.7 \cdot 10^{-4}$ . This is somewhat higher than the value suggested in the same Recommendation ( $K = 3.6 \cdot 10^{-5}$  according to eq. (10)).

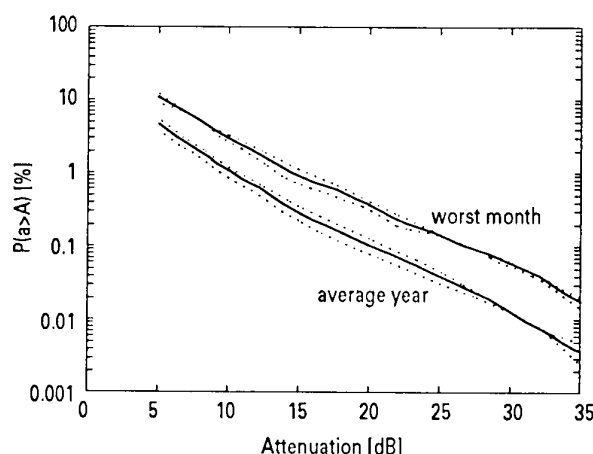


Figure 7: fading statistics (centre beam).

## 9. IMPROVEMENT BY BEAM SWITCHING

For 15 months (July 1988 until September 1989) the experiment was conducted as described in section 7. In this period the Bit Error Ratio of the centre beam signal was above  $1 \cdot 10^{-3}$  ("outage") for 1042 seconds. Simultaneous outage of the upper beam signal occurred during 105 of these 1042 seconds. Hence, the outage time improvement factor obtained with beam switching per second amounts to about 10.

The number of switch-overs that is required to obtain this improvement factor, is surprisingly low. Even in September 1989, the worst month of the measurement period, only 22 switch-overs between centre beam and upper beam were sufficient to keep the BER below  $10^{-3}$ .

The contribution of the lower beam to performance improvement is derived from the power measurements on this beam, for here the received signal was not demodulated. The power measurements on the lower beam are available from December 1988 until September 1989 (10 months). In this period 544 outage seconds of the centre beam were recorded. During centre beam outage, the signal level at the lower beam was only 20 seconds below the measurement range of the power detector (about 1 dB above the BER =  $10^{-3}$  threshold). The upper beam signal level was 75 seconds below threshold.

It is unlikely that simultaneous outage of centre and (upper or lower) diversity signal will occur when the diversity signal level is above threshold, since the starting point for the antenna design was that selective fading should always be sufficiently reduced, even in the (theoretical) worst case. Indeed this is the case for the upper beam: simultaneous outage (105 seconds between July 1988 and September 1989) only occurred when the diversity signal was below threshold. There is not much reason to believe that this will be different for the lower beam.

On the basis of this assumption the outage time reduction factor for the lower beam amounts to 27. This is a conservative estimate, since the floor of the measurement range was 1 dB higher than the BER =  $10^{-3}$  threshold.

Switching between three beams does not lead to a much higher improvement factor. Using the same procedure we find an improvement factor of about 32. Considering the more complex switching algorithm that would be required for three-beam switching, two-beam switching is the most favourable for

practical applications. It is however essential to determine whether the diversity beam should have a higher or a lower elevation angle than the centre beam.

When designing the angle diversity experiment, we decided to connect the second demodulator to the upper beam rather than to the lower beam, because publications on angle diversity tend to indicate that beams with positive elevation angles give higher improvement (for an overview see [5]). However, on the experimental link Lopik - Loon-op-Zand the lower beam performed better. This might be explained from the existence of permanent surface reflections, combined with a possible high occurrence of surface ducts (the hop runs parallel to the North Sea coast, about 50 km inland without significant barriers, and is surrounded by a flat area with many small water surfaces), so that the multiple rays predominantly have negative Angles-of-Arrival.

Probably an even higher improvement factor can be obtained by optimizing the diversity patterns. In section 3 it was stated that the optimum patterns follow from a compromise between the required reduction of selective fading and the permissible increase of flat fading. Since simultaneous outage of centre and upper beam occurred only during strong attenuation of the upper beam signal, the gain of the upper beam pattern near the Line-of-Sight appears to be too low. Increasing this gain by slightly decreasing the angular offset of the diversity beams would probably increase the improvement factors.

## 10. INSTALLATION OF ADAPTIVE COMBINING

In section 6 it was stated, on theoretical grounds, that beam switching gives higher angle diversity improvement than Maximum Power Combining. Still it is worthwhile to examine the impact of MPC's on angle diversity improvement, for two reasons:

- since many operators are familiar with the use of MPC's for space diversity systems, the operational introduction of angle diversity would be facilitated if satisfactory improvement with MPC's can be obtained;
- several publications on angle diversity experiments are based on the use of MPC's.

We tested the application of MPC's in three different configurations, all according to the general set-up shown in figure 8. The centre beam signal is divided into two parts. One part is demodulated (the "main channel"), the other part is combined with the upper beam signal (the "combiner channel"). Now it is of interest how the performance of the combiner channel compares to the main channel performance.

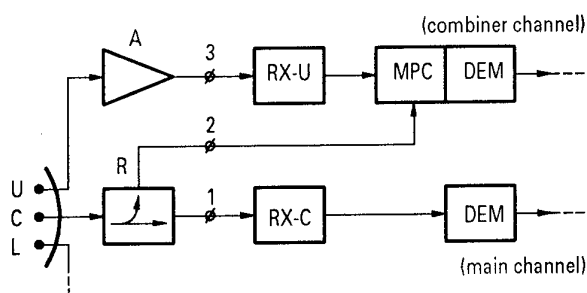


Figure 8: basic configuration with MPC.

The two variables are the gain  $A$  of the upper beam RF-amplifier and the split-off ratio  $R$  of the power splitter.

Concerning  $R$  it should be recognized that this parameter should be set to 3 dB to get a "fair" comparison between the main channel and the combiner channel. If  $R$  has a higher value, the combiner channel is at disadvantage. On the other hand, with a high value of  $R$  the main channel can still be considered as a standard, unprotected link (the margin reduction due to signal loss is negligible). For these reasons  $R$  was set to 10 dB in the first two configurations with MPC, and to 3 dB in the last configuration.

The value of  $A$  should be such that, ideally, the diversity beam signal is always weaker than the split-off part of the centre beam signal, unless the centre beam signal shows significant performance degradation. In the latter case the diversity signal should dominate.

To find the optimum value for  $A$ , use can be made of figure 9 (based on recordings of the first 15 months of the experiment). This figure shows the difference between the incident signal levels on the centre beam and the upper beam, respectively. Two different curves are drawn, one for the case that the Bit Error Ratio of the centre beam signal was better than  $10^{-8}$ , and one for the case that this BER was worse than  $10^{-3}$ . It can be seen that if the centre beam signal has a low BER, this signal is stronger than the upper beam signal for 95% of the time. In case of high BER (the BER  $\geq 10^{-3}$  curve) this percentage is reduced to about 50%.

The curves of figure 9 are also valid for the difference between the input signals at the combiner. However, as the signal from the centre beam is attenuated by  $R$  dB and the upper beam signal is amplified by  $A$  dB, an amount of  $(R + A)$  dB should be subtracted from the abscissa values. In other words: the 0 dB-point (where the two signals are equally strong) shifts to the right by  $(R + A)$  dB.

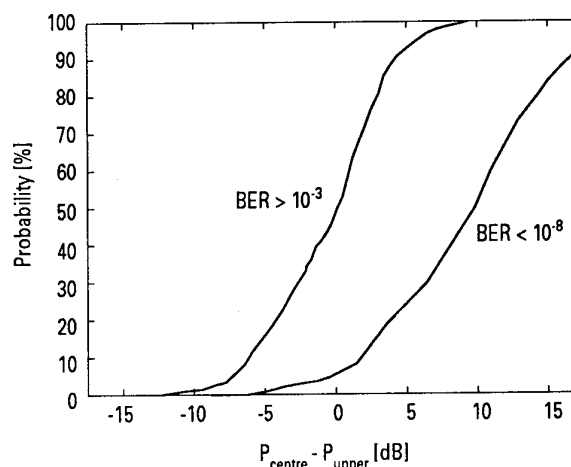


Figure 9: Difference between incident power on centre and upper beam, with centre beam BER as a parameter.

Ideally,  $R + A$  is chosen such that the curve for high centre beam BER-values is entirely on the left hand side of the 0 dB point, and the low-BER curve entirely on the right hand side. Then the diversity beam signal would always dominate in case of severe degradation of the main beam signal, whereas it would be weaker when the main beam performance is acceptable. However, from figure 9 it can be seen that this ideal situation cannot be reached. Hence, a compromise is required.

During the last four months of the experiment (April – July 1990), we tested three different configurations with MPC's. Table 2 lists how many weeks each configuration was under test. Moreover the signal levels are given as measured at the three points indicated in figure 8: the input of the main channel receiver (1), the input from the centre beam into the diversity combiner (2) and the input from the upper diversity beam into the combiner (3). The figures are in dB relative to the nominal centre beam level. The last column in table 2 gives the effective value of  $(R + A)$ , taking into account the splitter, the low-noise amplifier, insertion losses and a 3 dB attenuator in the diversity combiner at the input for the diversity signal.

Conf.	weeks	measured levels [dB]			$(R+A)_{\text{eff}}$
		1	2	3	
A	6	0	-10	-26	7
B	3	0	-10	-5	28
C	7	-3	-3	-19	7

Table 2: configurations with MPC.

## 11. RESULTS FOR ADAPTIVE COMBINING

### Configuration A:

The first configuration was realized with a 10 dB power splitter (in order to preserve the reference to a normal link without diversity) and without an amplifier. Taking account of the 3 dB attenuation of the diversity signal inside the MPC, the effective reduction of the power difference between the two signals, as compared to the abscissa values in figure 9, amounts to about 7 dB. This value was chosen because:

- the signal from the diversity beam will dominate most of the time when the centre beam signal is severely degraded;
- the relatively large portion of the low-BER curve that falls left of the new 0 dB-point (the 7 dB-point in figure 9) seems acceptable, because here the centre beam signal is probably much distorted already (in spite of the low BER). Nominally (50% of total measurement time) the difference between centre and upper beam signal level amounts to about 26 dB, so the low-BER curve corresponds already to a degraded situation.

During the 6 weeks that configuration A was installed, 166 seconds of main channel outage were recorded. In the same period outage of the combiner channel occurred for 154 seconds. Hence the improvement factor was very low, which is probably due to the fact that the combiner channel has a 10 dB lower fade margin.

### Configuration B:

The next 3 weeks we examined the effect of a strong amplification of the diversity signal. Effectively the signal level difference at the combiner input was reduced by 28 dB, such that the two input signals were equally strong under nominal conditions. The combiner channel performance turned out to be very poor: there were 559 seconds of outage, compared to 74 outage seconds of the main channel; an "improvement" factor of 0.13.

### Configuration C:

The last 7 weeks of the experiment the reference to a standard unprotected radio link was given up by inserting a 3 dB-power splitter in the main channel. With an appropriate choice of

the amplifier gain the same reduction of the input level difference was obtained as for configuration A, i.e. 7 dB. The main difference with configurations A is that now the main channel and the combiner channel have the same flat fade margin.

Surprisingly, the results were similar to those obtained with configuration A: 1263 (!) seconds of main channel outage and 1309 seconds of combiner channel outage, giving an improvement factor slightly less than 1. Excluding the last week of the measurements would give a different picture: the total outage time in six weeks was reduced from 268 to 50. This outage time reduction would have complied with our expectations: a moderate improvement factor, but significantly lower than the improvement obtained with switching.

In section 6 it was stated that the Maximum Power Algorithm was not the optimum for angle diversity, since in case of angle diversity the strongest signal is not necessarily the best signal. However, attempts to compensate for this by amplifying the diversity beam signal obviously failed. It seems therefore safer not to amplify the diversity signal, in order to avoid the risk that this signal unnecessarily degrades the performance of the centre beam signal.

## 12. CONCLUSIONS

The major advantage of angle diversity compared to space diversity, is that it can be realized with only one reflector. To achieve this, a compact antenna system is required. Delft University of Technology designed such an antenna for the 4 GHz band, suitable for beam switching in the vertical plane.

Measurements with the antenna show that beam switching with two beams, one aiming at the Line-of-Sight and one at a 2° lower elevation, reduces outage time ( $\text{BER} \geq 10^{-3}$ ) by a factor 27. Even higher improvement factors can probably be obtained with slightly adapted diversity patterns.

Maximum Power Combiners (MPC's), which are commonly used for space diversity, are less suitable for angle diversity. Optimization of the receiver configuration with MPC's turns out to be very difficult.

Further research should be directed to the issues of the optimum beam configurations, the elevation angles and reliable prediction methods.

## REFERENCES

- [1] Webster, A.R. and Merritt, T.S.: "Multipath Angles-of-Arrival on a Terrestrial Microwave Link" IEEE COM-38, No. 1, Jan. 1990, pp 25-30.
- [2] Ligthart, L.P.: "Design Criteria for Limited Scan Antennas at Digital Microwave Line of Sight Links" AGARD Conf. 363 on Propagation Influences on Digital Transmission Systems - Problems and Solutions, 1984, pp 15.1 – 15.7
- [3] Ligthart, L.P.: "Antenna Design and Characterization based on the Elementary Antenna Concept" PhD thesis Delft University of Technology, The Netherlands, 1985.
- [4] Beaufort, D. and Hoek, L. van der: "The effect of angle diversity on performance as measured on a digital radio relay link" Proc. of the 2<sup>nd</sup> ECRR, Padua (Italy), April 1989, pp 328 – 335.
- [5] CCIR Report 376-6 (1990): Diversity Techniques for Radio-Relay Systems; section 5.3.2.



## DISCUSSION

**Discussor's name :** G. S. Brown

**Comment/Question :**

Did you actually try to use your dual polarization capability, i.e. receiving on two orthogonal polarizations? There may be difficulties due to the cross-polarization properties of parabolic reflector antennas.

**Author/Presenter's Reply :**

For the experiment we only used the horizontal polarization.

**Discussor's name :** U. Lammers

**Comment/Question :**

1. Apparently you derive the greatest benefit from the lowest beam. Does it see ground reflected signals?
2. Rather than switching beams, would continuously tracking the optimum signal in angle further improve the BER?

**Author/Presenter's reply :**

1. It probably does: on the flat path ground reflections are likely to occur. Moreover, we assume that the proximity of the sea causes surface ducts to occur relatively often, leading to negative angles-of-arrival.
2. In principle, yes. It seems, however, very difficult to define a reliable tracking algorithm. Switching is much easier and has already given satisfactory results. Hence, switching is preferable.

# MITIGATION OF EFFECTS OF MULTIPLE PATH NULLS AT SUPER-HIGH FREQUENCIES THROUGH DIVERSITY AND NETWORKING

N. Dave  
NCCOSC RDT&E DIV Code 827  
53560 Hull St  
San Diego, CA 92152-5001 USA

## SUMMARY

The goal of this work is to investigate the design issues implied by multipath effects for a high bandwidth communication network consisting of platforms in a Navy battle group. This communication network is designed to operate using super-high frequency (SHF) or ultra-high frequency (UHF) line-of-sight (LOS) propagation, and must be robust to variations in link quality due to platform motion or deletion, as well as to the effects of multipath propagation. High bandwidth in this context implies data rate in excess of 1.544 megabits per second (Mbps), known as "T1" in the commercial world. Multipath nulls at the above frequencies can render links useless at certain ranges. In this work, we briefly discuss the well-known methods of height and frequency diversity, as well as a less frequently used but potentially powerful method of "path diversity" through networking, to alleviate the ill effects of multipath nulls. The communication system configurations discussed are appropriate for expected platform separations in post-Cold War battle group scenarios, which envision most platforms within line-of-sight (LOS) distance from each other, i.e., separated by no more than about 20 nautical miles (nmi).

## 1. SHF PROPAGATION STUDIES

We first examine the requirements for effective use of SHF propagation at data rates of T1 or higher. For an understanding of the cause of multipath interference in the SHF spectrum at LOS ranges, a ray optics (RO) treatment is adequate. Under the RO approximation, the LOS field may be viewed as resulting from the interference between straight-line air propagation of energy from the transmitting antenna and energy reflected from the surface (the ocean surface, for this work). Varying phase difference between the "direct" and "reflected" rays alternately causes constructive or destructive interference in the LOS region, resulting in maxima and minima in received energy as a function of range. Destructive interference of the two components may reduce signal intensity to zero at some ranges. Details of LOS field calculations are presented in Panter [1].

The performance of communication systems is dependent not only on propagation and system losses, but also on such parameters as the data rate

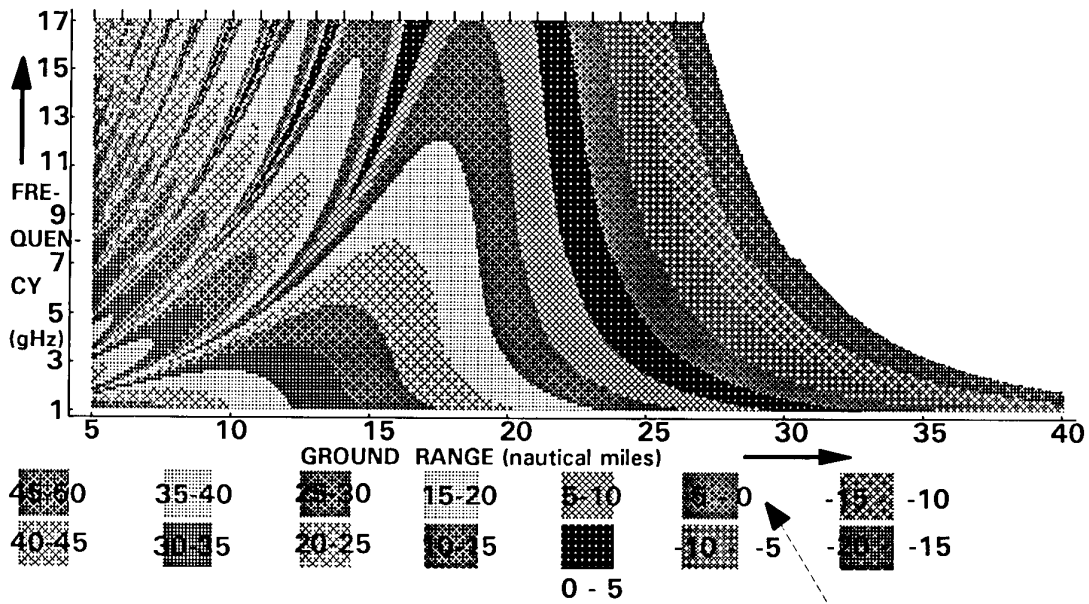
used, the average bit error rate (BER) which can be tolerated, the particular modulation method used for sending the data, the receiver noise figure, transmitter/antenna gains and antenna heights. System margin, defined as the ratio (in dB) of the available signal-to-noise ratio (SNR) to the SNR necessary for the required data rate, bit error rate, and modulation scheme, is a parameter which must preferably be significantly positive (by at least 10-20 dB) in the design of communication systems. We proceed to discuss margin studies for a typical high data rate naval communication system, based on computer prediction programs developed at NCCOSC.

A SHF propagation prediction program called Engineer's Refractive Effects Prediction System (EREPS) has been developed at NCCOSC [Hitney, et al., 2], [Patterson, et al., 3]. This program was used by James and Rockway [4] to graphically display the expected margin for SHF communication systems. James and Rockway [5] have developed a PC-based program called the SHF Link Analysis Model (SLAM), which uses EREPS for propagation prediction, to predict SHF communication system performance.

An improvement on the EREPS calculation method, called the "Radio Physical Optics" (RPO) method, has also been developed at NCCOSC [6]. This program calculates and plots range-dependent propagation loss on a height versus range display using a combination of Ray Optics (RO) and Parabolic Equation (PE) techniques. The RO techniques include the full amplitude divergence and integrated optical path length phase effects. The PE model mostly follows the method described by Dockery [7]. Although the RPO model is considered more accurate, the existing version of SLAM yields roughly the same results as the former, and in view of its simplicity of use, is adopted in the prediction of performance of SHF-LOS communication systems herein.

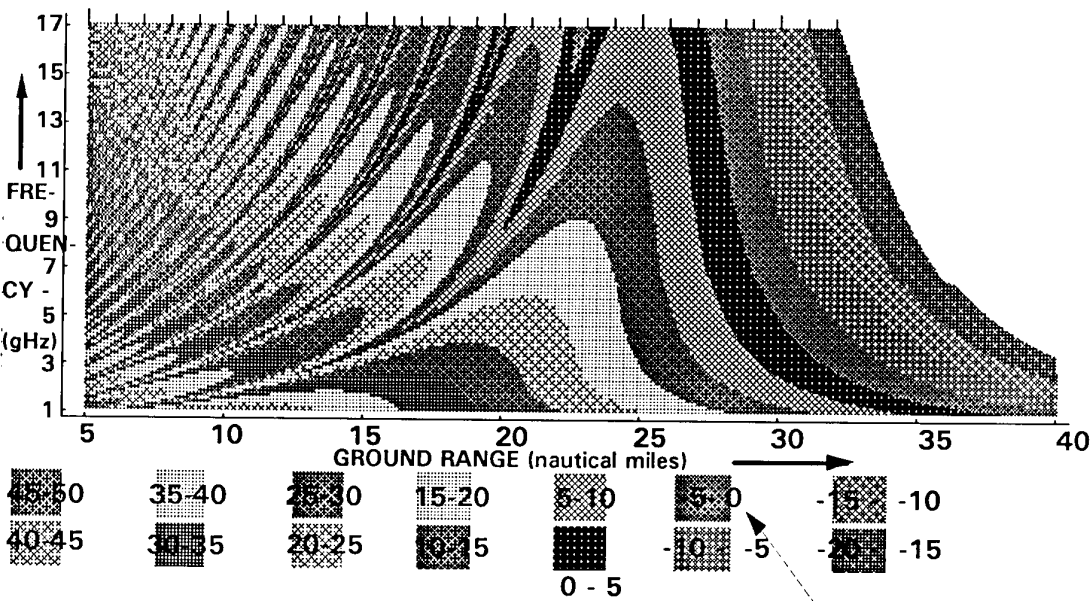
The main system configuration studied (called System A) involves a 100 Watt transmitter and omnidirectional transmit and receive antennas with +5 dB of gain each relative to isotropic (dBi), both at 100 ft elevations. Quadrature phase shift keying (QPSK) with a bit error rate (BER) requirement

of  $10^{-6}$  and a receiver noise figure of 5 dB are assumed. This implies a SNR requirement of 11 dB. No unusual propagation conditions, such as evaporation ducting, are assumed to be present. A 10 knot wind speed is



LEGEND: Shaded regions indicate MARGIN (dB) as noted in squares above, e.g.

Figure 1 - Margin for system configuration "A" (defined above), plotted in the frequency/ground range plane



Legend: Shaded regions indicate MARGIN (dB) as noted in squares above, e.g.

Figure 2 - Margin for system configuration "B" (defined above), plotted in the frequency/ground range plane

assumed, and rain is assumed to be absent. The study is done using an effective earth radius of  $r_k = 4/3$ , a world average of 399 N-units for the surface refractivity (which affects the tropospheric loss) and a world average of  $7.5 \text{ gm/m}^3$  for absolute humidity, which affects the absorption by water vapor molecules.

Figure 1 is a plot from the SLAM program of available margin for the above configuration in 5 dB increments shown as varieties of shading, with ground range on the abscissa and frequency on the ordinate. This study follows a method developed by Dave [8] for creating "mode structure diagrams" in high frequency (HF) propagation studies at high latitudes. According to Figure 1, this communication system maintains more than 10 dB margin at distances out to about 22 nmi in the 3-5 GHz spectrum and out to almost 26 nmi in the 1-2 GHz spectrum. These distances are adequate for the task force sizes mentioned above. However destructive interference between direct and reflected rays, or *multipath nulling*, which show up as "wedge" shaped regions of shading in Figure 1, can reduce the margin to very low or negative values at certain ranges. Figure 2 shows a study similar to Figure 1, but for transmit and receive antenna heights of 150 ft, all other parameters being identical. (This system is called System B.) Evidently, according to Figure 2, antenna heights of 150 ft will generate a 10 dB margin out to almost 28 nmi at 1-2 GHz for this system. Thus, increased antenna height yields longer effective range for the communication system. However, this improvement is accompanied by a marked increase in the number of multipath nulls in the LOS range.

The performance of systems having configurations with different gain parameters from the ones outlined above can be inferred from Figures 1-2 by adding to or subtracting from the plotted results the appropriate gain in dB. Additionally, every halving of the data rate will also increase the system margin by +3 dB, so that longer range links can be successfully operated at data rates lower than T1.

From Figures 1-2 it may be inferred that SHF-LOS is capable of providing high bandwidth service between tactical naval platforms situated within 20 nmi of each other, with however, significant deterioration of margin at certain ranges due to destructive multipathing. These multipath nulls can be mitigated by wind, which causes the ocean surface to become rough and hence

a weaker specular reflector of incident energy. However results from the SLAM program indicate that wind speeds in excess of 30 knots are required to mitigate multipath effects. In the next section, we discuss three possible system design methods for mitigating multipath nulls - one using height diversity, another using frequency diversity and a third using networks with strong enough connectivity to offer alternative, node-disjoint paths between a given pair of nodes, a property which may be called *path diversity*.

## 2 - DIVERSITY SYSTEMS FOR MITIGATING MULTIPATH EFFECTS

### 2.1 Height and Frequency Diversity

An example of how spatial, or height diversity systems can improve coverage for a SHF communication system operating at a given frequency is shown in Figure 3, wherein margin vs. range curves at 4 GHz and for antennas at 40 and 100 feet are plotted on the same set of axes. This figure shows that most of the nulls at one antenna height configuration occur at ranges where the other configuration has good margin. Thus, receiving the data from the antenna which happens to give the stronger signal of the two at the given range can significantly improve coverage out to 20 nmi. Of course, this requires additional equipment outlay and complexity to determine which antenna's signal should be fed to the receiver.

An alternative to height diversity is to exploit the differing positions of the nulls as a function of frequency shown by Figures 1-2. A set of frequencies could be assigned to each platform, which would be separated enough in the spectrum that at least one frequency would not experience a null at a given ground range. For example, for System A, 3 GHz and 4 GHz carrier frequencies for a given platform would be a good choice, as each of these frequencies has nulls at different ground ranges from the other. To use frequency diversity, intelligent decisions regarding which frequency to use would have to be made.

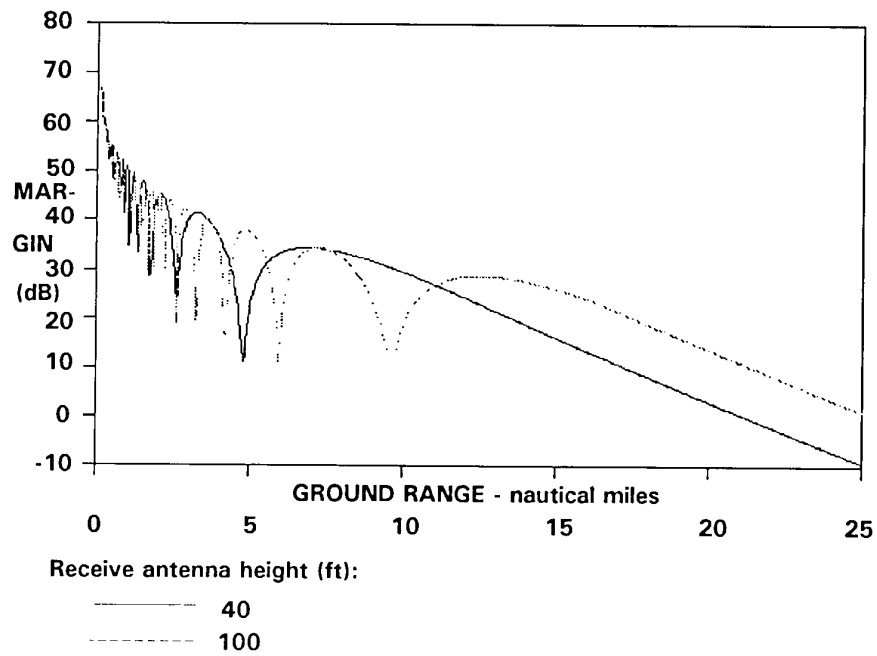


Figure 3 - Receive antenna height diversity  
as a means of mitigating multipath nulls

## 2.2 Diversity Through Network Design

### 2.2.1 Network Design Options

We now consider the mitigation of multipath effects possible by maintaining physical layer links from a given platform to more than one other platform in a communication network. Individual links in a communication network may be maintained, for example, by using different frequencies for each platform pair  $(i, j)$  - adequate bandwidth exists in the SHF spectrum to permit such multiple frequency assignments. Each platform is able to maintain as many links with other platforms as the number of carrier frequencies assigned to it. The platforms could selectively receive individual platforms by a "frequency division multiple access" (FDMA) protocol, under which each platform transmits at two or more different frequencies and receives on two or more other frequencies, with no frequency being reused by any other platform. Alternatively to FDMA, a time division multiple access (TDMA) scheme could be used, under which all platforms transmit at the same frequency, but at different times. Under either scheme, each platform may receive messages from more than one other platform by tuning its receiver suite to the transmission frequencies of the other platforms, or receiving only during the other transmitters' time slots. Existence of multiple links at each platform allows the possibility of relaying messages between platforms that are not directly connected. For example, in the case that two platforms are not within LOS distances of each other, relays could nevertheless be used to link them, thus forming a *virtual circuit*. (defined below in graph-theoretic terms). Relays also afford the possibility of more than one virtual circuit between node pairs, thus increasing robustness in a multipath or otherwise degraded link environment. A minimum of two carrier frequencies under FDMA (or two transmission time slots under TDMA) per platform is generally required to create a network with relays. Use of three or more carrier frequencies per platform increases the richness of connectivity possibilities in the network. Since links are expensive and complex to maintain, it is preferable to limit the number of links per platform.

We now discuss some network topologies involving two or three links per node, and their advantages and disadvantages

in terms of virtual circuit availability. The discussion uses terms from graph theory, in which the network is viewed as a *graph* or *topology*, consisting of *vertices* (or *nodes*) and *links* (or *arcs*) between them. The number of platforms or *nodes* in the network is called the *order* of the network, and the number of links assigned to each node is called the *degree* of that node. It is convenient to refer to the *degree of the topology* as the maximal degree of any node in the topology. A virtual circuit is thus a set of nodes and links joining them over which data can be sent between node pairs  $(i, j)$ . Two virtual circuits are said to be *node disjoint* if the only nodes that are included in both of them are the endpoints,  $(i, j)$ . An important parameter in this analysis is the number of links, or *hops*, known as *path length*, on a given virtual circuit between endpoint node pairs  $(i, j)$ . The problem discussed here is similar in nature to the minimum broadcast network problem studied by, for example, Mitchell and Hedetniemi [9], Liestman and Peters [10], and Bermond, et al. [11]. These references are useful for an overall discussion of this and similar problems.

### 2.2.2 Networks of Degree Two - Bus and Ring Topologies

A simple connectivity scheme for a topology of degree two is that in which each platform receives transmissions from only one or two other platforms and in turn transmits to only one or two other platforms. The simplest of these "topologies of degree two" is the bus topology of Figure 4, in which every node relays the messages which it receives from at most two other platforms.

An analysis of the mean and standard deviation of path lengths on a trunk is fairly straightforward (c.f. Figure 4); however each node has a different mean distance to other nodes, depending on its location on the trunk.

For a node at the endpoint of the trunk we have for the mean path length  $\bar{L}$  and its variance  $\sigma$ , in the limit of large  $n$ ,

$$\begin{aligned}\bar{L} &= n/2, \\ \sigma^2 &= n^2/48, \quad (1a)\end{aligned}$$

while for a node near the middle of the trunk,

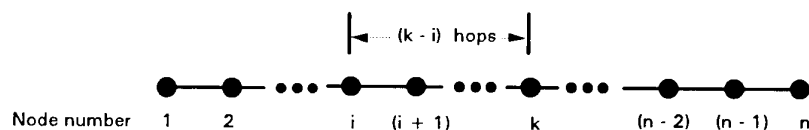


Figure 4 - Graph of trunk topology, illustrating a typical path length calculation

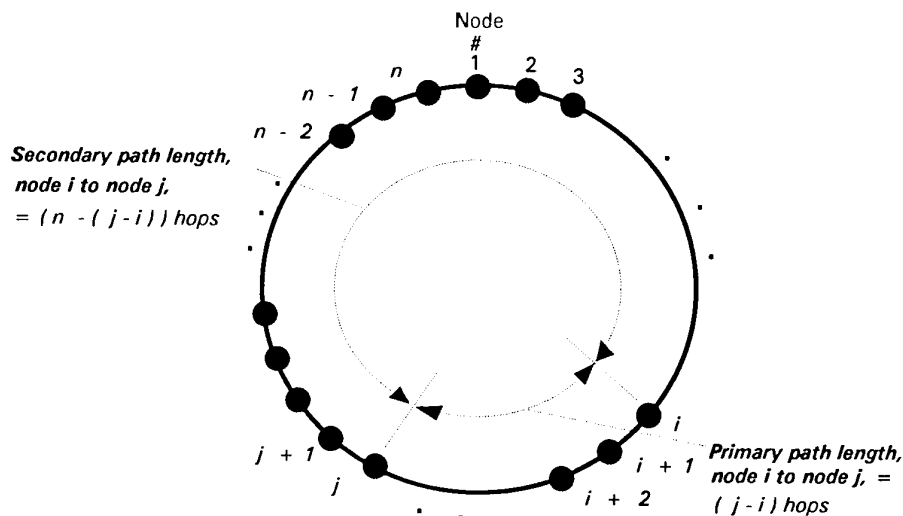
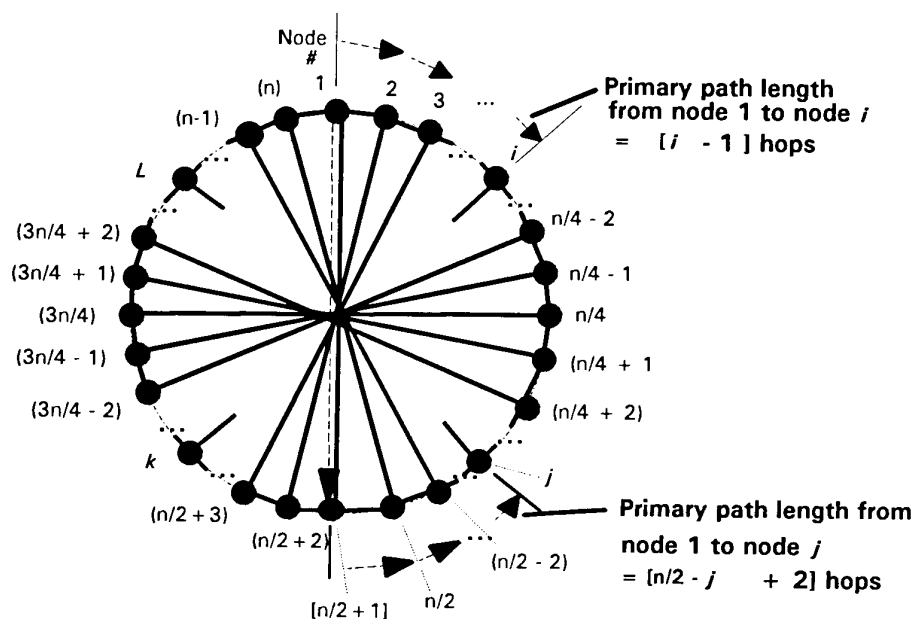


Figure 5 - Graph of ring topology, showing primary and secondary paths  $[i, j]$ , with  $j > i$



- N. B. :
- \*  $n \bmod 4 = 0$
  - \* General nodes  $i, i, k$ , and  $L$  with  $1 < i < j < k < L$ , are shown incompletely linked
  - \* No secondary or tertiary paths are shown.

Figure 6 - Augmented ring topology, with  $n \bmod 4 = 0$ , showing generalized nodes  $i, j, k$ , and  $L$ , and primary paths  $(1, i), (1, j)$

$$\bar{L} = n/4,$$

$$\sigma^2 = n^2/48 \quad (1b)$$

The major drawback of a bus topology is that if one link is inoperative the network becomes disconnected, and the bus must be reconfigured. This is because there is only one path in the bus between a node pair  $(i, j)$ . This renders the bus topology quite fault-intolerant.

A solution to this fault intolerance of the trunk or bus topology is to connect the nodes to form a ring topology as shown in Figure 5. If all nodes are within LOS of each other, a ring topology can always be created. It can also be created in cases where some nodes are beyond line-of-sight (BLOS) of each other. Again, two transmission frequencies or time slots per platform are required, as in the bus topology. The ring topology offers the advantage of two node-disjoint paths between each node pair  $(i, j)$  a minimum length path (which will hereinafter be referred to as the "primary" path) and another, longer path (hereinafter called the "secondary" path). The node-disjoint property of the two paths implies that even if one or more links on one of the paths is inoperative, the links on the alternate path may still be operational, since this alternate path involves different relays than the other. This path redundancy offered by the ring topology gives improved reliability over the trunk topology, as shown by the following analysis (c.f. Figure 5).

The mean,  $\bar{L}_p$ , of all primary paths on the ring from a given node to all other nodes is given by

$$\begin{aligned} \bar{L}_p &= \frac{1}{n-1} \left[ 2 \left( \sum_{i=1}^{n/2} i \right) - \frac{n}{2} \right] \\ &= \frac{1}{(n-1)} \left[ \frac{n}{2} \left( \frac{n}{2} + 1 \right) - \frac{n}{2} \right] \\ &= \frac{1}{(n-1)} \left[ \frac{n^2}{4} \right] \xrightarrow{n \rightarrow \infty} \frac{n}{4}, \quad n \text{ even}, \quad (2a) \end{aligned}$$

and

$$\begin{aligned} \bar{L}_p &= \frac{1}{n-1} \left[ 2 \sum_{i=1}^{(n-1)/2} i \right] \\ &= \frac{(n+1)}{4} \xrightarrow{n \rightarrow \infty} \frac{n}{4}, \quad n \text{ odd} \quad (2b) \end{aligned}$$

using a well-known summation formula.

Similarly, the variance  $\sigma_p^2$  for the primary paths can be calculated from the formula

$$\begin{aligned} \sigma_p^2 &= \frac{1}{(n-2)} \left[ \sum L_p^2 - (n-1)(\bar{L}_p)^2 \right] \\ &= \frac{1}{(n-2)} \left\{ 2 \left( \sum_{i=1}^{n/2} i^2 \right) - \left( \frac{n}{2} \right)^2 - (n-1) \left[ \frac{1}{n-1} \left( 2 \sum_{i=1}^{n/2} i \right) - \frac{n}{2} \right]^2 \right\} \\ &= \frac{1}{(n-2)} \left[ \frac{1}{6} n \left( \frac{n}{2} + 1 \right) (n+1) - \left( \frac{n}{2} \right)^2 - \frac{1}{(n-1)} \left( \frac{n^2}{4} \right)^2 \right] \\ &\xrightarrow{n \rightarrow \infty} \frac{n^2}{48}, \quad n \text{ even} \quad (2c) \end{aligned}$$

and

$$\begin{aligned} \sigma_p^2 &= \frac{1}{(n-2)} \left\{ 2 \left( \sum_{i=1}^{(n-1)/2} i^2 \right) - \left[ (n-1) \left[ \frac{1}{(n-1)} \left( 2 \sum_{i=1}^{(n-1)/2} i \right) \right]^2 \right] \right\} \\ &= \frac{1}{(n-2)} \left[ \frac{1}{6} (n-1) \left( \frac{(n-1)}{2} + 1 \right) (n) - (n-1) \left( \frac{(n+1)}{4} \right)^2 \right] \\ &\xrightarrow{n \rightarrow \infty} \frac{n^2}{48}, \quad n \text{ odd} \quad (2d) \end{aligned}$$

A similar analysis for the secondary paths in the ring is omitted for brevity, but shows that for large  $n$  these have mean length and variance given by

$$\bar{L}_s \xrightarrow{n \rightarrow \infty} 3n/4 \quad (3a)$$

and

$$\sigma_s^2 \xrightarrow{n \rightarrow \infty} n^2/48, \quad (3b)$$

with the subscript  $s$  denoting secondary. We note that the probability



that both primary and secondary paths between node pair  $(i, j)$  are inoperative is lower than that of a single path being inoperative, e.g., as in a bus topology. The topologies considered so far involve at most two links per node. If each platform is able to manage three links to other platforms, for example by the use of three different carrier frequencies per platform, then the possibilities for network topology become richer, as discussed below.

### 2.2.3 Networks of Maximum Degree Three - The Augmented Ring Topology

In configurations allowing use of three separate links (e.g., carrier frequencies) per platform, many topologies are possible. We now consider a topology of degree three, called the *augmented ring*, which has been chosen for economy in number of hops between nodes (i.e. path lengths). In this topology each node of the ring of Figure 5 is additionally connected to its diametrically opposite neighbor by a link, as shown in Figure 6. An odd number of nodes can be connected similarly to Figure 6, except that exactly one node is of degree two instead of degree three. Evidently the augmented ring topology exists only for an even number of nodes  $n$ , but it is nevertheless of interest, since the properties of an odd order augmented ring are about the same as those of the augmented rings closest in order to it.

In the augmented ring topology, there are three node-independent paths between any node pairs  $(i, j)$  - a shortest path (called the "primary" path), a second-shortest path (called the "secondary" path), and a longest path (called the "tertiary" path). Examples of the primary paths between node pairs  $(1, i)$  and  $(1, j)$  are shown in Figure 6. The secondary path between node pair  $(1, j)$  (not shown in Figure 6 to avoid cluttering) is the one which traverses counter-clockwise from node 1 to the node diametrically opposite to node  $j$ , and then over the diametric link to node  $j$ . The tertiary path from node 1 to node  $j$  traverses clockwise from node 1 to node  $j$ , without a diametric hop. (Note that in this case, both primary and secondary paths have the same lengths). The existence of three node-independent paths for each node pair implies increased reliability for communication circuits in the augmented ring topology, as we now show.

Omitting the details of the derivation of the means and standard deviations of the three different types of paths for this topology, we quote the results for large  $n$ . For primary paths, the mean path length and standard deviation are found by forming appropriate sums of

the shortest path lengths from a given node (say node 1 in Fig. 6) to all other nodes. We consider the case  $n \bmod 4 = 0$ . For nodes  $\leq n/4$  hops away, the

primary path leads clockwise or counter-clockwise from node 1, while

for nodes farther away, the primary path begins with a diametric hop across the ring followed by a clockwise or counter-clockwise traverse around the ring (e.g., path from node 1 to node  $j$ ). Thus, the formulae for mean path length and its variance on primary paths are (with  $n \bmod 4 = 0$ )

$$\begin{aligned} \bar{L}_p &= \frac{1}{(n-1)} \left( 4 \left( \sum_{i=1}^{n/4} i \right) - 1 \right) \\ &= \frac{1}{(n-1)} \left[ \frac{n}{2} \left( \frac{n}{4} + 1 \right) - 1 \right] \\ &\xrightarrow{n \rightarrow \infty} \frac{n}{8} \end{aligned} \quad (4a)$$

$$\begin{aligned} \sigma_p^2 &= \frac{1}{(n-2)} \left[ \sum L_p^2 - (n-1)(\bar{L}_p)^2 \right] \\ &= \frac{1}{(n-2)} \left[ 4 \left( \sum_{i=1}^{n/4} i^2 \right) - 1 - \frac{(n-1)}{(n-1)^2} \left[ \frac{n}{2} \left( \frac{n}{4} + 1 \right) - 1 \right]^2 \right] \\ &\xrightarrow{n \rightarrow \infty} \frac{n^2}{48} \end{aligned} \quad (4b)$$

while for secondary paths (omitting the details),

$$\bar{L}_s \xrightarrow{n \rightarrow \infty} n/8, \quad (5a)$$

$$\sigma_s^2 \xrightarrow{n \rightarrow \infty} n^2/48, \quad (5b)$$

and for tertiary paths,

$$\bar{L}_t \xrightarrow{n \rightarrow \infty} 3n/8, \quad (6a)$$

$$\sigma_t^2 \xrightarrow{n \rightarrow \infty} n^2/192, \quad (6b)$$

with the obvious interpretation of subscripts. The results for  $n \bmod 4 = 2$  are identical to Eq. 4-6 in the limit of large  $n$ . In Table 1 we summarize Equations 2-6 in the limit of large  $n$ ,

for the topologies considered in this and the previous subsection. The last column on the right in Table 1 gives specific information for the maximal

primary paths in the topology, and for the secondary and tertiary paths which are associated with them.

Table 1 - Comparison of path statistics for Bus, Ring, and Augmented Ring Topologies

GRAPH TYPE	PRIMARY PATH LENGTH (HOPS) $\overline{L_p}, \sigma_p$	SECONDARY PATH LENGTH (HOPS) $\overline{L_s}, \sigma_s$	TERTIARY PATH LENGTH (HOPS) $\overline{L_t}, \sigma_t$	MAXIMAL PRIMARY PATH LENGTH (AND ASSOCIATED SECONDARY AND TERTIARY PATH LENGTHS) (HOPS)
BUS	$\frac{n}{4}$ to $\frac{n}{2}$ , $\frac{n^2}{12}$ (node dependent)	N/A	N/A	$n$
RING	$\frac{n}{4}$ , $\frac{n^2}{48}$	$\frac{3n}{4}$ , $\frac{n^2}{48}$	N/A	$\frac{n}{2}$ , $\left(\frac{n}{2}\right)$
AUGMENTED RING	$\frac{n}{8}$ , $\frac{n^2}{48}$	$\frac{n}{8}$ , $\frac{n^2}{48}$	$\frac{3n}{8}$ , $\frac{n^2}{192}$	$\frac{n}{4}$ , $\left(\frac{n}{4}\right)$ , $\left(\frac{n}{4}\right)$

Table 2 - Circuit availability for the topologies considered, assuming a link reliability of  $p=0.8$

NETWORK TYPE	PROBABILITY THAT AT LEAST ONE CIRCUIT IS AVAILABLE (FOR NODES SEPARATED BY MAXIMAL PRIMARY PATHS)
BUS	0.035
RING	0.307
AUGMENTED RING	0.733

### 2.2.4 Comparison of Availability of Circuits in the Bus, Ring, and Augmented Ring Topologies

A reliability analysis can be used to compare the performance of the three topologies discussed above. We assume that network management at each node permits the user to determine which paths or circuits are available, and to choose the shortest path. In the bus topology of course, only one circuit is available, but in the ring, two are available (primary and secondary), while in the augmented ring, there are three available (primary, secondary, and tertiary). We further assume that each link in the topology has a probability  $p$  of transmitting data at or exceeding the quality of service required during the time that a circuit is being used, and that the probability of any link failing is independent of that of any other link failing. Under these assumptions, a path of length  $i$

hops has reliability  $p^i$ . The analysis is done in the limit of large  $n$ .

We consider circuits between node pairs  $(i, j)$  whose primary path lengths are maximal in the given topology, since these have the lowest reliability. These path lengths are tabulated in the rightmost column of Table 1. Thus, for the bus topology, with maximal path

length of  $(n-1)$  hops, the circuit

reliability,  $p_{bus}$ , is evidently

$$p_{bus} = p^{(n-1)} \quad (7a).$$

For the ring topology, wherein the

maximal primary path length is  $\frac{n}{2}$ , each

such path is associated with a secondary paths of the same length (i.e., traversing in the opposite sense on the ring). Hence, the probability,

$p_{ring}$ , that at least one of the paths will provide the required service is unity minus the probability that both paths are non-functional, i.e.:

$$p_{ring} \cong 1 - \left(1 - p^{\frac{n}{2}}\right) \left(1 - p^{\frac{n}{2}}\right) \quad (7b)$$

Finally, for the augmented ring, the

maximal path length is  $\frac{n}{4}$ , and each

such path is associated with secondary and tertiary paths of the same length (for large  $n$ , c.f. Figure 7), yielding

a reliability  $p_{augring}$  of

$$\begin{aligned} p_{augring} &= 1 - \left(1 - p^{\frac{n}{4}}\right) \left(1 - p^{\frac{n}{4}+1}\right) \left(1 - p^{\frac{n}{4}+1}\right) \\ &\cong 1 - \left(1 - p^{\frac{n}{4}}\right) \left(1 - p^{\frac{n}{4}}\right) \left(1 - p^{\frac{n}{4}}\right). \quad (7c) \end{aligned}$$

The probabilities of Equations (7) are evaluated for a network of order  $n=16$  assuming an individual link reliability of  $p=0.8$ . (The exact equations are used, not the approximations for large  $n$ ). The results, tabulated in Table 2, show that the augmented ring topology yields significantly higher performance potential than the other two in the face of deteriorated link margin due to multipathing. It is interesting to note that the augmented ring topology has a circuit reliability which is, under the assumed parameters, almost as high as that of any individual link.

### 3. CONCLUSION

Networking has been shown to be a possible method of introducing diversity into a communication system to mitigate the effects of multipath nulls. This method could be used to augment the effectiveness of height or frequency diversity in improving tactical naval communication effectiveness. Of course, network management is required to determine which circuits are available and which should be used in a given operational scenario. But a similar problem also confronts the other methods of mitigation - height and frequency diversity - discussed herein.

The topologies considered herein are not the optimal topologies for given degree, in terms of minimum path lengths between nodes (see, for example, Liestman and Peters [10] for a more complete discussion of optimal topologies for the minimum broadcast problem). However, the topologies presented here are easy to visualize and, therefore, to manage.

**ACKNOWLEDGMENTS** - Grateful acknowledgment is given to Mr. A. Shum for his careful reading of the manuscript. Helpful discussions with Mr. Shum and Mr. A. Legaspi (both of NCCOSC Code 827) are also acknowledged, with pleasure.

in bounded degree graphs", SIAM J. of Disc. Math., v. 5, n. 1, pp. 10-24, [Feb 1992]

## **5. REFERENCES**

1. Panter, P.F., Communication System Design: Line-of-sight and Tropo-scatter systems, McGraw-Hill Book Company, New York [1972]
2. Hitney, H.V., J.H. Richter, R.A. Pappert, K.D. Anderson, and G.B. Baumgartner, Jr, "Tropospheric Radio Propagation Assessment," Proceedings of the IEEE, vol. 73(2), [1985]
3. Patterson, W. L., C. P. Hattan, H. V. Hitney, R. A. Paulus, A. E. Barrios, G. E. Lindem, and K. D. Anderson, "Engineer's Refractive Effects Prediction Systems (EREPS) - Revision 2.0," NOSC TD 1342, NCCOSC, San Diego, CA, [February, 1990]
4. James, R.R., and J.W. Rockway, "Battle Force/Battle Group Communications: A Trunkline Backbone Concept", NOSC TR 1407 [October, 1990]
5. James, R.R., and J.W. Rockway, "Super High Frequency (SHF) Link Analysis Model (SLAM) for Non-Satellite Applications, NOSC TR 1350 [June, 1990]
6. Hitney, H. V. , "Hybrid ray optics and parabolic equation methods for radar propagation modeling", IEE Radar 92, 58-60, Brighton, UK, 12-13 Oct, 1992
7. Dockery, D.G., "Modeling Electromagnetic Wave Propagation in the Troposphere Using the Parabolic Equation," IEEE Trans. on Antennas & Propagation, Vol. 36, No. 10 [October 1988]
8. Dave', N, "The use of mode structure diagrams in the prediction of high -latitude HF propagation, Radio Science, v. 25, n. 4, pp 309-323, [July-August, 1990 ]
9. Mitchell, S. and Hedetniemi, S., "A census of minimum broadcast graphs", J. of Combin., Inform. and Sys. Sci., v. 5, n. 2, 141-151 [1980].
10. Liestman, A. L., and Peters, J. G., "Broadcast networks of bounded degree", SIAM J. of Disc Math, v. 1, n. 4, pp. 531-540 [1988]
11. Bermond, J., C., P. Hell, A. Liestman, and J. Peters, "Broadcasting

## DISCUSSION

**Discussor's name :** K. S. Kho

**Comment/Question :**

Do you plan to use the network for interactive voice communications?

Don't you envisage problems with the delays of the relayed messages (packets)?

**Author/Presenter's reply :**

Yes, we do hope to use the network for real-time voice. If TI data rates are in fact achievable it would appear that a 64 kbit/sec voice channel could be multiplexed into the TI data stream. Then, because of the large data rate, relaying would introduce negligible delay. For example under TDMA, a very few time slots would suffice for the voice channel, implying low values of delay. Video and imagery could also be incorporated, in near real time.

**Discussor's name :** G. Sales

**Comment/Question :**

Why was the complementary path on the augmented ring configuration not considered?

**Author/Presenter's reply :**

There are exactly three node-disjoint paths for every pair of nodes (i, j) on the augmented ring. A primary and its associated secondary or tertiary paths in the augmented ring do not form a complementary set. In fact, the total of all the nodes on a set of primary, secondary and tertiary paths on the augmented ring will still not, in general, employ all the nodes in the topology. Thus, complementarity of the paths does not apply to the augmented ring, but node-disjointedness does.

# MULTIPATH IMPACT ON GROUND-BASED GLOBAL POSITIONING SYSTEM RANGE MEASUREMENTS: ASPECTS OF MEASUREMENT, MODELING, AND MITIGATION

G. J. Bishop  
Phillips Laboratory, Air Force Materiel Command  
Geophysics Directorate, Ionospheric Effects Division  
29 Randolph Road  
Hanscom AFB, MA 01731-3010  
USA

E. A. Holland  
NorthWest Research Associates  
300 120th Avenue NE  
Bellevue, WA 98005  
USA

## 1 SUMMARY

Multiple mechanisms propagation paths (multipath) can be the most important error source in ground-based Global Positioning System (GPS) measurement of range to the satellites. This multipath error, arising from a combination of the direct path and reflections from objects relatively close to the receiving antenna, can at times exceed the ionospheric delay error, which the two-frequency (1228 and 1575 MHz) GPS signal format is designed to measure and correct. GPS multipath can seriously degrade Differential GPS (DGPS) navigation, geodetic measurements, ionospheric monitoring, and other GPS applications, yet the source of the problem may not be evident without the use of specialized tests. Several techniques have been proposed to reduce the effects of GPS multipath, these include: improved receiver technology, specialized antenna designs, and various modeling or filtering approaches. This paper illustrates the nature of the two-frequency GPS multipath problem with measurement data from typical ground-based installations, exhibiting variation in multipath conditions, ranging from low to quite high for the varying geometries of the available satellite tracks. Leading mitigation techniques are reviewed, with emphasis on multipath modeling. A new simple modeling approach currently being studied by Phillips Laboratory is discussed. This technique takes advantage of the daily repetition of the GPS observation geometry from a ground station to create a 'multipath template' specific to each satellite pass, and reduce multipath effects on successive days. Data is presented showing significant improvement in a severe multipath environment and contrasting the effectiveness of this approach with all-sky modeling techniques. Mitigation techniques for GPS multipath show potential to enable GPS ground-based range and ionospheric measurement to greatly reduce errors at low elevation angles, leading to improved accuracy and wider coverage area capability.

## 2. INTRODUCTION

The second frequency in the two-frequency GPS signal format (1.228 MHz, referred to as L2, while the L1 signal is at 1.575 GHz) was incorporated mainly to permit GPS receivers to measure the group delay of GPS

signals due to the ionosphere (Ref 1). The group delay represents a range error to the satellite being observed and affects the navigation solution of the GPS receiver. The physical parameter causing the signal group delay is the ionospheric total electron content (TEC) along the raypath to the satellite. TEC is defined as the total integrated quantity of electrons contained in a column of one meter-squared cross-section centered on the raypath (Ref 2). TEC is typically expressed in "TEC Units", where one TEC unit =  $1 \times 10^{16}$  electron/m<sup>2</sup>. In practice, a GPS receiver measures the differential group delay (DGD),  $\Delta\tau$ , between the precise code streams on L1 and L2, which can then yield the absolute ionospheric group delay on L1,  $\tau_{\text{GDL1}}$ , from equation [1] (Ref 3). The ionospheric delay is typically the largest contributor to GPS range errors.

$$\Delta\tau = \tau_{\text{GDL1}} [(f_{\text{L1}}/f_{\text{L2}})-1] \quad (1)$$

Since the ionosphere is charged by solar radiation, TEC typically exhibits a diurnal variation with a peak near 1400 local time and with low values at night, exceptions being in disturbed ionospheric regions such as the auroral zone (Ref 4). GPS measurements of TEC also show such diurnal variation, as illustrated in Figure 1. In this case, the plot abscissa is universal time, and 1200 local time occurs near 2400 universal. Also, the GPS satellites are not seen overhead, typically, but rather they are seen to trace long arcs across a wide range of azimuth and elevation, each satellite being visible for three hours or more. This limited time when each satellite is visible accounts for the TEC curve in Figure 1 being plotted in sections, each section is observing a different GPS satellite. The "x" and "+" symbols plot the latitude and longitude under the point where the raypath to a satellite penetrates the peak of the ionosphere, assumed at 350 km altitude. The TEC plotted in Figure 1 is converted (assuming a relatively uniform ionosphere) to the equivalent value seen looking vertically from that latitude/longitude. It may be easily seen, from the plotted symbols, that there is usually a significant change in look direction when there is a change of satellite.

Apparently the ionosphere was fairly uniform over the station viewing region on the day plotted in Figure 1, since the TEC discontinuities are very small at the satellite change points. Significantly greater variation with look direction is often seen, particularly near the more disturbed regions of the ionosphere (Ref 5). The right ordinate of Figure 1 is labelled in equivalent ns of differential delay and delay at the L1 frequency.

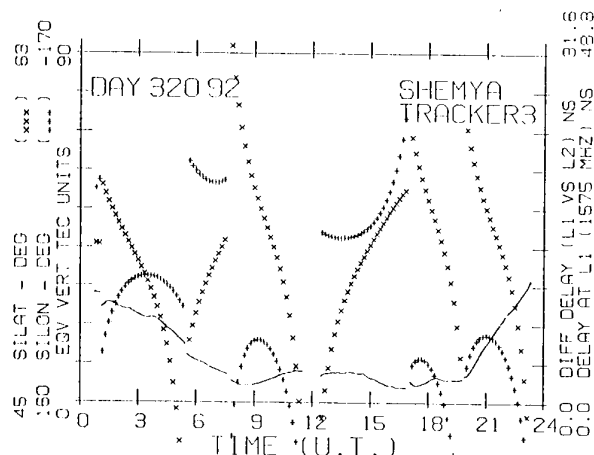


Figure 1. One day of ionospheric total electron content (TEC) observations, obtained by monitoring a sequence of GPS satellites, at Shemya, Alaska.

Multipath contamination (occurring when a GPS receiver acquires reflected signals from the ground or objects near the antenna) significantly affects the GPS DGD measurement, and in severe cases can actually exceed the ionospheric delay that two-frequency GPS signal is designed to measure and correct. This is particularly true for non-ideal antenna locations, such as typical building rooftops having vents, antennas, etc., and for observing GPS satellites at elevation angles near or below 15°. Such multipath contamination can be an important error source in GPS navigation as well as in ionospheric and geodetic measurements.

### 3. STRUCTURE OF TWO-FREQUENCY GPS MULTIPATH

Figure 2, is formatted as Figure 1, but shows 24 hours of ionospheric TEC data contaminated with multipath. The figure plots the TEC data for four smoothing cases: unsmoothed-raw samples taken at 6-second intervals, 18 sec smoothing, 1 minute and 5 minutes. The larger scale multipath is clearly seen in the similar structures evident in the 5 minute smoothed data of Figure 2 and the "before" data in Figure 5. The 1 minute data in Figure 2 shows an example where negative multipath is greater than the ionospheric TEC, yielding a negative overall TEC.

### 4. MITIGATION OF GPS MULTIPATH EFFECTS

Several techniques have been suggested or employed for multipath mitigation, including: use of an antenna that is desensitized (tapered) at low elevation angles (Ref 6),

mechanical 'jittering' of the antenna and ground plane with respect to the reflective surfaces (Ref 7), specialized receiver designs (Refs 7-10), directional antennas, smoothing the GPS differential group delay with differential phase [phase averaging] (Ref 11), and modeling multipath for the entire observation hemisphere (Ref 12).

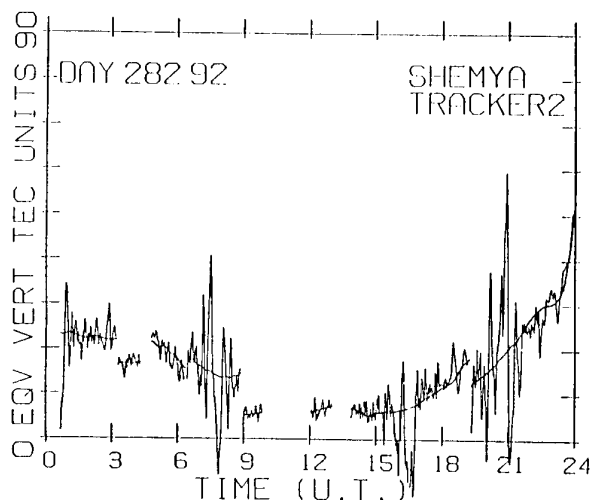


Figure 3. One day of ionospheric differential group delay data (TEC) showing multipath, with differential phase data (smooth curves) fitted to it by averaging.

The tapered antennas must necessarily sacrifice coverage of GPS satellites which reduces the choices available for navigation calculations and substantially shrinks the area of the ionosphere that can be monitored from a single site. To 'jitter' an antenna continuously, a very durable and reliable automatic mechanism must be employed, or else a multiple-antenna installation with electronic switching could be used (Ref 7). New receiver technology holds promise, but remains to be demonstrated. Directional antennas will require steered dishes or phased arrays, both of which are costly to implement compared to any standard antenna. Modeling multipath over the entire hemisphere of observation will be examined in a following section of this paper.

Smoothing the GPS differential group delay with differential phase (phase-averaging) takes advantage of the fact that GPS differential phase is two orders of magnitude less sensitive to multipath than the differential group delay (Ref 11). Figure 3 illustrates the application of this process. The data was acquired in a severe multipath environment typical of many installations. A non-tapered antenna was mounted on a six-foot pole above a reflective roof, with railing and other antennas nearby. The smooth lines in Figure 3 are the differential phase, fitted to the differential group delay data. Close examination of this data shows that if the interval of data available for phase averaging is of the same order as the period of large multipath, the average of the resulting group delay data may have significant,

oscillating errors. This concern can be minimized if satellites are tracked as long as possible, and the phase averaging product is not used until a long period of data has been collected. To make sure the phase data will be useable over such long intervals, techniques have been developed that are very efficient at correcting phase discontinuities (Ref 13). Another concern is the observation that multipath typically is not zero-mean (Refs 7, 10). However, the mean error tends to be quite small in real environments where there are a variety of reflectors, with reflection coefficients that vary as the satellite moves, and reflected signal delays are small compared to the GPS chip time. An approach that appears effective in reducing any residual non-zero multipath is to combine long satellite observations with selection of a low standard deviation subset of the satellite pass to use for the phase-averaging process.

A more critical concern for real-time applications is the fact that the period of large multipath may extend to an hour or more, (see Figure 3). When phase-averaging is applied to such data the result may not meet accuracy requirements until a data set from that satellite has been accumulated for much more than an hour. Figure 4 illustrates a simulated real-time phase-averaging situation for high multipath. The time required in this case to achieve a steady-state phase-average "fit" was approximately 80 minutes. This would mean that perhaps the first half of any satellite pass that experiences severe multipath

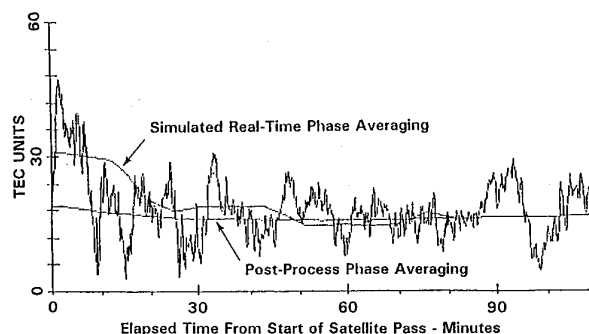


Figure 4. Illustration of potential error in real-time application of "phase averaging" process in a high multipath case.

would probably be untrustworthy. It would also mean that, even though an antenna with hemispheric (untapered) coverage would allow acquisition of satellites just above the horizon, the data from rising satellites would be unusable, possibly over a region as great as would have been lost to antenna tapering. However, setting satellites should be useful to the horizon, if acquired well above the horizon.

## 5. PHILLIPS LABORATORY SIMPLE MULTIPATH (TEMPLATE) MODELING TECHNIQUE

### 5.1 Technique Description

A simple multipath mitigation technique (Ref 14), that overcomes the real-time

limitations of phase-averaging, has been developed by Phillips Laboratory for ground-based applications. This technique takes advantage of the fact that the observation geometry of a satellite repeats almost exactly on successive days. Since this is the case, a 'template' model (Ref 15) of multipath may be constructed from each GPS satellite pass on a given day, and then used to remove multipath from the delay measurements on the following day(s). This is done by using the "phase-averaging" process to fit the differential phase measurements to the differential phase delay, and then subtracting the referenced phase data from the original delay data. This process yields a "template" consisting of the multipath structure for that satellite pass (with absolute level accurate to the degree that the multipath is zero-mean for that pass) and the system noise for that pass. To eliminate system noise either one-minute smoothing of the template or averaging of two successive days' templates has been performed.

Figure 5 illustrates the application of the template technique to "remove" multipath. The upper plot shows five minute smoothed differential group delay for seven satellite passes over an entire day, as in Figure 2. In the lower plot a template derived from the previous day's data has been subtracted prior to smoothing, thus "removing" the multipath. The resulting data in this lower plot is differential group delay data, it has not been phase averaged.

### 5.2 Effect of Template Age

In Figure 6 an example is given of the effect of the age of the template used to

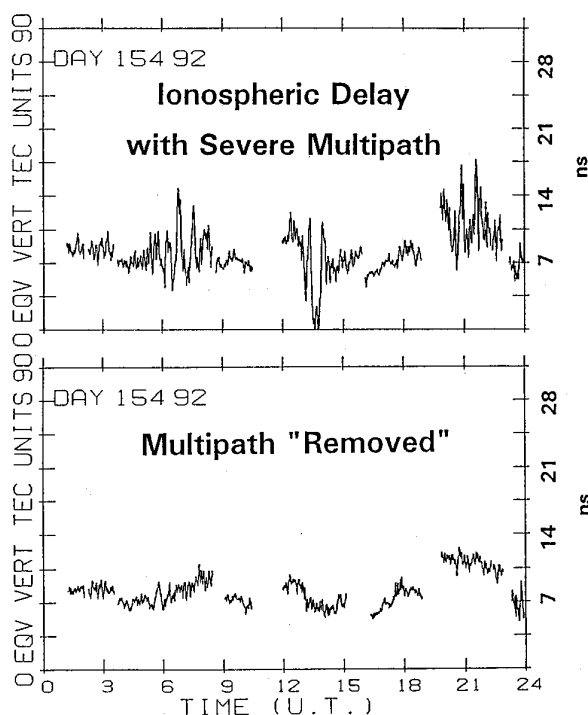


Figure 5. Illustration of results application of the "multipath template" technique to reduce the effects of severe multipath.



remove multipath. The upper plots are comparable to the lower (multipath removed using a template from the previous day) plot of Figure 5, showing cases of the resulting data with both one and five-minute smoothing. The lower plots of Figure 6 show the results of applying the same template to data obtained eight days later, so the template is nine days old at that point. All plots in Figure 6 show that the template technique has produced significant improvement, even with the older template. However, it is clear that the residual noise is much larger when the template is 9 days old.

Figure 7 is derived from the same data as Figure 6, but examines one satellite pass in fine detail. The plots on the left of Figure 9 show one minute smoothed data before application of a template, and the plots on the right show one minute smoothed data after template is applied. Comparing the left plots in Figure 7 shows that the basic multipath structure between these two days, eight days apart, remains similar. Comparing plots on the right shows the detail of the reduction in benefit (higher residual noise) as the template ages.

### 5.3 Sensitivity to Template Timing

Figure 8 gives an example of the sensitivity of the template technique to errors in time alignment between the template and the current data. Increase in noise starts to become evident as the misalignment reaches 45 seconds - as shown in the figure, (shifts of 3, 15, 30, and 60 seconds were also examined). In the upper plots the template is applied in raw form (including system noise), whereas in the lower plots the template is pre-smoothed over a sliding 1 minute interval. The pre-smoothed template used for the upper plots yields improved results, in general. This is expected, since the noise from the day sourcing the template should mostly be removed by the smoothing process, leaving only the noise from the day receiving the template to contribute to residual errors.

### 5.4 Template Day-to-Day Correlation

Table 1 lists the correlation coefficients between templates derived from satellite passes on two successive days, and again nine days apart. Raw data, and 1 and 5-minute pre-smoothed data is used for the three cases in the "successive days" comparison. It may be seen that the correlation between the templates derived from the raw data is much lower, certainly due to the noise on the two days, which will be uncorrelated. The 1-minute smoothed data shows significantly higher correlation, and is likely the best measure of the template correlation, since multipath can occur at 1-minute periods, and does exhibit detectable day-to-day changes (Ref 11). The 5-minute smoothed data show small improvement in correlation over the 1-minute case, but this may be due to removal of small day-to-day changes in multipath. The correlation results would imply that passes 1, 3, 5, and 7 have lower multipath effects, Figure 2, which plots the data covered by Table 1, may be seen to confirm this.

Table 1 also allows examination of an example of the change in correlation between templates separated two days versus nine days. The correlation drops off noticeably for the higher frequency multipath (one minute smoothing), but the slower and larger multipath maintains high correlation. This suggests that the template technique should maintain its effectiveness even if the template is not renewed for a week or more, (barring relocation of a satellite orbit).

Pass	Successive Days			9 Days Apart	
	Raw	1-min	5-min	1-min	5-min
1	-0.204	0.676	0.858	0.428	0.735
2	0.459	0.878	<b>0.927</b>	0.556	<b>0.883</b>
3	0.111	0.513	0.599	0.377	0.467
4	0.643	0.927	<b>0.963</b>	0.785	<b>0.951</b>
5	0.220	0.650	0.708	0.183	0.765
6	0.643	0.944	<b>0.970</b>	0.787	<b>0.895</b>
7	0.036	0.012	0.393	-0.013	0.225

Table 1. Correlation Coefficients of Templates from Different Days

### 6. A MEASURE OF MERIT FOR ALL-SKY MULTIPATH MODELING TECHNIQUES

One approach to correcting multipath involves attempting to model multipath over the entire hemisphere above the antenna site (Ref 12). A metric that should apply to any such technique is the maximum spatial separation in degrees that can be tolerated between a "known" point and an inferred point, before model accuracy becomes unsatisfactory. To examine the behavior of measured multipath with respect to such a metric, a set of the PL multipath data was analyzed to plot, and statistically summarize, the change in multipath as a function of angular separation of the data points. The data set used for this analysis is the one shown in Figure 3. Figure 9 plots the multipath templates for this data set.

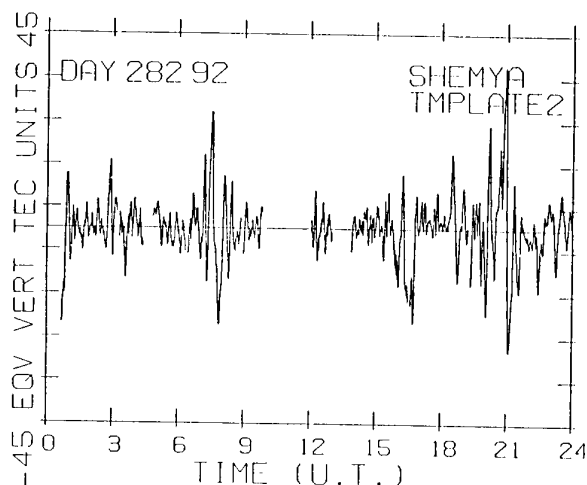


Figure 9. Multipath templates for entire data set used to test potential error in all-sky multipath modeling techniques.

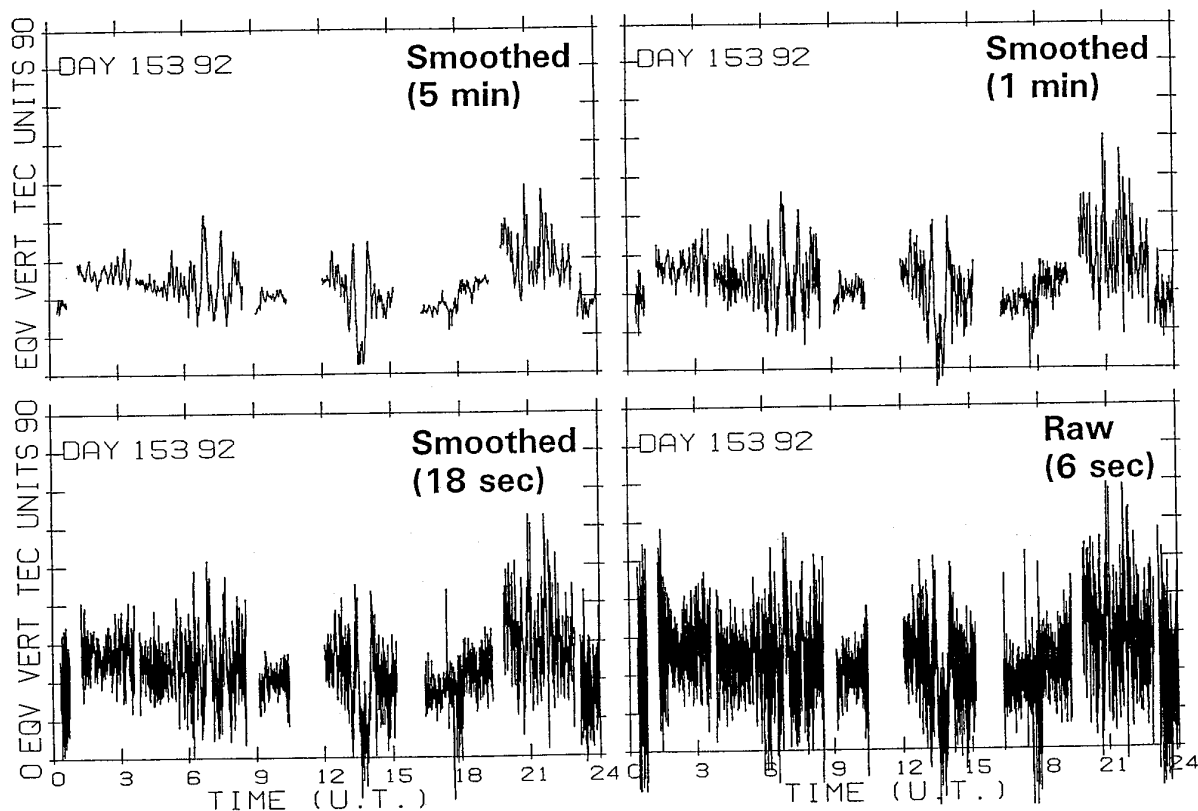


Figure 2. Structure of two-frequency GPS multipath illustrated in one day of ionospheric total electron data, taken at 6-second intervals and smoothed over 18 seconds, 1 minute and 5 minutes.

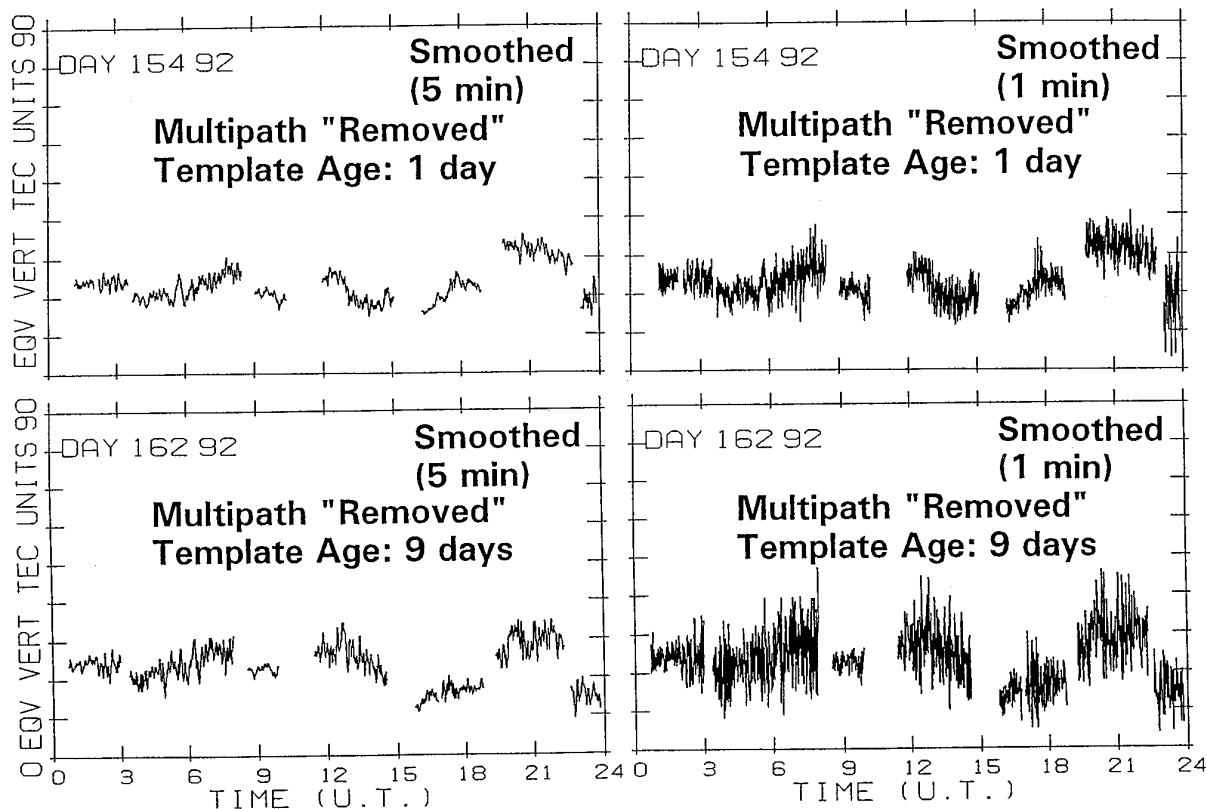


Figure 6. Example of effect of age of "multipath template" used to remove multipath, showing higher residuals from nine day old template than one day old template.

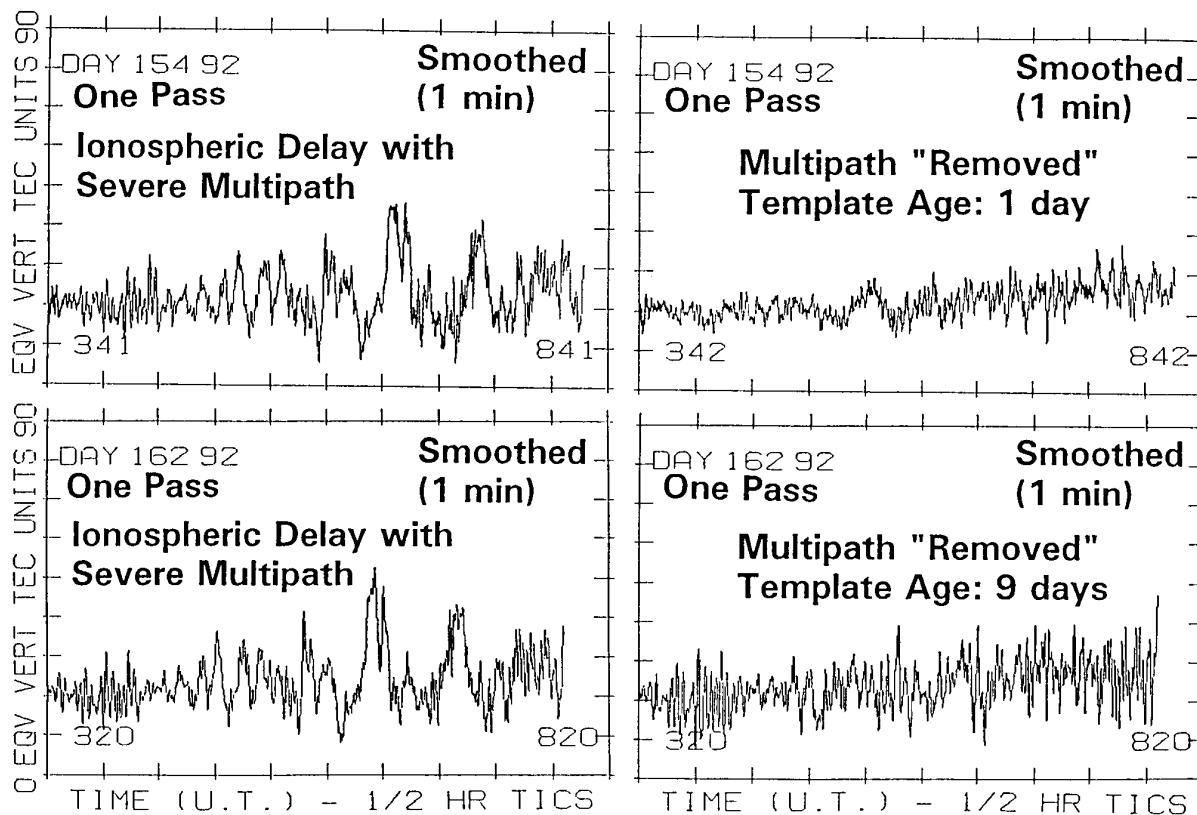


Figure 7. Fine detail of the effect of age of "multipath template" used to remove multipath, showing higher residuals from nine day old template vs one day old.

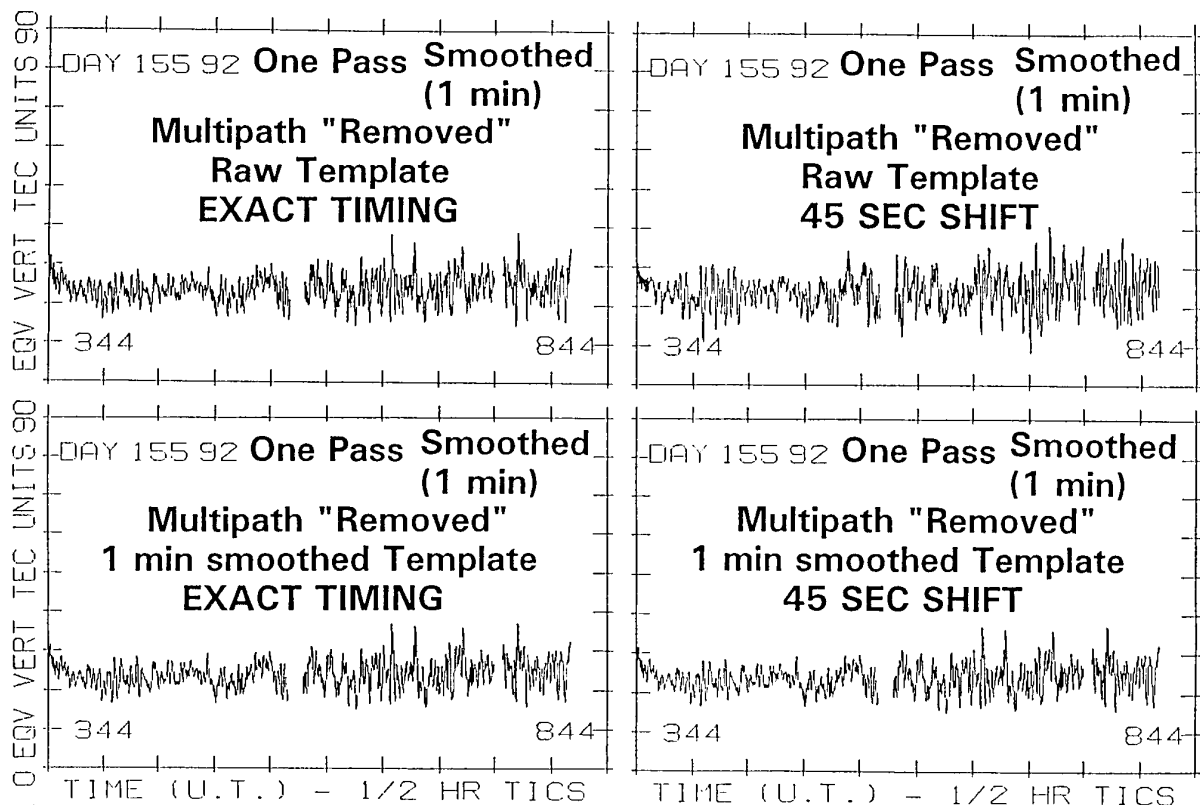


Figure 8. Example of the sensitivity of the "multipath template" technique to errors in time alignment between the template and the current data. For this data set residuals appear to increase for time shifts of 45 seconds or more.

Satellite Number	Multipath Level	Mean Actual Error (TEC units)	Std Dev Actual Error (TEC units)	Mean Absolute Error (TEC units)	Mean Percent Error
15	Medium	-1.54	11.41	8.77	398
20	Low	0.0	10.22	8.05	193
19	Low	0.52	5.67	4.55	12
16	High	-0.16	17.45	13.46	342
11	Low	-0.18	6.0	4.91	177
15	Low	-0.3	9.36	7.62	164
25	High	-0.14	10.92	7.94	-
28	High	-0.26	17.44	11.99	11

TABLE 2. Error in Using Multipath Data to Predict Value Spaced 5 Degrees Away

The data set was analyzed to obtain and plot the error in estimating multipath using a data point spaced five degrees away in spatial angle within the same template. Figure 10 presents data from two satellite passes from the data set, one with high and one with moderate multipath. The upper pair of plots in Figure 10 show the absolute group delay with differential phase fitted to it, and the resultant plot of phase-averaged equivalent vertical TEC adjusted for satellite bias and receiver offset. The middle plots give the derived multipath templates for each satellite pass, and the bottom plots give the actual error, in TEC units, in modeling multipath with five degree spacing. It is clear that at this spacing multipath cannot be acceptably modeled since the error magnitudes are at least of the same order as the original multipath. Table 2 summarizes the statistical results from all the passes in the data set. By comparing the "mean absolute error" in Table 2 to the smooth curves in Figure 3, it may be seen that the mean absolute error in this attempt to model multipath is of the order of 30% to 50% of the average TEC for each satellite pass.

These results suggest that all-sky modeling of multipath using empirical measurements as a base may give unacceptably high errors for available angular spacing. Figure 11 shows available azimuth-elevation spacing of the sky tracks of GPS satellites at the site where the data set was taken - there are few cases where even as close as 5° spacing is obtainable. These results also would indicate that any analytical all-sky multipath modeling technique should be carefully tested against high-resolution empirical data.

#### 7. PHILLIPS LABORATORY TECHNIQUE BENEFIT TO WIDE AREA COVERAGE AND RISING SATELLITES

The significant improvement shown in Figure 5, compared to the simulated performance of phase-averaging in Figure 4, suggests that the simple PL technique could extend capability to effectively monitor ionospheric delay (and correct GPS range) to much lower elevation angles where high multipath values are typically encountered. Capability to operate accurately to lower elevation angles would extend ionospheric monitoring coverage to a much wider region, and would extend and improve the available GPS navigation products from a site.

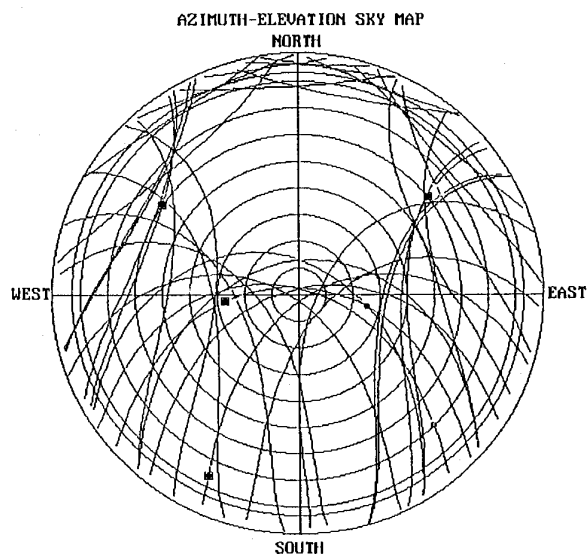


Figure 11. Skymap showing proximity of GPS satellite passes at Shemya, Alaska, 1992.

Extending the elevation coverage down toward the horizon from 15 degrees (typical cutoff of a "tapered" antenna) could as much as double the radius of coverage at ionospheric altitudes (Ref 4). This means a GPS-based ionospheric monitor using the PL technique could, in the limit, quadruple the area of the ionosphere monitored. Further, capability to apply a template to remove multipath from the start of a satellite pass would allow observation of satellites that are just rising (which phase-averaging does not support). Similarly, the quantity of GPS satellites visible and the dilution of precision shows significant improvement as elevation coverage is extended toward the horizon.

#### 8. CONCLUSIONS

Ionospheric delay is typically the largest contributor to GPS range errors. For this reason the GPS signal structure provides for accurate measurement of ionospheric delay as a range correction for GPS. GPS multipath is an artifact of the raypath reflection geometry at the receive antenna site and can, at times, exceed the ionospheric delay. Thus multipath measurement,

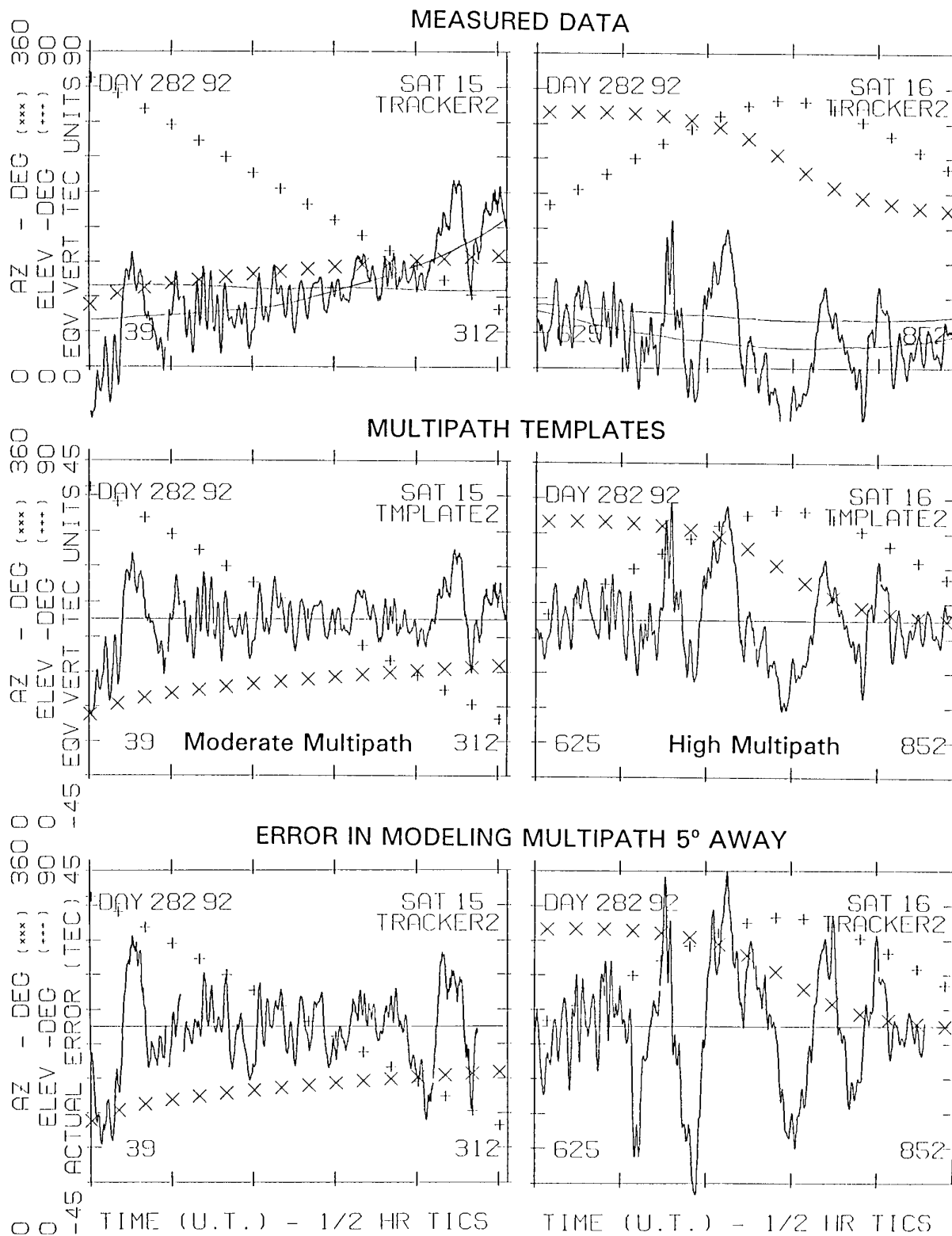


Figure 10. Data from two satellite passes, with moderate and high multipath, respectively, showing: the measured data, "multipath templates", and the error in using a given multipath datum to model multipath 5 degrees away from that data point.

modeling and mitigation is of consequence both to ionospheric monitoring and GPS navigation. Several techniques have been proposed for mitigating multipath effects. These have been reviewed with emphasis on modeling, and in particular emphasizing a new simple modeling approach currently being studied by Phillips Laboratory. This technique takes advantage of the daily repetition of the GPS observation geometry from a ground station to create a "multipath template" specific to each satellite pass, and reduce multipath effects on successive days. This approach has been shown to yield significant improvement in a severe multipath environment and to be relatively insensitive to template age and time alignment. The technique can correct multipath in real-time from the first acquisition of the satellite, in contrast to other approaches that may need an hour or more to start up. Thus the PL technique expands available real-time data, allowing use of data from lower elevations and rising satellites. In the limit this could quadruple the area of the ionosphere that may be monitored from a single GPS site, and improves availability of GPS satellites for navigation calculations. In contrast, a study of PL multipath data suggests that to achieve acceptable accuracy, "all-sky" multipath modeling techniques may require extremely fine angular resolution in multipath measurements or modeling validation. This suggests that such approaches may be impractical for ground-based applications, and at minimum, great care should be exercised with such techniques.

#### 9. REFERENCES

1. Hoffman-Wellenhof, B., H. Lichtenegger, and J. Collins, "GPS Theory and Practice", Springer-Verlag Wein, New York, 1992, p 95.
2. Bishop, G.J., J.A. Klobuchar, Lt Col A.E. Ronn, and Capt M.G. Bedard, "A Modern Trans-Ionospheric Propagation Sensing System", in "Operational Decision Aids for Exploiting or Mitigating Electromagnetic Propagation Effects", AGARD CP 453, May 1989, Paper 31.
3. Spilker, J.J., "GPS Signal Structure and Performance Characteristics", Navigation, 25, 2, Summer 1978.
4. Bishop, G.J., "Specification of Trans-Ionospheric Effects for Space Surveillance", in "Proceedings of the 1992 Space Surveillance Workshop", Lincoln Laboratory Project Report STK-193, Vol. 1, Contract F19628-90-C-0002, April, 1992.
5. Bishop, G.J., D.S. Coco, and C. Coker, "Variations in Ionospheric Range Error with GPS Look Direction", in "Proceedings of ION GPS-91", The Institute of Navigation, Washington, DC, September, 1991.
6. Tranquilla, J.M., and J.P. Carr, "GPS Multipath Field Observations at Land and Water Sites", Navigation, 37, 4, 393, Winter 1990-1.
7. Braasch, M.S., and F. van Graas, "Mitigation of Multipath in DGPS Ground Reference Stations", in "Proceedings of Institute of Navigation National Technical Meeting", San Diego, CA, January, 1992.
8. Van Dierendonck, A.J., P. Fenton, and T. Ford, "Theory and Performance of Narrow Correlator Spacing in a GPS Receiver", in "Proceedings of Institute of Navigation National Technical Meeting", San Diego, CA, January, 1992.
9. Iltis, R.A., "Joint Estimation of PN Code Delay and Multipath Using the Extended Kalman Filter", IEEE Trans. Comm., 38, 10, October 1990, pp 1677-1685.
10. van Nee, D.J.R., "Multipath Effects on GPS Code Phase Measurements", in "Proceedings of ION GPS-91", The Institute of Navigation, Washington, DC, September, 1991.
11. Bishop, G.J., J.A. Klobuchar, and P.H. Doherty, "Multipath effects on the determination of ionospheric time delay from GPS signals", Rad. Sci., 20(3), 388, 1985.
12. Cohen, C. E., and B. W. Parkinson, "Mitigating Multipath Error in GPS Based Attitude Determination", in "Guidance and Control, 1991, Volume 74, Advances in the Astronautical Sciences", R. D. Culp and J. P. McQuerry, eds, Univelt Inc., San Diego, Ca, 1991.
13. Coco, D.S., C.E. Coker, and G.J. Bishop, "A Real-Time GPS Ionospheric Monitor", in "Proceedings of the Ionospheric Effects Symposium", Alexandria, VA, May, 1993.
14. Bishop, G.J., and E.A. Holland, "A Simple Approach to Reducing Severe Multipath errors in GPS Ground-Based Measurements of Ionospheric Delay", Abstract G12B-9, Supplement to EOS, 20 April 1993.
15. Bishop, G.J. et. al., "GPS Application to Global Ionospheric Monitoring: Requirements for a Ground-Based System", in "Proceedings of ION GPS-92", The Institute of Navigation, September, 1992.

## DISCUSSION

**Discussor's name :** H. V. Hitney

**Comment/Question :**

You stated that you could mitigate multipath effects all the way to the horizon using your template method. Did your data include cases of elevation angle near zero degrees, or was there a mask angle in use that rejected signals below a few degrees?

**Author/Presenter's reply :**

The data probably includes a few cases near zero degrees elevation since we were emphasizing observation in one region, whenever possible. There was no "mask angle". The antenna used was a TI-4100 antenna, which has an approximately uniform pattern for the whole sky, to the horizon, as well as (unfortunately) backlobes. The point I wish to emphasize is that the 'template' technique applies to removal of repetitive artifacts (multipath) regardless of elevation. As one takes advantage of the template technique to extend observation to lower elevations, one must of course consider tropospheric propagation, ducting, refraction and other effects as appropriate.

# Impact of Propagation Mechanisms on Global Navigation Satellite System Performance

Stuart Riley, Peter Daly & Peter Raby

Satellite Communications Group  
Department of Electronic & Electrical Engineering  
The University of Leeds  
Leeds LS2 9JT, UK

## SUMMARY

Propagation mechanisms have a detrimental effect on the accuracy of satellite positioning systems such as GPS and GLONASS. The ionosphere at times of high activity will cause the greatest error due to the propagation medium. This paper describes a dual GPS/GLONASS receiver that is capable of measuring the ionospheric delay in the measured GLONASS pseudo ranges using both the code and carrier phases. This allows the pseudo ranges to be corrected for ionospheric delay and a more accurate position solution to be calculated. The paper describes the receiver architecture and fundamental accuracy; receiver measurement noise and calibration are also discussed before the impact of propagation mechanisms on the measurements are investigated. The measurement of the line of sight ionospheric delay, from a GLONASS satellite, is shown and compared with the GPS transmitted ionospheric model. An example of GLONASS P code navigation is given with and without correction for the ionosphere.

## INTRODUCTION

GPS and GLONASS are global navigation satellite systems (GNSS) operated by the USA and CIS respectively. When the systems become fully operational they will provide the user with 24 hour positioning in three dimensions. Both systems provide a coarse acquisition (C/A) code at L1 (1.6GHz) and precise (P) code at L1 and L2 (1.2GHz) frequencies. Both systems modulate the data message with a pseudo noise (PN) code. To demodulate the signal the receiver aligns a locally generated version of the code with the received signal, producing range information.

Navigation is achieved by measuring the electrical range between the receiver and four satellites and solving for  $x, y, z$  and time. The propagation effects of the troposphere and ionosphere together with multipath significantly reduce the achievable accuracies. Tropospheric and ionospheric effects can produce errors in the range measurements of up to 30m and 100m respectively for a mid-latitude station. Multiple propagation paths add low frequency non-Gaussian noise to the measurement with a typical amplitude of several metres.

The frequency of the PN code is commonly called the chipping rate with a chip being a single bit of the PN code[5]. The GLONASS C/A and P code chipping rates are 0.511MHz and 5.11MHz compared to the GPS codes

which are 1.023MHz and 10.23MHz. In a traditional receiver the P code, when compared to the C/A code, will have approximately an order of magnitude less receiver noise on the code phase observable for the same tracking bandwidth and signal to noise ratio (SNR). As the GPS chipping rate is twice that of GLONASS, with the same SNR and tracking bandwidths, the GPS code phase noise will be half that of GLONASS. However, the GLONASS system offers several advantages over GPS:-

- (i) The positioning accuracy is not deliberately degraded. GPS has the two dimensional positioning accuracy reduced to 100m 2drms by a deliberate accuracy degradation called selective availability (S/A). The GLONASS system offers an accuracy of approximately 40m 2drms[16].
- (ii) The GPS P code will be encrypted by Anti-Spoofing (A-S). Though the civilian user will still be able to monitor the ionospheric group delay the results will have a greater noise level. Coded receiver operation is not possible and so the tracking loops will operate with a lower SNR.
- (iii) The inclination of the GLONASS satellite orbits is  $64^\circ$  compared with  $55^\circ$  for GPS. This provides ionospheric measurements at higher latitudes.

## GNSS RECEIVER

The Leeds University GPS/GLONASS receiver is capable of measuring code and carrier phase from both system's C/A code. Additionally measurements of the GLONASS P code at both L1 and L2 frequencies can be made. GPS uses code division multiple access, each satellite transmitting a different PN code at the same frequency ( $L1=1575.42\text{MHz}$ ,  $L2=1227.6\text{MHz}$ ). This makes the RF/IF processing in a GPS receiver relatively straightforward. The inclusion of GLONASS significantly complicates the design as frequency division multiple access is used. Each GLONASS satellite transmits the same PN code but on a different carrier frequency given by,

$$\begin{aligned} \text{GLN } L1_i &= 1602.0 + 0.5625 \times i \text{ MHz} \\ \text{GLN } L2_i &= 1246.0 + 0.4375 \times i \text{ MHz} \quad (1) \\ i &= 1 \dots 24 \end{aligned}$$

Where  $i$  represents the satellite channel frequency.



The aim of the RF/IF processing was to accommodate both systems with as much common hardware as possible. To achieve this the architecture was designed as shown in Figure 1. A single antenna containing an internal pre-amplifier is connected to the receiver, with approximately 30m of cable. The antenna used is a commercially available GPS antenna, it performs reasonably well at the GLONASS L1 frequency but at L2 there is some degradation. In the receiver, the signal is amplified before being split into separate L1/L2 processing sections. Only the L1 section will be considered, the L2 is similar except the GPS L2 signal is not currently recovered.

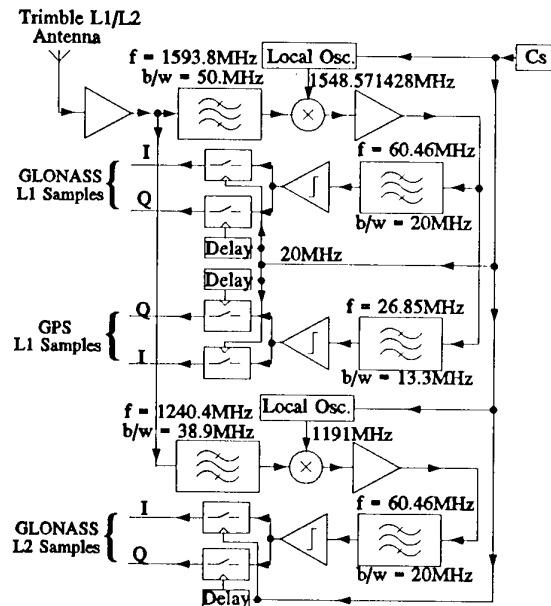


Figure 1 GPS/GLONASS IF/RF processing.

The L1 signal is bandpass filtered to remove the unwanted image signals. It is then downconverted using a single PLL oscillator locked to a reference Caesium clock (Cs). The signal is again amplified before being split into the GPS and GLONASS IF processing sections. The GLONASS IF band is centred at approximately 60MHz. This can be bandlimited to 20MHz incurring only a marginal correlation loss for the satellite channels at the edges of the band. After filtering the signal is one bit quantized both in phase(I) and Quadrature phase(Q). As quadrature sampling is used the sampling frequency of 20MHz satisfies the Nyquist criteria[19] and a digital image reject mix can be implemented to convert the signal to baseband. The spectrum of the sampling pulse train contains a harmonic at 60MHz. This is used to decimate the GLONASS IF band to a lower frequency which can be handled easily by digital devices. The one bit quantization results in an SNR loss of 1.96dB[18] but leads to a significant digital hardware simplification and eliminates the need for an automatic gain control. The GPS IF signal is at 26.85MHz, a bandpass filter of 13.3MHz will allow the future inclusion of the P code with minimal loss[5]. GPS undergoes an analogue to digital conversion(ADC) similar to GLONASS except the 20MHz harmonic of the sampler is used to decimate the signals to 6.85MHz.

The receiver contains ten independent hardware channels, all controlled by a single TMS320C30 microprocessor. The three sets of I/Q samples, from the ADC, enter each channel. The user selects the satellite and the software sets the hardware accordingly, switching the required samples in to the mix sub-section of the channel. The processing for the GPS and GLONASS signals is identical except different code generators are required as the PN codes are different.

The PN code is BPSK modulated on to the carrier, this suppresses the carrier and so it cannot be recovered using a PLL[5]. The normal method of recovering a suppressed carrier is the Costas loop. This consists of an oscillator a  $90^\circ$  phase shifter, three mixers and two low pass filters[18]. Using an image reject mix, the I and Q IF samples are mixed with the output of the carrier numerically controlled oscillator (NCO) producing baseband signals. The I and Q baseband energy is measured and an error signal is derived. This is applied to the carrier NCO to maintain lock by maximising the I signal. This process removes the IF, GLONASS channelization and the carrier frequency Doppler shift and provides the carrier phase measurement.

The PN modulation is at a greater frequency than the data rate, for GPS C/A code 1.023MHz compared with 50baud. This spreads the signal over a wide bandwidth. The receiver must reverse the spreading operation to recover the data message, this operation also provides the range measurement. This is achieved in the correlators which mix the baseband signals with a locally generated replica of the known PN modulation, accumulating the result. Each channel can generate the GLONASS C/A, P and the GPS Gold PN codes. The codes are generated using shift-registers with feed back, clocked by an NCO which is locked to the receiver reference oscillator. As all receiver oscillators and sample clocks are derived from the same source accurate code and carrier phase measurements are possible. Four correlators are used three I and one Q. One of the I correlators and the Q use the local replica code and are used by the Costas loop. The remaining two correlate the baseband I signal with an advanced and retarded local replica, usually called early and late. An error signal is derived from the correlation sums and applied to the code generator's NCO to maintain lock. This type of tracking loop is known as a delay lock loop (DLL)[18].

The correlation despreading process collapses the bandwidth to that of the information, increasing the SNR by the processing gain. Every millisecond, synchronous with the initial state of the code generator, the correlation sums are stored and transferred to the microprocessor. From the correlation sums the microprocessor calculates the code and carrier phase errors. These values are filtered, using  $2^{\text{nd}}$  order filters, before being applied to the appropriate NCO. Figure 2 provides a functional diagram of a receiver channel.

The microprocessor executes the tracking loop algorithms, extracts the data message and measures the code and carrier phase. The receiver is controlled by a PC which performs the satellite selection, data decoding and measurement processing. Communication between the PC

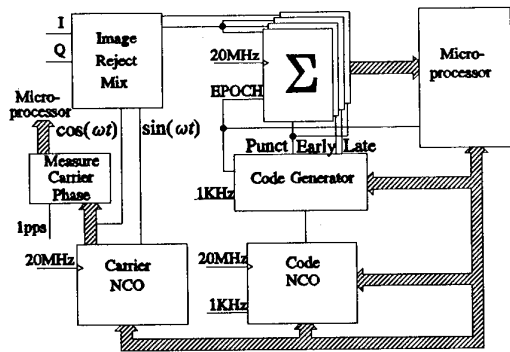


Figure 2 Channel architecture.

and microprocessor is achieved by using first-in first-out (FIFO) buffer memory, reducing the handshaking requirements. The PC (386 or 486) operates under the OS/2 operating system, running proprietary software developed at Leeds. The software utilises the multitasking capabilities of the operating system to simplify the software structure and provides a graphical user interface. Measurements of the code and carrier phase and SNR are stored to the PC hard-disk every second. The transmitted satellite position and clock data contained in the ephemerides and almanacs are stored when the parameters change. Figure 3 gives a block diagram of the receiver architecture.

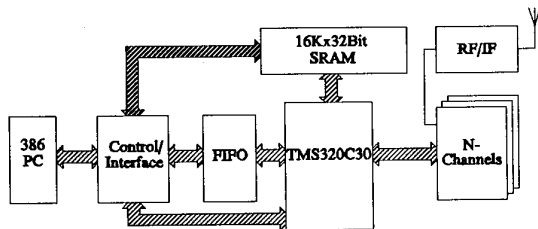


Figure 3 Receiver block diagram.

To minimise the number of components a combination of application specific integrated circuits and Xilinx XC3090 field programmable gate arrays are used. A two channel block requires two of the Xilinx devices, two Stanford Telecommunications STEL-1175 NCOs and a single Qualcomm Q2334 NCO. The original prototype receiver design had the capacity for sixteen channels[15]. A recently developed four layer PCB has ten-channels due to size and financial constraints.

## CORRELATOR SPACING

DLLs are classified by the correlator spacing, the time delay between locally generated early and late PN signals. Practically all GPS/GLONASS receivers have until recently employed a 1 chip spacing, or delay, between the correlators. Recently it has been shown that the noise on the early and late inputs to the DLL discriminator become more correlated as the spacing is reduced. Therefore, when they are subtracted to form the DLL error signal, noise cancellation occurs. Resulting in lower code phase measurement noise[7],

$$\sigma = \sqrt{\frac{B_L \Delta}{2 \frac{S}{N}} \left[ 1 + \frac{2}{\frac{S}{N} T(2-\Delta)} \right]} \quad \text{chips} \quad (2)$$

where,

- $B_L$  Code tracking bandwidth in Hertz
- $\Delta$  Correlator spacing in chips
- $T$  Integration interval in seconds
- $S/N$  Signal to noise ratio in a one Hertz bandwidth
- $\sigma$  Predicted code tracking standard deviation

This technique requires the received signal to have an ideal autocorrelation function. However, most GPS C/A code receivers bandlimit the IF to approximately 2.046MHz (the bandwidth between the first two spectral code nulls), this removes most of the transmitted PN code harmonics which smooths the data transitions and hence the autocorrelation function. This results in nonlinear operation of the DLL discriminator if the spacing is reduced below 1 chip, invalidating the above equation. The signal leaving a GPS satellite is bandlimited, before transmission, to 20.46MHz [12]. The GLONASS satellites do not contain any output filters[13]. The C/A code of both systems will therefore have reasonably sharp transitions and a near ideal autocorrelation function. By increasing the receiver IF bandwidth more of the transmitted harmonics remain, which sharpen the data transitions causing the received signal's autocorrelation function to have a sharper peak and validating equation (2). As the pre-correlation IF bandwidth has been made wide enough, in this receiver, to facilitate the P-code. The C/A code autocorrelation function peak is sufficiently sharp to allow narrow correlation to be implemented. Narrow correlation has been exploited, for the GPS C/A code, in the GPSCard™[7] and is used for both GPS and GLONASS C/A codes in this receiver. Presenting equation (2) graphically, Figure 4 for GPS, it can be seen that the tracking accuracy improvement is significant. The SNR will typically vary between 35 and 45dBHz dependent on satellite elevation. Additionally the method can reduce the effect of code multipath[20].

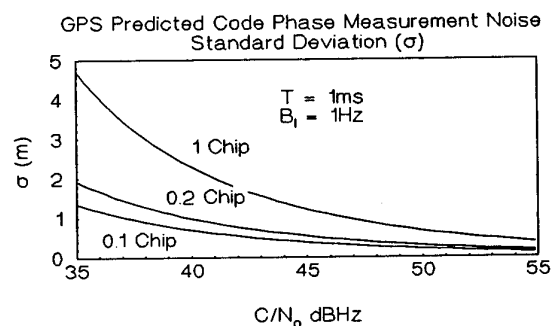


Figure 4 Predicted GPS code phase standard deviations.

The antenna positioning and type will determine the amount of multipath present. An environment with many metallic reflective surfaces may cause severe multipath problems. In this situation the use of absorbent matting as a ground plane for the antenna has been found to provide a high degree of multipath mitigation[11]. Alternatively choke rings can be used. The NovAtel GPSCard™ advertising

literature claims a 50% reduction in multipath when choke rings are used. Both GLONASS and GPS transmit right-hand circularly polarized signals. When the signal is reflected the polarization changes to left-handed. GPS antennas are generally designed to have very low gain for left-hand polarized signals, usually a gain less than -10dB is found. Only a standard GPS antenna, with no specific anti-multipath properties, was available for this work so multipath signals are still present. However this does allow an observation of multipath to be made.

### CARRIER MEASUREMENT ACCURACY

The carrier phase observable is the most precise measurement that can be obtained from the satellite signal. It is fundamental to geodetic survey applications and is often used in other applications to smooth the code phase. In designing the Costas loop the tracking accuracy must be considered, equation (3)[4] gives the predicted carrier tracking standard deviation,  $\sigma$ , in metres.

$$\sigma = \frac{\lambda}{2\pi} \sqrt{\frac{B_L}{C}} \text{ metres} \quad (3)$$

Where,

- $B_L$  Carrier tracking bandwidth in Hertz  
 $C/N$  Carrier to noise ratio in a one Hertz bandwidth  
 $\lambda$  Carrier wavelength in metres.

The Costas loop tracking bandwidth must be able to accommodate the satellite and receiver dynamics, local oscillator noise and drift, and to a lesser extent the ionospheric dynamics. The current receiver is static. The maximum rate of change of Doppler shift of the carrier for a static observer anywhere on the surface of the Earth will be less than 2 Hz/s. The local oscillators and digital sample clock are phase locked to a HP5061A Caesium clock that has a very low phase noise. Therefore, a bandwidth of 10Hz is used, below this very little tracking performance improvement occurs as the carrier phase multipath will dominate. The subsequent predicted tracking accuracy, calculated using equation (3), is plotted graphically in Figure 5 for GPS L1.

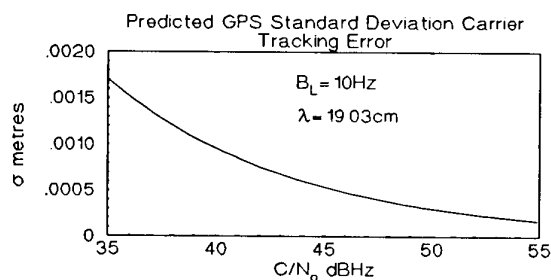


Figure 5 Predicted GPS L1 carrier tracking standard deviation ( $\sigma$ ).

### MEASUREMENT NOISE AND CALIBRATION

The measurement performance of the receiver is limited by the inherent capabilities of the hardware and software. The

limitations can be classified as the measurement bias and the measurement noise. The noise is caused by several sources, receiver thermal noise, local oscillator and reference source phase noise, phase and frequency tracking loop bandwidths and signal quantization together with measurement resolution. The use of a digital architecture as opposed to an older analogue design reduces the noise-narrower tracking loops are possible together with an increased immunity against temperature and ageing effects. The measurement bias can be divided into absolute, inter-channel and GLONASS inter-satellite channel biases.

The inter-channel bias is the measurement difference between two channels on the same receiver, simultaneously tracking the same satellite. This will typically be very small as the same samples are processed by all channels, the RF/IF noise will cancel. The absolute receiver bias is the total measurement bias caused by the entire receive chain, for navigation this is unimportant as the bias effects the time estimate and not the positioning accuracy. For accurate time transfer, however, this bias must be calibrated. All GPS satellites use the same nominal transmit frequency and so the group delay caused by the antenna unit, RF and IF sections is constant for all satellites. The group delay will not be constant for GLONASS as the delay through the bandpass elements will vary over the 20MHz band. The receiver architecture reduces the problems associated with GLONASS by downconverting and sampling the entire band but significant differential group delays, over 10ns, remain and need careful calibration. Additionally the L1-L2 bias needs to be established. The calibration has been achieved using a combination of an HP8510 network analyzer and a simple GLONASS satellite signal simulator. The expected accuracy of the calibration is a few nanoseconds but the stability with temperature has yet to be determined. For every nanosecond error in the L1-L2 calibration, the L1 group delay produced by combining the L1 and L2 measurements will have an additional 1.53125ns bias. The calibration of the carrier phase is much more difficult as a cycle at L1 is only approximately 19cm(0.63ns). The phase delay through the bandpass elements can change by several cycles between GLONASS channels[14]. Fortunately, accurate carrier phase calibration is not necessary for the processing methods employed in this paper.

There is also a bias between the L1 and L2 transmissions leaving the satellite. There have been several published attempts to measure the GPS satellite bias, summarized in[17]. The results are shown in Figure 6 along with the estimate of delay the GPS satellites transmit(GPS). JPL is a Jet Propulsion Laboratory study, IfE the University of Hannover and IAG the institute of Astronomy and Geodesy, Madrid. There is a significant difference between the transmitted corrections and the measured values, all the studies agree reasonably well. The satellite bias has been shown to remain relatively constant over time[3].

As GLONASS satellites do not filter the signals before transmission[13] the L1-L2 satellite delays may be lower than GPS. However, no pre-launch delay values are available and the satellites do not transmit an estimate of the bias. No study has yet attempted to determine what the

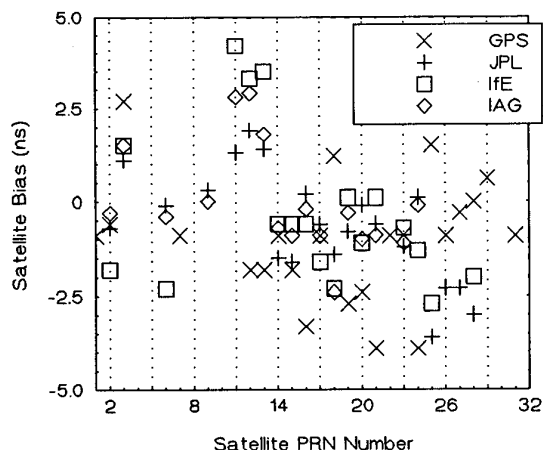


Figure 6 GPS L1-L2 satellite bias.

GLONASS bias is and this calibration has been set to zero in the results presented in this paper.

To show the receiver inter-channel bias and noise all channels were locked to the same satellite, the code phase measurements were differenced and averaged to form the inter-channel bias. Figure 7 shows an example of this measurement. The average bias between the two channels is -30ps (-9mm) with a standard deviation of 88ps (26mm), the satellite tracked was at an elevation angle of 40°. The low bias and spread is expected as only the digital and software sections of the measurement process are being tested. A similar test was performed by Keegan[9] to establish the performance of the Magnavox MX4200 6-channel GPS receiver, his results suggest a bias of 6cm and standard deviation of 86cm. This is very high, though the receiver is several years old.

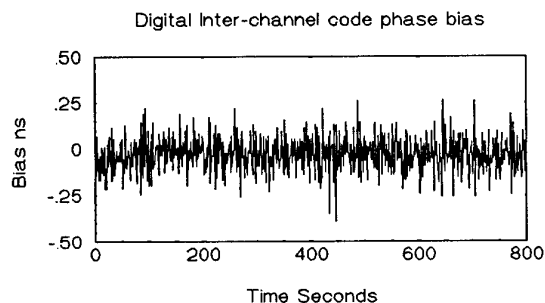


Figure 7 Inter-channel Code phase measurement noise.

The same measurement can be performed on the carrier phase, Figure 8, the offset is approximately zero with a standard deviation of 0.31ps (0.093mm). The coarseness of the graph is due to the measurement resolution of 0.17ps (0.05mm). For this measurement Keegan[9] obtains a standard deviation of 0.86mm. The inter-channel digital biases and noise are therefore several orders of magnitude less than those of the satellite and propagation medium and can be neglected.

In the previous experiment the same samples were simultaneously processed by several hardware channels, providing the receiver bias and the digital noise while

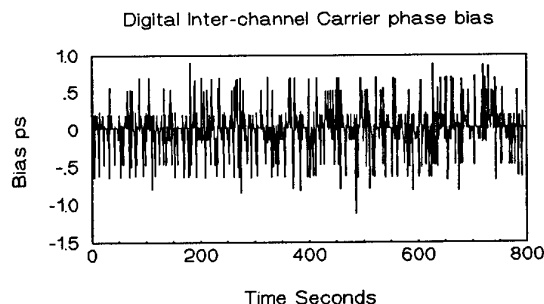


Figure 8 Inter-channel carrier phase measurement noise.

neglecting the RF and IF noise. To ascertain the total receiver measurement noise a different method is necessary, Figure 9. By using the same antenna and preamplifier to feed two separate receivers the system noise can be measured. If the same satellite is tracked on each receiver and the measurements are differenced, a single difference ( $\Delta\phi$ ) is obtained given by,

$$\Delta\phi = \text{chn } n_{rx0} - \text{chn } n_{rx1} \quad (4)$$

The propagation effects are removed as the same antenna is used and so cancel in the difference. The signal passes through separate RF, IF and ADC producing independent samples allowing the total receiver noise to be estimated. The same reference 20MHz oscillator is used by each receiver and the measurements occur almost simultaneously. A time difference will be caused by cable delays and the comparators, which convert the reference to a digital signal, though the difference is unlikely to exceed 100ns.

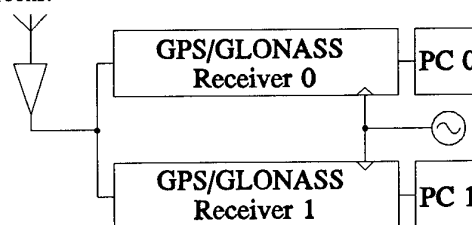
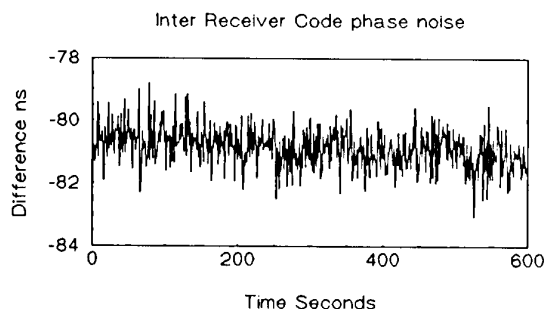


Figure 9 Single antenna receiver noise test.

Figures 10 and 11 show the differenced code and carrier phase results. The standard deviations are 606ps (18cm) and 2.47ps (0.74mm) respectively. To obtain the standard deviation on an individual receiver the results must be divided by the square root of two. Inspecting Figure 11, the carrier phase measurement has a significant random walk component, this is due to the phase noise of the L-band oscillator. In the normal operational mode this will cancel as all channels will be making measurements at the same time. The fundamental receiver noise is very low compared to noise that is caused by the propagation path.

## RESIDUAL MEASUREMENT

The carrier phase provides the change in satellite range between successive measurement epochs. Accumulating gives a carrier phase pseudo range, referred to as the accumulated delta range (ADR). Due to the very low carrier phase measurement noise, equation (3), the ADR is



**Figure 10** Zero-baseline inter-receiver code phase measurement noise.

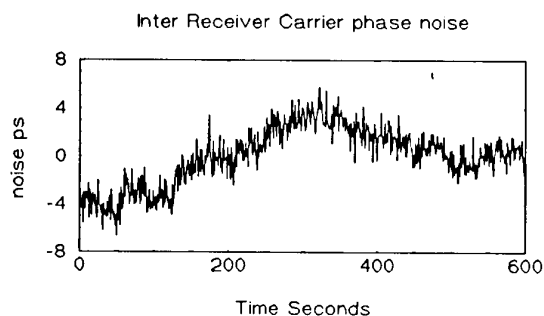


**Figure 11** Zero-baseline inter-receiver carrier phase measurement noise.

very precise. The carrier wavelength is approximately 19cm and 24cm at the L1 and L2 frequencies respectively and so there is an initial ambiguity in the measurement as the number of cycles between receiver and satellite will be unknown when the observation period begins.

If the difference is formed between the code phase pseudo range and the ADR a residual is produced[16]. This has the user and satellite clock and position errors removed and so gives an indication of the code phase measurement noise. The carrier phase measurement noise is much less than the code phase noise and can be neglected. As the ionospheric group and phase delays have opposite signs, twice the ionospheric term will remain. Measuring over an entire satellite pass allows the extent of the ionospheric group delay to be seen. When a satellite is at higher elevations the ionosphere will stay relatively constant and the code phase noise can be analyzed, giving an indication of the fundamental accuracy of the receiver and the effect of multipath.

Figure 12 shows the residual formed from GLONASS Almanac 22 on 17<sup>th</sup> March 1993 using 0.1 chip correlation spacing in the DLL. The satellite was tracked for approximately six hours starting at an elevation angle of 2°, reaching a maxima of 75° and terminating at 5°. The absolute value has been altered to provide a better presentation. As any ionospheric effect is doubled, a plot of twice the predicted ionospheric group delay, from the GPS model[10], is superimposed on the same graph. A high degree of correlation between the two curves can be seen. As there is one point per second for over 20,000 seconds, multipath, which has a typical period of a few

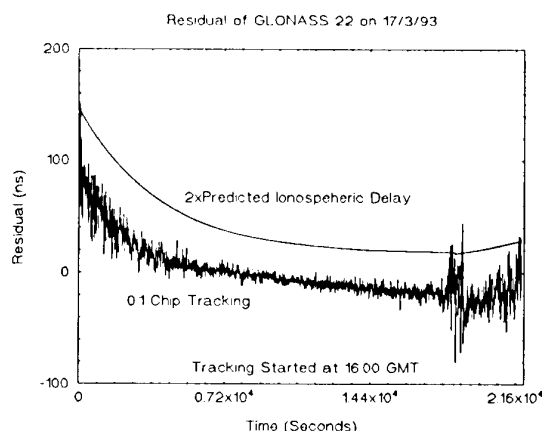


**Figure 12** Six hour GLONASS code phase - ADR residual measurement, 0.1 chip correlator spacing.

minutes, is hard to distinguish.

Figure 13 shows the residual from a GPS satellite (PRN14) on 21<sup>st</sup> August 1993. During the one hour segment of data the satellite was at its highest elevation relative to the receiver. The change in ionospheric group delay over the period is negligible so there is no visible code/carrier phase divergence, caused by the group and phase delays having opposite signs. Multipath can still be seen on the measurement given in Figure 13, despite the high elevation. It is characterized by large periodic deviations from the mean.

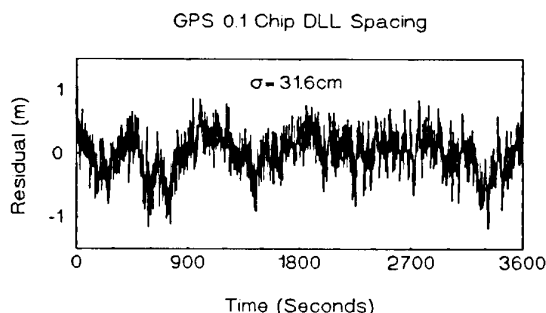


**Figure 13** One hour GPS code phase - ADR residual measurement, 0.1 chip correlator spacing.

To show the GLONASS code phase measurement noise five channels of the receiver were simultaneously locked to the same GLONASS satellite. Three channels tracked the C/A code with the three different correlation chip spacings the receiver can produce, the other two tracked the P code at L1 and L2 frequencies. The code tracking bandwidth of all five channels was set to 1Hz with a 1ms integration period and a 10Hz carrier tracking bandwidth. Figure 14 shows one measurement per second of the five residuals, the absolute values have been altered to ease presentation. The 0.1 chip C/A code GLONASS residual has a larger spread than the GPS measurement as the GLONASS chip length is 587m compared with the GPS length of 293m. The P code has a chip length of 58.7m this results in a theoretical noise level similar to the GPS 0.1 chip C/A code. The L2 P code has a much larger measurement noise than the L1 data as the received SNR is up to 10dB less

than is found at L1. This may be caused by the GPS antenna which is not ideal at the GLONASS frequencies. The received GPS L2 power is 3dB less than at L1[12]. It is likely that the GLONASS L2 transmission is lower in power than the L1 though probably not by 10dB.

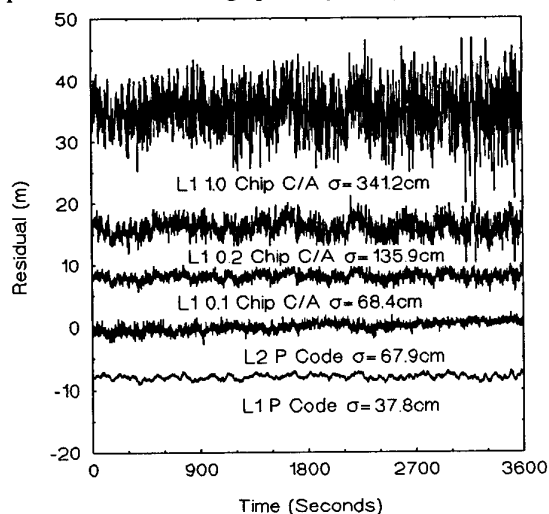


Figure 14 GLONASS code-phase - ADR residual measurements on 22<sup>nd</sup> August 1993.

### IONOSPHERIC GROUP DELAY

The Klobuchar model[10] is transmitted by GPS satellites. It consists of a third order polynomial fit to a half cosine, with a period of approximately one day, Figure 15 gives an example.

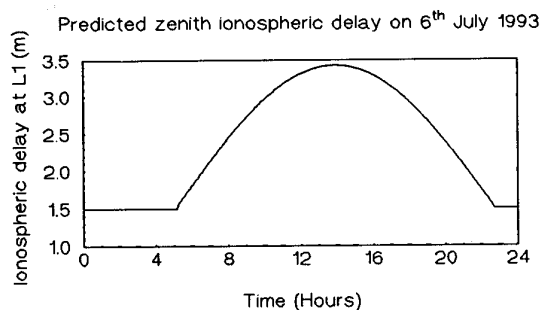


Figure 15 Predicted zenith delay, at Leeds, using the Klobuchar model parameters transmitted by GPS.

The model has a positive bias, as there will always be a small delay. The transmitted parameters produce variations in the model's period and amplitude. To convert to the required line of sight ionospheric delay a transformation is used[10]. The model is designed to operate with satellites down to an elevation angle of 5°, where the delay is approximately three times greater than at zenith. It has been observed to correct for 60% rms range error even at the peak of the solar-flux cycle[6]. The model coefficients are calculated from an empirical model of global ionospheric behaviour. The parameters broadcast are selected from a set of 370, based on the day of year and the average solar flux for the preceding five days[2]. The transmitted parameters change typically once a day. The

predicted peak value from the model is shown in Figure 16. Unfortunately we do not have the data for the end of 1990 and 1991. If the graph is compared to the monthly sunspot number[1], Figure 17, the same trend can be seen. Ionospheric activity is currently low.

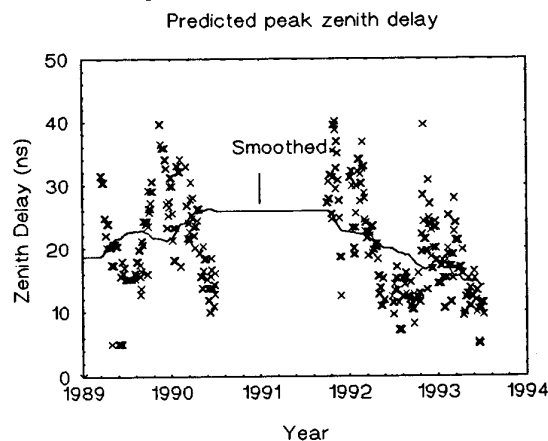


Figure 16 Peak zenith delay calculated from daily transmitted GPS model parameters.

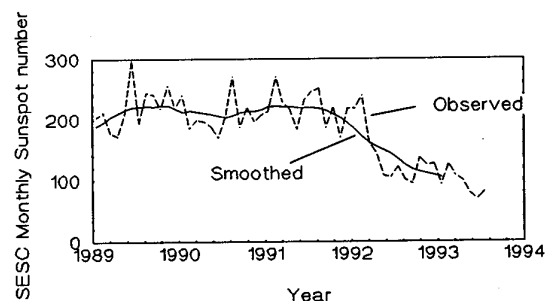


Figure 17 Monthly observed and smoothed sunspot numbers.

For some applications the model is too imprecise. For dual frequency GNSS users the effect of the ionosphere can be removed. The ionospheric delay is approximately inversely proportional to the square of the operating frequency. As GPS and GLONASS transmit at two widely spaced frequencies, L1 and L2, the ionospheric delay can be estimated by combining the measurements. As both code and carrier phase observables are available a very accurate estimate of the ionospheric delay can be obtained, subject to any calibration errors. The algorithms used to obtain the ionospheric delay are given in[16].

### DUAL FREQUENCY GLONASS MEASUREMENTS

Figure 18 shows the measured line of sight ionospheric delay to a GLONASS satellite. The measurement was obtained by combining code and carrier phase observables at both L1 and L2 frequencies. The measurement has low noise as the code phase data is only used to provide the absolute level of the ionospheric delay, the precise carrier phase data gives the profile information. Provided no cycle slips occur the profile, or change in ionospheric delay, is accurate to within a few centimetres. The absolute value of the measured ionosphere is less certain as the code phase

receiver calibration and satellite biases have a much larger uncertainty. The graph also includes the satellite elevation angle and the predicted ionospheric delay given by the GPS model. A decrease in ionospheric delay can be seen as the satellite is at a higher elevation and a clear correlation exists between the modelled and measured delay.

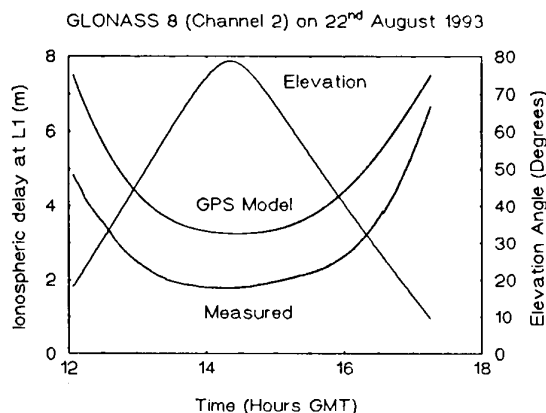


**Figure 18** GLONASS 8, measured ionospheric group delay.

### GLONASS DUAL FREQUENCY NAVIGATION

Figures 19 to 24 show GLONASS P code navigation on 29<sup>th</sup> August 1993. The receiver was locked to the P code, at L1 and L2 frequencies, of the four GLONASS satellites with the best geometry. The first three graphs show the calculated position error, from the surveyed WGS-84 antenna position, when only the L1 P code is used without any ionospheric correction. The second set of graphs were produced by calculating the ionospheric delay from the L1 and L2 code and carrier phases and subtracting the estimated delay from the L1 pseudo ranges. The corrected L1 pseudo ranges were processed using the same algorithm as the L1 only data. Comparing the graphs, the spread of the ionospherically corrected data is slightly worse than the L1 only data. This is because of initial transients in the ionospheric estimation filter[16]. However, all three coordinates show an improved average position, compared to the surveyed reference. The height shows the largest improvement. This is usually the case, due to the satellite geometry, the calculation of height is most susceptible to measurement error amplification. As was shown in Figures 16 and 17 the ionospheric behaviour is presently relatively quiet. Towards the end of the decade the activity will start to increase as the solar activity approaches an 11 year maxima early next century. The errors caused by the ionosphere in the navigation solution will then be more significant. Dual frequency navigation will be necessary for high accuracy.

### TROPOSPHERIC DELAY

A further source of range error is the troposphere. Errors are caused because signals are refracted, due to the atmosphere causing a change in the refractive index. This increases the propagation path length. To calculate the range error the refractive index must be integrated along the signal path length. The refractive index can be

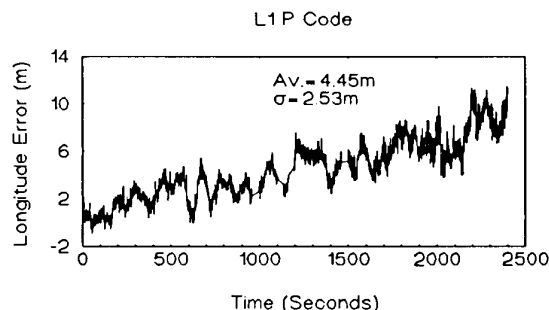


**Figure 19** GLONASS L1 P code longitude position error.

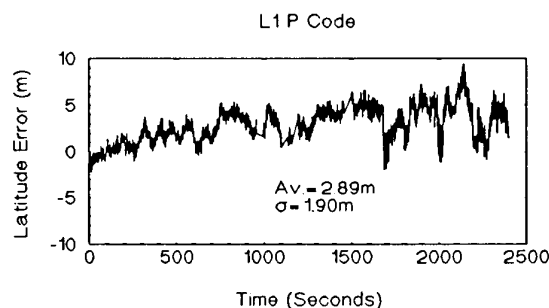


**Figure 20** GLONASS L1 P code latitude position error.

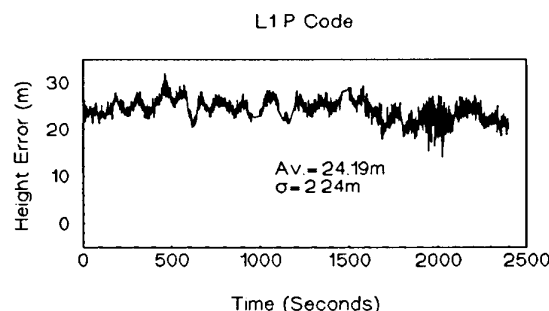


**Figure 21** GLONASS L1 P code height position error.

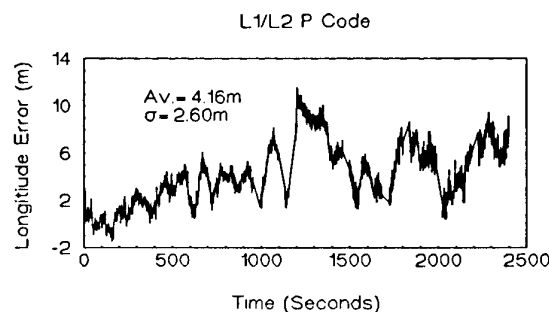


**Figure 22** GLONASS L1/L2 P code longitude position error.

calculated, using a suitable model, from simple atmospheric measurements:- temperature, pressure and water vapour content. The dry air component is the easiest to model, forming 80-90% of the total[18]. GPS provides a simple

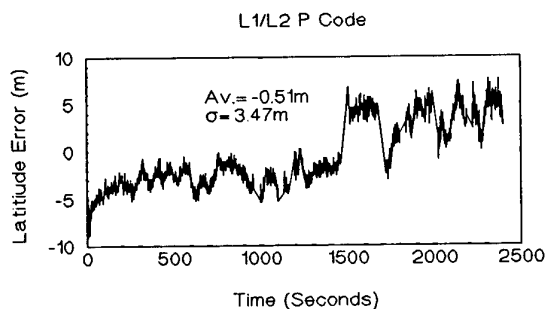


**Figure 23** GLONASS L1/L2 P code latitude position error.

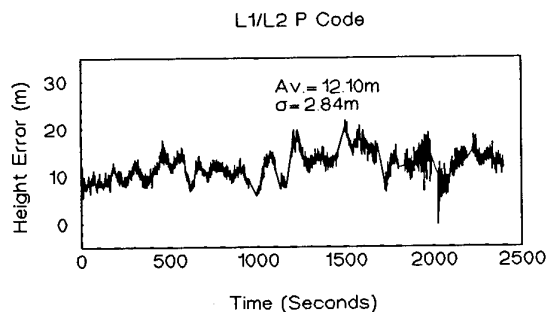


**Figure 24** GLONASS L1/L2 P code height position error.

tropospheric correction model, the only parameters necessary are receiver height and satellite elevation angle. The model can be used for GLONASS without modification, no parameters for the model are transmitted. The model requires height above mean sea level or the geoid and not above the WGS-84 ellipsoid. At Leeds the geoid is approximately 47m above the ellipsoid[12]. The model also requires the surface refractive index at mean sea level,  $N$ . The global mean is 324.8 with a standard deviation( $\sigma$ ) of 25.98[12]. The 95% confidence level of the model is 3.9m, this is sufficient for most single frequency applications as the ionospheric model error will be much greater. For dual frequency applications tropospheric error may dominate. Instruments exist for direct measurement of the tropospheric delay, but are expensive. Alternatively the prediction accuracy can be improved by using more detailed models[8]. Unfortunately more accurate modelling requires local weather data that is not always readily available. The GPS model alone has been used throughout this work. Figure 25 shows the model correction against satellite elevation for the Leeds reference antenna, 162m above the ellipsoid, 115m above mean sea level with the  $\pm 3\sigma$  values.

The facilities do not exist at Leeds to measure the tropospheric delay. However by using the carrier phase ADR the effectiveness of the model can be seen. The range correction provided by the model is most noticeable at low elevation angles. If the ADR is formed and subtracted from the calculated range produced by using the satellite ephemeris and the known position of the Leeds antenna the troposphere, ionosphere and receiver and satellite position uncertainties remain. If the calculation is performed on the

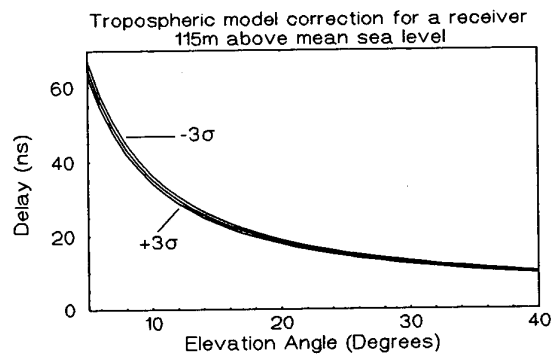


**Figure 25** Predicted Tropospheric delay at Leeds, for  $N_s = 324.8$  and  $\pm 3\sigma$

same data set with and without the tropospheric model the extent of the improvement can be shown. Figure 26 is an example of this measurement. The small jumps in both data sets are caused when the transmitted parameters, used to calculate the satellite position, change. The uncorrected curve has a large error when the elevation angle is low, characterized by a rapid departure from an almost straight line. This demonstrates the typical effect of the troposphere on the satellite ranging measurements.

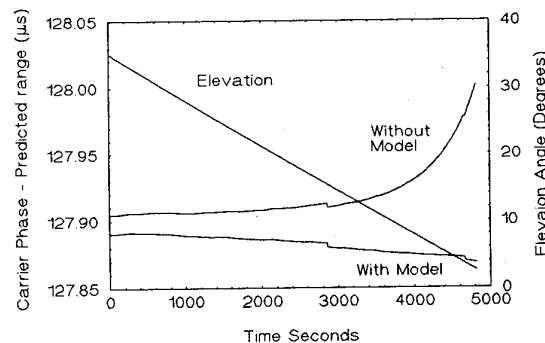


**Figure 26** ADR - calculated range with and without the tropospheric model.

## CONCLUSIONS

This paper has described the architecture of a multichannel GNSS receiver developed at the University of Leeds. The receiver is highly integrated using common hardware and software to process both GPS and GLONASS signals. The fundamental receiver noise due to hardware and software design has been demonstrated to be much less than the noise induced on the signal by the propagation medium. Use of the narrow correlation technique has helped to reduce the code phase noise to a level similar to that of the P code observable. By tracking and measuring the code and carrier phase observables of the GLONASS P code at the two transmitted frequencies, an estimate of the ionospheric delay on the signal can be obtained. An example of the line of sight ionospheric delay on a GLONASS signal over a continuous five hour tracking period has been shown. Though the measured and modelled ionospheric delay have similar profiles there is a significant difference allowing enhanced navigation to be performed using the L1/L2



estimate.

The receiver and satellite L1/L2 and inter-channel calibration is one of the major problems when making ionospheric measurements. Future work will attempt to measure the receiver biases more accurately and assess their change with temperature and age. Hardware improvements will be made to attempt to minimise and stabilise the inter-channel and inter-frequency biases. Once the receiver has been more accurately calibrated an attempt will be made to estimate the L1/L2 GLONASS satellite biases. A better antenna will be obtained which is less lossy at the GLONASS frequency. This will increase the SNR and so reduce the receiver measurement noise. Further work will be undertaken to reduce the multipath interference.

## ACKNOWLEDGEMENTS

The authors would like to thank the Department of Surveying at the University of Newcastle for the loan of GPS equipment and processing the data which determined the WGS-84 position of the antenna. This work has been supported by the Science and Engineering Research Council (UK).

## REFERENCES

- [1] "Monthly Review of Solar and Geophysical Activity", Summary for July 1993, Report compiled by the Solar Terrestrial Dispatch P.O. Box 357 Stirling, Alberta T0K 2E0, Canada
- [2] D.S.Coco, C.Coker and J.R.Clynch, "Mitigation of Ionospheric Effects For Single Frequency GPS Users", *Proc. ION GPS-90*, ION Satellite Division, 3<sup>rd</sup> International Technical Meeting, Colorado Springs, CO, September 19-21, 1990.
- [3] D.S.Coco, C.Coker, S.R.Dahlke and J.R.Clynch, "Variability of GPS Satellite Differential Group Delay Biases", *IEEE Trans. Aerospace and Electronic Systems*, Vol. AES-27, No. 6, November 1991.
- [4] C.E.Cohen and B.W.Parkinson, "Expanding the Performance Envelope of GPS-Based Attitude Determination", *Proc. ION-GPS 91*, ION Satellite Division, 4<sup>th</sup> International Technical Meeting, Albuquerque, New Mexico, September 9-13, 1991.
- [5] R.C.Dixon, *Spread Spectrum Systems*, John Wiley & Sons, 2<sup>nd</sup> Edition 1984.
- [6] W.A.Feess and S.G.Stephens, "Evaluation of GPS Ionospheric Time-Delay Model", *IEEE Trans. Aerospace and Electronic Systems*, Vol. AES-23, No. 3, May 1987.
- [7] P.C.Fenton, W.H.Falkenberg, T.J.Ford, K.Ng and A.J. Van Dierendonck, "NovAtel's GPS Receiver- the High Performance OEM Sensor of the Future", *Proc. ION-GPS 91*, ION Satellite Division, 4<sup>th</sup> International Technical Meeting, Albuquerque, New Mexico, September 9-13, 1991.
- [8] H.S.Hopfield, "Tropospheric effect of electromagnetically measured range: Prediction from surface weather data", *Radio Science*, Vol. 6, No. 3, March 1971.
- [9] R.Keegan, "The New Magnavox GPS Receiver Technology", *Proc. ION GPS-90*, ION Satellite Division, 3<sup>rd</sup> International Technical Meeting, Colorado Springs, CO, September 19-21, 1990.
- [10] J.A.Klobuchar, "Ionospheric Time-Delay Algorithm for Single Frequency GPS Users", *IEEE Trans. Aerospace and Electronic Systems*, Vol. AES-23, No. 3, May 1987.
- [11] G.Lachapelle, W.Falkenberg and D.Neufeldt, "Marine DGPS Using Code and Carrier In a Multipath Environment", *Proc. ION GPS-89*, ION Satellite Division, 2<sup>nd</sup> International Technical Meeting, Colorado Springs, CO, September 27-29, 1989.
- [12] NATO MAS Standardisation Agreement - NAVSTAR GPS System Characteristics. STANAG 4294 Draft Issue N, May 1991.
- [13] J.E.B.Ponsonby, "Spectrum Management and the Impact of the GLONASS and GPS Satellite Systems on Radioastronomy", *The Journal of the Royal Institute of Navigation*, Vol-44, No.3, September 1991.
- [14] P.Raby and P.Daly, "Using the GLONASS System for Geodetic Survey", *Proc. ION-GPS 93*, ION Satellite Division, 6<sup>th</sup> International Technical Meeting, Salt Lake City, Utah, September 22-24, 1993.
- [15] S.Riley, "An Integrated Multichannel GPS/GLONASS Receiver", *Proc. ION-GPS 92*, ION Satellite Division, 5<sup>th</sup> International Technical Meeting, Albuquerque, New Mexico, September 16-18, 1992.
- [16] S.Riley and P.Daly, "Performance of The GLONASS P-Code at L1 and L2 Frequencies", *Proc. ION-GPS 93*, ION Satellite Division, 6<sup>th</sup> International Technical Meeting, Salt Lake City, Utah, September 22-24, 1993.
- [17] E.Sardon and L.Wanninger, "Comparison of Several Data Sets of The Differential Instrumental Delays of GPS Satellites", IfE-Memo WA-03/93, Institut für Erdmessung (Institute of Geodesy) Universität Hannover, 1993.
- [18] J.J.Spilker, *Digital Communications by Satellite*, Prentice Hall, 1977.
- [19] R.G.Vaughan, N.L.Scott and D.R.White, "The Theory of Bandpass Sampling", *IEEE Trans. Signal Processing*, Vol. SP-39, No. 9, September 1991.
- [20] A.J.Van Dierendonck, P.Fenton and T.Ford, "Theory and Performance of narrow correlator spacing in a GPS receiver", ION National Technical Meeting, San Diego, CA, 27 January 1992.

## DISCUSSION

**Discussor's name :** G. J. Bishop

**Comment :**

You mentioned in your presentation that JPL had recently published new measurements of GPS LI-VS-L2 transmission delay bias (at the Institute of Navigation GPS-93 meeting). I would like to add that in their paper JPL claimed to have a significant improvement in accuracy in measurement of these biases, and they are seeing the biases as quite stable within their measurement accuracy. Our own measurements at Phillips Laboratory also appear to show good stability of these biases over several months, at least. Therefore, the good news is that these satellite biases appear to be diminishing as a calibration issue for GPS measurement.

## MITIGATION OF THE EFFECTS OF F LAYER IRREGULARITIES BY USING MULTIPLE PATHS

by

**Jules Aarons**  
Center for Space Physics  
Boston University  
725 Commonwealth Avenue  
Boston, Massachusetts 02215  
United States

### ABSTRACT

In recent military operations trans-ionospheric satellite to ground communications have been utilized in the equatorial region. One problem for the predominantly 250 MHz system has been fading due to irregularities in the region within plus and minus 20 degrees of the magnetic equator. A similar problem has been encountered at high latitudes. For minimizing the effect of the fading, one might expect that radio links sufficiently separated in frequency and polarization would be effective in combating scintillation. Unfortunately frequency separations would have to be of the order of 100 MHz to obtain an adequate diversity improvement. The use of right and left circular polarization or of orthogonal linear polarizations is not effective.

However, time diversity is a demonstrated procedure for overcoming scintillation but there is a loss in using coding or redundancy and a reluctance to complicate the system with modems. If the paths from a single satellite are sufficiently well separated then fading on two links is uncorrelated and diversity gain may be achieved. Unfortunately at equatorial latitudes separations of the order of a kilometer are involved.

Another use of "space diversity" can be effective. If the paths from two satellites with spacing between them are available and there is recognition that scintillation is causing the fading on the path to one satellite, then operators can utilize the path to a second satellite. For equatorial paths the operator must be alert as to the time development of irregularities and the dynamics of plume development. The differences in activity on the paths are due to two aspects of the irregularity plume i.e. the start time as the sunset moves westward and the spacing between plumes on very active days. Examples of the time difference between the start of equatorial scintillations on one path versus that of another have been recorded in many sectors of the world. The results of these studies as applied to the problem of multiple paths will be shown.

At high latitudes during moderate magnetic activity, it is possible to find paths that are not dominated by irregularities. However at auroral latitudes when a magnetic storm commences, the irregularity development moves equatorward with great rapidity and encompasses large areas. It is then difficult to find a path free of irregularities.

### INTRODUCTION

Satellites operating for communication purposes in the 250 MHz range are being used currently by the military. While this allows relatively low power systems, the use of the 250 MHz band also increases the effect of ionospheric irregularities on transmissions. It is the purpose of this paper to suggest one means of minimizing this problem.

### THE EQUATORIAL REGION

In recent military operations, trans-ionospheric satellite to ground communications has been utilized in the equatorial region. One problem for the predominantly 250 MHz system has been fading due to irregularities in the region within plus and minus 20 degrees of the magnetic equator. By knowing the characteristics of the F layer irregularities which affect transmissions, it is possible to transmit information with a minimum of fading.

Scintillations are predominantly a nighttime phenomenon. The development of the irregularities occurs after the westward moving sunset line has gone thru the region. The formation proceeds for periods of the order of a half hour to an hour from east to west. Once formed however the plume or thin layer moves with the wind i.e. to the east.

An example of fading at 250 MHz can be noted in recordings from Natal, Brazil in Figure 1. In this case the signal is approximately 18 dB above sky temperatures before the onset of scintillations. As time progresses thru the night there are periods of no scintillation followed by sporadic fading. Between periods of fading which can range from several seconds to many minutes, transmissions can move unaffected thru the system. The Natal site is near the magnetic equator and therefore has a more continuous flow of irregularities across its propagation path than sites distant from the magnetic equator. The sites distant from the equator will show more gaps than those within plus or minus 5 degrees of the equator. Thus one technique to minimize fading is to take advantage of the gaps between periods of fading.

## NATAL, BRAZIL

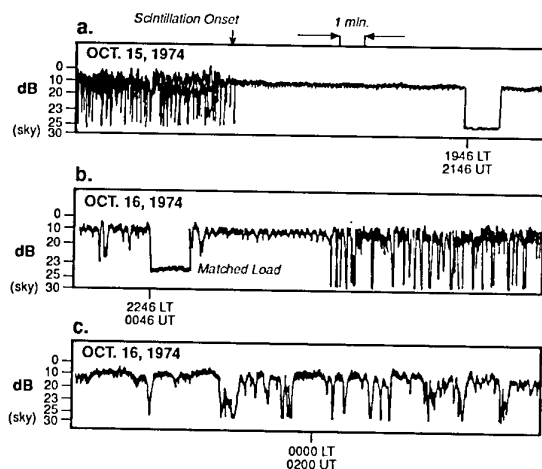


Figure 1. 250 MHz scintillation observations made in Natal, Brazil. With the onset of scintillations at 1955 Local Standard Time, the fluctuations are rapid. However later, for example at 2240 LST, there are gaps with low activity and even longer periods between fades near the midnight time period.

The high altitude plumes which are the main source of problems in the equatorial region contain irregularities at F layer heights and a depletion of electron density. Their high altitude over the magnetic equator affects the ionosphere of latitudes far from the equator. The turbulence is extended along the lines of force of the earth's field. The depletion of electrons can be sensed by optical methods which picture the entire sky over an observing point. One such study (Mendillo and Tyler, 1983) with a depletion image translated into irregularities observed south of the magnetic equator (Figure 2) shows both the extent of a single plume and the bifurcation of the plume at high altitudes (and at great distances from the magnetic equator). These are the gaps which can be utilized by operators if they understand the characteristics of these equatorial phenomena. The gaps between bursts of scintillation can be noted in the diagram from Goodman and Martin, 1982 (Figure 3a) which shows the scintillation levels on a satellite signal noted by a naval vessel at a magnetic latitude in or beyond the anomaly region. The times between gaps then should be used to concentrate sending and receiving signals. The Guam data (Paulson, 1983) shown in Figure 3b shows decreased scintillation between quite virulent scintillation activity.

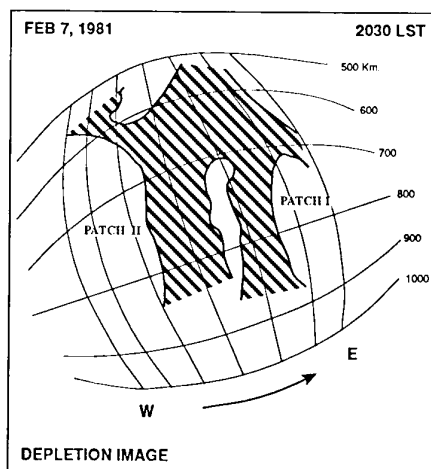


Figure 2. When depletion in a plume, as shown by optical methods, is noted above Ascension Island which is situated to the south of the magnetic equator, a single patch will often split into two sections with gaps between the bifurcated patches (Mendillo and Tyler, 1983).

SSR-1 Observed Max-Min AGC  
From USNS HAYES  
Mag. Lat: -21° Lat: -38.03° Lon: -57.51°  
January 28, 1981

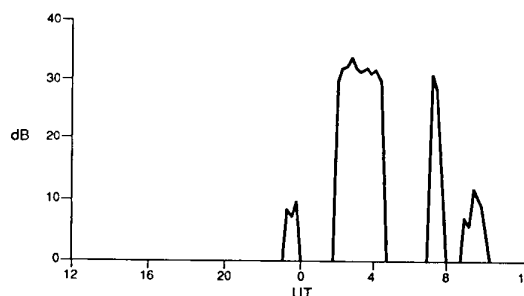


Figure 3a. Making shipboard observations of 250 MHz satellite transmissions from a site situated polewards of the accepted anomaly region, Goodman and Martin (1982) found deep peak to peak fades but with gaps between the periods of deep fading.

Scintillation Levels at Guam at 250 MHz  
(Paulson, 1983)

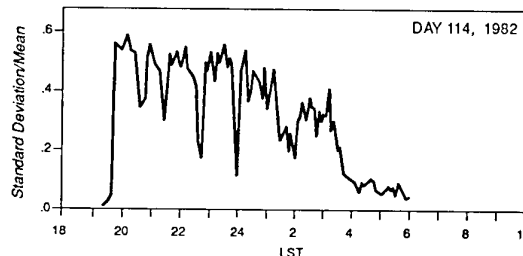


Figure 3b. On Guam, observing at 250 MHz from 1900 to 0600 LST, Paulson (1983) also found gaps in the fading, in this case closer to the magnetic equator.

Essentially the above method is a manner of dealing with a single propagation path. If paths to two satellites are available, then the possibility of using the two paths should be studied. The sunset line going west is the site of the setting up of the parameters necessary to generate the irregularities. In principle therefore the time when the irregularities develop on one path versus that on a second path should be related to the time difference between the two. As is usual in geophysics there are a substantial number of exceptions. Figure 4a illustrates the first appearance of high amplitude scintillations on two paths on a series of nights. The time difference between the 350 sub-ionospheric propagation longitudes was approximately one hour. The ATS-3 path at a more westerly location should be disturbed first, followed by the ATS-1 path which would then show scintillations later).

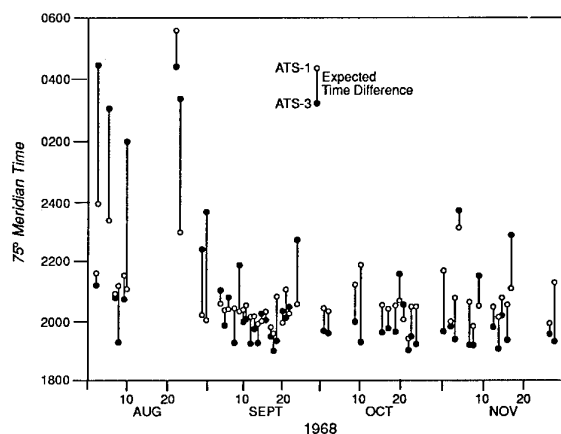


Figure 4a. Since the solar terminator moves westward, the development of the plume structures should be a function of local time on the propagation path. Most often it is but the time differences between onset varies. In addition there are days with no development of plumes and dates when the plumes develop only on the western path and then move eastward under the influence of zonal wind. At the top is the expected appearance of scintillation which is a function of local time of the propagation path to each satellite.

It can be seen that while there is a pattern of sequential commencement of scintillation activity starting on the eastern path and then on the western path. That is not always the case as can be seen on various days. Sometimes the irregularities start on the western path, develop and then move east. Similarly as shown in Figure 4b, the disappearance of the irregularities most often follows the pattern of the eastern satellite scintillation disappearing first from the observer's point of view. However localized effects play a role in the decay of the irregularities as can be noted from the many exceptions.

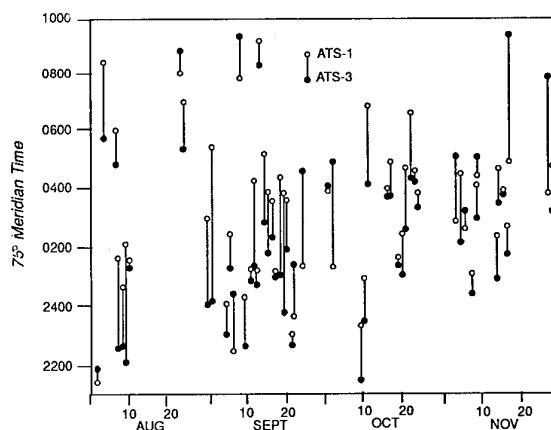


Figure 4b. In the case of the decay of the plume, the final disappearance of high amplitude scintillation should first be noted in the east and then in the west. While this occurrence is predominant both the length of time for the disappearance on each path and the sequence of events varies in many cases.

The data therefore from this and other observations indicates the need to switch paths if two satellite paths are available. The use of this method in a troublesome area should be considered. This could work in the equatorial region but would require the operator to be alert as to the time development of irregularities and to the dynamics of plume development.

#### FREQUENCY AND SPACE DIVERSITY IN THE EQUATORIAL REGION

For minimizing the effect of the fading, one might logically expect that radio links sufficiently separated in frequency, polarization, or time would be independent and could be effective in combating scintillation.

Unfortunately, this generalization is not true. Frequency separations would have to be of the order of 100 MHz to obtain an adequate diversity improvement in the frequency domain. Neither the use of right and left circular polarization or of linear polarizations is effective. However, time diversity is a demonstrated procedure for overcoming scintillation at UHF for disadvantaged mobile platforms; there is a loss in using coding or redundancy and a reluctance to complicate the system with modems.

For space diversity, separations of the order of a kilometer are involved and have been used on ground installations. However the useful minimum separations are certainly larger than ship dimensions. As a result, shipboard and airborne terminals must be designed to provide compensation through pursuit of other measures.

#### MIDDLE AND SUB-AURORAL LATITUDES

At latitudes below the auroral oval, there are means of utilizing different propagation paths. These can be effective during moderate magnetic activity but fail during magnetic storms.

From a site near Boston during a year of high solar flux, several satellites were observed continuously. While there was a small amount of movement in position of the satellites, the paths which could be termed sub-auroral, were substantially those shown in Figure 5a. In Figure 5b scintillations can be noted for hours on one path (in this case the path to ATS-3) while only relatively small fluctuations were noted on the path to the second 136 MHz satellite termed Canary Bird. The path to LES-5 with observations near 250 MHz was severely disturbed; these observations on a higher frequency are less sensitive than those on the 136 MHz CB signal path but the region thru the CB path was not covered with F-layer irregularities. On another night at the same local time as that of Figure 5b, the CB path was disturbed (Figure 5c) while the ATS-3 path was not. In these cases it appears as if substorm related mechanisms with their localized characteristics (narrow in time and in longitude) were responsible for the growth of irregularities.

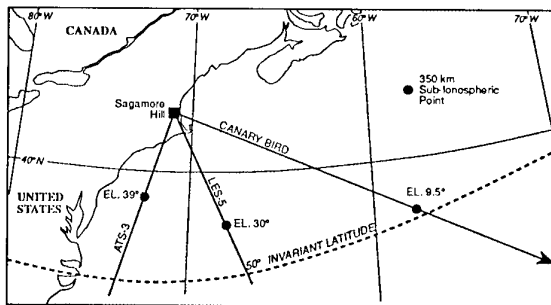


Figure 5a. A map of the propagation paths to three satellites observed from the Boston region. The 350 km sub-ionospheric point is marked. ATS-3 and the CB satellite transmit in the 136 MHz range and the Lincoln Experimental Satellite (LES-5) transmitted in the 250 MHz range.

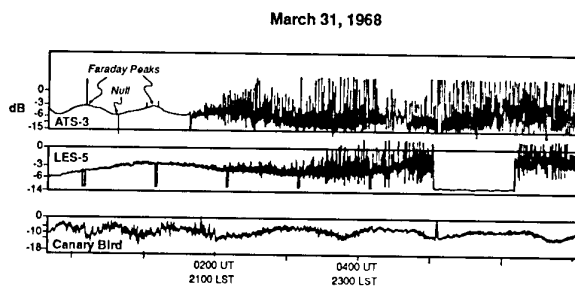


Figure 5b. In this diagram it can be noted that on this night with the first hour mark at 1900 LST (0000 UT), intense scintillations were noted on the ATS-3 path but relatively low level of the order of a few dB on the Canary Bird signal. Intense scintillation was also noted on the LES-5 path.

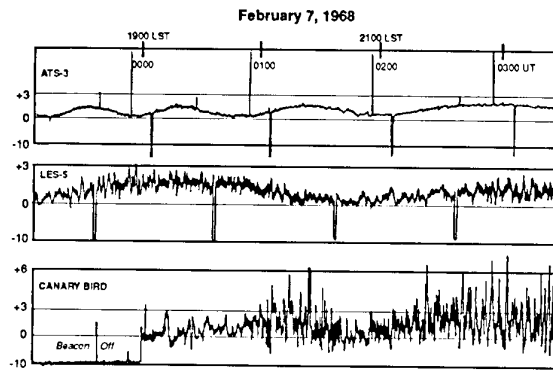


Figure 5c. On another night with the records starting at the same beginning time as those in Figure 5b, the ATS-3 path showed no scintillations while the CB path exhibited very high levels.

However these localized effects do not hold in the case of a major magnetic storm. A dramatic illustration of the effect of these storms on several paths to satellites from one observation point is shown in Figure 6 where the three paths show maximum scintillation activity almost simultaneously when the irregularity generating effects of a magnetic storm descend on a region.

Essentially the storm effects descend in time along a longitude, affect a single latitude and longitude region simultaneously as shown in Figure 7. As shown in Figure 8, the effects of the magnetic storm in time move equatorwards to lower latitudes, in this case over several hours. The total picture after the development of the magnetic storm is shown in Figure 9 where an entire longitude region is encompassed by strong irregularities. Thus during this period a single station even with multiple satellites under view would be suffer deep fading on all paths.

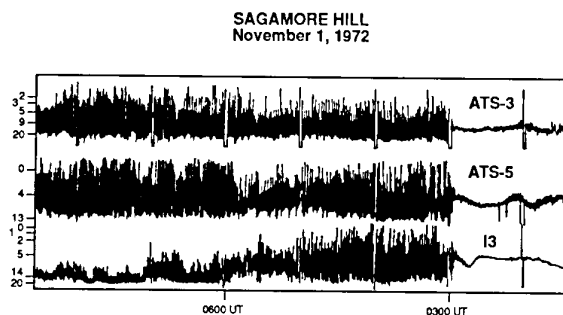


Figure 6. During a severe magnetic storm, paths over a large range of longitudes will be affected almost simultaneously. This is shown in observations of three satellites from a single site thru a path at 54 degrees Corrected Geomagnetic Latitude.

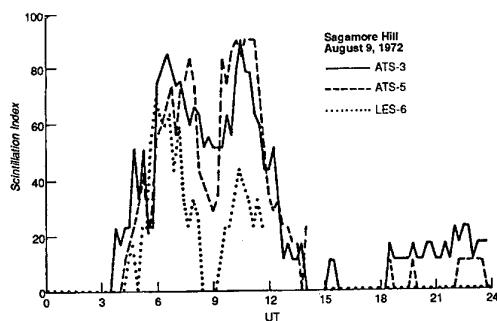


Figure 7. An analysis of data for another magnetic storm period is shown in this figure. The motion of the forcing function producing the irregularity development has slightly different rise times for paths with the same frequency. In this case the start time difference is approximately an hour.

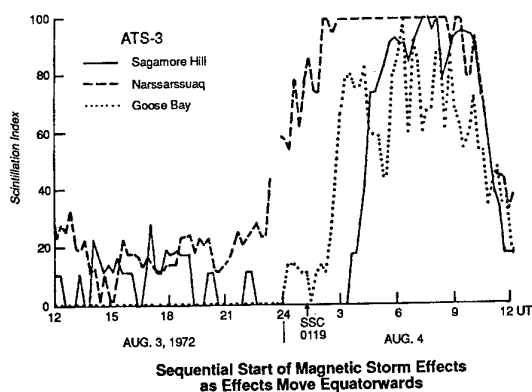


Figure 8. The irregularity region envelops various latitudes as its effects move equatorward. The first path affected is the intersection from Narssarsuaq at 63 degrees Corrected Geomagnetic Latitude. Then the intersection from Goose Bay at 60 degrees and finally the intersection at 54 degrees (Sagamore Hill, near Boston).

Area of Deep Fading  $\geq 10$  dB  
During the Intense Magnetic Storm of  
October 31, 1968

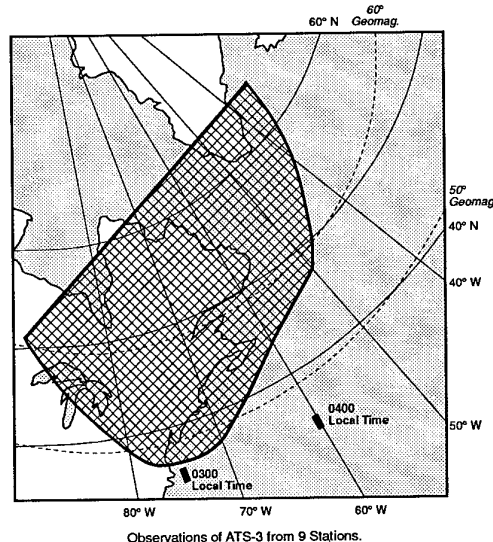


Figure 9. The area of deep fading (in this case  $>10$  dB on a 136 MHz signal) produced during a magnetic storm is shown. Observations from 9 stations were used.

## CONCLUSION

In the equatorial region the use of the intervals between plumes can yield useful time for communications and navigational needs. If more than one satellite is available the path difference may yield low fluctuation on one path and high on another.

In the sub-auroral region, which may include middle latitudes during magnetic storms, sub-storms may introduce irregularities on various paths. However even for a single station, it might be manageable to use distinctively separated paths to overcome scintillation on one path. During a major magnetic storm, the sub-auroral latitudes are severely affected simultaneously at a distinct longitude. The sub-auroral label may be attached to relatively low latitudes depending on the severity of the storm.

## ACKNOWLEDGEMENTS

The studies of Jules Arons are sponsored by the Office of Naval Research.

## BIBLIOGRAPHY

Goodman, J.G. and A.J. Martin (1982) A summary of propagation studies undertaken by the 1981 expedition of the U.S.N.S. Hayes. Naval Research Laboratory Report 4720

Mendillo, M. and A. Tyler, The geometry of depleted plasma regions in the equatorial ionosphere, J. Geophys. Res., 88, 5778, 1983.

Paulson, M.R., Equatorial scintillations of satellite signals and some drift characteristics of the scintillation, NOSC TR 911, 1983.

## DISCUSSION

**Discussor's name :** C. Goutelard

**Comment/Question :**

Une expérimentation mondiale nommée Année Internationale d'Etude de l'Ionosphère Equatoriale se déroule actuellement groupant différentes nations, et se poursuivra jusqu'à fin 94. Une importante banque de données va être constituée. Avez-vous connaissance de cette expérience.

**Translation :**

*A world-wide programme of experiments entitled "The International Year of the Study of the Equatorial Ionosphere" is under way at the present time and will continue until the end of 1994. A major data bank is being constituted. Do you know about this programme?*

**Author/Presenter's reply :**

I am quite interested in learning of this program. New data on regions beyond the anomaly region has been puzzling; these new studies may be very helpful.

**Discussor's name :** G. Sales

**Comment/Question :**

Do you have the data base to investigate the achievable networking through several widely-spaced ground stations using several satellites?

**Author/Presenter's reply :**

At equatorial latitudes, ground diversity using spacing greater than 100 meters has achieved considerable improvement (papers by Paulson). Therefore, I would expect widely spaced stations would be successful by networking. However, at high latitudes, networking has not been tried but time diversity has been successful (A. Johnson).



## ELECTROMAGNETIC WAVE REFLECTION FROM IRREGULAR PLASMA LAYERS

K. Papadopoulos  
University of Maryland  
Department of Physics  
College Park, MD 20742

R. Short and R. Shanny  
ARCO Power Technologies Inc.  
Washington, DC 20037

USA

## ABSTRACT

The general theory describing reflection of electromagnetic waves from irregular reflectors was formulated by using path integral techniques [Dashen, 1979; Flatte', 1979]. The general formulae reproduce the well known reflection coefficients for wave scattering from random rough surfaces derived by using Kirchhoff's theory or perturbation theory [Ogilvie, 1991]. The theory was used to determine the degradation of an OTH radar signal scattered from irregular Artificial Ionospheric Mirrors (AIM). The cases of density irregularities induced by fluctuations in the ambient neutral density and by fluctuations in the heater power were separately examined. Scaling laws and bounds for minimal signal loss were derived.

## 1. INTRODUCTION

Strategic air defense depends upon detecting and tracking potential threats approaching at long ranges, allowing adequate time for assessment and reaction. The threats of particular current interest are penetrators with small radar cross sections, including air launched and submarine launched cruise missiles (ALCM and SLCM). These threats will become more important in theater warfare as well over the next few decades. The ability to supplement current wide area surveillance with reliable, all weather, continuous detection and tracking of low flying, low observable targets is essential to the successful implementation of both strategic and tactical air defense.

Recognition of the performance limitations associated with use of the natural ionosphere to reflect Over The Horizon (OTH) radar signal motivated Artificial Ionospheric Mirror in the upper atmosphere, in order to reflect ground based radar signals for OTH surveillance [Drobot et al., 1987]. The AIM is produced by beaming sufficient electromagnetic power into the lower ionosphere to enhance the in situ ionization level to  $10^7 - 10^8$  electrons/cm<sup>3</sup> thereby providing an ionized layer capable of reflecting radar frequencies between 5-90 MHz. The advantages of an AIM system as a complement to existing OTH radars were discussed by Short et al. [1990] and are illustrated in Figure 1. An issue in the performance of AIM is the degree of degradation of the reflection, over that of a perfect reflector, due to the presence of random fluctuations in the electron density generated during the AIM formation. The objective of the present paper is to develop the reflection formulation and evaluate the extent of signal degradation due to natural and heater induced irregularities. The plan

of the paper is as following. The next section presents the mathematical formulation of the problem and its solution using path integral techniques [Feynman and Gibbs, 1965; Dashen, 1979; Flatte, 1979]. The results are then used to compute in sections 3 and 4 the reflection coefficient from irregular AIM clouds for isotropic and anisotropic fluctuations. The performance degradation for natural and heater induced fluctuations is presented in section 5.

## 2. PROBLEM FORMULATION

## 2.1 Path Integral in Propagation Problems

Consider a monochromatic wave with frequency  $\omega$  propagating through a medium with permittivity  $\epsilon(\mathbf{r})$ . Its propagation is described by the Helmholtz equation

$$\nabla^2 \psi(\mathbf{r}, t) + k_o^2 \epsilon(\mathbf{r}) \psi(\mathbf{r}, t) = 0 \quad (1)$$

$$k_o^2 \equiv \frac{\omega^2}{c^2}$$

where  $\psi(\mathbf{r}, t)$  is the wave amplitude. If we assume that the wave amplitude varies slowly with respect to the wavelength in its propagation direction, which we take as the x-direction, so that

$$\psi(\mathbf{r}) = E(z, r_{\perp}) e^{ik_o x} \quad (3)$$

equation (1) reduces to the usual "parabolic" equation

$$2ik_o \frac{\partial E(\mathbf{r})}{\partial x} + \nabla_{\perp}^2 E(\mathbf{r}) + k_o^2 (1 - \epsilon(\mathbf{r})) E(\mathbf{r}) = 0 \quad (4)$$

$\nabla_{\perp}^2$  is the gradient in the transverse direction. For reasons that will soon become apparent equation (4) is written as

$$\frac{i}{k_o} \frac{\partial E}{\partial x} + \frac{1}{2k_o^2} \nabla_{\perp}^2 E - U(\mathbf{r}) E(\mathbf{r}) = 0 \quad (5a)$$

$$U(\mathbf{r}) = -\frac{1}{2} [1 - \epsilon(\mathbf{r})] \quad (5b)$$

Equation (5) is formally identical to the two dimensional Schrodinger's equation,

$$i\hbar \frac{\partial \psi}{\partial t} + \frac{\hbar^2}{2m} \nabla_{\perp}^2 \psi - V(\mathbf{r}) \psi = 0 \quad (6)$$

if we make the following substitutions  $t \rightarrow x$ ,  $\hbar \rightarrow \frac{1}{k_o}$ ,  $m = 1$ ,  $V(\mathbf{r}) \rightarrow -\frac{1}{2} [1 - \epsilon(\mathbf{r})]$ . Notice that the analogy

indicates that geometric optics ( $k_o \rightarrow \infty$ ) is equivalent to the classical limit ( $\hbar \rightarrow 0$ ). This analogy can be exploited to write a general solution of equation (4) or (5) following the path integral technique formulated by Feynman. Notice that equation (5) is now an initial value problem, with  $x$  as an equivalent time variable. The problem can be formulated using a Green's function which can be integrated in  $x$  starting from an initial condition  $E(r_\perp, x = 0)$ .

Feynman's path integral technique relies on the fact that the response of an instrument located at a position  $B = (r_\perp, x_1)$  to a source located at a point  $A = (r_\perp, x = 0)$  is given by the sum over all the paths that connect the two locations. It is an infinite dimensional integral with  $2N-2$  integration variables. Following Dashen (1979) the path integral connecting B to be is given by

$$G(A \rightarrow B) = \int dr_p \times \exp \left[ ik_o \int_0^{x_1} \left[ \frac{1}{2} \left( \frac{dr_p}{dx} \right)^2 - U(r_p(x) + \hat{e}_z x) \right] dx \right] \quad (7)$$

where the integration is over all paths  $r_p$  connecting A to B.  $G(A \rightarrow B)$  is nothing more than the propagator of equation (5). The expression in the exponential of equation (7) is equivalent to a Lagrangian with a unit mass kinetic energy and negative potential energy  $U$ . The formal solution of equation (5) is given by

$$E(r_\perp, x) = \iint G(r_\perp, 0; r_\perp, x) E(r_\perp, 0) dr_\perp \quad (8)$$

The moments of  $E$  are found by taking ensemble averages of the power of equation (8). If we define

$$S(path) \equiv \int_0^{x_1} \left[ \frac{1}{2} \left( \frac{\partial y(x)}{\partial x} \right)^2 + \frac{1}{2} \left( \frac{\partial z(x)}{\partial x} \right)^2 - U(y(x), z(x), x) \right] dx \quad (9)$$

the average value of  $E$  can be written as

$$\langle E \rangle = \langle \int d(paths) \exp[ik_o S(path)] \rangle \quad (10)$$

The power of the technique is that it can produce physical transparent results in the case of weak scattering as well as for strong interaction through the use of asymptotic series. We apply the technique next to the case of reflection from irregular AIM clouds.

## 2.2 Reflection from Irregular Plasma Layers

For a plasma the dielectric function is

$$\epsilon(\omega) = 1 - \frac{\omega_e^2}{\omega^2} \quad (11)$$

where  $\omega_e$  is the plasma frequency. In the presence of density fluctuations given by  $n = \bar{n} + \delta n$  with  $\langle \delta n \rangle = 0$  the value of  $U(r)$  will be given by

$$U(r) = -\frac{1}{2} \left[ \frac{n(r)}{n_c} + \frac{\delta n(r)}{n_c} \right] \quad (12)$$

where  $n_c$  is the critical electron density defined as

$$n_c \equiv \frac{\omega^2 m}{4\pi e^2} \quad (13)$$

From the previous analysis and using the form of equation (9), we write

$$\langle E \rangle = \langle \int d(paths) \exp[ik_o S_o(path) + ik_o S_1(path)] \rangle \quad (16)$$

We assume next that the eikonal  $S_1(path)$  is a Gaussian variable and

- (i) Interchange averages and integrations;
- (ii) Use the fact that for a Gaussian variable

$$\langle e^{i\alpha} \rangle = \exp \left( -\frac{1}{2} \langle \alpha^2 \rangle \right)$$

Under these conditions equation (16) becomes

$$\langle E \rangle = \int d(path) \exp[ik_o S_o(path)] \times \exp \left[ -\frac{1}{2} k_o^2 \langle S_1^2(path) \rangle \right] \quad (17)$$

Equation (17) gives a physically transparent but deceptively simple looking result. The first term describes propagation in a smooth medium, while the term

$$R \equiv \exp \left[ -\frac{1}{2} k_o^2 \langle S_1^2(path) \rangle \right] \quad (18)$$

the modification of the propagation by the presence of fluctuations. For  $R = 1$  we recover the propagation through a smooth medium. From equations (17) and (18) the signal reduction  $\mathcal{L}$  in dB due to the presence of density irregularities will be given by

$$\mathcal{L} = -4.3 k_o^2 \langle S_1^2(path) \rangle \text{ dB} \quad (19)$$

This is an important result of the analysis. We would apply it below to the case of AIM reflection.

## 3. REFLECTION FROM AIM IN THE PRESENCE OF FLUCTUATIONS

### 3.1 Isotropic Case

From eqs. (17-19) we find that the deterioration of the signal due to inhomogeneities in the AIM surface, will be given by

$$\frac{\langle E \rangle}{\langle E \rangle_o} = \exp \left[ -\frac{1}{2} k_o^2 \langle S_1^2(path) \rangle \right] \quad (20)$$

Let us first examine the case of isotropic fluctuations with scale length much shorter than the path through the cloud. In this case (Rytov et al., 1990)

$$\langle S_1^2(path) \rangle = \delta \sigma_\phi^2 \quad (21)$$

The eikonal variation  $\delta\sigma_\phi^2$  is given by

$$\delta\sigma_\phi^2 = \pi^2 \int_0^{\ell_o(\theta)} \frac{ds}{\bar{\epsilon}[z(s)]} \int_0^\infty S_\epsilon(k, z(s)) k dk \quad (22)$$

where  $\ell_o(\theta)$  is the zero order path of the ray incident at an angle  $\theta$  and  $S_\epsilon(k, z)$  the spectrum of the fluctuations  $\delta\epsilon$  at the point  $z$ . Equation (22) can be analytically evaluated when  $S_\epsilon(k)$  is independent of position and the AIM layer has a linear profile with scalelength  $L$ . Such a profile can be described by

$$n(z) = n_c \frac{z}{L} \quad (23)$$

in this case the zero order ray follows a parabolic trajectory given by

$$z = x \cot\theta - \frac{1}{2} \frac{x^2}{L \sin^2\theta} \quad (24)$$

The ray turns at a level given by

$$z_t(\theta) = L \cos^2\theta \quad (25)$$

and exits the AIM cloud after traveling an horizontal distance  $\Delta(\theta)$  given

$$\Delta(\theta) = 4L \sin\theta \cos\theta \quad (26)$$

Integrating eq. (22) by using the path (24) we find

$$\delta\sigma_\phi^2(\theta) = 2\pi^2 L \left( \ell_n \frac{1 + \cos\theta}{1 - \cos\theta} \right) \int_0^\infty S_\epsilon(k) k dk. \quad (27)$$

For a Gaussian fluctuation spectrum

$$\psi_\epsilon(r) = \sigma_\epsilon^2 e^{-r^2/2\ell_\epsilon^2} \quad (28)$$

the integral in eq. (40) gives

$$2\pi^2 \int_0^\infty S_\epsilon(k) k dk = \sigma_\epsilon^2 \sqrt{\frac{\pi}{2}} \ell_o \quad (29)$$

so that

$$\delta\sigma_\phi^2 = \sigma_\epsilon^2 \sqrt{\frac{\pi}{2}} \ell_o L \left( \ell_n \frac{1 + \cos\theta}{1 - \cos\theta} \right) \quad (30)$$

The signal deterioration will be given by

$$L = -4.3 g \text{ dB} \quad (31a)$$

$$g = \sigma_\epsilon^2 \sqrt{\frac{\pi}{2}} (k_o \ell_o) (k_o L) \ell_n \left( \frac{1 + \cos\theta}{1 - \cos\theta} \right) \quad (31b)$$

From eq. (22) it is easy to see that  $\delta\sigma_\phi^2$  maximizes when  $\bar{\epsilon}(z)$  becomes small, i.e. near the turning regions of the layer. It is easy to find that 50% of the contribution to

$\delta\sigma_\phi^2$ , comes from a fraction of the layer near the top with width  $\Delta L$  given by

$$\frac{\Delta L}{z_t} = \frac{1}{2} \frac{\sin\theta(1 - \sin\theta)}{\cos^2\theta} \quad (32)$$

This corresponds to about a fifth of the layer at  $\theta = 45^\circ$  and 1/6 at  $\theta = 30^\circ$ . Notice that in this region the rays are almost parallel to  $x$ .

A simple but intuitive way to derive the above result is as follows. Consider phase fluctuations over a ray of length  $\ell$  and inhomogeneities with scale  $\ell_\epsilon$ . The ray path will accommodate  $N \sim \frac{\ell}{\ell_\epsilon}$  independent inhomogeneities. After a simple inhomogeneity the phase shift of the wave will be

$$\ell_\epsilon \frac{\omega}{c} \bar{\epsilon} \approx k_o \ell_\epsilon \delta\epsilon \quad (33)$$

Since the random quantities corresponding to the different inhomogeneities are independent, the total mean square of the phase shift will be

$$\begin{aligned} \langle S_1^2 \rangle &= N \langle (\ell_\epsilon k_o \delta\epsilon)^2 \rangle \approx \frac{\ell}{\ell_\epsilon} \ell_\epsilon^2 k_o^2 \sigma_\epsilon^2 \approx \\ &\approx (k_o \ell_\epsilon) (k_o z) \sigma_\epsilon^2 \end{aligned} \quad (34)$$

which is comparable to eq. (30).

### 3.2 Anisotropic Case

For a situation with anisotropic fluctuations eq. (34) becomes

$$\delta\sigma_\phi^2 = \frac{\pi}{2} \int_0^{\ell_o(\theta)} \frac{ds}{\bar{\epsilon}[z(s)]} \int_{-\infty}^\infty S_\epsilon(\underline{k}_\perp; z(s)) d^2 k_\perp \quad (35)$$

where  $\underline{k}_\perp$  refers to the transverse direction at every point on the path. The role of anisotropic fluctuations can be understood by considering the value of the integral

$$I = \int_{-\infty}^\infty S_\epsilon(\underline{k}_\perp, 0) d^2 k_\perp \quad (36)$$

for the case that the fluctuations are described by

$$\psi_\epsilon(\underline{r}) = \sigma_\epsilon^2 \exp \left[ -\frac{1}{2} \left( \frac{x^2}{a^2} + \frac{y^2}{b^2} + \frac{z^2}{c^2} \right) \right] \quad (37)$$

In this case  $\delta_\epsilon(\underline{r})$  has a spectrum

$$S_\epsilon(\underline{k}) = \frac{\sigma_\epsilon^2 abc}{(2\pi)^{3/2}} \exp \left[ -\frac{1}{2} (a^2 k_x^2 + b^2 k_y^2 + c^2 k_z^2) \right] \quad (38)$$

Assuming propagation on the  $x$ - $z$  plane at an angle  $\gamma$  to the  $z$ -axis

$$I(\gamma) = \frac{\sigma_\epsilon^2}{\sqrt{2\pi}} \frac{ac}{\sqrt{a^2 \cos^2 \gamma + c^2 \sin^2 \gamma}} \quad (39)$$

Notice that for propagation in the  $x$ -direction ( $\gamma = \frac{\pi}{2}$ ),

$$I\left(\frac{\pi}{2}\right) = \frac{\sigma_\epsilon^2 a}{\sqrt{2\pi}} \quad (40a)$$

and for  $\gamma = 0$ ,

$$I(0) = \frac{\sigma_c^2 c}{\sqrt{2\pi}} \quad (40b)$$

Namely the eikonal correlation is controlled by the correlation length along the propagation direction. From eqs. (35-38)

$$\delta\sigma_\phi^2(\theta) = \left(\frac{\sigma_c^2}{2}\right) \sqrt{\frac{\pi}{2}} a \times \alpha \times \int \frac{ds}{\bar{\epsilon}[z(s)]} \frac{1}{\left[\sin^2\gamma(s) + \frac{a^2}{c^2} \cos^2\gamma(s)\right]} \quad (41)$$

where  $\gamma(s)$  is the local propagation angle. For isotropic spectra  $a = c$  and we recover the result of eq. (28) with  $\ell_o$  replaced by  $a$ . Since the integral of eq. (41) maximizes when  $\bar{\epsilon}[z(s)]$  is minimum, i.e. near the turning regions,  $\gamma(s) \approx \frac{\pi}{2}$  and as long as  $\frac{a^2}{c^2} \cos^2\gamma(s) \ll 1$ ,

$$\delta\sigma_\phi^2(\theta) = \left(\frac{\sigma_c^2}{2}\right) \left(\sqrt{\frac{\pi}{2}}\right) \int_0^{\ell_o(\theta)} \frac{ds}{\bar{\epsilon}[z(s)]} \quad (42)$$

For a linear density profile eq. (42) gives

$$\delta\sigma_\phi^2(\theta) = \sigma_c^2 \left(\sqrt{\frac{\pi}{2}}\right) L \ell_n \left(\frac{1 + \cos\theta}{1 - \cos\theta}\right) \quad (43)$$

The result is similar to eq. (29) but with the isotropic scalelength  $\ell_o$ , replaced by the scalelength  $\alpha$  in the  $x$  direction. The value of  $g$  is given by

$$g(\theta) = \sigma_c^2 \sqrt{\frac{\pi}{2}} (k_o a) (k_o L) \ell_n \left(\frac{1 + \cos\theta}{1 - \cos\theta}\right) \quad (44)$$

#### 4. SOURCES AND SPECTRA OF PERMITTIVITY FLUCTUATIONS IN AIM

For practical AIM systems there are two sources of permittivity fluctuations  $\delta\epsilon(\underline{r})$ , caused by electron density fluctuations within the cloud. Both are associated with fluctuations in the local ionization rate. The first source is due to natural fluctuations in the ambient neutral density. The second is due to spatial variation of the incident RF power caused by scanning and heat control errors. In both cases the electron density fluctuations are induced by fluctuations in the ionization rate  $\nu(\underline{x})$ . In deriving the spectrum  $S_n(\underline{k})$  from the spectrum of the ionization rate fluctuations  $S_\nu(\underline{k})$ , we use two models. An upper limit on the value of  $S_n(\underline{k})$  can be found by ignoring self-absorption in the formation of the AIM cloud and assuming that

$$n(\underline{x}) = n_o e^{\nu(\underline{x})\tau} \quad (45)$$

where  $\tau$  is the pulse length of heater and  $n_o$  the initial electron density. A more realistic estimate can be found by considering the saturated case (i.e. including self-absorption) in which case

$$n(\underline{x}) \sim \nu^\alpha(\underline{x}) \quad (46)$$

with  $\alpha \approx 1 - 2$ . The spectrum  $S_n(\underline{k})$  is defined here in a normalized form, i.e.

$$S_n(\underline{k}) = \frac{1}{(2\pi)^3} \int \frac{\langle nn | \underline{x} \rangle e^{-i\vec{k} \cdot \underline{x}}}{\bar{n}^2} \quad (47)$$

so that

$$S_n(\underline{k}) = S_\nu(\underline{k}). \quad (48)$$

##### 4.1 Unsaturated Case

For the unsaturated case, we assume that the density at a point  $\underline{x}$ , is related to the ionization rate by eq. (46). We, furthermore, normalize  $\nu(\underline{x})$  to the pulse length  $\tau$ , so that  $\nu(\underline{x}) = \nu(\underline{x})\tau$ . As a result

$$\langle n(\underline{x})n(\underline{x}') \rangle = n_o^2 \langle e^{\nu(\underline{x})} e^{\nu(\underline{x}')} \rangle \quad (49)$$

Writing

$$\nu(\underline{x}) = \bar{\nu}(\underline{x}) + \delta\nu(\underline{x}) \quad (50)$$

we find

$$\langle n(\underline{x})n(\underline{x}') \rangle = n_o^2 e^{2\bar{\nu}(\underline{x})} \langle e^{\delta\nu(\underline{x})} e^{\delta\nu(\underline{x}')} \rangle \quad (51)$$

Assuming that

$$\langle \delta\nu(\underline{x}) \rangle = 0 \quad (52)$$

with

$$\langle e^{\delta\nu(\underline{x})} \rangle = \exp\left[\frac{1}{2} \langle \delta\nu^2(\underline{x}) \rangle\right] \quad (53)$$

we find that eq. (51) becomes

$$\langle n(\underline{x})n(\underline{x}') \rangle = n_o^2 e^{2\bar{\nu}(\underline{x})} e^{\langle \delta\nu^2 \rangle} \exp[\langle \delta\nu(\underline{x})\delta\nu(\underline{x}') \rangle] \quad (54)$$

As a result

$$\begin{aligned} \langle n(\underline{x})n(\underline{x}') \rangle &= \langle n^2(\underline{x}) \rangle \\ &= n_o^2 e^{2\bar{\nu}(\underline{x})} \exp[\langle \nu^2 \rangle] \times \exp[\langle \delta\nu(\underline{x})\delta\nu(\underline{x}') \rangle - 1] \end{aligned} \quad (55)$$

If we define

$$\begin{aligned} G(\underline{x} - \underline{x}') &\equiv \frac{\langle n(\underline{x})n(\underline{x}') \rangle - \langle n^2(\underline{x}) \rangle}{\langle n^2(\underline{x}) \rangle} = \\ &= \exp[\langle \delta\nu(\underline{x})\delta\nu(\underline{x}') \rangle - 1] \end{aligned} \quad (56)$$

the one dimensional electron density fluctuation spectrum, will be given by

$$S_n(k) = \frac{1}{2\pi} \int d\underline{x} e^{-i\vec{k} \cdot \underline{x}} G(\underline{x}) \quad (57)$$

or

$$S_n(k) = \frac{1}{2\pi} \int d\underline{x} e^{-i\vec{k} \cdot \underline{x}} \left[ e^{\langle \delta\nu\delta\nu | \underline{x} \rangle} - 1 \right] \quad (58)$$

Returning to dimensional variables and defining

$$\lambda \equiv \bar{\nu}\tau \quad (59)$$

and

$$S_\nu(\underline{x}) \equiv \frac{\langle \delta\nu\delta\nu | \underline{x} \rangle}{\bar{\nu}^2} = \sigma_\nu^2 F_\nu(\underline{x}) \quad (60)$$

with  $F_\nu(\underline{x} = 0) = 1$ ,  $F_\nu(\underline{x} \rightarrow \infty) = 0$ , eq. (58) becomes

$$S_n(k) = \frac{1}{2\pi} \int d\underline{x} e^{-i\vec{k} \cdot \underline{x}} \{ \exp[\lambda^2 \sigma_\nu^2 F_\nu(\underline{x})] - 1 \} \quad (61)$$

Notice that the value of  $\lambda^2 \sigma_\nu^2$  is the strength parameter, since  $F_\nu(\underline{x}) \leq 1$ . We distinguish the cases of weak,  $\lambda^2 \sigma_\nu^2 \ll 1$ , and strong,  $\lambda^2 \sigma_\nu^2 > 1$ , fluctuations.

#### 4.1.1 Weak fluctuations

We define as weak fluctuations if  $\lambda^2 \sigma_\nu^2 \ll 1$ . For example, if  $\lambda \approx 10$  weak fluctuations imply  $\frac{\delta \nu}{\nu} \leq .1$ . The practical applications require such as a condition. From eq. (61) we find

$$S_n(k) = \lambda^2 S_\nu(k) \quad (62)$$

Namely the spectral distribution of the density fluctuations will be similar to the ionization rate fluctuations, but their strength will increase by  $\lambda^2$ .

#### 4.1.2 Strong fluctuations

In this case  $\lambda^2 \sigma_\nu^2 \ll 1$  and

$$S_n(k) = \frac{1}{2\pi} \int dx e^{-ikx} \exp(\lambda^2 \sigma_\nu^2 F_\nu(x)) \quad (63)$$

In order to proceed we assume that

$$F_\nu(x) = \frac{b^2}{b^2 + x^2} \quad (64)$$

This is a Lorentzian spectrum with correlation length  $b$ . For  $F_\nu(x)$  given by eq. (64) the integral in eq. (61) can be performed, using the technique of stationary phase. We find

$$S_n(k) = \sqrt{\frac{\pi}{2k}} \exp\left(-\frac{k^2 b^2}{2\sigma_\nu^2 \lambda^2}\right) \quad (65)$$

The importance of this result lies in the fact that while for weak fluctuation there is essentially no spectral shift, for strong fluctuations there is a complete shift of the spectrum towards shorter wavelengths. The equivalent correlation length is smaller by  $\frac{1}{\sigma_\nu \lambda}$  and can be strongly reduced by adjusting  $\lambda$  to large values.

#### 4.2 Saturated Case

For the saturated case the density is connected to the ionization rate via eq. (46). In this case

$$\begin{aligned} \langle n(x)n(x') \rangle &= \langle \nu^\alpha(x') \nu^\alpha(x) \rangle = \\ &= \langle (\bar{\nu}(x) + \delta\nu(x))^\alpha (\bar{\nu}(x') + \delta\nu(x'))^\alpha \rangle = \\ &= (\bar{\nu}(x'))^{2\alpha} \left( 1 + \alpha^2 \frac{\langle \delta\nu(x') \delta\nu(x) \rangle}{\bar{\nu}^2} \right) \end{aligned} \quad (66)$$

From eq. (78) it is a straightforward to find that

$$S_n(k) = \alpha^2 S_\nu(k) \quad (67)$$

Namely the spectrum of the fluctuations remains the same but the amplitude is modified by the factor  $\alpha^2$ .

### 5. DEGRADATION OF AIM PERFORMANCE DUE TO FLUCTUATIONS IN THE LOCAL IONIZATION RATE

#### 5.1 Fluctuations of the Ambient Neutrals

The ionization rate is a linear function of the neutral density  $N$ . As a result, if all other factors are constant

$$S_\nu(k) = S_N(k) \quad (68)$$

Based on available measurements [Jursa, 1985] for the relevant altitude range of 60–80 km,  $S_N(k)$  can be described by an isotropic spectrum

$$S_N(|k|) = \frac{k_c}{k^4} \quad k > k_c \quad (69)$$

This corresponds to an isotropic spatial autocorrelation function  $\langle \delta N \delta N | r \rangle$  which for "small" distances has a linear decay with radius with scale length  $L_c = \frac{1}{4k_c}$ . The wavenumber spectrum of eq. (68) has a spectral index of  $p=4$ , i.e. decays as  $k^{-4}$ . The corresponding one dimensional wavenumber spectrum has a spectral index  $\alpha = p-2 = 2$ . From Fig. 2 and Table 1 we see that  $L_c \approx 4 \times 10^3$  km, giving  $k_c \approx 10^{-4}$  km $^{-1}$ .

For the AIM problem the maximum size of the inhomogeneities of interest corresponds to the minimum of either the Fresnel size  $L_F$ , which is of the order of a few kms, or of  $\Delta(\theta)$  defined by eq. (26). It is convenient to cast eq. (69) as

$$S_N(k) = A \frac{k_m}{k^4} \quad k > k_m \quad (70)$$

where

$$A \equiv \left( \frac{k_c}{k_m} \right) \quad (70a)$$

$$k_m = \max\left(\frac{1}{\Delta}, \frac{1}{L_F}\right) \quad (70b)$$

From eqs. (62) and (70)

$$S_\epsilon(k) = S_n(k) = A \lambda^2 \frac{k_m}{k^4} \quad k > k_m \quad (71)$$

For the linear profile eqs. (27) and (71) give

$$\begin{aligned} \delta \sigma_\phi^2 &= 2\pi^2 L \left( \ln \frac{1 + \cos \theta}{1 - \cos \theta} \right) (A \lambda^2) k_m \times \\ &\times \int_{k_m}^{\infty} \frac{dk}{k^3} = \end{aligned} \quad (72)$$

$$= 2\pi^2 L \left( \ln \frac{1 + \cos \theta}{1 - \cos \theta} \right) (A \lambda^2) \left( \frac{1}{2k_m} \right) =$$

$$= \pi^2 L \left( \ln \frac{1 + \cos \theta}{1 - \cos \theta} \right) (A \lambda^2) \frac{1}{k_m}$$

For the general AIM case  $\Delta < L_F$  and  $k_m = \frac{1}{\Delta}$ . As a result

$$\delta\sigma_\phi^2(\theta) = \pi^2 L \lambda^2 \left( \ln \frac{1 + \cos\theta}{1 - \cos\theta} \right) \frac{\Delta^2(\theta)}{L_c} \quad (73)$$

From eqs. (19) and (22) the signal loss will be given by

$$\mathcal{L} = -4.3\pi\lambda^2 (k_o L) (k_o \Delta(\theta)) \frac{\Delta(\theta)}{L_c} \times \ln \frac{1 + \cos\theta}{1 - \cos\theta} \text{ dB} \quad (74)$$

For a linear profile using the results of Section 3.1, eq. (74) becomes

$$\mathcal{L} = -1.1 \left( \frac{\lambda}{10} \right)^2 \left( \frac{L}{100m} \right)^3 \left( \frac{f}{10 \text{ MHz}} \right)^2 \left( \frac{4 \times 10^3 km}{L_c} \right) \times \left( \ln \frac{1 + \cos\theta}{1 - \cos\theta} \right) \sin^2\theta \cos^2\theta \text{ dB} \quad (75)$$

Equation (75) represents an upper limit in the fluctuations, since as it can be easily verified in this case the weak fluctuation limits is always valid. For the saturated case the loss will have the same form as in (75) but with  $\lambda$  replaced by  $\alpha$ . Since  $\alpha \approx 0(1)$  the loss rate will be totally negligible, in this case.

## 5.2 Effect of Heater Induced Fluctuations

### 5.2.1 Loss as a function of the density fluctuation level

Fluctuations in the electron density can also arise from the finite step of the heater during painting of the AIM cloud, as well as from any other heater phase errors [Short et al., 1990]. The analysis below addresses the constraints imposed by a heater step size. The analysis relevant to this case is the anisotropic analysis discussed in Section 3.2. Assuming that the heater induced fluctuations have a correlation length  $a$  in the ray direction equal to the step size  $a_o$  of the ionizing beam, we find that the power loss will be given from eqs. (19) and (44) as

$$\mathcal{L} = -2.1 \left[ \frac{\delta n/n_o}{.1} \right]^2 \left( \frac{f}{10 \text{ MHz}} \right)^2 \left( \frac{a_o}{10m} \right) \left( \frac{L}{100m} \right) \ln \left( \frac{1 + \cos\theta}{1 - \cos\theta} \right) \quad (76)$$

For a step size of 10m,  $f = 10 \text{ MHz}$  and  $L \approx 100m$ , the round trip loss will be 4-5 db for 10% density fluctuations. To achieve the same performance with 50 MHz the fluctuation level should be reduced to 2%. As discussed by Short et al. [1990] these can be easily achieved.

### 5.2.2 Loss as a function of heater power fluctuations

In this case the fluctuations will be anisotropic and we should use the equations derived in Section 2 to calculate the loss. We assume that the power fluctuation spectrum is given by

$$S_p(x) = \sigma_p^2 F_p \left( \frac{x}{a} \right) \quad (77)$$

and taking  $\nu \sim P$  we find

$$S_\nu(x) = \sigma_p^2 F_p \left( \frac{x}{a} \right) \quad (78)$$

For the case of weak fluctuations

$$\lambda^2 \sigma_p^2 \ll 1 \quad (79)$$

$$S_n(x) = \lambda^2 \sigma_p^2 F_p \left( \frac{x}{a} \right)$$

For a Gaussian spectrum  $F_p(\frac{x}{a})$ , in conjunction with eq. (19) gives

$$\mathcal{L} = -1.7 \left( \frac{\lambda}{10} \right)^2 \left( \frac{\sigma_p}{10^{-2}} \right) \left( \frac{a}{10m} \right) \left( \frac{L}{100m} \right) \left( \frac{f}{10 \text{ MHz}} \right)^2 \ln \frac{1 + \cos\theta}{1 + \sin\theta} \text{ dB} \quad (80)$$

Notice that  $\sigma_p = 10^{-2}$  corresponds to power fluctuations of 4-40 dB. According to Short et al. [1990] power fluctuations as low as -60 dB can be achieved. For the saturated case replacing  $\lambda$  by  $\alpha$  we find losses by at least an order of magnitude smaller.

### 5.2.3 Strong fluctuations

It is interesting to examine the upper limit of loss for the case of strong fluctuations in the sense of  $\lambda\sigma_p \gg 1$ . Such is the case if the heater power fluctuations are large (i.e. > 10 db). In this case using eq. (36) for  $\delta\sigma_\phi^2$ , with the spectrum given in eq. (66) we find

$$g(\theta) \approx \frac{1}{(\sigma_p \lambda)} (k_o b) (k_o L) \ln \left( \frac{1 + \cos\theta}{1 - \cos\theta} \right) \quad (81)$$

Notice that the correlation length has shifted to  $\frac{b}{\sigma_p \lambda}$  instead of  $b$ . The loss computed on the basis of eq. (91) is

$$\mathcal{L} = -8 \left( \frac{1}{\sigma_p} \right) \left( \frac{20}{\lambda} \right) \left( \frac{b}{10m} \right) \left( \frac{L}{100} \right) \ln \left( \frac{1 + \cos\theta}{1 - \cos\theta} \right) \text{ dB} \quad (82)$$

## REFERENCES

- Beckmann, P. and A. Spizzichino, "The Scattering of Electromagnetic Waves from Rough Surfaces", Pergamon Press, 1963.
- Dashen, R., Path Integrals for Waves in Random Media, Journal of Mathematical Physics, 148, 208-214, 1979.
- Drobot, A., K. Papadopoulos and R. Hirsch, "Artificial Ionization for Radar Applications", Presentation to Forecast II, US Airforce, 1987.
- Feynman, R. and D. Hibbs, "Quantum Mechanics and Path Integrals", McGraw-Hill, New York, 1965.
- Flatte, S.M., "Sound Transmission Through a Fluctuating Ocean" Cambridge University Press, Cambridge, 1979.
- Jursa, A. S., Handbook of Geophysics and the Space Environment, A. S. Jursa, Scientific Editor, Air Force Geophysics Laboratory, 1985.
- Ogilvie, T., "Scattering from Rough Surfaces", Pergamon Press, 1991.
- Rytov, S. M., Yu. A. Kravtsov and V. I. Tatarski, Principles of Statistical Radiophysics, Vol. 3, Springer Verlag, 1988.
- Short, R., P. Lallement, D. Papadopoulos, T. Wallace, A. Ali, P. Koert, R. Shanny, C. Stewart, A. Drobot, K. Tsang and P. Vitello, Physics Studies in Artificial Ionospheric Mirror (AIM) Related Phenomena, GL-TR-90-0038, Geophysics. Laboratory Air Force Systems Command, 1990.

Acknowledgement: Many discussions and careful critique of the work by Drs. N. Borisov, P. Sprangle, and Mr. T. Wallace are acknowledged and appreciated.

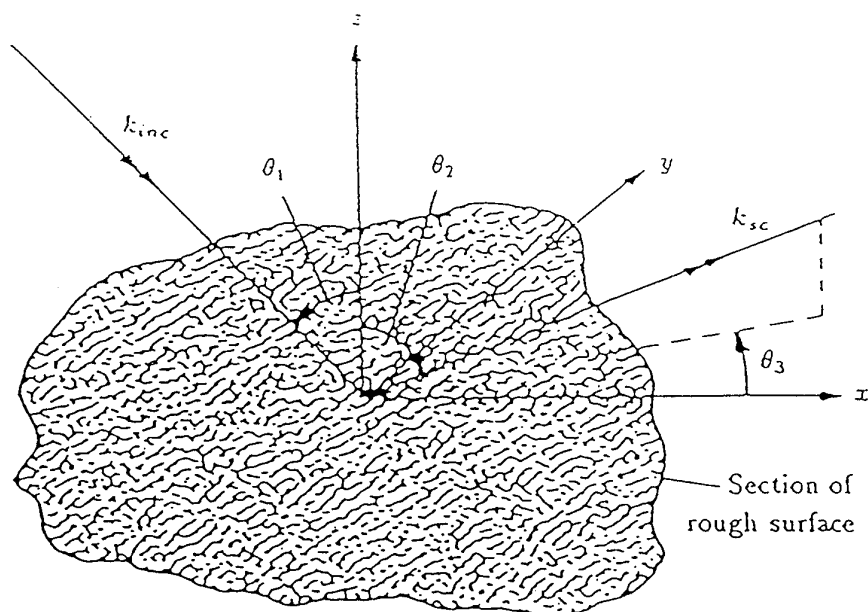


Figure 1 An AIM-based radar as a complement to a Skywave OTH radar.

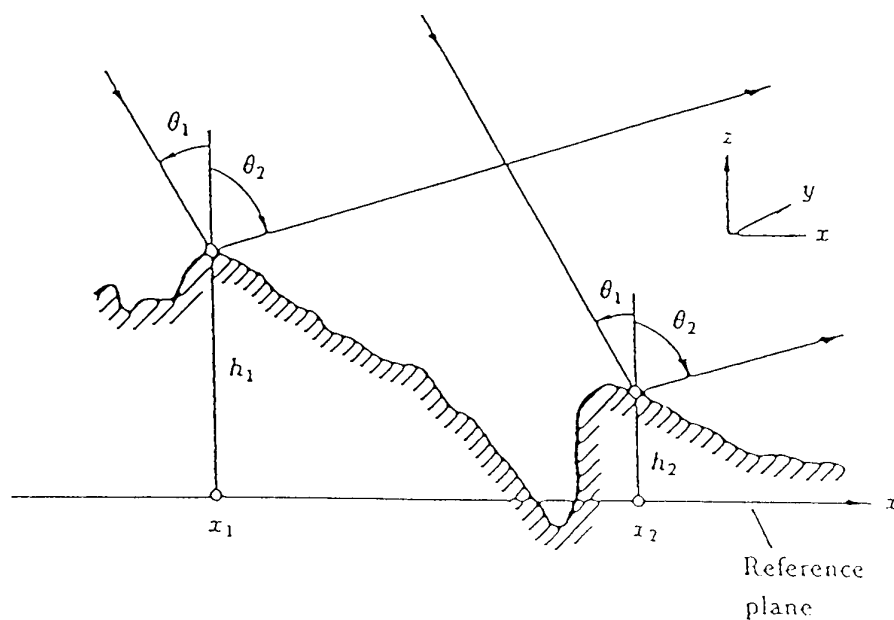


Figure 2 Decay of density correlations with distance at various altitudes in midlatitudes. [From Handbook of Geophysics and the Space Environment.]

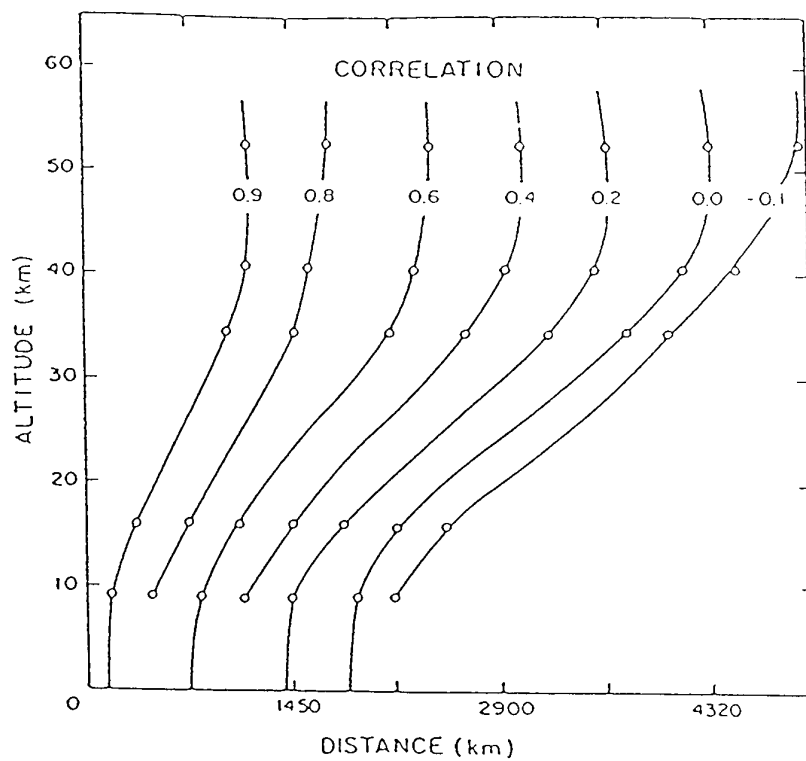


Figure 3.



Table 1. Estimated rms differences (% of mean) between densities at locations 90, 180, and 360 km apart during the midseason months in the tropics

Alt (km)	90	Jan 180 km	360	90	Apr 180 km	360	90	Jul 180 km	360	90	Oct 180 km	360
10	0.10	0.13	0.18	0.10	0.13	0.18	0.10	0.13	0.18	0.10	0.13	0.18
15	0.13	0.17	0.25	0.11	0.14	0.21	0.16	0.20	0.30	0.16	0.20	0.30
18	0.50	0.61	1.00	0.34	0.42	0.68	0.30	0.37	0.60	0.34	0.42	0.68
20	0.28	0.34	0.56	0.28	0.34	0.56	0.24	0.29	0.48	0.24	0.29	0.48
25	0.28	0.34	0.56	0.28	0.34	0.56	0.24	0.29	0.48	0.26	0.32	0.52
30	0.30	0.37	0.60	0.30	0.37	0.60	0.28	0.34	0.56	0.30	0.37	0.60
35	0.34	0.42	0.68	0.30	0.37	0.60	0.30	0.37	0.60	0.36	0.44	0.72
40	0.40	0.49	0.80	0.44	0.54	0.88	0.48	0.59	0.96	0.44	0.54	0.88
45	0.46	0.56	0.92	0.40	0.49	0.80	0.60	0.73	1.20	0.52	0.64	1.04
50	0.56	0.69	1.12	0.54	0.66	1.08	0.72	0.88	1.44	0.54	0.66	1.08
55	0.66	0.81	1.32	0.56	0.69	1.12	0.84	1.03	1.68	0.78	0.96	1.56
60	0.84	1.03	1.68	0.66	0.81	1.32	1.00	1.22	2.00	0.82	1.00	1.64

## DISCUSSION

**Discusser's name :** L. Bertel

**Comment/Question :**

What would be the effects of anisotropy on the performances of your system?

**Author/Presenter's reply :**

Physical mechanisms for creating anisotropic plasma effects have not been identified. For example, diffusion rates are much longer than projected plasma lifetimes, preventing the formulation of field-aligned irregularities. Therefore, anisotropic analysis has not been carried out.

**Discussor's name :** C. Goutelard

**Comment/Question :**

Les densités utilisés pour les chauffages dans les régions F sont de 0,1/0,2  $W/m^2$ . Vous devez utiliser ici de l'ordre de 45  $W/m^2$ . La puissance à utiliser pour le chauffage est beaucoup plus importante. Pouvez-vous nous dire si vous développez un système expérimental et donner ses caractéristiques?

**Translation :**

*The densities used for heating in the F regions are 0.1/0.2  $W/m^2$ . You should use of the order of 45  $W/m^2$  here. The power to be used for heating is much greater. Can you tell us if you are developing an experimental system and if so give its characteristics?*

**Author/Presenter's Reply :**

The plasma formulation is performed in the D-region at 70 km. Effective radiated power required at 425 MHz is 55 dbW. This requires a very large array (~1 to 2 km in diameter) with a large number of elements, 10 to 40 thousand. The practicality of the system is largely a function of cost and the technical feasibility of proving adequate phase control. From the stand-point of cost, any system with the area coverage and low frequency characteristics of AIM is expensive.

**Discussor's name :** P. Kossey

**Comment/Question :**

Have you considered the effects that variations in local meteorological conditions would have on the ability to focus the beam?

**Author/Presenter's reply :**

Meteorological variations across the array have been considered, and for conditions of heavy precipitation focusing problems can occur.

**Discussor's name :** U. Lammers

**Comment/Question :**

To obtain a sloping mirror you have to refocus in range. What does that imply in terms of the array size on the ground and its density of population? Do you have something like a grating lobe problem?

**Author/Presenter's reply :**

The range control is achieved by operating in the near-field at the heater array. This requires an array diameter of 1 to 2 km. The density is an issue of efficiency; the higher the density, the more power is focused on the ionization spot. Grating lobes are controlled by random placement of the elements.

# THE EFFECTS OF MULTIHOP HF PROPAGATION ON THE PERFORMANCE OF OTH BACKSCATTER RADARS

by

**J. Buchau & S. Dandekar**

Ionospheric Physics Laboratory  
Phillips Laboratory, Hanscom AFB, MA  
United States

**G.S. Sales**

University of Massachusetts Lowell  
Center for Atmospheric Research, Lowell  
450 Aiken Street, Lowell, Mass. 01701  
United States

**B. Weijers**

Rome Laboratory  
Hanscom AFB, MA  
United States

**D. Reynolds**

Radex Corporation  
Bedford, MA  
United States

## SUMMARY

Analysis of approximately one years data from an operational OTH radar shows that equatorial clutter, originating in the ionosphere in regions up to 14,000 km from the radar, directly impacts the radar's performance. The radio wave propagation to these regions often involve from three or more ground hops depending on the radar's azimuth. These phenomena are important to all OTH radar systems in that great circle paths always cross the magnetic equator.

The special data processing developed for this program uses both the long range (to 8000 nm) wideband (6 to 28 MHz) backscatter ionograms made routinely at selected azimuths and the radar's amplitude, range and Doppler data format, measuring the frequency of occurrence, location and intensity of the clutter as a function of time and azimuth. These data indicate that intense ionospheric irregularities connected with the nighttime equatorial activity produce sufficient Doppler spread scattered energy that directly affects the performance of the radar. With the Parametric Ionospheric Model developed at the Phillips Laboratory and numerical ray tracing the specific interaction regions for the radar signal and the ionospheric irregularities are shown and an explanation for the observed temporal behavior is proposed. Several mechanisms for Doppler spreading of the clutter signal are also reviewed.

## INTRODUCTION

The performance of high power HF radar systems (Over-the-Horizon - OTH) depends on the detectability of a backscattered target signal relative to the background noise level. These radar systems all make use of the fact that the relatively weak received signal from moving targets are shifted in frequency and with Doppler frequency spectrum processing, the target return becomes visible relative to the very strong unshifted backscatter from the ground (sea or land) clutter. Under ideal conditions the noise level, against which the target must be detected, is set by the ambient HF atmospheric noise level, to a great degree, determined by remote and local thunderstorm activity.

However, when the ionosphere, somewhere along the path of the radar signal, is disturbed, some significant fraction of the radar energy is backscattered and appears as wideband noise (known as ionospheric spread clutter), degrading the performance of the radar. For these radars, the Doppler frequency processing introduces a range ambiguity, which means that this wideband ionospheric clutter, often originating at great distances from the radar, is aliased into the primary coverage region, typically around 2000 km from the radar. The active nighttime equatorial ionosphere is often intercepted by the radar signal via multihop propagation at some point along the great circle path.

This paper first looks at the structure of this clutter as seen by the radar itself and by the wideband swept frequency backscatter sounder that supports the radar operation. The advantage of the backscatter sounder is that the continuous swept frequency waveform does not suffer range folding and the location of ionospheric clutter can be determined unambiguously. The sources of this ionospheric clutter and the mechanisms for returning the scattered energy back to the radar are investigated. In the equatorial region, which includes the anomaly regions lying north and south of the magnetic equator, the magnetic dip angles are relatively small and it is not possible for the ray path to achieve orthogonality with the field aligned F-region irregularities. Scatter mechanisms are proposed that can account for this clutter.

## RADAR PERFORMANCE

The primary source of radar data used here is from the USAF OTH system located in Maine (ECRS). Two types of data are used for this study. First, the Amplitude/Range/Doppler (ARD) display (Figure 1) which shows the radar backscattered signal amplitude as a function of range and for each range bin a Doppler frequency spectrum is generated with frequency limits of  $+WRF/2$  to  $-WRF/2$ . Typically, the waveform repetition frequency (WRF) is around 30 to 40 Hz, with a range ambiguity of 5000 km and 3750 km, respectively. From Maine, the distance to the equatorial regions is a function of the radar look direction, nominally, around 6000 to 10,000 km. These distances are to the equator and the southern anomaly region and reflect the fact, as discussed below, that the northern anomaly region seems to play little role in this clutter problem. The range to these likely clutter sources is beyond the nominal range coverage of the radar, usually defined in terms of a one hop propagation mode. However, range folding often causes the long range (two and three hop modes) clutter sources to be superimposed on the one hop target signal. Unless a low WRF waveform (10 Hz) is used by the radar, it is impossible to unscramble the range folding without supporting measurements such as the backscatter sounder data.

Combining a sequence of these ARD data, as the radar scans in azimuth, and using a qualitative measure of radar performance, a map of performance (Figure 2) shows the encroachment of the equatorial clutter into the coverage as the radar looks into the equatorial region at the post sunset times even while the radar site and local ionosphere is still illuminated by the sun. In the sectors indicated by the shaded areas, the radar performance has been degraded by spread multiplicative noise from backscatter by equatorial ionospheric irregularities. This phenomena progresses from east to west following the sunset terminator and often recovering sometime after midnight and certainly after sunrise in the equatorial region.

## BACKSCATTER IONOGRAMS

As part of this program, the backscatter sounders at the site are operated periodically in a long range mode (sweep rate is 25 kHz/s) with a maximum of 15,000 km. This permits an unambiguous view of the clutter sources out beyond the southern anomaly regions. An apparent feature on these ionograms that seems to correspond to the occurrence of spread Doppler clutter (the backscatter ionogram operating in the swept frequency mode cannot be used to determine the Doppler characteristics of any backscattered signal) are range independent traces across a large frequency band of 10 MHz or more (Figure 3).

Approximately one years data has been scaled and the location and extent of these traces has been plotted against local time at the equator in the particular sounder look direction (Figure 4). The predominant number of observations, from radar Segments II and III representing the southern  $120^\circ$  of the radar coverage, lies in the southern hemisphere between  $20^\circ$  and  $40^\circ$  dip latitude, beginning around sunset and apparently disappearing almost completely after 0200 LT. Around local midnight there is evidence of clutter originating at the magnetic equator ( $0^\circ$  dip angle). Similar traces in the Segment I observations seem lie around the northern anomaly but this appears to be associated with a midlatitude ionospheric upwelling that is discussed later.

Ignoring the time variations, Figure 5 shows the geographic distribution of these clutter traces on a global map, predominantly in the vicinity of the southern anomaly and sometimes beyond.

### BACKSCATTER IONOGRAM SIMULATION USING PARAMETRIC IONOSPHERIC MODEL (PIM)

To investigate the sources of these BSI clutter traces, extensive ray tracing in an ionospheric electron density model that realistically describes the magnetic equatorial region, was carried out. For this purpose PIM (Parametric Ionospheric Model) was chosen and sample profiles at 20 UT, 00 UT and 04 UT from the radar to the southern anomaly region, in a direction of  $180^\circ\text{T}$  were used with a ray tracing code to produce a set of rays at 20 MHz are shown in Figure 6. In Figure 7, with the same 00 UT profile, ray tracing at three frequencies; 12, 16 and 20 MHz was carried out. It is possible to see the formation of these clutter traces after the two hop mode skips over the equatorial "dome".

The sequence of synthesized backscatter ionograms using this technique, with 0.5 MHz frequency steps and  $0.5^\circ$  elevation steps, are shown in Figure 8 for the interval from 20 UT to 10 UT in 2 hour intervals for an azimuth of  $180^\circ\text{T}$  and the month of October. Figure 9 shows the a sequence of actual backscatter ionograms for the same period.

A similar analysis is carried out for a radar bearing of  $75^\circ\text{T}$  (Segment I). Figures 10, 11 and 12 show the same sequence as for the  $180^\circ\text{T}$  bearing. A very similar behavior is observed here except that the source of these traces is a domed structure that forms after sunset as the radar looks into the east. With the sun setting near the radar a minimum forms east of the radar but as the ray path moves southward toward the equator, even after sunset, the peak electron density increases. This produces a dome similar to the equatorial dome, but with a very different origin. This sunset dome produces similar ray bundling as for the equatorial dome. This appears to be the source of the Segment I clutter traces as seen on the backscatter ionograms and but probably does not represent a source of spread radar clutter. This subject is discussed in more detail below.

### RADAR CLUTTER SOURCES

As indicated earlier, it is easy to show that the radar signals propagating to long ranges in the southern hemisphere, within the equatorial and anomaly regions, cannot achieve orthogonality with field aligned ionospheric irregularities. Orthogonal backscatter is a relatively strong mode when it is present. Several alternative mechanisms are being considered, all of which involve specular scatter; orthogonal scatter is a special case of specular scatter. Specular scatter is defined as those scattering angles that make the same angle with the earth's magnetic field direction as the incoming ray at the scattering volume in the ionosphere. The locus of these scattering angles forms a cone with the magnetic field along the axis and the apex angle equal to the angle between the field and the incoming ray direction (Figure 13).

The width of the cone is relatively narrow, depending on the electron density correlation scale lengths along and across the magnetic field. For typical; scales of  $10^5$  to  $10^6$  m along the field and  $10^3$  m across the field the width of the cone is only one or two degrees. The specular scatter cone always includes the forward scatter component which is the strongest component in the scattering pattern.

Several theories for the generation of spread clutter involve the strong forward scatter component which uses the same propagation mode back to the radar after a ground scatter. The difficulty with the simple forward scatter mode is the small Doppler spreading associated with this mode, though some of the theories invoke strong phase fluctuations that compensate for the inherent small Doppler frequency spreading.

In other directions around the specular scatter cone, the amplitude of the scattered signal is relatively uniform, though smaller than the forward direction. On the other hand the Doppler spreading, particularly in the back edge of the scatter cone, is considerably larger than in the forward edge (direction) for the same irregularity random velocities. All directions around the scatter cone contribute to the total returned signal and the observed spectra are represented as the integral over all directions. These resultant spectra looks very much like the observed ARD spectra (Figure 14).

### SUMMARY

Although most OTH radar systems operate to detect moving targets at ranges from 1000 to 3000 km, within the one hop coverage area, the performance of the radar in terms of the detectability of small targets depends on the ray path through the ionosphere after several ground reflections where the path crosses the magnetic equator and sometimes the remote auroral region. With range folding, all of these sources of spread radar clutter affect the noise level, often over a significant portion of the Doppler spectrum, against which the target must be detected, essentially reducing the visibility of the desired target.

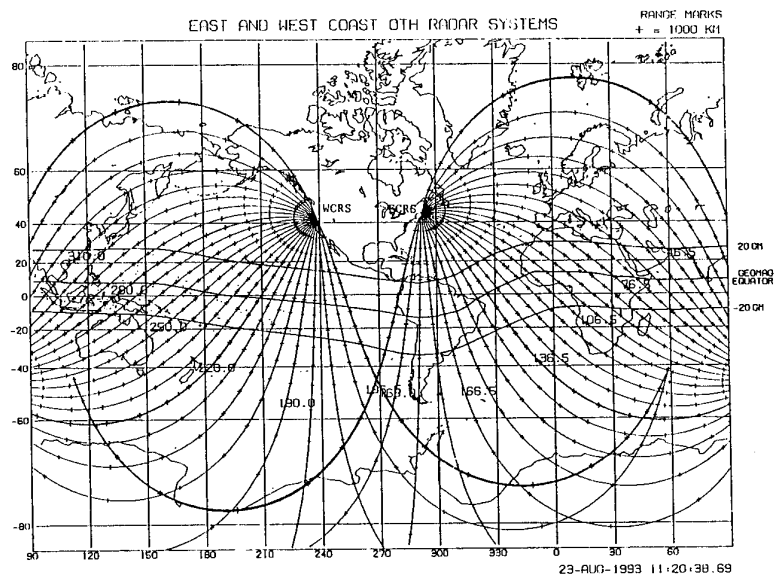


Figure 1. Look directions of the East and West Coast radar systems.

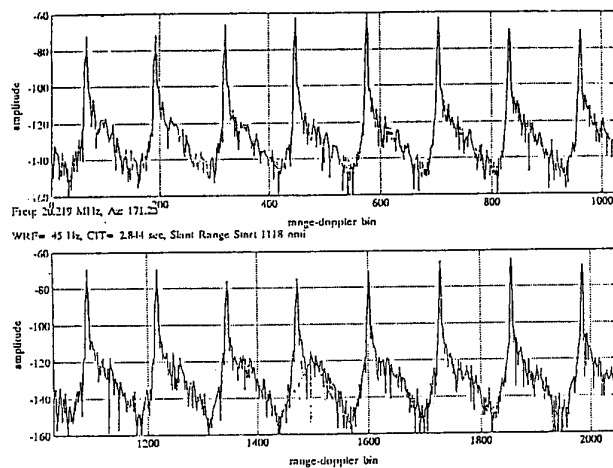


Figure 2. ARD data sample showing ionospheric clutter.

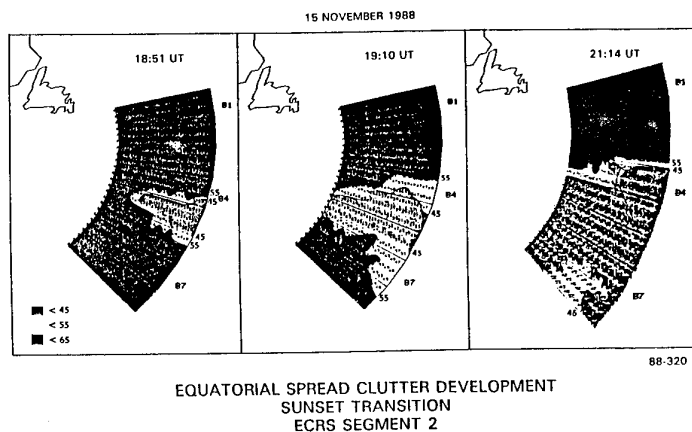


Figure 3. Sequence of clutter to noise ratio azimuthal maps showing clutter encroachment into the radar coverage.

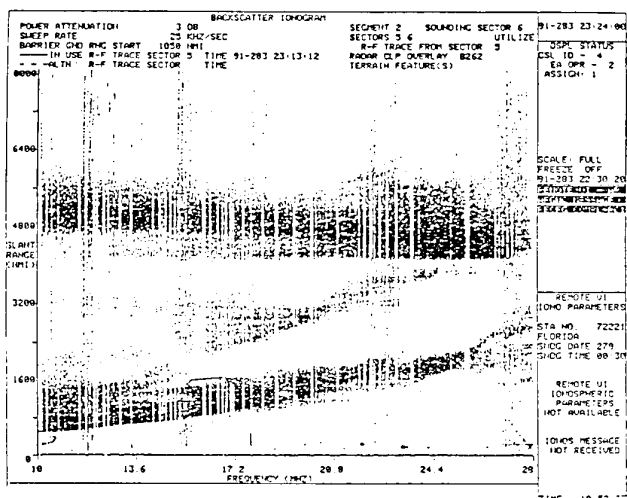


Figure 4. Sample backscatter ionogram clutter traces.

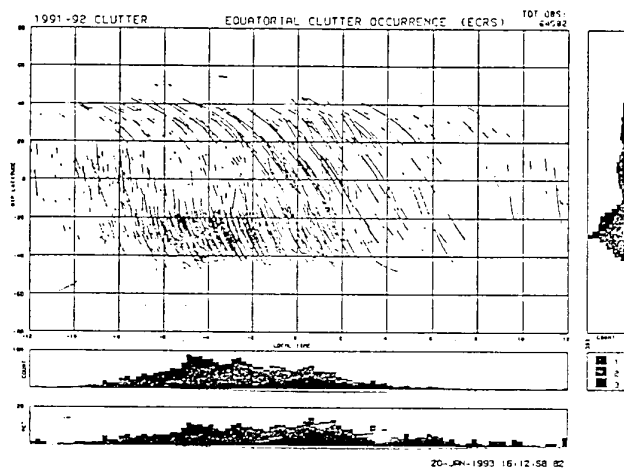


Figure 5. Magnetic dip angle vs local time for backscatter ionogram traces.

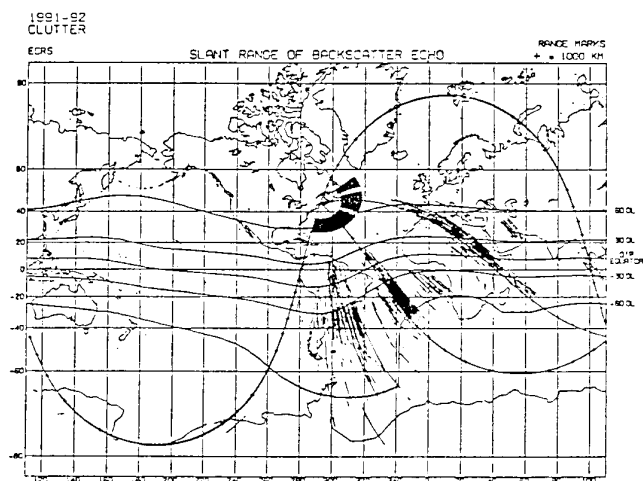


Figure 6. Geographical distribution of backscatter ionogram clutter traces.

OCT 15, 92 SSN=100

AZIM=180

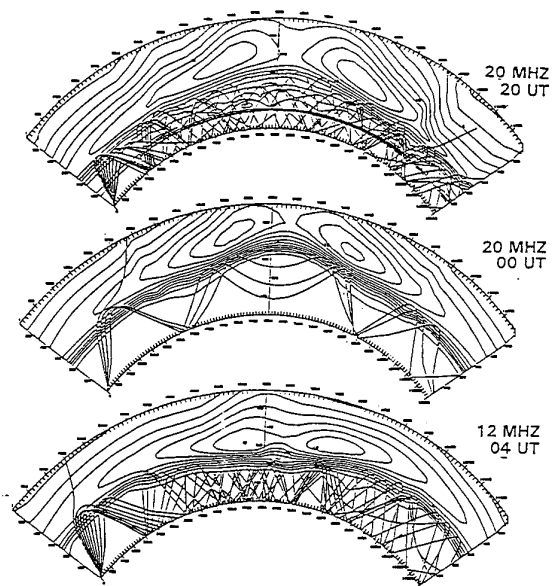


Figure 7. Electron density profiles using PIM for 20, 00, and 04 UT at 180°T with 20 MHz ray tracing.

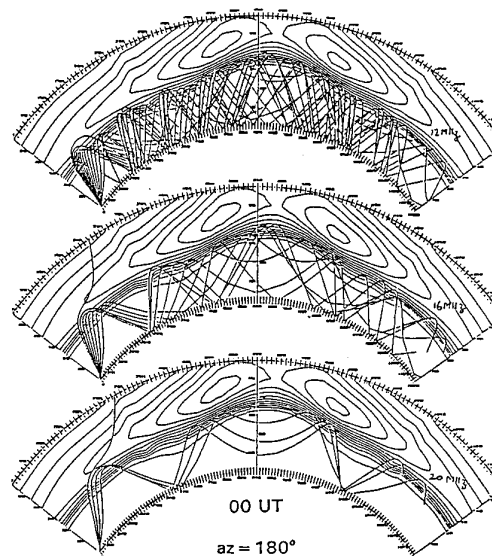


Figure 8. Electron density profiles using PIM at 00 UT with ray tracing at 12, 16 and 20 MHz.

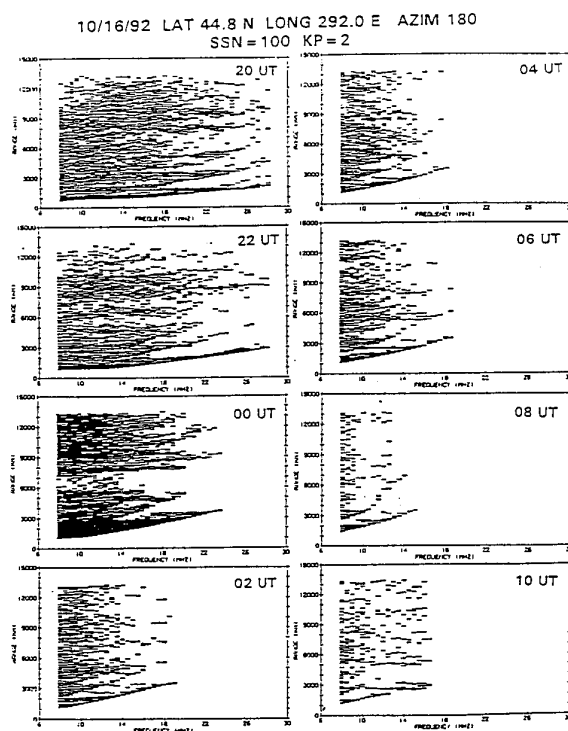
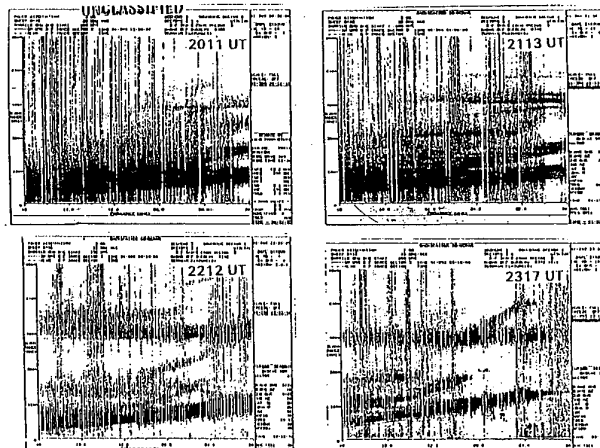


Figure 9. Synthesized backscatter ionogram for 180°T.

BACKSCATTER IONOGRAMS SEGMENT 3 SECTOR 4  
OCT-NOV 1991



BACKSCATTER IONOGRAMS SEGMENT 3 SECTOR 4  
OCT-NOV 1991

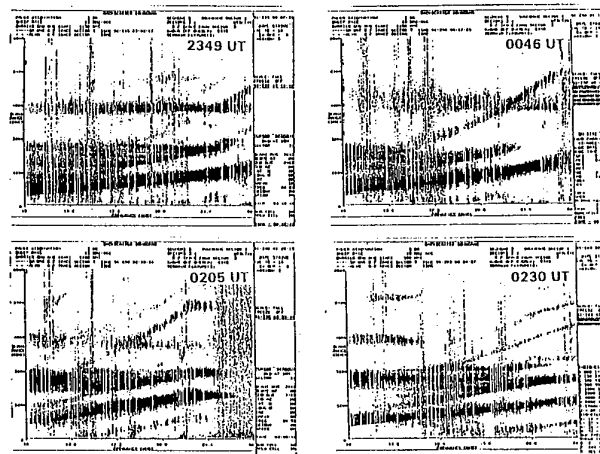


Figure 10. Measured backscatter ionogram for 180°T

SSN = 100

AZIM = 75

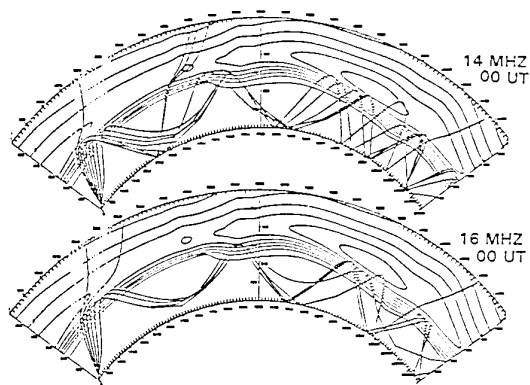
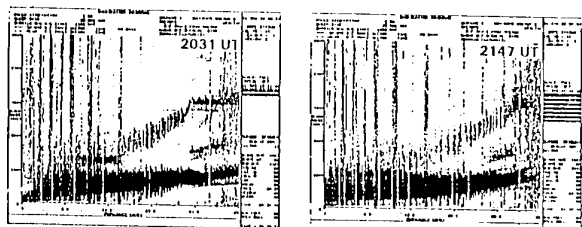
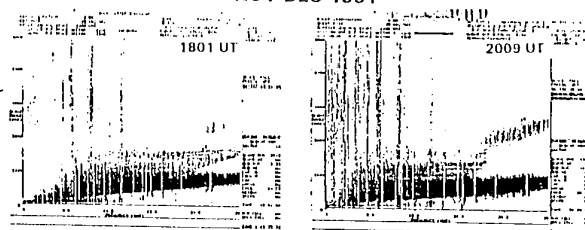


Figure 11. Electron density profiles from PIM at 00 UT with ray tracings at 12, 16 and 20 MHz for 75°T.

BACKSCATTER IONOGRAMS SEGMENT 1 SECTOR 8  
NOV-DEC 1991



BACKSCATTER IONOGRAMS SEGMENT 1 SECTOR 8  
NOV-DEC 1991

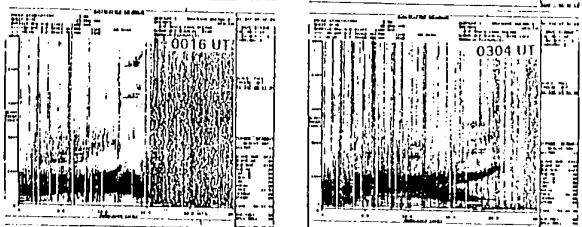
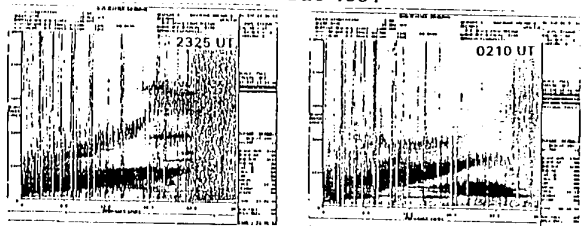


Figure 13. Measured ECRS backscatter ionogram for an azimuth of 75°T.

10/16/92 LAT 44.8 N LONG 292.0 E AZIM 75  
SSN = 100 KP = 2

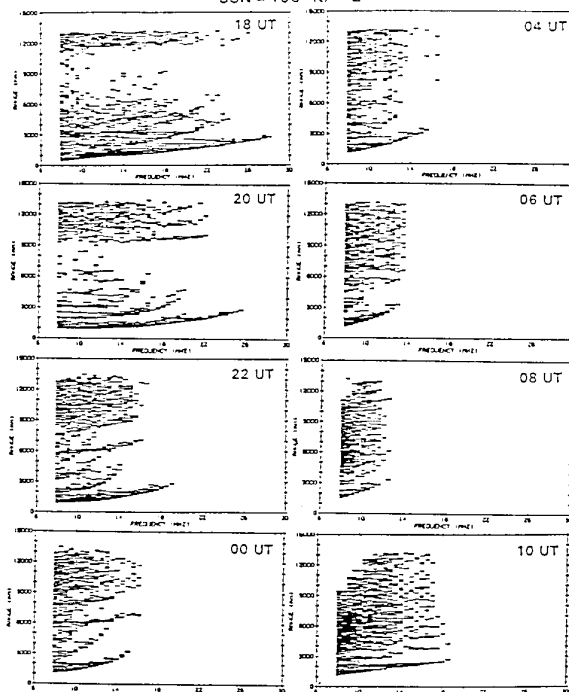


Figure 12. Synthesized backscatter ionogram for 75°T.

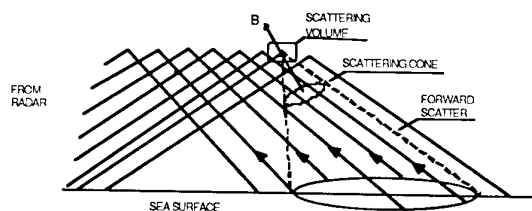


Figure 14. Illustrative volumetric scattering showing specular cone pattern and return path to OTH radar.

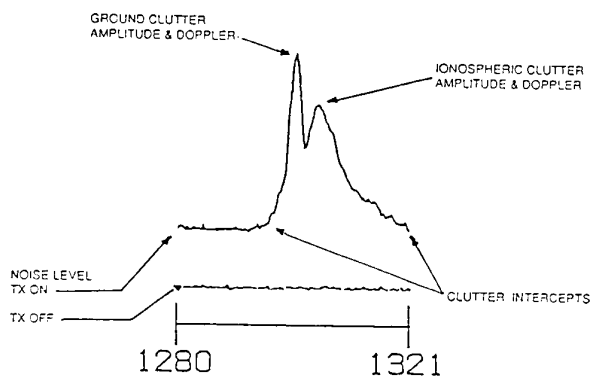


Figure 15. Simulated ARD spectrum;  $v_r = 100$  m/s.



## DISCUSSION

**Discussor's name :** J. Aarons

**Comment/Question :**

I believe clutter will be considerably reduced in years of low solar flux.

Question : measured irregularity scale sizes range from 18 cm to several kilometers. Aren't you affected predominantly by irregularities with spatial wavelengths corresponding to half the probing signal wavelength?

**Author/Presenter's reply :**

Our scattering theory assumes a spectrum of irregularity scales from kilometers to meters following  $k^{-2}$  and  $k^{-4}$  power laws. The radar selects the appropriate scale for maximum scatter according to the Bragg condition.

**Discussor's name :** P. S. Cannon

**Comment/Question :**

1. When looking north into the auroral zone from such a radar the Doppler Clutter Spectrum is often asymmetric. Do you see this asymmetry when you look into the equatorial region, and if you do can you comment on this?
2. Were your backscatter ionograms synthesised using an analytic or numerical ray tracing package? How long did it take to synthesise an ionogram?

**Author/Presenter's reply :**

1. The spread clutter spectra looking north towards the auroral region are almost indistinguishable from the equatorial clutter in terms of amplitude, Doppler spread and asymmetry.
2. We use numerical-ray tracing and it takes minutes to produce one ionogram.

# COMPORTEMENT TEMPOREL ET SPATIAL DES TRAJETS MULTIPLES DANS LES PROPAGATIONS IONOSPHERIQUES EN INCIDENCE OBLIQUE MESURE FRACTALE DES PERTURBATIONS

C. GOUTELARD, J. CARATORI, L. BARTHES

LETTI - Université Paris-Sud - 91405 ORSAY Cédex

## I. - GENERALITES -

La propagation des ondes électromagnétiques dans l'ionosphère est, on le sait, complexe, l'anisotropie et l'inhomogénéité introduisant des trajets multiples et la non stationarité des effets doppler. Les modèles ionosphériques habituellement utilisés permettent de rendre compte des trajets multiples et des décalages doppler. Selon ces modèles, basés sur des tracés de rayons, il apparaît, pour chaque trajet, un seul triplet (amplitude, doppler, temps de propagation) qui permet de tracer des diagrammes simples.

L'observation expérimentale montre que, si l'on retrouve effectivement les signatures prévues dans la théorie classique des tracés de rayons pour les signaux de grande amplitude, on observe, avec des systèmes de mesure de grande sensibilité, des signaux de faible amplitude qui semblent traduire l'existence de propagations diffuses.

Les résultats d'une étude en sondage oblique bistatique et d'une étude en sondage par rétrodiffusion donnés dans cette présentation, montrent l'apparition d'effets du second ordre. Une méthode de caractérisation de ces effets est proposée par l'introduction de la mesure de la dimension fractale des fonctions de diffusion, obtenues par une méthode d'analyse spectrale haute résolution.

## II. - ETUDE EN SONDAGE OBLIQUE BISTATIQUE -

L'inhomogénéité de l'ionosphère est connue depuis longtemps et, très tôt, les inhomogénéités à grande échelle telles que les transitions jour-nuit, les perturbations ionosphériques itinérantes, ou les instabilités de plasma dans les zones équatoriales ou polaires ont été étudiées. Des perturbations à plus petite échelle apparaissent en permanence et modifient les caractéristiques de la propagation. Afin de mettre en évidence ces effets, qui seront

dénommés du second ordre par la suite, on a mené une première étude en sondage oblique bistatique.

L'expérience a consisté à utiliser (figure 1) deux stations d'émission synchrones, STUDIO 1 et STUDIO 2, distantes de 17,5 km et une station de réception, STUDIO 3, située à 450 km ou 1 500 km des deux stations d'émission. On obtient ainsi deux géométries de propagation très voisines dont les points milieux sont théoriquement distants de 8,75 km.

Afin de pouvoir analyser les deux propagations simultanément, les fréquences d'émission des stations STUDIO 1 et STUDIO 2 sont séparées de 5Hz.

Une première série de mesures a été effectuée en mesurant la fonction de diffusion du canal qui représente le diagramme (amplitude, temps de propagation, doppler) de la réponse impulsionnelle. La figure 2 donne l'exemple d'un diagramme où apparaissent nettement trois modes de propagation différents. La qualité de ces résultats, obtenus à partir d'un signal codé, permet de voir autour des pics centraux de chaque mode attribuable à sa partie cohérente, des signatures d'amplitude plus faible qui mettent en évidence une partie non cohérente caractérisée par un étalement temporel et un étalement doppler que ne prévoit pas la théorie des tracés de rayons. On peut noter que ces parties diffuses sont à des niveaux très inférieurs à celui du pic central.

Ces phénomènes, observables sur les fonctions de diffusion, se retrouvent dans les expériences effectuées en utilisant des émissions cohérentes d'ondes sinusoïdales émises avec un décalage de 5Hz à partir des stations STUDIO 1 et STUDIO 2. La comparaison des signaux reçus simultanément à STUDIO 3 permet de mesurer la cohérence spatiale de l'ionosphère. La comparaison des spectres obtenus est présentée, sous la forme dont la figure 3 donne

un exemple, pour une configuration d'ionosphère calme le 10 décembre 1991 sur une liaison de 1 500 km à  $f_o = 11,363\text{MHz}$ .

La figure 3a donne l'évolution temporelle des deux spectres reçus, la figure 3b la répartition des amplitudes des voies doppler correspondantes, qui montre une décorrélation assez forte, et la figure 3c la variation des fréquences doppler des deux voies d'amplitude maximale de chacun des spectres, et qui révèle une excellente corrélation. Les variations régulières du doppler révèlent la présence d'une perturbation ionosphérique itinérante.

L'analyse a donc porté sur la corrélation des dopplers et des amplitudes sur chaque composante des spectres. On a, pour cela, rangé dans chaque spectre les composantes par amplitudes de valeurs décroissantes. On a appelé  $A_{ij}$  ces amplitudes où  $i = 1$  pour la station STUDIO 1 et  $i = 2$  pour la station STUDIO 2, et le rangement par ordre respectant la loi :

$$A_{i1} > A_{i2} > A_{i3} \dots A_{ij} > A_{ij+1}$$

On a appelé  $F_{ij}$  la fréquence doppler de la composante d'amplitude  $A_{ij}$ .

Les diagrammes ( $F_{1j}$ ,  $F_{2j}$ ) et ( $A_{1j}$ ,  $A_{2j}$ ) ont été tracés, ce qui a permis d'établir la corrélation entre les fréquences doppler  $F_{ij}$  et les amplitudes  $A_{ij}$ .

La figure 4 représente les graphes obtenus pour l'observation du 10 Décembre 1991 ( voir figure 3 ) et pour les valeurs  $j = 1, 2, 4, 6, 8, 10$ . Ceux-ci montrent l'évolution de la corrélation sur les fréquences doppler et l'absence de corrélation sur les amplitudes.

On a caractérisé les amplitudes des composantes spectrales par leurs valeurs moyennes établies sur les deux spectres par la relation :

$$\bar{A}_j = \frac{1}{N} \sum_{k=1}^N [A_{(1,j,k)} + A_{(2,j,k)}] \quad (1)$$

où  $k$  indique le  $k$ ème des  $N$  spectres mesurés dans l'enregistrement.

Les graphes de la figure 4 montrent qu'en présence d'une perturbation itinérante à grande échelle les fréquences doppler des composantes spectrales de grande amplitude sont très fortement corrélées ( $j = 1, 2, 3, 4$ ) puis que la corrélation décroît progressivement pour atteindre une décorrélation totale pour les composantes de bruit ( $j = 10$ );

En ce qui concerne les amplitudes, on peut constater que la dispersion des points traduit une mauvaise corrélation, même pour les amplitudes de valeurs élevées.

Pour mesurer la corrélation des fréquences doppler et des amplitudes, on a tracé pour chaque graphe la droite de régression obtenue par la méthode des moindres carrés :

$$y = Ax + B$$

en imposant pour les graphes d'amplitude  $B = 0$ .

On a alors déterminé, pour chaque cas, le coefficient de corrélation  $R$  des points obtenus, en notant  $R_f$  les coefficients de corrélation des fréquences doppler et  $R_A$  ceux relatifs à l'amplitude. Les valeurs de  $A$ ,  $B$  et  $R$  sont indiquées pour chaque enregistrement.

La figure 5 représente les mesures et les graphes tracés pour  $j = 1, 2, 4, 6, 8, 10$  et pour une période perturbée. On peut noter que les amplitudes demeurent décorréliées et que les fréquences doppler le sont également. Ceci indique que les trajectoires STUDIO 1 et STUDIO 2 à STUDIO 3 rencontrent des zones ionosphériques où les conditions sont différentes, ce qui traduit, compte tenu de la distance séparant les points milieu des liaisons - 8,75 km - l'existence de perturbations à très petite échelle.

On peut noter que, pour les périodes non perturbées (figure 4), la corrélation pour les fréquences doppler est toujours très bonne pour les composantes de forte amplitude, qu'elle s'altère pour les composantes de faible amplitude et que la décorrélation est totale pour les composantes de bruit.

Les amplitudes sont toujours mal corrélées. Les composantes de grande amplitude correspondent à des trajets principaux donnés par les modèles classiques de l'ionosphère, ce qui explique la cohérence doppler. La décorrélation sur les amplitudes peut s'interpréter par le fait que les amplitudes résultent de la sommation des composantes magnéto-ioniques et des éventuels modes à fréquences doppler identiques de la propagation. L'amplitude de la composante spectrale est donc le module de grandeurs complexes dont les arguments, définis modulo  $2\pi$ , se décorrélient très rapidement d'un spectre à l'autre, ne serait-ce qu'à cause de la différence des distances orthodromiques des liaisons.

La figure 6 montre les variations du coefficient de corrélation des fréquences doppler en fonction de l'amplitude normalisée des composantes. On peut constater que dans les configurations ionosphère non perturbée, le coefficient de corrélation est élevé sur les premières composantes tandis que dans les cas

d'ionosphère perturbée, la corrélation demeure toujours faible.

Ces résultats traduisent le fait que, sur deux trajectoires voisines pour lesquelles les points milieux sont théoriquement distants de 8,75 km, la corrélation des rayons principaux demeure en général forte. Cependant, lors de l'apparition de perturbations, la décorrélation constatée prouve l'existence de perturbations à petite échelle. Les composantes de faible amplitude qui apparaissent indiquent que des phénomènes, attribuables à des processus de diffusion dus à des instabilités locales, produisent des trajectoires fortement décorrélées. Ces trajectoires sont mises en évidence dans les enregistrements effectués grâce à la grande dynamique des systèmes de mesure. Pour analyser plus finement ces phénomènes, il a été fait appel au sondeur à rétrodiffusion installé à la station STUDIO 1. Celle-ci est dotée d'une grande sensibilité, et a permis de mettre en évidence les dimensions spatiales de ces irrégularités.

### **III. - ETUDE EN SONDAGE OBLIQUE PAR RETRODIFFUSION -**

#### **III.1. Performances de la station STUDIO.**

Le LETTI a implanté dans le sud de Paris une station de sondage par rétrodiffusion qui possède une grande sensibilité. Le système, dont le principe a été décrit en 1978 [1], a été améliorée et permet de faire actuellement des mesures de grande sensibilité.

La station monostatique repose sur un principe d'émission-réception alternées permettant, par l'utilisation de systèmes de codage particuliers, d'obtenir une protection importante sur le brouillage et le bruit.

La figure 7 donne un exemple des résultats obtenus. La figure 7a donne la réponse impulsionnelle du canal qui montre la présence de nombreux modes de propagation avec une dynamique affichée importante. La zone d'observation est limitée, dans cet exemple, à 7 650 km. La figure 7b montre l'évolution de la position des échos de rétrodiffusion en fonction du temps. Ce diagramme représente, avec le code de couleur utilisé dans la figure 7a, l'évolution des échos de rétrodiffusion pendant une période d'observation d'environ 30 minutes. On peut noter, compte tenu de l'échelle logarithmique utilisée, l'évolution rapide de certains échos de faible amplitude. La figure 7c donne une représentation de la fonction de diffusion qui est obtenue par la transformée de Fourier effectuée selon le temps courant de la réponse impulsionnelle du canal. Elle

donne, dans une représentation tridimensionnelle, l'amplitude des composantes spectrales en fonction de leur fréquence doppler et de leur temps de propagation. Dans l'exemple présenté, l'étalement doppler atteint une dynamique voisine de  $\pm 2,5$ Hz avec une résolution de 20mHz. Ces résultats ont été obtenus avec une puissance d'émission de 300W, chaque réponse impulsionnelle étant acquise avec un temps de traitement de 200 ms.

Cette grande sensibilité est illustrée par l'enregistrement de la figure 8 qui représente la réponse impulsionnelle similaire à la figure 7a et l'évolution temporelle similaire à la figure 7b pour une puissance d'émission de 100 mW. Ces deux enregistrements révèlent les possibilités de la station STUDIO et montrent que la qualité des mesures permet une étude fine de l'ionosphère.

Les résultats présentés sont obtenus par un procédé particulier de codage et de traitement du signal qui nécessite une puissance de calcul de 250 millions d'opérations par seconde. La fonction de diffusion, calculée en temps réel sur 65536 pixels, est révélatrice des analyses qui peuvent être faites.

La figure 9 montre un détail de fonction de diffusion obtenue par le système STUDIO. On y voit apparaître un premier écho obtenu par une réflexion sur la région E qui révèle les raies de diffraction de BRAGG, obtenues par une rétrodiffusion sur la mer. Un second écho, dû à la région F, apparaît à une distance voisine de 2 000 km. La structure de cet écho est conforme à la théorie qui avait été présentée en 1965 [2] et dans laquelle l'existence d'un rayon mixte avait été, à l'époque, prévue. Une perturbation ionosphérique itinérante est révélée par un décalage doppler qui apparaît à une distance de 1 500 km.

La signature spectrale de la région F - théoriquement de la région E également mais qui est peu visible en pratique - peut être vue à partir des schémas de la figure 10 extraite de [2]. Pour un temps de propagation donné, trois trajectoires d'un mode magnéto-ionique ont le même temps de propagation selon qu'elles empruntent le rayon bas à l'aller et bas au retour, haut à l'aller et bas au retour ou inversement, haut à l'aller et haut au retour. Sur les figures 10a et 10b, les distances atteintes au sol sont respectivement  $D_1$ ,  $D_2$ ,  $D_3$ . Le mode haut-bas a été appelé rayon mixte. L'effet de champ magnétique terrestre et de la dépolarisation des ondes ( faible en rétrodiffusion ), complique les processus et multiplie les modes comme le résume la figure 10c.

La figure 11 montre deux fonctions de diffusion obtenues le 17 janvier 1992, pour une fréquence d'émission de 25,932MHz à 11h01 T.U. et 11h02

T.U. dans la direction Est, où la rétrodiffusion des ondes s'effectuant sur le sol exclut toute apparition de la diffraction de BRAGG. On peut noter que ces deux fonctions, dont la forme générale est proche de la forme théorique, sont très ressemblantes et qu'aucune distinction ne peut être faite entre ces deux analyses. Pour effectuer une analyse des fluctuations à petite échelle de l'ionosphère, ces deux signaux ont été traités par des méthodes d'analyse spectrale haute résolution.

### III.2. Analyse haute résolution.

La figure 12 représente ces deux analyses haute résolution. Elle révèle l'existence de composantes spectrales qui ont évolué entre deux instants d'analyse. Cependant, la superposition des enregistrements révèle un recouvrement important de ces composantes. La cohérence spatiale de ces composantes montre que les perturbations qui en sont à l'origine s'étendent sur des distances relativement faibles - typiquement de l'ordre de 10 à 30 km.

### III.3. Mesure fractale des perturbations.

Si l'on admet que les diffusions n'apparaissent que dans l'ionosphère, on peut repérer un point de l'ionosphère par le vecteur  $\vec{r}$  dans un système de référence choisi. Le champ diffusé  $E_s$  est alors donné par l'expression :

$$E_s = \alpha \int_V E_0(\vec{r}) \mathcal{E}(\vec{r}, t) e^{j\vec{k}\vec{r}} d^3\vec{r} \quad (2)$$

où

$\alpha$  est une constante traduisant l'affaiblissement,

$E_0(\vec{r})$  est le champ incident dans le volume V

$\mathcal{E}(\vec{r}, t)$  est l'indice de réfraction du milieu

$\vec{k}$  est le vecteur d'onde.

Si l'on admet que les pertes introduites par la diffusion sont constantes et que la diffusion se produit dans un volume V suffisamment réduit, l'expression devient alors :

$$E_s = \alpha E_0 \int_V \mathcal{E}(\vec{r}, t) e^{j\vec{k}\vec{r}} d^3\vec{r} \quad (3)$$

Il apparaît que le champ diffusé  $E_s$  est une transformée de Fourier tridimensionnelle de l'indice de réfraction du milieu. On appelle pupille équivalente l'intégrale de la formule (2) et la fonction de diffusion apparaît comme l'image, à travers cette pupille, de la loi d'illumination de l'antenne d'émission.

L'analyse haute résolution fait apparaître les différentes composantes spectrales. La mesure de cette fonction de diffusion apparaît difficile pour traduire l'existence et la forme des différentes signatures élémentaires constituées par chacune des composantes qui s'étend dans l'espace et dans le domaine fréquentiel. L'objet ainsi constitué par l'ensemble des signatures peut être mesuré par sa dimension fractale. On s'est attaché à développer ce moyen de mesure et la méthode du pavage est apparue la plus simple à mettre en oeuvre.

Sur l'exemple de la figure 12 la mesure de la dimension fractale a été effectuée et a donné la valeur :

$$\Delta_D^F = 0,90$$

Des mesures ont été effectuées sur un ensemble de fonctions de diffusion telles que celles représentées sur la figure 13 qui donne l'analyse haute résolution de deux modes de propagation, le premier est un mode E où l'on reconnaît les raies de BRAGG, l'autre est un mode F qui apparaît sur des distances comprises entre 1 800 et 3 000 km. Les mesures des dimensions fractales apparaissent :

- Pour la région F, égales à  $\Delta_D^F = 92$ .

- Pour la région E, égales à  $\Delta_D^E = 0,95$ .

L'ensemble des mesures effectuées sur les fonctions de diffusion traitées a révélé que :

- Pour la région F, la dimension fractale  $\Delta_D^F$  se trouve être comprise entre 0,70 et 0,95.

- Pour la région E, la dimension fractale  $\Delta_D^E$  est comprise entre 0,85 et 0,95.

Ces mesures permettent de remarquer que :

- Les dimensions fractales attachées aux modes de propagation E sont plus proches de l'unité, ce qui traduit une structure plus régulière de la fonction de diffusion propre à la région E.

- Les dimensions fractales attachées aux modes de propagation F sont plus faibles que celles attachées aux modes E, ce qui traduit une structure moins régulière de la fonction de diffusion propre à la région F.

Il est possible d'attacher une dimension fractale à la répartition spatiale des structures par une projection de la fonction de diffusion sur l'axe temporel.

Les mesures effectuées font apparaître :

- Pour la région E, une dimension fractale voisine mais inférieure à 1.

- Pour la région F, une dimension fractale voisine de 0,65.

#### IV. - INTERET DE LA MODELISATION -

La modélisation fractale qui a été adoptée introduit un moyen de mesure de la fonction de diffusion évaluée en haute résolution. Deux dimensions fractales ont été introduites, l'une sur la fonction de diffusion complète qui s'intéresse donc à un objet défini dans un espace à deux dimensions, l'autre sur la projection de la fonction de diffusion sur l'axe spatial. La dimension introduite est donc celle d'un objet inclu dans un espace à une dimension.

L'intérêt de ce procédé est :

- De permettre la caractérisation des mesures effectuées par des méthodes haute résolution

- De caractériser la cohérence des milieux par la mesure de la dimension fractale.

- Par un traitement inverse, de déterminer la pupille équivalente de  $\mathcal{E}(\vec{r}, t)$ .

#### V. - CONCLUSION -

L'ionosphère est, on le sait, un milieu inhomogène, anisotrope, non stationnaire particulièrement hostile. On a, dans cette étude, mis en évidence les fluctuations à faible échelle de l'ionosphère en caractérisant leurs dimensions spatiales et temporelles.

Les mesures par l'introduction de dimensions fractales permettent d'avoir une approche quantitative de la stabilité des milieux. Cette mesure permet d'obtenir une caractérisation simple de l'état de l'ionosphère et, par là même, de pouvoir effectuer des interprétations théoriques.

Le calcul inverse de la fonction de diffusion permet, théoriquement, de caractériser la pupille équivalente offerte par le milieu et il s'agit là d'un problème difficile qui, pour l'instant, ne peut être résolu que par des traitements informatiques.

Les interprétations physiques que l'on peut en faire demeurent encore délicates, mais cette étude permet déjà de caractériser les dimensions spatiales des perturbations ainsi que leurs variations temporelles.

#### REMERCIEMENTS

*Les résultats présentés sur les figures 2 à 6 ont été traités par un programme informatique développé par M.FLEURY, et les résultats présentés sur les figures 7 à 9 ont obtenus grâce à un logiciel de présentation développé par P.NERI, que les auteurs remercient pour leur aide.*

#### BIBLIOGRAPHIE

[1] *Technique de sondage électromagnétique par échantillonnage spatio temporel des signaux de réception. Application à l'étude des inhomogénéités du plasma ionosphérique.*

C. GOUTELARD, J. CARATORI, A. JOISEL.  
Symposium AGARD - EPP - Londres 1978 - Proceeding n° 244.

[2] *La réflexion des ondes décimétriques par la surface terrestre en émission impulsienne et son rôle dans l'interprétation des spectres de fréquence des échos obtenus dans les sondages par rétrodiffusion.*

C. GOUTELARD.  
XIV Symposium AGARD - EPP - Sandefjord - Norvège. 19-23 Août 1968 - Proceeding n° 37.

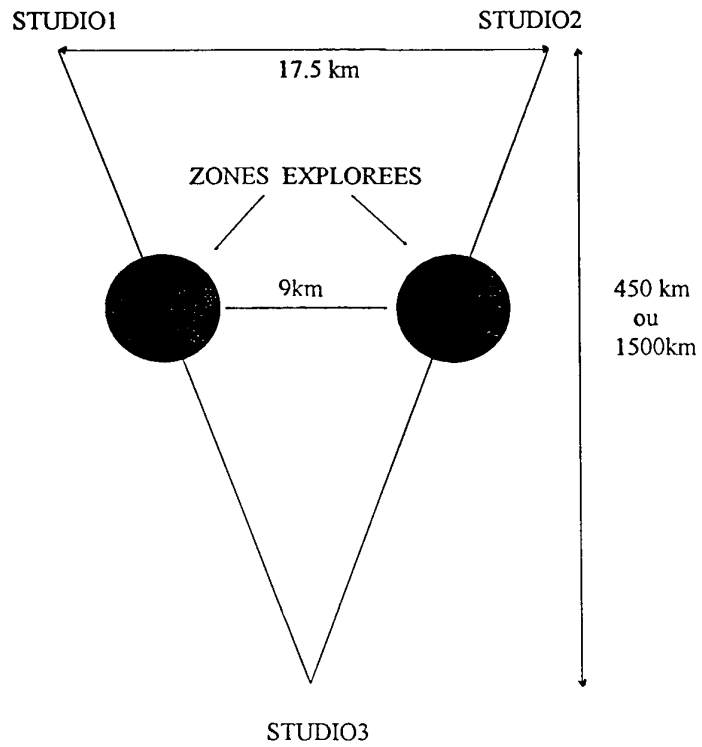


FIGURE 1  
Géométrie des liaisons bistatiques utilisée

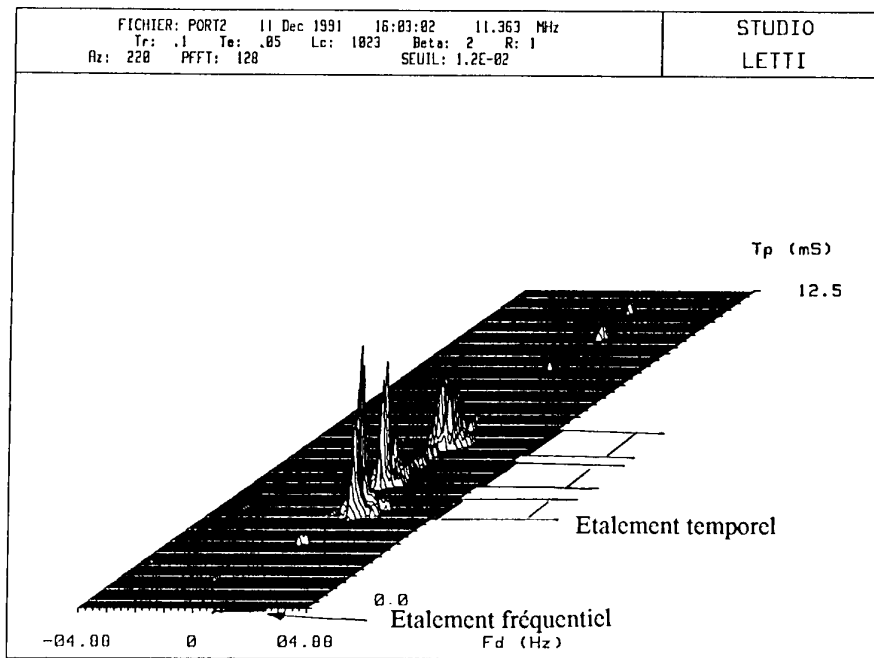
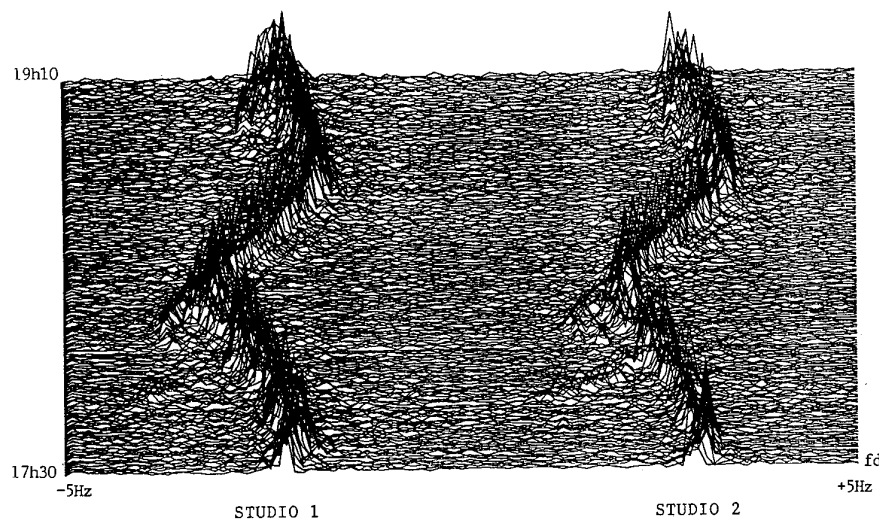
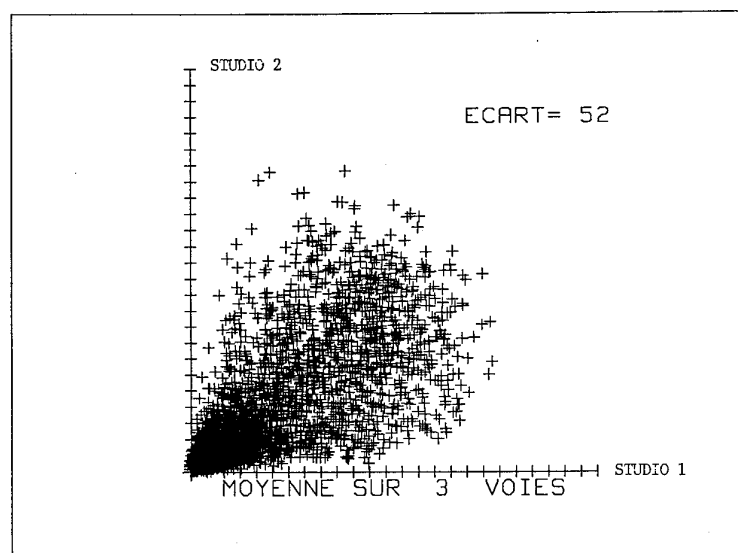


FIGURE 2  
Fonction de diffusion en sondage bistatique

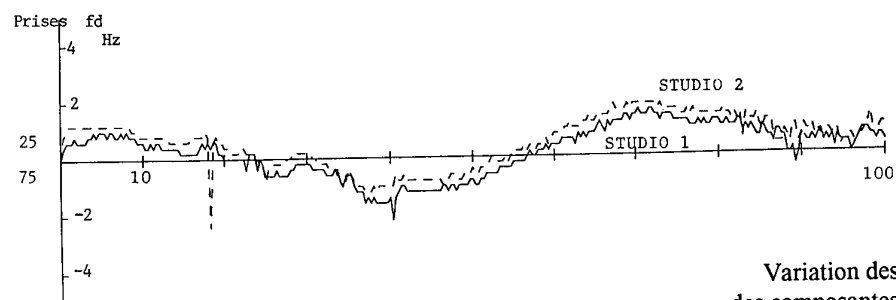


- a -

Variation temporelle des spectres



- b -

Répartition d'amplitude  
des composantes spectrales  
de même fréquence doppler

- c -

Variation des fréquences doppler  
des composantes d'amplitude maximale

FIGURE 3

Enregistrement en sondage bistatique de 17h30 à 19h10 T.U.  
le 10.12.1991. Réception à STUDIO 3. Emission à STUDIO 1 et STUDIO 2



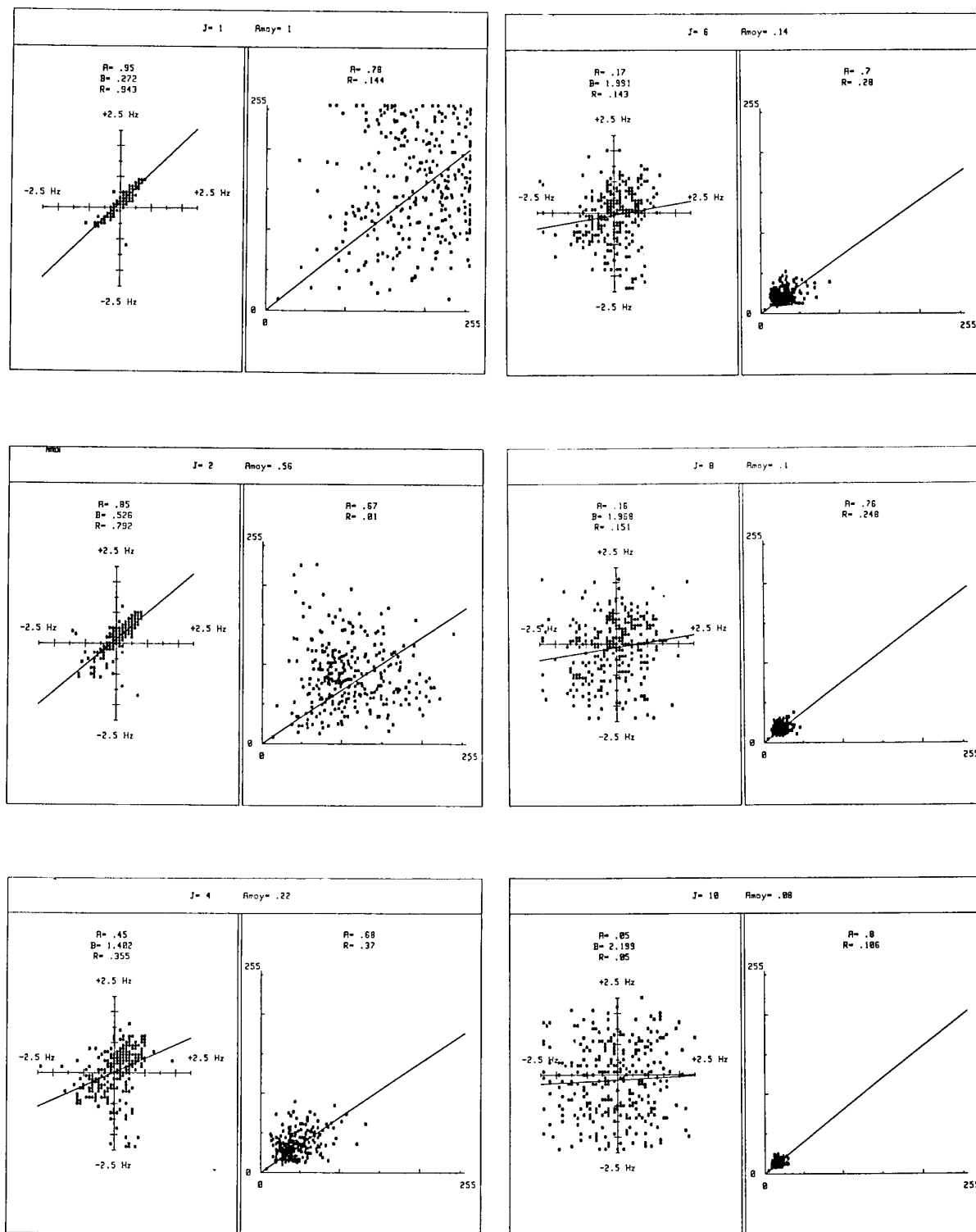


FIGURE 4  
Corrélation doppler et amplitude pour les composantes spectrales  
 $j = 1, 2, 4, 6, 8, 10$  de l'enregistrement de la figure 3

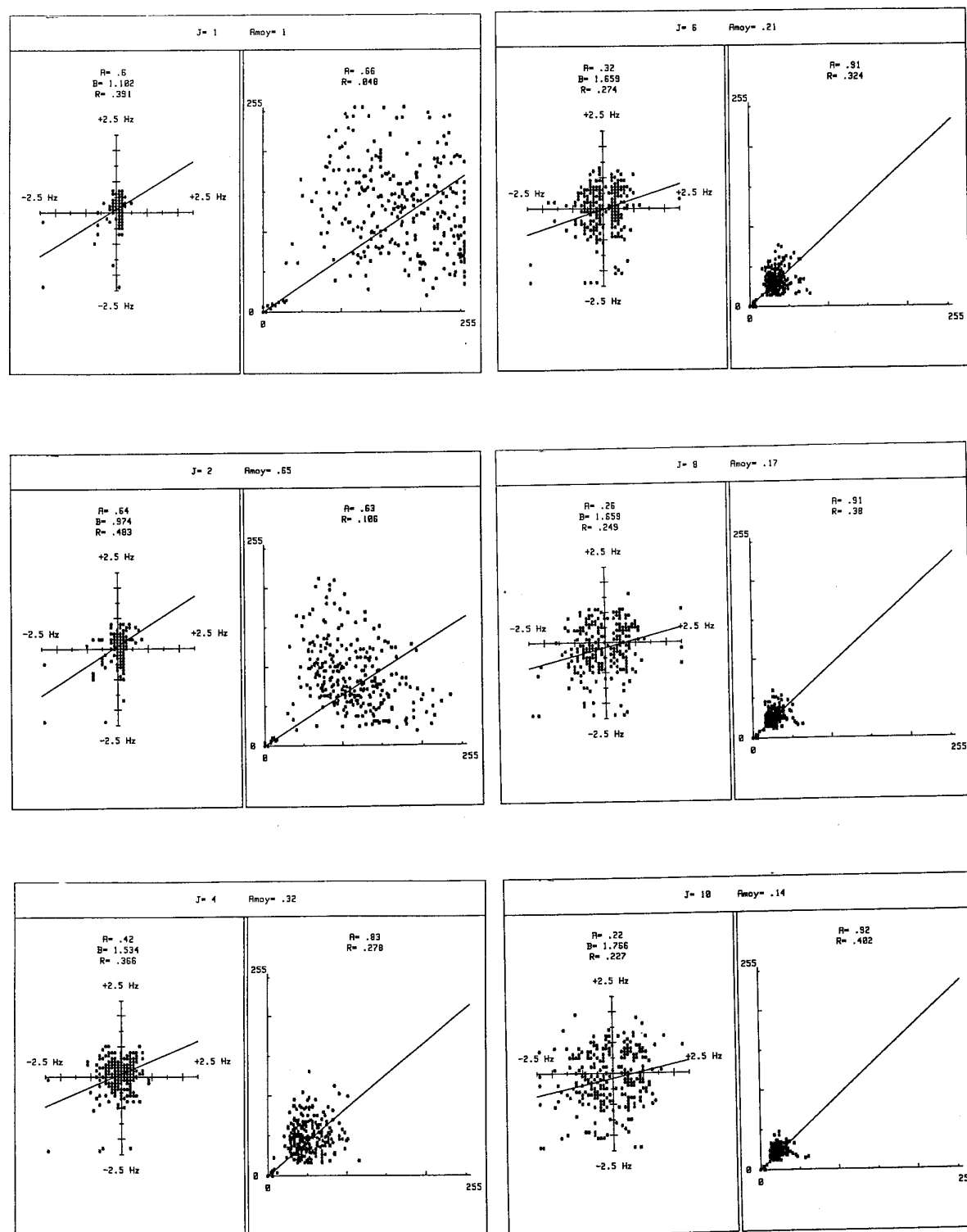
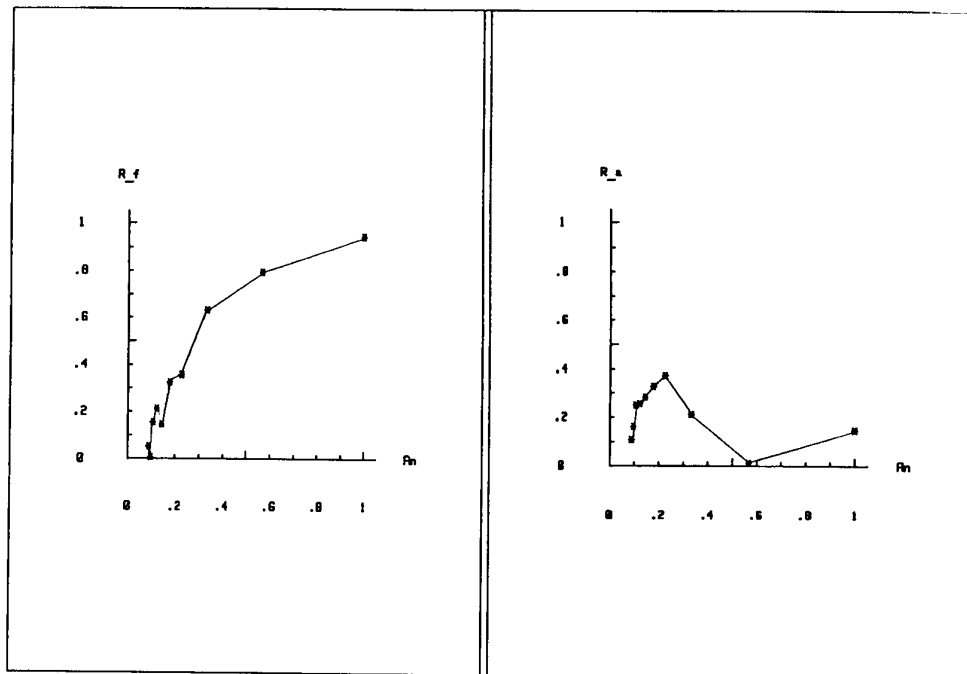


FIGURE 5  
Corrélations doppler et amplitude pour les composantes spectrales  
de l'enregistrement en période d'ionosphère perturbée  
du 12.12.1991 de 12h30 à 14h10 T.U.  
Emission à STUDIO 1 et à STUDIO 2

- a -

Enregistrement de 17h30 à 19h10 T.U. du 15.12.1991  
Cas d'une ionosphère non perturbée



- b -

Enregistrement de 12h30 à 14h10 T.U. du 12.12.1991  
Cas d'une ionosphère perturbée

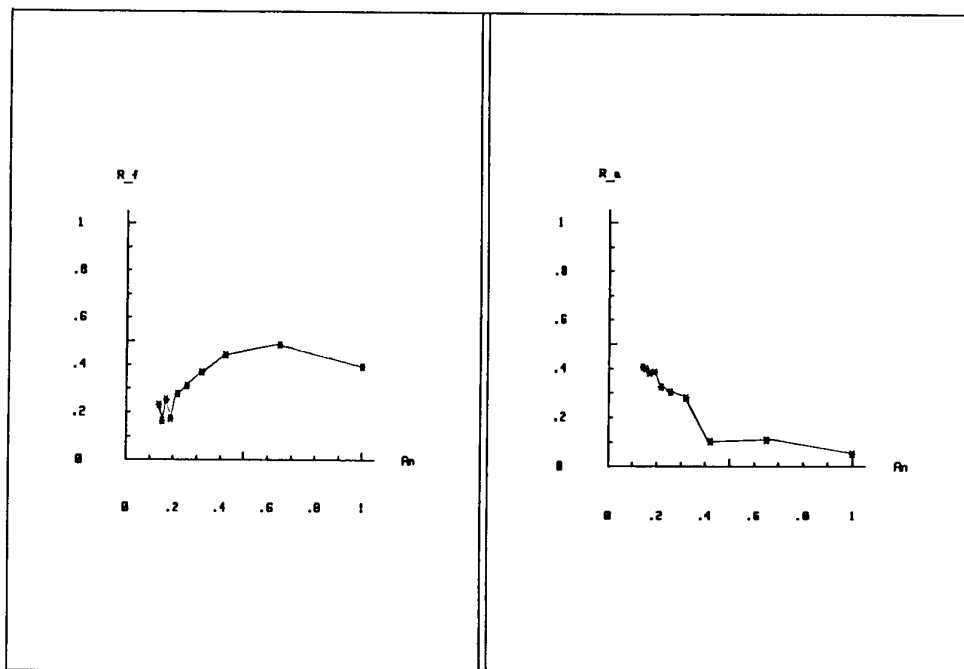
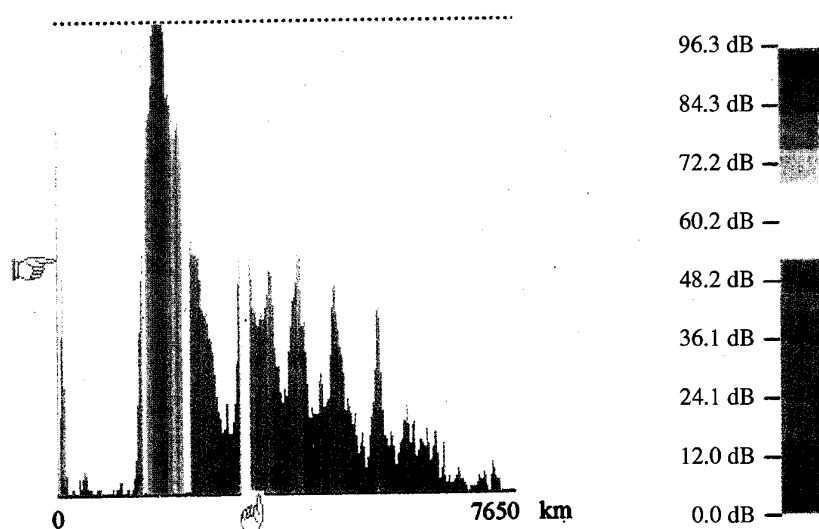


FIGURE 6

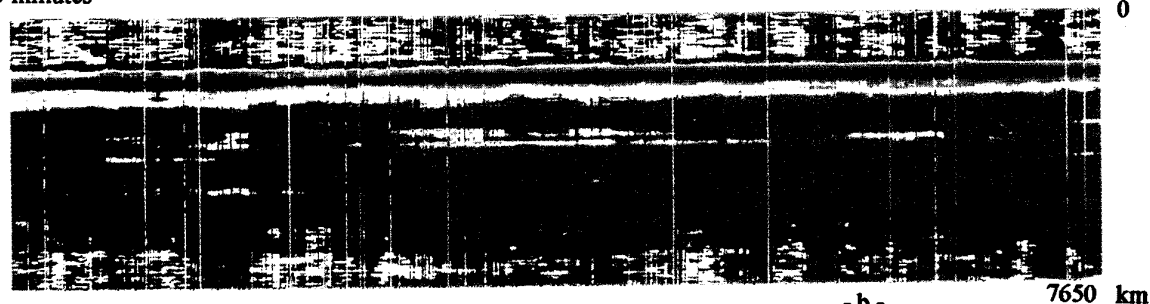
Variation des coefficients de corrélation des doppler et amplitude

Laboratoire d'Etude des Transmissions Ionosphériques  
Station STUDIO

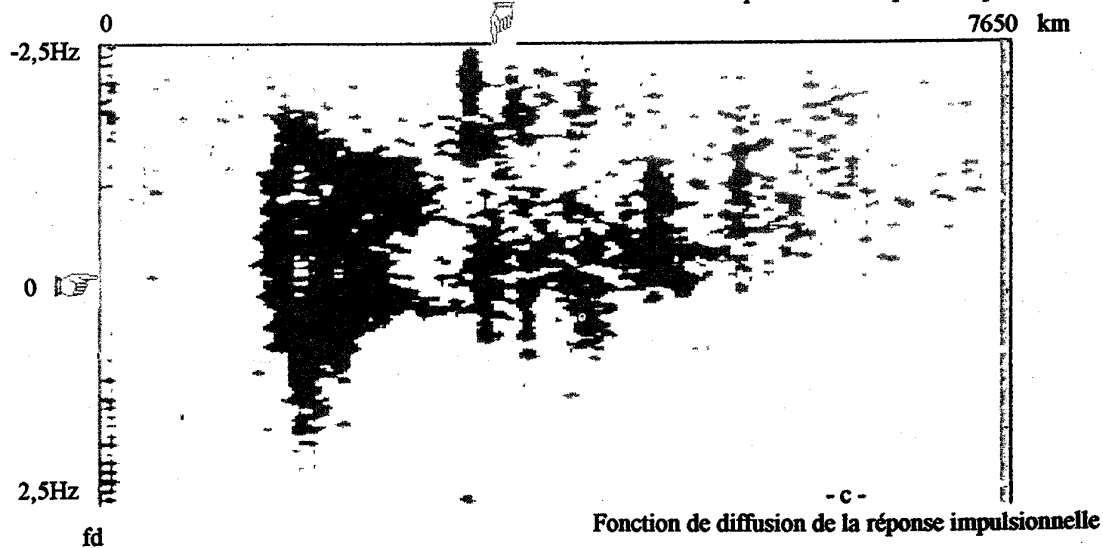


- a -  
Réponse impulsionnelle du canal

30 minutes



- b -  
Evolution temporelle de la réponse impulsionnelle



- c -  
Fonction de diffusion de la réponse impulsionnelle

FIGURE 7  
Résultats obtenus le 3 Décembre 1992 à la station STUDIO du LETTI  
Puissance du signal émis : 300W

Laboratoire d'Etude des Transmissions Ionosphériques  
Station SLS

30 minutes

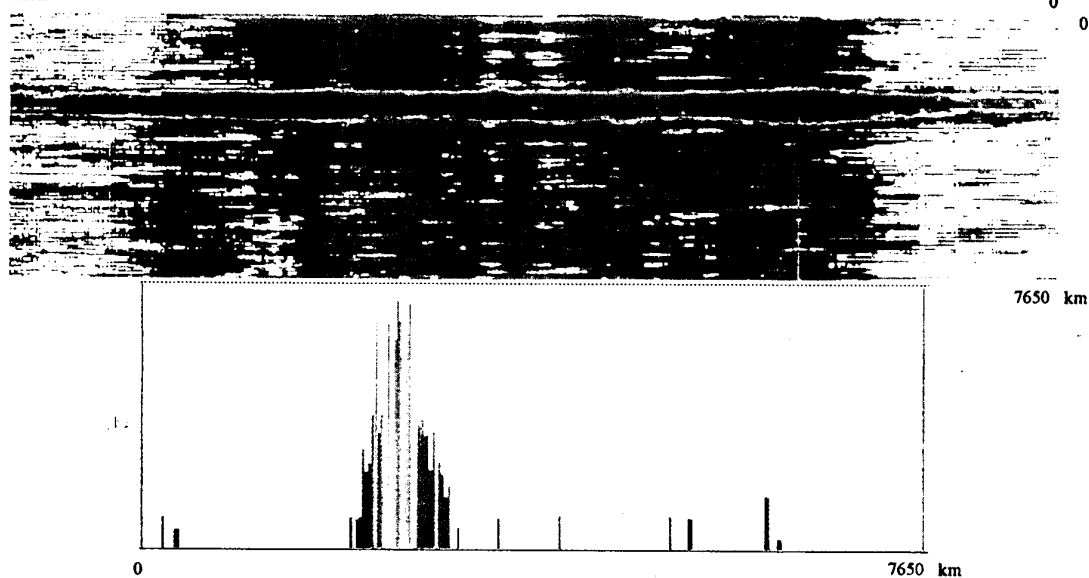
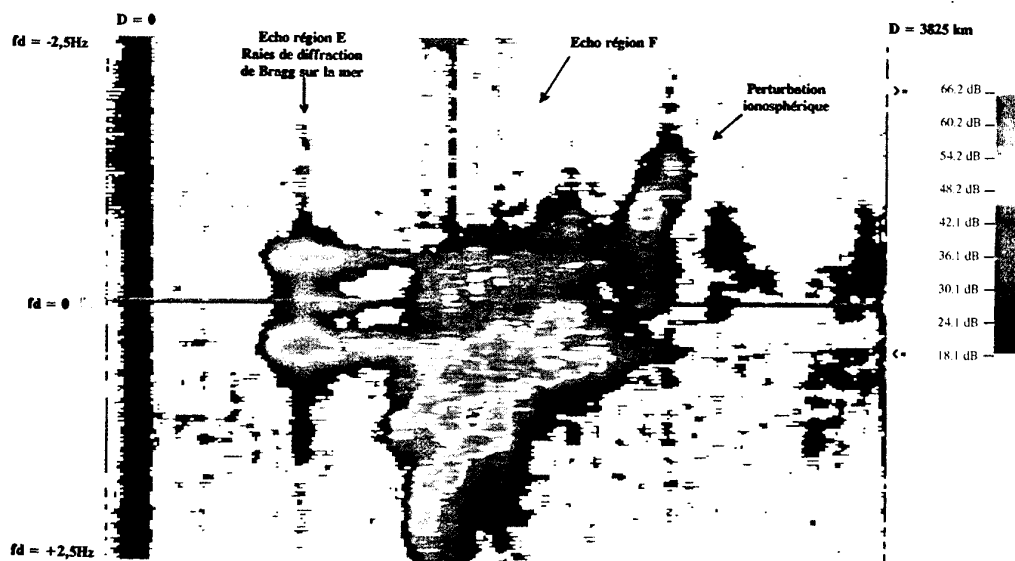


FIGURE 8  
Résultats obtenus le 3 décembre 1992 à la station STUDIO du L  
Puissance du signal émis : 0.1W

Laboratoire d'Etude des Transmissions Ionosphériques  
Station STUDIO

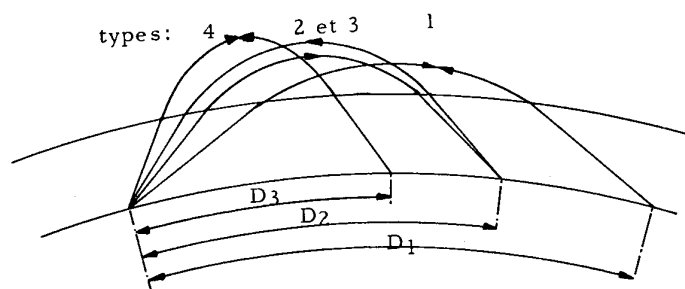


FONCTION DE DIFFUSION. ECHOS PROCHES.

FIGURE 9  
Fonction de diffusion obtenue le 18 Septembre 1992  
à la Station STUDIO du LETTI  
Puissance du signal émis : 300W

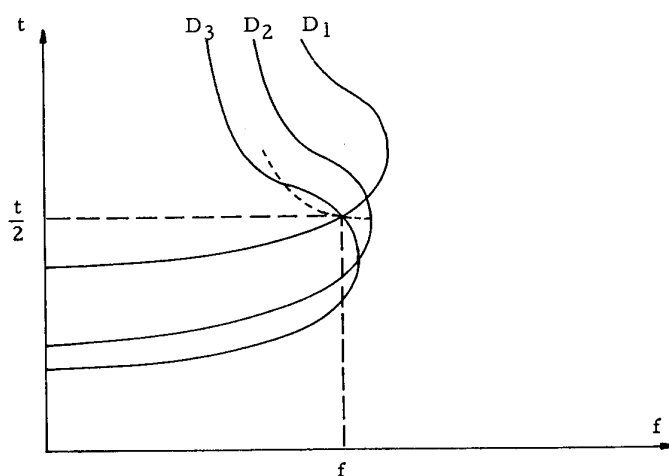
- a -

Géométrie des rayons de même temps de groupe



- b -

Détermination des distance à même temps de groupe



- c -

Multiplication des modes par l'effet magnéto-ionique  
et par dépolarisation

	Bas		Haut	
	Ordinaire	Extraordin.	Ordinaire	Extraordin.
Trajet aller	↓	↓	↓	↓
Effet du sol	Diffusion - Dépolarisation			
Trajet retour	↓	↓	↓	↓
	↓	↓	↓	↓
	↓	↓	↓	↓
	↓	↓	↓	↓

FIGURE 10

Existence du rayon mixte dans les sondages par rétrodiffusion

Figure extraite de [2]

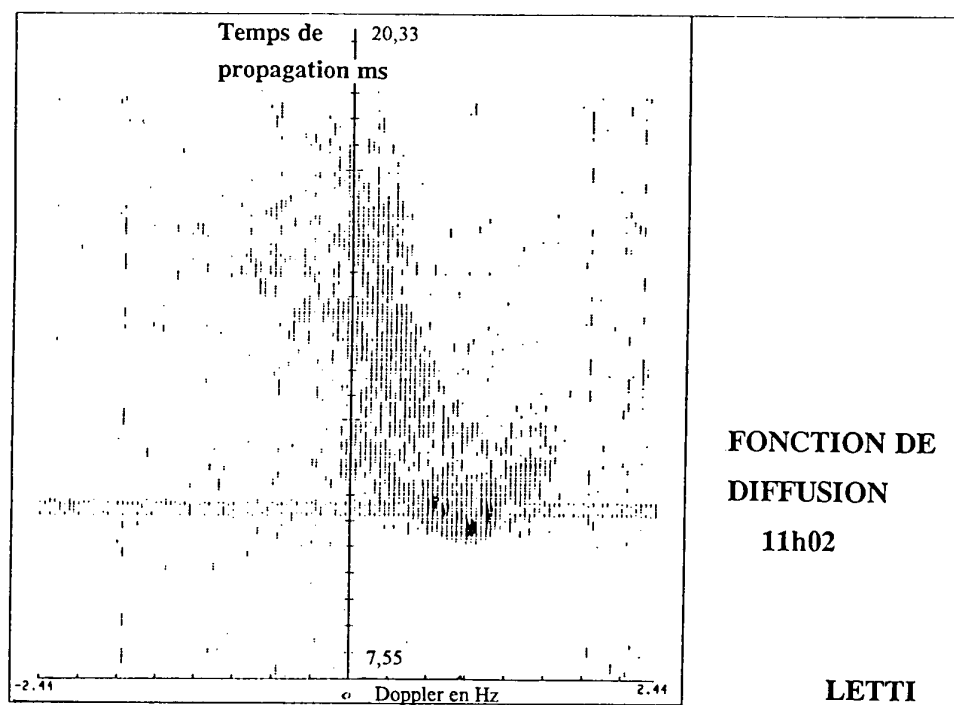
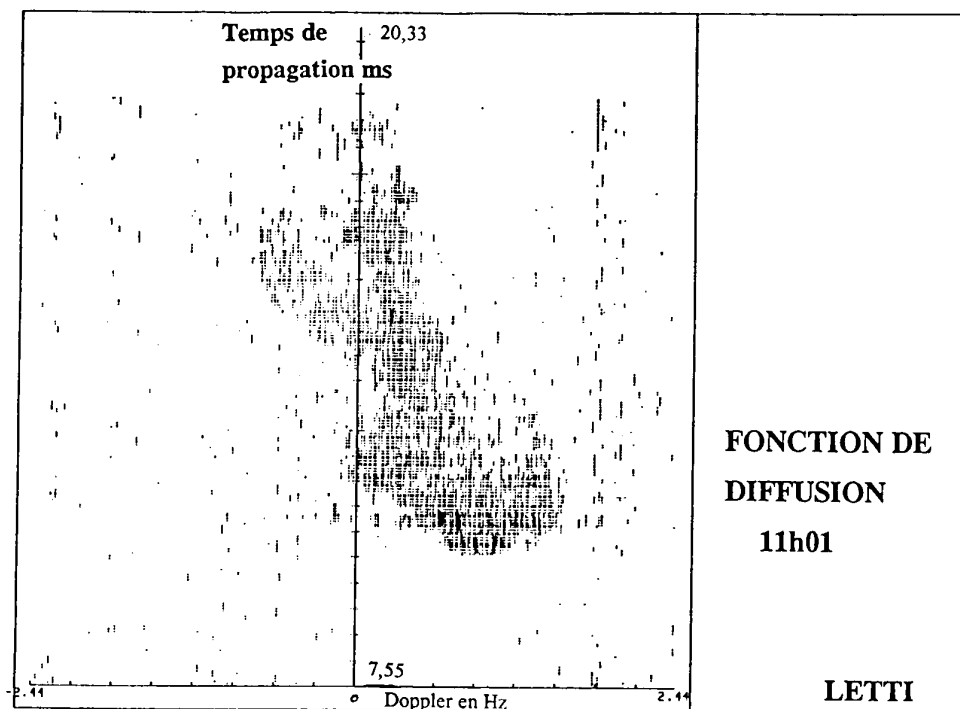
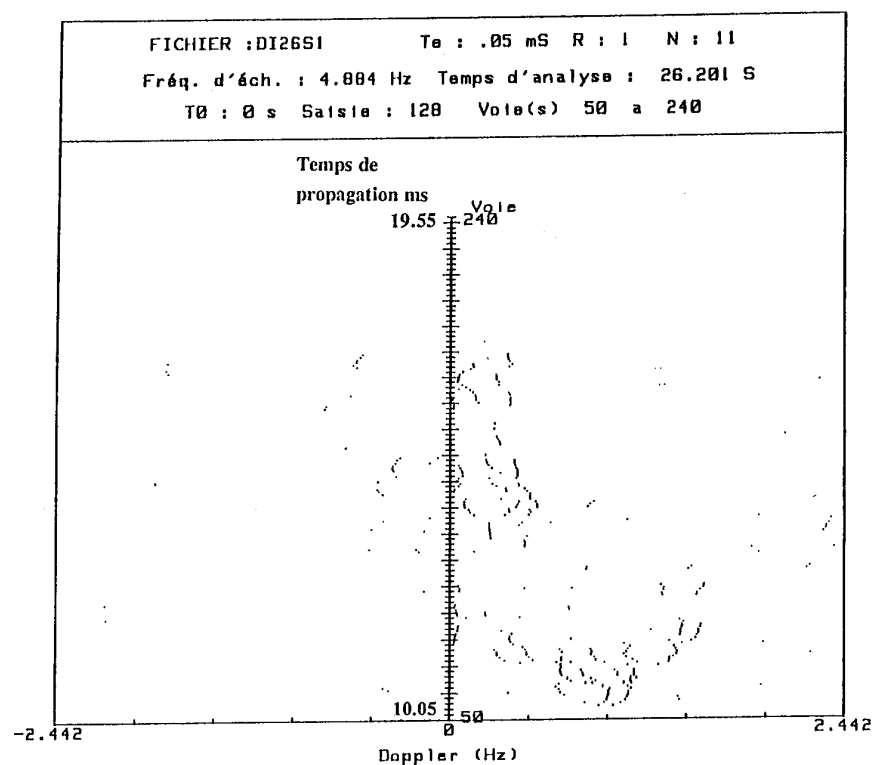


FIGURE 11

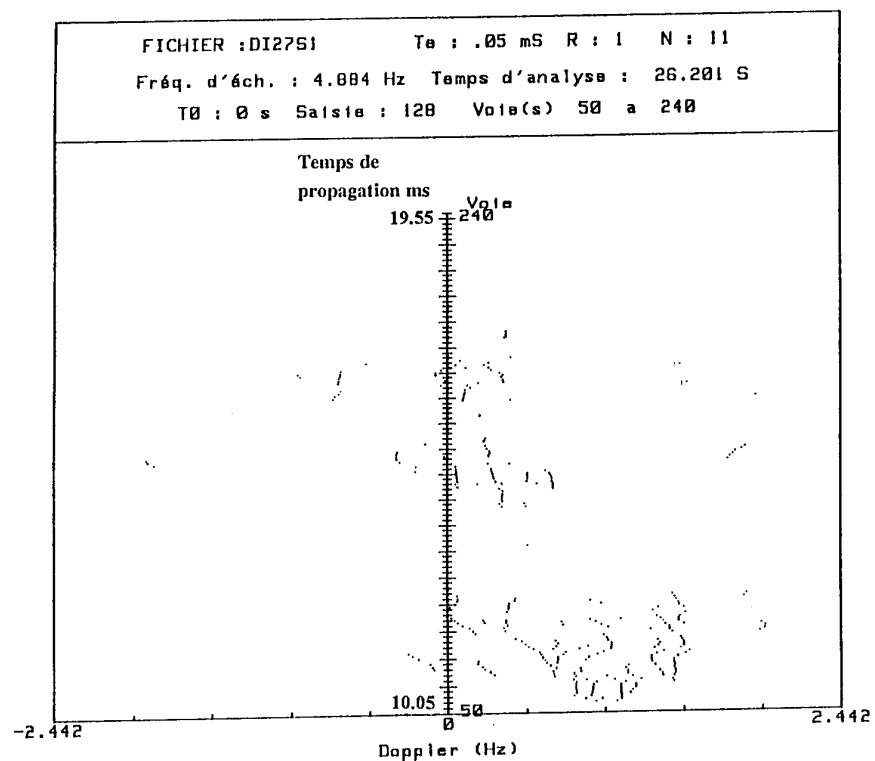
Fonctions de diffusion relevées à 11h01 et 11h02 T.U. le 17.01.1992

Rétrodiffusion sur le sol

Résolution distance : 7,5 km, doppler = 0,02Hz, F émission : 25,932MHz



FONCTION DE  
DIFFUSION  
11h01



FONCTION DE  
DIFFUSION  
11h02

LETTI

FIGURE 12  
Analyse par une méthode haute résolution des fonctions de diffusion  
de la figure 11





## DISCUSSION

**Discussor's name :** J-L. Rogier

**Comment/Question :**

L'hypothèse "sources ponctuelles" des méthodes haute résolution n'est-elle pas gênant pour analyser des composantes diffuses?

**Translation :**

*Isn't the "point source" assumption used in high resolution methods a nuisance when analysing diffuse components?*

**Author/Presenter's reply :**

Le système haute résolution filtre les composantes diffuses dont les amplitudes sont équivalentes, et ne retient évidemment que les composantes émergentes. Il s'agit d'un filtrage réel fort utile dans cette étude.

La pertinence des résultats est cependant rendue par le fait que les composantes qui apparaissent sur les cases distances consécutives sont parfaitement cohérentes alors qu'elles sont traitées séparément.

**Translation :**

*The high resolution system filters out diffuse components of equivalent amplitudes and, of course, only retains the emergent components. This is a type of real filtering which is extremely useful in this study.*

*The relevance of the results is however shown by the fact that the components which appear in consecutive range bins are perfectly coherent, whereas they were processed separately.*

**Discussor's name :** G. Sales

**Comment/Question :**

Can you compare your day-time results with those made at night.

**Author/Presenter's reply :**

La nuit, sur la région F, la forme générale de la fonction de diffusion est la même que le jour. Cependant, les structures fines sont différentes avec quelquefois des anomalies fortes.

**Translation :**

*At night, in the F region, the general form of the scatter function is the same as in the day. However, fine structures are different, and sometimes exhibit marked anomalies.*

# **DAMSON - A SYSTEM TO MEASURE MULTIPATH DISPERSION, DOPPLER SPREAD AND DOPPLER SHIFT ON MULTI-MECHANISM COMMUNICATIONS CHANNELS**

Nigel C Davies  
Paul S Cannon

Radio Propagation Exploitation Group  
Space and Communications Dept  
Defence Research Agency  
Malvern, Worcs, WR14 3PS  
United Kingdom

## **SUMMARY**

The performance of communications equipments (especially data modems) designed to work over high frequency paths which can propagate by a number of different mechanisms is dependant on their ability to work with a wide range of signal to noise conditions and with varying degrees of frequency and time dispersion. The latter phenomena are a particular problem for systems operating over high latitude paths and yet there appears to be little available data documenting their severity or frequency of occurrence.

DAMSON (Doppler And Multipath SOunding Network) is an oblique channel sounding system which has been developed by the UK Defence Research Agency (DRA) to measure a number of real-time channel parameters using low power pulse compression waveform transmissions. Extensive use is made of digital signal processing techniques. The system will allow signal time-of-flight, time dispersion (multipath dispersion), frequency dispersion (Doppler spread and Doppler shift) and signal strength to be measured over point-to-point communications paths. The DAMSON experiment is to be deployed to make measurements over a number of mid and high-latitude paths.

This paper provides an introduction to the DAMSON system, its basic operation and measurement performance. The initial experiments to be conducted and the associated system deployment are presented.

## **1. INTRODUCTION AND SCIENTIFIC OBJECTIVES**

Signal transmissions in the high-frequency (HF) band (2-30 MHz) can propagate by a number of different mechanisms (including ground wave, single and multi-hop skywave, sporadic-E etc). The various propagation mechanisms and other ionospheric effects can result in the signal suffering multipath dispersion, Doppler shifts and Doppler spreading (frequency dispersion) and attenuation. Whilst these effects occur all over the World, there is a particular interest in the high latitudes, where severe Doppler spreads and multipath dispersion occur. A survey of propagation literature has shown that little data exists which provides information on the magnitude and frequency of occurrence of multipath dispersion and (in particular) Doppler spread over these high-latitude paths. Available data suggests that Doppler spread may be encountered for substantial percentages of the time.

The first, and most fundamental, objective of the DAMSON experiment is to statistically quantify spectral spreads, Doppler shifts, multipath delay and signal strengths for a number of high-latitude and mid-latitude reference paths. This is to be achieved by collecting a large database of measurements over a period of many months. This data provide much of the basic information required to fulfil the project's other major objectives.

## **Assessment of HF data modem waveforms**

The information obtained from the experiment will be used to assess the affects of high-latitude propagation conditions on both current and future HF data modem waveforms. This information is particularly important for the specification of robust modulation schemes for use on high-latitude circuits where communications availability and reliability are critical.

## **Updating Propagation Prediction Codes**

It is hoped to use the measurements that are being made with DAMSON to derive 'empirical rules' for spectral spread (particularly on polar-cap and auroral links) and to incorporate this knowledge in future propagation prediction codes. The measured parameters will be assessed as a function of both the geographic and geomagnetic path positions and as a function of geophysical activity.

## **Application to HF Simulators**

The DAMSON measurements will be used to specify HF simulator characteristics to allow more representative (accurate) testing of communications systems and modems to be conducted. This will allow designers to predict modem performance over high-latitude path conditions with a much higher degree of confidence.

To date the fading algorithms utilised in many simulator implementations is based on the Watterson fading model. This model was derived from the analysis of data from just three 12 minute measurement periods on a single 1294 km mid-latitude path. While the Watterson model has been shown to be acceptable for modelling more benign mid-latitude paths [CCIR, 1990]<sup>1</sup> its applicability to high-latitude (and indeed other difficult) paths has yet to be verified.

## **2. INTRODUCTION TO MEASUREMENT SYSTEM**

The DAMSON system uses relatively low power coded transmissions between remote transmit and receive sites on a pre-selected range of frequencies to determine the following real time oblique channel parameters:

- Absolute time of flight ( $\leq 100$  ms)
- Multipath dispersion ( $\leq 100$  ms, max resolution  $100 \mu s^*$ )
- Doppler shift & spread ( $-100$  to  $100$  Hz, resolution  $1$  Hz)
- Signal strength
- Signal to noise ratio

\*Using 12 kHz measurement bandwidth. Resolution is  $400 \mu s$  in a 3 kHz bandwidth.

The system determines channel parameters using pulse compression sounding waveforms to increase the total energy available at the receiver (by increasing the transmission time) whilst maintaining the time resolution that could be obtained from a single pulse (equivalent to the compressed pulse

width). Timing resolution is determined by the system bandwidth, normally either 3 kHz or 12 kHz, which limits the minimum pulse width through the system. Pulse compression and integration over many pulses yields typical signal processing gains of ~35 dB (depending on the particular waveform in use).

The system is based on commercially available equipments (such as HF communications receivers, computers etc) and makes extensive use of Digital Signal Processing (DSP) techniques. High accuracy system timing is derived from the constellation of Navstar Global Positioning System (GPS) navigation satellites. This ensures that transmit and receive stations are accurately synchronised and also allows absolute time-of-flight measurements to be made.

It is not possible to measure all the channel parameters over the required ranges using a single waveform; some of the requirements are quite contradictory. In order to increase the performance and flexibility of the system, and in the light of these constraints, the particular waveforms in use and their characteristics (type, duration, bandwidth, pulse repetition frequency (PRF), number of pulses etc) can all be specified in a configuration file. Hence the waveform in use can be tailored to the particular measurement being made. The principal constraint on this flexibility is that waveform parameters must be pre-arranged between transmit and receive stations. The system has been designed to support a wide range of different pulse compression waveforms including, in particular, a variety of PSK modulated sequences (including Barker sequences, maximal length pseudo noise (PN) sequences and complementary sequences) as well as linear FM chirps, up-down chirps etc.

Measurements are made using a combination of four basic modes:

- Time of flight (TOF) search mode
- Delay Doppler (DD) measurement mode
- CW measurement mode
- Noise measurement (NM) mode

The time-of-flight (TOF) mode is used to determine both the basic signal time of flight and approximate multipath profile while the Delay-Doppler (DD) mode determines the channel multipath profile, Doppler spread and Doppler shift. Both modes can also collect signal strength information. Two additional measurement modes will be implemented. A CW measurement mode will allow the receiver gain to be automatically adjusted if required and then used to determine large frequency shift/dispersion conditions (useful for data 'pre-screening'). A noise-monitor (NM) mode will be used to determine the quiescent channel conditions (interference etc.) for accurate signal-to-noise calculation etc.

The following measurement schemes are supported:

- Fixed Frequency operation. Allows the investigation of a single frequency (or a number of specified frequencies). Typically the system would determine the signal TOF, multipath dispersion, Doppler spread and signal strength for a frequency using the TOF search mode followed by the DD measurement mode.
- Scanning Ionogram operation. The system steps through frequencies (across all or any part of the HF band) sounding channels to produce a conventional type ionogram together with TOF and Doppler information as required.

The DAMSON system software includes scheduler routines which allow measurement schemes to be repeated at selected intervals over any chosen time period.

By analysing data collected over a period of time the changing nature of the channel can be investigated. The instrument allows information on the frequency of occurrence and severity of time and frequency dispersion over different paths (especially high latitude and trans-auroral paths), diurnal and seasonal variations and the effect of ionospheric disturbances to be collected.

### 3. TRANSMIT STATION CONFIGURATION

A DAMSON transmit station (Fig.1) consists of an IBM compatible personal computer (PC) which is used to perform basic system control functions. Plugged into the PC is a DSP card which carries out both the real time processing and the digital to analogue conversion required to accurately generate waveforms and trigger their transmission. The baseband output of the DSP sub-system drives the modulation input of a HF single-sideband (SSB) drive unit. Basic transmit parameters such as frequency and transmit bandwidth are controlled by the PC via a serial communications interface. The HF drive has a high stability frequency reference (better than 1 in  $10^6$ ) and a number of software selectable SSB bandwidths including a maximum bandwidth of 12 kHz. The HF drive unit output is fed to a wide-band linear power amplifier which in turn feeds a maximum power of between 500 W and ~1 kW into the antenna system. For fixed operation on long or difficult paths it is envisaged that a (calibrated) directive antenna aimed at the receive site be used. System timing and hence synchronisation with the receive station is obtained from a GPS receiver card plugged into the PC.

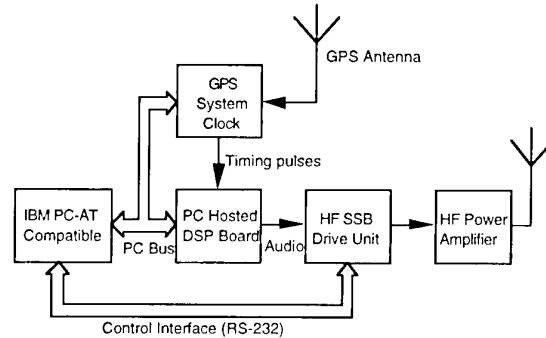


Fig.1- Configuration of Transmit System

### 4. RECEIVE STATION CONFIGURATION

The receive station (Fig.2) consists of a receive antenna system, a good quality HF communications receiver and a signal processing and data storage/analysis system. The receiver is fully software controllable using a serial control interface. It has a high quality stable oscillator (better than 1 in  $10^6$ ) and a one Hertz tuning accuracy. The receiver baseband output is fed to the analogue to digital converter (ADC) input of the DSP card. The receiver can be operated in either an automatic gain control (AGC) mode or in a manual (computer controlled) IF gain mode to allow more accurate signal strength and fading measurements to be made.

A PC is used to perform basic system control functions, data archiving, analysis and display. Plugged into the PC is a DSP card which both samples the received signal, using an on-board ADC, and carries out all the real time processing required to detect and process received transmissions. Sampling is performed at twice the Nyquist rate to allow in-

phase and quadrature (IQ) processing of the received signals. As with the transmitting station system timing is obtained from a GPS receiver card plugged into the PC.

Measurements made using the DAMSON system contain a large amount of data (upto ~50 kbytes for a 5 s measurement). This is initially stored to a large hard disk (One giga-byte capacity) and then periodically archived to digital audio tape (DAT).

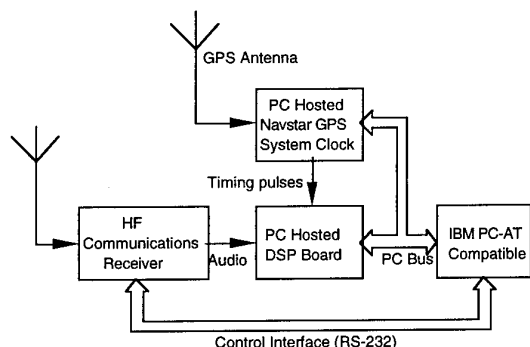


Fig.2 - Receive Station Configuration

### 5. TIME OF FLIGHT SEARCH MODE

In this mode the transmit station sends a number of accurately timed pulse compression waveforms in order to allow the receive station to determine the basic signal propagation delay (TOF) and a low resolution picture of the multipath structure. The principle requirement in this mode is for a waveform that gives good signal detectability in the presence of delay and Doppler dispersion rather than highly accurate time-of-arrival. A typical waveform for use in this mode is a bi-phase PSK modulated Barker-13 sequence which gives reasonably good detectability whilst being short enough to be robust in the presence of fading. In order to cater for all envisaged paths with no time (range) ambiguity, a pulse repetition interval (PRI) longer than the maximum anticipated TOF is required (up to at least 100 ms for longer paths). In order to increase the total energy available at the receiver the waveform is transmitted a number of times. The received pulses are detected and Doppler integrated (see section 6) to determine the basic TOF from the time-of-arrival and knowledge of the transmission time (accurately determined from the GPS timing source). In addition this mode will provide a low resolution picture of the multipath dispersion.

### 6. DELAY DOPPLER MEASUREMENT MODE

This mode is used to determine the detailed multipath dispersion and Doppler characteristics of a channel once the TOF search mode has been used to identify the approximate time window during which the received signals arrive. The transmit station sends a number of accurately timed pulse compression waveforms in order to allow the receiving station to determine multipath dispersion, frequency dispersion (Doppler spread and Doppler shift) and received signal strength.

Principal requirements of a pulse compression waveform to be used in the DD mode is that it gives good time resolution (approaching the maximum for a given channel bandwidth), has a large dynamic range (peak-sidelobe ratio) and that it performs adequately in a frequency dispersive environment (a non time coherent channel will generally reduce the observed peak-sidelobe ratios). Suitable pulse compression waveforms include BPSK modulated Barker sequences, periodic maximal length PN sequences and complementary sequences. The nominal peak-sidelobe performance of the latter sequences are

excellent but degrade quickly in the presence of fading and changing channel phase.

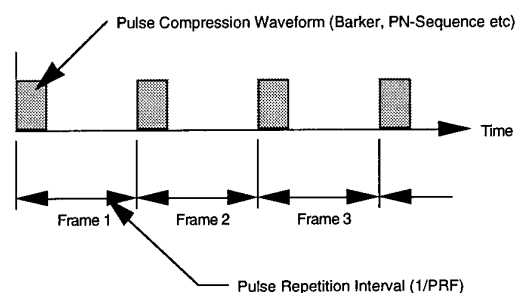


Fig.3 - Transmitted Waveform Frame Structure in Delay Doppler (DD) Measurements Mode

The pulse compression waveform is sent many times (typically 64, 128 or 256 times), the interval between the start of each waveform transmission being termed a frame (Fig.3). The period of a frame determines the multipath measurement time 'window'. If pulse-to-pulse coherence is maintained for the transmitted signal any spectral spreading/frequency shifts observed at the receiver will be due to ionospheric effects.

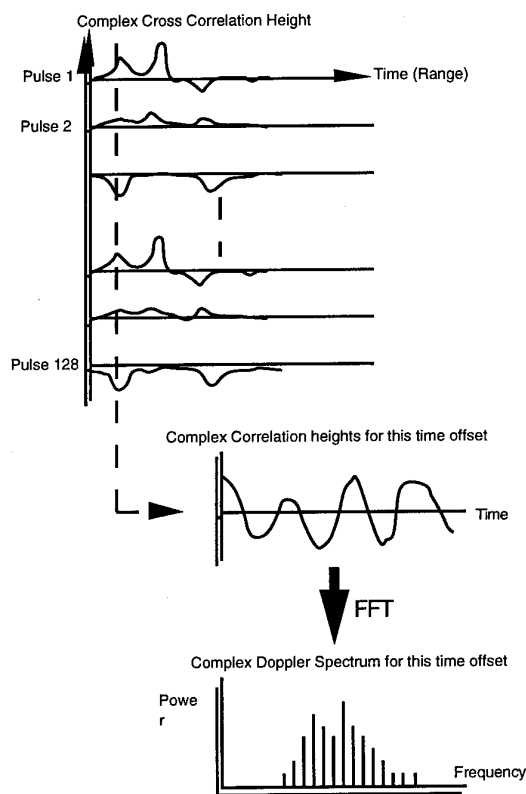


Fig.4 - Calculation of Doppler Spectra for Each Time Delay Interval Using Doppler Integration

The receiver detects the pulse compression waveform by continuously sampling the receiver output, converting the received signal to IQ and cross correlating it against a complex unit template of the pulse compression waveform transmitted. This process gives a complex cross-correlation height for each time offset (range). The output of the cross-correlator over the period of one frame is the complex channel impulse response (see Fig.4). If the channel caused no

frequency dispersion then the impulse response for each frame would be identical. However in the more general case fading would cause the received energy to be dispersed between the in-phase and quadrature channels (as shown in Fig.4, top left).

Once the complex impulse responses have been calculated for all the transmitted frames then the system can calculate the Doppler spectra for each time offset in the multipath window. This is done by making a time series of the complex cross-correlation heights at the same time offset in the multipath window for each successive frame and then taking its Fourier transform using a Fast Fourier Transform algorithm (FFT) to obtain the Doppler spectra for that time offset. The total power in the spectra is the received energy at that time offset integrated across all the received waveforms (Doppler integration). Hence the multipath profile, as measured by the system, is the total energy in the Doppler spectra for each time-offset plotted against its time offset.

The DAMSON system can thus determine both the channel multipath profile and the frequency spectra (Doppler shift and spread) for each received mode.

The maximum timing resolution possible is determined by the system bandwidth. Using a system bandwidth of 12 kHz and a 9600 baud PSK waveform would give a multipath dispersion resolution of  $\sim 100 \mu\text{s}$  (digitising resolution  $25 \mu\text{s}$ ). The multipath time period (range or multipath 'window') that can be investigated unambiguously is determined by the frame period. Larger multipath spreads than the frame period will cause interference in subsequent frames. The Doppler frequency range for a DD measurement is also determined by the frame period; it is  $\pm(\text{PRF}/2)$ , the PRF being  $1/(\text{frame period})$ . The presence of larger Doppler frequencies than this will cause aliasing and appear as lower frequencies within the measurement range. The unambiguous multipath and Doppler ranges that can be measured simultaneously must be traded off; as the unambiguous multipath range increases the Doppler range decreases. Hence compromises have to be made in choosing the measurement parameters. The Doppler resolution of the system is directly proportional to the total integration period (ie total receive time). An integration period of one second would give a resolution of 1 Hz whereas an integration time of 0.5 s would give a resolution of 2 Hz etc. Table.1 shows the trade-offs between Delay Range, Doppler range/resolution and total measurement time (maximum signal integration period).

Delay Range (ms)	Number of Frames	Doppler Range (Hz)	Doppler Resolution (Hz)	Integration Period (s)
5	64	$\pm 100$	3.12	0.32
5	128	$\pm 100$	1.56	0.64
5	256	$\pm 100$	0.78	1.28
5	512	$\pm 100$	0.39	2.56
10	64	$\pm 50$	1.56	0.64
10	128	$\pm 50$	0.78	1.28
10	256	$\pm 50$	0.39	2.56
10	512	$\pm 50$	0.19	5.12
15	64	$\pm 33$	1.04	0.96
15	128	$\pm 33$	0.52	1.92
15	256	$\pm 33$	0.26	3.84

Table.1 - Trade-offs between Delay Range, Doppler Range/Resolution and total DD Measurement Time (3 kHz bandwidth and 9600 samples per second)

## 7. DEPLOYMENT OF DAMSON EXPERIMENT

The DAMSON system is currently in phase one of its deployment with transmitters located at Farnborough (UK) and Harstad in Norway (see Fig.5). The transmitter in Harstad is under remote control using a modem link. Receivers are located at Oslo (Norway), Farnborough (UK) and Ottawa in Canada. A receiver is yet to be installed in Alta (Norway).

In phase two of the system's deployment (Fig.6) it is hoped to move the transmitter in Harstad to Svalbard (Spitzbergen) and to install an additional transmitter in Resolute (Canada) to increase the number of high-latitude paths.

## 8. CONCLUSIONS

The DAMSON system, which is in the final stages of development and testing (using an ionospheric simulator), is currently being deployed. Initial high latitude measurement paths will include Canada to Norway and the UK although other paths will also be used. The first major measurement campaign is due to commence in early 1994.

## 9. ACKNOWLEDGEMENTS

The authors wish to thank their colleagues at the Communications Research Centre (CRC), Ottawa, Canada and at the Norwegian Defence Research Establishment (NDRE), Oslo for their contributions and continued support to the DAMSON measurement programme.

## REFERENCES

1. CCIR, Report 549-3, HF Ionospheric Channel simulators, in Annex to volume III, XVIIth Plenary Assembly, Dusseldorf, CCIR, 1990.

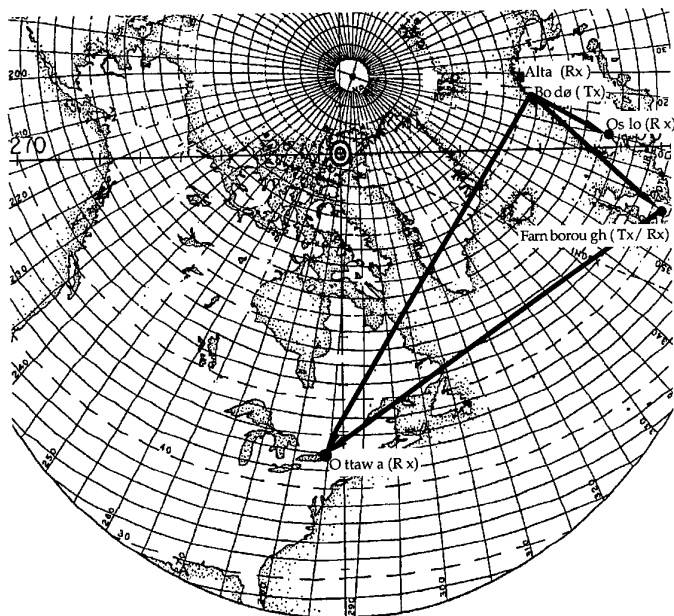


Fig.5 - Phase One DAMSON Deployment

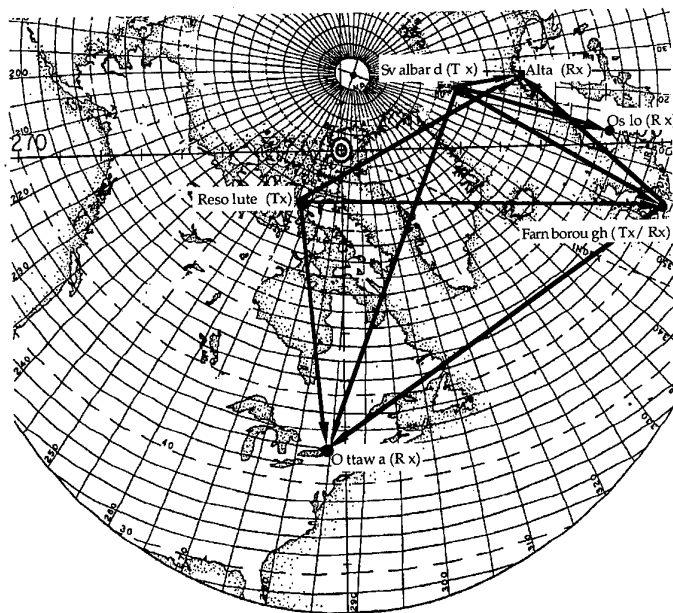


Fig.6 - Phase Two DAMSON Deployment

## DISCUSSION

### 3. Discussor's name : C. Goutelard

#### Comment/Question :

Avez-vous l'intention de corréler vos résultats avec des mesures ionosphériques faites dans les zones traversées par les liaisons que vous envisagez? Cela pourrait entre autre aider aux interprétations.

#### Translation :

*Do you intend to correlate your results with ionospheric measurements made in the zones crossed by the links which you envisage? Among other things, this could help with interpretation.*

#### Author/Presenter's reply :

- The most urgent requirement of the data from the DAMSON system is just to quantify the severity and occurrence statistics for multipath dispersion and Doppler spread.
- In terms of the longer term aims of the experiment other sources of scientific experimental data will be useful (perhaps essential). We anticipate using data from Digisondes, oblique sounders etc.

### 3. Discussor's name : G. Sales

#### Comment/Question:

Can you explain the apparent difference in the arrival times on the UK/Alaska path in the search mode and the multipath modes?

#### Author/Presenter's reply :

A mature experimental system was not used for these measurements; the data is only indicative that the system would work.



# IDENTIFICATION DES MODES ET TRAJETS DE PROPAGATION SUR DES LIAISONS HF A L'AIDE D'UN GONIOPOLARIMETRE .

A. EDJEOU, L. BERTEL, V. MASSOT.

Laboratoire Radiocommunications, URA CNRS 834, Université de RENNES 1  
Campus de Beaulieu- 35042 Rennes Cedex- France.

## RESUME

Dans cet article, nous décrivons un système qui permet la séparation des trajets de propagation et l'identification des polarisations des modes. Les liaisons radioélectriques étudiées se font entre Monterfil (latitude 48°05N, longitude 2°W) et tout émetteur travaillant sur porteuse et de position connue. L'analyse expérimentale est faite à l'aide d'un "goniopolarimètre" qui est un système déterminant à la fois les angles d'arrivée (fonction goniométrie) et le type de polarisation des ondes incidentes correspondantes. Le traitement s'appuie sur une méthode d'analyse fréquentielle non linéaire haute résolution associée à un filtrage de polarisation.

## SUMMARY

We present in this paper a system which is able to separate the propagation paths and also to identify the type of polarization of the modes. The studied links are between Monterfil (48°05N latitude, 2°W longitude) and all type of known location transmitter which works on carrier. The experimental analysis is performed using a "goniopolarimeter" which is a device determining both the arrival angles (goniometrical function) and the type of polarization of the corresponding incoming skywaves. We apply a high resolution non linear frequential analysis associated to a reiterated method of filtering matched to this polarization.

## 1. INTRODUCTION

L'anisotropie du canal ionosphérique influence la polarisation des ondes reçues. Lors d'une liaison point à point par ce milieu, plusieurs trajets et modes de propagation sont possibles. Les signaux correspondants à ces divers modes sont généralement fortement corrélés.

Plus précisément, les ondes suivant des trajets différents, sont affectées d'un doppler variable d'un mode à l'autre. Pour un trajet donné, deux modes appelés ordinaire "O" et extraordinaire "X" peuvent être voisins. Les performances de la mesure des angles d'arrivée des trajets très proches, sont limitées si l'on ne tient pas compte du caractère vectoriel de la propagation [1].

L'objectif de cet article est :

- de décrire un système qui permet l'identification des modes et trajets de propagation sur des liaisons HF. L'intérêt d'une telle identification avec séparation de modes, réside dans l'analyse plus fine du canal ionosphérique mettant en évidence les effets de polarisation des ondes.
- de rappeler la conception d'un tel système décrit par ailleurs [2] et d'en évaluer les limites et les conditions de bon fonctionnement.
- d'analyser des mesures effectuées sur des émetteurs de radiodiffusion de position connue.

Le système est de conception originale basée sur les travaux antérieurs de Bertel et al (1990) [3] et Baltazart

et al (1992) [1]. La méthode exposée, utilise des signaux à bande étroite (mesures effectuées sur porteuse) auxquels est appliqué un filtrage de polarisation associé à une analyse fréquentielle non linéaire. Elle est différente de celle proposée par Rogier et al (1991) [4], s'appuyant sur l'observation de signaux large bande et un traitement par l'algorithme haute résolution MUSIC. Elle diffère également de la technique développée dans le système Skyloc [5].

Nous présentons les procédures de traitement de signal qui conduisent à l'obtention des paramètres souhaités : identification du type de mode, doppler intermode, nombre de modes et de trajets de propagation, et pour chacun d'eux, leur puissance relative et leurs angles d'arrivée.

Nous donnons des exemples expérimentaux qui illustrent les théories développées et qui montrent l'intérêt d'un tel système, en particulier pour estimer les azimuts et élévations sur des modes de types différents.

## 2. HYPOTHESES PHYSIQUES A L'ORIGINE DU SYSTEME

Les liaisons radioélectriques par voie ionosphérique se font par des trajets multiples auxquels sont associés deux modes de polarisation "O" et "X". Des articles antérieurs [1] et [6] ont décrit un modèle de signal, qui s'appuie sur une connaissance a priori de la réponse des antennes utilisées. Le signal à la sortie d'une antenne, résulte de la contribution de chacune de ces ondes ayant transité par

l'ionosphère. Pour un capteur de type  $u$  dont la position dans le réseau est  $i$ , le signal  $\chi_{iu}(t)$  ramené en bande de base à la sortie de ce capteur, se met sous la forme analytique suivante [1] :

$$\chi_{iu} = \sum_{k=1}^M A_k \cdot e^{j\theta_k} \cdot e^{j\varphi_{ik}} F_{uk}(T_u, Az_k, E_k, P_k) + n_u \quad (1)$$

où :

$A_k$  est l'amplitude relative au mode  $k$ ,

$\theta_k$  la phase généralisée,

$F_{uk}$  la réponse du capteur qui dépend de son type ( $T_u$ ), des angles d'arrivée (élévation  $E_k$ , azimut  $Az_k$ ) et de la polarisation  $P_k$  de l'onde incidente,

$M$  le nombre de modes incidents au capteur,

$n_u$  représente un bruit additif,

$\varphi_{ik} = 2\pi \cdot \frac{R_i}{\lambda} \cdot \cos(E_k) \sin(Az_k)$  avec  $\varphi_{ik}$  le déphasage géométrique correspondant au mode  $k$  pour le capteur  $i$ ,  $\lambda$  la longueur d'onde et  $R_i$  la distance au centre du réseau.

En bande étroite, on pose  $\theta_k = \omega_k t$ , où  $\omega_k$  est la pulsation correspondant au mode  $k$  et nous écrivons [1] :

$$\omega_k = \omega_0 + \Delta\omega_k(t)$$

$\omega_0$  est la pulsation du signal émis et  $\Delta\omega_k$  traduit le décalage doppler.

Pour des mouvements suffisamment lents et pour simplifier la génération du signal pour une période de simulation typiquement inférieure à une heure, nous donnons au doppler une allure simple de type sinusoïdal déjà introduite dans [1] :

$$\Delta\omega_k = a \left( \frac{E_k \cdot T}{100} \right) \cdot \cos \left( \frac{2\pi t}{T} + \alpha_k \right) \quad (2)$$

où  $E_k$  est l'angle d'élévation exprimé en degrés,

$T$  est la période de perturbation (typiquement on prend 15 mn pour une onde de gravité),

$a$  est le terme d'amplitude des oscillations,

$\alpha_k$  est la phase à l'origine (fixée à 0 dans les simulations).

Les valeurs d'amplitude des oscillations et leur période sont déduites d'expérimentations [7]. Ce dernier

formalisme considère que les perturbations ont pour origine les ondes de gravité, et il néglige la composante continue du doppler moyen journalier; il rend toutefois bien compte des observations. Le décalage doppler est d'autant plus important que l'angle d'élévation est élevé (ou l'altitude de réflexion importante), ce qui, pour une liaison donnée, traduit l'influence de la pénétration de l'onde dans le milieu ionosphérique.

Les caractéristiques du signal reçu, impose au système l'ensemble des contraintes suivantes :

- une technique de réception à diversité de polarisation pour séparer les différents modes de propagation. Quand pour un même trajet, les trajectoires des modes "O" et "X" sont très proches, les doppler correspondants sont très voisins; il est alors difficile de séparer ces ondes sans utiliser cette technique de diversité de polarisation.
- une analyse fréquentielle pour identifier les trajets de propagation et une technique de goniométrie pour déterminer les angles d'arrivée.

La constitution du "goniopolarimètre", se présente en fait, comme un système passif de réception HF couplé à un module d'acquisition automatique des signaux et de traitement en temps différé des informations enregistrées.

### 3. DESCRIPTION DU DISPOSITIF EXPERIMENTAL.

#### 3.1 Banc d'Acquisition de Données (figure 1).

Le réseau actuel de réception est constitué de 3 capteurs (6 cadres croisés) disposés au sommet d'un triangle rectangle isocèle de 23 mètres de côté. Deux antennes cadres actives à polarisation croisée, orientées Est-Ouest (EW) et Nord-Sud (NS), forment un capteur. Les signaux HF acquis en parallèle sur 6 récepteurs cohérents, sont transposés en bande de base avec une largeur de bande variable entre 10Hz et 1KHz.

Une carte d'acquisition multi-voies permet d'échantillonner les signaux à la fréquence désirée ( $\leq 200$ Hz par voie pour une bande de sortie de 10Hz) et stocker les données. Les acquisitions sont programmées d'une façon automatique. L'analyse des signaux par trames de 10 secondes, respecte a priori l'hypothèse de stationnarité du canal ionosphérique aux latitudes moyennes, sous incidence oblique. Enfin, l'utilisation d'une antenne d'émission à polarisation verticale située à environ 200 mètres du système, permet de constituer des fichiers de calibrage du réseau pour chaque fréquence de travail.

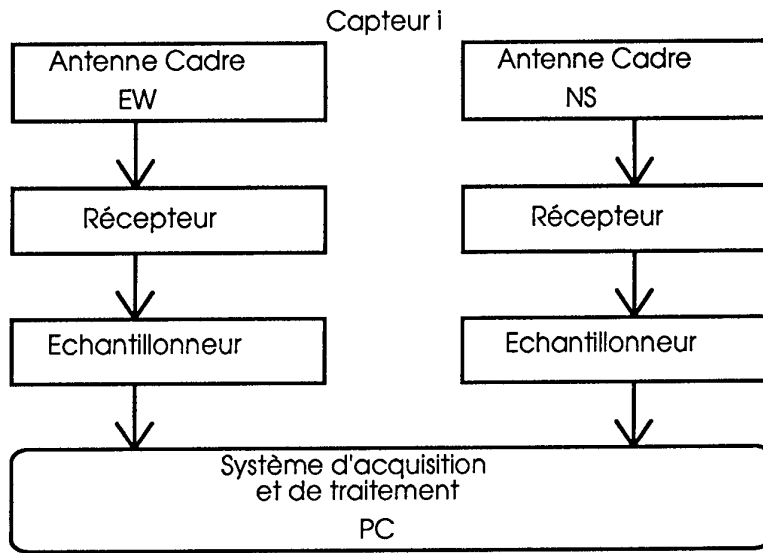


Figure 1 : Synoptique du banc d'acquisition des signaux

### 3.2 Traitement et Extraction des Paramètres (figure 2)

#### \* Filtrage de Hilbert

Le filtrage de Hilbert (trame par trame) consiste tout d'abord à générer à partir des signaux réels sur les antennes EW ( $\chi_{iEW}$ ) et NS ( $\chi_{iNS}$ ), les voies en phase et en quadrature.

L'intérêt d'avoir les signaux sous forme complexe est :

- de disposer de signaux d'où nous sortirons l'information phase,
- de pouvoir compenser l'erreur relative en amplitude et phase de chaque voie en utilisant les coefficients complexes résultant du calibrage du système.

#### \* Filtrage de polarisation

Si on suppose que la polarisation des modes de propagation est circulaire, ceci conduit à un filtrage de polarisation que nous dénommons "industriel" parce qu'il est utilisé dans de nombreux systèmes opérationnels.

A partir des signaux complexes  $\chi_{iEW}^*(t)$  et  $\chi_{iNS}^*$  du capteur i, obtenus après la transformée de Hilbert et le calibrage, deux signaux analytiques filtrés  $S_{iO}(t)$  et  $S_{iX}(t)$  correspondant aux modes "O" et "X" sont alors construits par une pondération simple ( $\alpha = \pm j$ ) :

$$S_{iX,O}(t) = \chi_{iEW}^*(t) \pm j \cdot \chi_{iNS}^*(t)$$

Le signe donne le type de mode suivant le sens de rotation de l'ellipse [8].

La polarisation des ondes incidentes dépend des angles d'arrivée, de la fréquence et de la localisation de la station de réception. Les calculs montrent alors que la polarisation des ondes incidentes aux antennes est généralement elliptique [9]. Le filtrage industriel n'est alors efficace que pour certaines directions d'arrivée.

De plus, la réponse des capteurs n'est pas isotrope; elle est fonction de la direction d'arrivée des ondes et de la nature du sol au voisinage des antennes.

Cette pondération simple limite les performances du filtrage "industriel" qui introduit donc des erreurs sur les estimations des angles d'arrivée [10].

De cette technique, il résulte toutefois des estimations qui restent voisines des valeurs introduites en simulation. Ces imperfections nous ont conduit à proposer un filtrage itératif qui utilise la réponse analytique des antennes [10].

Les coefficients itératifs de filtrage sont initialisés à partir des estimations des angles d'arrivée obtenus par filtrage "industriel".

Ces pondérations complexes ( $\alpha_O$ ,  $\alpha_X$ ) sont calculées à partir des conditions aux limites de Budden [8].

Les signaux analytiques relatifs aux modes "X" et "O" sont alors construits:

$$S_{iX,O}(t) = \chi_{iEW}^*(t) + \alpha_{X,O} \chi_{iNS}^*(t)$$

$$\text{avec } \alpha_O = -\frac{F_{XEW}}{F_{XNS}}, \alpha_X = -\frac{F_{OEW}}{F_{ONS}}$$

où F représente la réponse du capteur considéré (EW ou NS) pour le mode (O ou X).

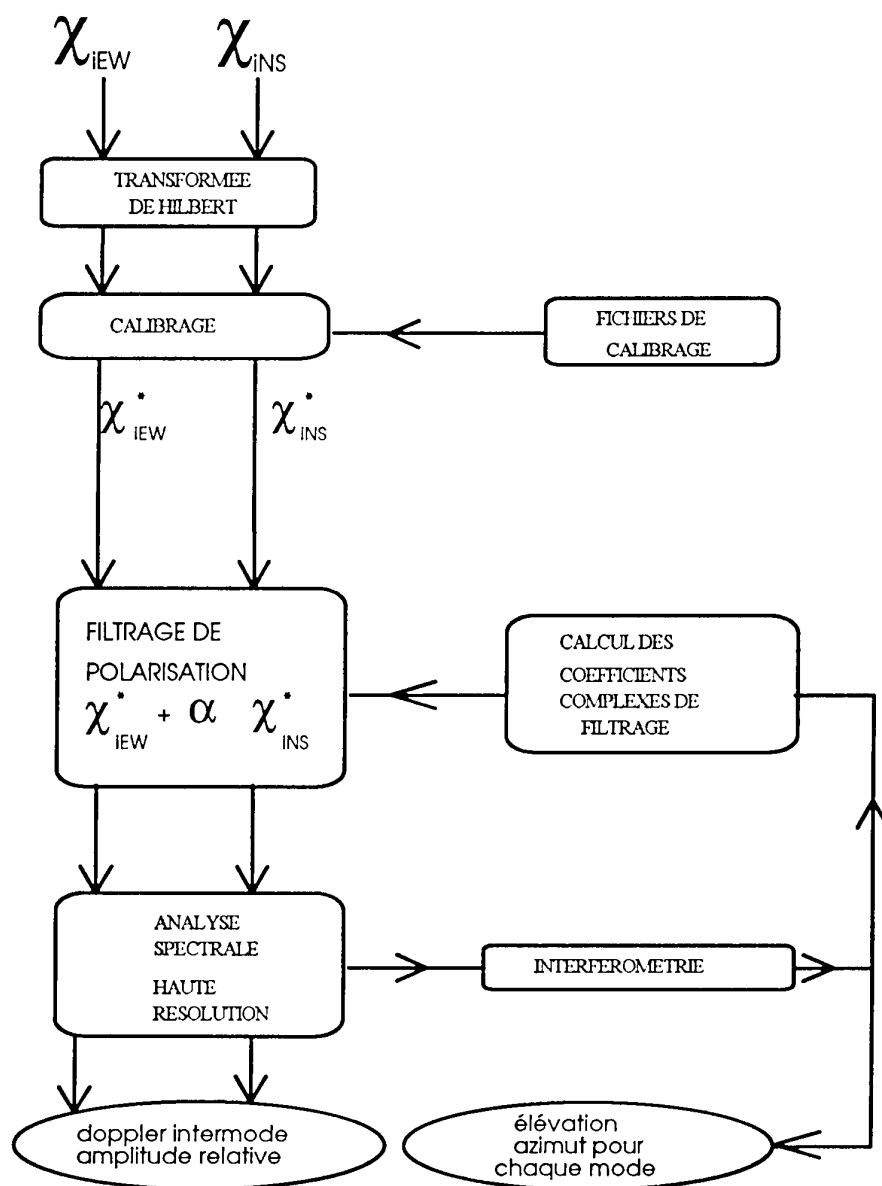


Figure 2 : Procédure de traitement.

Le filtrage itératif améliore les estimations des angles d'arrivée et la détection du nombre de modes incidents [10].

#### \* Filtrage fréquentiel

La durée d'analyse devra être faible compte tenu de la non stationnarité du milieu ionosphérique. Typiquement, nous prenons une durée de trame de 10 s.

En accord avec le modèle de signal et les résultats expérimentaux, le doppler intermode est faible, et il est nécessaire d'utiliser une analyse spectrale haute résolution pour séparer en fréquence les modes de propagation.

A partir de l'estimation de la densité spectrale (dsp) par l'algorithme de Burg [11], une détection des maxima d'amplitude de la dsp moyenne, permet de déterminer les fréquences de résonance.

Les informations d'amplitude et de phase, associées à chacun des pics spectraux correspondant au type de mode propagé, sont estimées en appliquant la Transformée de Fourier Discrète (DFT) sur la prédiction temporelle du signal complexe. Nous réduisons le temps de calcul imposé par la DFT, en opérant uniquement sur les pics spectraux.

\* Calcul des angles d'arrivée

Connaissant les phases différentielles des différentes voies filtrées, les angles d'arrivée des modes sont estimés en utilisant une technique simple de goniométrie (interférométrie).

#### 4. SIMULATIONS ET LIMITES DU GONIOPOLARIMÈTRE

Nous utilisons le modèle de signal décrit pour évaluer les effets des multitrajets sur le "goniopolarimètre". Le nombre de paramètres (élévation, azimut, doppler intermode, effet du sol, ...) étant important pour simuler un signal, ce qui suit ne constitue qu'une illustration des limites du système.

Les conditions de simulation sont les suivantes:

- le doppler intermode généré est donné par la relation (2),
- l'amplitude relative des oscillations est normalisée à 1 pour tous les modes,
- la fréquence d'échantillonnage est de 100 Hz, le signal en bande de base est de 6 Hz et la fréquence HF est fixée à 6 MHz,
- le sol naturel choisi a une permittivité relative de 15 et une conductivité de 0.01 S,
- la distance entre les antennes de réception est de 23 mètres.
- le modèle du signal ne prend pas en compte le bruit, excepté pour le cas étudié au paragraphe 4.7.

##### 4.1 Comportement du Système sans et avec Filtrage de Polarisation Industriel

Une goniométrie est faite sur une propagation où deux modes incidents sont attendus : un mode "O" (azimut (az) = 165° ; élévation (el) = 62° et un mode "X" ( az = 160° ; el = 60° ).

A l'aide d'un seul type d'antenne (EW), on trouve az = 161.9°, el = 61.1°; le résultat de l'élévation est la moyenne des élévations des deux modes attendus. Ceci est en accord avec les résultats publiés en [1].

En utilisant 3 capteurs à diversité de polarisation, le système détecte les deux trajets : un mode O ( az = 165.3°, el = 62.1°) et un mode X ( az = 159.8°, el =

59.9°). Nous remarquons que la séparation de deux modes de type différent est possible même si le doppler intermode est négligeable.

##### 4.2 Apport du Filtrage de Polarisation Itératif

Le filtrage de polarisation " industriel" est appliqué sur un exemple de propagation par 3 modes : deux modes "X" ( $X_1$  : az = 130°, el = 30°;  $X_2$  : az = 130°, el = 60°) et un mode "O" (az = 130°, el = 62°).

Dans cette simulation, nous introduisons une faible élévation pour le mode  $X_1$  et un doppler intermode entre  $X_2$  et "O" très réduit du fait des trajets voisins suivis, en accord avec le modèle de doppler. La figure 3a alors obtenue, montre que le système détecte 4 modes au lieu de 3. Ceci est dû à l'inadéquation filtrage-propagation.

La méthode itérative de filtrage de polarisation entraîne ainsi la disparition du mode parasite et une amélioration sensible de l'estimation des valeurs d'angle d'arrivée (figure 3b).

##### 4.3 Limites du Filtrage de Polarisation Itératif

Le résultat d'une estimation d'angles d'arrivée dans le cas d'une propagation par deux modes ( "X" : az = 130°, el = 10° et "O" : az = 130°, el = 20°), est le suivant :

"X" : az = 130.1°; el = 8.9°

"O" : az = 130.2°; el = 19.9°.

Il apparaît que le filtrage de polarisation itératif est limité pour des angles de site très faibles ( $\leq 10^\circ$ ).

Ceci peut s'interpréter puisque la polarisation des deux ondes tend vers une polarisation quasi-linéaire lorsque l'élévation décroît.

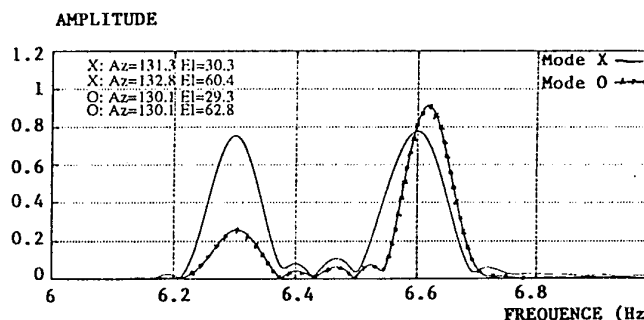


Figure 3a : Séparation des modes par filtrage de polarisation "industriel" (d'après [10]).

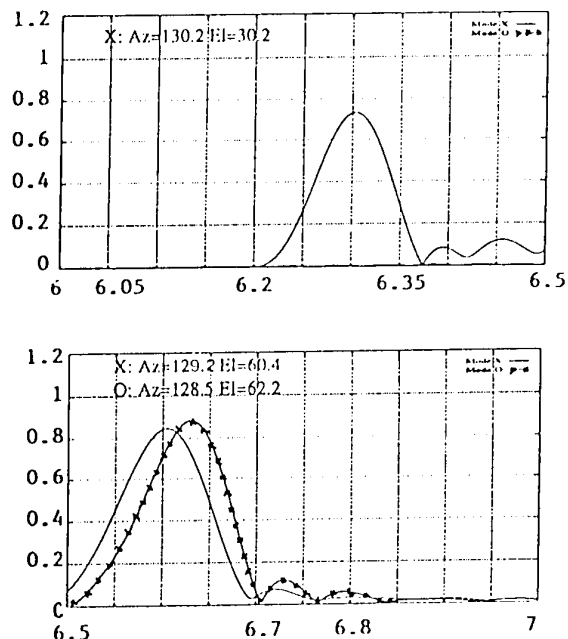


Figure 3b : Séparation des modes par filtrage de polarisation itératif (d'après [10]).

#### 4.4 Influence de la Non-Stationnarité du Milieu Ionosphérique .

L'ionosphère est non stationnaire et dans certains cas les signaux à analyser le sont ; ceci peut conduire à des erreurs d'interprétations.

En effectuant une goniométrie sur une propagation de 2 modes incidents ( "O" : az = 160°, el = 62°; "X" : az = 160°, el = 60°) et en variant la durée d'analyse, on obtient les résultats résumés dans le tableau ci-dessous.

La non-stationnarité de l'ionosphère (40.96s) et l'insuffisance du temps d'intégration (1.28s), donnent des résultats aberrants. Par contre, le système détecte bien les 3 modes pour une durée d'analyse de 5.12s et 10s.

Durée analyse [s]	Résultats de goniométrie	Remarques
1.28	X1: az=159.3°, el=60.3° X2: az=159.7°, el=59.5° O1: az=159.3°, el=62.4° O2: az=159.9°, el=61.5°	durée intégration insuffisante
5.12	X: az=160.0°, el=59.9° O: az=160.1°, el=62.2°	durée convenable
10.24	X: az=160.0°, el=59.9° O: az=159.9°, el=62.1°	durée convenable
40.96	X1: az=157.5°, el=62.1° X2: az=190.6°, el=54.2° O : az=158.6°, el=64.8°	durée trop grande : milieu non stationnaire

#### 4.5 EFFET DU DOPPLER INTERMODE SUR LES PERFORMANCES DU GONIOPOLARIMETRE

##### 4.5.1 Amplitude des Oscillations du Doppler

Pour deux modes incidents de même type (X1: az=160°, el=60°; X2: az=160°, el=65°), on obtient (X1: az=160.6°, el=60.4°; X2: az= 160.7°, el = 65.5°). Deux modes de même type peuvent être séparés à condition que leur doppler intermode soit supérieur ou égal à 0.05 Hz.

##### 4.5.2 Comportement du Filtrage de Polarisation en Fonction de la Variation Temporelle du Doppler

Une trame de 5.12s de signal est générée à différents instants suivant l'évolution du doppler de période T = 900s. Le tableau ci-dessous donne les résultats de goniométrie faite sur ce signal composé de deux modes incidents ("X" : az = 160°, el = 60°; "O" : az = 160°, el = 62°).

Instant de début du doppler [s]	Résultats de goniométrie
0	X : az=159.9°, el=59.8° O : az=160.9°, el=61.6°
T/8	X : az=160.0°, el=60.1° O : az=160.3°, el=62.3°
T/4	X : az=160.0°, el=59.9° O : az=160.1°, el=62.2°
T/2	X : az=160.1°, el=59.8° O : az=160.2°, el=62.5°

L'erreur sur la goniométrie reste du même ordre de grandeur montrant ainsi l'efficacité du filtrage de polarisation.

#### 4.6 Comportement du Bruit sur le Système.

Après un filtrage de polarisation industriel (figure 2), on injecte à l'entrée du filtre de Burg, un signal réel de 4000 échantillons acquis à partir de la liaison Monterfil (48°05 Nord, 2° Ouest) - Allouis (47° Nord, 2° Est). En sortie de ce filtre, le bruit expérimental de puissance relative 0.302 (-5 dBm), est récupéré. Ce bruit blanc, de densité spectrale (dsp) constante, est gaussien et de moyenne nulle (figure 4). La goniométrie est faite sur un signal (X : az = 160°, el = 60°; O : az = 160°, el = 62°) en variant sa puissance. Le tableau ci-dessous résume l'effet du rapport signal à bruit (S/B) sur les résultats obtenus.

Puissance du signal en entrée[dBm]	10	20	30
(S/B) à l'entrée [dB]	15	25	35
Puissance de bruit en sortie[dBm]	-21	-21	-12
(S/B) en sortie [dB]	X : 6 O : 6	X : 25 O : 25	X : 27 O : 27
Résultats de goniométrie	X : az=166° el=89°	X : az=160.1° el=59.8°	X : az=160.1° el=59.9°
	O : az=323° el=89°	O : az=160.1° el=62.2°	O : az=160.1° el=62.1°

Pour un rapport signal à bruit relativement faible ( $\leq 15$ dB), le système ne détecte pas les modes incidents. Plus (S/B) est important et plus la goniométrie devient efficace.

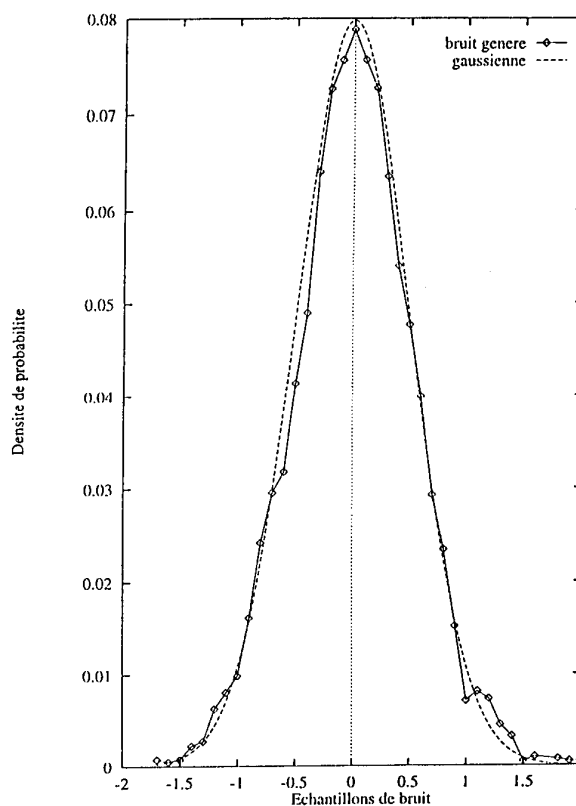


Figure 4 : Densité de Probabilité du Bruit

#### 4.7 Cas de la Présence de Plusieurs Modes Incidents.

L'exemple d'illustration est une propagation par 5 modes incidents :

X1 : az = 170°, el = 51°;  
X2 : az = 170°, el = 72°;  
X3 : az = 170°, el = 79°;  
O1 : az = 175°, el = 73°;  
O2 : az = 175°, el = 79°;

La goniométrie donne :

X1 : az = 169.6°, el = 50.5°;  
X2 : az = 170°, el = 71.7°;  
X3 : az = 169.1°, el = 79.8°;  
O1 : az = 175.1°, el = 72.6°;  
O2 : az = 174.2°, el = 78.3°;

Sur cet exemple on observe des erreurs inférieures au degré.

Quand le nombre de modes incidents devient important (plus grand que 5), le goniopolarimètre n'est plus performant.

## 5. Conséquences sur le Fonctionnement du Système

Nous récapitulons les domaines de validité du goniopolarimètre comme suit :

- angle d'élévation  $> 10^\circ$
- doppler intermode  $\geq 0.05\text{Hz}$  (dans le cas des modes de même type)
- nombre de modes incidents  $\leq 5$
- rapport signal à bruit nécessaire  $\geq 20\text{ dB}$
- durée d'analyse supérieure à 10s.
- erreur attendue sur les angles d'arrivée  $\pm 1^\circ$  au maximum.

### 5.1 Traitement de Données Réelles

Pour un mode  $k$ , l'interférométrie utilise 3 voies filtrées pour déterminer son élévation et son azimut. La moyenne de la dsp des 3 voies, est évaluée et une estimation des trajets de propagation est faite (détection des pics spectraux). Une goniométrie est réalisée sur chaque mode. Un traitement statistique évalue le nombre d'apparitions de chacun des trajets. Ce cumul de résultats d'interférométrie, nous permet un gain sensible dans l'identification des trajets. La validation de la présence du mode sur le réseau est donnée par la probabilité de son apparition.

La procédure est inadéquate aux instants où les dopplers intermodes sont nuls. La cohérence des résultats de goniométrie (angles d'arrivée, fréquences et amplitudes relatives) au cours du temps, élimine les incertitudes dues à ces mauvaises goniométries.

### 5.2 Ambiguïtés des Angles d'Arrivée

Si  $d_{ij}$  est la distance entre les capteurs  $i$  et  $j$ , le réseau peut être considéré comme une discrétisation dans l'espace, et la condition de Shannon impose :

$$d_{ij} \leq \frac{\lambda}{2 \cdot \cos(E_p)}$$

avec  $E_p$  l'angle d'élévation correspondant au mode  $p$ .

Puisque la longueur d'onde  $\lambda$  est variable, il arrive parfois que cette condition ne soit plus respectée. Ceci introduit des ambiguïtés sur les angles d'arrivée.

Nous proposons une solution qui, à partir de la configuration goniométrique du réseau à trois capteurs et des quatre cadrans du cercle trigonométrique, utilise l'azimut goniométrique  $A_{Z0}$  connu.

Suivant la position de  $A_{Z0}$  dans les cadrans du cercle, le retard ou l'avance du front d'onde sur le réseau, est

déterminé. On déduit ainsi le signe du déphasage  $\Delta\phi$ .

Dans le cas où  $\Delta\phi$  a un signe contraire à celui attendu, alors :

$$\text{si } \begin{cases} \Delta\phi < 0 \Rightarrow \Delta\phi = \Delta\phi + 360^\circ \\ \Delta\phi > 0 \Rightarrow \Delta\phi = \Delta\phi - 360^\circ \end{cases}$$

### 5.3 Avantages du Système

Le "goniopolarimètre" utilise un nombre restreint de capteurs (3 dans notre cas), contrairement aux systèmes [4] qui identifient un nombre de modes limité par celui des capteurs. D'autre part, la fréquence d'échantillonnage étant faible, la taille mémoire utile est réduite (3 Mégaoctets de mémoire paginée).

Par rapport à des systèmes actifs qui mesurent le temps de propagation des modes, le goniopolarimètre en estimant les angles d'arrivée, présente 4 avantages :

- il ne nécessite pas de synchronisation émission-réception,
- il peut étudier de nombreuses liaisons (émetteurs coopératifs),
- il identifie le type de polarisation des modes de propagation,
- il permet la mesure de plusieurs paramètres (azimut, élévation, type de mode, amplitude).

Dans la version actuelle du système, l'ordre de grandeur du temps de calcul sur un PC486, est moins de deux minutes pour une goniométrie faite pour 4 modes incidents sur une trame de 10.24s. Ce point fait du système un élément utile à des études du milieu mais non à des applications de détection de sources émettant de courts instants.

## 6. RESULTATS EXPERIMENTAUX

Le système expérimental décrit au paragraphe 3, est implanté à Monterfil (France).

Pour illustrer l'action des filtrages industriel et itératif, une goniométrie est réalisée sur une liaison Skelton (BBC) - Monterfil (distance = 705 km) et les résultats sont indiqués dans le tableau 1. Il apparaît que le filtrage de polarisation itératif donne des valeurs plus proches de celles des prévisions de propagation. Ces prévisions sont valables uniquement pour des trajets isotropes : modes "X" et "O" confondus. Les différences entre les résultats obtenus avec un filtrage industriel et les données attendues peuvent s'interpréter si on tient compte de la polarisation des ondes incidentes dans le plan d'onde. Pour une liaison dont l'émetteur est situé au nord (Skelton :  $355^\circ$ ) de la station (Monterfil), cette polarisation peut être linéaire pour certains angles d'élévation (environ  $25^\circ$ ) [9]. Pour les ordres de grandeur ( $17^\circ$ - $40^\circ$ ) des angles observés, le filtrage industriel



supposant les ondes polarisées circulairement, est donc complètement inadapté et explique pourquoi plusieurs itérations (6 dans ce cas) sont alors indispensables pour obtenir des valeurs cohérentes. Pour le mode O, on observe un comportement analogue.

Le tableau 2 montre les résultats typiques ( 3 cas ) obtenus pour la liaison Monterfil - Allouis. Dans la dernière colonne, figurent les données expérimentales du sondeur vertical de Poitiers. Cette station est située à environ 100 km du point milieu de la liaison étudiée.

Le cas 1 correspond à des situations couramment observées. On constate d'une trame à l'autre une bonne cohérence entre les mesures. Les paramètres du mode O de la trame 4 semblent signifier une propagation momentanée par la couche  $F_2$  alors que les autres valeurs sont relatives à une propagation par la couche  $F_1$ . L'accord entre les valeurs des hauteurs virtuelles déterminées par nos mesures et par sondage (données de Poitiers), est très bon dans ce cas.

Le cas 2 est très intéressant car outre la présence d'une propagation par une couche  $F_1$  (mode X) relativement stable, on observe la présence d'une liaison par une couche Es (trame 1) relayée (trame 2) par une couche E qui reste seule en trame 3. Ceci montre l'aptitude du système à détecter des angles d'arrivée voisins à élévations relativement faibles.

Le cas 3 montre que le mode X est relativement stable (élévation environ  $50^\circ$ ) et correspond à une propagation par  $F_1$ . On constate sur la trame 1 la présence de 2 modes O qui arrivent sous des azimuts voisins mais séparés en doppler d'une quantité suffisante ( $> 0.05$  Hz) pour assurer qu'il y a bien 2 trajets. Sur la trame 3, apparaissent 2 modes (X et O) de propagation qu'on peut attribuer à la présence des couches E et Es, respectivement.

Ces 3 cas permettent un suivi temporel des différents modes de propagation. L'interprétation des résultats reste délicate à cause de la présence des couches sporadiques (Es). Cependant, la comparaison entre les résultats expérimentaux et les prévisions de propagation ou les données de sondage, montre bien l'intérêt du système. Les déviations azimutales observées sont probablement dues d'une part aux erreurs instrumentales, et d'autre part aux effets tilts [2] et aux variations spatiales du milieu ionosphérique.

## 7. CONCLUSION

Le système décrit dans cet article permet la mesure des paramètres souhaités : angles d'arrivée, puissance relative des modes, doppler intermode, type de polarisation des ondes incidentes aux antennes.

L'amélioration de cette première réalisation du système passe par :

- une meilleure connaissance des réponses d'antennes,
- une augmentation de la dynamique de travail,
- des techniques de filtrage de polarisation encore plus efficaces (adaptées au mode filtré),
- l'utilisation d'un nombre accru de capteurs.

Les données obtenues par le système peuvent être appliquées pour une meilleure compréhension du canal de transmission HF et pour définir un modèle d'inclinaison de couches ionisées.

## 8. REFERENCES

- [1] Baltazart V., Bertel L., Fleury R., "Influence de la propagation sur la goniométrie haute fréquence et la localisation à station unique", AGARD, 50th symposium of the electromagnetic wave propagation panel on radiolocation techniques, Londres, 1-5 juin 1992.
- [2] Edjéou A., Lemur D., Bertel L., "Design and realization of a goniopolarimeter : application to Tilts study", Second South Pacific Step Workshop, University of Newcastle, Australia, 5-9 july 1993.
- [3] Bertel L., Le Ray B., Baltazart V., Le Saout J.Y., "Analysis of behaviour on small basis radiogoniometers using interferometry technique", Conference on radiowave propagation, Melbourne, february 1990.
- [4] Rogier J.L., Multedo G., Bertel L., Baltazart V., "Ionospheric multipaths separation with a high resolution direction finding algorithm mapped on an experimental system", IEE Proceedings, 339, juillet 1991.
- [5] Jeffrey Z.R., Middleton P.T. and Winkler C., "Accurate measurements of the total angle of arrival of HF skywaves", AGARD SYPOSIUM, CP-441, Munich, may 1988.
- [6] Rojas V.J., "Antennes filtre de polarisation dans la bande HF", Thèse d'Université, Rennes, 1987.
- [7] Gourvez P., Bertel L., Rojas V.J., "Measurements and analysis of the HF field received with a tripole antenna", IEE Conf. Pub., n° 274, pp. 108-111, 1987.
- [8] Budden K. G., "Propagation of Radio Waves", Cambridge University Press, 1985.
- [9] Bertel L., Rojas J.V., Cole D., Gourvez P. "Polarization and ground effects on HF receiving antenna patterns", Annales des Télécommunications, 44, n°7-8, 1989.
- [10] Bertel L., Edjéou A., Massot V., Erhel Y., "Méthode itérative de filtrage de polarisation : Application à la goniométrie HF", 14ième Colloque GRETSI, Juan les Pins, 13 au 16 septembre 1993.
- [11] Steven M.K., Stanley L.M., "Spectrum analysis. A modern perspective", Proceedings of the IEEE, vol. 69, n° 11, november 1981.

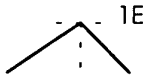

<b>CONDITIONS D'EXPERIMENTATION :</b> Liaison : Skelton (BBC) - Monterfil (Goniopolarimètre) Distance : 705 km Fréquence de l'émetteur : 9.75 MHz Date : 04/05/93 Heure : 9 H 30 TU Azimut géométrique : 355 ° Durée d'analyse : 10.24 s Fréquence d'échantillonnage : 100 Hz				
PREVISIONS DE PROPAGATION			MESURES	
Altitude de réflexion[km]	Angle d'élévation[°]	Type de couche	Filtrage industriel	Filtrage itératif
105	16.7		X: azimut= 345.8° élévation = 29.1°	azimut= 353.9° élévation = 16.8°
250 - 300	35 - 40		X: azimut= 351.8° élévation = 48.3°	azimut = 350.5° élévation = 39.8°

Tableau 1 : Influence du filtrage de polarisation

Tableau 2 : Suivi temporel des modes de propagation

Liaison : ALLOUIS-MONTERFIL : 325km

Fréquence de l'émetteur : 6.175MHz; Azimut géométrique : 110°

Durée d'analyse : 10.24s; Fréquence d'échantillonnage : 100Hz

CAS 1 : Date 12/02/93; Heure : 15H04 TU; angle d'élévation prédit : [50-58°] (1F2).

Séquence	Mode	Fréquence observée (Hz)	Azimut mesuré (°)	Elévation mesurée (°)	Puissance relative	Hauteur virtuelle estimée h (km)	Hauteur virtuelle de réflexion ( km) données de Poitiers
1	X	6.05	126.8	49.1	342.9	195.3	112, E 235, F <sub>1</sub> 269, F <sub>2</sub>
	O	6.03	124.3	51.1	313.0	210.0	
2	X	6.03	123.8	51.0	270.8	209.2	
	O	6.04	123.0	54.2	295.4	235.6	
3	X	6.06	126.6	51.6	340.7	213.8	
	O	6.04	125.8	53.9	343.7	232.9	
4	X	6.05	124.7	49.5	356.7	198.1	
	O	6.05	126.4	57.8	316.4	271.0	
5	X	6.03	122.6	50.6	411.5	206.2	
	O	6.03	127.1	49.6	351.3	198.8	

CAS 2 : Date 8/04/93; Heure : 8H30 TU; prévision de l'angle d'élévation : [30-40°] (1E).

Séquence	Mode	Fréquence observée (Hz)	Azimut mesuré (°)	Elévation mesurée (°)	Puissance relative	Hauteur virtuelle estimée h (km)	Hauteur virtuelle de réflexion ( km) données de Poitiers
1	X	6.18	108.5	45.5	266.9	171.9	112, E 144, Es
	O	6.11	109.8	37.0	94.5	126.9	
2	X	6.18	108.0	44.8	299.5	167.7	
	O	6.11	102.0	36.4	103.8	124.2	
	O	6.15	110.1	30.8	154.5	100.5	
3	X	6.18	108.2	45.0	345.6	168.9	
	O	6.19	117.0	31.1	209.2	101.6	

CAS 3 : Date 21/04/93; Heure : 7H30 TU; prévision de l'angle d'élévation : [30-40°] (1E); [50-58°] (1F2).

Séquence	Mode	Fréquence observée (Hz)	Azimut mesuré (°)	Elévation mesurée (°)	Puissance relative	Hauteur virtuelle estimée h (km)	Hauteur virtuelle de réflexion ( km) données de Poitiers
1	X	12.1	113.4	54.4	118.2	212.4	109, E 133, Es 220, F <sub>1</sub> 260, F <sub>2</sub>
	O	12.0	118.7	50.2	99.1	203.3	
	O	12.08	120.4	54.0	82.3	233.9	
2	X	12.08	117.4	50.4	140.1	204.8	
	O	12.07	117.0	51.6	101.1	214	
3	X	11.90	118.5	32.3	46.5	106.5	
	X	12.07	115.7	51.1	127.5	210.1	
	O	11.92	112.6	34.6	53.6	116.2	
	O	12.07	119.5	52.0	98.6	217.1	

## DISCUSSION

**Discussor's name :** C. Goutelard

**Comment/Question :**

Pouvez-vous préciser les problèmes que vous rencontrez aux faibles angles?

**Translation :**

*Could you specify the problems which you encounter at low angles?*

**Author/Presenter's reply :**

Les problèmes ont différentes origines:

- L'expérimentation elle-même : aux faibles angles le sursol (arbres, bâtiments, pylones, lignes électriques) peut perturber les mesures.
- La modélisation des capteurs peut s'avérer difficile (variation des caractéristiques du sol sur des distances de l'ordre de quelques longueurs d'onde).
- La technique elle-même: à élévation faible l'estimation devient délicate (ouverture du réseau faible, niveaux des signaux tels que le rapport signal à bruit décroît rapidement).

**Translation :**

*The problems are of different origins :*

- *The experiment itself : at low angles, the overground (trees, buildings, pylons, power lines etc.) may interfere with the measurements.*
- *Modelling of the sensors may prove difficult (variations in ground characteristics over distances of the order of a few wavelengths).*
- *The technique itself : estimation may be tricky at low elevation (narrow array aperture, signal levels such that signal to noise ratio falls off rapidly).*

## GEOGRAPHICAL DIVERSITY COMBINING TO EXPLOIT MULTI-MECHANISM PROPAGATION

M Darnell and T J Speight  
Hull-Lancaster Communications Research Group  
Department of Electronic Engineering  
University of Hull  
HULL, HU6 7RX  
United Kingdom

### 1. SUMMARY

The paper introduces the principles of a new macroscopic diversity scheme employing maximum likelihood, symbol-level, diversity combining. The performance of the scheme is compared with that of other classical post-detector diversity combining methods. It is shown that the new scheme has a performance similar to the classical techniques; however, its complexity is significantly lower.

The application of macroscopic diversity in the HF band is then described, and the results of practical on-air trials presented.

### 2. INTRODUCTION

Diversity reception is a well known technique which makes use of two or more uncorrelated, or partially correlated, versions of a signal transmitted over a radio channel. Combining, or selecting from, these multiple signals reduces the effect of deep fades, thus reducing the error rate in digital communications systems [1][2][3]. Conventionally, combination/selection is carried out at IF or baseband frequencies, and is termed either 'predetection' or 'postdetection' respectively. The combining/selecting techniques for these conventional cases are well documented and have been extensively analysed [3]; however,

the case where combining occurs at the fully demodulated symbol level has received little attention.

Symbol-level combining suffers from an inherent performance reduction when compared with postdetection or predetection combining because hard-decisions are made early in the receiver/combiner path. Another disadvantage is that duplicate demodulators are required at the diversity receiver sites, resulting in increased equipment costs. Despite these problems, combining at the symbol-level is useful in cases where the capacity of the interconnects between diversity receiving sites is limited; such is the case with macroscopic diversity applied to long-range radio systems, where base station sites may be tens to thousands of kilometres apart and optic fibre, microwave, or coaxial links are not feasible.

The first part of this paper is concerned with the philosophy of a new macroscopic diversity combining scheme; this is then compared with more conventional postdetection (baseband) combining techniques, such as selection, equal-gain and maximal-ratio. The performance is quantified in terms of error probability; it is shown that the new scheme approaches maximum likelihood closely, but is significantly less complex to implement than the more conventional techniques.

Effective implementation of the new combining technique requires the availability of channel state metrics for each branch. The effect of inaccuracies in these metric estimates on system performance is also considered.

Finally, the application of macroscopic diversity combining in the HF (2-30 MHz) context is described. Here, wanted signals and unwanted co-channel interference may propagate to and from the widely-separated sites by means of distinct mechanisms; hence, the scenario represents a multiple-mechanism path. The results of on-air trials, with different numbers of combining sites, are presented.

### 3. MAXIMUM LIKELIHOOD SYMBOL-LEVEL COMBINING

The operation of optimum symbol-level diversity combining relies on precise estimates of instantaneous probability of error, ie the probability that an individual symbol will be

demodulated erroneously, derived from information about the received signal over a given interval. The ideal estimator produces completely accurate instantaneous probability of error estimates. It is likely that the metric used by the ideal estimator will also be the variable upon which the final demodulation decision is based; for example, the outputs of the two matched filters in a binary FSK scheme.

The optimum (maximum likelihood) combining algorithm is simply to calculate the soft-distance of all received vectors from all the possible transmitted vectors, and select the transmitted vector at the minimum overall soft-distance. This is analogous to the optimum decoding of block codes; however, unlike a typical error control coding scheme, the number of possible transmitted vectors is small. In the binary case, there are only two: the all-1s vector and the all-0s vector (for an M-ary modulation scheme, there are M possible transmitted vectors).

Hence, the combining rule is

$$\prod_{\substack{\text{branches demodulated} \\ \text{as '1'}}} (1 - P_{e_j}) \prod_{\substack{\text{branches demodulated} \\ \text{as '0'}}} (P_{e_k}) > \prod_{\substack{\text{branches demodulated} \\ \text{as '0'}}} (1 - P_{e_k}) \prod_{\substack{\text{branches demodulated} \\ \text{as '1'}}} (P_{e_j}) \quad (1)$$

then combine to binary '1'

$$\prod_{\substack{\text{branches demodulated} \\ \text{as '1'}}} (1 - P_{e_j}) \prod_{\substack{\text{branches demodulated} \\ \text{as '0'}}} (P_{e_k}) < \prod_{\substack{\text{branches demodulated} \\ \text{as '0'}}} (1 - P_{e_k}) \prod_{\substack{\text{branches demodulated} \\ \text{as '1'}}} (P_{e_j}) \quad (2)$$

then combine to binary '0'

where  $P_e$  is the error probability; j and k are the number of branches demodulated as a 1 and 0 respectively, and  $j + k = M$ . It is unlikely that precise soft-decision information will be available for every symbol decision; in this case, soft-distance could be calculated for each received vector.

The use of a weight-and-vote algorithm reduces the complexity of the combiner and is used to derive an approximation to the theoretical error rate for the optimum symbol-level combining algorithm; this is described in the Section 4 below.

### 4. OPTIMUM WEIGHT COMBINING

Let the received symbol at the various combiner receiver-demodulators be represented by the vector y, where y is defined as:

$$y = (h_1, h_2, \dots, h_M) \quad (3)$$

where  $h_1, h_2, \dots, h_M$  are the received versions of the data at the M diversity branches. The maximum likelihood technique can now be extended to obtaining an optimum combining algorithm when applied to symbol-level combining with the vector y incompletely known. Figure 1 shows symbol-level combining with the various error probabilities

(listed at the top of the figure) when  $y$  is incompletely known. Here, binary signalling is assumed. The second column of Figure 1 is a listing of possible values of  $y$  in the form of correct and incorrect modulation decisions (C correct; I incorrect); these error patterns are denoted by  $EP_x$  (shown in the first column), where  $x$  is the decimal equivalent of the binary number created, assuming I as a binary '1' and C as a binary '0'; the branch with the lowest  $P_e$  is taken as the most significant bit. It is simpler to show the combiner inputs like this, rather than in actual binary form, since such a representation halves the number of patterns which need be considered. Pairs of error patterns are formed by inversion and hence, for example, in a 5-branch combiner, the pairs formed are:  $EP_0/EP_{31}$ ,  $EP_1/EP_{30}$ , ...,  $EP_{15}/EP_{16}$ . Decision confidence information gives the *a posteriori* instantaneous probability of bit error. The next step is to calculate the probability of each of the error patterns,  $P(EP_x)$  and to note which error pattern in each error pattern pair is most likely. The optimum combining algorithm is now the scheme which gives correct outputs for the identified error patterns, ie the bit pattern with the maximum *a posteriori* probability of occurrence. In Figure 1, the patterns italicised are those which the maximum likelihood scheme would combine to produce a correct output, since these have the greater value of  $P(EP_x)$ ; the other error patterns produce an incorrect output.

Once the nature of the maximum likelihood combiner has been defined, an implementation must be devised. One possibility is to use a weight-and-vote algorithm. This involves assigning a weight value calculation from the *a posteriori* error probability and adding the weight values of all those bits received as binary '0's; this sum is then compared with that obtained by adding the weight values of all those bits received as binary '1's.

Let  $a_1 \dots a_k$  be the weights corresponding to a binary '1' and  $b_1 \dots b_j$  be the weights corresponding to '0', where the weights are calculated as a function of  $P_e$

$$a_i = f(P_i(\text{error demodulated as '1'})) \quad (4)$$

$$b_i = f(P_i(\text{error demodulated as '0'}))$$

Binary decisions are then made on the following conditions

$$\text{if } \sum_{i=1}^k a_i > \sum_{i=1}^j b_i \text{ then output '1'} \quad (5)$$

$$\text{if } \sum_{i=1}^k a_i < \sum_{i=1}^j b_i \text{ then output '0'} \quad (6)$$

To obtain the maximum likelihood condition, correct selection of  $f(P_e)$  giving the weight values must be made. For this purpose, a number of rules can be defined for this function, termed the 'weighting function':

- (i) If any branch inputs have a binary data input which has an *a posteriori* error probability of 0.5, such branches should have no effect on the output of the combining receiver.
- (ii) If any input has a  $P_e$  of exactly 0.00 (always correct), then this input should have total control of the combiner output, regardless of the other inputs.
- (iii) If a diversity branch has a  $P_e$  of  $(x-\delta x)$  then this branch should have a larger weight value than another branch with  $P_e$  of  $x$ , even if  $\delta x$  is very small.

From the above rules, the following can be deduced about the weighting function,  $f(P_e)$ :

- (a) When  $P_e$  is 0.5, then  $f(P_e)$  is zero. The graph of  $P_e$  versus  $f(P_e)$  passes through the point (0.5,0).
- (b).  $f(P_e)$  tends to infinity as  $P_e$  tends to 0.0
- (c)  $f(P_e)$  has no maxima or minima.

Examples of empirical functions which obey these rules, but which are not necessarily optimum, are

$$f(P_e) = \frac{1}{(P_e^n)} - \frac{1}{(0.5^n)} \quad (7)$$

and

$$f(P_e) = -\ln\left(\frac{P_e}{n}\right) + \ln\left(\frac{0.5}{n}\right)$$

(8)

where  $n$  is a positive real number in both equations.

In Figure 1, the function described by equation (7) (with  $n=0.5$ ) is used to calculate weights in the combining process; a non-optimum result is obtained. Optimum weights are calculated by the use of an iterative algorithm, using the weights produced by the empirical function described by equations (7) or (8) as an initial estimate. The optimum performance, ie the maximum likelihood condition, can now be achieved using the weights calculated by this algorithm (also shown in Figure 1). This combining technique is termed 'Optimum Weight Combining'.

## 5. PERFORMANCE EVALUATION BY SIMULATION

Extensive theoretical analysis [4] has resulted in an analytical expression for the probability of error for optimum weight bit-level combining with non-coherent binary FSK, subjected to Rayleigh fading. Because of its complexity, this analysis is not reproduced here.

A comparison of optimum weight and more conventional baseband combining techniques is given in Figure 2. It is seen that a performance equivalent to equal-gain combining is achieved, but with a substantially reduced interconnect capacity requirement between diversity sites. Conventional combining schemes, such as equal-gain and maximal-ratio, require interconnects which have to support the transfer of baseband information received at the diversity sites to a central combining site. This requires interconnects which must transmit data at a minimum of the Nyquist rate for the highest signalling tone used by the transmitter in the modulation scheme. This is a considerably greater transmission rate than is required if optimum bit-level combining is employed; in such a case, a demodulation, decision together with a probability of instantaneous demodulation error for each bit/symbol period, is all that is necessary. An

improvement of approximately 1.5dB is obtained by the use of the new technique compared with conventional selection algorithm with  $M=4$ ; however, when  $M=2$  the techniques are equivalent.

Figure 3 is a plot of probability of error for empirically calculated weights and optimum weights for  $M=2,3,4$ . The empirical functions are a reasonable approximation to the use of optimum weights.

The optimum weight combining technique relies on a precise estimate of instantaneous  $P_e$  for each demodulation decision. In a real implementation of this combining method, inaccurate estimates of  $P_e$  will be used to calculate weights, thus causing a reduction in combiner performance. Figure 4 is a plot of optimum weight combiner performance with  $M=4$ , and various magnitudes of error in the determination of  $P_e$ . It is probable that in a real implementation the estimated  $P_e$ s will be distributed around the actual probability of bit error. In this analysis, the distribution was assumed to be of normal form, with the standard deviation being defined in terms of various percentages of the actual  $P_e$ . Thus, the plot shows estimation errors expressed in terms of the dispersion of the distribution; poorer estimates have a broader distribution than accurate ones. Smaller errors (<20%) produce a relatively small reduction in performance; only when the standard deviation is >50% of actual  $P_e$  does the reduction in performance become very significant.

## 6. HF TRIAL OF MACROSCOPIC DIVERSITY

Little work has been attempted to date in order to assess the value of macroscopic diversity in the HF band, although the technique has been proposed previously [5]. In [6], macroscopic diversity for the HF band was termed a 'geographical diversity' due to the very large distances required between diversity sites in order to achieve sufficiently decorrelated versions of the transmitted signal.

In addition to reducing the effects of long-term fading, the use of macroscopic diversity in the HF band also allows the reduction of the effects of co-channel interference, which is the main source of performance degradation for HF channels in Western Europe [7]. It has been shown that the correlation coefficient



between interference at sites separated by 150km varies from approximately 0.7 to 0.9 [8]. Although this is a significant correlation, a marked difference exists between interference spectra and thus diversity gain is potentially possible. In this experiment, the separation between diversity receiver sites is increased and it is shown that a substantial reduction in bit error rate for HF data transmission is possible via the use of macroscopic diversity combining.

Due to the large distances separating diversity sites, combining is carried out at the fully demodulated bit level; this reduces the required interconnect capacity. Thus, a more appropriate measure of potential combining gain is the degree to which the error patterns are correlated, rather than the signal correlation coefficient. Therefore, in this section an error correlation coefficient is defined and used with the experimental data.

A practical trial has been carried out to investigate the performance of a macroscopic diversity system; up to third order diversity

was employed. The location of the sites used for the trial was as follows:

#### **Transmitter (TX) site:**

University of Hull, Humberside, England

#### **Receiver (RX) sites:**

- (i) Cobbett Hill, DRA site, Surrey, England;
- (ii) University of Warwick, West Midlands, England;
- (iii) Wick, Highland Region, Scotland.

Figure 5 shows the locations of the transmitter and receiver sites on a map of the British Isles.

The modulation employed was 16-ary multiple FSK at 10 symbols/s. Blocks of 6000 random symbols were transmitted (representing a transmission time of 600s or 10 minutes) for 1 hour periods at various times over the course of 5 days; the schedule is shown in Table 1. Sequences were transmitted between blocks to enable correct synchronisation to take place between sites.

	Time of day on 26.11.90	27.11.90	28.11.90	29.11.90
Trial #1	16.10 - 17.10	--	--	--
Trial #2	22.30 - 23.30	--	--	--
Trial #3	--	12.00 - 13.00	--	--
Trial #4	--	--	8.20 - 9.20	--
Trial #5	--	--	--	17.00 - 18.00-

Table 1: Trial Schedule

The transmitting equipment consisted of a Skanti TRP8250 transceiver with an output power of 400W and an inverted-V antenna. The receiving sites employed Racal RA1187 receivers whose outputs were recorded by either Revox or Racal Store 4 magnetic recorders. The frequencies of operation were 2.162MHz, 5.75MHz, and 9.071MHz; one of these frequencies was selected as the transmission frequency at any time, depending on the prevailing channel state. The tapes made at the receiving sites were then returned to the University of Hull for analysis.

## **7. TRIALS RESULTS**

The algorithm specified by equations (1) and (2) is optimum for symbol-level combining.

However, to enable it to be implemented, outputs of all the multiple FSK demodulator filters are required to be available. The modem employed in the trial provided confidence information only for each symbol decision; thus a conventional selection diversity combining algorithm was used, with an estimated performance degradation over the optimum scheme of about 1-5dB.

Tables 2 to 6 show the symbol error rate results for optimum weight combining applied to the geographical diversity received data. The tables give the error rate for uncombined data, as well as for the selection from two and all three sites. This is only a sub-set of the analysed data available.

Receiving Site(s)	Error rate
Cobbett Hill	0.002875
University of Warwick	0.01708
Wick	0.002875
Cobbett Hill & University of Warwick	0.007778
Cobbett Hill & Wick	0.002536
University of Warwick & Wick	0.005918
All 3 Sites	0.0001691

Table 2 Error rate results for Trial 3.2:  
without combining, combining 2 sites and  
optimum weight combining applied to all 3  
sites

Receiving Site(s)	Error rate
Cobbett Hill	0.009842
University of Warwick	0.05988
Wick	0.01068
Cobbett Hill & University of Warwick	0.02252
Cobbett Hill & Wick	0.002836
University of Warwick & Wick	0.01184
All 3 Sites	0.003336

Table 4 Trial 4.2

Receiving Site(s)	Error rate
Cobbett Hill	0.02020
University of Warwick	0.01330
Wick	0.01128
Cobbett Hill & University of Warwick	0.008624
Cobbett Hill & Wick	0.01312
University of Warwick & Wick	0.004904
All 3 Sites	0.0006764

Table 3 Trial 3.3

Receiving Site(s)	Error rate
Cobbett Hill	0.007708
University of Warwick	0.040550
Wick	0.005697
Cobbett Hill & University of Warwick	0.014243
Cobbett Hill & Wick	0.001005
University of Warwick & Wick	0.005194
All 3 Sites	0.001173

Table 5 Trial 5.2

Receiving Site(s)	Error rate
Cobbett Hill	0.008362
University of Warwick	0.01502
Wick	0.001092
Cobbett Hill & University of Warwick	0.003754
Cobbett Hill & Wick	0.0006826
University of Warwick & Wick	0.004778
All 3 Sites	0.0003413

Figure 6 Trial 5.3

Figures 6 to 10 show the results of Tables 2 to 6 in graphical form, with numbers of errors plotted rather than error rate.

## 8. DATA ANALYSIS

Optimum combining requires uncorrelated signals to be available at the receiving sites. In the HF environment, correlated noise and interference can occur over large distances [8] such that, even with the macroscopic diversity system described by Figure 5, there will be some correlation of the received signals. The effectiveness of symbol-level combining is dependent on the extent to which the demodulation errors are uncorrelated at the different sites. Thus, an error correlation coefficient was computed to give a measure of the similarity between error patterns at the macroscopic diversity receivers shown in Figure 5.

The error correlation coefficient was obtained by partitioning the 600s data interval of the transmitted block into 60 blocks, each of duration 10s (100 symbols). The number of errors in each block is summed; in this way, two received data series  $k$  and  $I$ , can be represented as the vectors

$$\begin{aligned} k &= (k_1, k_2, k_3, \dots, k_{60}) \\ I &= (\lambda_1, \lambda_2, \lambda_3, \dots, \lambda_{60}) \end{aligned} \quad (9)$$

where  $k_x$  represents the number of errors in block  $x$  of received data series  $k$ , and  $\lambda_x$  represents the number of errors in block  $x$  of data series  $I$ .

The error correlation coefficient between the two vectors is now calculated from

$$\rho(k, I) = \frac{\sum_{i=1}^{60} (k_i \lambda_i)}{\sum_{i=1}^{60} \left( \frac{k_i + \lambda_i}{2} \right)^2} \quad (10)$$

The value obtained from equation (10) is a measure of the similarity of the distribution of errors in time for the two received data series. A value of 1 indicates exactly similar error distributions; a value of zero implies totally uncorrelated error patterns. Although this parameter is not an absolute correlation coefficient, it does give an indication of the correlation of the fading and noise. Also, for symbol-level combining, this parameter gives a better measure of potential combiner effectiveness than a correlated coefficient derived directly from the baseband signal.

Tables 7 to 11 show the error correlation coefficients for the trials 3.2, 3.3, 4.2, 5.2, 5.3 for all possible pairs of combiner sites. Table 12 shows the error correlation coefficients for all the data sent during the trial period.

	<b>Cobbett Hill</b>	<b>University of Warwick</b>	<b>Wick</b>
Cobbett Hill	--	0.210	0.921
University of Warwick	0.210	--	0.154
Wick	0.921	0.154	--

Table 7 Error correlation coefficient between receiving sites for trial 3.2

	<b>Cobbett Hill</b>	<b>University of Warwick</b>	<b>Wick</b>
Cobbett Hill	--	0.401	0.936
University of Warwick	0.401	--	0.0585
Wick	0.936	0.0585	--

Table 8 Error correlation coefficient between receiving sites for trial 3.3

	<b>Cobbett Hill</b>	<b>University of Warwick</b>	<b>Wick</b>
Cobbett Hill	--	0.649	0.779
University of Warwick	0.649	--	0.720
Wick	0.779	0.720	--

Table 9 Error correlation coefficient between receiving sites for trial 4.2

	<b>Cobbett Hill</b>	<b>University of Warwick</b>	<b>Wick</b>
Cobbett Hill	--	0.379	0.355
University of Warwick	0.379	--	0.647
Wick	0.355	0.647	--

Table 10 Error correlation coefficient between receiving sites for trial 5.2

	<b>Cobbett Hill</b>	<b>University of Warwick</b>	<b>Wick</b>
Cobbett Hill	--	0.372	0.247
University of Warwick	0.372	--	0.306
Wick	0.247	0.306	--

Table 11 Error correlation coefficient between receiving sites for trial 5.3

	Cobbett Hill	University of Warwick	Wick
Cobbett Hill	--	0.7471	0.8877
University of Warwick	0.7471	--	0.7072
Wick	0.8877	0.7072	--

Table 12 Error correlation coefficient between receiving sites for all trials

## 9. CONCLUDING REMARKS

The maximum likelihood condition for symbol-level combining has been presented in this paper and has been termed *optimum weight combining*. Simulation results show that, with precise probability of error metrics, performance approaching that obtained with equal-gain baseband combining can be achieved. Consideration of an approximation to the optimum weight case has also been presented.

The following conclusions can be drawn from the analysis presented in Sections 7 and 8:

- (i) The use of selection combining in a macroscopic diversity system has a significant effect on the error rate performance of the communications system. Figure 11 shows a plot of the average error rate for the 'on air' trials between 26.11.90 and 29.11.90 for 1, 2, and 3 diversity branches. Note that there is a factor of approximately 10 improvement in error rate when 3 branches are combined, in comparison with the single-branch (no-combining) case.
- (ii) The University of Warwick receiving site consistently gave poorer error performance than the other two receiving sites. This was probably due to a local interferer affecting this site. Theoretical analysis [9] indicates that if the confidence information is correct, then adding more branches to the combiner, no matter how poor the error rate performance of these new branches, will enhance the overall combiner output error rate; it cannot get worse. The results from trials 5.2 and 5.3 show that this is not the case in practice. For example, in trial 5.2 when the Cobbett Hill and Wick

sites are combined, 17 errors were detected; however, the addition of the Warwick site in the combining algorithm led to 20 errors. The calculation of the confidence metric is inaccurate, and will always be so since it is based on a single symbol demodulation; thus, it may be necessary to inhibit some of the diversity branches exhibiting much higher error rates than others in the diversity network.

- (iii) Correlation between receiving sites was in some cases quite high. This is demonstrated by the value of the error correlation coefficient shown in Tables 7 to 11. During trial 3, the correlation between receiver sites at Cobbett Hill and Wick was high (Trial 3.2,  $\rho = 0.921$ ; Trial 3.3  $\rho = 0.936$ ); therefore, the effectiveness of combining between these two sites was low. For Trial 3.2 (see Figure 6), the combining of Cobbett and Wick gives only a marginal improvement from 17 errors to 15 errors. In Trial 4.2, the correlation coefficients are all in the range 0.65 and 0.78 and here the combiner is perhaps the most effective of all the trial periods; 88, 64 and 49 errors in the individual branches combine to 2 errors. The signals appear to be least correlated in Trial #5; however, due to the fact that the Warwick site displayed far more errors than the other two sites, combining was not successful (see paragraph (ii) above).
- (iv) In general, the trials have shown that macroscopic diversity is an effective technique for reducing errors caused by both noise and propagation effects in the HF band. Further, the trials have shown that the symbol-level combining technique can be used in such a system.

## 10. ACKNOWLEDGEMENTS

The authors wish to thank the UK Science and Engineering Research Council (SERC) for their financial support of this work and the Defence Research Agency (Farnborough) for their assistance during the radio trials.

## 11. REFERENCES

1. Brennan D G, "Linear diversity combining techniques", Proceedings of IRE, Vol 47, pp 1075-1102, June 1958.
2. Barrow, B B, "Error probabilities for data transmission over fading radio paths", SHAPE Technical Memorandum TM-26, February 1962.
3. Schwarz M, Bennet W R, Stein S, "Communications systems and techniques", McGraw-Hill, New York, 1966.
4. Speight T J, Darnell M, "The performance of maximum likelihood symbol-level diversity combining", Submitted for publication to IEE Proceedings, Part I.
5. Thrane, E V, "Propagation II. Problems in HF propagation", AGARD Lecture Series, No 127, May/June 1983.
6. Darnell M, "Problems of mobile HF communication and techniques for performance improvement", IEE Proceedings, Vol 132, Part F, No 5, pp 433-440, August 1985.
7. Gott, G F, Dutta S, Doany P, "Analysis of HF interference with application to digital communications", Proceedings of the IEE, Vol 130, Part F, pp 452-458, 1983
8. Dutta S, Gott, G F, "Correlation of HF interference spectra with range", Proceedings of the IEE, Vol 128, Part F, No 4, pp193-202, August 1981.
9. Speight T J, "Improved design of distributed HF communications systems involving mobile terminals", PhD thesis, University of Hull, 1992.

$$P_{e1} = 5E-4 \quad P_{e2} = 2E-3 \quad P_{e3} = 5E-3 \quad P_{e4} = 4E-2$$

$$W_i = f(P_{ei}) = 1/(P_{ei}^{0.5}) - 2^{0.5}$$

$$W_1 = 43.31 \quad W_2 = 20.95 \quad W_3 = 12.73 \quad W_4 = 3.58$$

Using optimum weight iterative algorithm

$$W'_1 = 38.87 \quad W'_2 = 25.39 \quad W'_3 = 17.17 \quad W'_4 = 3.59$$

Error Pattern No.	Error Pattern	Probability of Occurrence	Voting using $f(P_e)$	Output (using $f(P_e)$ )	Voting Using $f_{opt}(P_e)$	Output using $f_{opt}(P_e)$	Inverse Error Pattern	Probability of Occurrence	Voting using $f(P_e)$	Voting Using $f_{opt}(P_e)$
EP <sub>0</sub>	CCCC	9.53E-1	80.57-0	C	85.02-0	C	EP <sub>15</sub>	2.00E-10	I	I
EP <sub>1</sub>	CCCI	3.97E-2	76.99-3.58	C	81.43-3.59	C	EP <sub>14</sub>	4.80E-9	I	I
EP <sub>2</sub>	CCI C	4.97E-3	67.26-12.73	C	67.85-17.17	C	EP <sub>13</sub>	3.98E-8	I	I
EP <sub>3</sub>	CCI I	2.00E-4	64.26-16.31	C	64.26-20.76	C	EP <sub>12</sub>	9.55E-7	I	I
EP <sub>4</sub>	CI CC	1.91E-3	59.62-20.95	C	59.63-25.39	C	EP <sub>11</sub>	9.98E-8	I	I
EP <sub>5</sub>	CI CI	7.96E-5	56.04-24.53	C	56.04-28.98	C	EP <sub>10</sub>	2.40E-6	I	I
EP <sub>6</sub>	CI I C	9.60E-6	46.89-33.68	C	42.46-42.56	I	EP <sub>9</sub>	1.99E-5	I	C
EP <sub>7</sub>	CI I I	4.00E-7	43.31-37.26	C	38.87-46.15	I	EP <sub>8</sub>	4.77E-4	I	C

Total error rate using empirically calculated weights :  $P_{e\text{total}} = 5.0E-4$

Optimum weights would give  $P_{e\text{optimum}} = 1.35E-5$

Figure 1 Example of optimum and empirical weight combining

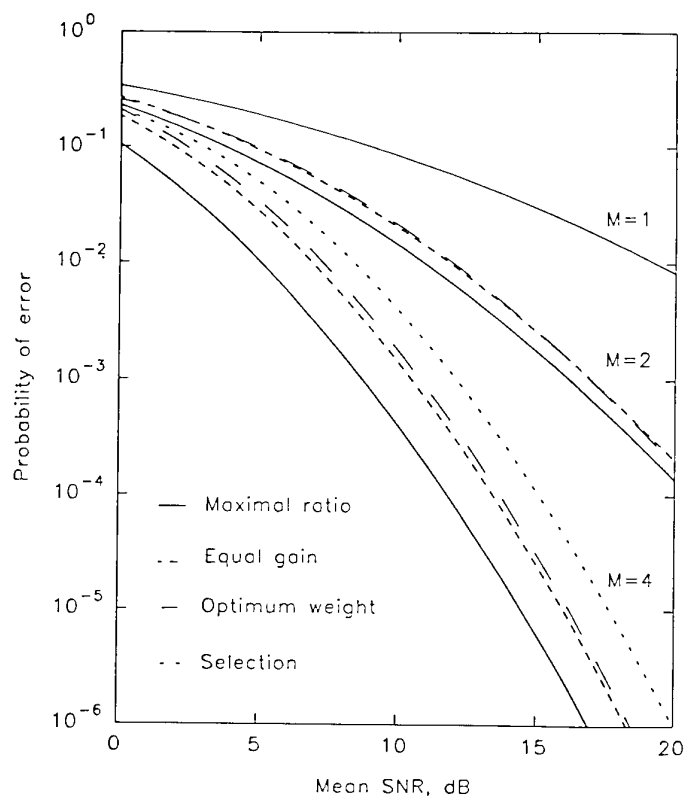


Figure 2 Comparison of optimum weight combining with various baseband combining techniques for  $M=1,2,4$

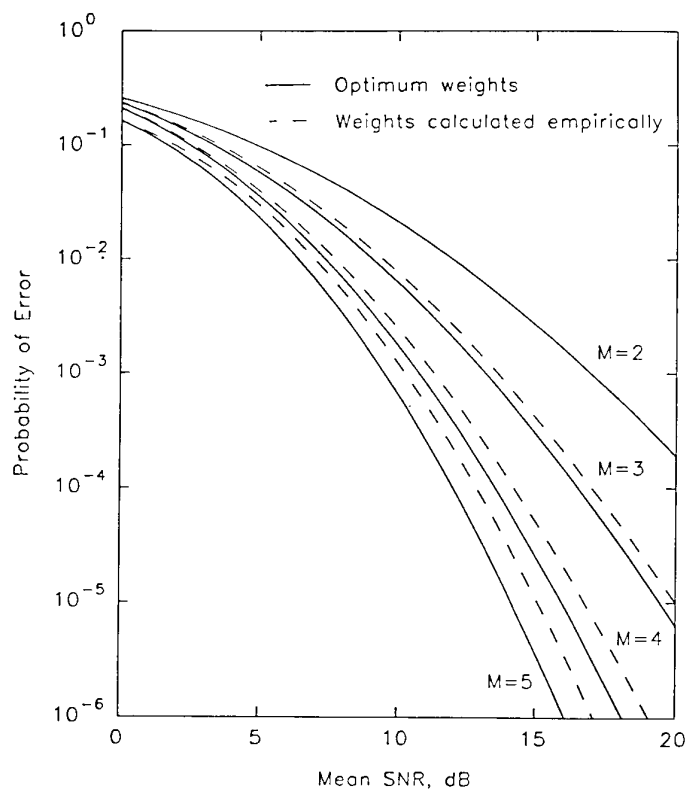


Figure 3 Comparison of bit level combining for optimum weights and weights calculated from an empirical function which is an approximation to the optimum function



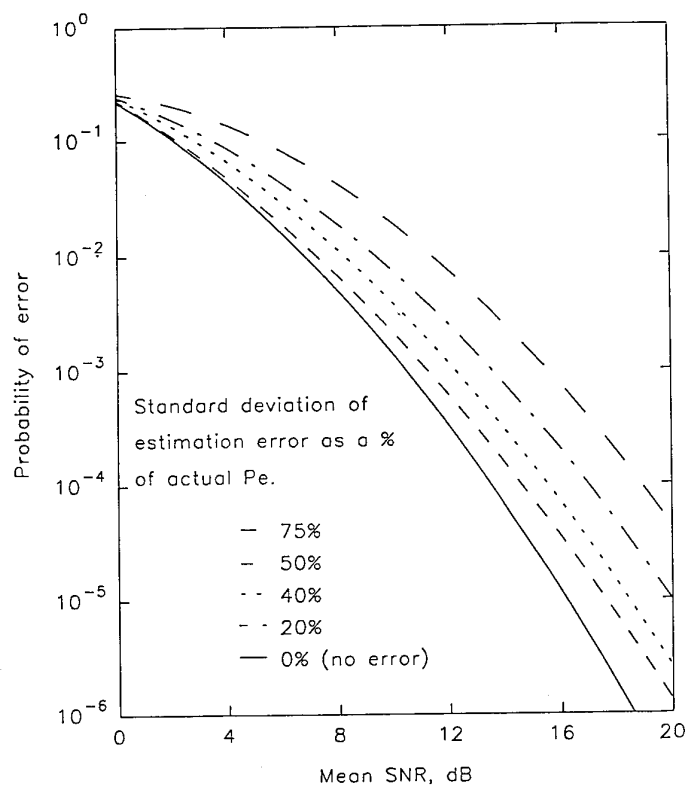


Figure 4 Effect of incorrect probability of error estimation on optimum weight combining

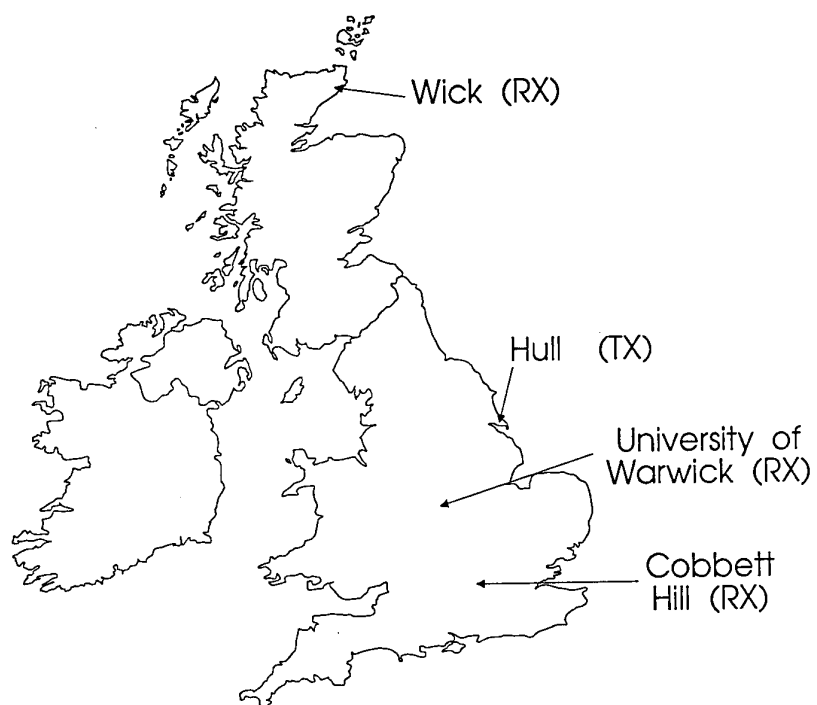


Figure 5 Geographical location of transmitter and receiver sites for the HF message system 'on air' trials.

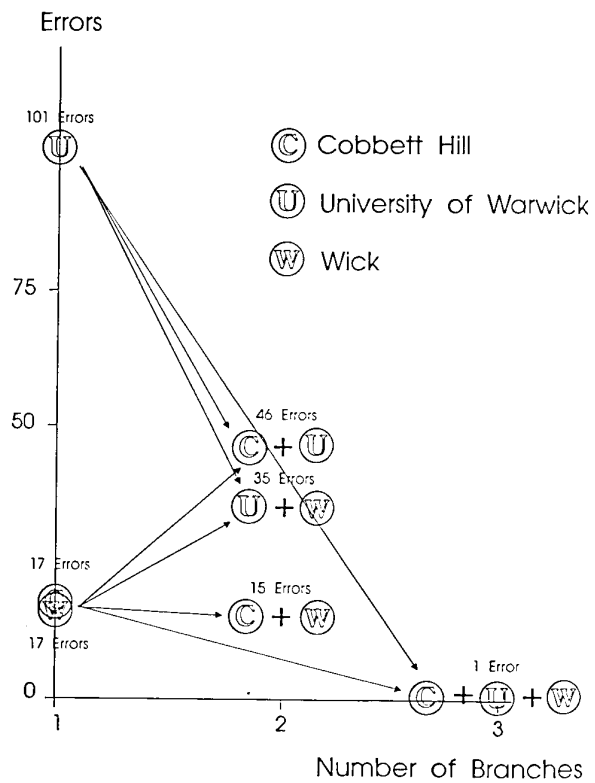


Figure 6 Graph of number of errors for no combining, combining 2 sites and combining of all 3 sites for Trial 3.2

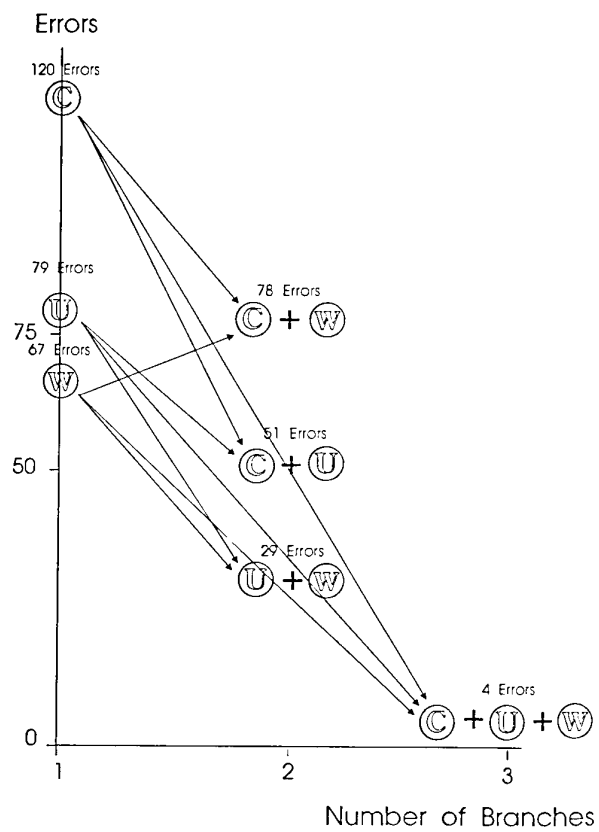


Figure 7 Graph of number of errors for Trial 3.3

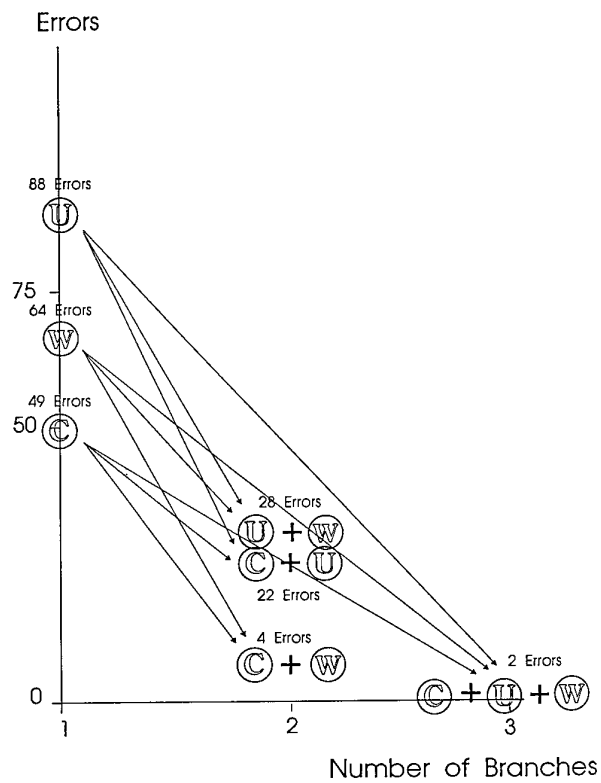


Figure 8 Graph of number of errors for Trial 4.2

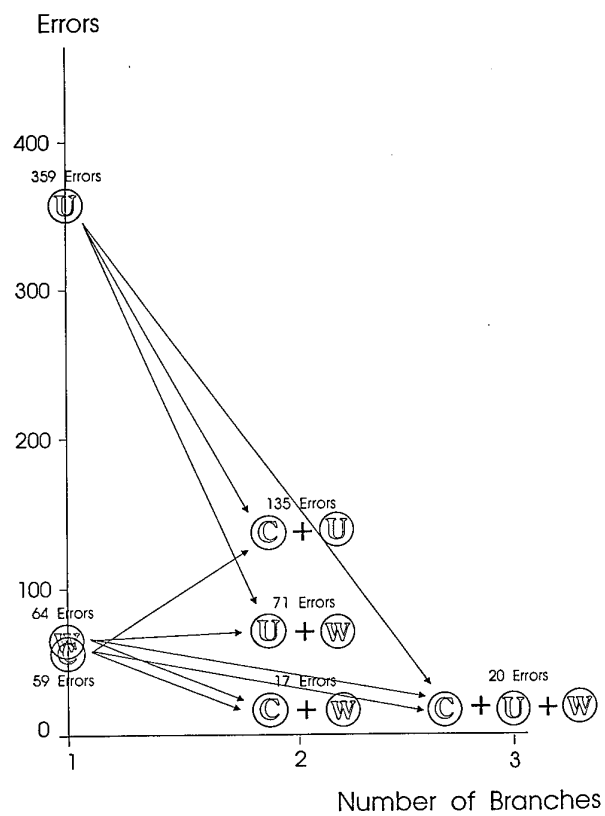


Figure 9 Graph of number of errors for Trial 5.2

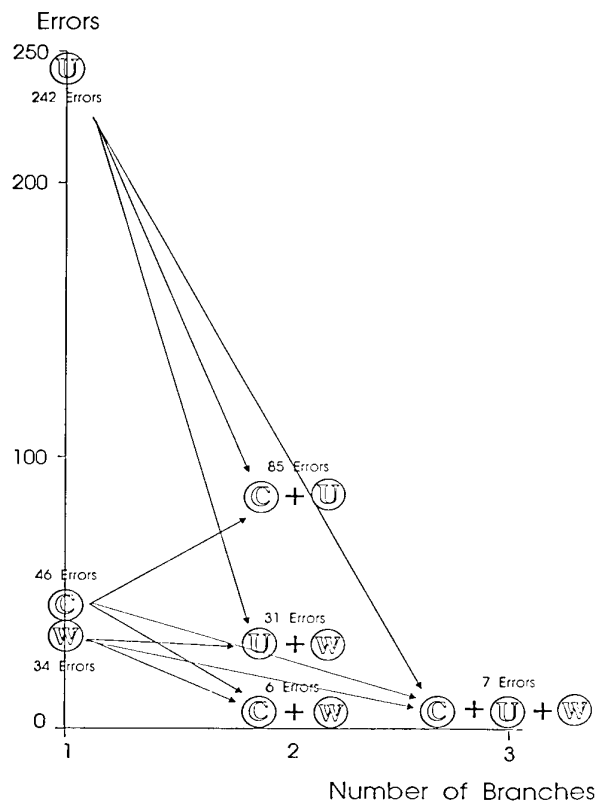


Figure 10 Graph of number of errors for Trial 5.3

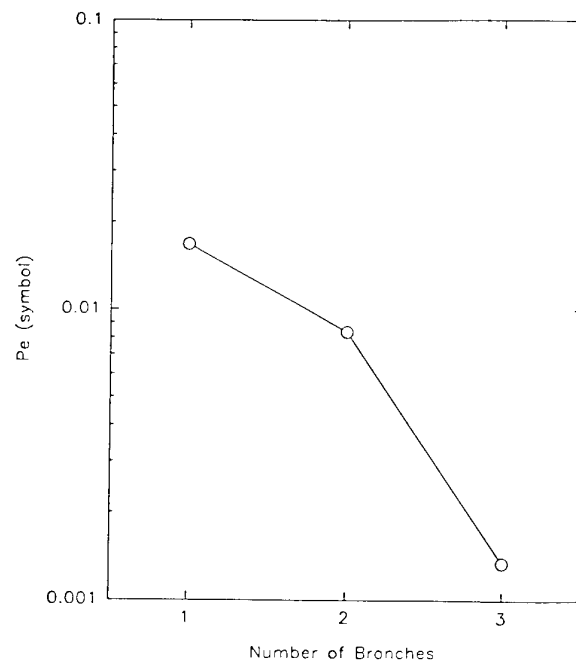


Figure 11 Graph of average error rate for 'on air' trials versus number of branch combining used

## DISCUSSION

**Discussor's name :** C. Goutelard

**Comment/Question :**

Le coefficient de pondération  $W_c$  que vous utilisez respecte les conditions limites que vous imposez pour  $P_c = 0,5$  et  $P_c = 1$ . On peut utiliser d'autres lois, comme par exemple  $W_c = (0,5 - P_c)/P_c$ . *(0,5 - P\_c) / P\_c*  
Avez-vous étudié l'optimalité de la loi à prendre sur  $W_c$ ?

**Translation :**

*The weighting coefficient  $W_c$  which you use obeys the limit conditions which you impose for  $P_c = 0.5$  and  $P_c = 1$ . We can use other laws, for example  $W_c = (0.5 - P_c)/P_c$ . Have you studied the optimality of the law to be used for  $W_c$ ?*

**Author/Presenter's reply :**

As you indicate, there are many possible functions which can be used to generate the combiner weights. The one we chose was computationally convenient, but not necessarily optimum.

**Discussor's name :** P. Melançon

**Comment/Question :**

How do you estimate the error rate for each channel, particularly in real time for radio channels with important multipath propagation?

**Author/Presenter's reply :**

For example, by running SNR measurements derived from demodulators, a decoder or a synchroniser.

The trials described in the paper made use of transmissions at 10 symbols/s; therefore multipath was not significant. At higher rates, metrics could be derived from an equaliser.

**Discussor's name :** NATO Delegate

**Comment/Question :**

What kind of information should be transmitted via the service channel to the combiner?

Are the service links also HF links?

**Author/Presenter's reply :**

The information to be transmitted to the combiner comprises the demodulated data plus running error probability estimates.

The interconnect links may be of any convenient form, but are likely to be established via a switched network. They could, however, be reliable radio links, e.g. troposcatter. The philosophy is to remove operational complexity from say a transmitting mobile (ship or aircraft) and allow complexity in the interconnected receiving network.

**Discussor's Name :** H. Vissinga

**Comment/Question :**

In the early sixties a system, called MUFTRA, was used in which a ship, simulating the strike fleet in the North Atlantic, was transmitting on a number of frequencies, which were received at a number of widely dispersed receiving sites. These signals were sent to a central point and there somehow composed into a final message.

**Author/Presenter's reply :**

Typically, all message versions could be fully printed out and compared manually to control errors. Also, prior to the 2nd World War, global navies had multiple possible receiving locations which were widely separated. Any message received satisfactorily at a given location would be forwarded to its destination by an appropriate command structure.

**Discussor's name :** D. Yavuz

**Comment/Question :**

Since we know that maximal ratio combining is optimal, would not a scheme simply transmitting the estimated bit sequence per frame, etc. and the S/N be "more" optimal and just as simple to implement?

**Author/Presenter's reply :**

In essence, our error probability metrics are a direct measure of S/N. Thus, we would not expect a substantial difference between optimum weight and maximal ratio combiner performance - an expectation confirmed by our simulation results.

# Superresolution Direction Finding Algorithms for The Characterisation of Multi-Moded H.F. Signals

M.A. Zatman

H.J. Strangeways

Dept. Electronic & Electrical Engineering,  
The University of Leeds, Leeds, LS2 9JT, United Kingdom

## SUMMARY

In this work three superresolution direction finding algorithms for use with arbitrary array geometries are described, all of which are capable of dealing with coherent signals, as typically found in the multi-path environment. DOSE is a quick single snapshot algorithm developed by the authors which operates on the received data vector. The IMP and Maximum Likelihood (ML) algorithms are used to process time averaged data covariance matrices. All three algorithms attempt in different ways to find a multi-dimensional solution to the inverse problem of direction finding. It is shown that calibration of arrays of identical elements is simplified by the use of these multi-dimensional algorithms when compared to 1 dimensional methods such as MUSIC. A common methodology for the implementation of these multi-dimensional algorithms is presented, and a quick method of implementing the ML algorithm and determining the number of signals present is described.

## LIST OF SYMBOLS

$a(\theta)$	Steering vector in direction $\theta$
$A$	Steering matrix
$E$	Steering matrix of directions to be nulled
$I$	Identity matrix
$L(\Theta)$	Likelihood of $\Theta$
$M$	Number of elements in the array
$N$	Number of wavefronts incident on the array
$P$	Projection matrix of $A$
$Q$	Null projection matrix of $E$
$R$	Covariance or correlation matrix of the received data
$S$	Matrix of powers and correlations among the wavefronts
$T$	Number of snapshots
$tr[\cdot]$	Trace operator
$x$	Received data vector
$y$	Conditioned data vector
$ \cdot $	Determinant or modulus operator

## 1. INTRODUCTION

In a stationary multipath environment the signal and/or its reflections incident on an array of antennas are coherent. In this case sub-optimal 1 dimensional superresolution direction finding (SRDF) algorithms which rely on the decomposition of the time averaged covariance matrix (such as MUSIC [1]) do not work without extra processing, which has significant drawbacks. At H.F. multi-moded signals are highly correlated, and are only incoherent due to the non-stationarity of the ionosphere. While algorithms such as MUSIC can be made to work under these circumstances with long time integration [2], the time integration reduces the optimality of the solution reached, since the direction of arrival (DOA) of each path is changing with time.

A better solution can be reached by the use of non subspace methods such as the ML estimator [3-5], the IMP algorithm [6]

and for single snapshot data the DOSE algorithm [7]. All of these methods find the solution to a multi dimensional inverse problem, either directly (ML) or by simultaneously solving a number of 1 dimensional problems (IMP and DOSE). Algorithms such as MUSIC are in fact 1 dimensional methods attempting to find the solution to a multi-dimensional problem. Commonly cited drawbacks of multi-dimensional algorithms are initialization procedures, the need to determine the model order and computational complexity.

In the multipath environment, the determination of model order is a particular problem, since AIC [8] and MDL [9] - the common methods - require decomposition of the covariance matrix, which gives incorrect results in this situation.

## 2. FORMATION OF THE PROBLEM

The waveforms received at the  $M$  elements of an array are linear combinations of the  $N$  incident wavefronts and the noise. The received  $M \times 1$  data vector  $x$  contains the complex value of the waveform at each sensor at a snapshot in time. The time averaged covariance matrix  $R$  is defined as:

$$R = \frac{1}{T} \sum_{k=1}^T x_k x_k^H \quad (1)$$

where  $T$  is the total number of snapshots, and  $x^H$  represents the hermitian transpose of  $x$ .

If  $a(\theta)$  is the 'steering vector' representing the transfer function between DOA  $\theta$  and the array,  $A$  the  $M \times N$  steering matrix of  $N$  steering vectors and  $S$  the  $N \times N$  matrix of amplitudes and correlations of the wavefronts, then the covariance matrix (without noise) is given by:

$$R = ASA \quad (2)$$

Finding the DOA of all the wavefronts incident on the array is thus an  $N$  dimensional problem where the  $N$  constituents of  $A$  are determined.

The ML technique is known to be an optimal solution to this problem and is calculated by maximising the following objective function:

$$L(\Theta) = \text{tr}[PR] \quad (3)$$

where  $P = A(A^H A)^{-1} A^H$ , i.e.  $P$  is the projection matrix onto the column space of  $A$ .

Now as the conventional beamformer (CBF) is an integral part of the DOSE and IMP algorithms we will take this opportunity to derive it's relationship to the ML estimator. This will also give us an insight into some of the subspace type algorithms and their relationship to the ML and CBF.

Theorem 1 : The CBF is a 1 dimensional realisation of the ML estimator, and is thus an optimal method of estimating the parameters of 1 wavefront.

Proof: The ML estimator is equivalent to finding:

$$\max(\text{tr}[PR]) \quad (4)$$

which is equivalent to:

$$\max(\text{tr}[\{A(A^H A)^{-1} A^H\}R]) \quad (5)$$

and for 1 signal becomes:

$$\max(\text{tr}[\frac{a a^H}{a^H a} R]) \quad (6)$$

which is mathematically equal to

$$\frac{a(\theta)^H R a(\theta)}{a(\theta)^H \cdot a(\theta)} \quad (7)$$

which is the expression for the CBF. If only one snapshot is processed this can be further simplified to :

$$\frac{|a(\theta)^H \cdot x|^2}{a(\theta)^H \cdot a(\theta)} \quad (8)$$

equivalent to the discrete fourier transform (DFT).

This result is useful in that it tells us that the CBF and the DFT, the core of the IMP and DOSE algorithms are optimal ways of estimating the parameters of a single wavefront, but are also non-optimal for estimating the parameters of more than one. From examination of eqns. (7) and (8) and the spectral equations of MUSIC and other similar subspace algorithms, it can be seen that such techniques merely use a different weighting instead of the covariance matrix or data vector in eqns. (7) and (8). By virtue of being 1 dimensional algorithms they are sub-optimal, but achieve higher spectral resolution of more than 1 signal than the CBF, at the expense of loss of performance at low SNRs and high wavefront correlation.

### 3. ARRAY CALIBRATION

The need for accurate array calibration is often cited in the literature on SRDF algorithms. However we will show that under certain circumstances (for multi-dimensional algorithms such as DOSE, IMP and ML) this is not true.

Assuming an array of identical antennas, each with arbitrary but identical gain patterns and orientation, and that the mutual coupling between the antennas is minimal, (achievable say by the use of small (compared with  $\lambda$ ) active antennas and/or suitably wide spacing between the elements of the array).

**Theorem 2:** An ML based estimator will correctly estimate signal DOAs without the knowledge of antenna gain patterns providing all of the antennas are identical.

Proof: The determinant of a projection matrix is zero.

$$|P| = |A(A^H A)^{-1} A^H| = 0 \quad (9)$$

The effect of eqn. (9) is most simply visualized by looking at the example of a simple 1 dimensional projection matrix of a vector with 2 elements. Take the vector  $v=[a, b]^T$ .

The projection matrix of  $v$  is

$$\begin{bmatrix} a \\ b \end{bmatrix} \left( \begin{bmatrix} a & b \end{bmatrix} \begin{bmatrix} a \\ b \end{bmatrix} \right)^{-1} \begin{bmatrix} a & b \end{bmatrix} = \frac{\begin{bmatrix} a^2 & ab \\ ab & b^2 \end{bmatrix}}{a^2 + b^2} \quad (10)$$

Suppose a gain term  $g$  is introduced into  $v$  so  $v'=[ga, gb]^T$  then the projection matrix of  $v'$  is:

$$\begin{bmatrix} ga \\ gb \end{bmatrix} \left( \begin{bmatrix} ga & gb \end{bmatrix} \begin{bmatrix} ga \\ gb \end{bmatrix} \right)^{-1} \begin{bmatrix} ga & gb \end{bmatrix} = \frac{\begin{bmatrix} g^2 a^2 & g^2 ab \\ g^2 ab & g^2 b^2 \end{bmatrix}}{g^2 a^2 + g^2 b^2} \quad (11)$$

eqn. (11) is of course numerically identical to eqn. (10) since all the  $g$ 's cancel.

The correctness of this result is illustrated by considering the case of 1 signal being processed with the CBF. Then if the gain terms are ignored the CBF will still estimate the DOA correctly, but will produce an incorrect amplitude. Knowledge of the gain characteristics of the antennas is much more important when estimating the DOAs of more than one signal with 1 dimensional algorithms like MUSIC and the CBF, when the DOA relies on finding multiple peaks or troughs in the spatial spectrum.

The fact that under certain circumstances the ML estimator, (and when seeking one signal the CBF & DFT - model order 1 realisations of ML) do not need the information on antenna gains allows faster computation of the algorithms through associated simplifications to the computer code, and also demonstrates the enhanced robustness of algorithms such as ML, IMP and DOSE over MUSIC and other subspace methods.

### 4. THE IMP AND DOSE ALGORITHMS

The IMP and DOSE techniques employ a similar methodology. Instead of directly trying to estimate the solution to a multi-dimensional problem, they both find a number of optimal one dimensional solutions to the problem through the use of the CBF (IMP) or the DFT (DOSE) and an adaptive nulling scheme. DOSE is faster than IMP by virtue of using vector operations to process the one snapshot data vector, whereas the IMP algorithm employs the time averaged covariance matrix, which though more cumbersome to process, also allows some time integration of the signal.

The IMP algorithm uses the following estimator:

$$P_{imp}(\theta) = \frac{a(\theta)^H Q R Q a(\theta)}{a(\theta)^H Q a(\theta)} \quad (12)$$

where  $Q$  is matrix which projects nulls in the direction of signals already found. If  $N$  signals arrive from DOAs  $\{\theta_1, \dots, \theta_N\}$ , corresponding to 'steering vectors'  $\{e_1, \dots, e_N\}$ , forming  $E$ , then

$$Q = I - E(E^H E)^{-1} E^H \quad (13)$$

When all but one of the signals are nulled, the IMP algorithm



is effectively the same as eqn. (7) the CBF, which will find the DOA of one signal optimally.

If  $y=Qx$ , then the DOSE spectral estimator starts as:

$$P_{dose}(\theta) = \frac{|a(\theta)^H \cdot y|^2}{a(\theta)^H Q a(\theta)} \quad (14)$$

The denominator can be decomposed into a number of dot products, so the square root of eqn. (15) (for example  $j$  signals being eliminated) is:

$$P_{dose}(\theta) = \frac{|a(\theta)^H \cdot y|}{k - \sum_{i=1}^j \frac{1}{k} |a(\theta)^H \cdot e_i|} \quad (15)$$

where the constant  $k=a(\theta)^H \cdot a(\theta)$ . Hence the DOSE algorithm is in the region of  $M$  times faster to compute than IMP. When all but one of the signals are nulled, DOSE is effectively the same as eqn. (8) the DFT which will find the DOA of one signal optimally.

#### 4.1 The Directed Search

The directed or guided search is an implementation methodology, which we use with the DOSE and IMP algorithms [10], and which we will also apply to our implementation of the ML estimator.

The philosophy is simple:

- 1) Solve the  $N=1$  problem.
- 2) Test the hypothesis  $N=1$ . If true end, otherwise
- 3) Solve the  $N=2$  problem.
- 4) Test the hypothesis  $N=2$ . If true end, otherwise
- 5) Solve the  $N=3$  problem...

and so on until the correct model order is reached. This methodology seems to provide optimum initialization for each stage, and used with appropriate tests for model order with the DOSE, IMP and ML estimators, provides a robust platform for the processing undertaken.

#### 4.2 Implementation of the Algorithms

The implementation of the DOSE and IMP algorithms involves following the directed search technique described above, the testing of the model order achieved by looking at the spectrum  $P(\theta)$  in the  $N+1$  case. When all  $N$  signals are nulled, the resulting spectrum should be just the noise. In practice a threshold is set at (say) 30dB below the amplitude found at the first stage, and when the amplitude of the spectrum falls below this level it is assumed that all the signals have been located, and the algorithm is terminated.

The algorithm runs as follows:

- 1) Calculate the CBF/DFT spectrum eqn. (7)/(8),  $no\_signals=1$ , assign peak to  $h_1$  and  $Threshold=|h_1|-30dB$ .
- 2) Form  $Q$  so as to make nulls at  $h_1$  to  $h_{(no\_signals)}$ , calculate the DOSE/IMP spectrum eqn. (12)/(15) and assign peak to  $h_{(no\_signals+1)}$ .
- 3) If  $|h_{(no\_signals+1)}| < threshold$  END. Else  $no\_signals+1$  and go to 4)
- 4) Alternately form  $Q$  to null  $no\_signals-1$  of the estimates  $h_1$  to  $h_{(no\_signals)}$  and calculate the DOSE/IMP spectrum for the signal not nulled.
- 5) Continue with 4 until all the estimates are stable, then go to 2).

An example of the DOSE algorithm in practice is shown in figures 1 and 2 and table I. Two wavefronts incident on a 7 element array from azimuths of  $50^\circ$  &  $60^\circ$  produce the DFT shown in fig.1, with a single peak at  $55^\circ$ . This is nulled, and a peak above the threshold is found at  $56^\circ$ . The two estimates are tracked (table I), and alternately nulled and re-estimated until stable estimates are reached at  $50^\circ$  and  $60^\circ$ . These are then both nulled, and the DOSE spectrum calculated. Since the peak is now below the threshold, the algorithm terminates.

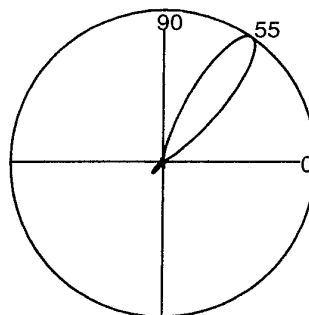


Figure 1. The DFT of the example described in the text.

Iteration	Amplitude	DOA
1	1	55
2	0.104	56
3	0.113	50
4	0.24	60
5	0.24	50
6	0.24	60
7	$3 \times 10^{-7}$	166

Table I

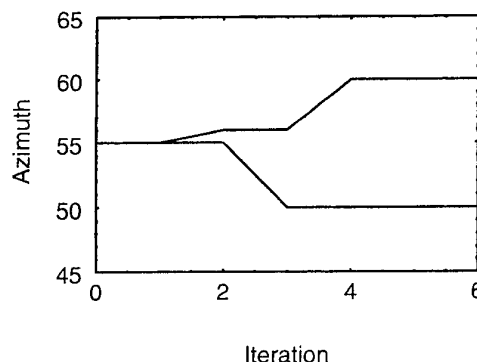


Figure 2. The paths tracked by the DOSE algorithm for the example given in the text and table I.

## 5. THE MAXIMUM LIKELIHOOD ESTIMATOR

Much has been written about the ML estimator, and various algorithms proposed. The implementation we describe is faster to compute than any of the methods cited earlier, follows the guided search principle, and has an effective means of determining the model order - even for the case of coherent wavefronts. The implementation consists of three separate sub-algorithms chained together:

- 1) The scan
- 2) Five-point surface fitting
- 3) The maximiser

### 5.1 The Scan

The scan is a search procedure that evaluates  $L(\Theta)$  (eqn. (3)) over a regular two dimensional (azimuth and elevation) grid and retains the highest value of the function. The scan is only used in one dimension, when incrementing model order. In order to achieve a fast scan, a widely spaced grid is used, with intersections on the grid being  $\frac{1}{2}$  of a CBF beamwidth apart. In our experience this spacing is narrow enough that the highest peak in the scan of  $L(\Theta)$  is always found.

### 5.2 Five Point Surface Fitting

The result of the scan will not be at precisely the maximum of the objective function, so the result of the scan, and the two adjacent points in both azimuth and elevation are taken, and fitted to a parabola using the three point method twice. Given  $U$ , the estimate of the highest peak in  $L(\Theta)$ , the adjacent points in azimuth or elevation,  $U^+$  and  $U^-$ , and the spacing between them  $h$ ;  $arg(F)$ , the peak of the parabola is located at:

$$arg(F) = arg(U) + \left( h \frac{\frac{|U^+| - |U^-|}{2}}{2|U| - |U^+| - |U^-|} \right) \quad (16)$$

It must be stressed that the parabola is only an approximation to the shape of the function in the dimension of  $L(\Theta)$  being scanned. With the spacing suggested, the scan will find the peak in that dimension to within 0.17 beamwidths, and with minimal extra processing the five-point surface fitting locates the peak to within about 0.03 beamwidths. To perform the scan at this resolution would increase the scan's computation by a factor of approximately 25, whereas the five-point curve fitting takes minimal time computationally compared to evaluating eqn. (3) in one dimension over even the widest of grids.

### 5.3 The Maximiser

The last part of this implementation of the ML estimation involves finding the global maximum of  $L(\Theta)$  in all the dimensions. The result from the five-point surface fitting is taken, and the value of  $L(\Theta)$  at this point, and every point adjacent to it in every dimension (including diagonally) calculated. The point corresponding to the largest value of  $L(\Theta)$  calculated is now taken, and the maximizer is now calculated with this point at its centre. This routine is repeated until the centre point of the maximizer does not shift, at which point the multi-dimensional maximum has been found. The maximizer must evaluate  $L(\Theta)$  at  $3^d$  points each time, where  $d$  is the number of dimensions being searched in both azimuth and elevation. This is implemented using a base 3 counter. The maximizer may be speeded up through the use of various 'tweaks'. Once it is known in roughly which direction the global peak lies,  $L(\Theta)$  does not need to be evaluated in

directions other than this, and those adjacent to it. So after the first run of the maximizer in a particular model order, the number of points at which  $L(\Theta)$  is evaluated can be reduced by more than half.

### 7.4 Determining Model Order

The final problem is to determine when all the wavefronts present have been found. Providing the directed search methodology is followed, and no attempt is made to calculate the same DOA in more than one dimension simultaneously, (when the projection matrix cannot be correctly calculated due to a singularity in the matrix to be inverted), then when all the signals have been correctly located, the amplitude of the objective function -  $|L(\Theta)|$  - saturates. When incrementing model order after this, the  $|L(\Theta)|$  does not increase. In fact, once all of the signals have been found the estimator will try to estimate the noise present in addition to the signals. Thus in practice a ratio (say 1.05:1) is set. If when increasing model order, the  $|L(\Theta)|$  is not greater than the previous value by the ratio set, it is then assumed that all signals have been found.

### 7.5 Implementation of an ML Algorithm

Putting the above together a quick and robust implementation of the ML estimator can be achieved as follows:

- 1) SCAN.
- 2) FIVE-POINT, no\_signals=1 and  $h=|L(\Theta)|$ .
- 3) SCAN.
- 4) FIVEPOINT.
- 5) If  $|L(\Theta)| < h \times \text{ratio}$  then END; else no\_signals+1 and  $h=|L(\Theta)|$ .
- 6) MAXIMIZE. if  $|L(\Theta)| > h$  then  $h=|L(\Theta)|$  and repeat 6); else  $h=|L(\Theta)|$  and goto 3).

An azimuth only example (same problem as used for DOSE before) of this implementation of the ML estimator is summarised in table II below.

ITN	MO	PART	$ L(\Theta) $	DOAs
1	1	S	479.13	54
1	1	F	480.96	55
2	2	F	490.33	54,55
2	2	F	491.34	55,56
3	2	M	491.39	54,57
4	2	M	491.50	53,58
5	2	M	491.62	52,59
6	2	M	491.71	51,60
7	2	M	491.73	50,60
8	2	M	491.73	50,60
8	3	S	491.73	50,60,0

Table II ITN = iteration number, MO = model order and PART = part of implementation (Scan, Five-point or Maximize)

## 6. PERFORMANCE OF THE ALGORITHMS

The performance of the algorithms proposed is assessed through Monte-Carlo simulations where the root mean square error (RMSE) of the estimator at a particular SNR is calculated from 100 test runs. The tests were undertaken with two wavefronts separated by  $5^\circ$  in DOA, incident on a 7 element array at correlation coefficients of 0.95 and 1.0, and also in the single snapshot case. Where the MUSIC algorithm gave correct results its performance has also been included. Further results are based on real data collected from a 7 element array, where the true answer is not known precisely. Here the significance is in the fact that the algorithms are shown to work on real data.

### 6.1 Simulation Results

The performance of the algorithms is plotted in figures 3, 4 and 5.

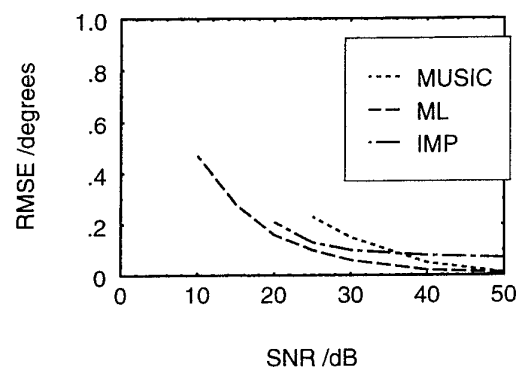


Figure 3. The performance of MUSIC, ML and IMP with a correlation coefficient of 0.95.

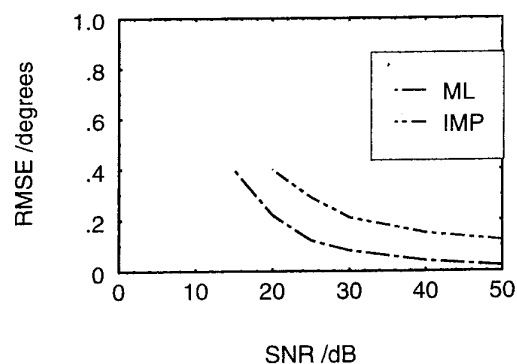


Figure 4. The performance of ML and IMP with a correlation coefficient of 1.0

The results in Figure 3 show ML to be the 'best' estimator, with the smallest RMSE at all SNRs. IMP seems to perform better than MUSIC at low SNRs while the converse is true at high SNRs. This anomaly is a result of the particular implementation of IMP, and applies to the DOSE results in Figure 5 too. Due to the finite step size used with the IMP implementation, if the convergence is slow IMP can seem to converge before the correct results are actually reached due to a failure to progress all the way to the next step. Hence there seems to be a residual RMSE of at least 0.08 degrees in the

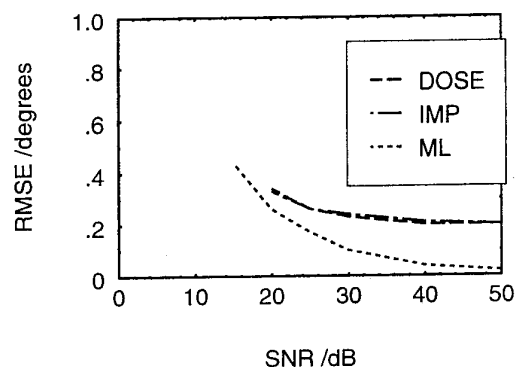


Figure 5. The performance of DOSE, IMP and ML in the one snapshot scenario.

IMP and DOSE results. This is not due to the inability of the estimator itself, but due to the fixed step sizes in the iterative implementation. The implementation of the ML algorithm used does not suffer from this problem because of the properties of the maximizer stage, however, similar problems have been noted with the alternating projection algorithm cited earlier. If smaller steps were used with the DOSE and IMP algorithms, then the performance in the simulation would be expected to be closer to that of the ML estimator.

The MUSIC algorithm is known not to perform at SNRs below about 20dB, due to the decomposition of the covariance matrix not leading to recognisable signal and noise subspaces. This is demonstrated in the results shown in Figure 3, but performance at low SNRs may be improved [11]. The IMP (and DOSE) algorithms do not seem to work at low SNRs either, and in this case the problem seems partly to lie with estimating model order and the setting of the threshold. The ML estimator was capable of working at lower SNRs than any of the other algorithms.

The results in Figures 4 and 5, where the MUSIC estimator failed completely, demonstrate the superior capability of the other algorithms to operate with coherent wavefronts and on single snapshot data. Computationally DOSE was the fastest algorithm, about a factor of 1.7 times faster than ML and 7.3 times faster than IMP.

### 6.2 Experimental Results

The following results were obtained using a 7 element array (on a site in Wiltshire, England) arranged in a V formation. The relative phases and amplitudes were measured by means of a 7 channel receiver, each channel being matched to the others and connected to one of the antennas. A computer controlled analogue to digital converter sampled the outputs of the receivers at a rate of 9 samples per second. The signal monitored is a transmission from Madrid, Spain on 9.570 MHz at 16.33 GMT. Less detailed DOA analysis of this (and other) data with interferometric techniques [12], and the MUSIC and DOSE algorithms [7] has previously been published. (We are grateful to Dr. E.M. Warrington, University of Leicester for the supply of this data). Due to a mixture of the low sampling rate and the non-stationarity of the signal being monitored time integration of the data was not appropriate, hence each snapshot was processed individually.

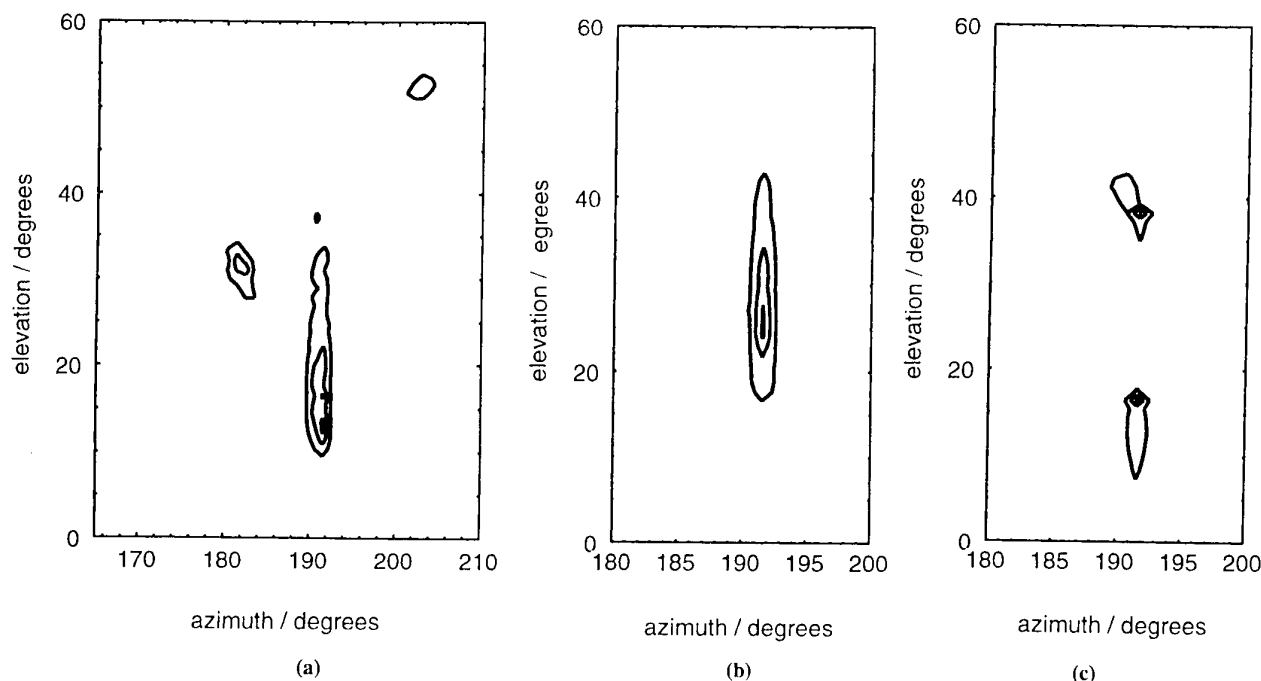


Figure 6. DOA measurements determined using a) Interferometry b) the CBF estimator and c) the ML algorithm.

The results of the DOA measurements using Interferometry, the CBF and the ML algorithms are shown in figures 6 a)-c). The contours plotted are for occurrence values of 10%, 50% and 90% of the peak number of occurrences. The results for the DOSE, IMP and ML algorithms were virtually identical, and unlike the interferometric and CBF analysis, DOSE, IMP and ML managed to resolve two ionospheric modes, 1 and 2 hop F region reflections. The DOSE algorithm, which produces estimates of signal powers simultaneously with estimates of DOA, measured the 1 hop path as being about 6dB stronger than the 2 hop path. This information would coincide with observed elevation estimates for the CBF and Interferometry being less than the average of the estimates produced for each path by the DOSE and ML algorithms. It is also of note that the DOSE and ML algorithms produced very sharp peaks in the figures plotted, whereas there is a much greater spread of readings on plots of data analyzed with the other methods.

### 9. TIME ANALYSIS OF DOA

In order to 'smooth' plots of DOA vs. time, some time integration by means of a moving window may be applied to the data [13]. In signal processing terms such a moving window is equivalent to a very simple low pass FIR filter. We have improved on the technique in [13] by constructing a 25 element low pass FIR filter with the aid of 'Hypersignal' and applying this to the data instead. The filter designed around a sampling frequency of 9Hz, has a 3dB cutoff at 2Hz, and a stopband attenuation of >30dB. The characteristic is plotted in Figure 7.

Filtering the DOA data has the effect of removing the short random variations in DOA <0.4s thus making underlying changes clearer. This method allows better time resolution and better reduction of noise variation than by processing a time averaged covariance matrix of the raw data to obtain an averaged DOA, and the problems with processing time averaged non-stationary signals are also removed.

Figure 8 shows a typical example of variation in elevation. The determined elevations of the two paths processed with the ML

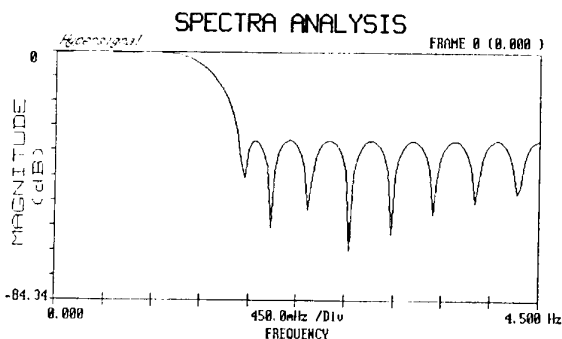


Figure 7 The response of the FIR filter used to smooth the DOA results.

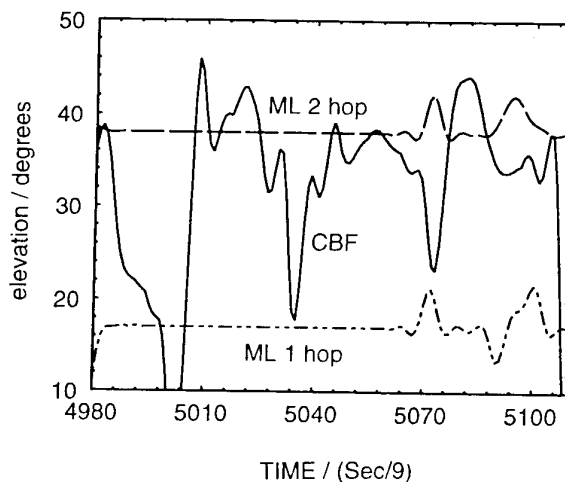


Figure 8 Plot of observed elevation vs. time.

estimator are fairly constant, whereas the elevations obtained from the CBF show a large temporal variation. The azimuth is plotted in Figure 9, and in this case the 1 hop path shows the least variation, the 2 hop path rather more and the CBF the greatest fluctuations.

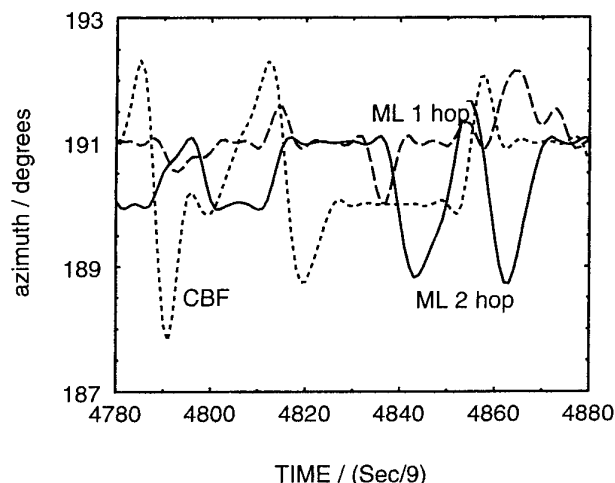


Figure 9 Plot of observed azimuth vs time

Figure 10, (note the different time scale) is of the data processed with the CBF. There is clearly a periodic variation of the elevation measurement, of a frequency of about 0.3Hz. It seemed likely that this effect was due to the phase between the 1 and 2 hop paths changing (due to different doppler shifts) and so a simulation was run to see if this effect on the CBF could be reproduced.

Two signals from DOAs of  $50^\circ$  and  $65^\circ$  (azimuth only) of relative amplitudes 1 and 0.2 separated by 0.3Hz in frequency and sampled at 9Hz were simulated as being incident on a 7 element circular array. The two signals were (just) within 1 CBF beamwidth of each other. The DOA determined by the CBF is shown in Figure 11, and clearly the periodic variation is similar to that of Figure 10. Incidentally, both DOSE and ML gave the DOAs of both signals correctly throughout the simulation. The explanation of this phenomena is also relatively straight forward. The DOA bias of one signal when estimated with the CBF due to the presence of another depends partly on the relative phases of the two signals, (the same is true of Fourier analysis in any domain). In this case the phase between the signals arriving by the two paths is changing by a rate proportional to the different doppler shifts introduced on the paths, and the estimate of DOA changes accordingly. Given the result of the above simulation, and the logic of the explanation, it would seem reasonable to estimate the doppler differential between the one and two hop paths as being in the region 0.3Hz. It seems as though this property of the CBF can be used to estimate the difference in frequency of signals incident on an array of antennas in a similar fashion to the amplitude beating which also occurs. Since the CBF is the order 1 calculation of the ML as proved earlier, then with the ML, IMP and DOSE implementations proposed above, the model order 1 data may be used to determine the difference in the frequencies of the signals being received either by inspection - as in this case, by use of Fourier analysis, or by using higher resolution methods such as MUSIC, DOSE and ML in the time / frequency domains.

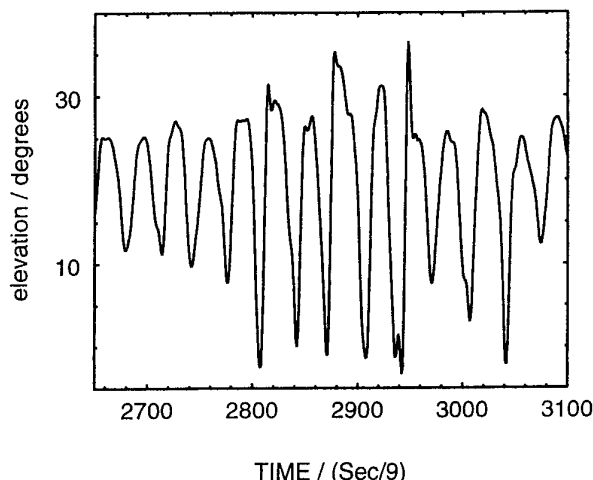


Figure 10 Observed elevation using CBF, note the periodic variation.

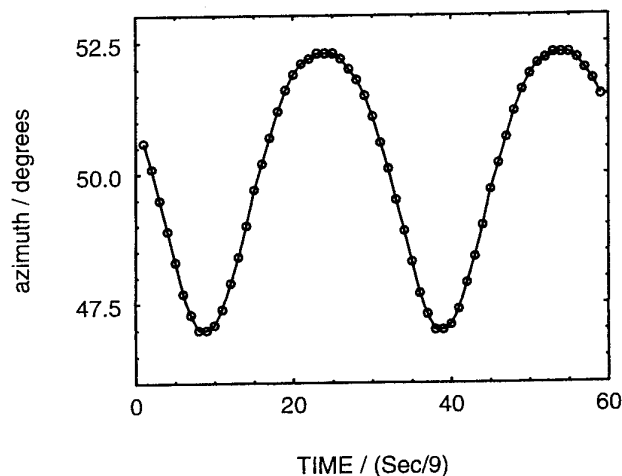


Figure 11 Simulation of CBF processing of two signals of different frequencies shows similar periodic variation to that in Figure 10.

## 8. CONCLUSIONS

Three algorithms - DOSE, IMP and ML - have been presented for superresolution DF analysis in the multipath environment. Efficient implementations of the algorithms using the directed search philosophy and a new method of determining the number of signals present with the ML algorithm (one which works in the presence of coherent signals) have also been described. Proofs that the CBF is an order 1 implementation of the ML estimator, and that array calibration may be simplified when using the above algorithms have also been given. The performance of the proposed algorithms was shown in simulation, and their ability to determine DOAs on real multimoded H.F. data demonstrated.

The DOA data was further analyzed with the use of an FIR filter for smoothing the results instead of using the usual moving window to provide time integration. It was also shown that the DOA variation occurs with the CBF due to the

frequency difference between the two modes resolved by the other methods. Since the CBF results are produced as a by product of the algorithms suggested, analysis of this is proposed as an alternative method for determining the difference in doppler shift of the two paths.

## 9. REFERENCES

- [1] Schmidt, R.O., "Multiple Emitter Location and Signal Parameter Estimation", *IEEE Trans. Ant. Prop.*, **34**, 1986, pp. 276-280.
- [2] Rogier, J.L., Multedo, G., Bertel, L., and Baltazart, V., "Ionospheric Multi-Paths Separation With a High Resolution DF Algorithm Mapped on an Experimental System" *IEE Conf. Publ.*, **339**, 5th Int. Conf. HF Radio Systems and Techniques, July 1991, pp. 117-121.
- [3] Bresler, Y., and Mazovski, A., "Exact Maximum Likelihood Parameter Estimation of Superimposed Signals in Noise", *IEEE Trans. ASSP*, **34**, 1986, pp. 1081-1089.
- [4] Ziskind, I., and Wax, M., "Maximum Likelihood Localization of Multiple Sources by Alternating Projection", *IEEE TRANS. ASSP*, **36**, 1988, pp. 1153-1560.
- [5] Miller, M.I., and Fuhrmann, D.R., "Maximum Likelihood Narrow-Band Direction Finding and the EM Algorithm", *IEEE Trans. ASSP*, **38**, 1990, pp. 1560-1577.
- [6] Mather, J.L., "Characterisation of the Iterative Multi Parameter (IMP) Algorithm", *Proc. I.O.A.*, **11**, 8, 1989, pp. 189-197.
- [7] Zatman, M.A., and Strangeways, H.J., "Resolution of Multi-Moded H.F. Transmissions Using the DOSE Superresolution Direction Finding Algorithm", *IEE Conf. Publ.*, **370**, 8th Int. Conf. on Antennas and Propagation, 1993, pp. 415-418.
- [8] Akaike, H., "A New Look at Statistical Model Identification", *IEEE Trans. AC*, **19**, 1973, pp.716-723.
- [9] Rissanen, J., "Modelling By Shortest Data Description", *Automania*, **14**, 1978, pp. 465-475.
- [10] Clarke, I.J., "Supervised Interpretation of Sampled data Using Efficient Implementation of Higher-Rank Spectrum Estimation" in "Advances in Spectrum Analysis and Array Signal Processing" (S. Haykin Ed.), **II**, Prentice Hall, 1992, pp. 65 -121.
- [11] Zatman, M.A., and Strangeways, H.J., "The Effect of the Number of Noise Eigenvectors Used and Quantization Errors on the Performance of the MUSIC Algorithm", *IEE Conf. Publ.*, **370**, 8th Int. Conf. on Antennas and Propagation, 1993, pp. 481-484.
- [12] Warrington, E.M., and Jones, T.B. "Measurements of the Direction of Arrival of HF Sky Wave signals and Single Site Location Using a Seven Element Wide Aperture Interferometer Array", *IEE Proc. H*, **138**, 1991, pp. 121-130.
- [13] Tedd, B.L., Strangeways, H.J., and Jones, T.B., "The Influence of Large Scale TIDs on the Bearings of geographically Spaced H.F. Transmissions", *J. Atm. and Terr. Phys.*, **46**, 1984, pp. 109-117.

## DISCUSSION

**Discussor's name :** L. Bertel

**Comment/Question :**

1. What kind of antenna did you use for your experiments?
2. Comment: with linear antennas it is impossible to separate the 0 and X mode. So in your graph you get the mean value for azimuth and elevation angles for the 2 modes. That means you found a mean value for a path.

**Author/Presenter's Reply :**

1. Elevated feed vertical monopoles.
2. Yes, that is correct. We did not choose or set up the antennas, but were just given the data, and were aware of this problem; and your work on this is referenced in our paper. (Reference number 2).

**Discussor's name :** C. Goutelard

**Comment/Question :**

Vous présentez des résultats avec des séparations d'angle de 10 degrés au plus. Avec l'algorithme MUSIC dont vous parlez, on obtient de meilleurs résultats.

De plus MUSIC permet de traiter, avec pénalisation il est vrai, des signaux corrélés.

Pouvez-vous indiquer la limite de votre méthode notamment en fonction du bruit et la comparer avec les résultats du MUSIC?

**Translation :**

*You present results with angle separations of 10 degrees at most. Better results can be obtained with the MUSIC algorithm which you mention.*

*Moreover, MUSIC, admittedly with some penalties, can be used to process correlated signals.*

*Can you indicate the limit of your method, in particular with respect to noise, and compare it with the results obtained using MUSIC?*

**Author/Presenter's reply :**

We have also processed data where we resolved low and high angle modes separated in bearing by 4 degrees. The methods we presented are all capable of outperforming MUSIC in simulation, and are capable of beating the Cramer-Rao lower bound with a special implementation we have devised.

In practice, the methods are all more robust than MUSIC, which was unable to process the data we presented here, and possess higher resolution.

In any real system our methods are limited by system errors and not the capabilities of the algorithm.

Yes, MUSIC can be forced to work with coherent sources, but this requires pre-processing which is dependent on array geometry and also reduces the array aperture, thus reducing spectral resolution. Our algorithms are far more robust, require no such pre-processing to resolve coherent sources, and are applicable to any array geometry.



# Mesures d'Angles d'Elévation en HF par une Méthode Haute Résolution utilisant la Diversité de Polarisation<sup>(1)</sup>

Cédric Demeure, Anne Ferréol, Jean-Luc Rogier

Thomson-CSF/RGS

66 Rue du Fossé Blanc, 92231 Gennevilliers, France

## 1. INTRODUCTION

Dans ce papier, nous présentons l'utilisation des techniques haute résolution et de la diversité de polarisation afin d'analyser les liaisons HF par propagation ionosphérique, liaisons qui se caractérisent en général par la présence de plusieurs modes de propagation donnant lieu à plusieurs ondes incidentes à la réception. Ces modes sont en général fortement corrélés et peuvent avoir des polarisations très différentes. Les techniques haute résolution possèdent la capacité de mesurer plusieurs ondes incidentes présentes simultanément dans un canal d'analyse fréquentiel donné, et sont donc adaptées tout particulièrement à des situations de brouillage où une séparation fréquentielle et/ou temporelle n'est plus possible. L'utilisation d'un réseau à diversité de polarisation permet, au delà de l'obtention de certains paramètres de polarisation, une augmentation de la résolution des méthodes envisagées, du fait de la différence de polarisation des modes. Une meilleure connaissance du phénomène de propagation des ondes dans ce milieu est le résultat escompté de l'application de ces techniques.

Pour une liaison donnée et en première approximation (on néglige les effets dus au tilt, ou au rebond sur un sol incliné), les modes arrivent sous le même azimut avec des angles d'élévation différents. Dans l'expérience décrite dans ce papier, la mesure des angles d'élévation est faite en supposant une connaissance de l'azimut. Ainsi nous utilisons un réseau linéaire et l'orientons de façon à obtenir de bonnes performances pour l'estimation des angles d'élévation. La méthode haute résolution à diversité de polarisation utilisée est la méthode MUSIC [1] adaptée afin de tenir compte de l'utilisation de capteurs ayant des gains différents en fonction de la polarisation de l'onde reçue [2].

## 2. PROPAGATION

L'ionosphère présentant des gradients de densité ionique, la propagation des ondes HF s'effectue suivant différents trajets. Les maxima de densité ionique étant traditionnellement associés à des couches, une situation typique de propagation peut se présenter de la manière suivante (voir figure 1):

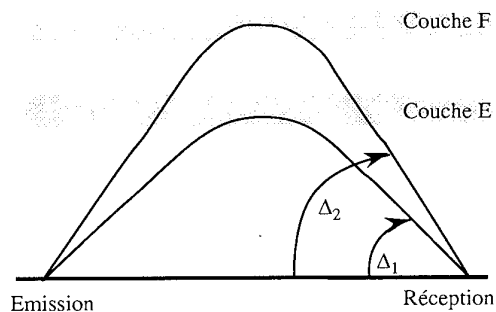


Figure 1 : Exemple de Propagation ionosphérique

On dit alors qu'il y a "réflexion" sur les couches E et F. Si l'on tient compte de l'anisotropie du milieu provoquée par la présence du champ magnétique terrestre, on constate que pour un trajet donné, deux modes de propagation appelés modes "O" et mode "X" (pour ordinaire et extraordinaire) peuvent exister. Ces deux modes ont en général des chemins de groupe très voisins, et de ce fait des angles d'élévation proches, soit donc des retards de groupe différentiels très faibles. Ils ont en revanche des polarisations très différentes. En outre, du fait des ondes de gravité, les couches sont affectées d'un mouvement, qui génère un décalage doppler pour l'ensemble des modes.

Ainsi, pour un seul émetteur, il est possible de recevoir plusieurs sources qui arrivent avec des angles d'élévation plus ou moins différents  $\Delta_1$ ,  $\Delta_2$ , etc ... Ces différents modes arrivent à la réception plus ou moins corrélés. Cette corrélation (spatiale et/ou temporelle) détermine la capacité de l'algorithme

<sup>1)</sup> Ce travail a été effectué dans le cadre du contrat DRET n° 90-34-473.

de goniométrie à séparer les différentes composantes du signal reçu. La décorrélation partielle des signaux observée est provoquée par les dopplers différentiels ainsi que par les retards de groupe différentiels entre les différents trajets de propagation. Dans la référence [3], en s'appuyant sur des modèles de signaux développés dans la référence [6], on montre que pour des dopplers et retards de groupe usuels, une bande de fréquence utile de 1 kHz ou une durée d'observation de quelques secondes apporte une décorrélation suffisante pour les algorithmes haute résolution.

Le système expérimental associé aux algorithmes proposés permettra de déterminer pour une liaison donnée le nombre de modes incidents, leurs sites, ainsi que certains paramètres relatifs à leur polarisation.

### 3. MODELE DE SIGNAL

On considère un réseau de  $N$  capteurs disposés linéairement et recevant  $M$  ondes. Pour un même émetteur, nous recevons donc sous un azimut  $\theta_0$  par rapport au nord.  $M$  modes avec des élévations différentes  $\Delta_m$ . L'objectif de cette étude est de déterminer les élévations de chacun des trajets associés en connaissant la direction  $\theta_0$  de l'émetteur. Le signal en sortie du  $n^{\text{ème}}$  capteur est donné par:

$$x_n(t) = \sum_{m=1}^M s_m(t) f_n(m) \exp\left\{j2\pi \frac{d_n}{\lambda} \cos(\Delta_m) \sin(\theta_0)\right\} + b_n(t)$$

- $M$  : nombre de sources reçues
- $f_n(m)$  : gain du capteur  $n$  pour la source  $m$
- $s_m(t)$  : amplitude complexe de la source  $m$
- $b_n(t)$  : bruit sur le capteur  $n$
- $\lambda$  : longueur d'onde
- $d_n$  : distance entre les capteurs 1 et  $n$
- $\Delta_m$  : angle d'élévation de la source (du mode)  $m$
- $\theta_0$  : azimut de l'émetteur ( $0$ =orthogonal à l'axe du réseau)

Ce modèle correspond à une hypothèse de front d'onde plan.  $\underline{a}$  représente un vecteur,  $\underline{a}^t$  son transposé,  $\underline{a}^*$  son complexe conjugué, et  $\underline{a}^{\dagger}=(\underline{a}^*)^t$ .

#### 3.1 Cas de capteurs identiques

Si les capteurs sont identiques et en supposant un modèle de propagation plan, la hauteur efficace complexe des antennes pour un mode donné (le facteur  $f_n(m)$ ) est indépendant de l'indice  $n$  et l'équation donnant le signal vectoriel reçu  $\underline{x}(t)=[x_1(t) \dots x_N(t)]^t$  peut s'écrire :

$$\underline{x}(t) = \sum_{m=1}^M s_m^*(t) \underline{a}(\Delta_m, \theta_0) + \underline{b}(t)$$

$$s_m^*(t) = f(m) s_m(t)$$

où le vecteur  $\underline{a}(\Delta, \theta)$  contient les réponses en gain des antennes pour l'azimut  $\Delta$  et l'élévation  $\theta$ . Le vecteur  $\underline{a}(\Delta_m, \theta_0)$  est appelé le vecteur directionnel ("steering vector") de la source  $m$ . Du fait que les antennes sont identiques, le vecteur  $\underline{x}(t)$  appartient (en l'absence de bruit) à l'espace vectoriel engendré par les vecteurs directionnels  $\underline{a}(\Delta_k)$  (si on suppose l'azimut connu) qui ne dépendent que de la géométrie du réseau et non pas de la polarisation. Celle-ci n'intervient que sur la puissance des sources reçue par les antennes.

#### 3.2 Algorithme MUSIC

L'algorithme de goniométrie haute résolution MUSIC ("Multiple Signal Classification") [1] exploite les propriétés de la matrice de covariance des observations sur les antennes  $R_x = E[\underline{x}(t) \underline{x}(t)^{\dagger}]$ , où  $E[\cdot]$  est l'espérance mathématique. En supposant que le bruit est spatialement blanc et décorrélé, le nombre de sources est estimé à l'aide d'un test sur les valeurs propres de  $R_x$  [3] ou à base de l'algorithme du maximum de vraisemblance. Par ailleurs, les vecteurs propres  $e_i$ , associés aux plus petites valeurs propres de  $R_x$  ( $M+1 < i < N$ ) forment une base qui est orthogonale à tous les vecteurs directionnels  $\underline{a}(\Delta_m)$  ( $1 < m < M$ ). Nous pouvons alors écrire  $E_b^{\dagger} \cdot \underline{a}(\Delta_m) = 0$ , où  $E_b = [e_{M+1}, \dots, e_N]$  est une base de l'espace "bruit".

L'algorithme de goniométrie MUSIC exploite cette propriété et la fonction de recherche de direction se met sous la forme :

$$P_{\text{music}}(\Delta) = \frac{\underline{a}^{\dagger}(\Delta) \Pi_b \underline{a}(\Delta)}{|\underline{a}(\Delta)|^2}$$

où  $\Pi_b = E_b E_b^{\dagger}$  est un projecteur sur l'espace bruit. Les estimées  $\Delta_m$  des sites sont les  $M$  minima de la fonction  $P_{\text{music}}(\Delta)$ , puisque si  $\Delta$  est une direction d'arrivée alors la fonction de recherche de direction s'annule. De manière traditionnelle, on utilise plutôt l'inverse de cette fonction qui est appelée "pseudo-spectre" à cause en particulier de pics bien formés aux fréquences dites spatiales ( $f=d/\lambda \cos(\Delta)$ ) des sources reçues, ce qui le fait ressembler à un spectre classique.

#### 3.3 Réseau à diversité de polarisation

Le champ électrique de toute onde peut se décomposer dans le plan d'onde comme une combinaison linéaire de deux champs  $E_1$  et  $E_2$ :

$$\vec{E} = \alpha \vec{E}_1 + \beta \vec{E}_2$$

Les coefficients complexes  $\alpha$  et  $\beta$  définissent la polarisation de l'onde incidente. Le réseau utilisé est supposé composé de deux types de capteurs sensibles à deux polarisations différentes. Ainsi, l'énergie d'une source se répartie entre les capteurs de type 1 et les capteurs de type 2. Les signaux sur ces capteurs peuvent s'écrire de la manière suivante :

$$x'_n(t) = \sum_{m=1}^M s_m(t) k'_m \exp\left\{j2\pi \frac{d'_n}{\lambda} \cos(\Delta_m) \sin(\theta_o)\right\} + b'_n(t)$$

$$x''_n(t) = \sum_{m=1}^M s_m(t) k''_m \exp\left\{j2\pi \frac{d''_n}{\lambda} \cos(\Delta_m) \sin(\theta_o)\right\} + b''_n(t)$$

$x'_n(t)$  : n ième capteur de type 1

$x''_n(t)$  : n ième capteur de type 2

$k'_m, k''_m$  : hauteurs efficaces complexes des antennes de type 1 et 2 dans la direction et pour la polarisation du mode m.

Les équations précédentes peuvent se mettre sous la forme vectorielle suivante:

$$\underline{x}'(t) = \sum_{m=1}^M s_m(t) \underline{k}'_m \underline{a}'(\Delta_m) + \underline{b}'_n(t)$$

$$\underline{x}''(t) = \sum_{m=1}^M s_m(t) \underline{k}''_m \underline{a}''(\Delta_m) + \underline{b}''_n(t)$$

avec  $\underline{x}'(t) = [x'_1(t) \dots x'_N(t)]^T$ ,  $\underline{a}'(\Delta) = [a'_1(\Delta) \dots a'_N(\Delta)]^T$  et  $a'_n(\Delta) = \exp(j2\pi (d'_n/\lambda) \cos(\Delta) \sin(\theta_o))$ , et de même pour le deuxième type de capteurs.

En concaténant les vecteurs observations  $\underline{x}'(t)$  et  $\underline{x}''(t)$  correspondant aux deux types d'antennes en un seul vecteur d'observation global  $\underline{x}(t)$ , et en définissant  $\underline{k}_m$  comme le vecteur normalisé constitué par les deux composantes  $k'_m$  et  $k''_m$ , l'observation de l'ensemble des sorties du réseau peut s'exprimer comme suit :

$$\underline{x}(t) = \sum_{m=1}^M \Gamma(\Delta_m) \underline{k}_m s_m(t) + \underline{b}(t)$$

$$\text{avec } \Gamma(\Delta) = \begin{bmatrix} \underline{a}'(\Delta) & \underline{0} \\ \underline{0} & \underline{a}''(\Delta) \end{bmatrix}, \text{ et } \underline{x}(t) = \begin{bmatrix} \underline{x}'(t) \\ \underline{x}''(t) \end{bmatrix}$$

Pour la suite, nous posons :  $\underline{a}(\Delta_m, \underline{k}_m) = \Gamma(\Delta_m) \underline{k}_m$ .

**Remarque** : L'intérêt d'un tel formalisme par rapport à celui de Ferrara-Parks [2] réside dans les points suivant :

- Les deux vecteurs colonnes de  $\Gamma$  sont orthogonaux par définition, ce qui simplifie notablement l'expression du pseudo-spectre comme nous le verrons par la suite.

- le vecteur  $\underline{k}$  à estimer n'est plus le vecteur de polarisation mais le vecteur des hauteurs efficaces des deux types d'antennes vis à vis de la source considérée. La connaissance de la réponse des antennes n'intervient que si l'on souhaite estimer la polarisation à partir de  $\underline{k}$ , ce qui n'est pas nécessaire si l'on se limite à une goniométrie.

Par contre, un tel formalisme n'est pas applicable dans le cas où l'on utilise plus de deux types de capteurs.

### 3.4 MUSIC avec diversité de polarisation

La généralisation s'obtient en considérant que le vecteur  $\underline{k}$  est un paramètre supplémentaire à estimer pour chaque source, en plus de l'angle d'élévation. L'orthogonalité entre l'espace bruit et les vecteurs directionnels de chacune des sources demeure, il suffit alors de minimiser la fonction de recherche de direction suivante :

$$P_{\text{music}}(\Delta, \underline{k}) = \frac{\underline{a}^\dagger(\Delta, \underline{k}) \Pi_b \underline{a}(\Delta, \underline{k})}{|\underline{a}(\Delta, \underline{k})|^2}$$

L'algorithme de Ferrara [2] permet d'éviter une recherche multidimensionnelle en effectuant la minimisation selon le paramètre  $\underline{k}$  de façon analytique, grâce à la théorie des faisceaux de formes quadratiques [8]. En remplaçant  $\underline{a}(\Delta, \underline{k})$  par son expression, nous obtenons :

$$P_{\text{music}}(\Delta, \underline{k}) = \frac{\underline{k}^\dagger \left( \Gamma(\Delta)^\dagger \Pi_b \Gamma(\Delta) \right) \underline{k}}{\underline{k}^\dagger \left( \Gamma(\Delta)^\dagger \Gamma(\Delta) \right) \underline{k}}$$

dont la valeur minimale selon  $\underline{k}$  s'exprime comme suit :

$$P_{\text{music}}(\Delta) = \lambda_{\min} \left\{ \Gamma(\Delta)^\dagger \Pi_b \Gamma(\Delta), \Gamma(\Delta)^\dagger \Gamma(\Delta) \right\}$$

$\lambda_{\min}$  désigne la valeur propre généralisée minimale du couple de matrices  $\{ \Gamma(\Delta)^\dagger \Pi_b \Gamma(\Delta), \Gamma(\Delta)^\dagger \Gamma(\Delta) \}$ , qui sont des matrices de dimension  $2 \times 2$ . Si l'on a pris soin de normaliser les vecteurs  $\underline{a}'$  et  $\underline{a}''$ , la matrice  $\Gamma(\Delta)^\dagger \Gamma(\Delta)$  est la matrice identité. La fonction de recherche de direction se réduit alors à calculer la valeur propre d'une matrice  $2 \times 2$ :

$$P_{\text{music}}(\Delta) = \lambda_{\min} \left\{ \Gamma(\Delta)^\dagger \Pi_b \Gamma(\Delta) \right\}$$

Tout comme pour l'algorithme MUSIC sans diversité, la détermination des incidences des sources se fait en recherchant les minima de cette fonction.

### 3.5 Calcul de la polarisation

Une fois les angles d'élévation obtenus, il est possible

de calculer la polarisation associée à chacune des incidences identifiées. Cela passe par une estimation des vecteurs des hauteurs efficaces  $\underline{k}_m$ . Rappelons ici que les deux composantes de ce vecteur représentent la réponse des deux types d'antennes à la polarisation de la source considérée. L'obtention du vecteur  $\underline{k}_m$  à partir de l'incidence estimée  $\Delta_m$  découle des propriétés algébriques suivantes : La projection du vecteur directionnel  $\underline{a}(\Delta_m, \underline{k}_m)$  de la source  $m$  sur l'espace bruit est nulle, soit  $\Pi_b \underline{a}(\Delta_m, \underline{k}_m) = 0$ , soit encore  $\Pi_b \Gamma(\Delta_m) \underline{k}_m = 0$  et finalement  $[\Gamma(\Delta_m)^* \Pi_b \Gamma(\Delta_m)] \underline{k}_m = 0$ . Le vecteur  $\underline{k}_m$  est donc le vecteur propre de la matrice  $[\Gamma(\Delta_m)^* \Pi_b \Gamma(\Delta_m)]$  associé à la valeur propre nulle (ou minimale).

L'estimation de la polarisation de l'onde se fait ensuite en faisant intervenir, via une modélisation des antennes, la connaissance des hauteurs efficaces des deux types d'antenne. On recherche alors quelle polarisation donne une réponse des deux types d'antennes colinéaire au vecteur  $\underline{k}_m$  estimé. Cette recherche peut se faire soit de manière analytique si l'on dispose d'une modélisation analytique simple des aériens, soit de manière exhaustive. Dans ce papier, nous nous limiterons à une identification des modes par leur direction d'arrivée, sans chercher à exploiter les mesures de polarisation.

### 3.6 Détermination de la puissance des sources

Afin d'estimer la puissance des sources, il est nécessaire d'avoir estimé les angles d'élévation et les vecteurs  $\underline{k}$  des sources ( $\Delta_m$  et  $\underline{k}_m$ ). La méthode proposée dans [1] s'adapte de manière immédiate à la goniométrie avec diversité de polarisation. Comme par ailleurs les valeurs propres minimales de la matrice de corrélation donnent une estimation de la puissance de bruit, une estimation du rapport S/B est également possible.

### 3.7 Limites théoriques de la méthode

Notons que la détermination de  $\lambda_{\min}$  impose que le rang minimal du projecteur bruit  $\Pi_b$  soit de 2. Le nombre maximum de sources goniométrables est donc  $N-2$ ,  $N$  désignant le nombre total de capteurs du réseau (au lieu de  $N-1$  pour un réseau de capteurs sans diversité de polarisation). Cette limitation est en pratique peu gênante car le nombre maximal de sources observables est donné plus par les ambiguïtés du réseau (cf ci-dessous) que par le pouvoir d'identification de la méthode.

Lorsque deux sources arrivent sous les mêmes angles et avec des polarisations différentes, les deux valeurs propres de la matrice  $[\Gamma(\Delta)^* \Pi_b \Gamma(\Delta)]$  s'annulent. C'est pourquoi, il

est nécessaire d'examiner les deux valeurs propres si l'on souhaite détecter la présence de deux modes sous la même incidence. Par contre, dans un tel cas de figure, du fait de la dégénérescence de la matrice, l'estimation du vecteur  $\underline{k}$  devient impossible. De ce fait, il est possible de détecter la présence de deux sources sous la même élévation  $\Delta_m$  et avec des polarisations différentes. Ceci correspond en général aux modes de propagation O et X d'un même trajet, très proches spatialement. Ce cas a été fréquemment obtenu, comme nous le verrons dans la partie consacrée aux résultats expérimentaux.

## 4. DISPOSITIF EXPERIMENTAL

### 4.1 Réseau antennaire

Les différents points suivants ont été abordés afin de déterminer le réseau le plus adapté à cette étude:

**Choix de l'antenne :** Les diagrammes de rayonnement des antennes sont susceptibles de privilégier des couples incidence-polarisation. Le choix des types d'antennes et de leur répartition dépend essentiellement du type de sources que l'on souhaite privilégier, ou inversement du désir de voir le maximum de sources possibles. Pour cette étude, nous avons utilisé des antennes de série cadres croisés TRC195-6, à comportement relativement omnidirectionnel, et dont les signaux en sortie peuvent être les combinaisons  $S_{NS} + j S_{EW}$  ou  $S_{NS} - j S_{EW}$ .  $S_{NS}$  et  $S_{EW}$  désignant les signaux venant des cadres Nord-Sud et Est-Ouest. Ces combinaisons sont adaptées au cas de sources arrivant à élévation élevée avec une polarisation circulaire droite ou gauche.

L'**ambiguïté** d'un réseau est caractérisée par le fait que plusieurs incidences peuvent donner des vecteurs directionnels relativement proches. Cette notion est relative à l'ensemble des incidences d'intérêt. Ainsi, pour une recherche en angle d'élévation dans l'intervalle  $[0, 90^\circ]$ , la non-ambiguïté est plus facile à réaliser que dans le cas général d'une recherche azimut-élévation. Les conséquences de l'ambiguïté d'un réseau sont les fausses goniométries, c'est à dire l'augmentation de la probabilité de fausse alarme, conjointement à la diminution de la probabilité de détection du fait que des fausses directions d'arrivée ont été substituées à des directions d'arrivée correctes.

La **précision** peut être définie sans faire intervenir d'algorithme particulier en faisant appel à la borne de Cramer-Rao. Cette borne exprime la variance minimale de tout estimateur pour le réseau considéré en fonction des paramètres : position des sources, rapport S/B, corrélation temporelle. Il est assez aisé de constater sur simulation que la précision et la résolution dépendent essentiellement de l'ouverture du réseau.

c'est à dire de sa dimension suivant l'axe orthogonal à la direction d'arrivée de la source.

Le système doit être apte à fonctionner dans une **gamme de fréquence** relativement étendue, sans avoir à reconfigurer le réseau antennaire. Pour cette étude, on se fixe une gamme de fréquence de 6 à 12 Mhz, gamme dans laquelle il est relativement aisé d'obtenir des situations de multi-trajets.

Dans le cadre de cette étude, la conception du réseau peut alors se résumer à trouver une géométrie d'ouverture maximale (dans l'axe d'azimut d'arrivée de l'émission de test) en respectant les contraintes précédentes. Afin de disposer de la diversité de polarisation sans modifier les antennes, celles-ci sont prises par paires, et disposées selon une configuration lacunaire dite à redondance minimale [7], choisie pour des raisons d'ambiguïté et de précision à ouverture donnée (voir figure 2).

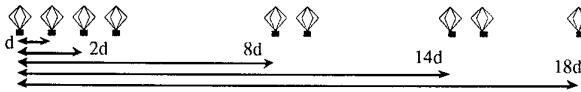


Figure 2 : Réseau d'antennes lacunaire utilisé

#### 4.2. Dispositif d'enregistrement

Un dispositif d'acquisition de dix voies simultanées similaire à celui décrit dans [3] a été utilisé. Une capacité d'enregistrement de 5 secondes sur 15 kHz de bande était disponible.

De manière à maîtriser tous les paramètres de la liaison (forme d'onde, puissance, azimut, ...), un émetteur coopératif a été utilisé lors des expérimentations. La liaison était de 350 km, avec un fort rapport signal sur bruit de manière à s'affranchir des problèmes de sensibilité et de fluctuations du bruit (ainsi que des non-stationnarités et/ou de la répartition spatiale non uniforme). Une forme d'onde dite large bande (modem numérique occupant 3 kHz) est utilisée de manière à bénéficier le plus possible de l'effet de décorrélation lié au produit Bande-Différence en retard de groupe des trajets.

#### 4.3. Décorrélation spatiale des modes O et X

Le coefficient de corrélation spatiale de deux sources permet d'évaluer l'aptitude d'un réseau à les séparer. Il est donné dans le cas général par le produit scalaire normalisé des vecteurs directionnels, soit dans notre cas :

$$c = \frac{2}{N} [k'_1 \hat{a}(\Delta_1) + k''_1 \hat{a}''(\Delta_1)]^\dagger [k'_2 \hat{a}(\Delta_2) + k''_2 \hat{a}''(\Delta_2)]$$

en supposant que les vecteurs  $\underline{k}$ ,  $\underline{a}'$  et  $\underline{a}''$  sont normalisés, il est alors aisé de calculer la corrélation spatiale entre deux modes O et X d'un même trajet, qui auraient des angles de site très voisins, ce qui permet de négliger la différence de phase géométrique :

$$c = k_1^* k_2' + k_1'' k_2'' = k_1^\dagger k_2$$

On constate donc que la corrélation spatiale de deux modes O et X arrivant sous des incidences très proches est donnée par le produit scalaire des vecteurs  $\underline{k}$ , et est donc indépendante de la disposition géométrique des antennes. Celle-ci va déterminer la capacité de séparation des trajets arrivant sous des incidences notablement différentes, alors que la séparation des modes O et X d'un même trajet va reposer sur les caractéristiques de polarisation des modes et sur le choix des deux types d'antenne utilisées.

Les valeurs de  $c$  ont été calculées pour différents azimuts en fonction du site, d'une part à l'aide d'une modélisation des antennes utilisées, et d'autre part à l'aide des conditions de Budden qui donnent la polarisation en sortie de l'ionosphère pour les modes considérés, selon une analyse similaire à la référence [5]. Un exemple est donné sur la figure 3 pour une fréquence de 6 MHz.

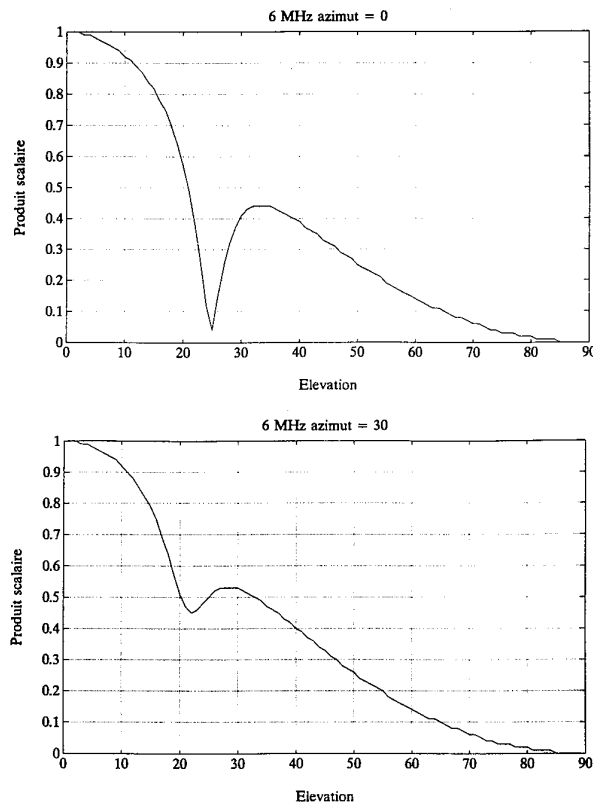


Figure 3 : Corrélation spatiale de O et X, fonction de l'élévation

La séparation des deux modes se fera d'autant mieux que leur corrélation spatiale vue par le réseau sera faible. On constate que bien que les polarisations des modes O et X sont orthogonales, cette orthogonalité n'est plus vérifiée sur les vecteurs constitués par la réponse des deux types d'antenne, surtout pour les angles d'élévation faibles où les antennes utilisées possèdent peu de diversité (non réception de la polarisation horizontale). Au delà de 20° d'angle d'élévation, la décorrélation est néanmoins suffisamment importante pour espérer une séparation des modes par l'algorithme goniométrique. Notons enfin la dépendance des résultats vis à vis de l'angle d'azimut qui reflète la non isotropie du milieu de propagation (champ magnétique terrestre).

## 5. RESULTATS EXPERIMENTAUX

### 5.1. Cas de deux modes non séparés en site

Afin d'identifier la présence de deux modes de propagation sur la même incidence, nous calculons simultanément les fonctions  $\lambda_{\min}|\Gamma(\Delta)^* \Pi_b \Gamma(\Delta)|$  (pseudo-spectre MUSIC avec diversité) et  $\lambda_{\max}|\Gamma(\Delta)^* \Pi_b \Gamma(\Delta)|$  afin d'en évaluer les minima. La figure 6 donne le tracé de ces deux valeurs propres, obtenu à partir d'un enregistrement expérimental (Fréquence 7.47 MHz). Dans un tel cas de figure, nous obtenons deux sources sous le même angle d'élévation ( $\Delta = 66^\circ$ ) avec des polarisations différentes, mais non mesurables du fait de ce qui vient d'être exposé ci-dessus. La figure 5, quant à elle donne un exemple comparable avec cette fois un second trajet de propagation à 30° d'élévation en plus du trajet à 63° comportant deux modes de propagation (Fréquence 8.4 MHz).

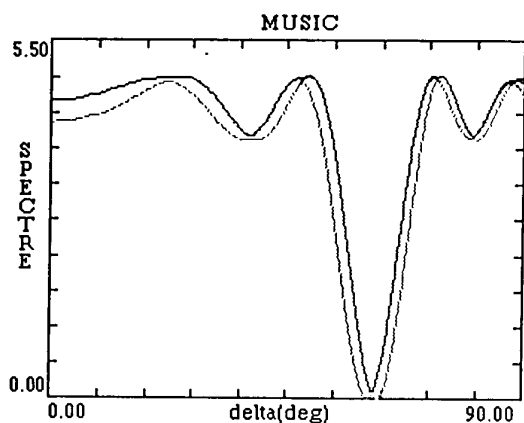


Figure 4 : Présence de modes O et X sur une même incidence - Pseudo-Spectres ( $\lambda_{\min}$  et  $\lambda_{\max}$ ).

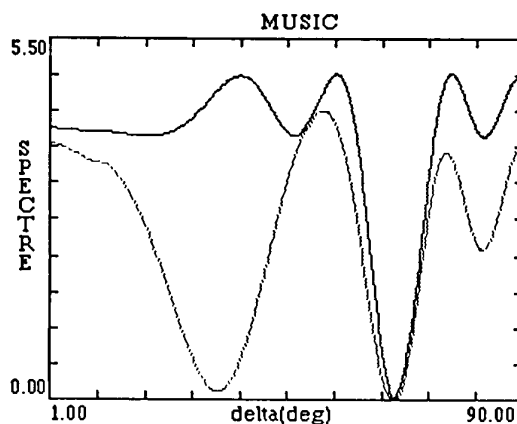


Figure 5 : Présence de modes O et X sur une même incidence - 2 trajets .Pseudo-Spectres ( $\lambda_{\min}$  et  $\lambda_{\max}$ ).

### 5.2. Evaluation du pouvoir séparateur en fonction de la corrélation en polarisation.

Lors d'une telle expérimentation, les performances absolues de l'algorithme de goniométrie MUSIC, en particulier en termes de précision, sont difficiles à évaluer car nous ne connaissons pas à priori les angles d'incidences exacts des trajets. Il est toutefois possible d'évaluer le pouvoir séparateur en examinant l'ensemble des goniométries obtenues. Comme nous l'avons vu précédemment, le pouvoir séparateur de la méthode est fonction du produit scalaire des vecteurs  $\underline{k}$  des deux sources que nous appellerons coefficient de corrélation en polarisation, et de leur espacement angulaire en site. Afin de connaître approximativement la résolution du système, chaque fois que nous séparons deux sources avec des élévations proches ( $\Delta_1$  et  $\Delta_2$ ), nous représentons le résultat dans le plan ( $dF$ ,  $r$ ), par un point :

$dF$  : séparation angulaire normalisée (égale à la fréquence spatiale dans le cas d'un réseau linéaire equi-espacé)

$r$  : coefficient de corrélation en polarisation.

avec

$$dF = \frac{d}{\lambda} [\cos(\Delta_2) - \cos(\Delta_1)] \quad r = \frac{|\underline{k}_2^+ \cdot \underline{k}_1|}{|\underline{k}_2| |\underline{k}_1|}$$

Il est en effet nécessaire de normaliser ainsi la séparation angulaire des sources, car du fait du caractère linéaire du réseau, les déphasages géométriques dépendent de la différence des cosinus des angles de site, et comme les expérimentations ont été réalisées à différentes fréquences l'ouverture du réseau en longueurs d'onde n'était pas constante. A titre d'indication, une séparation angulaire normalisée de 0.02 à 10 MHz pour des élévations proches de 60° correspond à une séparation angulaire de 4.5°.

L'ensemble de ces points se trouve sur la figure 6. Cette représentation nous permet de tracer la plus petite séparation "dF" observée en fonction du coefficient de corrélation en polarisation. Cette courbe nous permet de connaître la résolution en fonction de la différence de polarisation observable par les antennes.

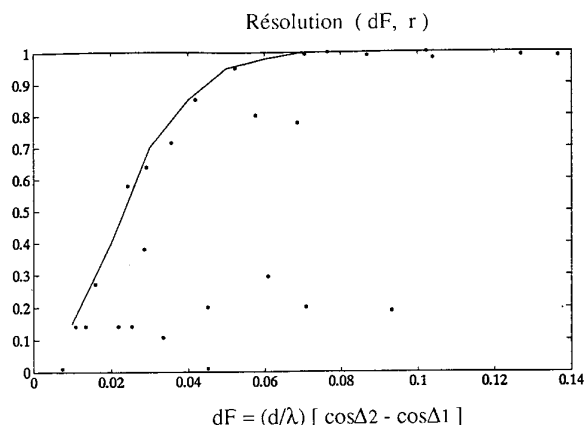


Figure 6 : Séparation en fonction de la corrélation en polarisation

Cette courbe confirme que plus les polarisations sont orthogonales ( $r=0$ ) meilleure est la résolution. Pour des polarisations colinéaires ( $r=1$ ), nous pouvons séparer deux sources à partir de  $dF=0,070$ . L'estimation théorique de la séparation angulaire est de  $dF=0,045$ . La diminution de la résolution provient des diverses erreurs instrumentales. Pour un coefficient de corrélation en polarisation de l'ordre de 0,5 la résolution est de  $dF=0,02$ . Pour des séparations angulaires quasiment nulles, il est difficile de calculer précisément les vecteurs  $\underline{k}_1$  et  $\underline{k}_2$ , c'est pourquoi nous ne pouvons obtenir des résultats dans la zone voisine du point ( $dF=0$ ,  $r=0$ ).

### 5.3. Apport de la diversité de polarisation

Le dispositif expérimental décrit plus haut permet également de mettre en œuvre l'algorithme MUSIC sans diversité de polarisation sur cinq antennes commutées de manière identique, le réseau sans diversité ayant la même ouverture que celui avec diversité. Il est en conséquence aisé d'évaluer l'intérêt de la diversité. Sur la figure 7 se trouve le spectre de MUSIC en diversité de polarisation d'une acquisition et sur la figure 8 le spectre sans diversité obtenu sur la commutation  $S_{NS} - j S_{EW}$  seulement.

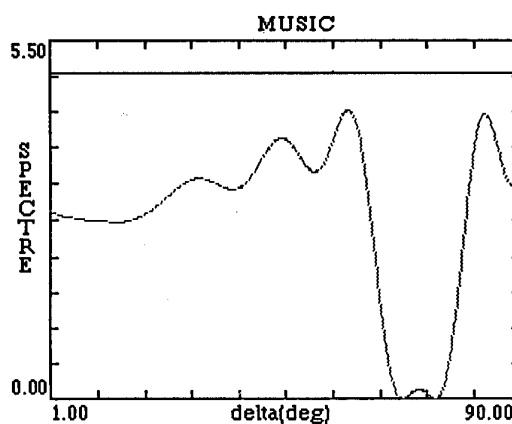


Figure 7 : Pseudo-spectre avec diversité de polarisation

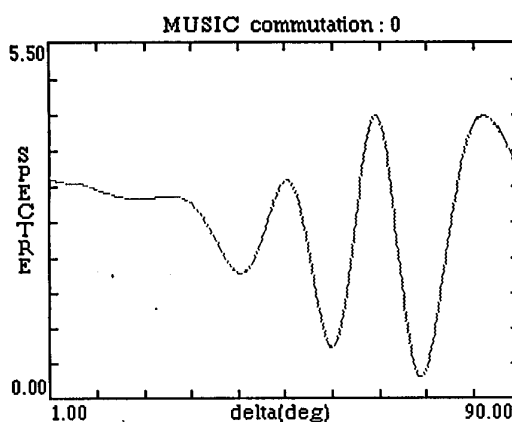


Figure 8 : Pseudo-spectre sans diversité de polarisation

Nous avons en fait deux sources qui se trouvent sous les élévations :  $\Delta_1 = 67^\circ$  et  $\Delta_2 = 74^\circ$ . En diversité de polarisation les puissances estimées sont de :  $[S/B]_1 = 35$  dB  $[S/B]_2 = 17$  dB. Sans diversité on trouve une seule source de puissance :  $[S/B] = 5$  dB. Dans ce cas la puissance estimée est plus faible car la commutation  $S_{NS} - j S_{EW}$  est mal adaptée aux ondes reçues. De plus, MUSIC ne trouve qu'un seul minimum à  $\Delta = 71,74^\circ$ , qui ne descend pas à zéro car la méthode ne sépare pas les deux trajets. Cela a pour conséquence de détériorer l'estimation de rapport S/B. Ce fichier montre qu'il est nécessaire d'avoir deux types d'antennes et d'exploiter de manière performante les signaux pour récupérer toute l'énergie de l'onde. Les deux séries d'antennes du réseau, font chacune un filtrage en polarisation et sont choisies de façon à filtrer des polarisations très différentes. Pour un même trajet, chacune des antennes récupère une partie de l'énergie. La diversité de polarisation permet de recombinaison de manière optimale les énergies de ces deux types de capteurs. Outre une amélioration évidente du pouvoir séparateur du système, on augmente notablement sa sensibilité.

#### 5.4. Stabilité temporelle des mesures

Finalement, nous montrons l'évolution d'une acquisition sur les 5 secondes d'enregistrement. Le signal étudié est sur la liaison CHOLET-COULOMMIERS. Comme le montre le spectre de MUSIC de la figure 9, nous sommes en présence de quatre sources.

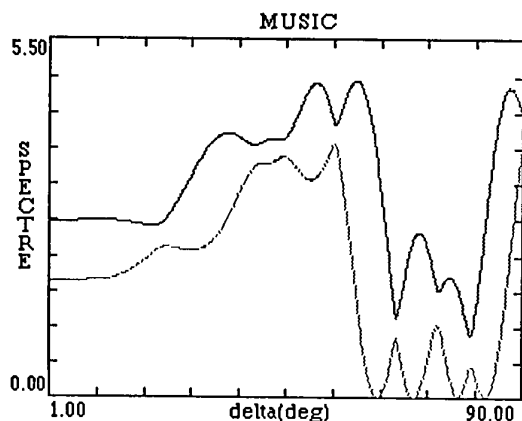


Figure 9 : Pseudo-spectre intégré sur 5 secondes

Ce signal comporte des trajets sous les élévations et les rapports signaux sur bruit estimés suivants:

$\Delta_1 = 62,7 \text{ deg}$	$[S/B]_1 = 26\text{dB}$
$\Delta_2 = 69,46 \text{ deg}$	$[S/B]_2 = 28\text{dB}$
$\Delta_3 = 77,85 \text{ deg}$	$[S/B]_3 = 12\text{dB}$
$\Delta_4 = 82,95 \text{ deg}$	$[S/B]_4 = 17\text{dB}$

Pour cette acquisition nous constatons que nous avons séparé des sources dans une dynamique de 15 dB. Afin d'analyser le signal plus finement la figure 10 représente l'évolution de des angles d'arrivées sur 5 s. Pour cela nous intégrons la matrice de covariance des mesures toutes les 150 ms.

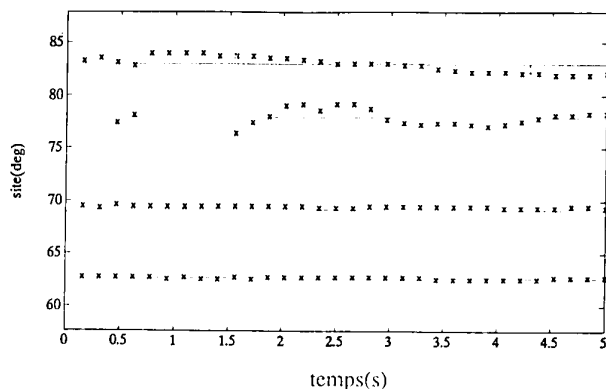


Figure 10 : Evolution des angles d'élévation sur 5 secondes

D'après ces résultats nous constatons que les sources qui ont la plus faible variance sont les plus fortes en puissance. La source qui se situe en 77,85deg n'est pas toujours détectée, d'une part parce qu'elle est 16dB en dessous de la plus forte, et d'autre part vraisemblablement à cause de l'évolution du décalage doppler différentiel. Pour cette source le temps d'intégration de 150 ms n'est pas toujours suffisant.

#### 6. CONCLUSION

Dans ce papier nous avons proposé une méthode permettant d'identifier les différents trajets et modes de propagation d'une liaison HF, par une technique de discrimination spatiale couplée à une discrimination en polarisation. La discrimination en polarisation s'avère particulièrement utile pour séparer des modes d'un même trajet qui arrivent sous des incidences très proches, mais qui d'après les conditions de Budden ont des polarisations orthogonales. L'exploitation optimale de cette orthogonalité est néanmoins sujette au choix des antennes de réception. Nous avons montré que si l'on se limite à une identification des trajets et modes par leur direction d'arrivée, la connaissance des fonctions caractéristiques d'antenne n'était pas indispensable, à condition de n'utiliser que deux types de capteurs dans le réseau. Il est par ailleurs envisageable d'exploiter les mesures de polarisation avec un modèle d'antenne performant. Ces techniques ont été appliquées sur un dispositif expérimental utilisant un réseau à ouverture relativement importante, mais dont la géométrie linéaire n'autorisait pas de mesure en azimut. Les résultats expérimentaux ont confirmé l'apport de la diversité de polarisation par rapport à une approche goniométrique classique, en termes de résolution et de sensibilité. La technique proposée constitue, pour une étude de la propagation ionosphérique, une alternative intéressante par rapport à des systèmes exploitant la mesure de retard de groupe qui nécessitent des modulations spécifiques et des largeurs de bande suffisamment importantes, car elle ne fait pas d'hypothèses sur le signal utilisé.

#### BIBLIOGRAPHIE

- [1] R.O SCHMIDT, "Multiple Emitter Location and signal Parameter Estimation" IEEE trans Ant.prop, Vol AP-34, n°3 pp 276-280, mars 1986
- [2] FERRARA, PARKS, "Direction finding with an array of antennas having diverse polarizations", IEEE trans. on antennas and propag. mars 1983.



[3] J.L. Rogier, G. Multedo, L. Bertel, V. Baltazart, "Ionospheric multi-paths separation with a high resolution direction finding algorithm mapped on to an experimental system," IEEE - Fifth International Conference on HF Radio Systems and Techniques, Edinburgh, United Kingdom, July 22-25 1991, pp. 117-121.

[4] L. Bertel, C. Brousseau, A. Ferreol, J.L. Rogier, C. Demeure, "Electronic Density Profile Updating From Arrival Angle Measurements on the HF Links", 7th Int. Ionospheric Effects Symposium, Alexandria, Virginia, USA, Mai 1993.

[5] L. Bertel, J. Rojas Varela, D. Cole, P. Gourvez,

"Polarisation and ground effects on HF receiving antenna patterns", Ann. Telecom., 44, n°7-8, 1989.

[6] P. Gourvez, L. Bertel, J. Rojas Varela, "Measurements and analysis of the H.F. Field received with a tripole antenna" IEE/ICAP/1987.

[7] David Pearson, S.U. Pillai and Y. Lee, "An algorithm for near-optimal placement of sensor elements," IEEE trans. on Inf. Theory, November 1990.

[8] F.R. Gantmacher, "Matrix Theory," Chelsea, New York, Vol. 2, 1974.

## DISCUSSION

**Discussor's name :** C. Goutelard

**Comment/Question :**

Pouvez-vous préciser la robustesse de MUSIC en diversité de polarisation, vis à vis du bruit de la gamme HF?

**Translation :**

*Can you specify the ruggedness of MUSIC in polarisation diversity compared to the HF range?*

**Author/Presenter's reply :**

L'hypothèse de décorrélation du bruit entre capteurs semble, d'après nos mesures, mieux vérifiée entre deux antennes de polarisation différentes espacées d'une demi longueur d'onde, conférant ainsi une robustesse satisfaisante à l'algorithme.

**Translation :**

*According to our measurements, the decorrelation assumption for noise between sensors seems to verify better for two antennas of different polarisation spaced a half-wavelength apart, which then gives the algorithms satisfactory ruggedness.*

# Measurements of radar backscatter from the ocean surface at 94 GHz as a function of wind speed, direction and the modulation by the ocean waves during the SAXON-FPN experiment.

Hans-Hellmuth Fuchs

Forschungsinstitut für Hochfrequenzphysik der FGAN e.V.  
Neuenahrerstr.20, D-53343 Wachtberg-Werthhoven, Germany

## ABSTRACT

As part of the joint German/US SAXON-FPN remote sensing experiment a series of mm-wave radar backscatter measurements were carried out in the German Bight of the North Sea in November 1990, 1991 and August 1992. The dependence of the reflectivity  $\sigma^0$  on wind speed and direction was determined by means of a 94 GHz (W-band) radar mounted on the German Research Platform North Sea (FPN). The radar backscattering measurements were performed at an incidence angle of  $45^\circ$  and at azimuth angles relative to the wind direction ranging from upwind to crosswind. Based on the data evaluation of the three measurement periods values for the wind speed exponent  $\gamma$  defined by an empirical relation between the reflectivity  $\sigma^0$  at vertical polarisation and the windspeed  $U$  measured at a height of 46 m above mean sea level at the FPN were obtained. The values of  $\gamma$  range between 2.33 and 2.50 depending on wind direction and the wave spectrum. This result shows that the wind speed exponent at W-band is higher than those at X-, Ku- and Ka-band indicating that either an enhanced generation of higher amplitudes of short waves in the millimeter range or other processes exist like specular scattering from facets reinforcing the backscatter cross section.

## 1. INTRODUCTION

Remote sensing of the ocean surface from space- or airborne platforms has become of increasing importance during recent years. The use of radars for imaging the ocean surface and for determining atmospheric and oceanographic parameters requires a good understanding of the backscattering process. Therefore, one of the primary objectives of the SAXON-FPN experiment was to investigate radar backscatter from the ocean surface at different environmental, especially high sea state conditions. The backscattering measurements were performed simultaneously with measurements of meteorological and oceanographic data to study in detail the dependence of the reflectivity on such parameters like the local wind vector, wind friction velocity, air-sea

temperature difference, surface wave slope and short wave spectral density. The radar frequencies used in this experiment ranged from microwaves at L-Band to millimeter waves at W-Band (94 GHz).

In theoretical considerations the radar backscatter for off-vertical incident angles from  $20^\circ$  to  $70^\circ$  is explained by a composite scale model based on perturbation techniques for a slightly rough surface where Bragg scattering is assumed to be the primary scattering mechanism [1]. In this theory the ocean surface is modeled as small-scale waves (capillary waves), which form the dominant scatterers and are induced by the surface friction velocities of the wind field. This shortwave spectrum is an equilibrium between wind forcing, wave breaking and dissipation due to viscous and turbulent effects, and is superimposed by large-scale waves (gravity waves) which have a tilting and modulating effect on the Bragg resonant waves. In a first-order scattering theory the Bragg wavelength  $\Lambda$  is related to the wavelength of the microwave  $\lambda$  interacting with the ocean surface wave by

$$\Lambda = \frac{\lambda}{2 \cdot \sin \theta} \quad (1)$$

where  $\theta$  denotes the incident angle. While at L-Band frequencies the Bragg wavelength is correlated with gravity waves and at X- and Ku-Band with gravity-capillary waves, the Bragg resonant waves correspond to the short capillary wave spectrum at millimeter wave frequencies (Ka- to W-Band). For 94 GHz the Bragg wavelength of sea surface waves is 2.2 mm at an incident angle of  $45^\circ$ . In this wavelength range a sharp cut-off in the spectral density of the capillary waves is expected and has been observed in wind-wave tank experiments. Therefore the backscatter cross sections should be considerably lower at 94 GHz compared to lower frequencies, but more sensitive to changes in this fall-off region of the spectral density.

Results of backscatter measurements of the ocean surface at 94 GHz from the Research Platform North Sea (FPN) are presented. The reflectivity was investigated as a function of wind speed and wind direction. Based on a data evaluation of the three measurement campaigns different wind speed exponents were determined using wind speed data measured at a height

of 46 m above the mean sea surface. Furthermore, the power spectra and auto-correlation function of  $\sigma^0(t)$  are discussed and compared to data from a wave-buoy located near the tower.

## 2. The Experiment

The experiment was carried out in November 1990, November 1991 and two weeks in August 1992 at the FPN which is located in the German Bight of the North Sea approximately 70 km west of the island of Sylt (Germany). The water depth in this area is about 30 m. The 94 GHz radar was mounted 31.5 m above mean sea level on the crane walkway on the northwest corner of the tower with a fixed azimuth angle of 319°N (antenna look direction). During the experiment the incident angle could be varied between 30° and 60°, but was kept predominantly at 45°.

Frequency, GHz	94.0
Peak power, W	4.0
Frequency chirp, MHz	300
Pulse length, ns	60
Pulse repetition frequency (max), kHz	50
Polarization (transmit, receive)	VV, VH
Minimum detectable signal at 300 MHz, dBm	-85
Dynamic range, dB	60
Output, power calibrated	log
Linearity, dB	± 1
Antenna	
Type	conical horn
3-dB beam width, deg	4.2
Gain, dB	29.5

Tab.1 Operational parameters of the 94 GHz radar

The incoherent 94 GHz radar consisted of a free running, pulsed IMPATT oscillator as the transmitting source whose inherent frequency chirp was band limited to 300 MHz and linearized by shaping the driving current pulse. The peak output power of 4 W was directed through a duplexer to a single conical horn-antenna for common transmission and reception. Range gating prevented unwanted spill-over into the receiver circuit. The 3-dB beamwidth was 4.2° resulting in an elliptical footprint area on the ocean surface of 12 m<sup>2</sup> for 45° incident angle. During transmission the radar was operated only in the vertical polarization mode. The received backscatter signal was split up by an orthomode transducer into the orthogonally polarized components VV and VH, down converted in two separate channels by mixers and a common GUNN local oscillator, detected, log converted and, finally, stored by a digital data acquisition system.

Tab.1 summarizes the operational parameters of the radar. The pulse repetition frequency was set to 6.4 kHz

due to the limited analog-digital conversion rate of the data acquisition system. Moreover, an integration of 256 pulses was performed to limit the amount of data on the storage medium, resulting in an average data rate of 25 Hz. For correlation purposes with mean values of environmental data 60-s averages of these reflectivity data were used.

The measured backscatter amplitudes were converted into reflectivity values  $\sigma^0$  in dBm<sup>2</sup>/m<sup>2</sup> (normalized radar cross section, NRCS) from the radar cross section  $\sigma$  of the illuminated area. A relative calibration of the radar system in NRCS values was twice established on the tower, before and after the experimental period, by measuring the radar backscatter from two trihedral reflectors of known cross section at a fixed distance. By this method an accuracy of 0.5 dB for the relative NRCS was achieved.

## 3. Experimental Results and Discussion

As an example Fig. 1 shows a 20-min time series of the measured reflectivity at 94 GHz for an incident angle of 45° with rapid changes in the wind field illustrating the influence of the environmental parameters on the back-scattering process at 94 GHz. The wind speed indicated by the dashed line with only a few available data points changed from about 12.5 m/s down to 3.5 m/s. The same tendency is observed for the reflectivity depicted by the solid line which is based on 60-s mean values using a sliding averaging technique. The wind direction ranged from 300°N to 330°N resulting in an upwind situation with respect to the azimuth orientation of the radar system. During the measurement the significant wave height of 0.9 m did not vary considerably, so that no change in the influence of the longer water waves on the reflectivity should be expected. The water temperature was higher than the atmospheric temperature ( $\Delta T < -3.5^\circ\text{C}$ ) resulting in an unstable air-sea boundary layer with higher wind speeds near the water surface. The variation of the reflectivity in Fig. 1 indicates an appreciable dependence on short time changes of the wind speed and a modulating influence of the larger gravity waves on the wind induced backscatter mechanism. But as soon as the average wind speed decreases, the reflectivity drops off in the same way.

In the following analysis the 94 GHz reflectivity  $\sigma^0$ , measured at an incident angle of 45° was correlated to wind speed  $U_{46m}$ . This data set was fitted to the empirical power law relation

$$\sigma^0(\lambda, \theta, \phi, p) = a(\lambda, \theta, \phi, p) \cdot U^{\gamma}(\lambda, \theta, \phi, p) \quad (2)$$

where  $a$  denotes the wind speed coefficient and the  $\gamma$  wind speed exponent. Both parameters depend on the wavelength  $\lambda$ , the polarization  $p$ ,  $\theta$  the incident angle of the electromagnetic wave and  $\phi$  its azimuth orientation relative to the wind direction.

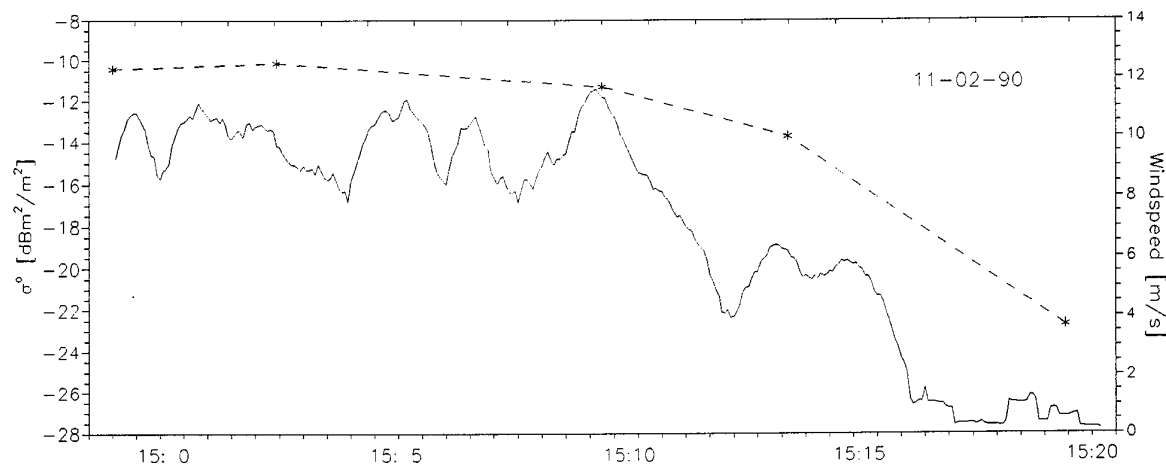


Fig.1: Measured reflectivity  $\sigma^0$  at 94 GHz, VV polarization, date 11-02-90, incident angle  $45^\circ$ , wind direction  $300^\circ$ - $330^\circ$  N (upwind)

For the first experiment in 1990 Fig. 2 shows a log-log representation of the measured reflectivity versus the windspeed  $U_{46m}$  for upwind directions within a sector of  $\pm 15^\circ$ . The condition of the boundary layer was always unstable ( $\Delta T < -2^\circ\text{C}$ ) during this measurement period. The solid line is the result of a regression analysis according to (2) yielding a wind speed exponent of 2.29. This value is in good agreement with data of previous 94 GHz scatterometer measurements (NARSHA 1987) at the same place represented here by the dashed line and the circles. Apart from a relative offset of both regression lines of 1 dB which may be attributed to differences in the calibration procedures, the limited data set show relatively large scatter. The reason was

that during both measurement campaigns only 10 min average values of the wind speed were available from the tower recordings with the additional problem of synchronizing them in time with the averaged backscatter data.

To overcome this problem for the following two experiments in 1991 and 1992 the wind speed and wind direction data were recorded simultaneously with the 94 GHz backscatter signal on the same data file giving at least a sufficient data set of 1 min averaged values for the correlation. Furthermore, modifications in the signal processing hardware unit improved the amplitude resolution of the system by 10 dB increasing the sensitivity for low reflectivity values especially during

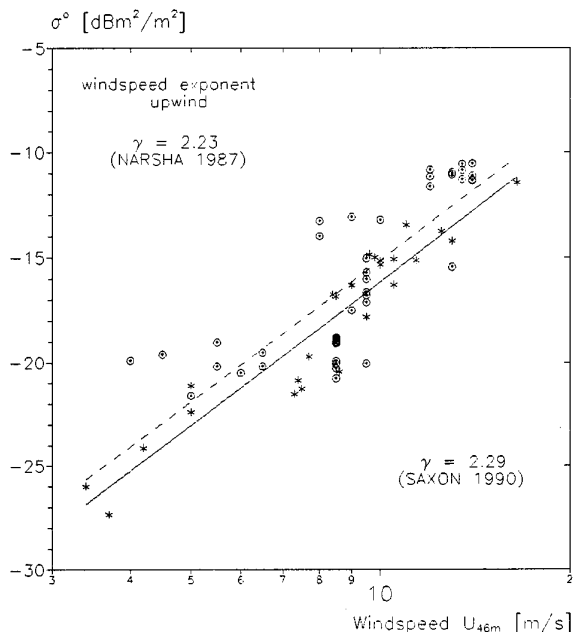


Fig.2: Reflectivity  $\sigma^0$  at 94 GHz versus windspeed for the wind direction interval  $300^\circ$ - $340^\circ$  (upwind) measured during the NARSHA experiment 1987 (dashed line) and SAXON-FPN 1990 (solid line).

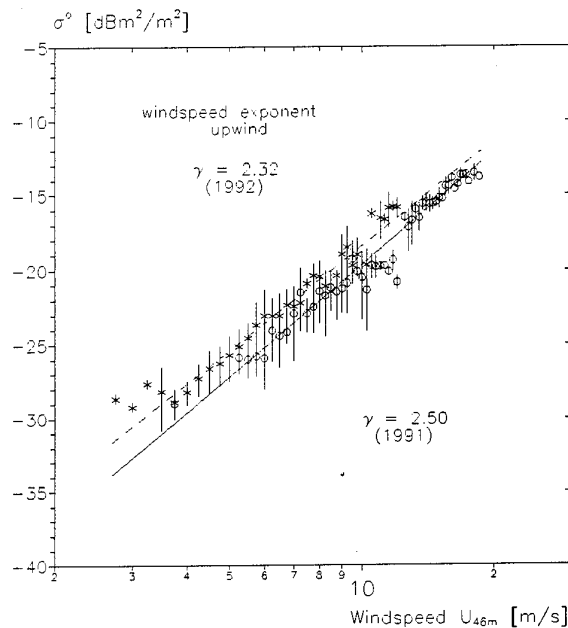


Fig.3: Reflectivity  $\sigma^0$  at 94 GHz versus windspeed for the wind direction interval  $300^\circ$ - $340^\circ$  (upwind) measured during the SAXON-FPN experiment 1991 (dashed line) and 1992 (solid line).

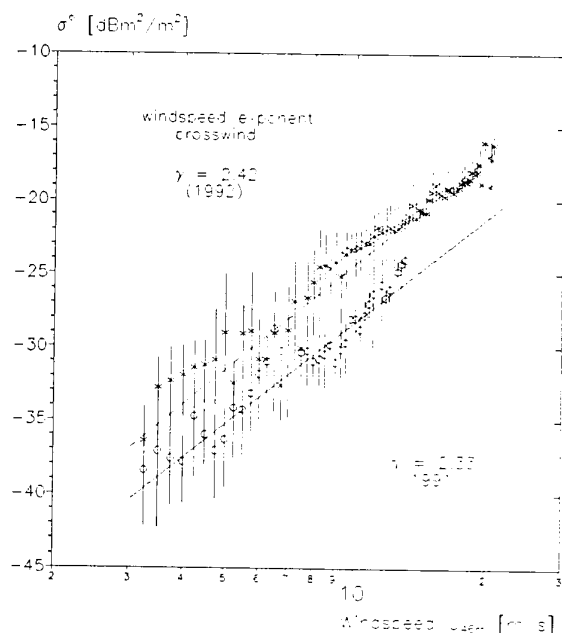


Fig.4: Reflectivity  $\sigma^0$  at 94 GHz versus windspeed for the wind direction intervals  $225^\circ$ - $240^\circ$  and  $30^\circ$ - $60^\circ$  (crosswind) measured during the SAXON-FPN experiment 1991 (dashed line) and 1992 (solid line).

low sea state and wind situations.

Fig.3 and 4 show the resulting  $\log \sigma^0 \propto \gamma \log U$  relation for upwind and crosswind conditions. The dashed regression line represents the 1992 experiment, the solid line the 1991 experiment. The corresponding data points are averages of reflectivity values grouped in wind speed intervals of 0.25 m/s. Vertical error bars are included indicating the variance of the measured reflectivity. The data points exhibit an expected average

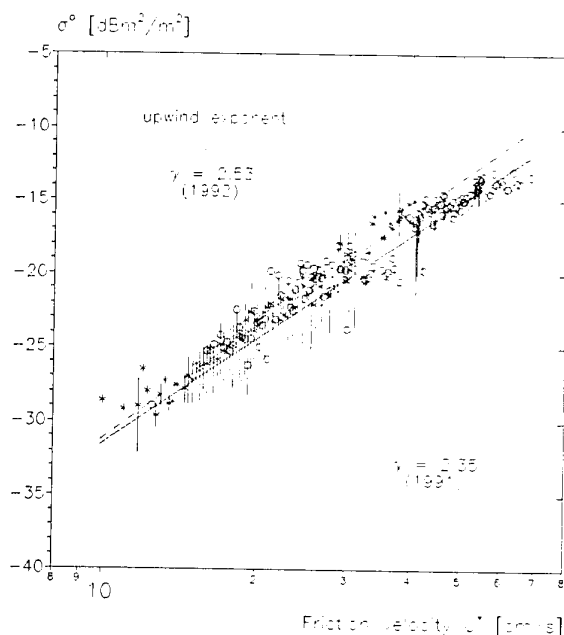


Fig.5: Reflectivity  $\sigma^0$  at 94 GHz versus calculated friction velocity  $U^*$  for upwind, other data same as Fig.3

upwind/crosswind ratio of  $\sim 4$  dB which is in good agreement with similar results at longer wavelength for that incident angle. However, both figures show a similar relative offset of the data sets as in the previous experiments (1987/90). But these differences cannot only be explained by an incorrect calibration because the trend for the upwind and crosswind case is different,  $\sim 2$  dB and  $\sim 4$  dB, respectively. One possible reason is that during the viewed time periods the ocean wave conditions varied with different wave spectra, directions and slopes. Another reason might be that changes in the stability of the air-sea interface and consequently in the vertical wind profile affect the backscatter process. Therefore it is more suitable to use the height independent friction velocity  $U^*$  of the wind field for the correlation with the backscatter data.

Assuming a wind speed profile of the form

$$U(z) = \frac{U^*}{k} \left[ \ln\left(\frac{z}{z_0}\right) - \Psi\left(\frac{z}{L}\right) \right] \quad (3)$$

according to the similarity theory of Monin-Obukhov [2] for the turbulence in boundary layer, where  $k$  ( $=0.4$ ) denotes the von Karman constant,  $z$  the height,  $z_0$  the roughness length and  $\Psi(z/L)$  the stability function with  $L$  as the Obukhov-length.  $U^*$  may be calculated from the measured wind speed at 46 m height. The other input parameter is the air-sea temperature difference  $\Delta T$  which determines the stability function  $\Psi(z/L)$  given here by an expression by Large and Pond [3].

In Fig. 5 and 6 the corresponding  $\log \sigma^0 \propto \gamma \log U$  relations are plotted for upwind and crosswind showing no major changes in the observed differences except an increased scatter of the calculated values and different slopes of the regression curves. During the time periods

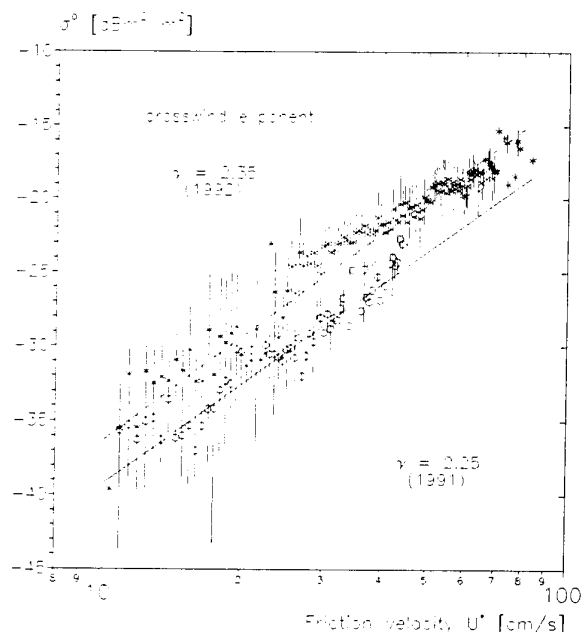


Fig.6: Reflectivity  $\sigma^0$  at 94 GHz versus calculated friction velocity  $U^*$  for crosswind, other data same as Fig.4

considered here only moderately unstable to neutral conditions of the boundary layer were encountered. At friction velocities  $> 50$  cm/s (upwind 1991, crosswind 1992) the 94 GHz reflectivity tends to become more insensitive to increasing  $U^*$ . Similar results were obtained at longer wavelength in previous experiments. As a result from Fig. 3-6 the regression analysis yielded wind speed exponents  $\gamma$  between 2.32 and 2.50 for  $U_{46m}$  and between 2.25 and 2.53 for  $U^*$ . No dependence of  $\gamma$  on azimuth orientation is discernable. The spread of  $\gamma$  lies within a deviation of 11% which may be attributed to changes in the environmental conditions especially to different sea states, directional wave spectra and slopes.

In comparison with investigations at lower frequency bands the wind speed exponents  $\gamma$  exhibit a considerable dependency on wind speed. Assuming Bragg-scattering at W-band frequencies and following [4] these exponents are plotted together with values of other investigations [4-11] in Fig. 7 as a function of the Bragg wavenumber

$$k_B = (4\pi/c) v \sin \theta \quad (4)$$

where  $v$  is the radar frequency and  $c$  the speed of light. Even at higher wavenumbers corresponding to a wavelength of 2-3 mm the wind speed exponent increases. This result should confirm the expected sensitivity of the reflectivity to changes in the spectral density of the capillary waves, especially in the fall-off region. But the comparable large reflectivity values indicate that either an enhanced generation of higher amplitudes of short waves in the millimeter range or, more likely, other processes exist like specular scattering from facets or wedge shaped crests [12] or wave breaking reinforcing the backscatter cross section.

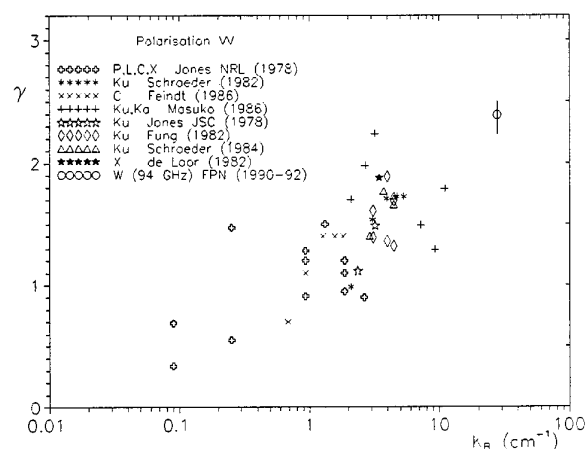


Fig.7: Wind speed exponents  $\gamma$  for VV polarization at 94 GHz (circle) and other frequencies, ranging from P- to Ka-band [4-11], as a function of Bragg wave number  $k_B$ .

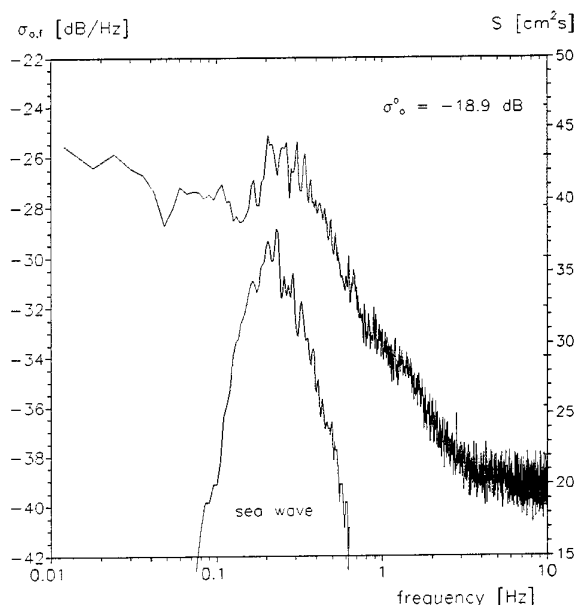


Fig.8: Spectrum of  $\sigma^0(t)$  and power spectrum of the sea waves measured on Nov. 29, 1990, 2h10-3h10, incident angle  $45^\circ$ , VV polarization, upwind, wind speed 5.5 m/s.

To evaluate the spectral characteristics of the measured reflectivity amplitudes selected time periods of the 1990 experiment were analysed. For comparison some wave spectra of a pitch and roll wave buoy were available. This buoy was located about 400 m southeast of the platform and delivered averaged wave spectra of 1 hour measurement periods. Fig.8 gives a typical example of a calculated spectrum of  $\sigma^0(t)$  together with the power spectrum of the sea. The modulation of the backscattered signal by the long ocean waves is obvious. The maximum of the wave spectrum agrees well with one spectral peak of the reflectivity, but there are several comparable spectral components of  $\sigma^0$  at higher frequencies which have only counterparts of minor power in the wave spectrum. This indicates that the backscattering process is also coupled to other dominant sources than the wave spectrum alone. In this consideration the aspect angle of the radar relative to the sea swell and the spot size illuminated by the radar have to be taken into account.

Due to the fact that the radar system used throughout these experiments had no coherence properties to extract Doppler information a calculation of the modulation transfer function (MTF) could not be established. The MTF was introduced to describe the modulation of the backscattered signal by the long ocean waves due to the tilting effect and the hydrodynamic-aerodynamic modulation of the small-scale waves. Instead, an evaluation procedure was applied outlined by de Loor et al. in [13]. Assuming sinusoidal sea waves  $\sigma^0(t)$  may be expanded to

$$\sigma^0(t) = \sigma^0 \left\{ 1 - \sum_{n=1}^N A(v_n) \sin(2\pi v_n t + \phi_n) \right\} \quad (5)$$

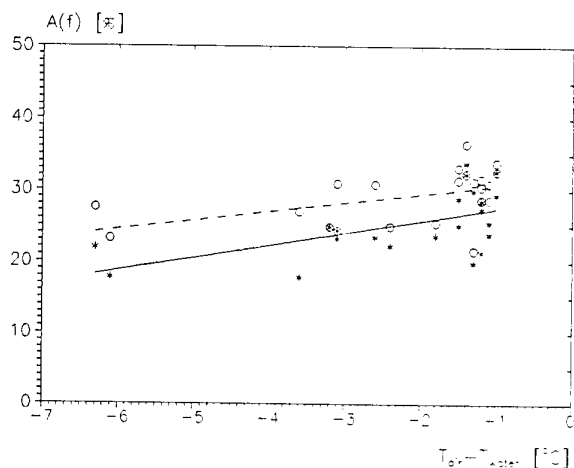


Fig.9: Modulation index  $A(v_0)$  (solid line) and  $A(v_m)$  (dashed line) as a function of the sea-air temperature difference for upwind situations, measurement time periods 1h.

where  $\sigma_0^0$  is the long time average reflectivity and  $A(v_n) = \sigma_0(v_n)/\sigma_0^0$  the modulation index at the spectral component  $v_n$ . From this modulation index the dependancy of the reflectivity on wave parameters and influences due to variations of the air-sea interface may be inferred. For some selected time periods where wave spectra were available from the wave buoy some values of  $A(v_0)$  were calculated at the frequency  $v_0$  of the dominant ocean wave. It was found that the wind speed  $U_{46m}$  and its azimuth orientation relative to the radar look direction have no influence on  $A(v_0)$ . Only a weak dependency on the air/sea temperature difference which is responsible for the stability of the boundary layer

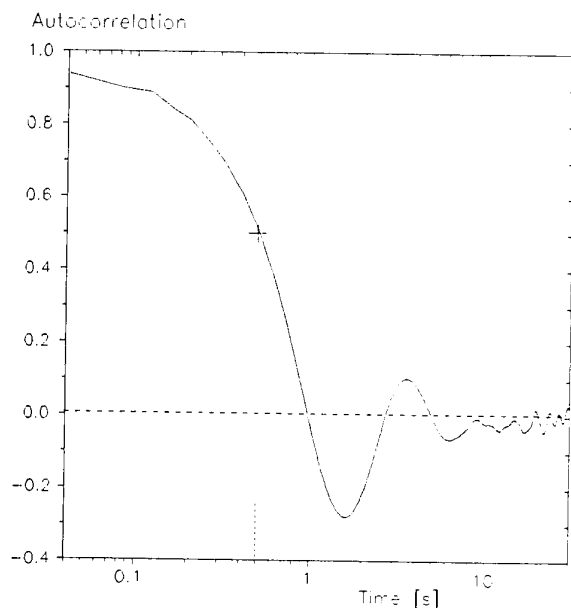


Fig.10: Autocorrelation function of  $\sigma^0(t)$  (same time period as Fig.8)

was discernible (Fig.9). In this plot a second data set of  $A(v_m)$  and the corresponding dashed regression line are inserted for comparison. These modulation index values are related to the maximum spectral component of the is reflectivity at frequency  $v_m$  which differs from the dominant ocean wave frequency  $v_0$ . They show the same weak dependency.

Finally the autocorrelation function was calculated. Fig.10 gives an example which corresponds to the spectrum of  $\sigma^0(t)$  in Fig.8 and is generally typical for all other investigated time periods. Comparing the resulting curve with results obtained by de Loor et al. [13] at X-band only two regions can be distinguished separated here by a decorrelation time at half of the total correlation level. For time shifts greater than this point ( $\sim 0.5s$ ) the relatively low correlation is mainly determined by the wave period of the long ocean waves and varies with the sea state. For shorter time shifts the curve exhibits in this region a comparably strong correlation. This is in contrast to the above mentioned observation at X-band where this latter region is split up into two components, one at very short time lags with a higher degree of correlation and an intermediate plateau-like one with about 50 % decorrelation. Adopting the assumption [13] that the first component can be attributed to resonance effects at capillary waves (Bragg scattering) and the second intermediate one to facets on the wave slope it can be concluded that at W-band (94 GHz) specular reflections from facets form the dominant part in the backscattering process [12].

### Conclusions

The results of this investigation showed that the backscattering from the ocean surface at millimeter-wavelength (94 GHz) is considerably dependent on the windfield. Applying the empirical relation  $\sigma^0 \sim \gamma \log U$  to the data set a windspeed exponent of  $\gamma = 2.39 \pm 0.11$  was determined for vertical polarisation. It is nearly independent of the azimuth orientation of the radar beam relative to the wind direction. The measured reflectivity shows an expected upwind/crosswind ratio of  $\sim 4$  dB. But differences between the correlation curves exhibit additional dependencies on other environmental parameters affecting the ocean wave spectrum and the stability of the air-sea interface. The evaluation of amplitude spectra of  $\sigma^0(t)$  indicates that the backscattering process at millimeter wavelength is more determined by specular scattering from facets or wedge shaped crests than Bragg scattering from capillary waves. This should be subject to further investigations and measurements including the evaluation of the MTF for the 94 GHz backscatter.

### References

- [1] Donelan, M.A. and Pierson, W.J., Radar scattering and equilibrium ranges in wind-generated waves application to scatterometry, *J.Geophys.Res.*, Vol.92, May 1987, pp.4971-5029.

- [2] Monin, A.P., Obukhov, A.M., Basic laws of turbulent mixing in the air near ground, *Tr. Geofiz. Inst. Akad. Nauk. SSSR*, 24(151), 1954, pp.153-187.
- [3] Large, W., Pond, P., Open ocean momentum flux measurements in moderate to strong winds, *J. Phys. Oceanogr.*, 11, 1981, pp.324-3361.
- [4] Feindt, F., Wissmann, V., Alpers, W., Keller, W.C., Airborne measurements of the ocean radar cross section at 5.3 GHz as a function of wind speed, *Radio Science*, Vol.21, No.5, 1986, pp.845-856.
- [5] Jones, W.L., Schroeder, L.C., and Mitchell, J.L. Aircraft measurements of the microwave scattering signature of the ocean, *IEEE J. Oceanic Eng.*, OE-2(1), 1977, pp.52-61.
- [6] Schroeder, L.C., D.H. Boggs, G. Dome, W.L. Jones, I.M. Halberstam, W.J. Pierson, and F.J. Wentz, The relationship between wind vector and normalized radar cross section used to derive Seasat-A satellited scatterometer winds, *J. Geophys. Res.*, 87(C5), 1982, pp.3318-3336.
- [7] Masuko, H., K. Okamoto, M. Shimada, S. Niwa, Measurement of microwave backscattering signatures of the ocean surface using X-band and Ka-band airborne scatterometers, *J. Geophys. Res.*, Vol.91, No.C11, 1986, pp.13065-13083
- [8] Jones W.L. and L.C. Schroeder, Radar backscatter from the ocean: Dependence on Surface friction velocity, *Boundary layer Meteorol.*, 13(1-4), 1978, pp.133-149.
- [9] Fung, A.K., and K.K. Lee, A semi-empirical sea-spectrum model for scattering coefficient estimation, *IEEE J. Oceanic Eng.*, OE-7(4), pp.166-176, 1982.
- [10] Schroeder L.C., W.L. Jones, P.R. Schaffner and J.L. Mitchell, Flight measurement and analysis of AAFE RADSCAT wind speed signature of the ocean, *Nasa Tech. Memo.*, TM-85646, 1984.
- [11] de Loor, G.P., Tower mounted radar backscatter measurements in the north sea, *J. Geophys. Res.*, 88, 1983, pp.9785-9791.
- [12] Kwok, D.S.W., and B.M. Lake, A deterministic, coherent, and dual-polarized laboratory study of microwave backscattering from water waves, 1, short gravity waves without wind, *IEEE J. Oceanic Res.*, OE-9, 1984, pp.291-308.
- [13] De Loor, G.P. Hoozeboom, P., Radar backscatter measurements from platform Nordwijk in the north sea, *IEEE J. Oceanic Eng.*, OE-7(1), 1982, pp.15-20

## DISCUSSION

**Discussor's name :** F. Christophe

**Comment/Question :**

Does the radar equipment you used allow for cross-polarized backscattering measurement, and do you think it could be useful for analysing the scattering mechanisms?

**Author/Presenter's reply :**

Our radar system has the capability for cross-polarized backscattering - and it is indeed very useful to analyse cross-polarized features in the backscattering process. Unfortunately, we had some technical problems with the VH-channel, so an evaluation could not be made.



# Calibration du Sondeur à Rétrodiffusion de l'île Losquet en Présence de Multi-Trajets

F. Gauthier, J.Y. Le Saout, R. Fleury

France Telecom / Centre National d'Etudes des Télécommunications

LAB/PTI/GER

B.P. 40, 22301 Lannion Cedex, France

## RESUME

La localisation précise des zones de l'ionosphère sondées par les radars HF transhorizon, dépend des paramètres caractéristiques de la propagation au moment du sondage, et nécessite souvent l'utilisation de techniques de calibration. Pour calibrer les données du sondeur à rétrodiffusion de l'île Losquet, le Centre National d'Etudes des Télécommunications (CNET) a mis en oeuvre un répondeur radar HF monofréquence mobile. On présente dans cette communication des résultats de sondages obtenus en mode de "balayage de site" alors que ce répondeur était opérationnel et implanté à environ 1000 km de l'île Losquet; ces données sont utilisées pour calculer la position du répondeur. On montre que les multi-trajets sont essentiellement à l'origine d'une erreur statistique de localisation en distance radiale et que l'emploi de méthodes simples de traitement permet la réduction de cette erreur.

## 1. INTRODUCTION

Les radars HF transhorizon qui utilisent l'ionosphère comme réflecteur permettent la télé-détection du profil de densité électronique à des distances comprises entre environ 250 km et 2000 km du site du sondeur. La localisation précise des zones sondées nécessite la mise en oeuvre de systèmes annexes de sondage du milieu de propagation afin de permettre la calibration des résultats de sondage du radar principal [1]. Parmi les systèmes couramment utilisés on peut citer les sondeurs verticaux ou obliques ainsi que les répondeurs radar.

Pour calibrer les données du sondeur à rétrodiffusion de l'île Losquet, le Centre National d'Etudes des Télécommunication (CNET) a mis en oeuvre un répondeur radar HF monofréquence [2]. On présente dans cet article des résultats de sondages obtenus au cours d'une campagne de mesures en mode de "balayage de site" alors que le répondeur était opérationnel à environ 1000 km du site de sondage.

L'effet des multi-trajets E-F sur la calibration du sondeur est évalué en comparant les résultats de quatre méthodes simples de localisation d'un répondeur HF faisant intervenir la directivité et l'agilité en site du radar. Ces méthodes, basées sur l'utilisation du théorème de Breit et Tuve, diffèrent dans la manière de sélectionner les données de sondage utilisées pour le calcul de la position du répondeur. La première méthode utilise la totalité des mesures. La seconde méthode utilise des résultats de sondages verticaux pour sélectionner les données. La troisième méthode consiste à ne prendre en compte que les signaux propagés via la couche F2. Pour la quatrième méthode on procède à un filtrage des angles mesurés avant d'appliquer la troisième méthode.

## 2. DESCRIPTION EXPERIMENTALE

### 2.1 Description des installations

Le sondeur à rétrodiffusion du CNET est implanté en Bretagne (France), sur l'île Losquet (48.8° N ; 3.6° W). Deux réseaux circulaires et concentriques sont utilisés pour l'émission (32 antennes biconiques) et la réception (64 antennes actives) [3]. La conformation du diagramme de directivité, schématisés figure 1, est effectuée indépendamment pour chacun des deux réseaux, à l'aide de déphaseurs digitaux. Ce système dédié à l'étude de la propagation des ondes décimétriques dans l'ionosphère utilise les fréquences radioélectriques comprises entre 6 et 30 MHz. La géométrie circulaire des réseaux permet le pointage du lobe principal en azimut, sur 360°, ainsi qu'en site entre 0° et 90°.

L'utilisation de ce sondeur en conjonction avec un répondeur radar HF (ou balise) est une des méthodes qui permet la calibration des mesures d'angle et de distances effectuées par le radar [2]. Le principe de fonctionnement de cette balise monofréquence, schématisé figure 2, est le suivant: les impulsions transmises par le sondeur, à la fréquence  $F_1 = 10.8$  MHz, sont réfractées par l'ionosphère et captées par le répondeur implanté au sol à grande distance du site radar. Les signaux reçus par la balise sont filtrés, transposés à la fréquence  $F_2 = 10.4$  MHz, après quoi ils sont amplifiés et réémis. Après une seconde réfraction dans l'ionosphère les signaux réémis sont détectés par le sondeur qui effectue la mesure de l'amplitude et du temps de propagation des impulsions transmises. En fixant la géométrie de sondage, la technique utilisée permet la suppression de l'écho de rétrodiffusion naturel se produisant à la fréquence  $F_1$ . La balise se comportant comme un point brillant pour le sondeur, le système permet l'étude du milieu de propagation.

### 2.2 Description des mesures

Les données analysées ci-dessous ont été obtenues au cours d'une campagne de mesures qui s'est déroulée sur 9 jours entre le 30/03/92 et le 18/04/92 alors que le répondeur était implanté à 1014 km de l'île Losquet dans l'azimut 119° du sondeur (l'azimut 0° est le Nord géographique et les angles sont comptés positivement vers l'Est). La figure 3 est un exemple de résultat moyenné de sondage, effectués dans l'azimut de visée correspondant aux coordonnées géographiques du lieu d'implantation du répondeur, alors que le sondeur fonctionnait en mode de balayage de site, entre 0° et 60°, par pas de 3°. Pour chaque angle de pointage du lobe principal du diagramme de directivité, l'amplitude des signaux reçus a été mesurée en fonction du temps de propagation des impulsions transmises entre le sondeur et le répondeur. La résolution en temps de groupe était de 0.3 ms et le temps d'acquisition était d'environ 1.3 s pour chaque angle de pointage utilisé. Pour accroître le

rapport signal sur bruit 9 balayages successifs ont été moyennés et enregistrés. Après quoi, ces fichiers ont été moyennés deux à deux pour minimiser l'influence des perturbations ionosphériques de courtes périodes. Les données de sondages exploitées sont alors représentatives des conditions moyennes de propagation sur des durées d'environ 8 mn.

La figure 3 est un résultat de sondage obtenu à l'aide de la technique décrite précédemment. On constate sur cette figure la présence d'un maximum d'énergie unique, bien localisé en temps de groupe alors que le signal présente un étalement en site. La dispersion angulaire est en partie due à la largeur du lobe du diagramme de directivité (produit émission-réception) qui dépend de la fréquence radar et de l'angle de visée. Dans notre cas, l'ouverture à 3 dB est d'environ 17° à la fréquence de 10 MHz et pour une élévation de visée de 30°.

Il est important de remarquer que le résultat de sondage présenté figure 3 est représentatif des mesures réalisées de nuit pour lesquelles seule la couche F2 intervient dans la propagation. Les sondages réalisés le jour présentent généralement plusieurs maxima provenant de la présence des couches basses de l'ionosphère F1, E et Es. La figure 4 illustre ce phénomène.

La méthode de sondage présentée ci-dessus permet l'identification des modes dominants, propagés en un bond, pour lesquels l'énergie reçue est a priori plus importante que celle obtenue lors de propagations en plusieurs bonds.

### 3. EFFET DES MULTI-TRAJETS

La première étape intervenant dans le traitement des données a consisté à relever les coordonnées (élévation - temps de groupe) associé à la position du ou des maxima d'énergie présents dans les résultats de sondage moyennés. Les variations de la valeur des angles d'élévation obtenus sont présentés figure 5 en fonction de l'heure TU pour les différents jours de la campagne: on constate que la faible cohérence temporelle des mesures ne permet pas la mise en évidence d'angles d'arrivées privilégiés.

La dispersion angulaire importante observée sur la figure 5 peut être due à des conditions de propagation perturbées ou à la méthode de mesure utilisée. L'examen des ionogrammes verticaux de Lannion et Poitiers ainsi que celui des valeurs prises par l'indice magnétique planétaire Kp au cours de la campagne montrent que, seule la journée du 06/04/92 était perturbée par un début d'orage magnétique. Par contre, il a été montré [4] que la présence simultanée, sur le réseau de réception, de signaux propagés par des trajets différents peut perturber la mesure des angles lorsque l'amplitude de ces modes est comparable et que l'écart angulaire entre les directions d'arrivées est inférieur à la largeur du lobe principal du diagramme de réception.

### 4. TRAITEMENT DES MESURES ANGULAIRES

#### 4.1 Méthode générale

L'influence des multi-trajets sur les résultats de mesures a été évaluée en calculant la position du répondeur, à partir des coordonnées - élévation ( $El_m$ ), temps de groupe ( $Tg_m$ ) -, en supposant que les couples de mesures ( $El_m, Tg_m$ ) correspondent à des modes "purs" et en utilisant le théorème de Breit et Tuve [5]. La distance au sol (D) du répondeur est alors donnée par la relation:

$$(1) \quad D = 2.R0.[\arctg(A)-El]$$

avec

$$A = [(Tg/2 + \sin(El).R0)/(\cos(El).R0)] - El$$

où D est la distance au sol en km, Tg est le temps de groupe exprimé en km, El est l'angle de visée en radians,  $R0=6370$  km est le rayon terrestre.

Il est à noter que l'utilisation de cette méthode de calcul, qui néglige le champ magnétique terrestre et suppose une stratification horizontale de l'ionosphère, peut être à l'origine d'un biais.

Cette représentation simple de la géométrie de la liaison permet, par ailleurs, le calcul de l'altitude virtuelle de réflexion ( $h'$ ) des signaux transmis en utilisant les mêmes informations ( $El_m, Tg_m$ ) et le théorème de Martyn [5]:

$$(2) \quad Tg = 2.h'.\sec(I)$$

où  $I = \pi/2 - El$  est l'angle d'incidence des rayons à la base de l'ionosphère.

On décrit dans les paragraphes suivants les résultats du calcul de la distance au sol obtenus à l'aide de la relation (1). Quatre méthodes simples sont comparées: elles diffèrent dans la manière de sélectionner les données utilisées pour le calcul de la position.

#### 4.2 Méthode 1

##### 4.2.1 Informations obtenues sur la position

La première méthode suppose qu'aucune des mesures n'est affectée par la présence de multi-trajets. L'ensemble des mesures présentées figure 5 a été utilisé pour calculer les distributions journalières des distances avec une résolution spatiale de 45 km qui correspond à la largeur des impulsions transmises. Les distributions obtenues sont présentées figure 6 et la position réelle du répondeur (1014 km) est repérée par une flèche. La barre d'erreur de  $\pm 75$  km représente les incertitudes de mesures associées aux paramètres de sondage utilisés (pas de 3° en angle de site et résolution temporelle de 0.3 ms).

Cette figure montre que: i) les distances calculées sont comprises entre 910 km et 1225 km ce qui correspond à une erreur maximale de 21% sur la distance ii) l'erreur maximale commise n'est pas accrue, le 06/04/92, en période de forte activité magnétique. iii) l'allure générale des distributions indique la présence d'un biais.

La valeur du biais observé sur la figure 6 a été évaluée en calculant la moyenne des distributions journalières ainsi que la moyenne de la distribution des distances obtenues sur l'ensemble de la campagne. Les valeurs des moyennes calculées sont reportées dans la première colonne du tableau -1- et montrent que la méthode utilisée est affectée d'un biais positif d'environ 50 km par rapport à la valeur réelle. L'écart type des distances calculées est de 58 km.

##### 4.2.2 Informations obtenues sur l'altitude virtuelle

Les altitudes virtuelles de réflexion ont été calculées à l'aide de la relation (2) pour l'ensemble des couples de mesures ( $El_m, Tg_m$ ) obtenus au cours de la campagne.

Pour évaluer l'effet de la dispersion angulaire des mesures sur le résultat de ces calculs, les altitudes virtuelles calculées à l'aide des données de sondage oblique ont été comparées à celles

relevées sur les ionogrammes de Poitiers à la fréquence verticale équivalente. Le résultat de ces comparaisons est présenté sur les figures 7 et 8, pour chaque jour de sondage ainsi que pour l'ensemble de la campagne. Afin de faciliter les comparaisons la bissectrice a également été représentée sur les figures. Ces figures mettent en évidence la présence d'un biais associé au calcul des altitudes inférieures à 200 km alors que, pour les altitudes supérieures à 200 km correspondant à des propagations par la couche F, il existe un bon accord entre les altitudes virtuelles de réflexion obtenues à l'aide du répondeur et celles relevées à Poitiers. Il est par ailleurs clair que les altitudes calculées à partir des données du sondeur ne permettent pas à elles seules la séparation entre les modes propagés par les couches E et F, alors qu'elle est très visible sur les résultats de l'ionosonde de Poitiers. La continuité des valeurs des altitudes calculées est en partie due à la dispersion angulaire des mesures qui s'explique par la présence simultanée, sur le réseau de réception de l'île Losquet, de multi-trajets au moment de la mesure. Il est à noter que des trajets aller et retour non identiques peuvent aussi être à l'origine de la continuité observée: l'hypothèse des modes "purs" n'est plus vérifiée dans ce cas.

#### 4.3 Méthode 2

La deuxième méthode consiste à sélectionner les mesures pour lesquelles l'altitude virtuelle de réflexion calculée est la même que celles mesurée, à la fréquence équivalente, sur les résultats de sondages verticaux de Poitiers. Pour tenir compte d'éventuels gradients horizontaux de densité électronique, entre la zone de réfraction des ondes transmises sous incidence oblique et la verticale du sondeur de Poitiers, une erreur de  $\pm 25$  km sur la détermination de l'altitude a été utilisée lors de la sélection des mesures. La précision avec laquelle sont effectués les sondages de Poitiers (5 km) est comprise dans cette erreur.

Les distributions de distances calculées à l'aide des mesures sélectionnées sont présentées figure 9. La comparaison de ces distributions avec celles obtenues sans filtrage des mesures (figure 6) montre que la sélection effectuée élimine une part importante des mesures correspondant aux distances situées en dehors de la barre d'erreur incluant la position du répondeur.

Les valeurs du biais et de l'écart type associés à ces distributions sont présentées dans la deuxième colonne du tableau -1- qui montre que l'utilisation de la méthode -2- réduit le biais à 25 km et l'écart type à 49 km.

Les distributions cumulatives des distances obtenues à l'aide des méthodes -1- et -2- sont présentées sur la figure 10. On constate que l'utilisation de la méthode -2- filtre environ 50% des mesures et qu'elle réduit la largeur de la distribution.

#### 4.4 Méthode 3

La méthode suppose que la présence simultanée de signaux propagés par les couches E et F est la principale cause de la dispersion angulaire observée dans nos mesures.

La technique de traitement utilisée ici consiste à sélectionner, pour le calcul de la distance, les modes propagés via la couche F2: seules les mesures pour lesquelles l'altitude virtuelle de réflexion, calculée à l'aide des données de sondages obliques, est supérieure à 200 km ont donc été retenues.

Les distributions journalières des distances calculées après filtrage sont présentées sur la figure 11. La comparaison de cette figure avec les résultats obtenus en utilisant l'ensemble des données (figure 6) montre que le filtrage supprime la quasi-

totalité des mesures pour lesquelles les distances calculées ne correspondent pas à la position du répondeur. Cet effet valide la méthode de sélection utilisée.

La distribution cumulative des distances obtenues à l'aide de la méthode -3- est présentée figure 12. Les valeurs du biais et de l'écart type associées à cette distribution, présentées dans la troisième colonne du tableau -1-, sont respectivement d'environ 10 km et de 45 km. Par ailleurs, la valeur de la distance moyenne (1031 km) se trouve dans la cellule de résolution (1000-1045 km) correspondant à la position du répondeur.

#### 4.5 Méthode 4

La technique utilisée ici prend en compte les résultats obtenus à l'aide de la méthode 3 montrant que 80% de la valeur du biais obtenue sans traitement (méthode 1) et environ 20% de l'écart type peuvent être attribués aux multi-trajets E-F au moment de la mesure. La méthode que nous proposons consiste à filtrer les angles avant d'appliquer la méthode 3. Le filtre que nous avons utilisé est un filtre glissant à trois points sélectionnant la valeur angulaire la plus importante ainsi que le temps de groupe associé. Ce filtrage sélectionne à priori les données, obtenues par des propagations via la couche F, peu affectées par les propagations E.

La comparaison des distributions obtenues à l'aide de la méthode 4 (figure 13) avec celles obtenues par la méthode 3 (figure 11) montre que le filtrage permet d'augmenter la valeur des distributions à l'intérieur de la barre d'erreur incluant la position du répondeur.

La distribution cumulative des distances obtenue à l'aide de cette méthode (figure 14) présente un biais résiduel faible, d'environ 3 km, et un écart type de 47 km qui est du même ordre de grandeur que celui obtenu à l'aide des méthodes 2 et 3.

### 5. DISCUSSION ET CONCLUSION

Dans cet article, l'effet des multi-trajets E-F sur la calibration du sondeur de l'île Losquet a été évalué en comparant quatre méthodes simples, de localisation d'un répondeur radar HF, qui diffèrent dans la manière de sélectionner les données de sondage obtenues.

Les résultats, du calcul des distances, obtenus à l'aide de ces méthodes sont présentés dans le tableau 1 et peuvent être résumés comme suit:

La méthode -1-, retenant l'ensemble des mesures, est affectée d'un biais de 50 km correspondant à une erreur d'environ 5% sur la position effective du répondeur (1014 km); cette méthode présente un écart type de 58 km.

La méthode -2-, utilisant des résultats de sondages verticaux, sélectionne 50% des données de sondage et réduit le biais à 25 km ainsi que l'écart type à 49 km.

La mise en oeuvre de la méthode -3- minimise l'influence des multi-trajets E-F et sélectionne aussi 50% des mesures. Elle conduit à un biais d'environ 10 km et un écart type de 45 km.

La méthode -4-, qui consiste à effectuer un filtrage d'angles avant d'appliquer la méthode -3-, permet d'obtenir le biais le plus faible (3 km) alors que l'écart type (47 km) est du même ordre de grandeur que celui obtenu par les méthodes -2- et -3-. Ce biais résiduel peut en partie être attribué aux approximations utilisées dans le calcul de la distance: champ magnétique et gradients horizontaux négligés.

Les résultats des traitements présentés dans cette communication montrent que, de manière générale, la présence simultanée de trajets E et F sur le réseau de réception perturbe la mesure des angles d'arrivée des signaux ce qui est en accord avec les résultats des travaux effectués en radiogoniométrie [4]. Les méthodes -3- et -4-, qui minimisent l'influence des mesures correspondantes à ces situations, montrent que ces trajets multiples sont essentiellement à l'origine du biais associé au calcul de la distance.

Ces deux dernières méthodes, utilisant uniquement les données du sondeur à rétrodiffusion de l'île Losquet et présentant un biais réduit, sont plus avantageuses à mettre en oeuvre en temps réel.

## 6. REFERENCES

1. Earl G.F. and Ward B.D., "The frequency management system of the Jindalee over-the-horizon backscatter HF radar", Radio Sci., vol.22, n°2, pp 275-291.
2. Ruelle N., Gauthier F., Le Saout J.Y., Bertel L. and Baltazart V., "A calibration technique for the CNET HF backscatter radar", AGARD Conf. Proc., n° 502, 32,1991.
3. Le Saout J.Y., and L. Bertel, "Les systèmes d'aériens utilisés par le radar HF à rétrodiffusion du CNET", JINA 88 Conf. Proc., pp 509-513, 1988.
4. Le Saout J.Y., Gauthier F., Ruelle N. and R. Fleury, "Utilisation du réseau de réception du sondeur à rétrodiffusion de l'île Losquet en radiogoniométrie", AGARD Conf. Proc., n° 528, 23, 1992.
5. Davies K., "Ionospheric Radio", IEE Electromagnetic wave series 31, Peter Peregrinus Ltd, 1990.

DATE	METHODE 1		METHODE 2		METHODE 3		METHODE 4	
	D (km)	N	D (km)	N	D (km)	N	D (km)	N
01/04/92	1066	27	1040	13	1002	11	1002	20
02/04/92	1074	20	1052	9	1013	5	1008	9
03/04/92	1085	36	1060	18	1036	13	1034	24
06/04/92	1077	28	1045	10	1054	10	1062	17
07/04/92	1074	58	1053	25	1031	26	1027	41
08/04/92	1110	25	1055	11	1050	13	1036	20
09/04/92	1071	12	1052	6	1042	7	1031	11
10/04/92	1060	25	1018	10	1018	10	1006	14
14/04/92	1048	48	1030	29	1029	36	1017	44
TOTAL	1071	279	1044	131	1031	131	1025	200
BIAIS	49		25		9		3	
SIGMA	58		49		45		47	

Tableau 1 : Moyennes des distributions journalières et moyenne de la distribution des distances obtenues sur l'ensemble de la campagne, pour les méthodes -1-, -2-, -3- et -4-. N représente le nombre d'échantillons.

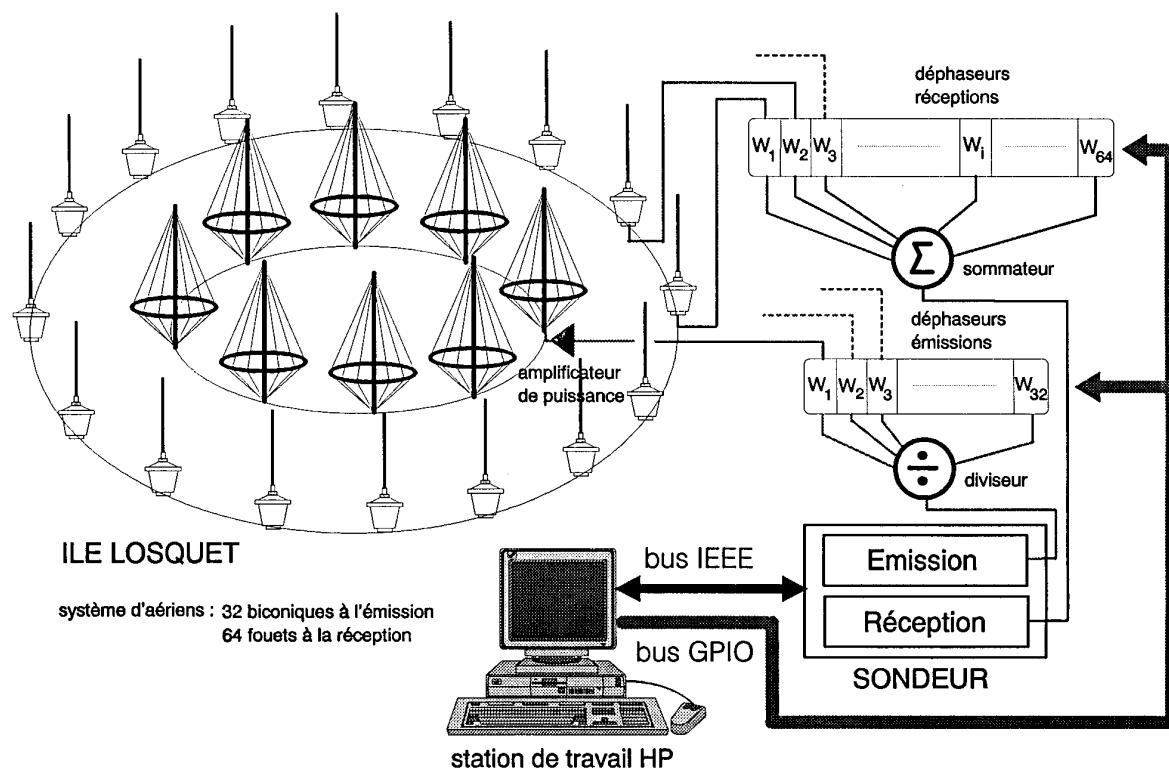


Figure 1: Synoptique du sondeur à rétrodiffusion du CNET

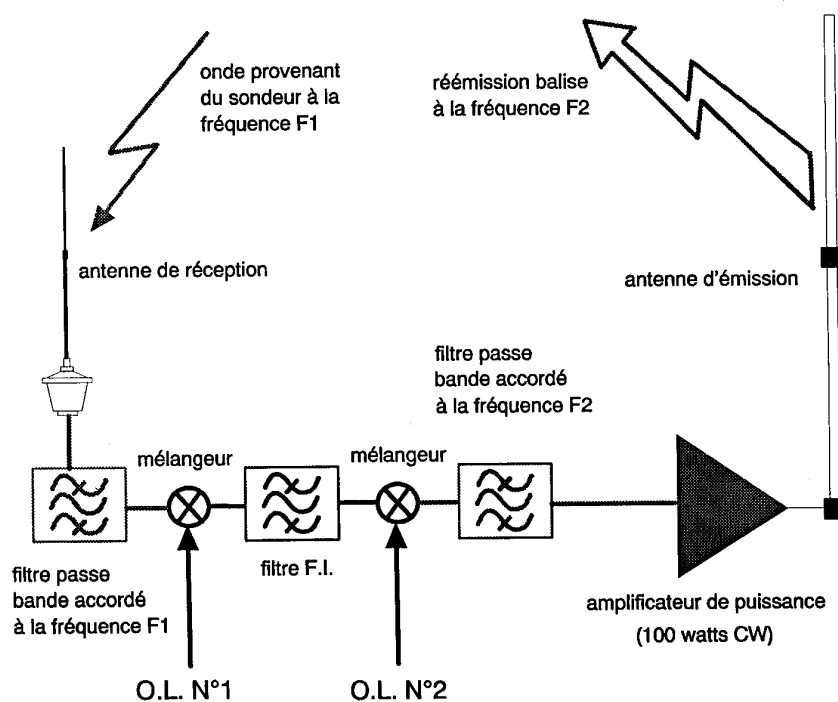


Figure 2: Synoptique du répondeur radar HF (balise monofréquence)

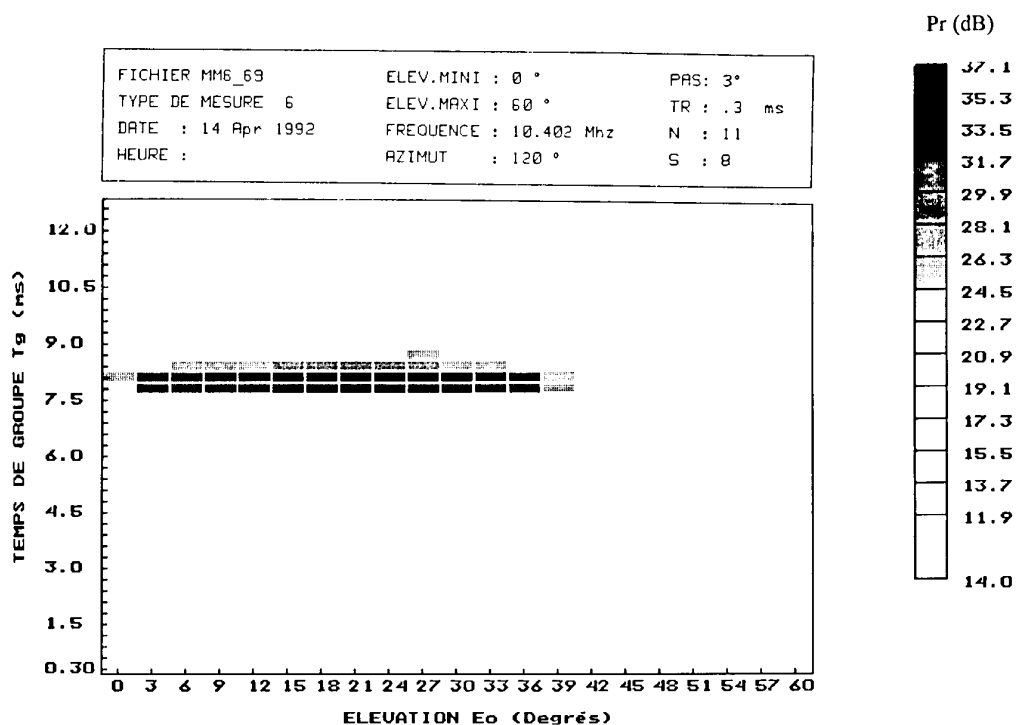


Figure 3: Résultat de sondage moyenné de nuit

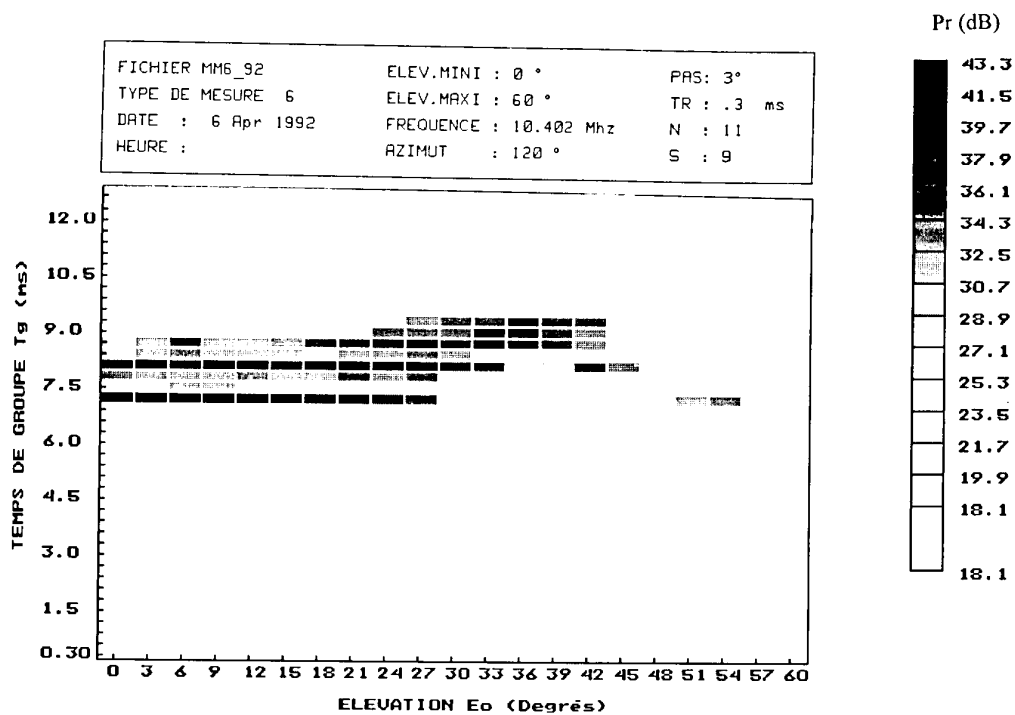


Figure 4: Résultat de sondage moyenné de jour

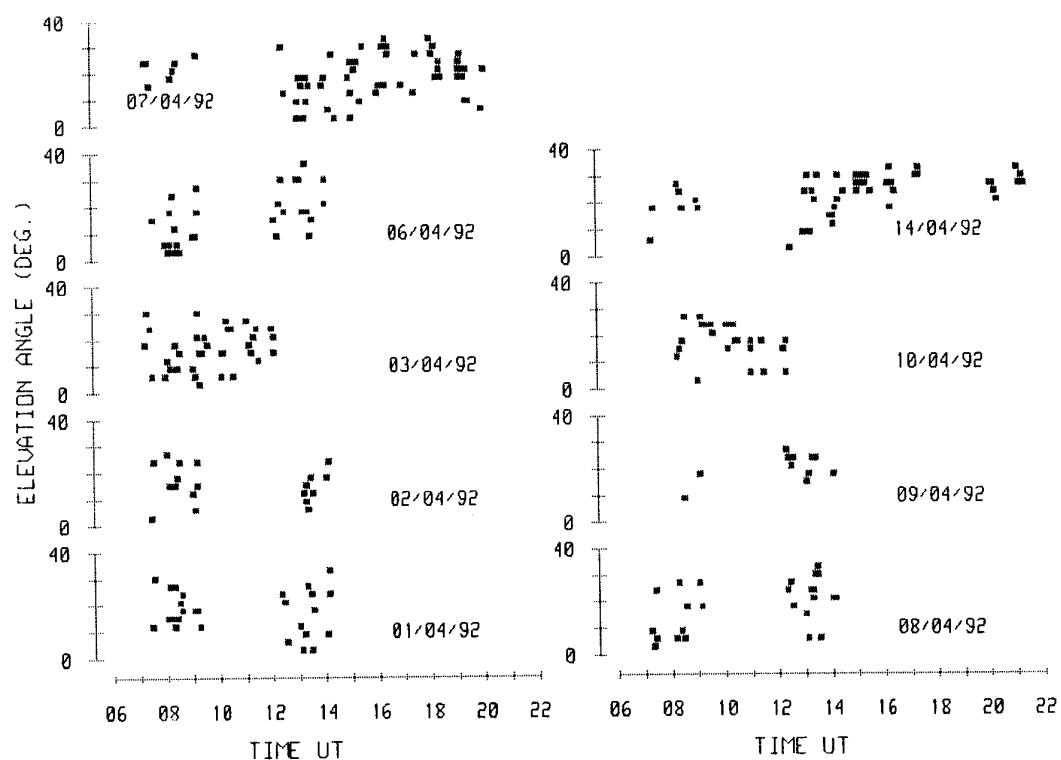


Figure 5: Angles mesurés correspondant aux maxima de puissance

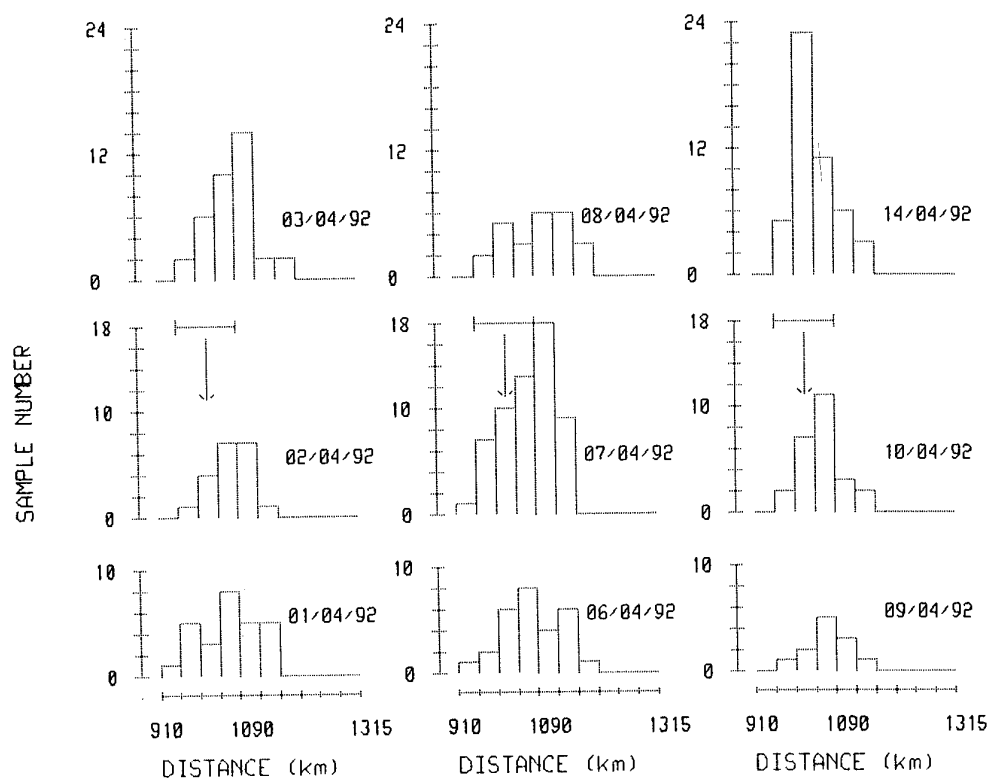


Figure 6: Distributions journalières des distances obtenues à l'aide de la méthode -1-. La position du répondeur est repérée par une flèche.

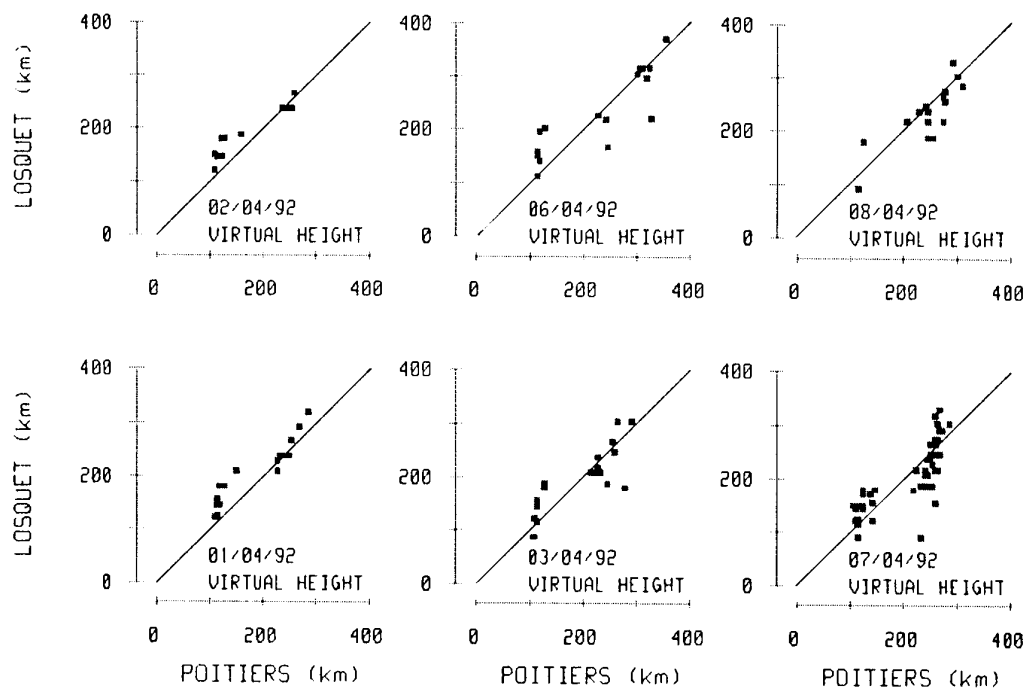


Figure 7: Comparaison journalières des altitudes virtuelles de réflexion calculées avec celles relevées sur les ionogrammes de Poitiers.

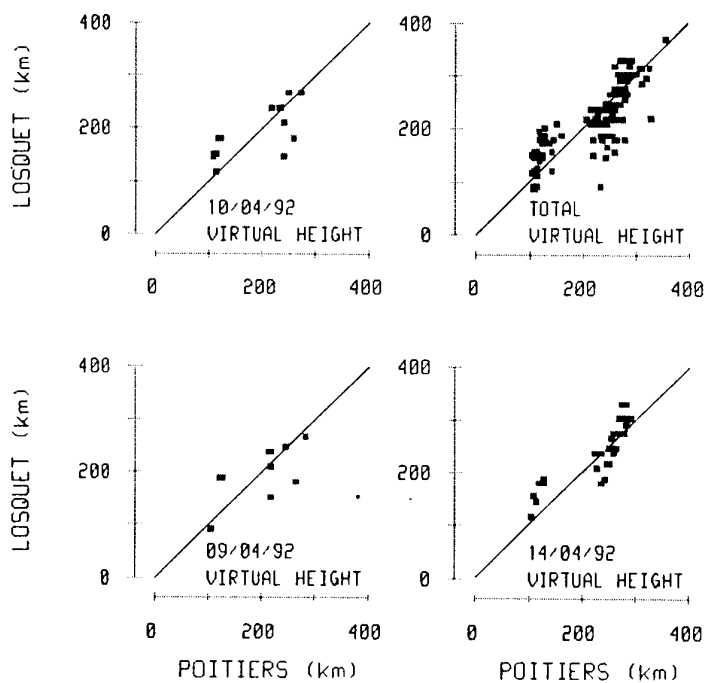


Figure 8: Comparaison journalières des altitudes virtuelles de réflexion calculées avec celles relevées sur les ionogrammes de Poitiers. "Total" correspond à l'ensemble des mesures.



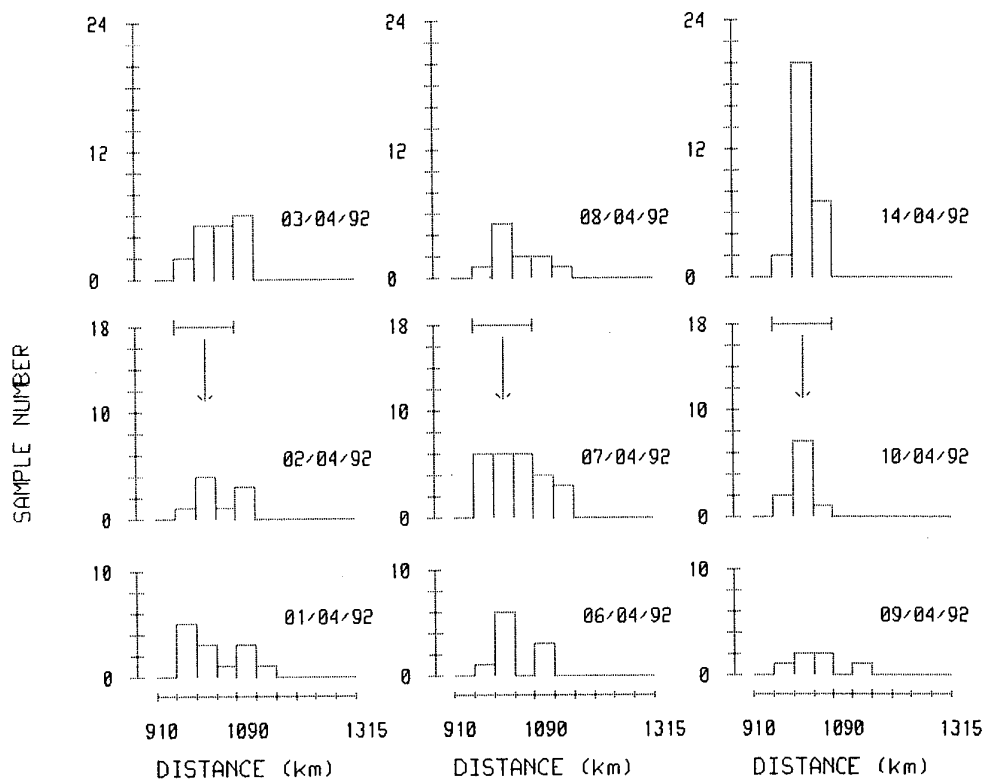


Figure 9: Distribution journalières des distances obtenues à l'aide de la méthode -2-.

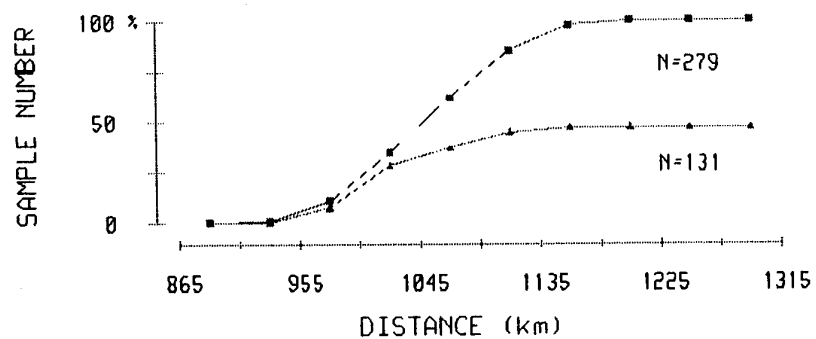


Figure 10: Distributions cumulatives des distances obtenues à l'aide des méthodes -1- (■) et -2- (▲). N correspond au nombre d'échantillons.

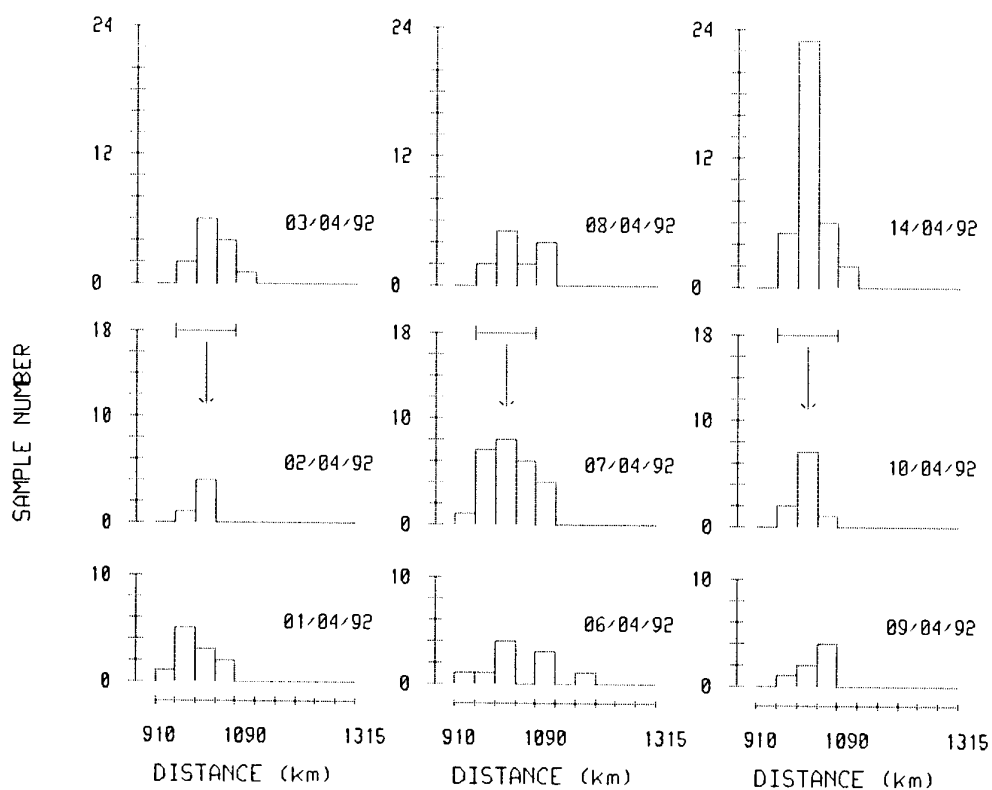


Figure 11: Distributions journalières des distances obtenues à l'aide de la méthode -3-.

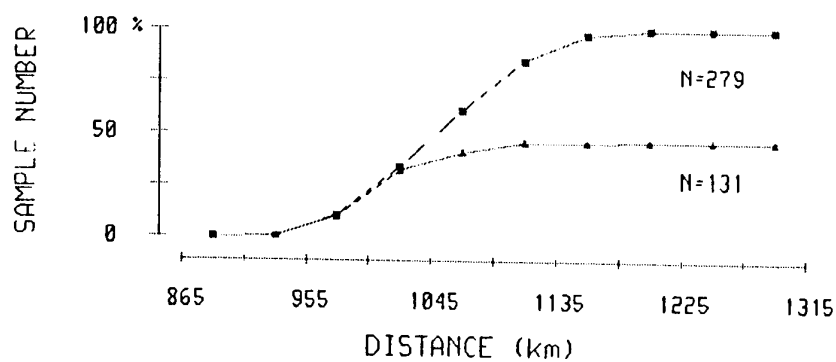


Figure 12: Distributions cumulatives des distances obtenues à l'aide des méthodes -1- (■) et -3- (▲). N correspond au nombre d'échantillons.

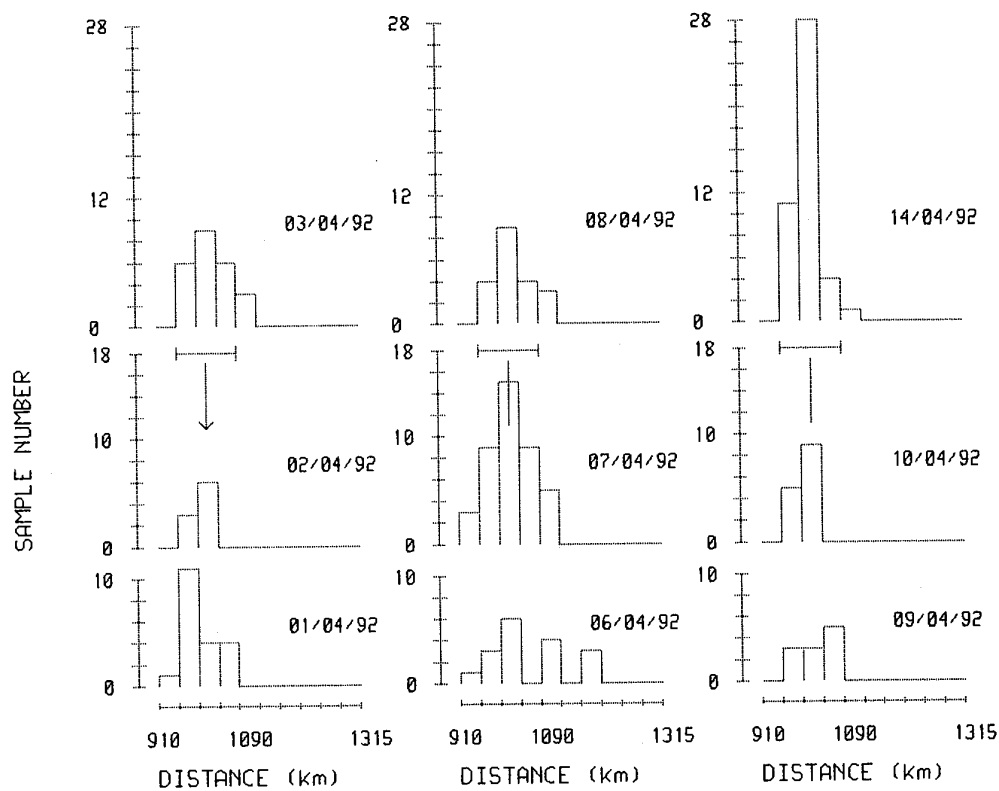


Figure 13: Distributions journalières des distances obtenues à l'aide de la méthode -4-.

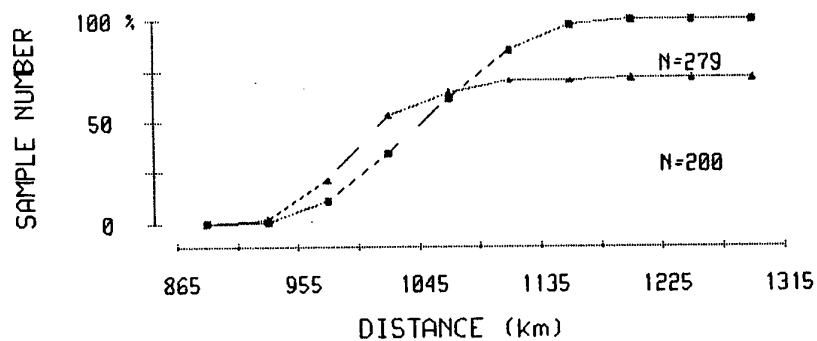


Figure 14: Distributions cumulatives des distances obtenues à l'aide des méthodes -1- (■) et -4- (▲). N correspond au nombre d'échantillons.

## DISCUSSION

**3. Discussor's name :** C. Goutelard

**Comment/Question :**

Avez-vous une interprétation des écarts que vous avez observé entre Losquet et Poitiers. Est-ce dû à des perturbations?

**Translation :**

*Do you have an explanation of the divergence which you have observed between Losquet and Poitiers? Is this due to interference?*

**Author/Presenter's reply :**

La mesure des angles intervenant dans le calcul de l'altitude virtuelle, les écarts observés proviennent essentiellement de la présence simultanée de multi-trajets incidents sur le réseau de réception de l'île Losquet à l'instant de la mesure. Par ailleurs, la cohérence spatiale des perturbations de moyenne échelle étant du même ordre de grandeur que la distance entre la zone de réfraction des signaux transmis et la verticale de Poitiers, ces phénomènes peuvent également être à l'origine de ces écarts. Par contre, la faible dispersion des variations temporelles des altitudes virtuelles relevées à Poitiers (non présentées dans les communications) indique une influence réduite de ce type de perturbation au cours de la campagne de mesures.

**Translation :**

*As angle measurement is part of the calculation of virtual altitude, the divergence observed arises mainly from the simultaneous presence of incident multipaths on the receiver network on the Isle of Losquet at the time of the measurement. Moreover, as the spatial coherence of the medium scale interference is of the same order of magnitude as the distance between the zone of refraction of the signals transmitted and the Poitiers perpendicular, these phenomena may also explain the divergence. However, the small amount of scatter of the temporal variations of the virtual altitudes measured at Poitiers (not presented in the papers) indicated the reduced influence of this kind of interference during the measurement campaign.*

LIST OF PARTICIPANTS

**AARONS** Dr J. AARONS, United States  
Center for Space Physics, Boston University, 725 Commonwealth Avenue, Boston MA 01115

**ALBRECHT** Dr H.J. ALBRECHT, Germany  
FGAN - Neuenahrerstrasse 20 - D-5307 Wachtberg-Werthhoven

**ALTENA** Major General drs D. ALTENA, The Netherlands  
Armaments Director and Procurement Executive - P O Box 20703 - The Hague

**BAARS** Dr E.P. BAARS, Germany  
FGAN-FHP - Neuenahrerstrasse 20 - D-5307 Wachtberg-Werthhoven

**BARRIOS** Dr A.E. Barrios, United States  
NCCOSC RDT&E Div. - NRaD - Code 54 - San Diego - CA 92152-5230

**BEAUFORT** Dr D. BEAUFORT, The Netherlands  
PTT Research - P O Box 421 - NL-2260 AK Leidschendam

**BERTEL** Prof L. BERTEL, France  
Université de Rennes - Laboratoire Radiocommunications - 35042 Rennes Cedex

**BILODEAU** Dr C. BILODEAU, Canada  
Communications Research Center - 3701 Carling Avenue - Ottawa - Ontario K2H 8S2

**BISHOP** Mr G.G. BISHOP, United States  
Phillips Laboratory/GPIA - 29 Randolph Road - Hanscom AFB - MA 01731-3010

**BLANCHETIERE-CIARLETTI** Dr V. BLANCHETIERE-CIARLETTI, France  
CRPE - 10/12 Avenue de l'Europe - 78140 Velizy-Villacoublay

**BOSSY** Prof L. BOSSY, Belgium  
UCCLE - 174 Avenue Winston Churchill - Brussels

**BROWN** Prof G. BROWN, United States  
Dept. of Electrical Engineering - Virginia Polytechnic Institute and State University - Blacksburg - VA 24061-0111

**BUONOMO** Dr S. BUONOMO, The Netherlands  
ESA/ESTEC XEP - Keplerlaan 1 - 2200 AG Noordwijk

**BUSSON** Mr P. BUSSON, France  
CELAR - ITES/GR - 35170 Rennes Cedex

**CANNON** Dr P.S. CANNON - United Kingdom  
Defence Research Agency - Malvern, Worcs. WR14 3 PS

**CARIGLIA** Lt-Col. R. CARIGLIA, Italy  
AGARD - EPP Executive - 7 rue Ancelle - 92200 Neuilly sur Seine - France

**CASSARA'** Lt-Col. A. CASSARA', Italy  
Aeronautica Militare - 00040 Pratica di Mare

**CHEVRIER** Mr F. CHEVRIER, France  
Laboratoire de Radiocommunications - Université de Rennes 1 - 35042 Rennes Cedex

**CHRISTOPHE** Mr F CHRISTOPHE, France  
ONERA-CERT - 2 Avenue Edouard Belin - 31055 Toulouse

**COSTA** Dr J.J. COSTA, Portugal  
INESC - Largo Mompilher 22 - Apartado 4433 - 4007 Porto

LP-2

<b>CRAIG</b>	Dr K. H. CRAIG, United Kingdom Rutherford Appleton Laboratory - Chilton - Oxon. OX11 0QX
<b>DARNELL</b>	Prof M. DARNELL, United Kingdom Department of Electrical Engineering - University of Hull - Hull HU6 7RX
<b>DASSIOS</b>	Prof G. DASSIOS, Greece University of Patras - GR 265 00 Patras
<b>DAVE</b>	Dr N. DAVE, United States NCCOSC RDTE Div 827 - 53560 Hull Street - San Diego - CA 92152-5001
<b>DAVIES</b>	Dr N.C. DAVIES, United Kingdom Radio Propagation Laboratory - Defence Research Agency - Farnborough? - Hants GU14 6TD
<b>DE LEENEER</b>	Eng. I. de LEENEER, Belgium Royal Military Academy - Renaissance Avenue 30 - 1040 Brussels
<b>DEGAUQUE</b>	Prof P. DEGAUQUE, France Laboratoire de Radiopropagation - 59655 Villeneuve d'Ascq Cedex
<b>DEMEURE</b>	Mr C. DEMEURE, France Thomson-CSF - Division RGS - 66 rue du Fosse Blanc - 92231 Gennevilliers
<b>DEUBACH</b>	Mr G. DEUBACH, Germany FGAN-IFE - Neunahrer Str. 20 - 53343 Wachtberg-Werthoven
<b>ELLIOTT</b>	Mr M. ELLIOTT, Belgium ARFA - CIS Division - IMS, NATO HQ - B-1110 Evere
<b>EL ZEIN</b>	Dr G. EL ZEIN, France LCST - INSA - 20 Avenue des Buttes de Coesmes - 35043 Rennes Cedex
<b>FLOOD</b>	Dr W.A. FLOOD, United States Chief, Env.Sci.Branch, US Army Research Office PO Box 12211, Research Triangle Park, NC 27709-2211
<b>FOURNIER</b>	Dr M. FOURNIER, France Le Centre Thomson d'Applications Radars - 6 rue Nieuport - 78143 Velizy-Villacoublay
<b>FUCHS</b>	Dr H-H. FUCHS, Germany FGAN - Neuenahrer Str. 20 - 5307 Wachtberg-Werthoven
<b>FUERXER</b>	L'Ing. En chef de l'Arm. FUERXER, France CNET - 38-40 rue du General Leclerc - 92131 Issy les Moulineaux
<b>GHICOPOULOS</b>	Dr B. GHICOPOULOS, Greece Hellenic Air Force - KETA - Post Office Terpsitheas - 16501 Glyfada - Athens
<b>GOUTELARD</b>	Prof C. GOUTELARD, France Université Paris-Sud - 91405 Orsay Cedex
<b>HITNEY</b>	Dr H.V. HITNEY, United States NCCOSC RDT&E Div. - NRAd, Code 54 - San Diego, CA 92152-5230
<b>HÖHN</b>	Dr D.H. HÖHN, Germany FGAN - Forschungsinstitut für Optik (FfO) - Schloss Kressbach - 7400 Tübingen
<b>HONARY</b>	Dr B. HONARY, United Kingdom Department of Engineering - Lancaster University - Lancaster LA1 4YR
<b>JORGE AFONSO</b>	Major Eng. A. JORGE AFONSO, Portugal CLAFa, Direcção de Electrotecnica - Base de Alfragide - 2700 Amadora

**KARAVASSILIS** Dr N. KARAVASSILIS, The Netherlands  
SHAPE Technical Centre - Communications Division - P O Box 174 - The Hague

**KHO** Mr K.S. KHO, Belgium  
ARFA Staff - NATO HQ - IMS ICIS - 1110 Brussels

**KOSSEY** Dr P.A. KOSSEY, United States  
Ionospheric Effects Division - Phillips Laboratory - PL/GPI - Hanscom AFB, MA 01731-5000

**LAMMERS** Dr U. LAMMERS, United States  
Rome Laboratory (RL/ERCT) - Hanscom AFB - MA 01731-5000

**LANUSSE** Dr A.F. LANUSSE, France  
DRET/SDR - Groupe 2 - 26 Boulevard Victor - 00460 Paris Armees

**LE JANNIC** Mr J-C. LE JANNIC, France  
CELAR - ITES/GR - 35170 Bruz

**LE ROUX** Dr Y-M. LE ROUX, France  
CNET - Laboratoire PTI - BP 40 - 22300 Lannion Cedex

**LE SAOUT** Dr Y. LE SAOUT, France  
CNET - Laboratoire PTI - BP 40 - 22300 Lannion Cedex

**LEVY** Dr M.F. LEVY, United Kingdom  
Rutherford Appleton Laboratory - Chilton - Didcot - Oxon OX11 0QX

**LIENARD** Dr M. LIENARD, France  
Université de Lille - Laboratoire de Radiopropagation - 59655 Villeneuve d'Ascq Cedex

**LIGTHART** Prof L.P. LIGTHART, The Netherlands  
Delft University - Electrical Engineering Department - Mekelweg 4 - 2628 CD Delft

**MARC** Mr P. MARC, France  
S.E.F.T. - Fort d'Issy - 92131 Issy Les Moulineaux

**MARKOW** Major M.S. MARKOW, United Kingdom  
Communications Branch - EOARD - 223/231 Old Marylebone Street - London NW1 5TH

**MCLAUGHLIN** Dr D.J. MCLAUGHLIN, United States  
Dept. of Electrical & Computer Engineering - Dana Research Center - Northeastern University - Boston - Mass 02155

**MELANCON** Dr P. MELANCON, Canada  
Communications Research Center - 3701 Carling Avenue - Ottawa - Ontario K2H 8S2

**MOORE** Mr M.R. MOORE, United Kingdom  
AWWAG - HM Naval Base - Portsmouth PO1 3LE

**PALMER** Dr F. PALMER, Canada  
Defence Research Establishment - Ottawa - Ontario K1A 0Z4

**PATRICIO** Eng. J.F. PATRICIO, Portugal  
Rua Alferes Barrilaro Ruas - No. 1, 8 Direito - 1800 Lisbon

**PROHOROFF** Dr Ir S. PROHOROFF, Belgium  
ULB - Ecole Polytechnique - Av. F.D. Roosevelt 50 - B-1050 Brussels

**RAVARD** Mr O. RAVARD, France  
Laboratoire de Radiocommunications - 35042 Rennes Cedex

**RICHTER** Dr J.H. RICHTER, United States  
NCCOSC - RDT&E Division, Code 54 - San Diego - CA 92151-5000

<b>RILEY</b>	Mr N. RILEY, United Kingdom Dept. of Electrical Engineering - University of Hull - Hull HU6 7RX
<b>RILEY</b>	Mr. S. RILEY, United Kingdom Dept. of Electrical Engineering - University of Leeds - Leeds LS2 9JT
<b>ROGGE</b>	Mr J. ROGGE, The Netherlands Koninklijk Militaire Academie - Postbus 90.154 - 4800 RG Breda
<b>ROTHER</b>	Dr Ing. D. ROTHER, Germany Alcatel SEL, AG - 7000 Stuttgart 40
<b>SALES</b>	Prof G. SALES, United States University of Massachusetts Lowell - 450 Aiken Street - Lowell - Mass. 01701
<b>SCHWEICHER</b>	Prof Dr E. SCHWEICHER, Belgium Ecole Royale Militaire - Chaire OM - 30 Avenue de la Renaissance - B-1040 Bruxelles
<b>SHORT</b>	Dr R.D. SHORT, United States ARCO Power Technologies, Inc. - Suite 850 - 1250 Twenty-Fourth Street, N.W. - Washington DC 20037
<b>SOMBROEK</b>	Captain (Ret) Ir L SOMBROEK Netherlands Delegation to AGARD - National Aerospace Lab. - P O Box 90502 - 1006 BM Amsterdam
<b>SPOELSTRA</b>	Dr T.A. SPOELSTRA, The Netherlands NFRA Radio Observatory - P O Box 2 - 7990 AA Dwingeloo
<b>STRANGWAYS</b>	Dr H.J. STRANGWAYS, United Kingdom Dept. Electronic & Electrical Engineering - University of Leeds - Leeds - W.Yorks LS2 9JT
<b>TAAGHOLT</b>	Mr J. TAAGHOLT, Denmark Danish Polar Center - Hausergade 3 - DK-1128 Copenhagen K
<b>TAMVACLIS</b>	Dr C. TAMVACLIS, The Netherlands SHAPE Technical Centre - P O Box 174 - The Hague
<b>TOKER</b>	Prof Dr C. TOKER, Turkey Middle East Technical University - Ankara
<b>TORUN</b>	Capt E. TORUN, Turkey Research & Development Department - Ministry of Defence - Ankara
<b>VAN DE CAPELLE</b>	Prof A. van de CAPELLE, Belgium Université Catholique de Louvain, Heverlee, B-3001
<b>VAN DER VORST</b>	Prof A. van der VORST, Belgium Université Catholique de Louvain, Heverlee, B-3001
<b>VAN DOOREN</b>	Mr G. van DOOREN, The Netherlands Technical University Eindhoven - P O Box 513 - 5600 MB Eindhoven
<b>VAN GAALLEN</b>	Mr W.J. van GAALLEN, The Netherlands Toezichtorgaan Stralingshygiëne - Defensie - P O Box 382 - 3720 AJ Bilthoven
<b>VANHOENACKER</b>	Dr D. VANHOENACKER, Belgium U.C.L. - Microwaves Laboratory - 3 Place du Levant - B-1348 Louvain-la-Neuve
<b>VISSINGA</b>	Ir H. VISSINGA, The Netherlands van Kempenstraat 30 - 2252 VH Voorschoten



**VOGEL** Dr M H VOGEL, The Netherlands  
TNO Physics and Electronics Lab. - P O Box 96864 - 2509 JG The Hague

**VONGAS** Mr G VONGAS, United Kingdom  
Defence Research Agency - Portsmouth West - Cosham - Hants PO64AA

**WALKER** Mr P.F. WALKER, United Kingdom  
Electronic Engineering Dept. - University of Hull - North Humberside HU6 7RX

**YAVUZ** Dr D. YAVUZ, The Netherlands  
SHAPE Technical Centre - The Hague - The Netherlands

**ZATMAN** Dr M.A. ZATMAN, United Kingdom  
Dept. Electronic & Electrical Eng. - The University of Leeds - Leeds - W.Yorks LS2 9JT

# REPORT DOCUMENTATION PAGE

<b>1. Recipient's Reference</b>	<b>2. Originator's Reference</b>	<b>3. Further Reference</b>	<b>4. Security Classification of Document</b>
	AGARD-CP-543	ISBN 92-835-0750-9	UNCLASSIFIED/ UNLIMITED
<b>5. Originator</b>	Advisory Group for Aerospace Research and Development North Atlantic Treaty Organization 7 rue Ancelle, 92200 Neuilly sur Seine, France		
<b>6. Title</b>	MULTIPLE MECHANISM PROPAGATION PATHS (MMPPs): THEIR CHARACTERISATION AND INFLUENCE ON SYSTEM DESIGN		
<b>7. Presented at</b>	the Electromagnetic Wave Propagation Panel Symposium, held in Rotterdam, The Netherlands, 4th--7th October 1993.		
<b>8. Author(s)/Editor(s)</b>	Various		<b>9. Date</b> July 1994
<b>10. Author(s)/Editor's Address</b>	Various		<b>11. Pages</b> 428
<b>12. Distribution Statement</b>	There are no restrictions on the distribution of this document. Information about the availability of this and other AGARD unclassified publications is given on the back cover.		
<b>13. Keywords/Descriptors</b>	<div style="display: flex; justify-content: space-between;"> <div> Multipath transmission Radio transmission Design </div> <div> Electromagnetic noise Atmospheric propagation </div> </div>		
<b>14. Abstract</b>	<p>This publication reports the papers presented to a specialists' meeting held by the Electromagnetic Wave Propagation Panel at its Fall 1993 meeting.</p> <p>The topics covered on the occasion of that symposium on the subject of "Multiple Mechanism Propagation Paths (MMPPs): Their Characterisation and Influence on System Design" included:</p> <ul style="list-style-type: none"> <li>• Propagation and Noise Aspects</li> <li>• Examples of MMPP Systems</li> <li>• System Design to Exploit or Reduce the Effects of MMPPs</li> <li>• Future Work.</li> </ul>		

<p>AGARD Conference Proceedings 543 Advisory Group for Aerospace Research and Development, NATO MULTIPLE MECHANISM PROPAGATION PATHS (MMPPs): THEIR CHARACTERISATION AND INFLUENCE ON SYSTEM DESIGN Published July 1994 428 pages</p> <p>This publication reports the papers presented to a specialists' meeting held by the Electromagnetic Wave Propagation Panel at its Fall 1993 meeting.</p> <p>The topics covered on the occasion of that symposium on the subject of "Multiple Mechanism Propagation Paths (MMPPs): Their Characterisation and Influence on System Design" included:</p> <p>P.T.O.</p>	<p>AGARD-CP-543</p> <p>Multipath transmission Radio transmission Design Electromagnetic noise Atmospheric propagation</p>	<p>AGARD Conference Proceedings 543 Advisory Group for Aerospace Research and Development, NATO MULTIPLE MECHANISM PROPAGATION PATHS (MMPPs): THEIR CHARACTERISATION AND INFLUENCE ON SYSTEM DESIGN Published July 1994 428 pages</p> <p>This publication reports the papers presented to a specialists' meeting held by the Electromagnetic Wave Propagation Panel at its Fall 1993 meeting.</p> <p>The topics covered on the occasion of that symposium on the subject of "Multiple Mechanism Propagation Paths (MMPPs): Their Characterisation and Influence on System Design" included:</p> <p>P.T.O.</p>	<p>AGARD-CP-543</p> <p>Multipath transmission Radio transmission Design Electromagnetic noise Atmospheric propagation</p>
<p>AGARD Conference Proceedings 543 Advisory Group for Aerospace Research and Development, NATO MULTIPLE MECHANISM PROPAGATION PATHS (MMPPs): THEIR CHARACTERISATION AND INFLUENCE ON SYSTEM DESIGN Published July 1994 428 pages</p> <p>This publication reports the papers presented to a specialists' meeting held by the Electromagnetic Wave Propagation Panel at its Fall 1993 meeting.</p> <p>The topics covered on the occasion of that symposium on the subject of "Multiple Mechanism Propagation Paths (MMPPs): Their Characterisation and Influence on System Design" included:</p> <p>P.T.O.</p>	<p>AGARD-CP-543</p> <p>Multipath transmission Radio transmission Design Electromagnetic noise Atmospheric propagation</p>	<p>AGARD Conference Proceedings 543 Advisory Group for Aerospace Research and Development, NATO MULTIPLE MECHANISM PROPAGATION PATHS (MMPPs): THEIR CHARACTERISATION AND INFLUENCE ON SYSTEM DESIGN Published July 1994 428 pages</p> <p>This publication reports the papers presented to a specialists' meeting held by the Electromagnetic Wave Propagation Panel at its Fall 1993 meeting.</p> <p>The topics covered on the occasion of that symposium on the subject of "Multiple Mechanism Propagation Paths (MMPPs): Their Characterisation and Influence on System Design" included:</p> <p>P.T.O.</p>	<p>AGARD-CP-543</p> <p>Multipath transmission Radio transmission Design Electromagnetic noise Atmospheric propagation</p>

<ul style="list-style-type: none"> <li>• Propagation and Noise Aspects</li> <li>• Examples of MMPP Systems</li> <li>• System Design to Exploit or Reduce the Effects of MMPPs</li> <li>• Future Work.</li> </ul> <p>ISBN 92-835-0750-9</p>	<ul style="list-style-type: none"> <li>• Propagation and Noise Aspects</li> <li>• Examples of MMPP Systems</li> <li>• System Design to Exploit or Reduce the Effects of MMPPs</li> <li>• Future Work.</li> </ul> <p>ISBN 92-835-0750-9</p>
<ul style="list-style-type: none"> <li>• Propagation and Noise Aspects</li> <li>• Examples of MMPP Systems</li> <li>• System Design to Exploit or Reduce the Effects of MMPPs</li> <li>• Future Work.</li> </ul> <p>ISBN 92-835-0750-9</p>	<ul style="list-style-type: none"> <li>• Propagation and Noise Aspects</li> <li>• Examples of MMPP Systems</li> <li>• System Design to Exploit or Reduce the Effects of MMPPs</li> <li>• Future Work.</li> </ul> <p>ISBN 92-835-0750-9</p>

AGARD

NATO OTAN

7 RUE ANCELLE · 92200 NEUILLY-SUR-SEINE

FRANCE

Télécopie (1)47.38.57.99 · Télex 610 176

DIFFUSION DES PUBLICATIONS

AGARD NON CLASSIFIEES

Aucun stock de publications n'a existé à AGARD. A partir de 1993, AGARD détiendra un stock limité des publications associées aux cycles de conférences et cours spéciaux ainsi que les AGARDographies et les rapports des groupes de travail, organisés et publiés à partir de 1993 inclus. Les demandes de renseignements doivent être adressées à AGARD par lettre ou par fax à l'adresse indiquée ci-dessus. *Veuillez ne pas téléphoner.* La diffusion initiale de toutes les publications de l'AGARD est effectuée auprès des pays membres de l'OTAN par l'intermédiaire des centres de distribution nationaux indiqués ci-dessous. Des exemplaires supplémentaires peuvent parfois être obtenus auprès de ces centres (à l'exception des Etats-Unis). Si vous souhaitez recevoir toutes les publications de l'AGARD, ou simplement celles qui concernent certains Panels, vous pouvez demander à être inclu sur la liste d'envoi de l'un de ces centres. Les publications de l'AGARD sont en vente auprès des agences indiquées ci-dessous, sous forme de photocopie ou de microfiche.

#### CENTRES DE DIFFUSION NATIONAUX

##### ALLEMAGNE

Fachinformationszentrum,  
Karlsruhe  
D-7514 Eggenstein-Leopoldshafen 2

##### BELGIQUE

Coordonnateur AGARD-VSL  
Etat-Major de la Force Aérienne  
Quartier Reine Elisabeth  
Rue d'Evere, 1140 Bruxelles

##### CANADA

Directeur du Service des Renseignements Scientifiques  
Ministère de la Défense Nationale  
Ottawa, Ontario K1A 0K2

##### DANEMARK

Danish Defence Research Establishment  
Ryvangs Allé 1  
P.O. Box 2715  
DK-2100 Copenhagen Ø

##### ESPAGNE

INTA (AGARD Publications)  
Pintor Rosales 34  
28008 Madrid

##### ETATS-UNIS

NASA Headquarters  
Code JOB-1  
Washington, D.C. 20546

##### FRANCE

O.N.E.R.A. (Direction)  
29, Avenue de la Division Leclerc  
92322 Châtillon Cedex

##### GRECE

Hellenic Air Force  
Air War College  
Scientific and Technical Library  
Dekelia Air Force Base  
Dekelia, Athens TGA 1010

##### ISLANDE

Director of Aviation  
c/o Flugrad  
Reykjavik

##### ITALIE

Aeronautica Militare  
Ufficio del Delegato Nazionale all'AGARD  
Aeroporto Pratica di Mare  
00040 Pomezia (Roma)

##### LUXEMBOURG

Voir Belgique

##### NORVEGE

Norwegian Defence Research Establishment  
Attn: Biblioteket  
P.O. Box 25  
N-2007 Kjeller

##### PAYS-BAS

Netherlands Delegation to AGARD  
National Aerospace Laboratory NLR  
P.O. Box 90502  
1006 BM Amsterdam

##### PORTUGAL

Força Aérea Portuguesa  
Centro de Documentação e Informação  
Alfragide  
2700 Amadora

##### ROYAUME UNI

Defence Research Information Centre  
Kentigern House  
65 Brown Street  
Glasgow G2 8EX

##### TURQUIE

Milli Savunma Başkanlığı (MSB)  
ARGE Daire Başkanlığı (ARGE)  
Ankara

**Le centre de distribution national des Etats-Unis ne détient PAS de stocks des publications de l'AGARD.**

D'éventuelles demandes de photocopies doivent être formulées directement auprès du NASA Center for Aerospace Information (CASI) à l'adresse ci-dessous. Toute notification de changement d'adresse doit être fait également auprès de CASI.

#### AGENCES DE VENTE

##### NASA Center for

AeroSpace Information (CASI)  
800 Elkridge Landing Road  
Linthicum Heights, MD 21090-2934  
United States

##### ESA/Information Retrieval Service

European Space Agency  
10, rue Mario Nikis  
75015 Paris  
France

##### The British Library

Document Supply Division  
Boston Spa, Wetherby  
West Yorkshire LS23 7BQ  
Royaume Uni

Les demandes de microfiches ou de photocopies de documents AGARD (y compris les demandes faites auprès du CASI) doivent comporter la dénomination AGARD, ainsi que le numéro de série d'AGARD (par exemple AGARD-AG-315). Des informations analogues, telles que le titre et la date de publication sont souhaitables. Veuillez noter qu'il y a lieu de spécifier AGARD-R-nnn et AGARD-AR-nnn lors de la commande des rapports AGARD et des rapports consultatifs AGARD respectivement. Des références bibliographiques complètes ainsi que des résumés des publications AGARD figurent dans les journaux suivants:

Scientific and Technical Aerospace Reports (STAR)  
publié par la NASA Scientific and Technical  
Information Program  
NASA Headquarters (JTT)  
Washington D.C. 20546  
Etats-Unis

Government Reports Announcements and Index (GRA&I)  
publié par le National Technical Information Service  
Springfield  
Virginia 22161  
Etats-Unis

(accessible également en mode interactif dans la base de données bibliographiques en ligne du NTIS, et sur CD-ROM)



Imprimé par Specialised Printing Services Limited  
40 Chigwell Lane, Loughton, Essex IG10 3TZ

AGARD

NATO  OTAN

7 RUE ANCELLE · 92200 NEUILLY-SUR-SEINE

FRANCE

Telefax (1)47.38.57.99 · Telex 610 176

**DISTRIBUTION OF UNCLASSIFIED  
AGARD PUBLICATIONS**

AGARD holds limited quantities of the publications that accompanied Lecture Series and Special Courses held in 1993 or later, and of AGARDographs and Working Group reports published from 1993 onward. For details, write or send a telefax to the address given above. *Please do not telephone.*

AGARD does not hold stocks of publications that accompanied earlier Lecture Series or Courses or of any other publications. Initial distribution of all AGARD publications is made to NATO nations through the National Distribution Centres listed below. Further copies are sometimes available from these centres (except in the United States). If you have a need to receive all AGARD publications, or just those relating to one or more specific AGARD Panels, they may be willing to include you (or your organisation) on their distribution list. AGARD publications may be purchased from the Sales Agencies listed below, in photocopy or microfiche form.

NATIONAL DISTRIBUTION CENTRES

**BELGIUM**

Coordonnateur AGARD — VSL  
Etat-Major de la Force Aérienne  
Quartier Reine Elisabeth  
Rue d'Evere, 1140 Bruxelles

**CANADA**

Director Scientific Information Services  
Dept of National Defence  
Ottawa, Ontario K1A 0K2

**DENMARK**

Danish Defence Research Establishment  
Ryvangs Allé 1  
P.O. Box 2715  
DK-2100 Copenhagen Ø

**FRANCE**

O.N.E.R.A. (Direction)  
29 Avenue de la Division Leclerc  
92322 Châtillon Cedex

**GERMANY**

Fachinformationszentrum  
Karlsruhe  
D-7514 Eggenstein-Leopoldshafen 2

**GREECE**

Hellenic Air Force  
Air War College  
Scientific and Technical Library  
Dekelia Air Force Base  
Dekelia, Athens TGA 1010

**ICELAND**

Director of Aviation  
c/o Flugrad  
Reykjavik

**ITALY**

Aeronautica Militare  
Ufficio del Delegato Nazionale all'AGARD  
Aeroporto Pratica di Mare  
00040 Pomezia (Roma)

**LUXEMBOURG**

See Belgium

**NETHERLANDS**

Netherlands Delegation to AGARD  
National Aerospace Laboratory, NLR  
P.O. Box 90502  
1006 BM Amsterdam

**NORWAY**

Norwegian Defence Research Establishment  
Attn: Biblioteket  
P.O. Box 25  
N-2007 Kjeller

**PORTUGAL**

Força Aérea Portuguesa  
Centro de Documentação e Informação  
Alfragide  
2700 Amadora

**SPAIN**

INTA (AGARD Publications)  
Pintor Rosales 34  
28008 Madrid

**TURKEY**

Milli Savunma Başkanlığı (MSB)  
ARGE Daire Başkanlığı (ARGE)  
Ankara

**UNITED KINGDOM**

Defence Research Information Centre  
Kentigern House  
65 Brown Street  
Glasgow G2 8EX

**UNITED STATES**

NASA Headquarters  
Code JOB-1  
Washington, D.C. 20546

**The United States National Distribution Centre does NOT hold stocks of AGARD publications.**  
Applications for copies should be made direct to the NASA Center for AeroSpace Information (CASI) at the address below.  
Change of address requests should also go to CASI.

SALES AGENCIES

NASA Center for  
AeroSpace Information (CASI)  
800 Elkridge Landing Road  
Linthicum Heights, MD 21090-2934  
United States

ESA/Information Retrieval Service  
European Space Agency  
10, rue Mario Nikis  
75015 Paris  
France

The British Library  
Document Supply Centre  
Boston Spa, Wetherby  
West Yorkshire LS23 7BQ  
United Kingdom

Requests for microfiches or photocopies of AGARD documents (including requests to CASI) should include the word 'AGARD' and the AGARD serial number (for example AGARD-AG-315). Collateral information such as title and publication date is desirable. Note that AGARD Reports and Advisory Reports should be specified as AGARD-R-nnn and AGARD-AR-nnn, respectively. Full bibliographical references and abstracts of AGARD publications are given in the following journals:

Scientific and Technical Aerospace Reports (STAR)  
published by NASA Scientific and Technical  
Information Program  
NASA Headquarters (JTT)  
Washington D.C. 20546  
United States

Government Reports Announcements and Index (GRA&I)  
published by the National Technical Information Service  
Springfield  
Virginia 22161  
United States  
(also available online in the NTIS Bibliographic  
Database or on CD-ROM)



Printed by Specialised Printing Services Limited  
40 Chigwell Lane, Loughton, Essex IG10 3TZ

ISBN 92-835-0750-9